

Renewable Energy Sustainable Energy



BY
Xiaohong Gu, Xian Liangjun,
and Shikun Guo

Nanotechnology for Sustainable Energy

ACS SYMPOSIUM SERIES 1140

Nanotechnology for Sustainable Energy

Yun Hang Hu, Editor

*Michigan Technology University
Houghton, Michigan, United States*

Uwe Burghaus, Editor

*North Dakota State University
Fargo, North Dakota, United States*

Shizhang Qiao, Editor

*The University of Adelaide
Adelaide, South Australia, Australia*

**Sponsored by the
ACS Division of Energy and Fuels**



American Chemical Society, Washington, DC

Distributed in print by Oxford University Press



Library of Congress Cataloging-in-Publication Data

Nanotechnology for sustainable energy / Yun Hang Hu, Uwe Burghaus, Shizhang Qiao, editors ; sponsored by the ACS Division of Energy and Fuels.

pages cm. -- (ACS symposium series ; 1140)

Includes bibliographical references and index.

ISBN 978-0-8412-2813-9 (alkaline paper) 1. Electric batteries--Congresses. 2.

Nanotechnology--Congresses. 3. Energy storage--Congresses. 4. Renewable energy sources--Congresses. I. Hu, Yun Hang. II. Burghaus, U. (Uwe) III. Qiao, Shizhang. IV. American Chemical Society. Division of Energy and Fuels.

TK2941.N36 2013

621.042--dc23

2013027669

The paper used in this publication meets the minimum requirements of American National Standard for Information Sciences—Permanence of Paper for Printed Library Materials, ANSI Z39.48n1984.

Copyright © 2013 American Chemical Society

Distributed in print by Oxford University Press

All Rights Reserved. Reprographic copying beyond that permitted by Sections 107 or 108 of the U.S. Copyright Act is allowed for internal use only, provided that a per-chapter fee of \$40.25 plus \$0.75 per page is paid to the Copyright Clearance Center, Inc., 222 Rosewood Drive, Danvers, MA 01923, USA. Republication or reproduction for sale of pages in this book is permitted only under license from ACS. Direct these and other permission requests to ACS Copyright Office, Publications Division, 1155 16th Street, N.W., Washington, DC 20036.

The citation of trade names and/or names of manufacturers in this publication is not to be construed as an endorsement or as approval by ACS of the commercial products or services referenced herein; nor should the mere reference herein to any drawing, specification, chemical process, or other data be regarded as a license or as a conveyance of any right or permission to the holder, reader, or any other person or corporation, to manufacture, reproduce, use, or sell any patented invention or copyrighted work that may in any way be related thereto. Registered names, trademarks, etc., used in this publication, even without specific indication thereof, are not to be considered unprotected by law.

PRINTED IN THE UNITED STATES OF AMERICA

Foreword

The ACS Symposium Series was first published in 1974 to provide a mechanism for publishing symposia quickly in book form. The purpose of the series is to publish timely, comprehensive books developed from the ACS sponsored symposia based on current scientific research. Occasionally, books are developed from symposia sponsored by other organizations when the topic is of keen interest to the chemistry audience.

Before agreeing to publish a book, the proposed table of contents is reviewed for appropriate and comprehensive coverage and for interest to the audience. Some papers may be excluded to better focus the book; others may be added to provide comprehensiveness. When appropriate, overview or introductory chapters are added. Drafts of chapters are peer-reviewed prior to final acceptance or rejection, and manuscripts are prepared in camera-ready format.

As a rule, only original research papers and original review papers are included in the volumes. Verbatim reproductions of previous published papers are not accepted.

ACS Books Department

Preface

Increased energy prices and the growing attention on global warming are motivating the creation of economically viable alternatives to fossil fuels. Nanotechnologies have been recognized as one effective approach to solve energy problems. Therefore, to promote the improvement of research and to foster professional collaboration among researchers in energy-related nanotechnologies, we organized a symposium on “Nanotechnology for a Sustainable Energy Economy” as a part of the 243rd American Chemical Society National Meeting, which took place March 25–29, 2012 in San Diego, California, USA. Forty-four contributors from 12 countries presented their research works from industrial, university, and national laboratories in nanotechnology areas related to energy and fuel technologies. This ACS Symposium Series book was developed from this symposium.

This book presents a very useful and readable collection of reviews and research papers in nanotechnologies for energy conversion, storage, and utilization, offering new results which are sure to be of interest to researchers, students, and engineers in the field of nanotechnologies and energy. The book focuses on the following topics: Li batteries (Chapters 1–4), supercapacitors (Chapter 5), dye-sensitized solar cells (Chapter 6), photocatalysis (Chapters 7–9), fuel cells (Chapter 10), electrocatalysis (Chapter 11), and electron beam lithography (Chapter 12). All 12 chapters were recruited from oral presentations at the symposium. All contributed manuscripts were sent to referees, and only those that passed through the peer review process became the chapters in this book.

We thank all the authors of the chapters for their contributions to this ACS book as well as to the ACS symposium. We also would like to express our appreciation to the peer reviewers for their efforts. We gratefully acknowledge the ACS Division of Energy and Fuels and the ACS Books Department for the opportunities to organize the symposium and to publish this book, respectively. Finally, we wish to thank Arlene Furman, Tim Marney, and Bob Hauserman of the ACS Books Department for their great effort and support through the entire peer-review and production process of this book.

Yun Hang Hu

Department of Materials Science and Engineering
Michigan Technological University
Houghton, Michigan 49931-1295, USA

Uwe Burghaus

Department of Chemistry and Biochemistry
North Dakota State University
Fargo, North Dakota 58108-6050, USA

Shizhang Qiao

School of Chemical Engineering
The University of Adelaide
Adelaide, SA 5005, Australia

Chapter 1

Nanoscale Tin Heterostructures for Improved Energy Storage in Lithium Batteries

Gregorio Ortiz, Ricardo Alcántara, Pedro Lavela, and José L. Tirado*

Laboratorio de Química Inorgánica, Universidad de Córdoba, Edificio Marie Curie, Campus de Rabanales, 14071 Córdoba, Spain
E-mail: iq1ticoj@uco.es. Tel.: +34957218637

Heterostructure composites including nanoscale tin species together with polymers, carbon nanomaterials (carbon nanotubes, fullerenes and graphene) or self-assembled titania nanotubes can be envisaged as efficient materials to avoid the undesirable lack of cycling stability commonly found in electroactive tin for Li-ion cells. Tin heterostructures cushion the stresses in the lithium intermetallic compounds and prevent aggregation of the nanoparticles, maintaining the mechanical integrity of the electrode during electrochemical cycling while improving the electrical contact between the particles, and allowing a better use of their capacity. Particularly, the use of TiO_2 nanotube layers was proven particularly useful to achieve large areal capacities and opens a new strategy for the electrochemical fabrication of advanced heterostructures for the electrodes of future lithium batteries.

1. Introduction

Around ten years ago it was realized that nanomaterials would contribute significantly to the replacement of graphitic materials from the anode of future Li-ion batteries. As compared with synthetic graphite, the milestones of the new materials developed so far include higher available energy density, rate capability, coulombic efficiency and cycle life. The combined achievement of all of these milestones is a difficult task. A fruitful approach is the use of composites in which the synergistic action of two or more components at the nano scale may mitigate the particular drawbacks of each one individually. Not all the components need

to be electroactive, but may include electronic or ionic conductors, or may form a matrix to maintain electrical connectivity and mechanical stability.

On the other hand, the use of alloys or intermetallic compounds allows for greater storage density of lithium and therefore higher energy storage than graphite is achieved (1). The difficulty in using the electrodes based on elements which form reversibly alloys with lithium, such as tin, silicon or antimony, lies in the abrupt volume change experienced during the electrochemical reaction with lithium. These volume changes in the crystals generate stresses that lead to a significant fragmentation after several charge-discharge cycles, finally leading to steep losses of battery capacity. The volume changes can be neutralized using electrodes “nano-structured” containing metallic elements that do not form alloys with lithium (inactive), such as cobalt and iron. These transition elements can cushion the stresses in the intermetallic compounds and prevent aggregation of the nanoparticles, maintaining the mechanical integrity of the electrode during electrochemical cycling. Furthermore, the presence of carbon improves the electrical contact between the particles, allowing a better use of its capacity.

Among the different alloying elements, tin has leaded the developments in the field of lithium-ion batteries for many years. Thus, the use of tin-based electrodes has given interesting results and a commercial product. Even though silicon is a more promising option in terms of theoretical gravimetric capacity (3576 mAhg⁻¹ for $\text{Li}_{15}\text{Si}_4$ vs. 993 mAhg⁻¹ for $\text{Li}_{22}\text{Sn}_5$) and natural abundance, its development is taking place at a significantly lower rate. The experimental capacity of silicon on prolonged cycling is commonly well below the theoretical value, due to the fact of having the highest change in volume during the electrochemical reaction with lithium ($\Delta V/V = 310\%$ for Si and 260 % for Sn). Also the electronic conductivity of pure silicon is low and its volumetric capacity is close to that of tin (8330 mAhcm⁻³ for $\text{Li}_{15}\text{Si}_4$ vs. 7310 mAhcm⁻³ for $\text{Li}_{22}\text{Sn}_5$). Antimony falls significantly below tin and silicon in terms of theoretical capacity (660 mAhg⁻¹ for Li_3Sb).

A first example of the industrial interest of tin for lithium batteries aroused when the photography company FujiPhoto Celtech Co. (Japan) announced in 1997 a glass material for the anode of rechargeable lithium-ion cells (2). The solid was based on tin oxide, with the stoichiometry SnM_xO_y , where M is a member of the group of glass-forming elements such as B(III), P(V) and Al(III). The amorphous solid contains Sn(II) as active center for lithium insertion and network-MO-built by the other elements of glass, which expands the network, allowing rapid diffusion of lithium. Electrodes formed by these materials showed capacities greater than 600 mAhg⁻¹ for the reversible insertion of lithium. These values are considerably larger than the theoretical capacity of graphite (372 mAhg⁻¹). The volumetric capacity - 2200 mAhcm⁻³ - is twice the value in the carbonaceous materials of highest yield (ca. 1200 mAhcm⁻³).

Later the electrochemical behavior of various tin oxides that can act as electrodes for lithium insertion was reviewed (3, 4). These include crystalline SnO , SnO_2 , Li_2SnO_3 , SnSiO_3 and Sn_2BPO_6 glasses. The resulting cells showed a discharge capacity of about 1000 mAhg⁻¹, whereas the reversible capacity ranged from 200 to 700 mAhg⁻¹. These results showed a first process that produces lithium oxide and tin metal irreversibly, followed by formation of alloy Li/Sn for lower voltages, with a limit of composition 4.4 Li/Sn.

More recently, SONY Company commercialized a new type of lithium-ion battery under the trade mark *Nexelion* (5). *Nexelion* batteries used a nano-composite material containing tin, cobalt and carbon, among others, as negative electrode, and represented a considerable change from the lithium-ion batteries more conventional. In this way, graphite and intermetallic tin-lithium have been used in the negative electrode of two successive generations of commercial rechargeable lithium batteries developed by SONY: Li-ion and *Nexelion*.

One of the major concerns in the extended use of Sn-based electrodes relies on the limited tin resources and reserves of the element. According to the USGS, tin reserves were estimated to be 8 million metric tons (6). These numbers were considered to be adequate to meet the world's future tin requirements. Assuming that world primary tin consumption will be about 200,000 metric tons per year, these reserves would last ca. 40 years. Most tin reserves are in Asia (mainly in Yunnan and Guangxi autonomous regions, China and Malaysia) and South America (Brazil and Bolivia). Other countries with tin resources to a certain extent are Russia, Australia and Thailand (6, 7). Leaving aside geopolitical considerations and catastrophic premonitions, a sufficiently long life is expectable for tin, and not only as solder element.

2. Tin-Polymer Composites

Tin nanoparticles can exhibit better ability to accommodate the volume changes during the charge-discharge processes of the lithium ion batteries in comparison with larger particles that can suffer pulverization and battery failure. Unfortunately, the initial tin nanoparticles tend to form larger particles after cycling as a way to reduce their surface energy, and consequently the growth large particles can be broken and pulverized again after further electrochemical cycling. As a way to overcome this drawback, the tin nanoparticles may be encapsulated within a non-metallic matrix to inhibit the tin grain growth. Since the phases with covalent bonds use to be less brittle than the metallic particles carbonaceous materials and organic polymers have been proposed to buffer the volume changes of the tin nanoparticles. On the other hand, the encapsulation of the metallic nanoparticles can protect them from oxidation in the air. The electrode materials containing metallic particles and organic polymers are classified into the organic-inorganic hybrid materials.

Ideally, the polymer matrix protecting the tin nanoparticles should be flexible, ease of manufacturing, being able to give interparticle binding strength to accommodate the volume changes of the active material, conductive, stable and chemically inert (8, 9). On the contrary to the most common binder used in batteries, it is preferred that the polymer matrix does not require other conductive additives.

The electronically conducting polymers (e.g. polyaniline, polythiophene and polypyrrole) can be very useful to form tin-polymer hybrid electrodes that are being recently explored for lithium ion batteries. On the other hand, polymers that usually are not electronic conductors such as polyacrylonitrile can exhibit

certain electronic conductivity when the polymer chain is very short and is grafted to a metallic surface (10). One of the first polymers that was known to form tin-polymer composites was polyaniline (8). More recently, the cathodic deposition of polypyrrole (ppy) in the presence of tin ions leads to the formation of spherical ppy particles coated with tin nanoparticles (11).

The pyrolysis of a polymer can be chosen as a method to prepare pure carbon (12). A first criterion for the optimization of the polymer is its ability to produce carbon. Another requirement is the absence of oxygen in its composition to prevent tin oxidation during the pyrolysis. The possible physicochemical interactions between the polymer molecules and tin particles may also influence on the final product, thus, it would be desired that the polymer could entrap appreciable quantities of the tin precursor. Polyacrylonitrile (PAN) is a versatile polymer with interesting properties such as the ability to adhere onto metallic surfaces, pyrolyzation at low temperatures and easy graphitization (13). The use of pyrolytic PAN to encapsulate spherical nanosized tin particles (Lc=28 nm) was reported by He et al (14). Poly(L-lactic acid) fibers with diameter smaller than 1 μ m were used for embedding tin nanoparticles (ca. 30 nm size) through using electrospinning (15). Tetraphenyltin and polystyrene were used by Patel et al (12).

A plethora of research efforts to prepare tin compound-polymer materials is being carried out in the last years. The tin compounds here discussed mainly involve intermetallics and oxides. PAN can be a suitable electrolyte for solid state batteries. In fact, PAN molecules are plasticized in LiPF₆/ethylene carbonate liquid solutions. Another way to improve the plasticization and gel formation of PAN is by addition of dimehtyl formamide (DMF). The ionic conductivity of PAN (-[CH₂-CH(CN)]_n-) is provided by the interactions between the Li⁺ ions and the -C≡N groups. Polyacrylonitrile can be electrodeposited on amorphous cobalt-tin alloy previously electrodeposited on a metal surface such as titanium (16). For this purpose, the monomer (acrylonitrile) is electropolymerized. The ionic and surface layer resistances increase for the the PAN-coated alloys while the charge transfer resistance becomes much more stable upon cycling, according to AC impedance results (16). These electrode materials containing thin films of tin alloys and polymers may be rather used for lithium ion microbatteries with areal capacities in the order of around 1-10 mAhcm⁻².

Nanocrystalline tin compounds such as CoSn₂ surrounded by a carbonaceous shell provided by PAN pyrolysis can be prepared by reducing the metal ions in the presence of PAN dissolved in DMF (17). This procedure to yield CoSn₂@PAN and then CoSn₂@C is successful because of the easy Co-Sn alloying process. However, the Fe-Sn intermetallics are no so easily formed (18). On the other hand, the shell of PAN molecules that surrounds the intermetallic particles prevent the particles growth during the annealing for PAN pyrolysis. In addition, the irradiation with high-intensity ultrasounds during the synthesis is useful to reduce the particle size and crystallinity of the tin-based phases in the composite material (Fig. 1) (19). The incomplete carbonization of PAN may be harmful for the electrochemical cycling probably due to the loss of electric conductivity. Henceforth, the relative amount of PAN-active material and the pyrolysis conditions must be optimized to achieve excellent electrochemical behavior.

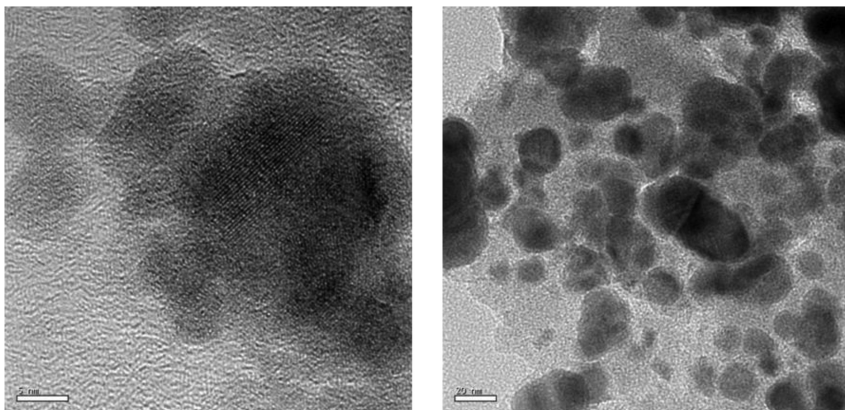


Figure 1. HRTEM images of $\text{CoSn}_2@\text{PAN}$ before (left) and after (right) annealing at 490°C under inert atmosphere.

A goal for the next future is the assembly of an entire battery in a three-dimensional architecture to achieve small footprint area electrode. Recently Gowda et al. reported the fabrication of a conformal layer of ~ 25 nm thick poly(methyl methacrylate) (PMMA) (separator/gel electrolyte) around an individual nanostructured electrode (Ni-Sn intermetallic nanowire) using a hard template assisted drop coating technique (20). The conformal PMMA layer soaked in liquid electrolyte solution formed the gel electrolyte and separator, and the observed areal capacities were typically around 0.8 mAhcm^{-2} .

The formation of tin oxide-polymer materials is also the objective of some studies. SnO_2 has been coated with polyaniline by using microemulsion polymerization method (21). An interesting porous carbon/ SnO_2 nanocomposite monolith was prepared by Wang et al (22). These authors used poly-methyl methacrylate spheres mixture containing a phenol-formaldehyde as carbon precursor and then SnO_2 were loaded via a vapor infiltration technique.

3. Tin-Nanocarbon Structures

Irrespective of the good electronic conductivity of metallic tin, carbon additives are a commonly accepted source of electrode stability. They are particularly necessary because of the low mechanical stability associated with lithium alloying-dealloying with tin. Carbon provides a substrate for the anchoring of particles and/or an electrical network to preserve electrical contacts for most of the electrode volume, thus allowing an improved utilization of the capacity of electroactive elements.

3.1. Tin-Carbon Nanotubes

Two main groups of heterostructures are found in this group: carbon fibers or nanotubes with decorated surface by tin oxide nanoparticles, and tin nanowires

encapsulated in carbon nanotubes (Sn@CNT). Concerning the former group, an early report showed the formation of SnO₂-vapor grown carbon nanofiber composite materials by the hydrothermal treatment of the fibers in the presence of tin oxalate (23). The size of tin dioxide crystallites was controlled by the duration of the hydrothermal treatment. The capacity delivered by tin augmented the limited capacity of the carbon fibers. The fibers themselves could be further activated by opening their inner surfaces by refluxing with acid solution, the reversible capacity thus increasing over 400 mAh⁻¹. According to ⁷Li MAS NMR data, the enhanced capacity could be ascribed to lithium that exhibits purely ionic character. More recently, a nanocomposite electrode synthesized by hydrothermal processes was also reported. The SnO₂ nanoparticles were attached to multi-walled carbon nanotubes (MWCNTs) with surfaces functionalized by an acid treatment that yielded carboxylate anions. The absence of SnO₂ aggregation in the MWCNT/SnO₂ nanocomposites, allowed a better access to the electrochemical lithium insertion and capacities higher than that of graphite were recorded for more than 100 cycles (24). A variant of these methods is the use of electrospinning techniques, the SnO₂/CNFs heterostructures with a good control on the coverage of SnO₂ nanoparticles on the surface of the CNFs could be achieved. The electrochemical response in lithium test cells revealed excellent capacitive performance due to the enhancement of the electric conductivity of SnO₂ by the 1-D properties of the fibers. In addition, an increased electrochemical utilization of SnO₂ and a rapid transport of the electrolyte ions were reported in SnO₂/CNFs heterostructures (25).

From first principles calculations, Zheng et al. showed that the interaction of Sn with the outer surface of a CNT is about two to three times stronger than with the inner surface, which hinders tin encapsulation inside the CNT by conventional methods (26). Nevertheless, different Sn@CNT heterostructures have been reported in which the encapsulation of tin nanowires by carbon nanotubes is carried out by using chemical vapor deposition procedures. Li et al. (27) obtained amorphous carbon nanotubes by coating tin nanowires and ensuring sufficient void space, good electrical contact, and good mechanical stability to accommodate the large volume changes in successive lithium insertion/extraction cycles. The CNT-encapsulated Sn nanostructure reported by Wang et al. (28) showed a particularly high reversible capacity and good cyclability.

3.2. Tin-Graphene

The vast amount of research work currently devoted to graphene has facilitated a rapid development of different Metal Oxide/Graphene Nano Sheets (MO/GNS) heterostructures. SnO₂ nanoparticles can be homogeneously attached to GNS by an *in situ* chemical reduction processes leading to flexible 3D architectures. According to Yao et al. (29), the mixing of graphene nanosheets and SnO₂ nanoparticles at the molecular level allows a reversible specific capacity of 765 mAh⁻¹ in the first cycle and enhanced cyclability. The observed capacity of the SnO₂/GNS heterostructure is only slightly lower than the theoretical capacity of SnO₂ (781 mAh⁻¹) even after 30 cycles, thus being a direct evidence of the synergistic effect of the composite (29). Somewhat lower capacities were

achieved by Paek et al. (30) by reassembling graphene nanosheets dispersed in ethylene glycol, in the presence of SnO_2 nanoparticles. According to these authors, the confinement of the SnO_2 nanoparticles by the surrounding graphene limits the volume expansion upon lithium insertion and the void spaces buffer volume changes and preserve the electrode from being pulverized.

One of the major concerns in the possible use of SnO_2/GNS heterostructures as commercial electrodes is their limited production rates. Recently, a nonaqueous Atomic Layer Deposition (ALD) technique was also used to prepare SnO_2/GNS heterostructures (31). SnCl_4 was used to anchor $-\text{O}-\text{SnCl}_3$ groups to the surface of graphene by a gas-solid reaction, followed by hydrolysis. The versatility of this technique is remarkable due to the possible formation of both amorphous and nanocrystalline SnO_2 depending on the temperature at which the surface reactions takes place. The method is also suitable for the production of large quantities, that could facilitate its potential application in the field of Li-ion batteries (31).

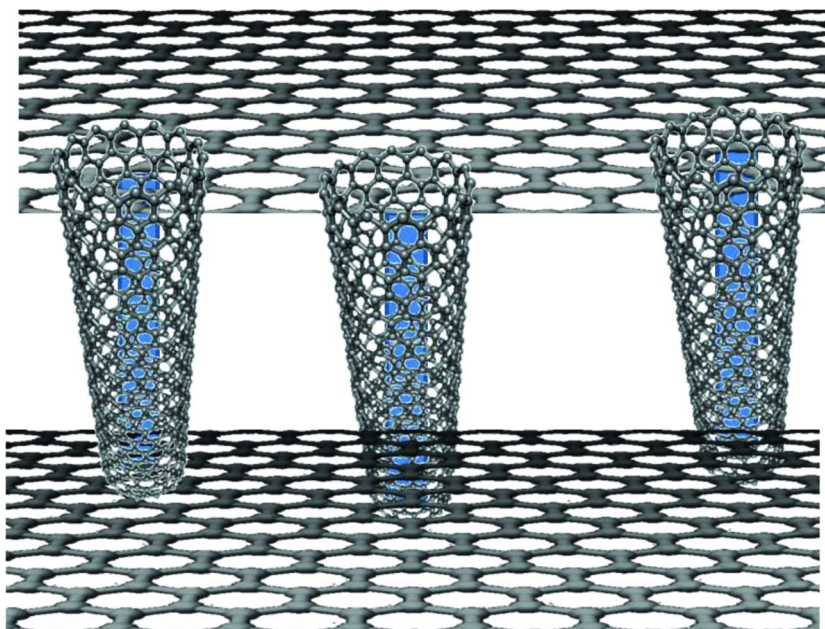


Figure 2. Artist's impression of a hierarchical graphene-Sn@CNT composite. Shaded areas correspond to metallic tin nanowires inserted in CNT.

Finally the combined use of tin, graphene and carbon nanotubes has recently generated exciting results. A hierarchical graphene-Sn@CNT composite (Fig. 2) showed a distinctive synergistic effect when evaluated as an anode material for Li-ion batteries. The electrochemical evaluation revealed extraordinary large reversible capacities (1160–982 mAh $^{-1}$ in 100 cycles) and excellent high-rate performances, which were ascribed to the absence of graphene agglomeration, and the combined electrical conductivity and volume buffering effects of CNT and GNS (32). Later, tin-core/carbon-sheath coaxial nanocables with uniform

diameter and high aspect ratio could be produced in large-scale by a CVD process using Reduced Graphene Oxide-based hybrid material as a substrate. These nanocables were tested in lithium cells that provided high reversible specific capacities and interesting rate capabilities. The advantages of structures with marked 1-D character can also be highlighted for this particular material (33).

4. Electrodeposited Tin Nanoarchitectures

Electrochemical deposition is an extensively developed technique that has been explored for the fabrication of different structures over the years. In the field of nanotechnology, the improved properties of one-dimensional structures such as rods, wires or fibers encouraged the scientific community to make further processing designs (34–36). Recently, we developed a template-free approach as novel electrode architecturation procedure. It consists of vertically grown tin and tin oxide nanowires onto self-organized TiO_2 nanotubes for application in Li-ion batteries (37).

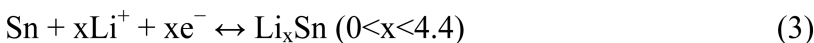
On the other hand, an exciting result has been recently reported by using hollow microspheres with SnO_2 inner shell ($\text{SnO}_2@ \text{TiO}_2$ composites) prepared by a templated self-assembly process from anatase TiO_2 nanosheets, which developed unusually enhanced capacity retention on cycling vs. lithium. The origin of such improvement was explained by the integration of hollow structure with the TiO_2 shell composed of highly functional nanosheets (38). With this result in mind, herein we discuss an electrochemical procedure to prepare $\text{SnO}_x\text{-TiO}_2$ nanocomposites in the form of thin films. This part of the chapter introduces to a new kind of hierarchically nanostructured electrode materials for lithium ion batteries, and we will discuss the pros and cons in the use of nanomaterials and make a comparison with other micron-scale systems.

Self-organized TiO_2 nanotube layers can be obtained by anodization of Ti substrates in a conventional two electrode cell which can be re-used as substrate for tin electrodeposition. In a typical potentiostatic experiment, a constant voltage of e.g. 0 V is applied between the working electrode consisting of titanium foil, and a platinum foil that serves as a counter electrode. The electrolyte can be a mixture of H_3PO_4 , NaOH and HF aqueous solutions (37). In the next step, tin is electrodeposited on TiO_2 nanotubes using a simple three electrode configuration with a commercial saturated calomel electrode (SCE), and a platinum grid acted as counter electrode.

Subsequently, tin and tin oxide nanowires can be growth with a vertical orientation or lying onto the surface of the substrate. Electrodeposition experiments were described by using room temperature galvanostatic conditions at with a current density of - 1 mA cm^{-2} during 3-6 min. The electrolytic bath consisted of tin dichloride and sodium citrate with a molar ratio of ca. 0.3 (39). SEM images show the different deposits that can be obtained. Fig. 3a-c shows tin electrodeposited on titania nanotubes and on a compact layer of titania. These parallel oriented tin and tin oxides nanostructures are influenced by the alignment of the titania nanotubes supporting them because presented empty spaces both outside and inside the nanotubular structure (37). Different morphologies of

tin and tin oxides can be obtained according to the electrolyte composition and concentration, and electrodeposition time (39–41). The most remarkable nanoarchitecturization is that of tin nanowires measuring 2 μm in length and 100–200 nm in diameter. It is worth noting that the nanowire population depends on the concentration of the electrolyte. For samples annealed at 350°C in air, SnO nanowires are also obtained (Fig. 3d). Similar morphologies are observed in others tin deposited species when using a titania compact layer. In this case larger particle sizes (0.5–2 μm) horizontally laid on the flat surface of the compact layer can be obtained (Fig. 3c). It becomes patently the orientational effect of the ntTiO₂ seed layer with different titania length of 500 and 900 nm (Fig. 3a,b,d). The nucleation of Sn on titania nanotubes is instantaneous according to the theory of Scharifker and Hills, consistent with the model of 3D nucleation with diffusion-controlled growth (39, 41, 42). Another nanocomposite tin-titania with a sponge-like morphology and particles forming an interconnected porous network can be obtained (Fig. 3e). The layer is about 1.5–1.6 μm thick and the agglomerate seems to be formed of small SnO nanowires of about 200 nm diameter. Tin-doped titania nanotubes were also fabricated having lengths of ~1.20 μm and diameters of ~90 nm (Fig. 3f) (43). It has been confirmed that as-prepared tin deposits presented a preferred growth orientation by the higher intensity ratio between the (200) and (101) diffraction peaks of β -Sn, while those samples annealed at 350°C presented partial conversion to SnO (39, 40). Moreover, metallic tin is still present after annealing, the oxidation is not complete. The results are consistent with the model of oxide growth limited by oxygen diffusion through the oxide layer (44). It is worth noting that the as-prepared titania nanotubes exhibited X-ray amorphous character, while those thermally annealed revealed a partial crystallization in the anatase structure (37, 45).

As well as the nanoarchitecturization of the materials, the working potential window effects on the cycling of tin-based electrodes, being the subject of numerous studies. For evaluating its impact, one of goals is the minimization of capacity fading in actual lithium test cells. The capacity per unit area of tin-titania composite films was measured as a function of the cycle number up to 50 cycles (39). A first selected galvanostatic discharge/charge curve can provide an insight to understand the undergoing reactions:



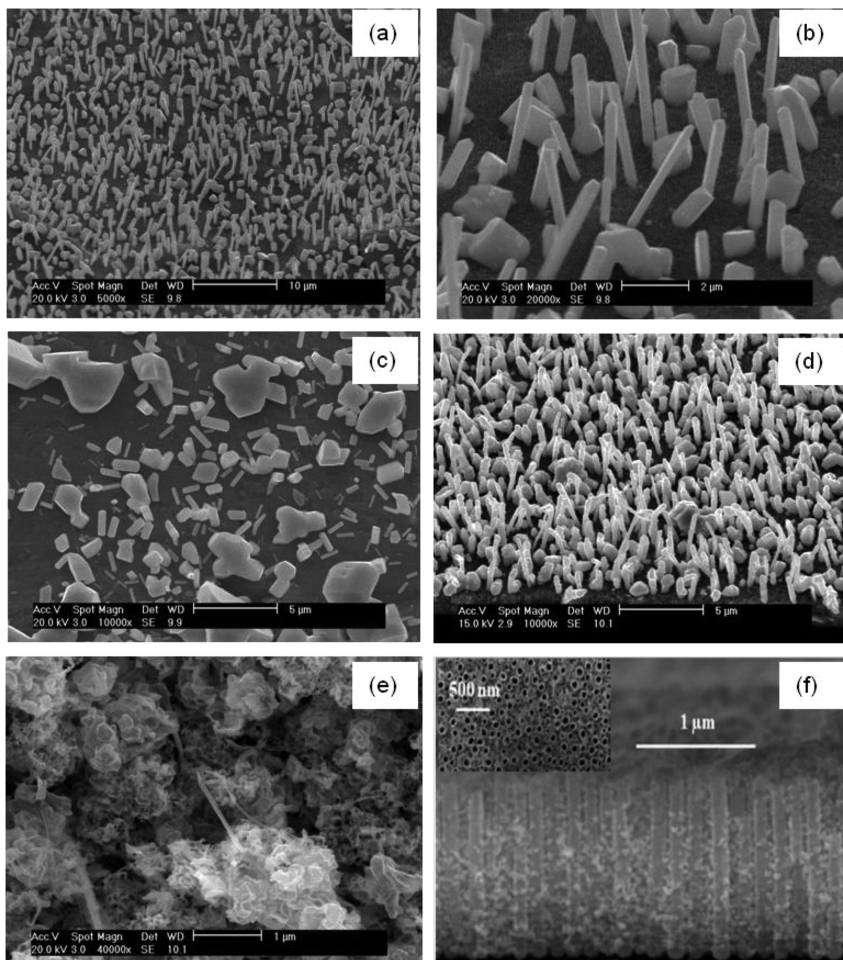


Figure 3. SEM images of: (a, b) Tin nanowires electrodeposited on titania nanotubes (900 nm length), (c) tin deposited on a titania compact layer, (d) tin oxide nanowires on titania nanotube layer, Sn crystallites electrochemically grown on TiO₂ nanotubes (500 nm length), (e) tin sponge on amorphous titania layer, and (f) Sn-doped TiO₂ nts. Fig. 3e is reproduced with permission from reference (40). Copyright 2009 The Electrochemical Society. Fig. 3f is reprinted with permission from reference (43). Copyright 2012 Elsevier.

The titania matrix provided a reasonable conductive substrate for the electrodeposition of tin. At 1.75 V, lithium is inserted into titania and the conductivity is increased during discharge. From 1- 0.7 V, tin monoxide reduction is observed (reaction 2). The latter two steps irreversibly consume lithium because of the de-intercalation from titania nanotubes do not proceed in further cycling due to the imposed voltage limitation in charge up to 1.2 V. Also, 2 Li⁺ ions per oxygen atom are irreversibly trapped to yield Li₂O and the irreversible formation of a solid electrolyte interface must be taken into account. For electrodes containing solely tin, the tin oxide reduction peak is not observed. In a third step, the metallic tin nanoparticles can accept Li⁺ ions up to the final stoichiometry of LiSn_{4.4} (3, 46). This reaction is responsible for the reversible capacity delivered by the cell.

One of the common solutions to reduce the poor capacity retention originated by Li-Sn alloys volume changes is the addition of electrochemically inactive materials, acting as buffers to accommodate the strains. The tin-titania nanocomposite described above represented a different and promising solution to the volume change issue. We moved from conventional micro-structures to novel micro and nano-architectures which provides empty voids for accommodating strains. Fig. 4b-d shows several examples in which the nanoarchitected tin-titania samples always exhibited superior capability. Depending of the loaded tin, the areal capacities may vary (Fig. 4c,d). For instance, considering Faraday's law, 0.22 mg of tin were electrodeposited onto 1 cm² of titania nanotubes; and the results expressed in terms of gravimetric capacities are of 675 mA h g⁻¹ for first reversible capacity at 2C rate keeping 85% of initial capacity over 50 cycles. These good performances are most likely due to the nanoarchitected tin- and tin oxide-nanowires tandem with titania nanotubes directly growth onto the current collector. This nanoarchitecture probably prevents the pulverization of pristine material in smaller particles during cycling. The improved strain relaxation allows using nanowires with increased diameter and length without breaking the pristine microstructure. The nanowire anode configuration provides an efficient 1D electron transport (see schematic representation inset Fig. 4b).

Finally, it should be noted that here we deal with free-additives electrodes which implies a 10 % reduction in battery pack weight and volume (47). This fact undoubtedly contributes to decrease the undesirable irreversible capacities.

5. Anodized Tin-Based Composites

The aim of this approach is the development of a novel synthesis route mainly based on an anodization method that can provide a relatively good control for the growth and final fabrication of hybrid electrode materials. Up to date, a limited number of reports based on the formation of tin and tin oxides nanostructures by anodization of bulk tin foils for the application on Li-batteries are found. Some of the preparation routes for 1D tin oxide structures such as nanotubes, nanoribbons, or nanorods can be found in literature (48–50). The most classical examples are those of anodic formation of self-ordered porous oxide films on aluminum and other valve metal such as Ti, Ta, W, or Zr (51–55).

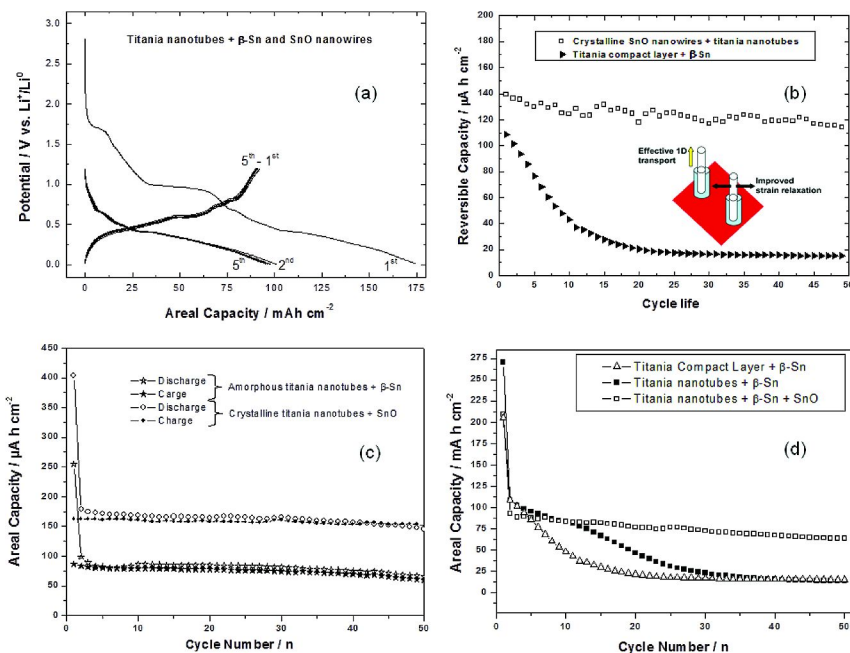


Figure 4. (a) Galvanostatic discharge/charge curves during the first five cycles of crystalline tin and tin oxides nanowires supported on crystalline titania nanotubes. Cycling life behavior of: (b) Tin oxide nanowires supported on titania nanotubes (900 nm length) compared to a titania compact layer cycled at $50 \mu\text{A cm}^{-2}$, (c) tin and tin oxides nanowires on titania nanotubes (500 nm length) cycled at $50 \mu\text{A cm}^{-2}$, and (d) specific capacity of the $\text{SnO}/\text{crystalline TiO}_2$ and $\text{Sn}/\text{amorphous TiO}_2$ films as a function of cycle number cycled at $100 \mu\text{A cm}^{-2}$. Hollow and solid symbols represent the discharge and charge, respectively. Fig. 4c is reproduced with permission from reference (40). Copyright 2009 The Electrochemical Society.

The electrochemical set up for tin anodization is easily constructed by using a high purity tin foil as a working electrode, and a platinum wire as a counter electrode. The electrolyte is a solution of polyethylenglycol (PEG) and oxalic acid. Constant voltages of 10 V during were applied for several minutes up to one hour (56). The anodization process can be followed by the current response of the anodization cell. After applying the potential, the current drops rapidly in the first few seconds and a compact oxide layer on Sn surface is formed. Afterwards, the current density increases because pores are formed through the barrier oxide layer, exposing again the tin foil to the electrolyte solution. During the process, a detachment of the tin oxide already formed on the electrode surface along with tin due to oxygen evolution is observed. The precipitation of tin oxides due to concentration of species above their solubility products near the electrode surface is another interpretation to the phenomena therein (57).

In order to know the oxidation state and local environment of tin-based materials, ^{119}Sn Mössbauer spectra of anodized tin foils are shown in Fig. 5a. The measured spectral intensities of the tin atoms are the product of the recoil-free-fractions (f) and the atomic fractions. The values of the recoil-free fractions have been taken from the literature: $f(\text{SnO}_2) = 0.56$, $f(\text{SnO}) = 0.12$, $f(\beta\text{-Sn}) = 0.06$ (58, 59). The as-prepared anodized sample exhibited an spectrum with signals ascribable to Sn(II), Sn(IV) and Sn(0) atoms with an atomic fraction value of 2, 11, and 87%, respectively. For annealed samples at 350°C no signal of Sn(II) is detected, meaning that the annealing process favored Sn(II) disproportion in Sn(IV) and β -Sn along with a partial oxidation to SnO_2 . Large micrometric particles with irregular shapes, according to SEM images, were collected. From a top view, a heterogeneous porous texture appears randomly distributed on the surface sample (Fig. 5b). Pore size and wall thickness ranged between 50 - 150 and 10 - 15 nm, respectively. A salient property found in these materials is the preservation of this complex texture after annealing at temperatures above the melting point of tin (Fig. 5c). A reasonable interpretation of this surprising phenomenon is that the tin oxide component forms a skull - as in skull-melting techniques - that prevents shape modification of the melted metal. This behavior is in agreement with the results reported in literature (48).

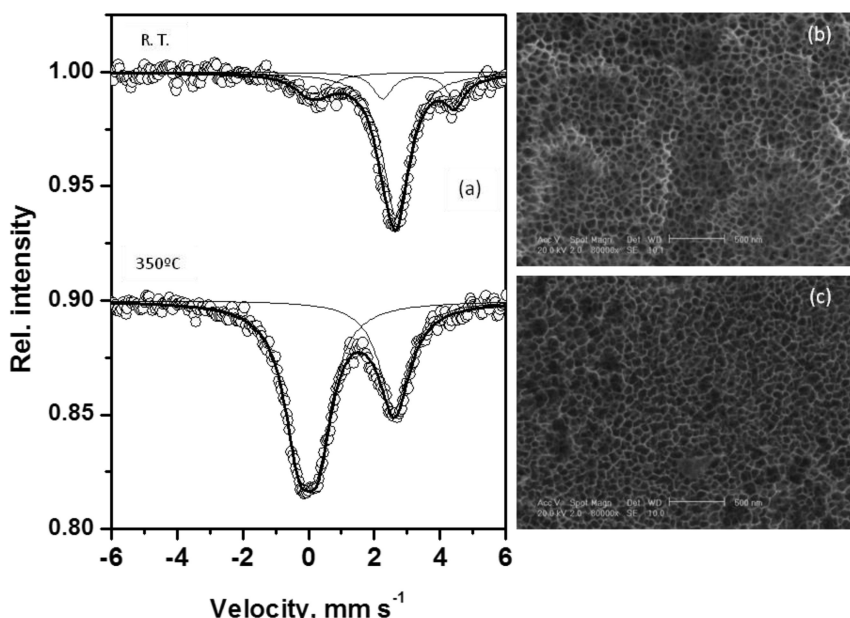


Figure 5. ^{119}Sn Mössbauer spectra (a) and SEM images of nanoporous tin-based materials obtained by anodic process at room temperature (b) and annealed at 350°C (c). Note that Fig. 5a is reproduced with permission from reference (56).

Copyright 2011 The Electrochemical Society.

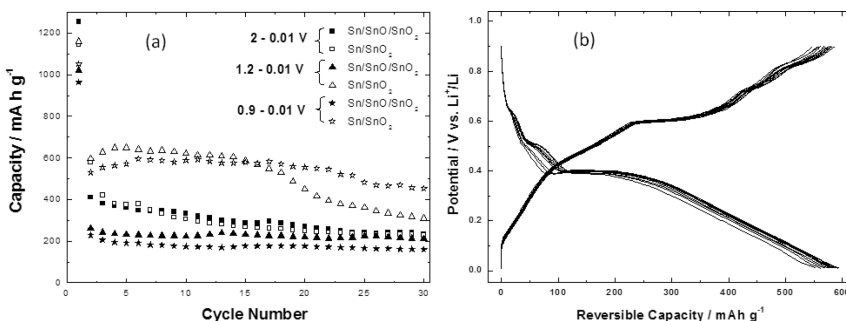


Figure 6. (a) Cycling study of tin-based electrodes performed at a C rate and using special operational voltage windows. Note: all the experiments are performed at a C rate and for the end of the discharge the lower potential was fixed on 0.01 V. (b) Galvanostatic discharge/charge curves during the first reversible 20 cycles for anodized and annealed tin-based material using 0.9 - 0.01 V range. Fig. 6a is reproduced with permission from reference (56).

Copyright 2011 The Electrochemical Society.

Next, a study related to the minimization of the volume changes of Li-Sn alloys during charge-discharge reactions in Li test cell is shown. The reversibility and stability of the Li reaction with tin-based electrodes is dependent on the operational voltage window and the selected kinetics (Fig. 6) (56). For the sake of clarity, experiments performed at 1C rate are shown in Fig. 6. The specific capacity for Sn-SnO₂ electrodes was around 600 mA h g^{-1} during the first reversible cycle, and according to the voltage limits the capacity is different. For example, when using a range of 2-0.01V there is an indication of capacity fading below 300 mA h g^{-1} just after the first 5 cycles. Otherwise, the capacity is retained over long cycling for narrow voltage limits. Thus, a capacity value of 330 mA h g^{-1} is kept after 30 cycles, what involves a 55% of efficiency when the voltage window was set between 1.2 - 0.01 V. The reversibility of the reactions is reasonably preserved on further cycling, especially when cycling between 0.9 - 0.01 V, because the hybrid nano-structure obtained at 350°C (Sn-SnO₂) showed an enhanced capacity (455 mA h g^{-1}) over 30 cycles entailing ~ 80% of reversibility. In order to see the impact of the capacity values and efficiency presented in this work, the capability values recorded for related tin-based electrodes are listed: (i) a nanoscale meshed SnO electrode delivered a specific capacity of 320 mA h g^{-1} (20th cycle) at a current density of 0.1 A g^{-1} (60), or (ii) other SnO₂ nanowires achieved 300 mA h g^{-1} (30th cycles) at a current density of 0.1 A g^{-1} (61), or (iii) commercial tin-based powder with a capacity fading below 250 mA h g^{-1} after 10 cycles (23, 60, 61). The improvement of the electrochemical behavior of our hybrid composite should be attributed to the 1D structure with a large surface area and high pore length / pore diameter ratio. This hybrid 1D Sn-SnO₂ structure with 75-80% porosity could provide more reaction sites on the surface, and the small pore diameter provides a short diffusion length for Li⁺ alloying, that may enhance the charge transfer and electron conduction. To identify the electrochemical

reactions, the galvanostatic discharge/charge curves of the reversible reactions are shown in Fig. 6b. The profile shows three apparent reduction peaks around 0.65, 0.5, 0.4 V during the discharge and 0.6, 0.74 and 0.84 V during the charge cycles, which are related to the formation of Li-Sn alloys with different stoichiometry (see the reaction in the previous chapters).

The achievement of a stable and high specific capacity is a result of the ability of the materials to accommodate the volume changes occurring during the cycling process. Equally important is the way of processing the materials. As we have shown, anodization is a practical technique for synthesizing promising nano-structures capable to offering long charge/discharge cycles life. Recent research and future directions focus on developments on manipulating materials morphology at the nanometer scale with thin film or derived 3D architectures for the future generation of lithium ion batteries.

6. Low-Cost Carbon-Tin Heterostructures

In order to be competitive with other energy storage devices, lithium ion batteries must be fabricated at the lowest price. The way to do that mainly resides in reducing the cost of materials and synthetic routes. The two main elemental components in carbon-tin heterostructures are abundant resources and hence are cheap. Graphitic carbon is highly reversible for lithium insertion, non-toxic and low cost but the limited theoretical capacity is restricting the future applications of Li-ion batteries. Otherwise, amorphous carbon prepared at low temperatures offers interesting possibilities due to its higher capacity than graphitic carbon and economical preparation route. Concerning tin, this element is an abundant source which provides an increased capacity to the cycled electrode as compared to graphite (62).

Unfortunately the sole presence of these elements does not provide an optimized performance to the anode material. Since the announcement of Sony that the revolutionary Nexion concept was based on an “amorphous tin–cobalt–carbon” material, a large number of studies have been devoted to unveil the role of the transition metal in the electrochemical reaction. Dahn et al. performed a combinatorial study of the structural and electrochemical properties of sputtered libraries $[Sn_{0.55}Co_{0.45}]_{1-y}C_y$ ($0 < y < 0.5$). From these results it was concluded that for y values close to 0.4, the local atomic structure remained unchanged after at least for 25 cycles (63). Cobalt is an expensive metal which presence in a high concentration would increase the cost of the electrode material. Although, the amount of cobalt needed for a proper anode cycling behavior is not high, great efforts are currently done to reduce its content in the anode. The resorcinol/formaldehyde polymerization–carbonization method was employed to prepare Sn–Co–C composites. The electrochemical results evidenced that cobalt plays a determining effect even in amorphous domains and relatively small (64).

Alternatively, the substitution of cobalt by cheaper transition metals as manganese or iron has been proposed in numerous contributions. One of the first attempts to use Sn-Fe-C composites as anode revealed a progressive growth of the grain size of the Li–Sn alloy and Sn–Fe domains upon cycling leading to

electrical disconnection and consequently cell failure (65). More recently, several solutions have been proposed to improve the mechanical stability and hence reducing the particle stress that eventually gives rise to cracks and the deleterious loss of electrical contact. Sohn et al. have prepared a $\text{Sn}_2\text{Fe}/\text{Al}_2\text{O}_3$ (3 wt.%)/C nanocomposite electrode in which the active material is mechanically reinforced by embedding Al_2O_3 particles resulting in a decrease of the initial irreversibility and enhanced performance. The improvement is attributed to a low crystallite size and highly dispersed active material (66). Manganese is another low cost element which has been essayed to prepare ternary Sn-Mn-C composites with potential application as anode in Li-ion batteries (67, 68). The microstructural analysis of the nanometric two-phase mixtures showed the occurrence of nanoscopic grains (10 nm) of the coexisting phases. The electrochemical study of the active materials revealed that tin atoms located at the grain boundaries of nanostructured SnMn_3C were able to react reversibly with lithium for large number of cycles.

Another possibility to diminish the production cost of tin-carbon heterostructures involves the use of facile methods of synthesis. Microwave plasma chemical vapor deposition (MPCVD) has been proposed as an easy, fast and inexpensive method for the direct formation of nano-dispersed tin-carbon composite thin-film anodes for Li-ion batteries (69). Mechanical alloying based on either ball milling or vertical-axis attritor milling has been extensively used to prepare tin-carbon heterostructures with small grain sizes in a large number of studies (70). Scrosati et al. have revealed promising results for the $\text{Sn}_{0.31}\text{Co}_{0.28}\text{C}_{0.41}$ composition prepared by ball milling. This active material was able of sustaining large capacity values retention upon prolonged cycling (71). Ferguson et al. showed that it was possible to prepare nanostructured $\text{Sn}_{30}\text{TM}_{30}\text{C}_{40}$ and of $\text{Sn}_{30}\text{Co}_{15}\text{TM}_{15}\text{C}_{40}$, ($\text{TM} = \text{Mn, Fe, Co, Ni, Cu}$) by mechanical attrition. This experimental approach allows an economical and industrially scalability. Those composites containing either Co or Ni had excellent capacity retention for at least 100 cycles at around 425 and 250 mA h g^{-1} , respectively. These successful results were ascribed due to the absence of crystalline phases (72).

The use of inexpensive carbonaceous products is also a low cost solution for the preparation of tin-carbon heterostructures. The petroleum industry produces large amounts of green cokes as secondary by-products. Their reduced cost is an added value for commercial purposes. Also, their low structural ordering offers a large variety of reactive sites to which lithium can be reversibly inserted hence contributing to the overall capacity. Sn-Co-C composites can be prepared by ball milling of green cokes and metal oxides followed by carbothermal reduction. This is a cost-effective procedure for the large-scale production of electrode materials. Scanning electron microscopy images of $\text{Sn}_8\text{Co}_4\text{C}_{88}$ showed sub-micrometric metallic particles homogeneously dispersed in the carbon matrix (Fig. 7). $\text{Sn}_7\text{Co}_1\text{C}_{92}$ and $\text{Sn}_8\text{Co}_4\text{C}_{88}$ composites galvanostatic cycled delivered 400 mA h g^{-1} at 35 mA g^{-1} after 40 cycles. Low internal impedances and a major CoSn_2 contribution in the pristine samples, revealed by Mössbauer spectroscopy, were beneficial factors in the most performing electrodes (73).

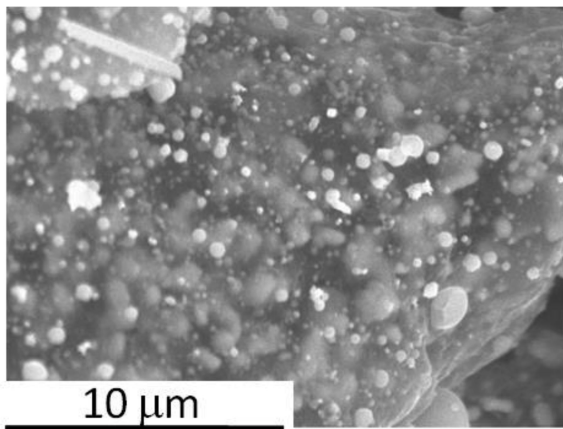


Figure 7. Scanning electron micrograph of Sn₈Co₄C₈₈.

Moreover, the fluidized state of vacuum residua carbon precursor during the copyrolysis reaction produced finely dispersed intermetallic phases embedded in the carbon matrix. It was reported a proportional increase of the reversible capacity with the inclusion of tin. Otherwise, the increase of the carbonization temperature induced a decrease of the irreversible capacity. The stabilizing and muffing effect of the carbonaceous matrix against the volumetric changes during the formation and deformation of the Li–Sn alloys was effective allowing maintain 500 mA h g⁻¹ for a number of cycles (Fig. 8). The analysis of cycled electrodes by spectroscopic techniques revealed that Li–Sn intermetallic compounds were produced on discharging but only partially removed at the end of the charge sweep. It can be responsible for irreversibility observed in sample carbonized at the lowest temperature (74).

7. Concluding Remarks

While tin era is still alive and nano-heterostructures provide means to overcome the limitations of individual electrode components, a shiny future is still expectable for the anode of advanced lithium batteries based on composite tin nanoarchitectures. An evidence of such phenomenon is the existence of commercial products based on this technology and the continuous improvement in both fundamental and industrial applications. A noteworthy example is the update received by the Nexelion technology in 2011, which allowed increasing their capacity from 2.2 Ah to 3.5 Ah (75). Previously unnoticed success is now expected for nanotechnology products involving heterostructures of polymers, carbon nanomaterials – particularly graphene – or self-assembled TiO₂ nanotubes together with different tin species.

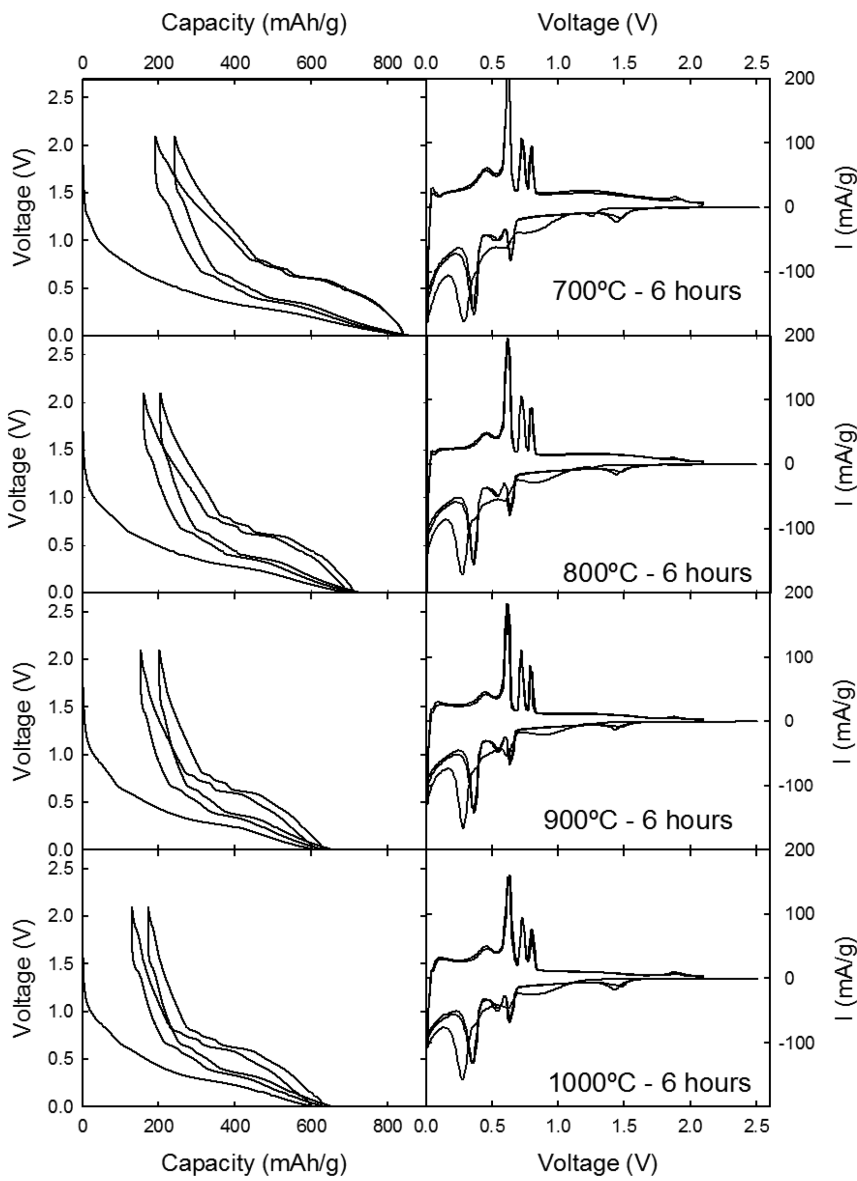


Figure 8. Discharge/charge curves for the composite materials using vacuum residue as a carbon precursor and carbonized at different temperatures (700, 800, 900 and 1000 °C). Reproduced with permission from reference (74).

Copyright 2007 Elsevier.

Acknowledgments

The authors would like to acknowledge for the support of Spanish Ministry of Science and Innovation (MICINN), contract MAT2011-22753, Junta de Andalucía (Research group FQM288)

References

1. Yang, J.; Winter, M.; Besenhard, J. O. *Solid State Ionics* **1996**, *90*, 281–287.
2. Idota, Y.; Kubota, T.; Matsufuji, A.; Maekawa, Y.; Miyasaka, T. *Science* **1997**, *276*, 1395–1397.
3. Courtney, I. A.; Dahn, J. R. *J. Electrochem. Soc.* **1997**, *144*, 2045–2052.
4. Courtney, I. A.; Dahn, J. R. *J. Electrochem. Soc.* **1997**, *144*, 2943–2948.
5. <http://www.sony.net/SonyInfo/News/Press/200502/05-006E/> (last access: 14/09/2012).
6. Carlin, J. F. Tin. *Minerals Yearbook* U.S. Geological Survey: 2000; pp 79.2–79.7.
7. Liu, S.; Ge, B.; Song, B.; Wang, W. *Adv. Mater. Res.* **2012**, *496*, 453–456.
8. Zhang, X. W.; Wang, C. S.; Appleby, A. J.; Little, F. E. *J. Power Sources* **2002**, *109*, 136–141.
9. Maxfield, M.; Jow, T. R.; Gould, S.; Sewchok, M. G.; Shacklette, L. W. *J. Electrochem. Soc.* **1988**, *135*, 299–305.
10. Lecayon, G.; Bouzien, Y.; Le Gressus, C.; Reynaud, C.; Boiziau, C.; Juret, C. *Chem. Phys. Lett.* **1982**, *91*, 506–510.
11. Jung, Y.; Singh, N.; Choi, K. S. *Angew. Chem., Int. Ed.* **2009**, *48*, 8331–8334.
12. Patel, P.; Kim, I. S.; Maranchi, J.; Kumta, P. *J. Power Sources* **2004**, *135*, 273–280.
13. Reynaud, C.; Boiziau, C.; Juret, C.; Leroy, S.; Perreau, J.; Lecayon, G. *Synth. Met.* **1985**, *11*, 159–165.
14. He, X.; Pu, W.; Wang, L.; Ren, J.; Jiang, C.; Wan, C. *Solid State Ionics* **2007**, *178*, 833–836.
15. Yagi, S.; Nakagawa, T.; Matsubara, E.; Matsubara, S.; Ogawa, S.; Tani, H. *Electrochem. Solid-State Lett.* **2008**, *11*, E25–E27.
16. Nacimiento, F.; Alcántara, R.; González, J. R.; Tirado, J. L. *J. Electrochem. Soc.* **2012**, *159*, A1028–A1033.
17. Nacimiento, F.; Alcántara, R.; Tirado, J. L. *J. Electrochem. Soc.* **2010**, *157*, A666–A671.
18. Nacimiento, F.; Alcántara, R.; Tirado, J. L. *J. Power Sources* **2011**, *196*, 2893–2898.
19. Nacimiento, F.; Alcántara, R.; Nwokeke, U. G.; González, J. R. *Ultrason. Sonochem.* **2012**, *19*, 352–357.
20. Gowda, S. R.; Reddy, A. L. M.; Shajumon, M. M.; Zhan, X.; Ci, L.; Ajayan, P. M. *Nano Lett.* **2011**, *11*, 101–106.
21. He, Z.; Xiong, L.; Liu, W.; Wy, X.; Chen, S.; Huang, K. *J. Cent. South Univ. Technol.* **2008**, *15*, 214–217.

22. Wang, Z.; Fierke, M. A.; Stein, A. *J. Electrochem. Soc.* **2008**, *155*, A658–A663.
23. Ortiz, G. F.; Alcántara, R.; Lavela, P.; Tirado, J. L. *J. Electrochem. Soc.* **2005**, *152*, A1797–A1803.
24. Jin, Y. H.; Min, K. M.; Seo, S. D.; Shim, H. W.; Kim, D. W. *J. Phys. Chem. C* **2011**, *115*, 22062–22067.
25. Mu, J.; Chen, B.; Guo, Z.; Zhang, M.; Zhang, Z.; Shao, C.; Liu, Y. *J. Colloid Interface Sci.* **2011**, *356*, 706–712.
26. Zheng, J. W.; Nai, S. M. L.; Ng, M.-F.; Wu, P.; Wei, J.; Gupta, M. *J. Phys. Chem. C* **2009**, *113*, 14015–14019.
27. Li, R.; Sun, X.; Zhou, X.; Cai, M.; Sun, X. *J. Phys. Chem. C* **2007**, *111*, 9130–9135.
28. Wang, Y.; Wu, M.; Jiao, Z.; Lee, J. Y. *Chem. Mater.* **2009**, *21*, 3210–3215.
29. Yao, J.; Shen, X.; Wang, B.; Liu, H.; Wang, G. *Electrochem. Commun.* **2009**, *11*, 1849–1852.
30. Paek, S. M.; Yoo, E. J.; Honma, I. *Nano Lett.* **2009**, *9*, 72–76.
31. Meng, X.; Geng, D.; Liu, J.; Banis, M. N.; Zhang, Y.; Li, R.; Sun, X. *J. Phys. Chem. C* **2010**, *114*, 18330–18337.
32. Zou, Y.; Wang, Y. *ACS Nano* **2011**, *5*, 8108–8114.
33. Luo, B.; Wang, B.; Liang, M.; Ning, J.; Li, X.; Zhi, L. *Adv. Mater.* **2012**, *24*, 1405–1409.
34. Zhu, J. J.; Liao, X. H.; Zhao, X. N.; Chen, H. Y. *Mater. Lett.* **2001**, *49*, 91–95.
35. Lieber, C. M. *Solid State Commun.* **1998**, *107*, 607–616.
36. Xia, Y. N.; Yang, P. D.; Sun, Y. G.; Wu, Y. Y.; Mayers, B.; Gates, B.; Yin, Y. D.; Kim, F.; Yan, Y. Q. *Adv. Mater.* **2003**, *15*, 353–389.
37. Ortiz, G. F.; Hanzu, I.; Djenizian, T.; Lavela, P.; Tirado, J. L.; Knauth, P. *Chem. Mater.* **2009**, *21*, 63–67.
38. Chen, J. S.; Luan, D.; Li, C. M.; Boey, F. Y. C.; Qiao, S. Z.; Lou, X. W. *Chem. Commun.* **2010**, *46*, 8252–8254.
39. Ortiz, G. F.; Hanzu, I.; Lavela, P.; Knauth, P.; Tirado, J. L.; Djenizian, T. *Chem. Mater.* **2010**, *22*, 1926–1932.
40. Ortiz, G. F.; Hanzu, I.; Knauth, P.; Lavela, P.; Tirado, J. L.; Djenizian, T. *Electrochem. Solid-State Lett.* **2009**, *12*, A186–A189.
41. Hanzu, I.; Djenizian, T.; Ortiz, G. F.; Knauth, P. *J. Phys. Chem. C* **2009**, *113*, 20568–20575.
42. Scharifker, B.; Hills, G. *Electrochim. Acta* **1983**, *28*, 879–889.
43. Kyeremateng, N. A.; Hornebecq, V.; Knauth, P.; Djenizian, T. *Electrochim. Acta* **2012**, *62*, 192–198.
44. Kolmakov, A.; Zhang, Y. X.; Moskovits, M. *Nano Lett.* **2003**, *3*, 1125–1129.
45. Ortiz, G. F.; Hanzu, I.; Knauth, P.; Lavela, P.; Tirado, J. L.; Djenizian, T. *Electrochim. Acta* **2009**, *54*, 4262–4269.
46. Li, N.; Martin, C. R.; Scrosati, B. *J. Power Sources* **2001**, *97-98*, 240–243.
47. Patil, A.; Patil, V.; Shin, D. W.; Choi, J. W.; Paik, D. S.; Yoon, S. J. *Mater. Res. Bull.* **2008**, *43*, 1913–1942.
48. Shin, H. C.; Dong, J.; Liu, M. *Adv. Mater.* **2004**, *16*, 237–240.
49. Feng, S.; Tang, Y.; Xiao, T. *J. Phys. Chem. C* **2009**, *113*, 4809–4813.

50. Ortiz, G. F.; Hanzu, I.; Lavela, P.; Tirado, J. L.; Knauth, P.; Djenizian, T. *Int. J. Nanotechnol.* **2012**, *9*, 260–294.
51. Masuda, J.; Fukuda, K. *Science* **1995**, *268*, 1466–1468.
52. Macak, J. M.; Tsuchiya, H.; Schmuki, P. *Angew. Chem., Int. Ed.* **2005**, *44*, 2100–2102.
53. Sieber, I. V.; Schmuki, P. *J. Electrochem. Soc.* **2005**, *152*, C639–C644.
54. Watcharenwong, A.; Chanmanee, W.; de Tacconi, N. R.; Chenthamarakshan, C. R.; Kajitvichyanukul, P.; Rajeshwar, K. *J. Electroanal. Chem.* **2008**, *612*, 112–120.
55. Tsuchiya, H.; Macak, J. M.; Sieber, I.; Schmuki, P. *Small* **2005**, *1*, 722–725.
56. Ortiz, G. F.; Lavela, P.; Knauth, P.; Djenizian, T.; Alcántara, R.; Tirado, J. L. *J. Electrochem. Soc.* **2011**, *158*, A1094–A1099.
57. Hossnia, S. M.; Abdel-Rahman, E. S.; Abd, M.; Hany, E. L. *J. Solid State Electrochem.* **2009**, *13*, 1279–1290.
58. Hightower, A.; Delcroix, P.; Le Caer, G.; Huang, C. K.; Ratnakumar, B. V.; Ahn, C. C.; Fultz, B. *J. Electrochem. Soc.* **2000**, *147*, 1–8.
59. Courtney, I. A.; Dunlap, R. A.; Dahn, J. R. *Electrochim. Acta* **1999**, *45*, 51–58.
60. Uchiyama, H.; Hosono, E.; Honma, I.; Zhou, H.; Imai, H. *Electrochem. Commun.* **2008**, *10*, 52–55.
61. Park, M. S.; Wang, G. X.; Kang, Y. M.; Wexler, D.; Dou, S. X.; Liu, H. K. *Angew. Chem., Int. Ed.* **2007**, *46*, 750–753.
62. Concheso, A.; Santamaría, R.; Blanco, C.; Menéndez, R.; Jiménez-Mateos, J. M.; Alcántara, R.; Lavela, P.; Tirado, J. L. *Carbon* **2005**, *43*, 923–936.
63. Todd, A. D. W.; Mar, R. E.; Dahn, J. R. *J. Electrochem. Soc.* **2006**, *153*, A1998–A2005.
64. Lavela, P.; Nacimiento, F.; Ortiz, G. F.; Tirado, J. L. *J. Solid State Electrochem.* **2010**, *14*, 139–148.
65. Mao, O.; Dunlap, R. A.; Dahn, J. R. *Solid State Ionics* **1999**, *118*, 99–109.
66. Lee, J.-M.; Jung, H.; Hwa, Y.; Kim, H.; Im, D.; Doo, S.-G.; Sohn, H.-J. *J. Power Sources* **2010**, *195*, 5044–5048.
67. Beaulieu, L.; Larcher, D.; Dunlap, R. A.; Dahn, J. R. *J. Alloys Compd.* **2000**, *297*, 122–128.
68. Beaulieu, L.; Dahn, J. R. *J. Electrochem. Soc.* **2000**, *147*, 3237–3241.
69. Marcinek, M.; Hardwick, L. J.; Richardson, T. J.; Song, X.; Kostecki, R. J. *J. Power Sources* **2007**, *173*, 965–971.
70. Chen, Z.; Qian, J.; Ai, X.; Cao, Y.; Yang, H. *J. Power Sources* **2009**, *189*, 730–732.
71. Hassoun, J.; Mulas, G.; Panero, S.; Scrosati, B. *Electrochem. Commun.* **2007**, *9*, 2075–2081.
72. Ferguson, P. P.; Martine, M. L.; George, A. E.; Dahn, J. R. *J. Power Sources* **2009**, *194*, 794–800.
73. Nacimiento, F.; Lavela, P.; Tirado, J. L.; Jiménez-Mateos, J. M. *J. Solid State Electrochem.* **2012**, *16*, 953–962.
74. Tirado, J. L.; Santamaría, R.; Ortiz, G. F.; Menéndez, R.; Lavela, P.; Jiménez-Mateos, J. M.; Gómez García, F. J.; Concheso, A.; Alcántara, R. *Carbon* **2007**, *45*, 1396–1409.

75. <http://www.sony.co.jp/SonyInfo/News/Press/201107/11-078/> (last access: 14/09/2012).

Chapter 2

Studying the Localized Electrochemical Phenomena in Rechargeable Li-Ion Batteries by Scanning Probe Microscopy Techniques

Jing Zhu and Kaiyang Zeng*

Department of Mechanical Engineering, National University of Singapore,
9 Engineering Drive 1, Singapore 117576

*E-mail: mpezk@nus.edu.sg

Rechargeable Li-ion batteries have many important applications in today's information rich society. In recent years, the optimization of energy density and life-time of the Li-ion batteries has become an essential step for the advances of the Li-ion battery, this optimization requires a comprehensive understanding of the electrochemical mechanisms at all length scales. In recent years, Scanning Probe Microscope (SPM) has therefore emerged as a powerful and sometimes the only tool to characterize the multi-functionalities of the energy storage materials including Li-ion batteries. In this chapter, we will review some of the recent progresses on the studies of the localized electrochemical phenomena in rechargeable Li-ion batteries by using various SPM techniques, including ex-situ Atomic Force Microscope (AFM), in-situ Electrochemical Atomic Force Microscope (EC-AFM), in-situ Kelvin Probe Force Microscopy (KPFM), in-situ Electrostatic Force Microscope (EFM), Conductive AFM (c-AFM), Electrochemical Strain Microscopy (ESM), and Contact Resonance AFM (CR-AFM). These SPM techniques have made significant contributions to enhance current understandings of the electrochemical functionalities and aging mechanisms of the rechargeable Li-ion batteries at meso- to nano-scales.

Introduction

Rechargeable Li-ion batteries are the most common and practical energy storage systems for many electronic products at various scales since the first commercialized product by Sony in 1991 (1–4). In the past decades, the Li-ion batteries have been extensively used in portable and mobile devices such as digital cameras, mobile phones and laptop computers, accounting for about 63% of worldwide market share in portable batteries (1–7). Recently, Li-ion batteries are used in larger and more durable products such as hybrid electrical vehicles (HEVs), space satellite and temporary buffering system for renewable energy sources such as solar and wind energy (5–7). For those applications, prolonged lifetime and higher energy density are very essential (8). In addition, due to the increased requirements of today's information rich society and emerging ecological issues, it is necessary to develop new, low-cost, and environmental-friendly materials for Li-ion batteries as well as new generation energy storage systems beyond Li-ion batteries, such as metal-ion batteries (9). Both the optimization of current battery material and the development of new energy storage systems require the comprehensive understanding of the electrochemical phenomena ranging from macro to nano-scales.

Similar to any battery structures, a typical Li-ion battery cell consists of a positive electrode (cathode), a negative electrode (anode) and an intervening electrolyte which is a good ionic conductor and electron insulator. Due to different electrochemical potential in the two electrodes, Li-ion battery can store electrical energy in chemical form and converts this chemical energy into electricity through the spontaneous electrochemical reactions. During the discharge process, Li-ions are released by the chemical reaction at the anode and then transfer into the cathode through the electrolyte (in either liquid or solid state); at the same time, the liberating electrons are transferred in the same direction through the external circuit to maintain the charge balance. In this way the chemical energy in the battery is electrochemically extracted to generate electricity. During the charge process, Li-ions transfer from the cathode into the anode and this will consume the external supplied electrical energy. Figure 1 schematically shows these charge/discharge processes in the rechargeable Li-ion batteries. During these processes, the Li-ion undergoes following oxidation and reduction reactions (redox) at the electrodes:



where M indicates the metal elements, such as Co, Mn, Ni, Fe etc.

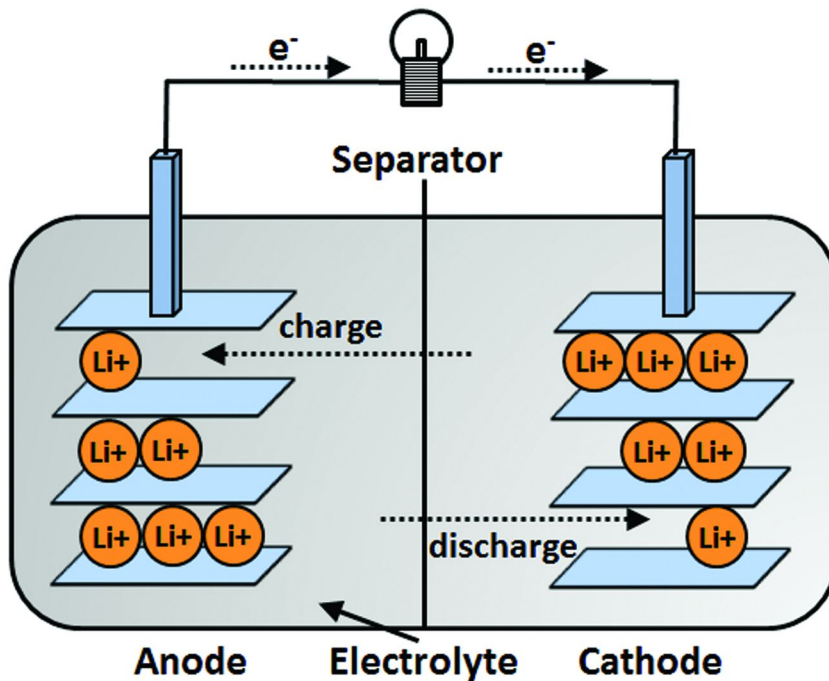


Figure 1. Schematic drawing of the charge and discharge processes of a lithium-ion rechargeable battery.

In recent years, various types of cathode materials have been developed with the purposes of optimizing the energy density as well as the lifetime of Li-ion batteries. The development of any new battery materials (especially cathode materials) requires in-depth understanding of the electrochemical phenomena at various states (such as solid-liquid or solid-solid) from macroscopic to nanoscopic length scales. Among those, the macroscopic electrochemical mechanisms have been extensively investigated by both academics and industries. However, due to the limitations of the experimental and analysis methodologies, the detailed electrochemical mechanisms from mesoscopic to nanoscopic levels, such as electronic and ionic transportation, local phase transformation (redox reaction), charge/vacancy trapping, solid-solid, solid-liquid and even solid-gas interfacial phenomena, as well as the roles of surface/structural defects on electrochemical process, are still not very clear. In the past two decades, Scanning Probe Microscopy (SPM) technique has emerged as a powerful, ideal and sometimes the only tool to characterize the multiple physical and chemical properties at nanoscale for numbers of functional materials, such as piezoelectric, ferroelectric, magnetic, and even tribological properties of semiconductors, multi-ferroelectrics and biological materials (10–21). Therefore, SPM techniques provide possibilities and unique characterization capabilities in the understanding and optimization of the rechargeable Li-ion batteries and other energy storage systems at sub-micron and nanometer levels (9).

Generally speaking, SPM-based techniques can be used to characterize the functionalities of the Li-ion battery based on different detection principles: such as force-based, potential-based and current based (9). The most classical force-based SPM technique is Atomic Force Microscope (AFM) imaging, in which provides detail information on topographical features with very high spatial resolution. AFM technique measures the mechanical response to the applied force through the probe tip; it can be used for Li-ion batteries with either solid-state or liquid-state electrolyte to investigate the surface topography and roughness change of the battery materials. In addition, AFM also provides the measurement of the force-deflection curve, which reflects the surface elasticity and adhesion properties of the materials. On the other hand, Electrochemical Atomic Force Microscope (EC-AFM) is also a force-based technique combining with a specially-designed electrochemical cell, which is commonly used for the characterization of the battery materials or structures with liquid electrolyte. The potential-based SPM techniques are based on the detection of long range cantilever-surface electrostatic force in response to the locally applied bias, these techniques include such as Kelvin Probe Force Microscopy (KPFM) and Electrostatic Force Microscope (EFM), in which have been widely used for the imaging of local electrical properties such as dipole moment and work functions. Finally, conductive Atomic Force Microscopy (c-AFM) is the most common current-based SPM technology, which is based on the detection of local current response to the tip bias, providing important information on conductance distribution on the sample surface.

As shown in Fig.2, there are various operation regimes of SPM based-techniques for battery characterizations. For example, SPM can be used to study the response to the applied bias in a single battery element which is the Li-ion contained cathode materials [Fig.2(a)]; or in two battery element or half-cell which is the electrode plus electrolyte [Fig.2(b)]; or in a full battery structure which includes anode, electrolyte and cathode [Figs.2(c) to 2(e)]. Furthermore, the SPM techniques can be used to investigate either the localized electrochemical properties [Figs.2(a), (b), (d) and (f)] or global behaviour [Figs.2(c) and (e)]. To study the global electrochemical behaviour, the battery structure is usually controlled by external potentiostat unit, and the SPM tip is used to measure the changes of surface morphologies or properties due to the application of the external field. To study the localized behaviour, the SPM tip is used for both applying the bias and measuring the property changes. In addition to the normal measurements in the vertical direction [Figs.2(a) to (d)], the SPM techniques can also be used for measure the battery behaviour in lateral orientations [Figs.2(e) and (f)], so that the interfacial transportation can be monitored directly. However, the battery fabrication in such orientation is still very challenge, for example, one of the problems is to avoid the short circuit in such structure arrangement.

Currently, various in-situ and ex-situ SPM techniques have been developed and applied to characterize various energy storage materials including Li-ion batteries, so that the local electrochemical functionality and aging mechanisms can be investigated. In this chapter, we will therefore provide an overview of recent studies on localized electrochemical phenomena in battery materials and

devices by using various SPM techniques, including the surface topography studies using ex-situ AFM, in-situ EC-AFM and in-situ EFM techniques; the electrochemical process investigation using KPFM; the electronic and ionic transportation studies using c-AFM and Electrochemical Strain Microscopy (ESM) techniques; and the surface mechanical degradation using Contact Resonance Atomic Force Microscopy (CR-AFM), as well as the studies using the newly-developed Electrochemical Strain Microscopy (ESM) technique.

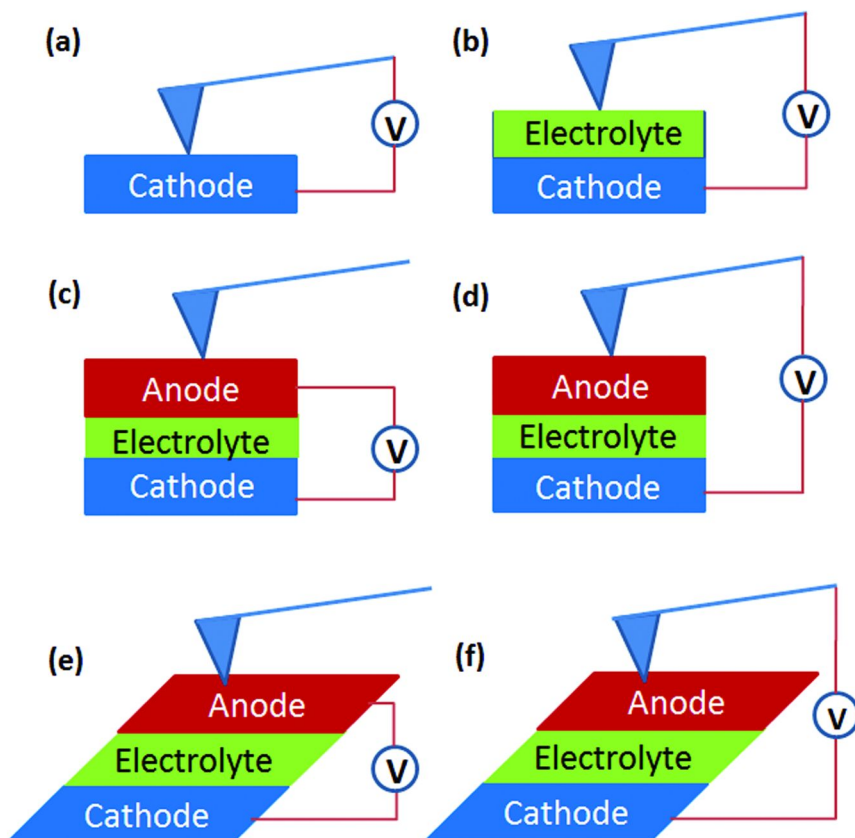


Figure 2. Schematic drawing of different SPM operation regimes for characterization of Li-ion battery: (a) single battery element – cathode material with Li-ion; (b) half-cell - cathode plus electrolyte (solid or liquid); for (a) and (b), the SPM tip is used to apply bias and scanning; (c) full battery controlled by an external potentiostat, the SPM tip measures the global properties; (d) full battery, SPM tip is used to apply bias and measure the localized behaviour; (e) full battery in lateral orientation controlled by an external potentiostat, SPM tip is used to measures the global properties; and (f) full battery in lateral orientation, SPM tip is used to apply bias and measure the localized behaviour.

Morphological Studies by AFM, EC-AFM and EFM Techniques

AFM (Atomic Force Microscopy) is the most-commonly used and direct SPM technique to image the surface topography and measure surface roughness of materials. In this operation mode, the SPM tip scans across the surface and the SPM control unit measures the cantilever deflection. This technique can provide surface topographic information at very high spatial resolution. In general, the AFM applications in battery characterization can be classified into three categories (9): (i) simple topographic imaging – only the topographic information such as grain size and shape, surface roughness can be obtained; (ii) in situ topographic imaging - the evolution of surface structure during the electrochemical process can be observed; and (iii) deformation (strain) mapping – the evolution of surface topography during the electrochemical process is performed under the conditions that allow absolute values of surface deformation (strains) to be extracted. In this section, we will discuss the principles and applications of ex-situ AFM topographic, in-situ EC-AFM (electrochemical AFM) and in-situ EFM (Electrostatic Force Microscopy) studies on Li-ion battery materials.

Ex-Situ AFM studies

AFM consists of a cantilever with a sharp tip which is used for surface scanning of the specimen. For topographic imaging, the cantilever is typically silicon or silicon nitride with the tip radius on the order of nanometres. Generally, AFM uses a laser beam deflection system, when the tip is brought into the sample surface; the forces between the tip and the sample are generated. In this case, the laser spot is reflected from the back of the AFM cantilever onto a position-sensitive detector, the deflection of the cantilever is controlled by the cantilever's spring constant according to Hooke's law. Due to AFM's versatility, it can be applied in a number of modes, depending on many applications. The primary imaging modes of AFM operation can be divided into two types: static mode (named contact mode) and dynamic mode (named non-contact or tapping mode). In contact mode, the AFM tip is dragged across the sample surface and measured using the deflection of the tip directly. In this mode, the force between the tip and the sample is constant by maintain a constant deflection. In non-contact mode, the AFM tip does not contact the sample surface, which is extremely oscillated at a frequency slightly above its fundamental resonance frequency or a harmonic. In this mode, the oscillated amplitude, phase and frequency are modified by tip-sample interactions.

For battery materials and structures, both anode and cathode surfaces undergo significant changes during the charge/discharge cycling, owing to the ionic diffusion processes between the anode and cathode, as well as Li-ion intercalation/de-intercalation processes. Numerous research works have demonstrated that the ex-situ AFM technique can be used to observe the surface topography change of both anode and cathode materials during charge/discharge cycling (22–25). Figure 3 shows the three-dimensional (3D) surface topography changes of $\text{LiNi}_{1/3}\text{Co}_{1/3}\text{Mn}_{1/3}\text{O}_2$ thin film cathode at different cycling stages. The as-deposited $\text{LiNi}_{1/3}\text{Co}_{1/3}\text{Mn}_{1/3}\text{O}_2$ thin film is uniform and almost defect-free,

consisting of almost close-packed grains with the average grain size of about 80 nm [Fig.3(a)]. With the increase of cycling number, the nano-sized grains in the $\text{LiNi}_{1/3}\text{Co}_{1/3}\text{Mn}_{1/3}\text{O}_2$ thin film seem to be self-agglomerated [Fig.3(d)], and the electrical contact within these nano-sized grains has become poor due to the presence of many voids, resulting in an increase in contact resistance and a reduction in capacity. In addition, the topography change can lead to an increase in surface roughness (in terms of RMS - root mean square) of $\text{LiNi}_{1/3}\text{Co}_{1/3}\text{Mn}_{1/3}\text{O}_2$ thin film cathode [Figure 4]. The similar surface topography changes have also been observed in other thin film cathode material (e.g., LiMn_2O_4), and anode materials (e.g., TiO_2 and RuO_2) (26–28). However, for anode material, the topography change is more significant. Due to the Li-ion insertion, the surface of thin film anode is substantially expanded, swelled and protruded from the substrate, forming island-like structures, which are electrically isolated from the rest regions of thin film (26–28). Overall speaking, the changes in the surface topography have significant effects on the capacity fading and mechanical degradation of the electrode materials (both cathode and anode); this has been discussed in detail in the previous studies (26–28) and will not be repeated here.

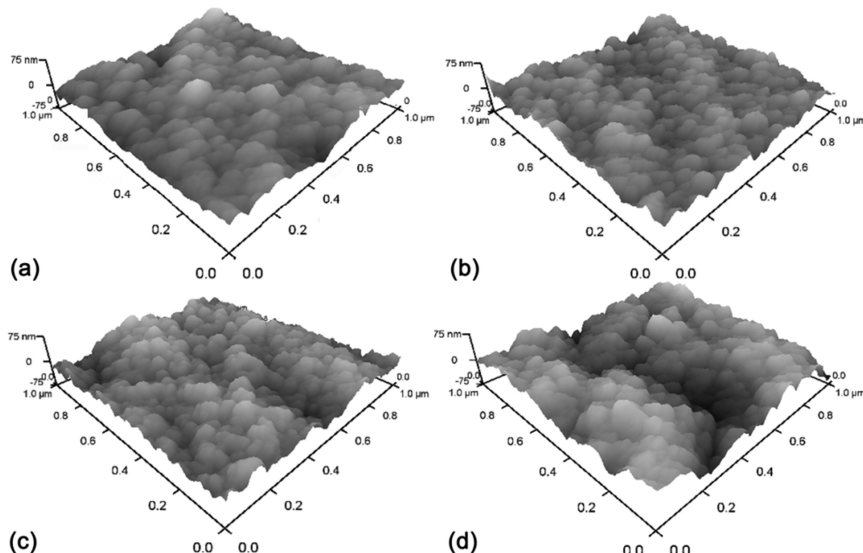


Figure 3. Surface morphology changes of $\text{LiNi}_{1/3}\text{Co}_{1/3}\text{Mn}_{1/3}\text{O}_2$ thin film cathode material during charge/discharge cycles: (a) as-deposited; (b) after 10 cycles; (c) after 50 cycles; and (d) after 100 cycles.

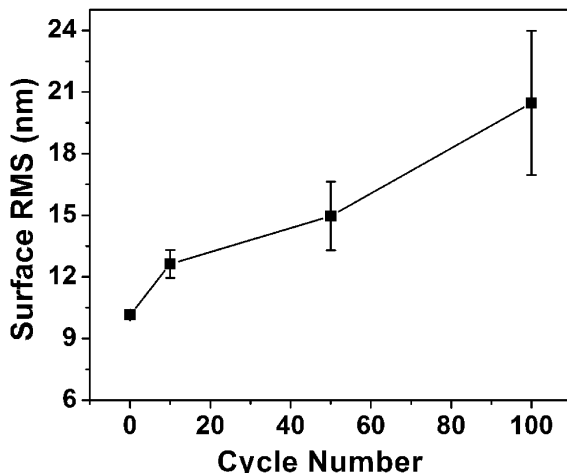


Figure 4. Surface roughness (RMS) changes of the $\text{LiNi}_{1/3}\text{Co}_{1/3}\text{Mn}_{1/3}\text{O}_2$ thin film cathode during charge/discharge cycles.

The ex-situ AFM measurements on battery materials are usually conducted after the batteries were subjected to the charge/discharge cycles with external devices (such as potentiostat). Generally-speaking, such battery was usually fabricated with liquid electrolyte, and then subjected to the charge/discharge processes, after that it was disassembled and the electrode materials were washed for the AFM studies (26–28). This study is ex-situ as the AFM measurements are conducted on the disassembled battery components which have subjected to the charge/discharge cycles, therefore, the process of the evolution of the surface change cannot be observed. Because of this reason, various in-situ methods are developed. Electrochemical AFM (EC-AFM) is one of the popular tools for such studies.

In-Situ Electrochemical AFM (EC-AFM) Studies

EC-AFM is a versatile platform for electrochemical experiments combining with the high resolution AFM imaging capability by using a special-designed electrochemical cell. Generally speaking, various electrochemical processes such as deposition, oxidation/reduction, corrosion, and mass transfer of metals and other materials can be investigated using EC-AFM technique. More significantly for battery materials, nanoscale topographical changes induced by electrochemical reactions can also be precisely monitored simultaneously, *i.e.*, *in-situ* studies of the surface topographic changes induced by Li-ion intercalation/de-intercalation between the anode and cathode, this can provide deeper insight into the electrochemical mechanisms of the Li-ion battery.

As shown in Fig.5, an electrochemical cell (EC-cell) should be integrated with the third-party potentiostat through the junction box to control all electrochemical processes. For the purpose of both measuring and controlling of the potential,

at least a three-electrode EC-cell is needed, *i.e.*, a working electrode (WE), or indicator electrode, which is the electrified interface to be studied; the reference electrode (RE), which can maintain a well-defined reference potential from which the potential of the WE can be both determined and controlled; the third electrode is the counter or auxiliary electrode (CE) which is used as a current source or sink, enabling the potentiostat electronics to control the WE potential with respect to that of the RE. The AFM probe is then used to scan the surface to obtain the surface morphology changes during the electrochemical reactions controlled by the potentiostat. The evident advantage of EC-AFM is the capability to characterize batteries with liquid electrolyte; hence it can also be used for various energy storage materials in addition to the Li-ion batteries.

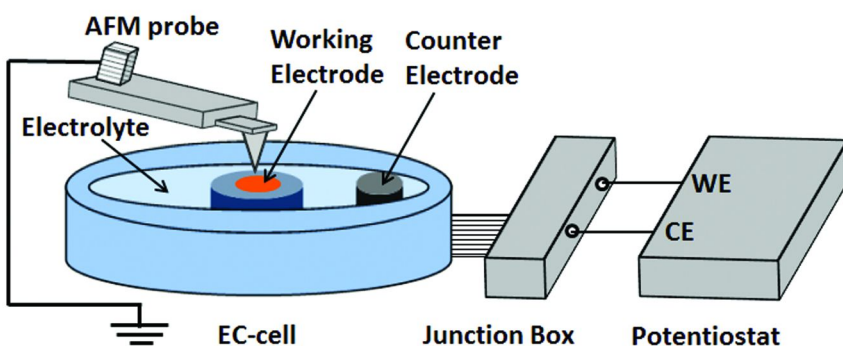


Figure 5. Schematic drawing of EC-AFM set-up for *in-situ* characterization of Li-ion battery.

In recent years, *in-situ* EC-AFM has been extensively applied to investigate the surface topographical changes of various electrode materials in Li-ion battery during charge/discharge processes. Many electrode materials, such as lithium metal, composite graphite, V_2O_5 , $LiCoO_2$ and $LiMn_2O_4$, have been studied (29–38). In addition, the decomposition of the liquid electrolyte, the formation of the so-called solid electrolyte interphase (SEI) film, and the related interfacial phenomena during the electrochemical cycling can be also investigated by this *in-situ* EC-AFM technique (39). For example, an *in-situ* EC-AFM study was conducted on composite graphite anode in Li-ion battery by Jeong et al. (34). Figure 6 shows the observed surface morphology changes of the composite graphite electrode during the charge/discharge cycling with constant current density of $30 \mu A cm^{-2}$ in $1 M LiClO_4/EC+DEC$ liquid electrolyte. At the open circuit potential of 3.3 V before charging [Fig.6(b)], the surface consists of graphite flakes with clear edges. As shown in Fig.6(c), when the open circuit potential reaches to 1.4 V, the graphite particle edge begins to curl up. With the decrease of open circuit potential during charging process [Figs.6(d) and 6(e)], the curling up of particle edge continues further. At the open circuit potential of 0.8 V [Fig.6(f)], the particle edge even swells and partially exfoliates. It is found that the significant topographic change is observed evidently in the vicinity of particle

edge. It was concluded that the surface topographical changes, including curling, swelling and exfoliation, were mainly attributed to the intercalation of Li-ion into graphite layers (34). This example clearly demonstrates the application and the results of the EC-AFM for *in-situ* topographic studies of the battery materials.

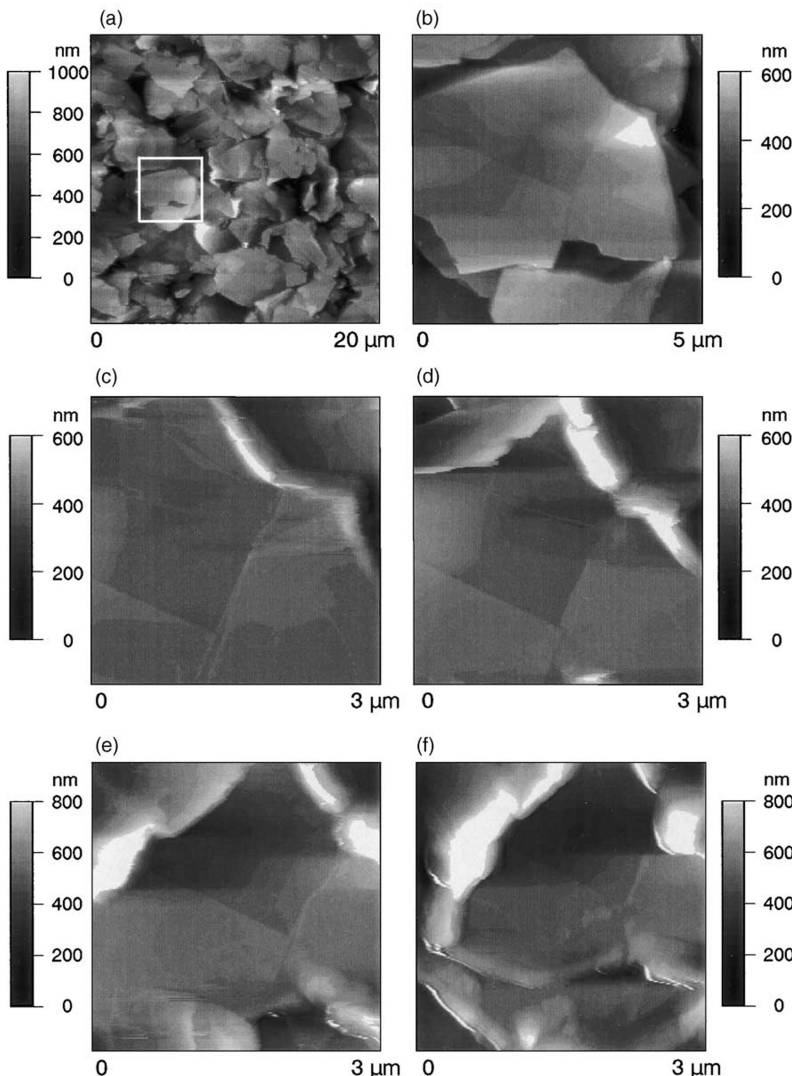


Figure 6. In-situ topography images of composite graphite electrode surface obtained at the open circuit potential: (a and b) 3.3V, (c) 1.4V, (d) 1.1V, (e) 1.0V and (f) 0.8V during constant current charging at $30 \mu\text{Acm}^{-2}$ in 1 M LiClO_4 /(EC+DEC) liquid electrolyte. (Reprinted from Ref. (34), Journal of Power Sources, Vol.119-121, Jeong et al, AFM study of surface film formation on a composite graphite electrode in lithium-ion batteries, Figure 1, page 556, Copyright (2003), with permission from Elsevier).

In-Situ Electrostatic Force Microscopy (EFM) Studies

Although most of previous in-situ SPM studies on Li-ion batteries were conducted using EC-AFM technique, *in-situ* EFM (Electric Force Microscopy) can be also used to simulate the charge/discharge cycling processes in Li-ion battery by inducing the reversible Li-ion diffusion through the biased SPM tip (usually is Si tip with conductive coatings such as Pt, Au, PtIr *etc*), whereas at the same time, the SPM tip scans and monitors the changes of the surface topography, volume and phases of the electrode surface (40). In the EFM set-up, the cantilever is usually driven to oscillate near its resonance above the surface while a bias is applied between the tip and the sample surface, a force gradients between the tip and the sample is generated and cause a shift in the phase between the drive and response of the cantilever, a lock-in amplifier is then used to detect the phase lag between the tip and sample as a result of an electric field gradient. It is noted that EFM can map electric properties of a sample surface by measuring the electrostatic force between the surface and a biased AFM cantilever. In addition, during EFM operation, a direct voltage (DC) can be applied to the sample surface through the conductive tip scanning over the sample surface. This technique is especially useful for all-solid-state Li-ion battery (40). Figure 7 shows the schematic drawing of the in-situ EFM measurement on all-solid-state thin film Li-ion battery as well as the cycled bias used in the study by Zhu *et al.* (40). In that work, an effective battery area covering the entire cathode/electrolyte/anode structure was scanned by SPM tip under the ambient condition while the substrate was electrically connected to the SPM system [Fig.7(a)] (40). It is well known that, due to different electrochemical potentials of lithium ions in the two electrodes, Li-ion diffusion from the cathode through the electrolyte into the anode can be compensated by the transfer of electron from the anode to the cathode through the external circuit. When a positive bias is applied to the anode surface, positive potential difference is created between the anode and cathode, this situation is similar to the case when the battery is charged, therefore, Li-ions are forced to diffuse from cathode through the electrode into the anode. On the other hand, when negative bias is applied through the EFM tip on the anode surface, the negative potential between the anode and cathode is built, hence the Li-ions are forced to leave the anode and diffuse through the electrolyte back into cathode, providing situation similar to the discharge process. Therefore, a series of biases is applied through the conductive tip in contact mode (dc-writing) EFM and this induces the cyclic Li-ion diffusion, this is followed by SPM scanning at the biased region [Fig.7(b)]. Additionally, the advantage of using this symmetrical voltage (± 3 V) is to ensure that the total amount of Li-ion diffusion within the battery is reversible and consistent.

Figure 8 shows the results of in-situ EFM measurements of surface morphology, amplitude and phase changes on TiO_2 thin film anode within all-solid-state thin film Li-ion battery subjected to cyclic voltages (40). It is found that the as-deposited TiO_2 film consists of scale-shaped grains with average grain size less than 30 nm [Fig.8(a)]. After the first Li^+ insertion cycle by applying +3 V, thin film surface has become flat since the nano-sized grains grow and expand almost in all directions with the grain boundaries contacting seamlessly [Fig.8(b)].

This is mainly attributed to the Li⁺ diffusion from LiNi_{1/3}Co_{1/3}Mn_{1/3}O₂ cathode into TiO₂ anode under the electric field. During the first Li⁺ extraction cycle by applying -3 V, the shrinkage of thin film anode can be observed evidently as Li⁺ is removed from the anode; and the gaps between the inter particles have become sharper [indicated by the black arrows in Fig.8(c)]. During the second Li-ion insertion cycle, thin film anode expands along the original gap lines as Li-ion is inserted back into the thin film anode [Fig.8(d)], and followed by an obvious contraction during the second Li⁺ extraction cycle [Fig.8(e)]. In addition, the subsequent Li-ion insertion/extraction cycles show similar topography changes, *i.e.*, expansion/shrinkage of particle gaps or boundaries, which become smaller through lithiation and larger and deeper through de-lithiation. It is proved that the reversible morphology changes are not surface damage made by scratch of the EFM tip, but attributed to the cyclic processes of the Li-ion diffusion. This insertion/extraction behavior of Li-ion is similar to the findings on graphite anode by Koltypin *et al.* (35). Therefore, similar to traditional electrochemical measurements, the local cyclic biases applied through SPM tip can also induce analogous Li⁺ diffusion and morphology changes, providing opportunities to in-situ model the charge/discharge processes at the length scale compatible to the characteristic microstructures of the electrode materials.

In addition to the surface topographic changes, the phase images also show interesting changes with the applied bias cycles (40). The phase image reflects the variations of the compositions and other surface properties, such as surface energy. The differences in the chemical compositions and surface properties near the sample surface lead to phase angle shift and hence reflected on the phase images. During the in-situ EFM images, the changes in the phase images are clearly visible. For example, there were almost no obvious contrasts in the phase image for as-deposited anode film [Fig.8(a)], however, a new phase appeared [green colour phase in the phase image of Fig.8(b)] after the battery was first polarized to +3V. It was also found that this new phase disappeared after the battery was polarized to -3V [Fig.8(c)], and re-appeared again when the battery was re-polarized to +3V [Fig.8(d)] and disappeared again at -3V (2nd time) [Fig.8(e)]. These changes show that the phase images from the in-situ EFM can be used to identify the phase transition of the battery materials during the charge/discharge processes. It was also noted that some residual phases were located at some grain boundaries when the battery was polarized to -3V, this most likely indicated that where and how the Li-ion might be trapped in the battery during the charge/discharge processes.

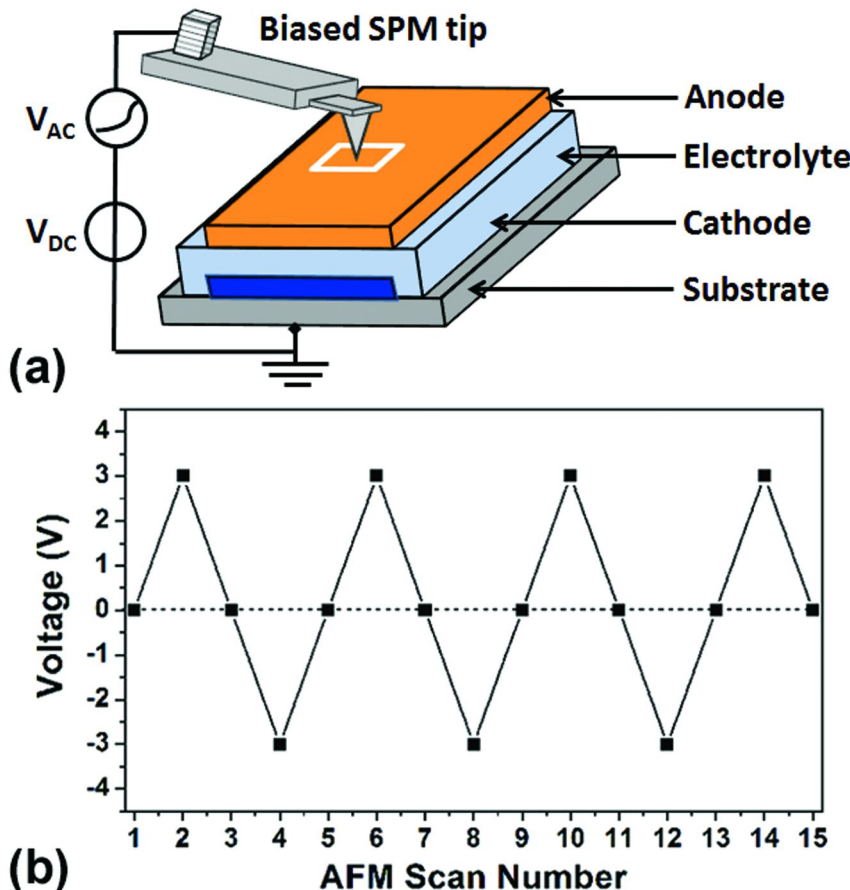


Figure 7. (a) Schematic of in-situ EFM measurement on all-solid-state thin film battery, which is the overlapping portion of anode/electrolyte/cathode (indicated by white frame); and (b) cyclic electrical field applied to the battery vs. SPM scan number.

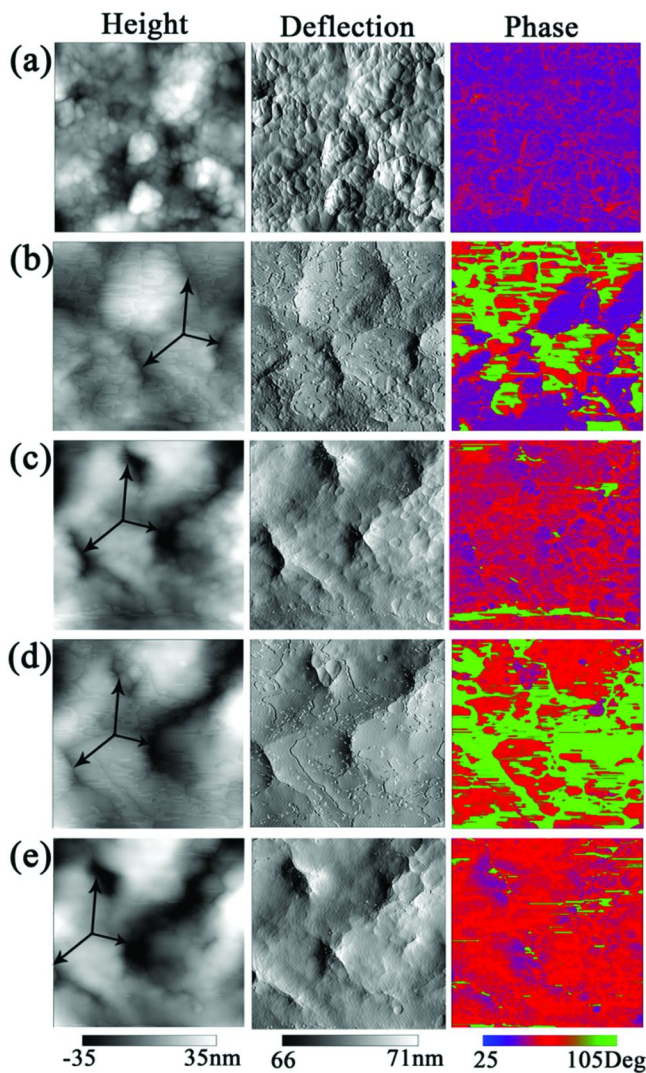


Figure 8. *In-situ* topography, amplitude and phase images of TiO_2 thin film anode in lithium ion microbattery polarized to cyclic potential: (a) 0V; (b) +3V; (c) -3V; (d) +3V (2nd time), and (e) -3V (2nd time). (Reprinted from Ref. (40), Journal of Power Sources, Vol.197, Zhu et al, *In situ* study of topography, phase and volume changes of titanium dioxide and in all-solid-state thin film lithium-ion battery by biased scanning probe microscopy, Figure 8, page226, Copyright (2012), with permission from Elsevier).

Surface Electrical Properties Studies by KPFM and c-AFM Techniques

Kelvin Probe Force Microscopy (KPFM) Studies

Studies on surface electrical properties, such as contact surface potential and charge distribution, can give new insights into the aging mechanisms of Li-ion batteries. KPFM is a non-contact SPM technique and widely used to quantitatively measure surface potential distribution at nanoscale in various functional materials, such as semiconductors, multi-ferroelectrics and organic materials (41). Generally speaking, the surface potential measured by KPFM is closely related to various physical phenomena depending on the electrical conductivity of samples. For insulators, surface potential reflects surface charge distribution in real space since charges cannot flow between the sample and the tip. For semiconductors, surface potential should be interpreted by both Fermi energy level shift and charge trapping effect (42). Due to the well-known space-charge-layer (SCL) near the semiconductor surface, the surface charge screening phenomenon can also affect the local electrostatic properties significantly. Due to the charge screening, the positive (negative) charges rearrange themselves around the negative (positive) charges to minimize the total electrostatic energy. Finally, for conductive samples, surface potential reflects the local work function difference between the sample and the tip since charges can flow freely from the sample to the SPM tip.

Figure 9 shows the operation principle of the KPFM measurement. In the KPFM operation, two-trace scanning is performed; the first scan is used to generate the topographic image, which is similar to the standard tapping mode AFM. The second scan is conducted in non-contact mode by lifting the conductive tip up to a fixed distance (ΔZ) along the first trace, in order to measure the surface potential difference between the conductive tip and sample surfaces. Due to the difference in the work functions between the electrically connected sample (Φ_{sample}) and the conductive tip (Φ_{tip}), an electrostatic contact potential difference (V_{CPD}) can be created and defined as (43):

$$V_{CPD} = \frac{\Phi_{tip} - \Phi_{sample}}{e} \quad (1)$$

During KPFM operation, an oscillating AC voltage (V_{AC}) is applied to the tip during the second scan, resulting in an electrostatic force that is proportional to the potential difference (V_{CPD}) between the tip and the sample surface, which can be detected by a lock-in amplifier (Fig. 9). When an AC voltage is applied to produce an electrostatic force, the tip and sample surface can be modeled as a parallel plate capacitor. In this case, the electrostatic force between the two plates is proportional to the square of the applied voltage as:

$$F = \frac{1}{2} \frac{\partial C}{\partial z} V^2 \quad (2)$$

Therefore, the total potential difference between the tip and the sample surface is the sum of the oscillated AC voltage (V_{AC}), the contact potential difference to measure (V_{SP}), and the DC voltage (V_{DC}) applied:

$$V = V_{SP} + V_{DC} + V_{AC} \sin \omega t \quad (3)$$

If Eq.(3) is substituted into Eq.(2) and rearranges the resulting equation, a new equation can be obtained as:

$$F = \frac{1}{2} \frac{\partial C}{\partial z} \left[\left[(V_{DC} - V_{SP})^2 + \frac{1}{2} V_{AC}^2 \right] + 2 \left[(V_{DC} - V_{SP}) V_{AC} \sin(\omega t) \right] - \left[\frac{1}{2} V_{AC}^2 \cos(2\omega t) \right] \right] \quad (4)$$

There are three force terms summed together. The first force (V_{DC}) is static with no frequency dependence. The second force (V_{SP}) occurs at the drive frequency ω . The third force (V_{AC}) oscillates at twice the drive frequency 2ω . Therefore, if an external applied voltage (V_{DC}) is adjusted by a potential feedback loop control to nullify the oscillation electrostatic force, the amount of this compensating voltage (V_{DC}) is just equal to the work function difference between the tip and the sample ($V_{DC} = V_{SP}$), thus, yielding the surface potential map of sample surface (41, 44, 45). It is noted that the measured surface potential is equal to the work function difference only if the KPFM measurements are performed in vacuum condition. In ambient conditions, the surface screen charge and polarization charge of materials also play significant roles in potential mapping.

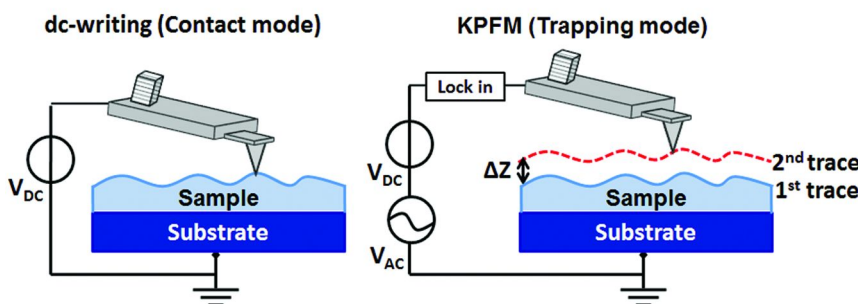


Figure 9. Operation Principle of Kelvin Probe Force Microscopy (KPFM: left image –first scan; and right image –second scan.

Although KPFM technique has been widely used to characterize various physical phenomena in semiconductors, ferroelectrics, organic materials, as well as in wear and corrosion studies, its applications in lithium-ion batteries are still limited. Using ex-situ KPFM technique, Nagpure *et al.* has investigated the surface potential of fresh and aged LiFePO₄ cathode from cylinder Li-ion batteries, establishing a preliminary relationship between the surface electrical modification and battery aging phenomena (46). It was found that the aged LiFePO₄ cathode showed lower surface potential compared to that of the un-aged sample under

the same applied bias, and indicated smaller charge sustaining capacity after the charge/discharge processes. The surface potential change is mainly attributed to the changes in physical and chemical properties of the electrode materials, such as the phase of surface layer, particle coarsening, nanocrystalline deposits and loss of carbon coating. Recently, by combining EFM and KPFM techniques, the surface potential change of all-solid-state thin film Li-ion battery due to the bias-induced Li⁺ diffusion were in-situ observed successfully (47). Figure 10(a) shows the surface potential shift of the TiO₂ anode film in comparison with that of the single layer TiO₂ film as well as the corresponding applied cyclic voltage (47). For TiO₂ thin film anode and single layer TiO₂, positive (negative) potential is induced by positive (negative) polarization, due to the upward (downward) shifting of Fermi level under the applied bias. For single layer TiO₂, both positive and negative polarization result in almost equivalent increment/reduction in surface potential during the first cycle, indicating similar amounts of positive and negative screening charges. However, for TiO₂ thin film anode in battery structures, the reduction of surface potential after negative polarization is much smaller than that of the increment of surface potential after positive polarization. This phenomenon can be explained by the less negative charge trapping sites due to Li-ion extraction. Figure 10(b) shows surface potential hysteresis loop formed on TiO₂ thin film anode, where the potential increases by a positive bias and decreases by a negative bias. It was observed that the surface potential decreased after three cycles, indicating the surface electrical property modification involving Li-ion intercalation/de-intercalation processes (47).

Conductive AFM (c-AFM) Studies

Aging studies on Li-ion batteries are usually based on the current measurements using various electrochemical technologies, including potentiostat and galvanostatic intermittent titration techniques (PITT and GITT), cyclic voltammetry (CV) and electrochemical impedance spectroscopy. Therefore, current-based SPM technique can provide opportunities to extend the current measurement on battery materials to micro- to nanoscopic levels. In conductive AFM (c-AFM) or current-sensing AFM (CSAFM) measurements, the conductive SPM tip acts as a moving electrode and image the local current response to the applied DC bias between the SPM tip and the grounded sample, and this provides valuable information on local surface conductance distribution around the sample surface. In addition, c-AFM can simultaneously map the topography and current response of sample surface, allowing the precise correlations between the topographical features and the conductivity.

The conductive AFM usually consists of a specially-designed cantilever holder or sample holder, which includes a transimpedance amplifier. Standard values of the gain of amplifier range from the orders of 10⁷ to 10⁹ volts/amp. The voltage is applied through either a conductive tip or sample holder whereas the sample or tip is grounded so that to complete the current loop. In principle, the conductive AFM measures the current using an electric circuit, according to the Ohm's equation:

$$V = IR \quad (5)$$

where V is the DC voltage applied between the tip and the sample, R is the resistance of the entire circuit, and I is the current passing through the tip and the sample, which can vary from the order of few pA up to several nA range. All images in the c-AFM measurement are obtained in the contact mode hence the tip must have good wear resistance.

Kuriyama *et al.* have correlated the surface morphology change with current response in spinel LiMn_2O_4 cathode (48). The schematic of AFM measurement is shown in Fig.11(a). In this study, the negative bias was applied to the conductive AFM tip to attract Li-ion toward LiMn_2O_4 cathode surface. In this case, Li-ion is extracted from the tetrahedral sites of the inner layer to the empty octahedral sites in LiMn_2O_4 lattice, resulting in Jahn-Teller phase transformation accompanying with the surface topography change and current increase. It was found that the current is gradually changed with the increase of tip bias, and increased abruptly at around 5.5 V. The peak value was observed at around 6.5 V, indicated electrical conduction related to the movement of Li^+ toward LiMn_2O_4 surface [Fig.11(b)]. Figure 11(c) showed the AFM topographic images taken under different bias voltages. As a result, surface morphology shows no significant change till 5.5 V. However, the whole surface is covered by scale-shaped grains at around 6.5 V. In summary, the evident surface morphology change corresponding to the current peak was induced by the Jahn-Teller instability in spinel LiMn_2O_4 cathode (48). Furthermore, several researchers have also applied c-AFM or CSAFM technique to correlate the surface conductance loss to the capacity fading of battery materials, as well as to investigate the variability in current response between different grains and grain boundaries (49–51). Figure 12 shows surface topography and current images of as-deposited and 50th cycled LiMn_2O_4 thin film cathode at 3.0 V tip voltage. As a result, the current image of as-deposited sample shows excellent electronic conductivity and only few insulating area. The current response has slightly decreased after 50 charge/discharge cycles. This reduction of surface conductance is closely related to the observed capacity fading as well as the degradation of electrochemical activity.

In summary, c-AFM technique is a very important and powerful tool to explore the electronic conductivity and surface electrical properties for electrode materials in Li-ion batteries. However, the main limitation of these current-based techniques is the extreme sensitivity to surface state and environmental conditions, such as humidity. In addition, c-AFM cannot detect ionic currents to explore ionic conductivity, which is very significant for battery materials. This has led to the development of Electrochemical Strain Microscopy (ESM) technique, in which will be discussed in the next section.

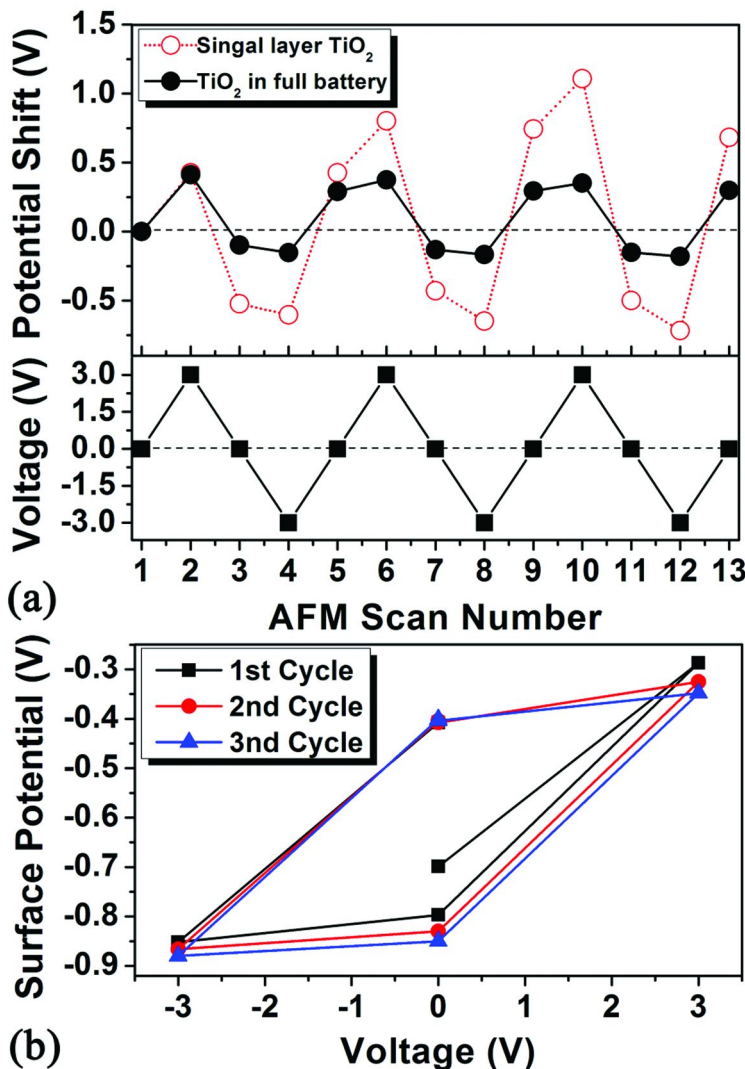


Figure 10. (a) Surface potential shift vs SPM scan number for both TiO_2 thin film anode and single layer TiO_2 ; and (b) Surface potential loops of TiO_2 thin film anode under the reversible electrical field. (Reprinted from Ref. (47), Journal of Applied Physics, Vol.111, Zhu et al, In-situ nanoscale mapping of surface potential in all-solid-state thin film Li-ion battery using Kelvin probe force microscopy, Figure 4, page 063723-4, Copyright (2012), with permission from American Institute of Physics).

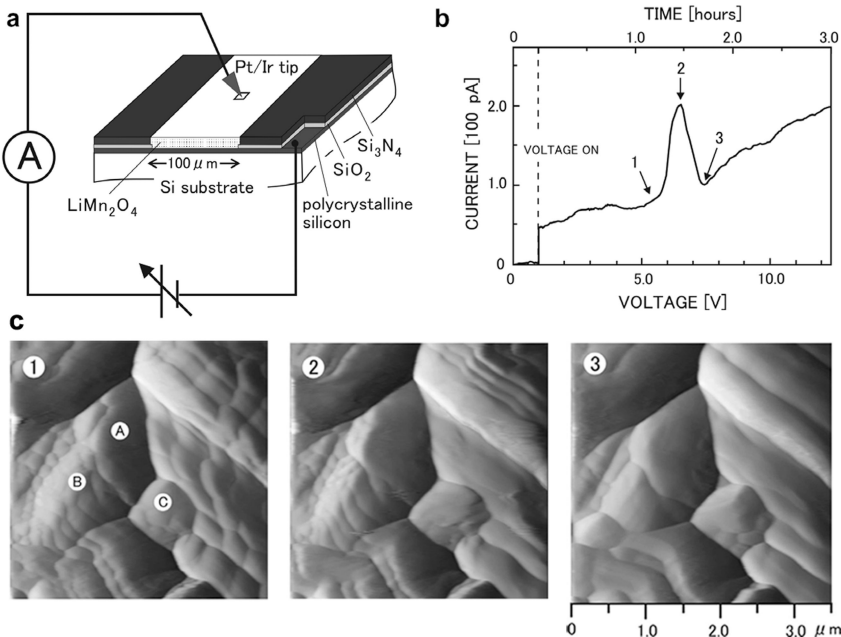


Figure 11. (a) Schematic of the c-AFM measurement. (b) Bias voltage dependent of the tip current measured at each point which the AFM tip passed through while scanning the $3.5 \times 3.5 \mu\text{m}^2$ area on spinel LiMn_2O_4 surface. (c) AFM images taken under different bias voltage: (1) 5.5V, (2) 6.5V and (3) 7.5V as indicated in (b). (Reprinted from Ref. (48), *Surface Science*, Vol.601, Kuriyama et al, *Atomic force microscopy study of surface morphology change in spinel LiMn_2O_4 : possibility of direct observation of Jahn-Teller instability*, Fig.2, page 2257 and Figure 4, page 2259, Copyright (2007), with permission from Elsevier. The figures are re-arranged to fit the lay-out of this chapter).

Ionic Diffusion Studies by Electrochemical Strain Microscopy (ESM) Technique

Electrochemical Strain Microscopy (ESM) is a new SPM technique developed in recent years and it is capable of probing electrochemical reactivity and ionic diffusion in solids at micro- to nano-meter levels (52–56). Therefore, ESM is an ideal and valuable tool for a broad range of electrochemical applications, such as lithium ion batteries, solar cells and fuel cells. The operation principle of ESM is very similar to the well-known Piezoresponse Force Microscopy (PFM) with the major difference of the bias-deformation coupling mechanisms. PFM measures the deformation induced by an applied electrical field due to the piezoelectric properties of the materials, while ESM detects the electrochemical

strain or deformation originated from the bias-induced ionic diffusion and the related volume change in the battery materials (57–60). The operation principle of ESM technique is illustrated in Figure 13. In the ESM approach, bias is applied through the cantilever tip which contacts with the sample surface. The applied bias induces a concentrated electrical field in a nanoscale volume of battery material, leading to the changes of electrochemical potential of Li-ion, and thus the ionic diffusion and redistribution in this small volume. The changes in ionic concentration can result in the molar volume change and oscillatory surface displacement of the battery material. Using a lock-in technique, the amplitude of oscillatory displacement is detected as the local electrochemical strain which is directly related to the Li-ion diffusion. This technique has applied to various battery materials and the name (ESM) was given by the research group from Oak Ridge National Laboratory (ORNL) (56–60).

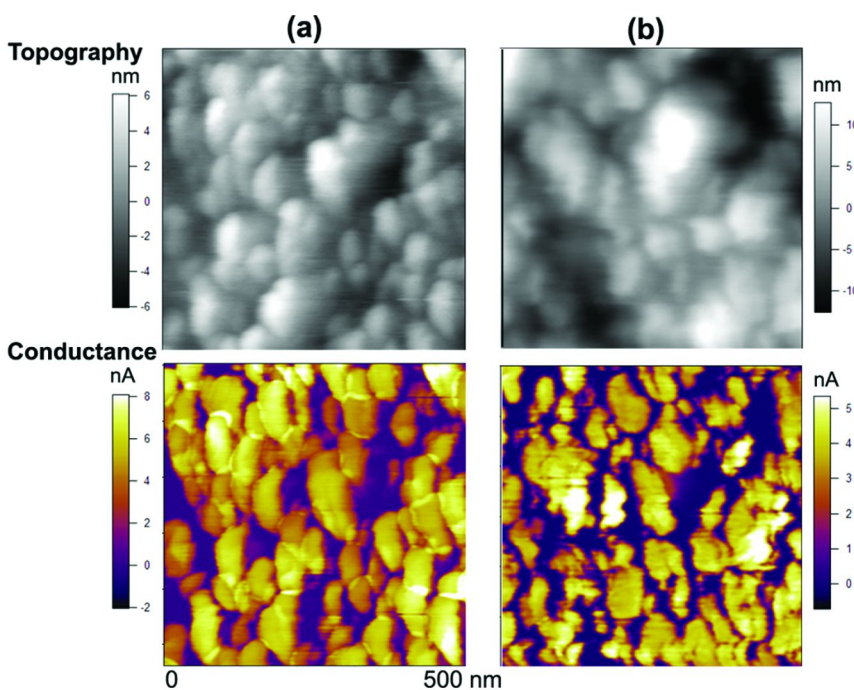


Figure 12. Surface topography and current images of LiMn_2O_4 thin film cathode at 3.0 V tip voltage: (a) as-deposited sample; and (b) cycled sample after 50 cycles.

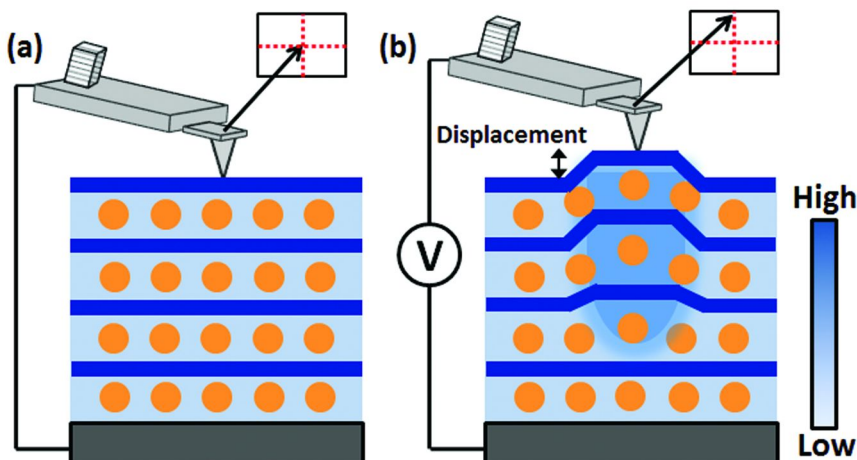


Figure 13. Operation principle of Electrochemical Strain Microscopy (ESM): left image – before applying local bias; and right image: after applying the local bias.

In addition, in order to enhance the signal and track the response on contact resonance frequency, ESM technique can be used together with multi-frequency AFM technique, such as Band Excitation (BE) method to form a BE-ESM image and analysis (57, 61–65). The BE approach is a new multifrequency SPM approach and can provide an alternative to traditional single frequency and frequency-sweep methods. During BE-ESM measurement, the cantilever is excited using a synthesized digital signal which spans a continuous band of frequencies; and the mechanical response can be monitored at all frequencies within the frequency band simultaneously (53). In such a way, the cross-talk between the topography and properties images can be avoided. This band of frequencies is usually with the contact resonance frequency as the center. As a result, the cantilever responses (amplitude vs. frequency and phase vs. frequency) are detected and Fourier transformed at each point, and stored as 3D data arrays (x, y, amplitude and x, y, phase) using a high-speed data-acquisition system. All response curves are fitted using the damped simple harmonic oscillator (SHO) model, which is described by three independent parameters namely resonant frequency (ω_0), amplitude at the resonance (A_{max}), and quality factor (Q) that describes the energy loss in the system (66, 67):

$$A(\omega) = \frac{A_{max} \omega_0^2 / Q}{\sqrt{(\omega_0^2 - \omega^2)^2 + (\omega_0 \omega / Q)^2}} \quad (6)$$

where ω_0 and A is closely related to the tip-sample force gradient and the driving force, respectively. In addition, the phase frequency response can be expressed as:

$$\tan \varphi(\omega) = \frac{\omega_0 \omega}{Q(\omega_0^2 - \omega^2)} \quad (7)$$

In addition to the electrochemical strain, surface elasticity and energy dissipation mapping can also be obtained by using BE-ESM measurement, providing valuable information on surface mechanical properties as well as their correspondence with the microstructure of the battery materials. ESM can be further used to obtain three-dimensional image, i.e., Vector ESM. The full surface displacement in vector ESM is a vector has three components, which can be determined by both cantilever deflection and torsion measurements. Using this method, both vertical (out-of-plane) and lateral (in-plane) surface displacements for the electrode materials with different crystal orientations or microstructure heterogeneous can be obtained.

Furthermore, BE-ESM can be cooperated with spatially-resolved spectroscopic techniques, including time spectroscopic and voltage spectroscopic techniques. Using these methods, the electrochemical reaction and Li-ion transportation can be separated. In ESM time domain spectroscopy, the ESM signal is measured after the application of a single voltage pulse to the probe, and the response is measured over a long period which is comparable to the diffusion time of Li-ion within the battery (68). This qualitative spectroscopic method is somewhat reminiscent of the widely-used potentiostatic and galvanostatic electrochemical techniques. Better yet, the ESM measurement can be used to investigate the time-dependent electrochemical behaviour at nanoscale. In ESM voltage domain spectroscopy, the voltage pulse of increasing and decreasing amplitude is applied to the probe, and the resultant surface deformation is measured after each pulse. In this case, the measured ESM signal as a function of bias pulse magnitude can provide information on bias-induced electrochemical reaction and ionic diffusion.

Figure 14 shows an example of ESM time spectroscopy of amorphous Si anode within an all-solid-state Li-ion battery (53). The evolution of ESM activity on the anode surface at different cycling stages can be observed clearly [Figs.14(a) to (d)]. It is noted that the defect-related “hot-spots” gradually disappear with the increase of cycling number, while the Li-ion concentration at grain boundaries increases evidently. This phenomenon is mainly attributed to the Li-ion accumulation at boundary-like features. In addition, the evolution of ESM displacement hysteresis loops at the grain boundaries is illustrated in Fig.14(e). The area under the hysteresis loop opening is proportional to the changes in Li-ion concentration directly, which is induced by the applied voltage cycle. As a result, the area of loop opening increases with the increase of cycling number, providing a direct observation of Li-ion diffusion and distribution in Si anode at nanoscale. In summary, ESM technique is an ideal tool for exploring the relationship between the electrochemical activity and nanostructure of electrode materials, which is critical in design and fabrication of Li-ion batteries.

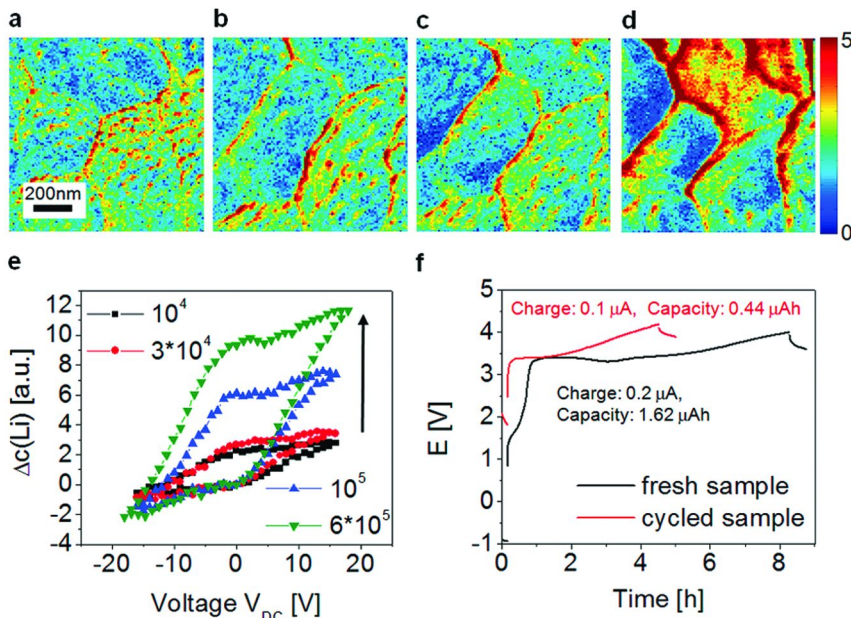


Figure 14. Evaluation of displacement loop opening maps after (a) 10^3 , (b) 10^4 , (c) 3×10^4 and (d) 10^5 cycles. (e) Strain hysteresis of the boundary regions for increasing cycle number. (f) Charging curves of fresh and high frequency cycled battery. (Reprinted with permission from Ref. (53), Balke et al, Real space mapping of Li-ion transport in amorphous Si anodes with nanometer resolution, *Nano Letters*, Vol.10, Figure 4, page 3423. Copyright (2010) American Chemical Society).

Future Perspectives of SPM Studies on Li-Ion Battery

Local Mechanical Property Studies

Besides the electrochemical issues, mechanical properties of electrode materials are also very significant in the optimization and prediction of performance and reliability of Li-ion batteries. However, the in-depth understanding and reliable quantification of mechanical properties at nanoscale is still very challenge. These issues have not been studied extensively for battery materials. In recent years, the high spatial resolution AFM techniques provide mechanical information on very small length scale, establishing the relationship between the local mechanical properties and microstructural features of battery material. Based on tip-sample dynamics, there are a number of non-destructive AFM techniques, including Contact-Resonance AFM (CR-AFM), Atomic Force Acoustic Microscopy, Ultrasonic Force Microscopy, Friction Force Microscopy, Torsional Harmonic Dynamic Force Microscopy, and Heterodyne

Force Microscopy (69, 70). Among of these, CR-AFM is the most practical technique, due to its minimal instrumentation and direct result interpretation.

In general, CR-AFM is used to excite one or more resonant vibrational modes of the AFM cantilever or sample in contact mode. Therefore, CR-AFM is conducted using a high frequency contact resonance sample holder, which includes a smart electronics module and a sample holder positioned in the AFM scanner. The sample should be glued on the sample holder very well using the special epoxy. This contact resonance sample holder can provide a wide-band and frequency independent excitation of the sample, allowing the evaluation of mechanical properties of materials. In the CR-AFM measurements, the contact resonance frequency is a measurement of the conservative tip-sample interactions, which can be converted into local tip-sample contact stiffness, by considering the cantilever-sample contact geometry and the dynamics of clamped-spring coupled cantilever. In addition, the quality factor (Q-factor) is a measurement of the energy dissipation due to the tip-sample interactions. In another word, the measured contact resonance frequency can qualify the material's ability to store the energy elastically, *i.e.*, storage modulus (E'), while Q-factor can qualify the material's ability to damp out energy, *i.e.*, loss modulus (E''). The phase vector incorporating these two capabilities is the complex dynamic modulus (E^*), namely Young's modulus. Therefore, CR-AFM can provide isolated information on conservative elastic properties and dissipative damping properties of sample surface at nanoscale simultaneously.

CR-AFM has been applied for both local point measurements as well as surface mapping of the elastic and viscoelastic properties of the materials. Using this technique, local elastic properties of various materials have been quantified successfully, such as piezoelectric ceramics, polymer materials, thin films and nanotubes (71–76). However, this powerful technique has not been used in the research and characterization of the battery materials to determine the local mechanical degradation during the electrochemical processes. Figure 15 shows a recent preliminary study (unpublished) using the CR-AFM technique to characterize the changes of surface elasticity and energy dissipation of the LiMn_2O_4 thin film cathode before and after charge/discharge cycles (50 cycles), whereas the changes of contact resonance frequency (conservative energy or surface elasticity) and Q-factor (dissipation energy) are obvious [Figs.15(a) and (b)]. It can be seen that the resonance Q-factor mapping shows strong variations between the grains and grain boundaries, corresponding very well to the surface topography features. On the other hand, Q-factor decreases at grain boundaries (red color) and increases at area within individual grains (blue color), indicating higher energy dissipation at the topographical depressions and lower energy dissipation at the protrusions. The contact resonance frequency image indicates the changes of the surface elasticity. More areas in the resonance frequency image have become darker after 50 charge/discharge cycles, indicating lower contact stiffness and storage elastic modulus in those areas. This result is consistent with the previous results from nanoindentation studies by Zhu *et al* (26–28), but more detail can be revealed by using the CR-AFM technique, whereas the nanoindentation only reveals an average surface elastic modulus value. This preliminary study shows that the CR-AFM technique is a very useful

and promising technique to detect the changes related to the surface mechanical properties of the battery materials, this information has not been extensively studied for battery materials yet.

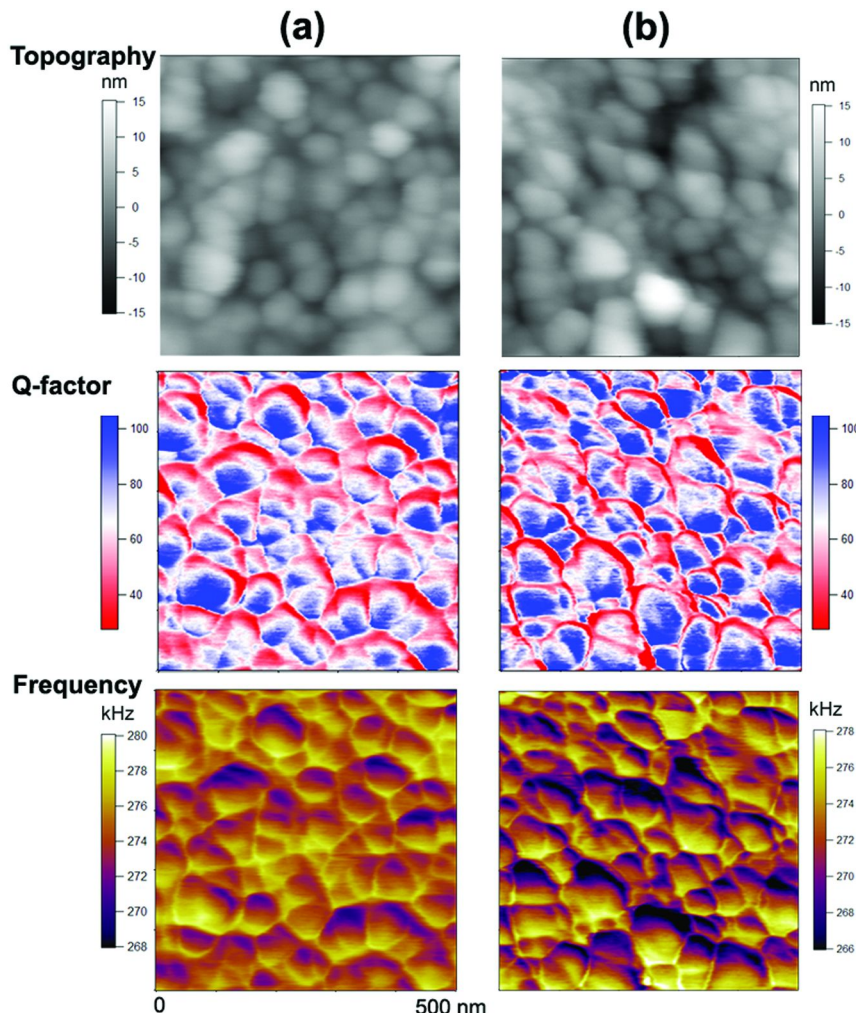


Figure 15. CR-AFM image of the cathode materials before (a) and after (b) charge/discharge cycles.

Combining Various SPM Techniques To Study the Coupling Effects

The electrochemical aging mechanisms in Li-ion battery are very complex processes with many interrelated factors acting together at the same time. Therefore, a single SPM technique such as we discussed so far (AFM, EFM, KPFM, c-AFM, ESM, EC-AFM, CR-AFM *etc*) may not be able to completely capture all of the electrochemical phenomena. Hence, a combination of several

SPM techniques is necessary in order to have a comprehensive understanding of the electrochemical processes in battery system.

It is well known that the electrode material in Li-ion battery is a mixed electronic/ionic conductor. Therefore, the capacity fading is attributed to the degradation of both electronic transportation and ionic diffusion capabilities. However, it is still difficult to make a clear distinction between these two contributions to the battery aging. Currently, the combination of ESM and c-AFM techniques provides the opportunities to investigate the electronic and ionic transportation separately. In particular, ESM contrast is closely related to Li-ion concentration distribution, whereas the c-AFM contrast is induced by the current flow and electron transportation. In addition, the changes in Li-ion concentration during BE-ESM measurement include both ionic diffusion (concentration driven) and ionic migration (field driven). Among these, the electrical field driven ionic migration largely depends on the sample electronic conductance. Higher sample electronic conductance can result in smaller effective potential drop, and thus lower field driven force for Li-ion migration. Therefore, through the combination of these two SPM techniques, the coupling effect between the ionic and electronic diffusion can be investigated successfully, improving the understanding of electrochemical processes and aging mechanisms underpinning Li-ion battery operation.

Summary

In this chapter, we have reviewed various Scanning Probe Microscopy techniques (AFM, EC-AFM, KPFM, c-AFM, ESM and CR-AFM) and their applications in electrochemical studies on rechargeable Li-ion batteries. The results observed from SPM images and analysis, such as changes in surface topography, electronic/ionic conductivity and other electrochemical phenomena at nanoscale, are closely related to the changes in the properties of Li-ion batteries, such as the increases in impedance and capacity fading. Therefore, these SPM techniques, including both ex-situ and in-situ techniques, provide unique opportunities to investigate the electrochemical functionalities and aging mechanisms of Li-ion battery at nanoscale, paving new ways for the performance improvement and design optimization for energy storage systems. It is also believed that these SPM techniques will be used more and more in the future research and development of the Li-ion batteries and even beyond the Li-ion battery.

Acknowledgments

The authors would like to thank the help and comments from our colleagues during the preparation of this chapter. This work is supported by Ministry of Education, Singapore through National University of Singapore under Academic Research Funds (R-265-000-305-112 and R-265-000-406-112).

References

1. Goodenough, J. B.; Kim, Y. *Chem. Mater.* **2010**, *22* (3), 587–603.
2. Patil, A.; Patil, V.; Wook Shin, D.; Choi, J.-W.; Paik, D.-S.; Yoon, S.-J. *Mater. Res. Bull.* **2008**, *43* (8–9), 1913–1942.
3. Ritchie, A. G. *J. Power Sources* **2004**, *136* (2), 285–289.
4. Wakihara, M. *Mater. Sci. Eng. R* **2001**, *33* (4), 109–134.
5. Tarascon, J. M. *Philos. Trans. R. Soc. A* **2010**, *368*, 3227–3241.
6. Tarascon, J. M.; Armand, M. *Nature* **2001**, *414* (6861), 359–367.
7. Vetter, J.; Nov'ak, P.; Wagner, M. R.; Veit, C.; M'oller, K. C.; Besenhard, J. O.; Winter, M.; WohlfahrtMehrens, M.; Vogler, C.; Hammouche, A. *J. Power Sources* **2005**, *147*, 269–281.
8. Nagpure, S. C.; Bhushan, B. Atomic force microscopy studies of aging mechanisms in lithium-ion batteries. In *Applied scanning probe methods XIII: biomimetics and industrial applications*; Bhushan, B., Fuchs, H., Eds.; Springer: New York, 2009; pp 203–233.
9. Kalinin, S. V.; Balke, N. *Adv. Mater.* **2010**, *22*, E193–E209.
10. Benstetter, G.; Biberger, R.; Liu, D. *Thin Solid Films* **2009**, *517* (17), 5100–5105.
11. Hansma, H. G.; Kim, K. J.; Laney, D. E. *J. Struct. Biol.* **1997**, *119*, 99–108.
12. Jaquith, M.; Muller, E. M.; Marohn, J. A. *J. Phys. Chem. B* **2007**, *111* (27), 7711–7714.
13. Jesse, S.; Lee, H. N.; Kalinin, S. V. *Rev. Sci. Instrum.* **2006**, *77* (7), 073702.
14. Kalinin, S. V.; Bonnell, D. A. *Appl. Phys. Lett.* **2001**, *78* (9), 1306–1308.
15. Kalinin, S. V.; Bonnell, D. A. *Mater. Res. Soc. Symp. Proc.* **2002**, *699*, R1.2.1–R1.2.6.
16. Kalinin, S. V.; Morozovska, A. N.; Chen, L. Q.; Rodriguez, B. J. *Rep. Prog. Phys.* **2010**, *73* (5), 056502.
17. Kalinin, S. V.; Rodriguez, B. J.; Jesse, S.; Maksymovych, P.; Seal, K.; Nikiforov, M.; Baddorf, A. P.; Kholkin, A. L.; Proksch, R. *Mater. Today* **2008**, *11* (11), 16–27.
18. Rohwerder, M.; Isik-Uppenkamp, S.; Stratmann, M. *Electrochim. Acta* **2009**, *54* (25), 6058–6062.
19. Rosenwaks, Y.; Shikler, R.; Glatzel, T.; Sadewasser, S. *Phys. Rev. B* **2004**, *70* (8), 085320.
20. Sorokina, K. L.; Tolstikhina, A. L. *Crystallogr. Rep.* **2004**, *49* (3), 476–499.
21. Snitka, V.; Ulcinas, A.; Mizariene, V. *Mater. Charact.* **2002**, *48* (2–3), 147–152.
22. Chen, J.; Bull, S. J.; Roy, S.; Kapoor, A.; Mukaibo, H.; Nara, H.; Momma, T.; Osaka, T.; Shacham-Diamand, Y. *Tribol. Int.* **2009**, *42*, 779–791.
23. Fleutot, B.; Martinez, H.; Pecquenard, B.; Ledeuil, J. B.; Levasseur, A.; Gonbeau, D. *J. Power Sources* **2008**, *180* (2), 836–844.
24. Patil, A.; Patil, V.; Choi, J. W.; Kim, H. J.; Cho, B. H.; Yoon, S. J. *J. Electroceram.* **2009**, *23* (2–4), 230–235.
25. Song, S. W.; Striebel, K. A.; Reade, R. P.; Roberts, G. A.; Cairns, E. J. *J. Electrochem. Soc.* **2003**, *150* (1), A121–A127.

26. Zhu, J.; Zeng, K. Y.; Lu, L. *Metall. Mater. Trans. A* **2011**, *44* (1) (Supplement), 26–34.
27. Zhu, J.; Zeng, K. Y.; Lu, L. *Electrochim. Acta* **2012**, *68*, 52–59.
28. Zhu, J.; Zeng, K. Y.; Lu, L. *J. Solid State. Electrochem.* **2012**, *16* (5), 1877–1881.
29. Beaulieu, L. Y.; Beattie, S. D.; Hatchard, T. D.; Dahn, J. R. *J. Electrochem. Soc.* **2003**, *150* (4), A419–A424.
30. Beaulieu, L. Y.; Hatchard, T. D.; Bonakdarpour, A.; Fleischauer, M. D.; Dahn, J. R. *J. Electrochem. Soc.* **2003**, *150* (11), A1457–A1464.
31. Beaulieu, L. Y.; Rutenberg, A. D.; Dahn, J. R. *Microsc. Microanal.* **2002**, *8*, 422–428.
32. Clemenccon, A.; Appapillai, A. T.; Kumar, S.; Shao-Horn, Y. *Electrochim. Acta* **2007**, *52* (13), 4572–4580.
33. Doi, T.; Inaba, M.; Tsuchiya, H.; Jeong, S.-K.; Iriyama, Y.; Abe, T.; Ogumi, Z. *J. Power Sources* **2008**, *180* (1), 539–545.
34. Jeong, S. K.; Inaba, M.; Iriyama, Y.; Abe, T.; Ogumi, Z. *J. Power Sources* **2003**, *119-121*, 555–560.
35. Koltypin, M.; Cohen, Y. S.; Markovsky, B.; Cohen, Y.; Aurbach, D. *Electrochem. Commun.* **2002**, *4* (1), 17–23.
36. Kushida, K.; Kuriyama, K. *Appl. Phys. Lett.* **2004**, *84* (18), 3456–3458.
37. Semenov, A. E.; Borodina, I. N.; Garofalini, S. H. *J. Electrochem. Soc.* **2001**, *148* (11), A1239–A1246.
38. Swiatowska-Mrowiecka, J.; Maurice, V.; Klein, L.; Marcus, P. *Electrochem. Commun.* **2007**, *9* (9), 2448–2455.
39. Kong, F.; Kostecki, R.; Nadeau, G.; Song, X.; Zaghib, K.; Kinoshita, K.; McLarnon, F. *J. Power Sources* **2001**, *97-98*, 58–66.
40. Zhu, J.; Feng, J.; Lu, L.; Zeng, K. Y. *J. Power Sources* **2012**, *197*, 224–230.
41. Melitz, W.; Shen, J.; Kummel, A. C.; Lee, S. *Surf. Sci. Reports* **2011**, *66* (1), 1–27.
42. Huang, H.; Wang, H.; Zhang, J.; Yan, D. *Appl. Phys. A: Mater.* **2009**, *95* (1), 125–130.
43. Glatzel, T.; Lux-Steiner, M. C.; Strassburg, E.; Boag, A.; Rosenwaks, Y. Principles of Kelvin probe force microscopy. In *Scanning probe microscopy*; Kalinin, S., Gruverman, A., Eds.; Springer: New York, 2007; pp 113–131.
44. Kalinin, S. V.; Bonnell, D. A. *Nano Lett.* **2004**, *4* (4), 555–560.
45. Rosenwaks, Y.; Shikler, R.; Glatzel, T.; Sadewasser, S. *Phys. Rev. B* **2004**, *70* (8), 085320.
46. Nagpure, S. C.; Bhushan, B.; Babu, S. S. *J. Power Sources* **2011**, *196* (3), 1508–1512.
47. Zhu, J.; Zeng, K. Y.; Lu, L. *J. Appl. Phys.* **2012**, *101*, 063723.
48. Kuriyama, K.; Onoue, A.; Yuasa, Y.; Kushida, K. *Surf. Sci.* **2007**, *601* (10), 2256–2259.
49. Kostecki, R.; McLarnon, F. *Electrochem. Solid State Lett.* **2002**, *5* (7), A164–A166.
50. Kostecki, R.; McLarnon, F. *Electrochem. Solid State Lett.* **2004**, *7* (10), A380–A383.

51. Kerlau, M.; Marcinek, M.; Srinivasan, V.; Kostecki, R. M. *Electrochim. Acta* **2007**, *52* (17), 5422–5429.
52. Balke, N.; Jesse, S.; Kim, Y.; Adamczyk, L.; Ivanov, I. N.; Dudney, N. J.; Kalinin, S. V. *ACS Nano* **2010**, *4* (12), 7349–7357.
53. Balke, N.; Jesse, S.; Kim, Y.; Adamczyk, L.; Tselev, A.; Ivanov, I. N.; Dudney, N. J.; Kalinin, S. V. *Nano Lett.* **2010**, *10* (9), 3420–3425.
54. Balke, N.; Jesse, S.; Morozovska, A. N.; Eliseev, E.; Chung, D. W.; Kim, Y.; Adamczyk, L.; Garcia, R. E.; Dudney, N. J.; Kalinin, S. V. *Nat. Nano* **2010**, *5* (10), 749–754.
55. Chung, D. W.; Balke, N.; Kalinin, S. V.; Garcia, R. E. *J. Electrochem. Soc.* **2011**, *158* (10), A1083–A1089.
56. Guo, S.; Jesse, S.; Kalnajs, S.; Balke, N.; Daniel, C.; Kalinin, S. V. *J. Electrochem. Soc.* **2011**, *158* (8), A982–A990.
57. Jesse, S.; Kalinin, S. V. *J. Phys. D: Appl. Phys.* **2011**, *44*, 464006.
58. Jesse, S.; Kumar, A.; Kalinin, S. V.; Gannepalli, A.; Proksch, R. *Microsc. Today* **2010**, *18*, 34–40.
59. Kalinin, S.; Kumar, A.; Balke, N.; McCorkle, M.; Guo, S. L.; Arruda, T.; Jesse, S. *Adv. Mater. Process.* **2011**, *169* (11), 30–34.
60. Soergel, E. *J. Phys. D: Appl. Phys.* **2011**, *44*, 464003.
61. Jesse, S.; Kalinin, K. V.; Proksch, R.; Baddprf, A. P.; Rodriguez, B. J. *Nanotechnology* **2007**, *18*, 435503.
62. Solares, S. D. *J. Appl. Phys.* **2012**, *111*, 054909.
63. Garcia, R.; Herruzo, E. T. *Nat. Nanotechnol.* **2012**, *7*, 217–226.
64. Guo, S.; Solares, S. D.; Mochalin, V.; Neitzel, I.; Gogotsi, Y.; Kalinin, S. V.; Jesse, S. *Small* **2012**, *8* (8), 1264–1269.
65. Kareem, A. U.; Solares, S. D. *Nanotechnology* **2012**, *23*, 015706.
66. Jesse, S.; Mirman, B.; Kalinin, S. V. *Appl. Phys. Lett.* **2006**, *89* (2), 022906.
67. García, R.; Pérez, R. *Surf. Sci. Rep.* **2002**, *47* (6-8), 197–301.
68. Kalinin, S.; Balke, N.; Jesse, S.; Tselev, A.; Kumar, A.; Arruda, T. M.; Guo, S.; Proksch, R. *Mater. Today* **2011**, *14* (11), 548–558.
69. Stan, G.; Krylyuk, S.; Davydov, A. V.; Vaudin, M. D.; Bendersky, L. A.; Cook, R. F. *Ultramicroscopy* **2009**, *109* (8), 929–936.
70. Killgore, J. P.; Yablon, D. G.; Tsou, A. H.; Gannepalli, A.; Yuya, P. A.; Turner, J. A.; Proksch, R.; Hurley, D. C. *Langmuir* **2011**, *27* (23), 13983–13987.
71. Hurley, D. C. Measuring mechanical properties on the nanoscale with contact resonance force microscopy methods. In *Scanning Probe Microscopy of Functional Materials*; Kalinin, S. V., Gruverman, A., Eds.; Springer: New York, 2010; pp108–137.
72. Shin, J.; Rodriguez, B. J.; Baddorf, A. P.; Thundat, T.; Karapetian, E.; Kachanov, M.; Gruverman, A.; Kalinin, S. V. *J. Vac. Sci. Technol. B* **2005**, *23* (5), 2102–2108.
73. Hurley, D. C.; Kopycinska-Müller, M.; Kos, A. B.; Geiss, R. H. *Meas. Sci. Tech* **2005**, *16*, 2167–2172.
74. Hurley, D. C.; Shen, K.; Jennett, N. M.; Turner, J. A. *J. Appl. Phys.* **2003**, *94* (4), 2347–2354.
75. Stan, G.; Price, W. *Rev. Sci. Instrum.* **2006**, *77*, 103707.

76. Yamanaka, K.; Maruyama, Y.; Tsuji, T. *Appl. Phys. Lett.* **2001**, *78* (13), 1939–1941.

Chapter 3

Co₃O₄/Carbon Composite Nanofibers for Use as Anode Material in Advanced Lithium-Ion Batteries

Shuli Li, Kun Fu, Leigang Xue, Ozan Toprakci, Ying Li, Shu Zhang,
Guanjie Xu, Yao Lu, and Xiangwu Zhang*

Fiber and Polymer Science Program, Department of Textile Engineering,
Chemistry and Science, North Carolina State University, Raleigh,
NC 27695-8301, USA

*E-mail: xiangwu_zhang@ncsu.edu

Co₃O₄/carbon composite nanofibers were prepared by a combination of electrospinning and carbonization methods using 10 - 30 nm and 30 - 50 nm Co₃O₄ nanoparticles, respectively, and their potential use as the anode material in rechargeable lithium-ion batteries was investigated. The composite Co₃O₄/carbon nanofiber electrode containing 30 - 50 nm Co₃O₄ nanoparticles showed large reversible capacities and good cycleability with charge capacities of 677 and 545 mAh g⁻¹ at the second and twentieth cycles, respectively. In contrast, the composite Co₃O₄/carbon nanofiber electrode containing 10 - 30 nm Co₃O₄ nanoparticles showed fast capacity fading during cycling due to severe nanoparticle aggregation. Results suggested that the good electrochemical performance of Co₃O₄/carbon nanofiber electrode containing 30 - 50 nm Co₃O₄ nanoparticles was ascribed to the combination of the properties of both Co₃O₄ nanoparticles (large Li storage capability) and carbon nanofiber matrix (long cycle life), and therefore this electrode material could be potentially used in high-energy rechargeable lithium-ion batteries.

Keywords: Cobalt oxide; composite nanofiber; nanoparticle aggregation; electrospinning; lithium-ion battery

Introduction

Lithium-ion batteries are considered as promising energy storage devices due to their eco-friendliness, low cost, large specific energy storage ability (1–3). They are playing increasingly important role in wireless communication devices, hybrid electric vehicles, and emerging smart grids (4). In order to meet the growing application requirements of novel energy storage, numerous materials and structures are thoroughly investigated in order to find new electrode materials with superior Li storage ability, improved cycleability, and lower cost.

Among various electrode materials, transition metal oxide tricobalt tetraoxide (Co_3O_4) has received significant attention due to its relatively high theoretical specific capacity of 890 mAh g⁻¹, low electrode potential, high Columbic efficiency, long cycle life, and high level of safety (5, 6). However, Co_3O_4 electrodes suffer from large initial irreversible capacity loss, low electrical conductivity, and poor cycling stability that is related to the severe particle aggregations and relatively large volume change during lithium insertion/extraction process (5–8). The agglomeration of Co_3O_4 particles and relatively large volume change could lead to the pulverization of the active particles and the loss of particle-particle electrical contact during repeated lithiation and delithiation processes, and thus cause serious detriment of the cycling stability (5, 7).

One possible strategy to alleviate these problems is to prepare nanometer-sized composite material with carbon nanofiber matrix, which has been proved to be an effective solution to enhance the cycling performance of Co_3O_4 anode materials (6, 9, 10). Carbon nanofibers demonstrate good capability of buffering the volume change in the electrode structure, short lithium-ion diffusion pathway, and relatively high conductivity. The carbon matrix can accommodate the internal mechanical stress induced by the volume change of Co_3O_4 nanoparticles and preserve the integrity of the anode. In addition, the matrix is electronically conductive and helps electron transport during lithium insertion and extraction processes (11). In this chapter, the size effect of the Co_3O_4 nanoparticles are investigated with 10 - 30 nm and 30 - 50 nm Co_3O_4 nanoparticles imbedded in carbon nanofibers produced by electrospinning technology.

Experimental

PAN (Mw = 150,000) and solvent N, N-dimethylformamide (DMF) were purchased from Sigma Aldrich. Co_3O_4 nanoparticles were obtained from US Research Nanomaterials, Inc., and their particle sizes were 10 - 30 nm and 30 - 50 nm, respectively. Co_3O_4 nanoparticles were added in DMF solution of 8 wt% PAN to prepare spinning solutions at 60 °C. Co_3O_4 concentration used was 20 wt% (compared to PAN). Mechanical stirring was applied for at least 48 h in order to obtain homogeneous dispersion of the nanoparticles.

Electrospinning process was carried out with a flow rate of 0.1 ml h⁻¹, needle-to-collector distance of 15.5 cm, and voltage of 15 kV supplied by Gamma ES40P-20W/DAM. Dry fibers were accumulated on the grounded collector and formed free-standing fibrous mats. The electrospun Co_3O_4 /PAN nanofibers were firstly

stabilized in air environment at 280 °C for 5.3 h (heating rate: 5 °C min⁻¹), and then carbonized at 700 °C for 1 h in an argon atmosphere (heating rate: 2 °C min⁻¹).

The morphology of the resultant Co₃O₄/C nanofibers were evaluated with scanning electron microscope (SEM, JEOL 6400F Field Emission SEM at 5 kV). The diameters of electrospun fibers were obtained by measuring fifty fibers randomly selected in SEM images using Revolution v1.6.0 software. Fibers were also analyzed with a transmission electron microscope (TEM, Hitachi HF-2000 TEM at 200 kV). Analysis of the composition and crystal structure of Co₃O₄/C nanofibers was conducted using a Rigaku SmartLab X-ray diffractometer at a scan rate of 5° min⁻¹.

Electrochemical experiments were performed using coin-type half cells containing carbonized Co₃O₄/C composite nanofibers as the working electrode and Li foil as the counter electrode. Co₃O₄/C composite nanofibers formed freestanding, conductive nonwoven mats, and they were directly used as the working electrodes without using any polymer binder or conductive filler. The electrolyte used was a 1 M LiPF₆ solution in ethylene carbonate (EC)/dimethyl carbonate (DMC) (1:1 v/v). Galvanostatic charge and discharge experiments were conducted using a battery test instrument (LAND CT2001A) at a current density of 50 mA g⁻¹ over the potential range from 0.01 to 2.50 V.

Results and Discussion

Morphology

Figure 1 exhibits SEM images of Co₃O₄/C nanofibers with different Co₃O₄ particle sizes of 10 - 30 nm and 30 - 50 nm, respectively. The Co₃O₄/C nanofibers are relatively straight and exhibit uniformly-distributed diameters. Bead-like structures can be seen from both Co₃O₄/C nanofibers containing 10 - 30 nm and 30 - 50 nm Co₃O₄ nanoparticles. Compared with Co₃O₄/C nanofibers containing 30 - 50 nm Co₃O₄ nanoparticles in Figure 1C, Co₃O₄/C nanofibers containing 10 - 30 nm Co₃O₄ nanoparticles in Figure 1A exhibit more irregular spherical beads with diameters around 500 nm. Under a higher magnification (Figures 1B and D), it is seen that the bead-like structures basically contain aggregations of Co₃O₄ nanoparticles on the fiber surface.

Figure 2 shows TEM images of Co₃O₄/C nanofibers containing 10 - 30 nm and 30 - 50 nm Co₃O₄ nanoparticles. It is seen that the majority of the nanoparticles are dispersed inside the carbon nanofiber matrix. A small portion of nanoparticles are not encapsulated inside in the nanofibers, but they appear to be attached to the fiber surface tightly. Most Co₃O₄ nanoparticles are separated from each other; however, some nanoparticles form aggregates of 100 nm or greater. Comparing Figures 2A and B, it is seen that more individual Co₃O₄ nanoparticles can be found in Co₃O₄/C nanofibers containing 30 - 50 nm Co₃O₄ nanoparticles; on the other hand, Co₃O₄/C nanofibers containing 10 - 30 nm Co₃O₄ nanoparticles have more Co₃O₄ nanoparticle clusters, which are larger than 100 nm. In other words, 10 - 30 nm Co₃O₄ nanoparticles have poorer dispersion than 30 - 50 nm Co₃O₄ nanoparticles. This phenomenon can be explained that smaller particles have

higher surface energy and tend to agglomerate into irregular and large secondary particles or clusters (12–14).

To further investigate the effect of particle size on the morphology of $\text{Co}_3\text{O}_4/\text{C}$ composite nanofibers, the fiber diameters are measured and their distributions are shown in Figure 3. The average fiber diameters of $\text{Co}_3\text{O}_4/\text{C}$ composite nanofibers with 10 - 30 nm and 30 - 50 nm Co_3O_4 nanoparticles are 294 and 269 nm, respectively. When the particle size is smaller, the particles tend to form more agglomerates in the electrospinning solutions and result in higher solution viscosity. Nanofibers produced from high-viscosity solution typically have larger fiber diameters (15). This result confirms the SEM and TEM observation (Figures 1 and 2) that the agglomerations of 10 - 30 nm Co_3O_4 nanoparticles are severer than the 30 - 50 nm ones with same concentration of Co_3O_4 in the composite nanofibers.

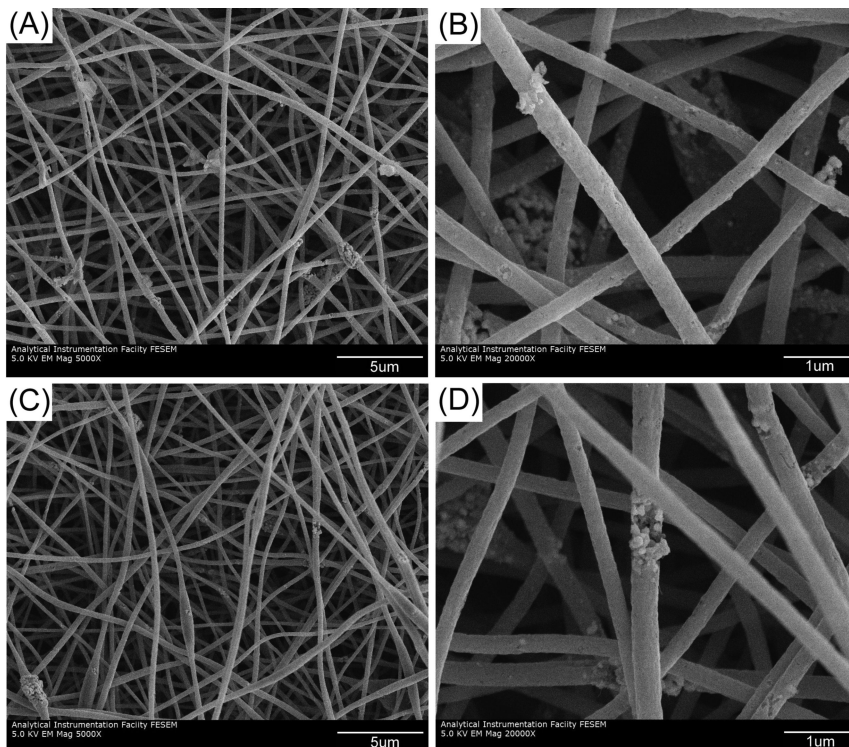


Figure 1. SEM images of $\text{Co}_3\text{O}_4/\text{C}$ composite nanofibers. Co_3O_4 particle size: (A,B) 10 - 30 nm, and (C,D) 30 - 50 nm.

Figure 4 illustrates the XRD pattern of $\text{Co}_3\text{O}_4/\text{C}$ composite nanofibers with 30 - 50 nm Co_3O_4 nanoparticles. Peaks at $2\theta = 19.00, 31.28, 36.86$, and 65.25° can be indexed to the pure cubic phase of Co_3O_4 (JCPDS File No. 43-1003) (16). Co_3O_4 peaks are small because of the very fine grain size of Co_3O_4 particles. From Figure 4, a broad carbon peak is also found at near $2\theta = 25^\circ$, corresponding to the (002) graphite layers; however, this peak is also weak, indicating low crystallinity of the carbon matrix (11).

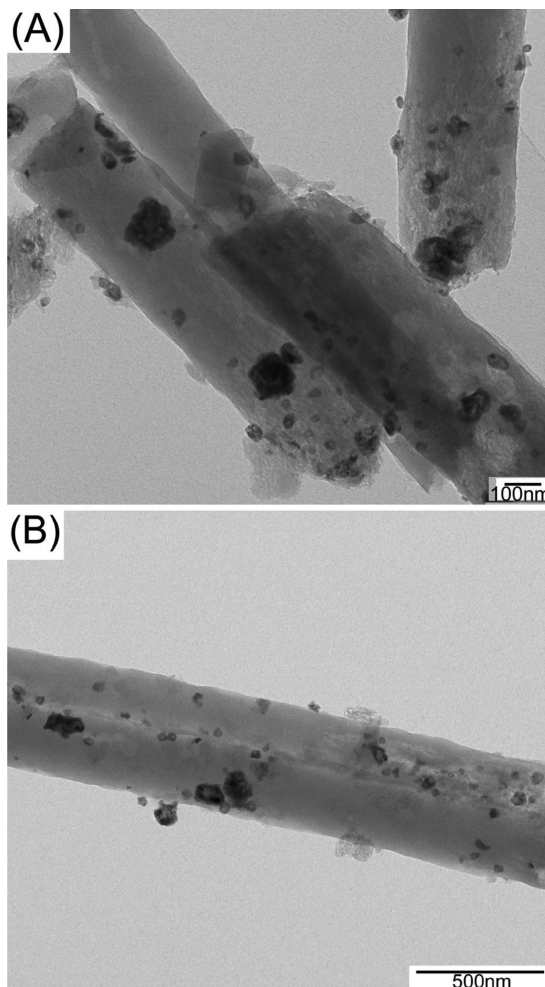


Figure 2. TEM images of $\text{Co}_3\text{O}_4/\text{C}$ composite nanofibers. Co_3O_4 particle size: (A) 10 - 30 nm, and (B) 30 - 50 nm.

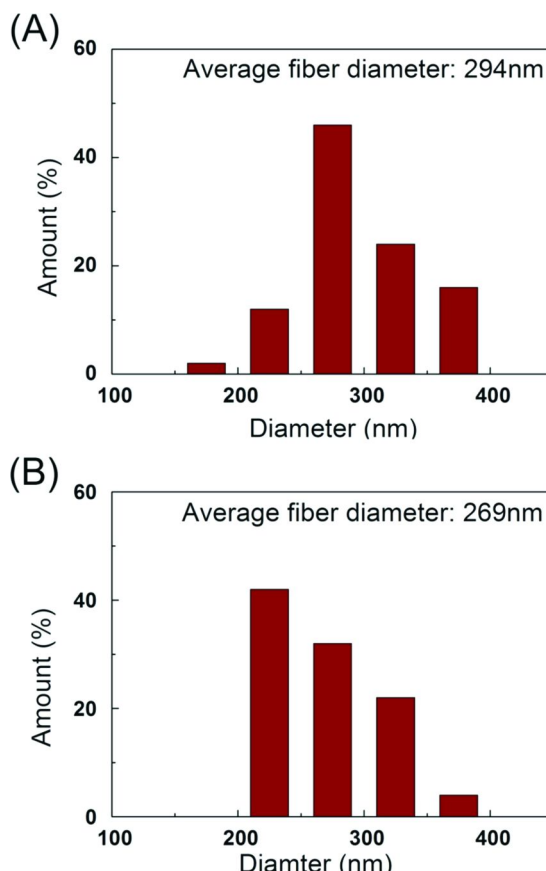
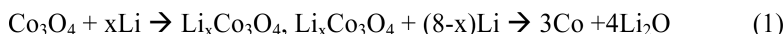


Figure 3. Fiber diameter distributions of Co₃O₄/C composite nanofibers. Co₃O₄ particle size: (A) 10 - 30 nm, and (B) 30 - 50 nm.

Electrochemical Performance

Galvanostatic charge-discharge experiments were carried out at a current density of 50 mA g⁻¹ within a voltage window of 0.01 - 2.50 V to evaluate the electrochemical performance of Co₃O₄/C composite nanofibers without using any binder or conductive additive.

Figure 5 exhibits the Galvanostatic charge-discharge profiles of $\text{Co}_3\text{O}_4/\text{C}$ composite nanofibers at the first, second and twentieth cycles. It is seen in Figure 5A that, during the first discharge process, $\text{Co}_3\text{O}_4/\text{C}$ composite nanofibers containing 10 - 30 nm Co_3O_4 particles present a small voltage plateau at 0.90 V and then a sloping voltage profile from 0.90 V to the cut-off voltage of 0.01 V. For $\text{Co}_3\text{O}_4/\text{C}$ composite nanofibers containing 30 - 50 nm Co_3O_4 particles, the voltage plateau slightly increases to around 1.00 V. The voltage plateau can be attributed to the decomposition of the electrolyte and the formation of solid electrolyte interface (SEI) (17). $\text{Co}_3\text{O}_4/\text{C}$ composite nanofibers containing 10 - 30 nm Co_3O_4 particles show an initial discharge capacity of 1030 mAh g⁻¹ and charge capacity of 450 mAh g⁻¹, respectively. $\text{Co}_3\text{O}_4/\text{C}$ composite nanofibers containing 30 - 50 nm Co_3O_4 particles have an initial discharge capacity of 1020 mAh g⁻¹ and charge capacity of 480 mAh g⁻¹, respectively. The first-cycle discharge capacities are greater than the theoretical capacity of pure Co_3O_4 (890 mAh g⁻¹), which further confirms the formation of SEI film (7). However, the first-cycle reversible capacities of $\text{Co}_3\text{O}_4/\text{C}$ composite nanofibers are low due to a phase transition during the initial lithiation process, which have been examined by Larcher and others (5-7, 16, 18-20). It has been reported that the large initial irreversible capacity is caused by the phase transition of $\text{Li}_{1.47}\text{Co}_3\text{O}_4$ from an intermediate lithiated phase to an amorphous phase (18). $\text{Li}_{1.47}\text{Co}_3\text{O}_4$ is produced by one of the two competing mechanisms to reach the full decomposition of the Co_3O_4 electrode into Co nanograins during lithium insertion process. The two competing mechanisms are (18):



In their research, Larcher and coworkers have exemplified the Co_3O_4 obtained at 500°C or higher would mainly go through the first mechanism during lithiation process, which has caused the consequences of the phase transition and reduced the initial reversible capacity (9, 18). However, other researchers have argued that the low initial reversible capacity is related to the formation/decomposition of Li_2O produced by the second mechanism as well as SEI film formation (21, 22). They have concluded that Li_2O is known to be electrochemically inactive and the incomplete decomposition of Li_2O is responsible for the large irreversible capacity loss of Co_3O_4 anode during cycling (9, 16, 19, 20).

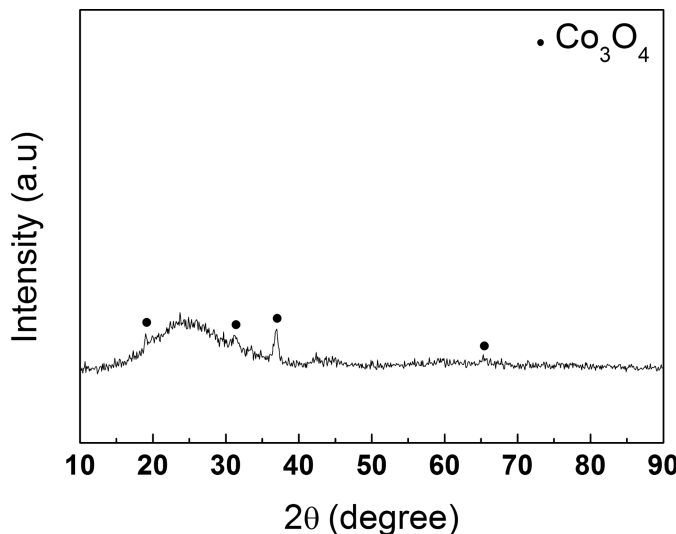


Figure 4. XRD pattern of $\text{Co}_3\text{O}_4/\text{C}$ composite nanofibers. Co_3O_4 particle size: 30 - 50 nm.

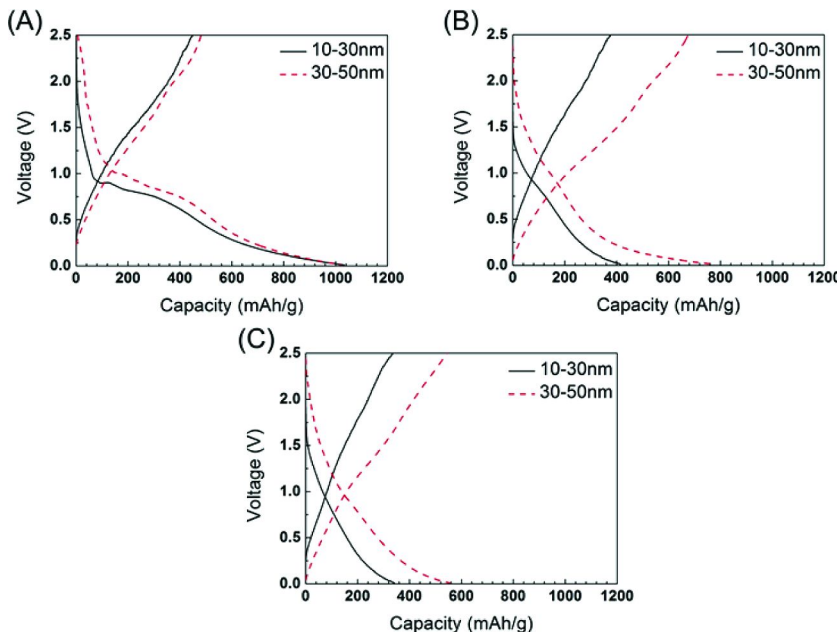


Figure 5. Galvanostatic charge-discharge curves of $\text{Co}_3\text{O}_4/\text{C}$ composite nanofibers with different Co_3O_4 particle sizes. (A) The first cycle, (B) the second cycle, and (C) the twentieth cycle.

From Figures 5B and C, which exhibit the Galvanostatic charge-discharge curves of the second and twentieth cycles of $\text{Co}_3\text{O}_4/\text{C}$ composite nanofibers, it is seen that the reversible capacities of nanofibers containing 30 - 50 nm Co_3O_4 nanopartiles increase while those containing 10 - 30 nm Co_3O_4 nanopartiles decrease. The reversible capacities of $\text{Co}_3\text{O}_4/\text{C}$ composite nanofibers containing 10 - 30 nm Co_3O_4 particles are 378 and 337 mAh g^{-1} , respectively, at the second and twentieth cycles, while the reversible capacities of $\text{Co}_3\text{O}_4/\text{C}$ composite nanofibers containing 30 - 50 nm Co_3O_4 particles are much larger: 677 and 545 mAh g^{-1} , respectively.

Figure 6 shows the cycling performance of $\text{Co}_3\text{O}_4/\text{C}$ composite anodes with 10 - 30 nm and 30 - 50 nm Co_3O_4 nanoparticles, respectively. The reversible capacities of the $\text{Co}_3\text{O}_4/\text{C}$ anode with 10 - 30 nm Co_3O_4 nanoparticles decline drastically with increase in cycle number. While the $\text{Co}_3\text{O}_4/\text{C}$ anode with 30 - 50 nm Co_3O_4 nanoparticles shows relatively good cycling stability with a high reversible capacity of 545 mAh g^{-1} at 20th cycle, compared to commercial Co_3O_4 anodes (less than 200 mAh g^{-1}) performed by others (6). This result indicates that the carbon nanofiber matrix, which buffers the volume change of Co_3O_4 nanoparticles in the composite, plays an important role in the improvement of the cycling performance of $\text{Co}_3\text{O}_4/\text{C}$ anode.

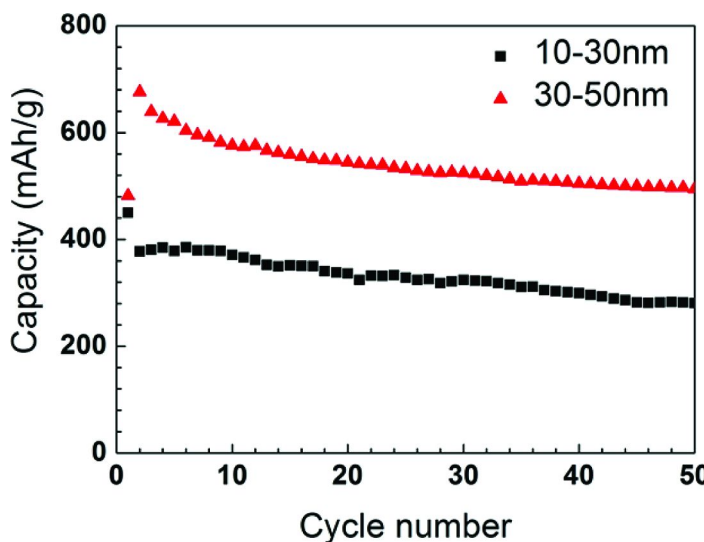


Figure 6. Cycling performance of $\text{Co}_3\text{O}_4/\text{C}$ composite nanofibers with different Co_3O_4 particle sizes.

For the $\text{Co}_3\text{O}_4/\text{C}$ composite anodes with 10 - 30 nm Co_3O_4 nanoparticles, the fast fading of charge-discharge capacities may be caused by two reasons. One reason is that 10 - 30 nm Co_3O_4 nanoparticles possess large surface area and the surface layer participates in the progressive cycling and loses the

electrochemical reactivity gradually during cycling (9). Another reason is that too much agglomeration of the Co_3O_4 nanoparticles results in pulverization, loss of active material, and electrical isolation during the charge and discharge processes. Similar results are shown in other work (17).

The comparison of the Coulombic efficiencies of $\text{Co}_3\text{O}_4/\text{C}$ composite nanofiber anodes containing 10 - 30 nm and 30 - 50 nm Co_3O_4 nanoparticles is shown in Figure 7. The Coulombic efficiencies of the first cycle of $\text{Co}_3\text{O}_4/\text{C}$ composite nanofiber anodes with 10 - 30 nm and 30 - 50 nm Co_3O_4 nanoparticles are 44% and 48%, respectively. The Coulombic efficiencies of the second cycle are 92% and 87%, as well as 99% and 99% for twentieth cycle. As discussed, the relatively low Coulombic efficiencies of the first cycle are mainly due to: *i*) the decomposition of the electrolyte and formation of the SEI film which hinders the ability of delithiation of the electrode, and *ii*) a phase transition during the reduction of Co_3O_4 to nanograin Co, amorphous $\text{Li}_{1.47}\text{Co}_3\text{O}_4$ and Li_2O . However, during the second discharge, the delithiation process releases Li ions and oxidizes nanograin Co to Co_3O_4 , which increases the second reversible capacities and therefore, the Coulombic efficiencies. In addition, it is possible that amorphous $\text{Li}_{1.47}\text{Co}_3\text{O}_4$ confines the volume change of Co_3O_4 nanoparticles and raises the conductivity of the composite nanofibers by connecting the active materials. After five cycles, the Coulombic efficiencies reach almost 100% for both $\text{Co}_3\text{O}_4/\text{C}$ composite nanofiber anodes containing 10 - 30 nm and 30 - 50 nm Co_3O_4 nanoparticles.

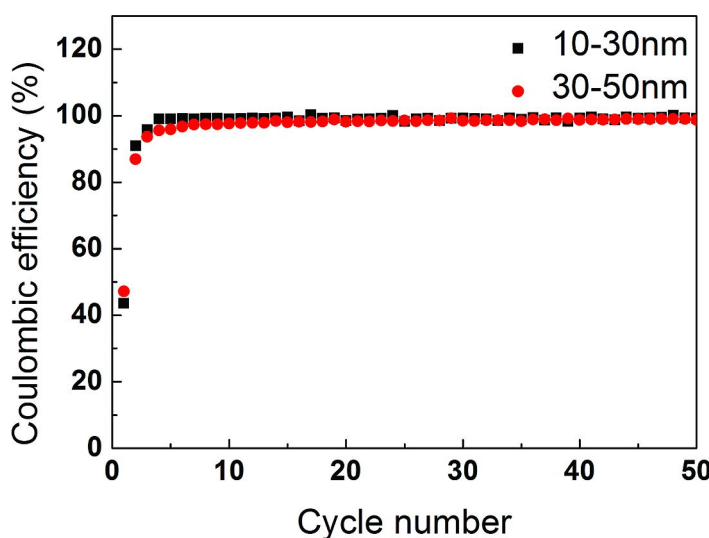


Figure 7. Coulombic efficiencies of $\text{Co}_3\text{O}_4/\text{C}$ composite nanofibers with different Co_3O_4 particle sizes.

Conclusion

$\text{Co}_3\text{O}_4/\text{C}$ composite nanofibers containing 10 - 30 nm and 30 - 50 nm Co_3O_4 nanoparticles were fabricated through electrospinning and thermal treatment processes. Compared with $\text{Co}_3\text{O}_4/\text{C}$ nanofibers containing 10 - 30 nm Co_3O_4 nanoparticles, $\text{Co}_3\text{O}_4/\text{C}$ anodes with 30 - 50 nm Co_3O_4 nanoparticles exhibited high reversible capacity, improved Coulombic efficiencies, and good cycling stability when used as binder-free anode material for lithium-ion batteries. In contrast, the $\text{Co}_3\text{O}_4/\text{C}$ composite nanofibers with 10 - 30 nm Co_3O_4 nanoparticles showed low charge-discharge capacities due to the pulverization of the electrode and the degradation of the electrochemical activity resulting from severe nanoparticle aggregation and large surface area. However, after the second cycle, both $\text{Co}_3\text{O}_4/\text{C}$ nanofibers displayed Coulombic efficiencies of almost 100%. The relatively good cycling performance of $\text{Co}_3\text{O}_4/\text{C}$ composite nanofibers derived from $\text{Co}_3\text{O}_4/\text{PAN}$ nanofibers could be attributed to their unique composite structure with an improved dispersion of Co_3O_4 nanoparticles, the unique one-dimensional fiber structure, and the shorter lithium ion diffusion distance in the nanofibers.

Acknowledgments

This research was supported by the U.S. Department of Energy under Grant No: DE-EE0001177, Advanced Transportation Energy Center, and ERC Program of the National Science Foundation under Award Number EEC-08212121.

References

1. Lin, Z.; Ji, L. W.; Woodroof, M. D.; Zhang, X. W. *J. Power Sources* **2010**, *195* (15), 5025–5031.
2. Ji, L. W.; Zhang, X. W. *Energy Environ. Sci.* **2010**, *3* (1), 124–129.
3. Ji, L. W.; Zhang, X. W. *Carbon* **2009**, *47* (14), 3219–3226.
4. Ji, L. W.; Lin, Z.; Alcoutlabi, M.; Zhang, X. W. *Energy Environ. Sci.* **2011**, *4* (8), 2682–2699.
5. Wen, W.; Wu, J. M.; Tu, J. P. *J. Alloys Compd.* **2012**, *513*, 592–596.
6. Yao, W. L.; Wang, J. L.; Yang, J.; Du, G. D. *J. Power Sources* **2008**, *176* (1), 369–372.
7. Zhang, P.; Guo, Z. P.; Huang, Y. D.; Jia, D. Z.; Liu, H. K. *J. Power Sources* **2011**, *196* (16), 6987–6991.
8. Needham, S. A.; Wang, G. X.; Konstantinov, K.; Tournayre, Y.; Lao, Z.; Liu, H. K. *Electrochim Solid.-State Lett.* **2006**, *9* (7), A315–A319.
9. Yao, W. L.; Yang, J.; Wang, J. L.; Tao, L. A. *Electrochim. Acta* **2008**, *53* (24), 7326–7330.
10. Yao, W. L.; Chen, J. Q.; Li, A. Y.; Chen, X. B. *Adv. Mater. Res.* **2011**, *197–198*, 1113–1116.
11. Ji, L. W.; Jung, K. H.; Medford, A. J.; Zhang, X. W. *J. Mater. Chem.* **2009**, *19* (28), 4992–4997.
12. Mao, J.; Dai, K. H.; Zhai, Y. C. *Electrochim Acta* **2012**, *63*, 381–390.

13. Ishizaki, C.; Raharjo, P.; Sato, K.; Ishizaki, K. *J. Ceram. Soc. Jpn.* **2001**, *109* (1), 16–22.
14. Zarzycki, J.; Prassas, M.; Phalippou, J. *J. Mater. Sci.* **1982**, *17* (11), 3371–3379.
15. Wang, T.; Kumar, S. *J. Appl. Polym. Sci.* **2006**, *102* (2), 1023–1029.
16. Rahman, M. M.; Wang, J. Z.; Deng, X. L.; Li, Y.; Liu, H. K. *Electrochim. Acta* **2009**, *55* (2), 504–510.
17. Yuan, Z. Y.; Huang, F.; Feng, C. Q.; Sun, J. T.; Zhou, Y. H. *Mater. Chem. Phys.* **2003**, *79* (1), 1–4.
18. Larcher, D.; Sudant, G.; Leriche, J. B.; Chabre, Y.; Tarascon, J. M. *J. Electrochem. Soc.* **2002**, *149* (3), A234–A241.
19. Lei, X. F.; Ma, J. X.; Sun, Y. Y. *Int. J. Electrochem. Sci.* **2011**, *6* (3), 573–580.
20. Liu, Y.; Mi, C. H.; Su, L. H.; Zhang, X. G. *Electrochim Acta* **2008**, *53* (5), 2507–2513.
21. Fu, L. J.; Liu, H.; Li, C.; Wu, Y. P.; Rahm, E.; Holze, R.; Wu, H. Q. *Solid State Sci.* **2006**, *8* (2), 113–128.
22. Guo, H. J.; Sun, Q. M.; Li, X. H.; Wang, Z. X.; Peng, W. J. *Trans. Nonferrous Met. Soc. China* **2009**, *19* (2), 372–376.

Chapter 4

Recent Advances in the Development of LiCoPO₄ as High Voltage Cathode Material for Li-Ion Batteries

Sergio Brutti^{*,1,2} and Stefania Panero³

¹Dipartimento di Scienze, Università della Basilicata, Potenza, Italy

²Istituto dei Sistemi Complessi, Consiglio Nazionale delle Ricerche (ISC-CNR) UOS Sapienza, Roma, Italy

³Dipartimento di Chimica, Sapienza Università di Roma, Roma, Italy

*E-mail: sergio.brutti@unibas.it

Polyanion-type materials, like lithium iron phosphate, are one of the great success in the research field of applied electrochemistry. Within this family, LiFePO₄ is a now mature material and its properties have been largely optimized thus opening the door to commercial exploitation. Only in recent years the attention of the scientific community is focusing the great advantage of the substitution of iron with manganese, cobalt or nickel in the olivine lattice. In fact the Mn³⁺/Mn²⁺, Co³⁺/Co²⁺ and Ni³⁺/Ni²⁺ couples show increasing redox potentials, all higher than the Fe³⁺/Fe²⁺, thus opening the door to large improvements in the energy performances of post-LiFePO₄ olivine based Li-ion cells.

This chapter reviews the most relevant reports about the LiCoPO₄ material and its use in lithium cells. The goal is to provide an overview of the reported advancements concerning LiCoPO₄ physical properties, synthesis routes, electrochemical lithium de-insertion/insertion mechanism, effect of doping/substitution and effect of coating on the battery performances.

In summary LiCoPO₄ is a valuable candidate material for next generation high voltage and high energy Li-ion cell. Although the research efforts dedicated so far by the scientific community, some fundamental aspects of the material

properties and reaction mechanisms in lithium cells are not completely understood. In particular the investigation of the possible occurrence of terminal solid solution in the first stages of de-lithiation of LiCoPO_4 , the characterization of the intermediate $\text{Li}_{0.7}\text{CoPO}_4$ phase, the effect of doping as well as a more careful understanding of the parasitic interactions with electrolytes are key aspects that have not been successfully tackled yet. Moreover, although a large phenomenological description of the structure/morphology/performances relationship has been developed so far, there is a lack of synthetic and fundamental explanations concerning the role of defects, the ion conduction mechanism, the electronic conductivity and the microscopic effect of crystal growth conditions. Owing to this, large room for improvements in the performances in Li-cells of LCP is expected by assessing the synthesis route, the coatings, the doping/substitution and the electrolyte additives in order to boost its ability to reversibly cycle lithium and minimize the unavoidable parasitic interaction with electrolytes at high voltage.

Introduction

Polyanion-type materials, like lithium iron phosphate, are one of the great success of recent years in the research field of applied electrochemistry. Since the experimental reports by Padhi and co-workers in 1997 (1, 2), the ability of LiFePO_4 (LFP) to reversibly de-insert/insert lithium in electrochemical cells has attracted an enormous attention within the scientific community. In the last decade, the fundamental chemistry that drives an effective use of LFP as cathode material in lithium and Li-ion cells has been widely instigated: nowadays lithium iron phosphate is one of the most deeply studied and understood electroactive material for secondary non-aqueous Li-ion cell applications (3–5). Hundreds of research papers and patents have been published in the last ten years on a wide variety of synthetic routes to prepare an LFP powder tailored for battery applications: LFP is a now mature material and its properties have been largely optimized thus opening the door to its commercial exploitation (3–5). Nowadays LFP is commonly employed in batteries for last generation power tools.

On the other hand, the other members of the olivine homologous series, i.e. LiMnPO_4 (LMP), LiCoPO_4 (LCP), LiNiPO_4 (LNP), are not as studied as their “most famous big brother” LFP. Only in recent years the attention of the scientific community is realizing the great advantage of the substitution of iron for manganese (6–8), cobalt (9–11) or nickel (12–14) in the olivine lattice. In fact the $\text{Mn}^{3+}/\text{Mn}^{2+}$, $\text{Co}^{3+}/\text{Co}^{2+}$ and $\text{Ni}^{3+}/\text{Ni}^{2+}$ couples show increasing redox potentials, all higher than the $\text{Fe}^{3+}/\text{Fe}^{2+}$ couple. In the olivine structures, where a PO_4^{3-} polyanionic framework surrounds the metal ions, the reduction potentials of the mentioned olivines are 3.5, 4.1, 4.8, 5.1 V vs. Li^+/Li^0 for Fe, Mn, Co and Ni, respectively (15). In the table 1 the basic properties of these compounds

are compared with other cathode materials currently used, or under study, in lithium-ion batteries (16).

Table 1. Properties of the LFP, LMP, LCP and LNP olivine compounds compared with other cathode materials currently used in lithium-ion batteries (16)

<i>Cathode materials</i>	<i>Discharge voltage vs. Li Volts</i>	<i>Theoretical capacity mAhg⁻¹</i>	<i>Density g cm⁻³</i>	<i>Energy cost US\$ kWh⁻¹ US\$ 18650 cell vs. graphite (LP30 electrolyte)^a</i>
LiFePO₄	3.4	170	3.6	158
LiCoO₂	3.6	137	5.1	198
LiAl_{0.05}Co_{0.15}Ni_{0.8}O₂	3.6	265	4.7	158
LiMn₂O₄	3.9	117	4.2	168
LiMnPO₄	4.1	171	3.4	150
LiNi_{0.5}Mn_{1.5}O₄	4.7	146	4.4	141
LiCoPO₄	4.8	167	3.7	142
LiNiPO₄	5.1	167	3.9	123

^a LP30 electrolyte: 1 M LiPF₆ in 1:1 w/w ethylene carbonate/dimethyl carbonate.

The three manganese-, cobalt- and nickel-based olivines are extremely interesting materials showing an estimated energy cost comparable or smaller than all the other materials. On the other hand, they show poor properties in terms of ionic or electronic conductivities and, in the cases of Co and Ni, operate at working potentials at the boundary or beyond the capability of any assessed electrolyte for Li-ion cells (16). In particular the greatest theoretical performances and smaller energy costs are given by LiNiPO₄ albeit at a voltage well outside the thermodynamic stability window of any contemporary electrolyte.

LCP, which operates at a slightly safer voltage, is apparently the best compromise: it incorporates the advantage of a higher working potential compared to LFP, with the larger theoretical performances and reduced cobalt weight fraction per formula unit compared to the commercial LiCoO₂. As a consequence, if compared with LFP, the larger raw material costs (LCP is approximately 67% more expensive in weight than LFP (16)) are counterbalanced and the resulting energy cost is greatly reduced. Its cost performances compare with the spinel LiNi_{0.5}Mn_{1.5}O₄ (LNMO) material that is at the centre stage for the development of high energy Li-ion cells (17). However phosphates have safety advantages compared to oxides (18–21) and such hazard factors must be carefully taken into account in the development of next generation high-voltage Li-ion cells. Furthermore the power performances reported so far in the literature for the LFP olivine cathodes have not yet been reached by LNMO (22, 23). Owing to

this LCP has apparently the potential to be the next decade success story in Li-ion technologies and to find large application in the next generation Li-ion cells (16, 23).

This chapter reviews the most relevant reports about the LCP material and its use in Li-ion cells. The goal is to provide an overview of the reported achievements for the olivine LCP about its physical properties, synthesis routes, electrochemical lithium de-insertion/insertion mechanism, effect of doping/substitution and effect of coating on the battery performances.

Physical Properties

The LCP crystal belongs to the olivine family of the triphylite lithium orthophosphates: it crystallizes in an orthorhombic lattice described either by the Pmna or Pmnb space groups. The crystal assembles two types of polyhedra: CoO_6 octahedra that are corner shared and cross-linked with the PO_4 tetrahedra. This combination forms a three-dimensional network with channels occupied by Li ions along the [010] and [001] directions. This connectivity has a strong impact on the electronic conductivity and ion mobility. In fact the CoO_6 sub-units share only corners between each other and the electron delocalization is hence difficult. Furthermore lithium conductivity is not 3D like in the case of the LMNO spinel (17) but occurs mainly along the [010] channels like the in the LFP lattice.

The lattice parameters, derived from single crystal neutron diffraction, are $a=10.159 \text{ \AA}$, $b=5.90 \text{ \AA}$ and $c=4.70 \text{ \AA}$ in Pnma description (24): the cell constants may vary depending on the synthetic route. A summary of the reported lattice constants are presented in table 2 and the trend of the cells volumes in function of the annealing temperatures is shown in figure 1, separately for the materials annealed in air or under inert atmospheres.

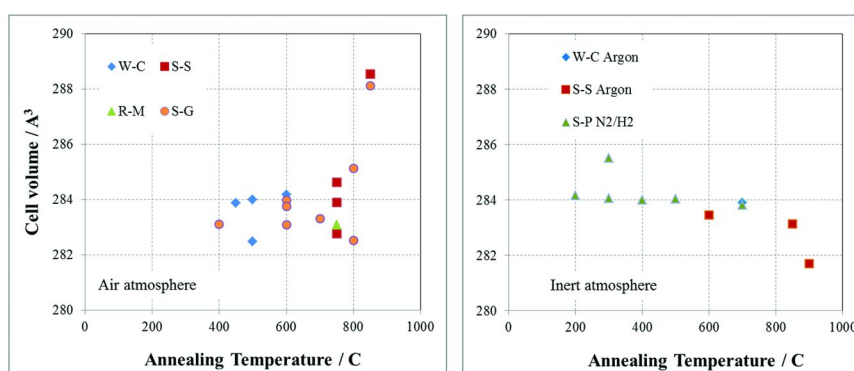


Figure 1. Cell volume observed for LiCoPO_4 derived from data reported in the table 2 (W-C= wet chemistry; S-S= solid state; R-M= rheological method; S-G=sol-gel; S-P=spray pyrolysis).

Table 2. Lattice constants reported in the literature for LiCoPO₄.

<i>Synthesis route</i>	<i>Annealing conditions</i>		<i>Lattice constants</i>			<i>Notes</i>	<i>Ref.</i>
	<i>Gas</i>	<i>Temperature/°C</i>	<i>a/Å</i>	<i>b/Å</i>	<i>c/Å</i>		
Wet chemistry	Air	450	10.203	5.921	4.699	(25)	(25)
		500	10.193 10.205	5.913 5.921	4.687 4.700		(26)
		600	10.206	5.923	4.701		(25)
Solid state	Air	750	10.202	5.922	4.699	(9)	(27)
			10.206	5.926	4.706		(28)
			10.188	5.904	4.701		(29)
Rheological phase method	Air	850	10.24	5.97	4.72	(28)	(30)
		750	10.178	5.909	4.707		
Solid state	Microwave heating		10.205	5.925	4.702	(31)	(31)
Sol-gel			400	10.187	5.918		
Air	600	10.201	5.923	4.700	(32)	(33)	
		10.195	5.918	4.692			
		10.194	5.925	4.698		(34)	
Air	700	10.195	5.914	4.699	(34)	(35)	
	800	10.2	5.91	4.73		(34)	
		10.180	5.901	4.703			
	850	10.286	5.927	4.726		(36)	

Continued on next page.

Table 2. (Continued). Lattice constants reported in the literature for LiCoPO₄.

<i>Synthesis route</i>	<i>Annealing conditions</i>		<i>Lattice constants</i>			<i>Notes</i>	<i>Ref.</i>
	<i>Gas</i>	<i>Temperature/°C</i>	<i>a/Å</i>	<i>b/Å</i>	<i>c/Å</i>		
Solid state	Ar	600	10.196	5.919	4.697	(11)	(37)
		650	10.209	5.923	4.716		
	N ₂	750	10.192	5.917	4.695	(38)	(39)
		800	10.195	5.920	4.698		
Molten salt	Ar	900	10.159	5.90	4.70	Single crystal	(24)
Sol-gel	Ar	700	10.202	5.921	4.700		(40)
Spray pyrolysis	N ₂ / 3% H ₂	200	10.206	5.923	4.701	(41)	(42)
		300	10.21	5.95	4.7		
		400	10.206	5.922	4.700	(41)	(41)
		500	10.203	5.921	4.701		
		700	10.202	5.924	4.700	(41)	(43)
	N ₂ / 5% H ₂		10.199	5.921	4.700		

Although the two trends observed in the figure 1a-b are partially biased by the large variety of the synthesis conditions (e.g. chemical nature of the precursors, duration of the annealing, heating rates, static vs. dynamic annealing atmospheres), it is possible to highlight two diverging evolution of the cell volumes upon increasing the annealing temperature. Different competitive phenomena can be responsible for such variations, likely related to the formation of lattice defects: specific studies have not been reported so far. On the other hand there is an abundant literature available for the isostructural LFP compound that can be used as starting point for discussion.

Among the LCP powders prepared under inert gas flow, the cell parameters decrease upon increasing the annealing temperature. It is noticeable that the single crystal sample studied by Tian et al. (24) shows the smaller cell volume compared to all the others samples ($\Delta V=1\text{--}2\text{ }\text{\AA}^3$). This single-crystal has been obtained at the highest reported annealing temperature followed by a very slow cooling with a $0.7^\circ/\text{h}$ temperature decreasing rate. Similar large volume contractions have been observed by Lu et al. (44) for the isostructural LFP microcrystals grown by hydrothermal route: in this case the authors speculate that such shrinking can be related to the ordering of the metal atoms in the lattice. In fact it is widely accepted that the LFP cell volume is an indirect measure of the cation disorder (e.g. metal vacancies, metal anti-site disorder) (44, 45). These native defects are believed to be responsible for the loss of electrochemical activity of LFP in lithium cells due to the blockage of lithium channels as an example by metal anti-site defects (46).

Turning to the powders prepared under air, a slight increasing trend in the cell volume is observed upon increasing the annealing temperature. Such expansion, that becomes dramatic at $T>800^\circ\text{C}$, can be also related to the formation of lattice defects. In fact, under air at high temperature, the oxidation of Co^{2+} to give Co^{3+} is thermodynamically favoured (47), similarly to what occurs for Fe^{2+} in the case of LFP. Zhagib et al. (48) observed that in LFP nano-crystallites free from impurity and defect, the surface is highly disordered and iron ions on the surface are often in the Fe^{3+} low spin ($S=1/2$) configuration. Such disorder is found to have dramatic effects on the electrochemical properties of LFP in lithium cells (formation of a solid solution): it can be strongly reduced by the growth of a carbon coating at 750°C , which switches the Fe^{3+} ions in the surface layer to the high spin ($S=5/2$) configuration. Although in the case of LCP there are not reports that tackles this point specifically, one can speculate that the oxidation of the surface Co^{2+} ions are likely to induce further vacancies in the other metal sites, thus increasing the local lattice disorder. This effect can be responsible for the cell expansion observed for the LCP samples prepared in air at high temperatures.

The electronic structure of the LCP crystal has been studied by Le Bacq and co-workers (49–51), Lin (52, 53), Amador (54), Zhou (55), Kang (56) and Shang (57) by density functional theory calculations in either local density or generalized gradient approximations. All authors agree that satisfactory calculations are obtained only if the d-states are treated by the explicit many-body theory adopting standard Hubbard models. In particular LDA+U calculations give acceptable good predictions for what concerns the cell volume ($274\text{ }\text{\AA}^3$) and correctly predict the insulating (band gap 2.9 eV) and antiferromagnetic character of the lattice

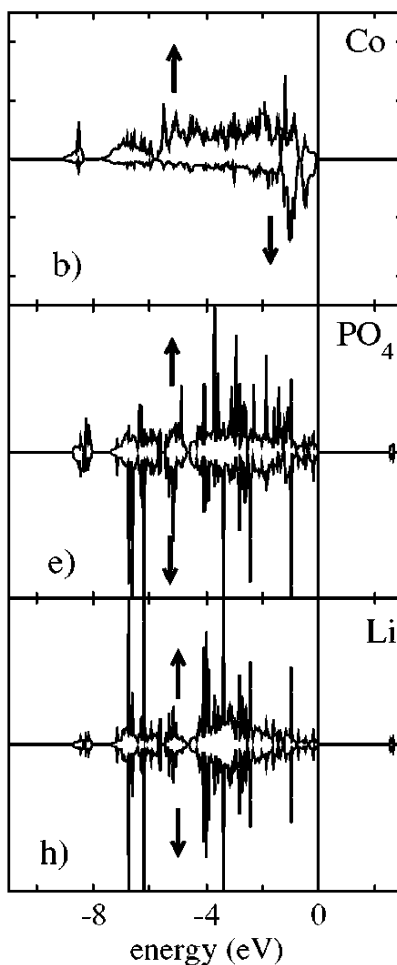


Figure 2. Density of states of (a) Co ion, (b) PO_4 fragment and (c) Li site in LCP calculated by DFT+U theory with the projector augmented wave method (LDA+U approximation). The Fermi energy is represented by a vertical line (49). Reprinted with permission from ref. (49). Copyright (2004) American Physical Society.

The LDA+U approximation predicts the formation of a wide Co-band constituted by two e_g - and t_{2g} -like bands, spreading out from -8 eV to the Fermi energy. The translation of the two partially filled e_g - and t_{2g} -like bands by the U addend leads to the expected insulator character differently from what predicted by LDA or GGA calculations. LDA+U calculations predict a potential of approximately 4.6 V vs. Li^+/Li for the $LiCoPO_4/CoPO_4$ oxidation in very

good agreement with the experimental values of 4.8 V vs. Li⁺/Li (see the other sections); other exchange-correlation functionals, i.e. LDA or GGA, largely fail by underestimating the intercalation potential of about 1-2 Volts.

The insulating character of LCP affects its electrical conductivity: Tadanaga and co-workers (58) and Wolfenstine (59–61) measured electrical conductivity values of $1 \cdot 10^{-10}$ (58) and $1 \cdot 10^{-9}$ S cm⁻¹ (59), respectively, by using a two or four point DC method. Deposition of carbon coatings or precipitation of Co₂P surface contaminants under high temperature annealing in inert atmosphere lead to a drastic increase of about 10^4 – 10^5 of the electrical conductivity of LCP materials (more details are discussed in the next sections) (59–61).

The ionic mobility in the LCP lattice has been studied by Morgan and co-workers (62), Shanmukaraj (26) and Prabu (36, 63). Lithium diffusion coefficients of 10^{-9} , $3.5 \cdot 10^{-14}$ (26), $2.3 \cdot 10^{-14}$ and $2.9 \cdot 10^{-15}$ cm²s⁻¹, respectively, have been estimated by firsts principles methods (62) or derived from bulk conductivities measured by impedance spectroscopy measurements (26, 36, 63). The experimental values are in close agreement with the diffusion coefficient measured for the isostructural LFP phase (14).

Synthesis

Solid State Method

This very common method has been used by many authors to synthesize LCP: this route involves the mixing of stoichiometric amounts of starting materials and the heat-treatment of the resulting mixture in a furnace. The main differences among the various adopted strategies deal with the chemical nature of the precursors, the mixing procedure (hand grinding or mechanical mixing) and the annealing conditions (air vs. inert atmosphere, annealing temperature and time, heating and cooling rates). As an example Li₂CO₃, Co₃O₄ and (NH₄)₂HPO₄ have been mixed in stoichiometric amounts by Amine et al. (9): this mixture has been grinded in agate mortar, pressed into a pellet and then calcined in air at 350 C for 9 h followed by a further air annealing step at 750C for 30h. The pre-annealing at 350C is necessary to obtain pure LCP material free from contaminants such as Li₅P₃O₁₀. Other precursors for Li (Li₃PO₄, LiOH·H₂O), Co (CoO, Co(OH)₂, Co(NO₃)₂·6H₂O, NH₄CoPO₄·H₂O, Co(OCOCH₃)₂·4H₂O) and P (P₂O₅, Co₃(PO₄)₂, NH₄H₂PO₄) have been used by other groups always obtaining single phase materials (9, 11, 12, 24, 27, 28, 37–39, 56, 64–66). Only the use of NH₄CoPO₄·H₂O with Li₃PO₄ leads, after calcinations in air in the temperature range 350–800C, to the precipitation of Co₃O₄ as admixture (the maximum contamination has been estimated below 5%) (39).

The LCP crystal and particles formation at high temperature have been investigated by Grigorova et al. (67) by thermogravimetry, differential scanning calorimetry, scanning electron microscopy (SEM) and X-ray diffraction (XRD), in order to develop a thermodynamic model capable to identify the most suitable conditions for solid state annealing. In particular Grigorova et al. suggest that pure LCP can be prepared in one step annealing (without intermediate temperature and grinding steps) if the treated precursor mixture is formed as thin plate with

thickness < 0.5 mm. Micrometric and homogeneous aggregates of pure LCP can be obtained by fast heating (1500 degree h⁻¹) under Ar-flow and annealing for 2 hours at 750C. Following this protocol particles have been obtained well shaped and similar in size.

On the other hand, although from the crystallographic point of view the use of inert gas or air has a certain influence on the lattice constants, the morphologies are apparently not much altered by the use of inert gas flows instead of air. In the figure 3 the comparison between two low magnification SEM images is shown for the samples synthesized by Bramnik et al. (68) under nitrogen at 800C and Rabanal et al. (27) in air at 750C.

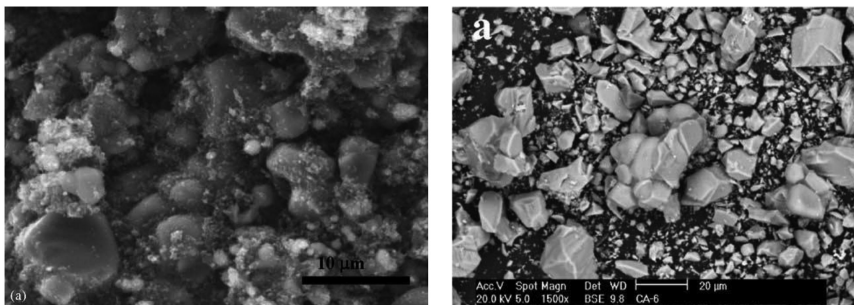


Figure 3. Comparison between the low magnification SEM of the samples synthesized (left) by Bramnik et al. (39) under nitrogen at 800C and (right) Rabanal et al. (27) in air at 750C. Reprinted with permission from ref. (27) and (39). Copyright (2005-2006) Elsevier publishing.

As expected for solid state routes, the particles are, in both cases, strongly agglomerated and inhomogenous in shape and size. This heterogeneous morphology has been also confirmed by transmission electron microscopy (TEM) investigation by Tan et al. (28): particles with irregular shapes are severely agglomerated thus making difficult the evaluation of the mean particle size.

As expected, mechanical grinding with vibratory mills leads to fragmentation of the larger aggregates and loss of crystallinity: however these phenomena occur in parallel with the undesired precipitation of Co₂P₂O₇ (27). The addition of small amount of carbon black to the LCP sample before mechanical milling prevents the precipitation of other phases even for long milling times (10 h) (27, 68). More details about the effect of carbon addition and the formation of LCP/C composites are discussed in the section 4f.

An interesting alternative to traditional high temperature annealing has been proposed by Han et al. (30). A stoichiometric mixture of precursors has been pelletized and then heated in a microwave oven covered with activated carbon. The precursors mixture has been obtained by vibratory milling for 2 h. The resulting material is LCP single phase with an homogeneous crystallite dispersion and particle size below 100 nm.

Wet Chemistry Methods

This method, also quoted as co-precipitation route, is very simple and the precipitates are generated simultaneously and uniformly throughout the solution. The typical precursors (e.g. LiH_2PO_4 , $\text{LiOH}\cdot\text{H}_2\text{O}$, $(\text{NH}_4)_2\text{HPO}_4$, $\text{Co}(\text{NO}_3)_2\cdot 6\text{H}_2\text{O}$, $\text{Co}(\text{HCOO})_2\cdot 2\text{H}_2\text{O}$) are simply dissolved in water and then precipitated: the resulting fine suspension is then filtered and the precipitate annealed at high temperatures under controlled atmospheres (10, 26). The precipitation of phosphate-based water-unsoluble precursors is driven by the pH of the solution as the chemistry of Co(II)-phosphate- H_2O system is rather complex. In the figure 4 the solid state repartition and solubility diagrams for the Co(II) system is shown (10).

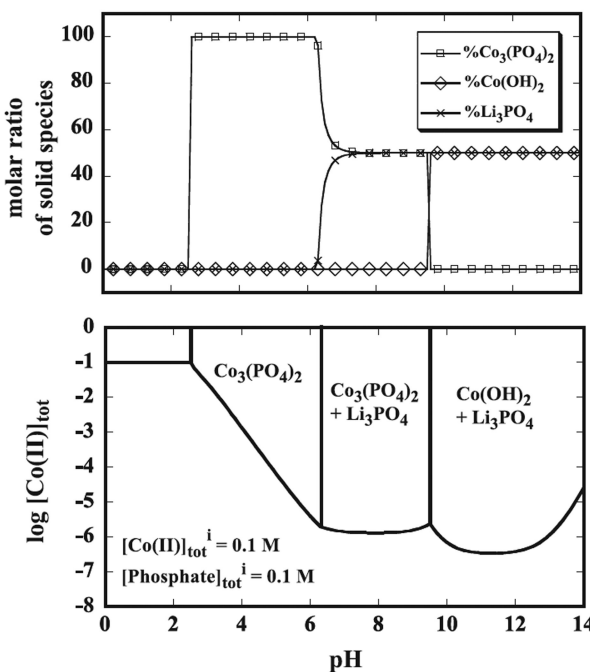


Figure 4. Solid state repartition and solubility diagram for Co(II)-phosphate- H_2O system from ref. (10). Reprinted with permission from ref. (10). Copyright (2004) Elsevier publishing.

The most probable pH-range for the precipitation of LiCoPO_4 apparently falls between 6.3 and 9.5. However, contrary to what expected, the filtered precipitate from a 0.1 M solution of Co(II) and phosphate in excess of Li^+ at pH=7.5 is formed at least by two phases (Li_3PO_4 and $\text{Co}_3(\text{PO}_4)_2$) as reported by Delacourt et al. (10). A careful heating at $T>500\text{C}$ leads to the formation of pure LiCoPO_4 .

A variant of the classic wet-chemistry route has been developed by Koleva et al. (25) by freeze-drying a slightly acidified (pH=3 by HCOOH) transparent water equimolar solution of LiH_2PO_4 and $\text{Co}(\text{HCOO})_2 \cdot 2\text{H}_2\text{O}$. The solution has been instantly frozen by liquid nitrogen and the dried under vacuum at -20°C. After drying the solid precursors have been annealed in two steps (350°C for 3h and at least 400°C for 10 hours in static air). The resulting material is pure LCP with homogeneous particle size dispersion and nanometric crystallites (65-105 nm from XRD Rietveld refinement): a SEM image of the excellent morphology of the LCP sample produced by Koleva et al. (25) at 450°C is shown in figure 5.

Another modified wet-chemistry route has been proposed by Fuertes et al. (69) in order to obtain LCP nanoparticles confined within an hollow carbon sphere. Carbon capsules with a macroporous hollow core and a mesoporous shell have been carefully impregnated with an aqueous solution of LiH_2PO_4 and cobalt nitrate. The conversion to encapsulated LCP nanoparticles has been obtained by annealing at 600°C in N_2 for 1h. The obtained composite material shows inorganic particles with homogenous sizes of approximately 150 nm in diameter, occupying the hollow core of the carbon capsule (see figure 6). The carbon shell keeps large part of its original mesoporosity and in fact the resulting surface exceeds $400 \text{ m}^2\text{g}^{-1}$.

Sol-Gel Method

The sol-gel routes are successful strategies to overcome many of the disadvantages of the solid-state and simple wet-chemistry (co-precipitation) syntheses. In fact sol-gel routes operate at relatively low processing temperatures and guarantee high chemical and morphological homogeneity, allowing a careful control of the size and shape of the materials particles. This synthetic approach improves the standard wet-chemistry route by tuning the precipitation step by the addition of chelatig and jellifying agents. The obtained viscous gel is then dried and calcined at high temperatures. Such methods usually also lead to the in situ precipitation of carbon coating on particles when Ar flows (or other inert gases) are used in the final annealing step.

Sol-gel recipes have been developed to prepare LCP by many research groups (31-35, 40, 51, 63, 70-77). As an example, stoichiometric amounts of LiNO_3 , $\text{Co}(\text{NO}_3)_2 \cdot 6\text{H}_2\text{O}$ and $(\text{NH}_4)_2\text{HPO}_4$ have been dissolved in aqueous citric acid (Citric acid mediated, CAM, sol-gel route) by Deniard and co-workers (51): the resulting liquid has been polymerized by the addition of propylene glycol which increases the solution viscosity due to the formation of an ester-type three dimensional network. Subsequently this gel has been aged in a microwave oven and then calcined at 500C degrees in air. The obtained material shows a particle size around 200 nm.

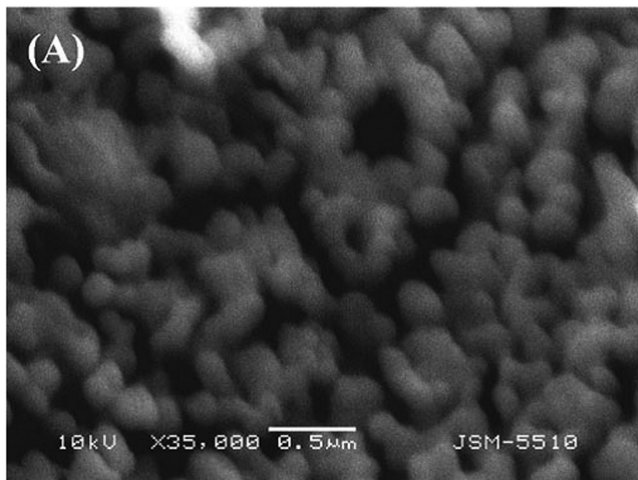


Figure 5. SEM micrograph showing the morphology of the LCP sample produced by Koleva et al. (25) at 450°C. Reprinted with permission from ref. (25). Copyright (2010) Wiley Blackwell publishing.

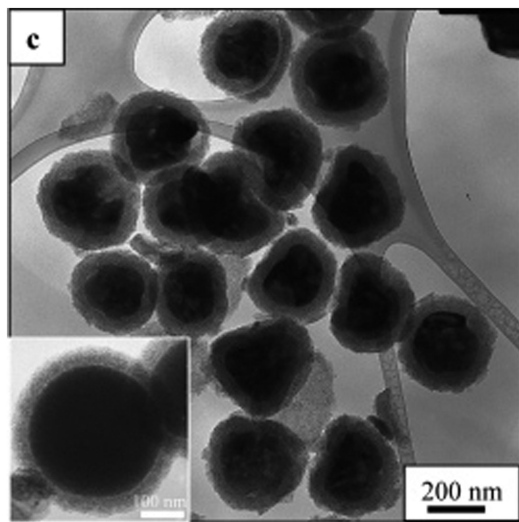


Figure 6. TEM micrograph showing the LCP nanoparticle encapsulated into the carbon hollow sphere (69). Reprinted with permission from ref. (69). Copyright (2007) American Chemical Society.

CAM sol-gel syntheses have been used also by other groups slightly changing the experimental conditions by varying the precursors, additives and the annealing conditions. Ehrenberg et al. (32) suggest the use of the sole citric acid and to induce the jellification by prolonged mild heating. Bhuvaneswari et al successfully use ethylene glycol as CAM-jellifying agent (70) obtaining plated-like particles with grain size of about 0.75 microns. Stronger nanometrization of well-formed crystal particles have been obtained by Kim et al. (31) by using a glucose-assisted CAM route (XRD crystallites with an approximate size of 450 nm), and by Xing et al. (76) by a careful optimization of the annealing (Ar and Air) and microwave oven ageing of the precursor gel (240-350 nm grain size estimated by SEM and TEM).

The polymerization of an aqueous solution has been also optimized by Bhuvaneswari et al. (35) by using a mixture of citric acid, acryl amide and N-N'-methylene-bis-acryl-amide. These additives lead to a rapid formation of a transparent gel that after a prolonged drying at 110°C and a two-step annealing at 300 and 800 °C in air turns to LCP. The resulting material shows nanosized and prismatic single crystal particles (approx. 50 nm) as shown in figure 7.

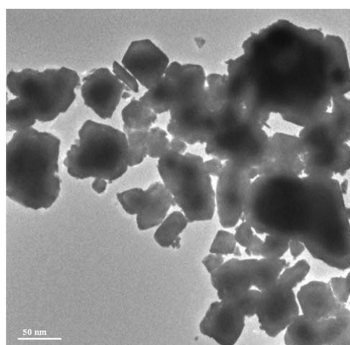


Figure 7. TEM micrograph showing the LCP nanoparticle obtained by a CAM sol-gel route by Bhuvaneswari et al. (35). Reprinted with permission from ref. (35). Copyright (2009) Springer publishing.

In a series of recent publications, a non-aqueous sol-gel route has been discussed by Dimesso and Ehrenberg (71-74) to help the infiltration of LCP precursors into 3D carbon architectures (nanotubes, nanofibers and foams). Stoichiometric amounts of cobalt and lithium nitrates have been dissolved in ethanol (0.1M) and this solution has been added dropwise to an ethanol solution of triethyl phosphite. The presence of hydrate water in the nitrate salts leads to the immediate formation of a sol that after prolonged ageing in air (24-48 h) is dried in Ar-flow until a viscous liquid is obtained. The final annealing is carried out at 700°C under Ar flow. In order to impregnate 3D carbon architectures, the porous carbon materials have been dispersed in the triethyl phosphite solution thus allowing the in situ formation of the sol. A TEM image of carbon nanofibers/LCP composite is shown in the figure 8.

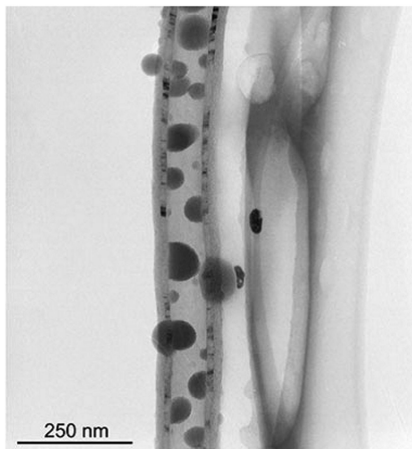


Figure 8. TEM micrograph showing a carbon nanofibers/LCP composite obtained by a non aqueous sol-gel route by Sarapulova *et al.* (74). Reprinted with permission from ref. (74). Copyright (2012) Springer publishing.

Hydro- and Solvo-Thermal Methods

Hydro- and solvo-thermal routes are soft-chemistry methods to prepare inorganic materials: these strategies allow to precipitate materials at low temperatures (from room temperature to 200-300 C) often avoiding the need of a further high temperature step. Such conditions help a careful control of the crystal growth (both shape and size) thus opening the door to a strong nanometrization of the crystallites, excellent morphological homogeneity and limited particle agglomeration. The main disadvantages of such methods are the high costs and the complicated synthetic procedures that make hard the scaling up to pilot plant production.

The synthesis of pure single phase LCP materials by hydrothermal and solvothermal routes has been reported by few groups (78-86). SEM images of some of the materials prepared by hydro and solvothermal syntheses are shown in the figure 9 as examples in order to highlight the large variety of homogeneous crystal morphologies reported so far.

The hydrothermal synthesis of LCP has been reported for the first time by Huang *et al.* (78), starting from an aqueous solution of Li^+ and Co^{2+} salts with H_3PO_4 (pH=8.5 by ammonia addition) treated at 220C. The final material is constituted by well-shaped micrometric LCP prisms (size 1-6 microns). On the contrary the hydrothermal synthesis in an acidic solution (pH=5.7) leads to the precipitation of a single phase material constituted by cobalt phosphate hydrate.

Thin foil-like LCP particles with a large surface area ($21.3 \text{ m}^2\text{g}^{-1}$) and nanometric particles size (tenths of nanometers) have been synthesized by Markevich *et al.* (79) by hydrothermally treating a mixture prepared from aqueous solution of LiOH , a soluble Co salt and orthophosphoric acid. The obtained hydrothermal product has been filtered, washed and subsequently mixed with a

carbon precursor. After drying the mixture has been pyrolysed at 750C under inert atmosphere.

Hedgehog-like polycrystalline particles have been obtained by a solvothermal route by Wang et al. (80). These particles are LCP single crystal shaped as 100 nm thick prismatic nanorods. Stoichiometric amounts of LiOH, CoSO₄, (NH₄)₃PO₄ and glucose (mole ratio 3:1:1:0.5) have been dissolved in an 1:1 water/benzyl alcohol mixed solvent and then heated in autoclave at 200C for 8 h. The simple hydrothermal synthesis has been also checked by Wang et al. in the same conditions obtaining prismatic micrometric LCP rods and verified the effect of high temperature annealing at 750C under Ar. This last step apparently do not alter the obtained nano-morphologies due to the formation of a thin carbon coating that encapsulate the single crystals thus limiting the coalescence at high temperature.

LCP nanocrystals with [010] orientation have been synthesized by Su et al. (81) using a poly(vinyl pirrolidone) (PVP) assisted ethanol solvothermal route at 180C for 2 days. After drying at 80C the obtained material is constituted by single phase LCP needles (diameter < 100 nm) assembled in isolated single straw-like structures. Without the use of PVP or by replacing it with glucose or polyethylene glycol 20000, the final material shows strong aggregation among the nanoparticles. Apparently PVP is capable to finely tune and control crystal growth and the morphology of the LCP material.

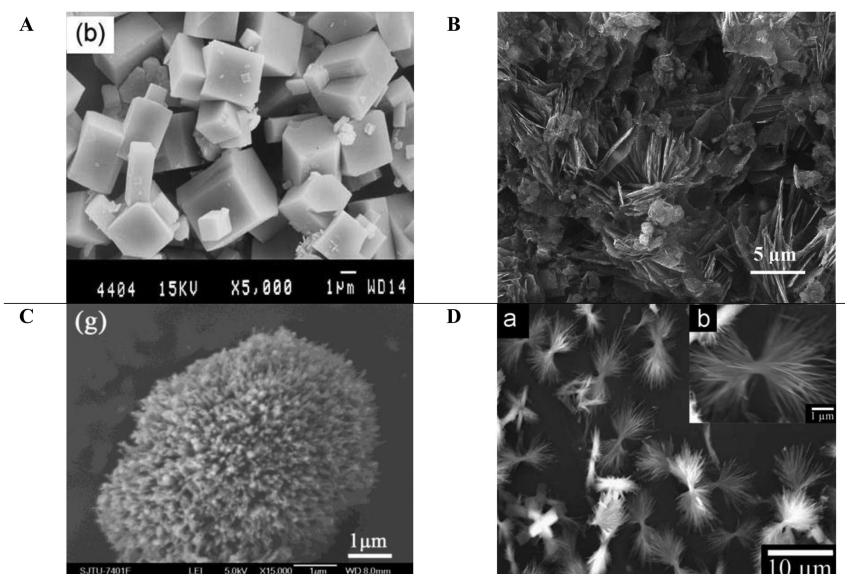


Figure 9. SEM images of hydro- and solvo-thermal LCP materials obtained by: (A) Huang et al. (78) (B) Markevich et al. (79), (C) Wang et al. (80) and (D) Su et al. (81). Reprinted with permission from ref. (78–81). Copyright (2005,2011) Elsevier publishing.

Spray Pyrolysis and Other Synthesis Methods

Spray pyrolysis allows the synthesis of nanocrystals intimately mixed with carbon nanoparticles assembled in large micron-sized nanoporous spherical assemblies. Such composite multidimensional materials can be easily packed in electrodes films thus circumventing the unavoidable small tap density and poor carbon dispersion of standard electrodes constituted by nanoparticles mixed with high surface area carbons.

LCP materials have been prepared by Long Doan et al. (41, 42, 87) starting from an aqueous solution of Li and Co nitrates with H₃PO₄. The precursor solution has been atomized at a frequency of 1.7 MHz by an ultrasonic nebulizer and the sprayed droplets have been transported to the reactor by a N₂/3%H₂ flow. Spray pyrolysis temperature has been set in the range 200-500C. The resulting particles have been collected at the reactor exit by an electrostatic precipitator operated at 170C. The as-prepared LCP powders have been then milled with 10% of acetylene black in ethanol by a planetary high energy ball milling. After ball-milling the samples have been annealed at 500C for 4 hours in a N₂/3%H₂ flow. The obtained composite material is constituted by single phase LCP crystals with primary particle size of 100 nm finely mixed with carbon nanoparticles and assembled in micron-sized spherical composite particles. A similar morphology has been obtained by Liu et al. (43) without the final ball milling step with acetylene black by forming an in situ a carbon coating during the spray pyrolysis at 700C. A SEM image of spray pyrolysis LCP material obtained by Long Doan et al. is presented in figure 10.

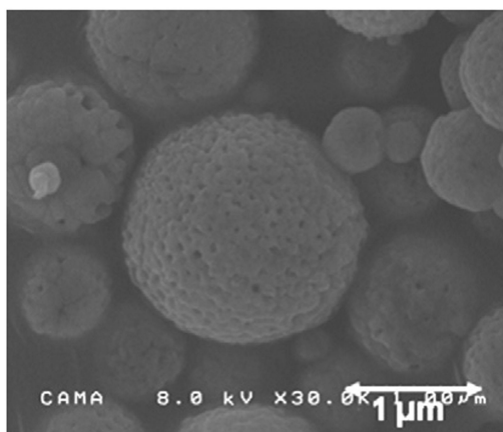


Figure 10. SEM image of spray pyrolysis LCP/carbon composite material obtained by Long Doan et al. (41). Reprinted with permission from ref. (41).

Copyright (2012) Elsevier publishing.

Single crystals of LCP have been obtained by Tian et al. (24) by LiCl molten salt methods in Pt crucibles sealed under Ar atmosphere at 900 C degrees. Other authors also report the synthesis of LCP materials by optical floating zone method (88), radio frequency magnetron sputtering (89), electrostatic spay deposition technique (90) and microwave heating (91).

Carbon Coating

The formation of a conductive carbon layer on the surface of crystal particles is a key factor to allow LFP to reversibly cycle lithium in electrochemical cells at high rates (3, 4). This is likely to be true also for LCP that shows electron conductivity values at room temperature comparable to LFP. In fact, as discussed above, deposition of carbon coatings or precipitation of Co²P under high temperature annealing in inert atmosphere lead to a drastic increase of about 10⁴-10⁵ of the electrical conductivity of LCP (38, 59-61).

Four main strategies have been explored to prepare LCP/carbon composite materials.

1. Infiltration of LCP sol or aqueous precursors in pre-formed 3D carbon architectures followed by annealing at high temperature to precipitate LCP particles on the surface or within the carbonaceous matrix (11, 39, 69, 71-74).
2. Intimate mixing of high surface carbon nanoparticles with pre-formed LCP micron- or nano-sized particles by mechano-chemical milling without or with a solvent to mitigate the energy of the ball impact on LCP crystals (27, 36, 38, 41, 42, 61, 66, 87).
3. In situ growth of a conducting carbon coating from organic precursors on pre-formed LCP particles followed by high temperature annealing in inert or reducing gas flow (34, 79).
4. One step in situ growth of a conducting carbon coating on LCP particles during their synthesis by high temperature annealing in inert or reducing gas flow (31, 40, 43, 70, 76, 80, 91, 92).

Examples of the first synthetic route have been reviewed in the previous sections and a detailed analysis is omitted to avoid redundancies (see materials shown in figure 6 and figure 8 and the corresponding discussion in the text). Briefly this strategy is a modification of the classic hard template route to precipitate nanoparticles within the pores of pre-formed 3D architectures. In this case the hard template is constituted by pre-formed carbon nanoparticles, hollow spheres, nanofibers, nanotubes or foams. By infiltrating the liquid LCP precursors mixture in the pores of the host matrix, and after high temperature annealing in Ar (or microwave ageing (30)), it is possible to obtain LCP nanoparticles homogeneously spread throughout the porous carbon material (11, 39, 69-74).

The formation of an intimate mixture of carbon nanoparticles with LCP particles obtained by mechanical milling has been proposed for the first time by Rabanal et al. (27) that mechanically grinded for 10 h in a vibratory ball mill pre-formed LCP samples prepared by solid state route with 8 wt.% of

black carbon. As already discussed, such addition prevents the precipitation of other phases such as $\text{Co}_2\text{P}_2\text{O}_7$ during the ball milling (27) and mitigates the unavoidable amorphization of the LCP particles due to impact with the balls upon milling. Many research groups have reported similar strategies mainly varying the nature and amount of the carbon nanoparticles and the experimental condition of mechanical milling (frequency, milling time, ball to material weight ratio) (36). Some authors suggested after mechanical milling a further annealing step at high temperature under Ar or N_2/H_2 flows to help the adhesion of carbon nanoparticles onto the LCP particles (38, 41, 42, 61, 66, 87). The effect of this further pyrolysis-step has been investigated by Wolfenstine et al. (61): they observe evidences of the carbothermal reduction of LiCoPO_4 at high temperature and the formation of small amounts of Co_2P as admixture (2-9 wt.%). This contamination has a strong beneficial effects of the electronic conductivity of LCP: a 9 wt.% Co_2P content leads to an electronic conductivity of $\sim 4 \cdot 10^3 \text{ S cm}^{-1}$, a factor of 10^{10} greater than for pure LCP. On the other hand, contaminations by Co_2P larger than 4-5 wt.% result in a detrimental reduction in the ability of the LCP material to reversibly cycle lithium in electrochemical cells. This effect has been attributed by Wolfenstine et al. to: (a) the reduced amount of LCP due to the carbothermal consumption and (b) the more difficult mobility of Li^+ ions through the electrolyte/electrode interphase due to the thick layer of Co_2P covering the LCP surfaces.

The *in situ* growth of a conducting carbon coating from organic precursors on pre-formed LCP particles can be obtained by thermally treating in inert or reducing gas flow a mixture of LCP particles with an organic precursor (79) such as sucrose (34). In this way a porous carbon layer precipitated on the surfaces of the LCP particles (see figure 11A).

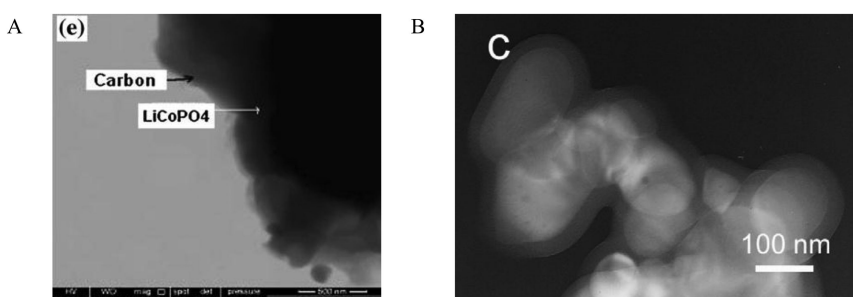


*Figure 11. TEM images of a (A) (bright field) LCP particles coated *in situ* with carbon nanoparticles by using a sucrose precursor on pre-formed LCP particles (34) or (B) (dark field) prepared in a one-step sol-gel synthesis using citric acid as carbon source (40). Reprinted with permission from ref. (34). Copyright (2011,2012) Springer and Elsevier publishing.*

One step *in situ* growth of a conducting carbon coating on LCP particles during their synthesis can be achieved by the addition of a proper organic substance (carbon precursor) into the LCP precursor mixture dissolved in solution (wet-chemistry, sol-gel, hydro- and solvo-thermal and spray pyrolysis

routes), followed by an high temperature annealing in inert or reducing gas flow (pyrolysis). In this way nanometric-sized carbon particles precipitate in situ during the formation of LCP crystals. These carbon nanoparticles uniformly cover the LCP particles thus forming a porous and continuous carbon coating (see figure 11B) with improved morphology compared to the other coating methods. Many authors report the precipitation of a carbon layers on LCP by using one-step sol-gel routes followed by high temperature pyrolysis: ethylene glycol/citric acid in mixture (70) or as single additives (40, 76, 92) have been used as carbon precursors as well as glucose/citric acid mixtures (31). Wang et al. have obtained a similar one step in situ formation of a compact carbon coating on LCP nanoparticles by a solvothermal route, using glucose as the carbon precursor, followed by inert gas annealing at 750 °C (80). Li et al. have synthesized a similar carbon coated LCP material by a one-step microwave heating route (91) and Liu et al. by spray-pyrolysis (43). It is to be noted that Dimesso et al. (92) observed that heat treatments at temperatures higher than 700 °C or prolonged annealing time ($t \geq 12$ h) of such “one step precursor mixture” lead to the formation of $\text{Li}_4\text{P}_2\text{O}_7$ and Co_2P as secondary phases. The formation of admixtures, particularly Co_2P , occurs due to the carbothermal reduction at the grain boundaries of the LCP crystallites.

Electrochemical Activity of LCP in Lithium Cells

LCP electrochemical activity has been proved by Amine and coworkers (9). Experimental galvanostatic lithium load curves and cyclic voltammetry are reported in the figure 12A-B.

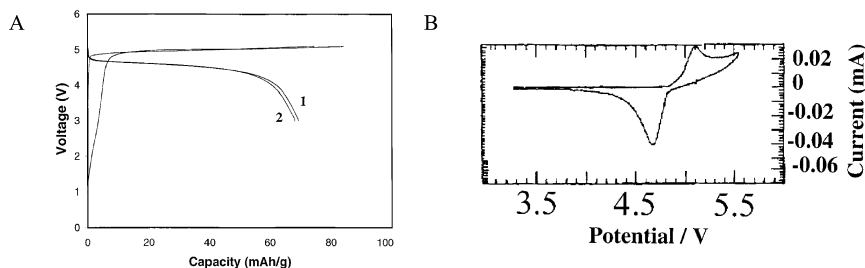


Figure 12. Electrochemical lithium load curve at 17 mAh g^{-1} ($= \text{C}/10$) and cyclic voltammetry (scan rate 0.5 mV min^{-1}) measured by Amine et al. (9) for the cell (Li/Sulfolane LiPF_6 /84% LCP 8% C 8% binder) at room temperature.
(Reproduced with permission from (9)).

LCP reversibly de-incorporates and incorporates lithium ions in electrochemical cells at approximately $\text{V} \sim 4.8 \text{ V}$ vs. Li^+/Li : apparently the oxidation/reduction steps occur in two stable plateaus similarly to LFP. However at such high potential the electrolyte components can oxidise: the increasing current at $\text{V} > 5.4 \text{ V}$ vs. Li^+/Li in the cyclic voltammetry test suggests the onset of parasitic reactions even in sulfulane-based electrolytes.

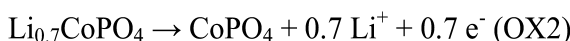
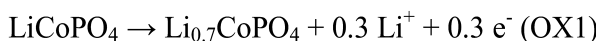
The chemical oxidation of LCP has been investigated by Wolfenstine and co-workers (64). An acetonitrile solution of nitronium tetrafluoroborate can promote the oxidation of Co^{2+} to Co^{3+} as the NO^+/NO redox potential is 5.1 V vs. Li^+/Li , larger than the potential experimentally observed for LCP oxidation in lithium cells. The ex situ XRD experiment after 7 days of chemical oxidation reveals that: (a) no new crystalline peaks appeared in the diffraction pattern, (b) only an additional large broad band appeared and (c) a slight shift of the original LCP peaks to lower angles has been observed together with their broadening and fading in intensity. Such results are in contrast with analogous studies carried out on the parent phases LFP and LMP thus suggesting that the delithiation mechanism of LCP is different from what observed for LFP and LMP (6).

Parallel theoretical studies carried out by Le Bacq (49, 50) and Zhou (55) predicts an oxidation voltage of 4.6 V vs. Li^+/Li for the $\text{LiCoPO}_4 = \text{Li}^+ + \text{e}^- + \text{CoPO}_4$ electrochemical reaction in good agreement with the experiments (9). Such reaction path has been assumed by the authors from the behaviour in lithium cells for the LFP and LMP olivines: calculations predicts also a volume shrinking of about -6.8% upon lithium extraction.

More detailed and systematic studies about the electrochemical lithium de-incorporation/incorporation mechanism of LCP have been carried out by Bramnik and co-workers (11, 32, 93) by electrochemical techniques (cyclic voltammetry, galvanostatic cycling, PITT, impedance spectroscopy) and XRD. Both conventional and synchrotron X-ray sources have been recorded ex situ on partially and completely charged/discharged samples and in situ upon electrochemical oxidation/reduction in a lithium cell coupled with an X-ray synchrotron source.

Current evolution in PITT experiments by Bramnik et al. (11) is shown in the figure 13 together with the differential charge plot from potentiodynamic cycling at C/30 and two selected regions in the diffraction patterns taken in situ during the first charge/discharge galvanostatic cycle.

Upon electrochemical oxidation in lithium cells LCP undergoes to a double consecutive two-phase transformation:



The first oxidation step (OX1) is a two-phase reaction that involves the consumption of the pristine LCP (phase 1 in the figures 13C-D) and the concomitant formation of a Li-poor olivine-like lattice, $\text{Li}_{0.7}\text{CoPO}_4$ (phase 2 in the figures 13C-D), obtained by extracting 0.3 equivalents of lithium ions. The second process (OX2) is another two-phase reaction that leads to a completely de-lithiated olivine-like lattice, CoPO_4 (phase 3 in the figures 13C-D) by releasing 0.7 equivalents of lithium ions upon oxidation. The lithium stoichiometry of the Li-deficient olivine lattice has been confirmed by Ehrenberg et al. by ex situ Neutron diffraction (32). It is to be noted that the de-lithiation/lithiation mechanism of LCP differs from the reaction path known for LFP and LMP due to the existence of an intermediate phase.

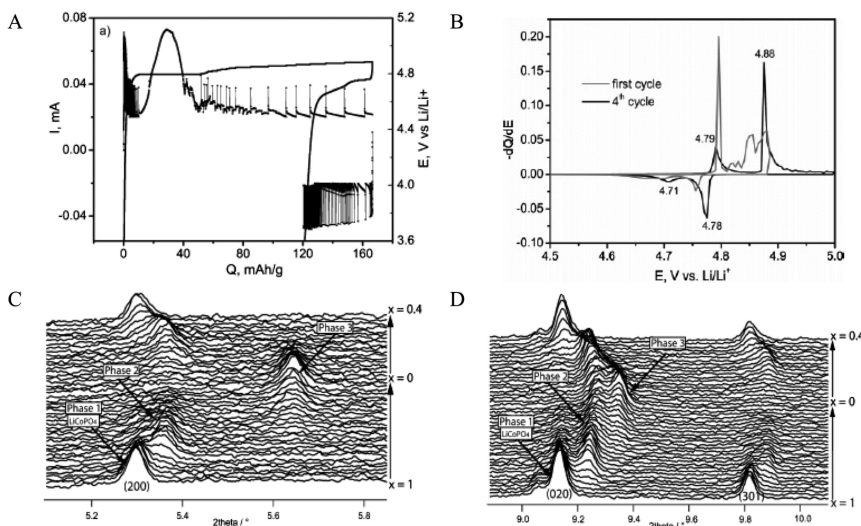


Figure 13. (A) Current measured in PITT experiments, (B) differential charge plot from potentiodynamic cycling at 5.6 mA g^{-1} ($= C/30$) and (C-D) evolution of two selected regions in the diffraction patterns (synchrotron radiation, $\lambda = 0.47189 \text{ \AA}$) upon galvanostatic charge/discharge at C/7 in lithium cells (Li/EC:DMC 2:1 LiPF_6 1M/75% LCP 20% C 5% binder) by Bramnik et al. (11). Copyright (2007) American Chemical Society.

The lattice parameters and atomic positions for the pristine, intermediate and de-lithiated phases obtained by Rietveld Refinement from ex situ Neutron experiments are summarised in the table 3. A volume contraction upon lithium removal of about -6.9% is observed, in excellent agreement with the computational prediction of -6.8% by Le Bacq et al. (50).

Besides these two consecutive two-phase reactions Bramnik et al. speculate about the possible existence of a terminal solid solution domain in the pristine LCP, at the beginning of charge and at the end of discharge. In situ synchrotron XRD and PTT experiments clues supports the hypothesis of a limited solid solution in the first stages of lithium extractions although in the lack of further experimental or computational study this point still remains open (11).

Turning to the performances in lithium cells, there is a general consensus that the reversibility of LCP in the lithium de-insertion/insertion greatly improves by growing a continuous carbon coating on the surface of the particles. As already discussed in the section 3f such carbon coating can contain Co_2P depending on the synthetic and pyrolysis conditions. In the figure 14 the performances in lithium cell are shown for a bare or carbon coated LCP materials prepared by Li et al. (91) using a microwave assisted method.

Table 3. Lattice constants and atomic positions for the three olivine-like phases observed by Bramnik et al. (32) in Neutron experiments on partially and totally charged LCP materials (space group Pnma)

Phase	Cell parameters				Atomic coordinates
	$a/\text{\AA}$	$b/\text{\AA}$	$c/\text{\AA}$	$V_{cell}/\text{\AA}^3$	
LiCoPO ₄	10.2012	5.9234	4.7000	284.0	Li ($\frac{1}{2}$ $\frac{1}{2}$ $\frac{1}{2}$) Co (0.2775 $\frac{1}{4}$ 0.9780) P (0.0943 $\frac{1}{4}$ 0.4190) O(1) (0.0972 $\frac{1}{4}$ 0.7420) O(2) (0.4543 $\frac{1}{4}$ 0.2037) O(3) (0.1663 0.043 0.2817)
Li _{0.7} CoPO ₄	10.0890	5.8544	4.7208	278.8	Li ($\frac{1}{2}$ $\frac{1}{2}$ $\frac{1}{2}$) ^a Co (0.2799 $\frac{1}{4}$ 0.9744) P (0.0971 $\frac{1}{4}$ 0.4163) O(1) (0.1047 $\frac{1}{4}$ 0.7416) O(2) (0.4498 $\frac{1}{4}$ 0.1878) O(3) (0.1680 0.043 0.2791)
CoPO ₄	9.5811	5.7888	4.7690	264.5	Co (0.2684 $\frac{1}{4}$ 0.9444) P (0.0928 $\frac{1}{4}$ 0.3820) O(1) (0.1178 $\frac{1}{4}$ 0.7016) O(2) (0.4339 $\frac{1}{4}$ 0.1590) O(3) (0.1595 0.029 0.2334)

^a Refined site occupancy 0.728

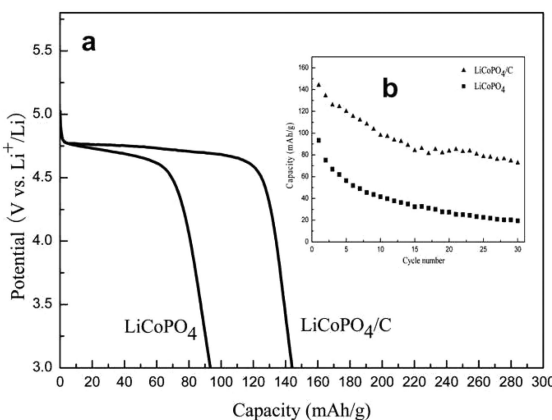


Figure 14. Performances in lithium cell (Li/EC:DMC 1:1 LiPF₆ 1M/LCP 75% C 20% binder 5%) for bare or carbon coated LCP materials prepared by Li et al. (91) using a microwave assisted method (current 17 mA g⁻¹=C/10, cycling between 5.1-3V). Copyright (2009) Elsevier publishing.

However the increase of the carbon content in the electrode formulation does not necessarily improve the performances that are apparently more carefully driven by the carbon coating synthetic procedure and the LCP preparation route. This has been demonstrated by Ni et al. (40) by preparing and studying two LCP-based materials by sol-gel, one calcined in Ar (LiCoPO₄/C-in-situ in figure 15a) and the other in Air. The first material, after Ar pyrolysis, shows a compact a continuous carbon coating covering the surface of the LCP particles (see figure 11b). The second material, i.e. annealed in air, has been submitted to a subsequent mild milling with acetylene black and heated at 550C to form an intimately mixed LCP/C composite (LiCoPO₄/C-ex-situ in figure 15a). In the figure 15a the discharge capacities reported by Ni et al (40) are shown for both materials. Although the amount of carbon in the two materials is comparable the morphology of the carbon coating makes the difference by improving the supporting a reversible cycling of lithium by LCP above 100 mAhg⁻¹ for 40 cycles.

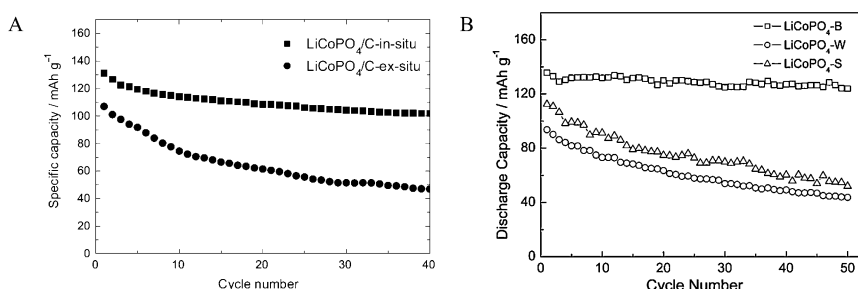


Figure 15. Performances in lithium cell reported by Ni et al (40) (Li/EC:DMC 1:1 LiPF₆ 1M/LCP 80% C 10% binder 10%; current 17 mAhg⁻¹=C/10, cycling between 5.2-3V) and Wang et al. (80) (Li/EC:DMC 1:1 LiPF₆ 1M/LCP 70% C 20% binder 10%; current 17 mAhg⁻¹=C/10, cycling between 5.2-3V) for a series of LCP carbon coated materials. Copyright (2009) Elsevier publishing.

The effect of the synthesis procedure and particles morphology has been studied by Wang et al. (80) in particular focusing on the capability of carbon coated LCP materials to reversibly de-insert/insert lithium in prolonged galvanostatic cycling. The performances in lithium cells of carbon coated LCP materials prepared by hydrothermal (LiCoPO₄-W in figure 15b), solvothermal (LiCoPO₄-B in figure 15b) and solid state (LiCoPO₄-S in figure 15b) routes are shown in the figure 15b thus suggesting that improved crystal and particles morphologies can greatly enhance the cyclability of LCP-based materials.

Good performances in lithium cells have been achieved also by LCP/C materials prepared by spray pyrolysis (41, 43) even at elevated current rates. In the figure 16 the performances reported by Doan et al. (41) for a LCP/C nanocomposite prepared by spray pyrolysis are shown.

It is therefore important to stress that the ability of LCP materials to reversibly cycle lithium in electrochemical cells is apparently strongly related to the crystal morphology, the synthetic strategy and the nature of the carbon coating.

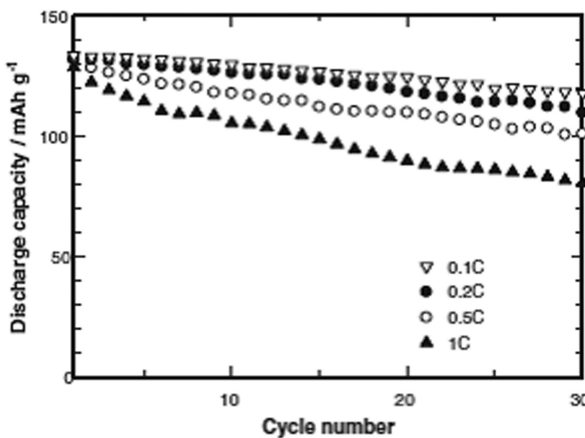


Figure 16. Performances in lithium cell reported by Doan *et al* (41) (Li/EC:DMC 1:1 LiPF₆ 1M/LCP 70% C 20% binder 10%; cycling between 5-2.5V). Copyright (2012) Elsevier publishing.

As a final point it is worth to mention that large part of the reported performances show only discharge capacities and neglect to report the coulombic efficiencies. As shown in figure 11a, and in many of the cited references, the efficiency of the electrochemical lithium de-insertion/insertion process from the LCP lattice is poor in the first cycle. However such poor reversibility is observed also in the subsequent cycles: where shown the coulombic efficiency never exceed 95% even after prolonged cycling (see as an example figure 6 in ref. (87)). More comments about the nature of this charge loss are discussed in the section 6.

Effect of Doping/Substitution

The beneficial effect of doping on the performances in lithium cells of LFP has been reported by many authors (3). The positive effect has been attributed to the improved intrinsic electronic conductivity and the increased Li-ion diffusion coefficient induced by cation substitutions. The electronic conductivity of LFP has been reported to increase by two to eight order of magnitude as a result of doping induced charge compensation. Although such simple picture is still under debate the beneficial effect of doping on LFP is straightforward.

Turning back to LCP only few studies about lattice doping/substitutions have been reported so far in the literature. Two different strategies have been computationally or experimentally tackled:

1. **“Metal doping”.** The substitution of metal sites (both Co²⁺ and Li⁺) with small amount of Cu⁺, Fe²⁺, Fe³⁺, Cr³⁺ and V⁵⁺ (30, 33, 38, 52, 56, 60, 94);
2. **“Solid solution”.** The formation of extended solid solutions by large substitution of Co²⁺ with Ni²⁺ and Mn²⁺ (12, 26, 42, 53, 83).

The goal of “metal doping” is to improve the electrical conductivity and lithium ion diffusivity in LCP lattice by altering the band-structure and inducing the formation of 0D defects (vacancies induced by charge compensation).

The computational modeling of Li-site (by Na and Cr) and Co-site (by isovalent Ni, Zn, Ca, Mg, and aliovalent Cu, Al, In, Mo and Zr) doped LCP by Lin et al. (52) suggests that doping in the Li-site may block the 1D channel diffusion path as both sodium and chromium are strongly bonded and difficultly extracted from the structure. On the other hand, doping in the Co-site may reduce the volume change upon lithium extraction/insertion thus suggesting that appropriate cobalt-site doping in LCP can enhance the structure stability of the materials promoting good reversibility and long cycle life.

From the experimental side, Wolfenstine (60) proved that limited doping with Cu^+ or Cr^{3+} does not alter significantly the electrical conductivity of LCP that is mainly affected by the precipitation of a surface layer of Co_2P . In fact the electronic conductivity of all undoped or doped samples are about 10^{-9} or 10^{-4} S cm^{-1} , all identical within the experimental uncertainties, for materials annealed in air or Ar, respectively. On the other hand, as observed by Wang et al. (38), doping with V^{5+} results in a slight increase of the electronic conductivity of LCP/C composites, from $6.8 \cdot 10^{-4}$ to $3.6 \cdot 10^{-3}$ S cm^{-1} , for the undoped and doped materials, respectively. This improvement apparently enhances the performances in lithium cells.

Many authors studied the LCP doping by Fe^{2+} that always results in the improvement of the electrochemical performances (30, 33, 56, 94) by boosting the kinetics of the lithium insertion/extraction reaction. In particular Kang and co-workers observed that Fe^{2+} doping suppress the Li-Co antisite mixing in the olivine structure by a combined computational and experimental approach. This effect is due to the preferential occupation of the Co-site by iron that induces an expansion of the oxygen octahedra and widens the Li^+ transport channels thus improving lithium diffusion.

Turning to large metal substitutions only a limited number of research groups have studied the formation of extended solid solution (12, 26, 42, 53, 83). The goal is to enlarge the ability of the resulting olivine-based material to reversibly cycle lithium in Li-cells.

The synthesis and characterization of $\text{LiCo}_{1-x}\text{Ni}_x\text{PO}_4$ solid solutions have been carried out by Wolfenstine (12) and Shanmukaraj et al. (26). Both groups suggest that the substitution of cobalt with nickel has negative effects on the materials properties: in particular the electrical conductivity apparently decreases with increasing concentration of Ni. Furthermore the discharge capacity of the $\text{LiCo}_{1-x}\text{Ni}_x\text{PO}_4$ solid solutions is associated entirely with the $\text{Co}^{3+}/\text{Co}^{2+}$ redox couple. Thus the effect of large Ni substitution is the reduce the length of the 4.7-4.8 V vs. Li^+/Li plateau in Li-cells as the $\text{Ni}^{3+}/\text{Ni}^{2+}$ is inactive even after charging to as high as 5.8-6.0 V vs. Li^+/Li .

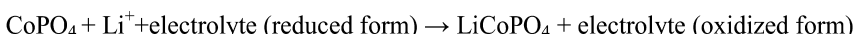
On the contrary, large substitutions with Mn^{2+} apparently lead to minor improvements in cyclability in Li-cells (42, 83). However such slight improvements are counterbalanced by the two-plateaus character of the voltage profile observed in galvanostatic cycling. The first plateau is observed at 4.1 and the second at 4.7-4.8 V vs. Li^+/Li due to the $\text{Mn}^{3+}/\text{Mn}^{2+}$ and $\text{Co}^{3+}/\text{Co}^{2+}$ redox couples, respectively. Such material, when coupled with an low voltage anode in

a full Li-ion configuration, would lead to a two plateaus full cell, thus implying the need of tailored electronics and electrical components to power any device.

Parasitic Processes

LCP working potential overcomes the capability of any existing electrolyte. The thermodynamic stability windows of the standard carbonate-based electrolytes is limited to 4.4-4.5 V vs. Li⁺/Li at the anodic side: above this limit the solvent molecules of the electrolytes start to oxidize at the cathode side. In the case of the LNMO spinel cathode material that works at 4.7-4.8 V vs. Li⁺/Li, the formation of a passivation film, by a limited decomposition of the electrolyte in the first charge, prevents self-discharge and further parasitic reaction upon cycling (95). Specific surface coatings further improves the reversibility of the LNMO cycling in Li-cells by limiting the electrode-electrolyte parasitic interactions (96).

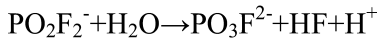
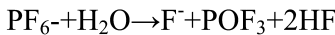
Bramnik et al have proved unambiguously the occurrence of parasitic reaction upon electrochemical lithium extraction from LCP by comparing the lithium content estimated by Rietveld refinement of in situ XRD patterns and the total charge exchanged electrochemically (11). Furthermore the occurrence of spontaneous self-discharge has been also observed in electrochemically de-lithiated LCP electrodes (11). In particular the self-relaxation of the charged LCP cathode is accompanied by a stepwise change in the open circuit voltage (OCV) and an increase in the total cell impedance. The shape of the self-discharge OCV shows two plateaus during relaxation, very similar to the galvanostatic discharge curve (see for comparison figures 13a and 14). Moreover prolonged relaxation leads to the formation of the pristine compound, from which lithium can be newly electrochemically extracted. Bramnik et al. (11) have speculated that such behaviour can be justified by considering the following reaction:



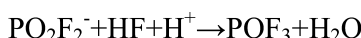
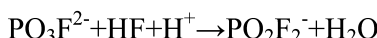
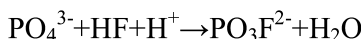
The spontaneous lithium insertion upon self-discharge proceeds via decomposition of the electrolyte. The products of such parasitic reactions, that may occur also upon charge, may contribute to the formation of a surface film on the cathode electrode. This hypothesis is in agreement with the increase in the resistance of medium frequency semi-circles in impedance spectroscopy tests carried out at OCV upon self-discharge. Unfortunately specific studies focused to the detailed understanding of such parasitic redox reactions and the identification chemical species involved are missing.

Besides self-discharge, many authors have observed a large capacity fading for LCP-based electrodes upon cycling (see as examples the inset figure 14 and figures 15-16) in conventional F-containing electrolytes. This behaviors may be a clue of parasitic reactions upon cycling. Sharabi et al. (82) have verified that the use of SiO₂-containing separators improves the LCP capacity retention compared to cells with polyethylene separators. The fast capacity fading in this last case apparently results from the degradation of the olivine structure upon cycling and lithium depletion from the lattice. These detrimental processes are probably related to the interaction of the charged material with HF, a contaminant

unavoidably present in traces in any electrolyte containing the LiPF₆ salt. HF spontaneously forms in the electrolyte due to the hydrolysis of PF₆⁻ anions with the residual traces of water:



The use of HF-scavenging SiO₂ separators reduces the capacity fading and do not lead to large alteration of the olivine structure upon cycling. This interpretation has been confirmed by the same research group in (84, 85) by nuclear magnetic resonance, Raman and X-ray photoelectron spectroscopy measurements. The capacity fading of LCP electrodes in LiPF₆-containing electrolytes is apparently induced by a nucleophilic attack of F⁻ anions on the P atoms of the de-lithiated olivine phase followed by the breakdown of the P-O bonds in the phosphate anions with the formation of the PO₂F₂⁻ anion that is highly soluble in the electrolyte solution. This parasitic electrode-electrolyte interaction follows the following reaction scheme:



The two reported reaction sequences are self-sustaining and likely lead to a progressive damaging of the surface of the charged electrode. It is to be noted that these processes are not charge consuming and therefore should occur also spontaneously on the pristine electrodes unless Co³⁺ ions are involved in other parallel parasitic redox reaction. Bramnik et al. (11) have observed that the total impedance of the not-charged LCP electrodes in lithium cells after a slightly increase does not show any significant changes for more than 18 hours. Owing to this it is likely that the detrimental parasitic reactions described by Sharabi and co-workers explain some aspects of the overall electrolyte decomposition but a further effort is needed to evaluate the role of Co³⁺ ions.

Strategies to tackle the capacity fading by mitigating the electrolyte/electrode parasitic interactions have been suggested by Eftekhari (97), Allen (33), Hu (75) and Xing et al. (76).

The capacity fading can be apparently mitigated by the growth of a film of Al₂O₃ directly on the surface of LCP as verified by Eftekhari (97), thus limiting the direct contact of the charged active material with the electrolyte components. On the other hand the use of additives to the electrolyte, such as tiophene (76), lithium difluoro(oxalate)borate (75) and tris(hexafluoroisopropyl)phosphate (33) improves the performances by enhancing the total discharge capacity and reducing the capacity fading upon cycling.

Conclusions

LCP is a valuable candidate material for next generation high voltage and high energy Li-ion cells. Although large efforts have been devoted by many research groups to the study of this material, some fundamental aspects of the material properties and reaction mechanisms in lithium cells are not completely understood. In particular the investigation of the possible occurrence of terminal solid solution in the first stages of de-lithiation of LCP, the characterization of the intermediate $\text{Li}_{0.7}\text{CoPO}_4$ phase and a more careful understanding of the parasitic interactions with electrolytes containing fluorinated anions are key aspects to be tackled. Moreover also the study of defects (e.g. Li-Co antisite defects, Li-vacancies, Co state of oxidation on the surface, ...) and the related effect of doping and substitutions is still at the pioneer stages of research.

Owing to this large room for improvements in the performances in Li-cells of LCP is expected by tailoring the synthesis route, the coatings, the doping/ substitution and the electrolyte additives in order to boost its ability to reversibly cycle lithium and minimize the unavoidable parasitic interaction with standard carbonate-based electrolyte.

Acknowledgments

The authors would like to thank Prof. B. Scrosati and Dr. Priscilla Reale for the fruitful discussions.

References

1. Padhi, A. K.; Nanjundaswamy, K. S.; Masquelier, C.; Okada, S.; Goodenough, J. B. *J. Electrochem. Soc.* **1997**, *144*, 1609–1613.
2. Padhi, A. K.; Nanjundaswamy, K. S.; Goodenough, J. B. *J. Electrochem. Soc.* **1997**, *144*, 1188-.
3. Zhang, W.-J. *J. Power Sources* **2011**, *196*, 2962–1194.
4. Jugovic, D.; Uskokovic, D. *J. Power Sources* **2009**, *190*, 538–544.
5. Song, H.-K.; Lee, K. T.; Kim, M. G.; Nazar, L.; Cho, J. *Adv. Funct. Mater.* **2010**, *10*, 3818-.
6. Delacourt, C.; Poizot, P.; Morcrette, M.; Tarascon, J. M.; Masquelier, C. *Chem. Mater.* **2004**, *16*, 93–99.
7. Chen, G.; Wilcox, J. D.; Richardson, T. J. *Electrochem. Solid-State Lett.* **2008**, *11*, A190–A194.
8. Bramnik, N. N.; Ehrenberg, H. *J. Alloys Compd.* **2008**, *464*, 259–264.
9. Amine, K.; Yasuda, H.; Yamaguchi, M. *Electrochem. Solid State Lett.* **2000**, *3*, 178–179.
10. Delacourt, C.; Wurm, C.; Reale, P.; Morcrette, M.; Masquelier, C. *Solid State Ionics* **2004**, *173*, 113–119.
11. Bramnik, N. N.; Nikolowski, K.; Baehtz, C.; Bramnik, K. G.; Ehrenberg, H. *Chem. Mater.* **2007**, *19*, 908–915.
12. Wolfenstine, J.; Allen, J. *J. Power Sources* **2004**, *156*, 150–153.
13. Wolfenstine, J.; Allen, J. *J. Power Sources* **2005**, *142*, 389–390.

14. Park, M.; Zhang, X.; Chung, M.; Less, G. B.; Sastry, A. M. *J. Power Sources* **2010**, *195*, 7904–7929.
15. Hautier, G.; Jain, A.; Ong, S. P.; Kang, B.; Moore, C.; Doe, R.; Ceder, G. *Chem. Mater.* **2011**, *23*, 3495–3508.
16. Howard, W. F.; Spotnitz, R. M. *J. Power Sources* **2007**, *165*, 887–891.
17. Santhanam, R.; Rambabu, B. *J. Power Sources* **2010**, *195*, 5442–5451.
18. Martha, S. K.; Haik, O.; Zenigrad, E.; Exnar, I.; Drezen, T.; Miners, J. H.; Aurbach, D. *J. Electrochemical Soc.* **2011**, *158*, A1115–A1122.
19. Xiang, H. F.; Wang, H.; Chen, C. H.; Ge, X. W.; Guo, S.; Sun, J. H.; Hu, W. Q. *J. Power Sources* **2009**, *191*, 575–581.
20. Jiang, J.; Dahn, J. R. *Electrochem. Commun.* **2004**, *6*, 39–43.
21. Martha, S. K.; Markevich, E.; Burgel, V.; Salitra, G.; Zinigrad, E.; Markovsky, B.; Sclar, H. *J. Power Sources* **2009**, *189*, 288–296.
22. Wang, G.; Liu, H.; Liu, J.; Qiao, S.; Lu, M.; Munroe, P.; Ahn, H. *Adv. Mater.* **2010**, *22*, 4944–4948.
23. Kraytsberg, A.; Ein-Eli, Y. *Adv. Eng. Mater.* **2012**, *2*, 922–939.
24. Tian, W.; Li, J.; Lynn, J. W.; Zarestky, J. L.; Vaknin, D. *Phys. Rev. B* **2008**, *78*, 184429.
25. Koleva, V.; Zhecheva, E.; Stoyanova, R. *Eur. J. Inorg. Chem.* **2010**, 4091–4099.
26. Shanmukaraj, D.; Murugan, R. *Ionics* **2004**, *10*, 88–92.
27. Rabanal, M. E.; Gutierrez, M. C.; Garcia-Alvarado, F.; Gonzalo, E. C.; Arroyo-de Dompablo, M. E. *J. Power Sources* **2006**, *160*, 523–528.
28. Tan, L.; Luo, Z.; Liu, H.; Yu, Y. *J. Alloys Compd.* **2010**, *502*, 407–411.
29. Okada, S.; Sawa, S.; Egashira, M. *J. Power Sources* **2001**, *97*, 430–432.
30. Han, D. W.; Kang, Y. M.; Yin, R. Z.; Song, M. S.; Kwon, H. S. *Electrochem. Commun.* **2009**, *11*, 137–139.
31. Kim, E. J.; Hu, H. Y.; Lim, J. S.; Kang, J. W.; Gim, J. H.; Mathew, V.; Kim, J. *J. Solid State Electrochem.* **2012**, *16*, 149–155.
32. Ehrenberg, H.; Bramnik, N. N.; Senyshyn, A.; Fuess, H. *Solid State Sci.* **2009**, *11*, 18–23.
33. Allen, J. L.; Jow, T. R.; Wolfestine, J. *J. Power Sources* **2011**, *196*, 8656–8661.
34. Poovizhi, P. N.; Selladurai, S. *Ionics* **2011**, *17*, 13–19.
35. Bhuvaneswari, G. D.; Kalaiselvi, N.; Jayaprakash, N.; Periasamy, P. *J. Sol-Gel Sci. Technol.* **2009**, *49*, 137–144.
36. Prabu, M.; Selvasekaranpadian, S.; Reddy, M. V.; Chowdari, B. V. R. *J. Solid State Electrochem.* **2012**, *16*, 1833–1839.
37. Sun, Q.; Luo, J. Y.; Fu, Z. W. *Electrochem. Solid State Lett.* **2011**, *14*, A151–A153.
38. Wang, F.; Yang, J.; Li, Y. N.; Wang, J. *J. Power Sources* **2010**, *195*, 6884–6891.
39. Bramnik, N. N.; Bramnik, K. G.; Baehtz, C.; Ehrenberg, H. *J. Power Sources* **2005**, *145*, 74–81.
40. Ni, J.; Wang, H.; Gao, L.; Lu, L. *Electrochim Acta* **2012**, *70*, 349–353.
41. Long Doan, T. N.; Taniguchi, I. *Powder Technol.* **2012**, *217*, 574–580.

42. Taniguchi, I.; Long Doan, T. N.; Shao, B. *Electrochim. Acta*. **2011**, *56*, 7680–7685.
43. Liu, J.; Conry, T. E.; Song, X.; Yang, L.; Doeff, M. M.; Richardson, T. J. *J. Mater. Chem.* **2011**, *21*, 9984–9987.
44. Lu, Z.; Chen, H.; Robert, R.; Zhu, B. Y. X.; Deng, J.; Wu, L.; Chung, C. Y.; Grey, C. P. *Chem. Mater.* **2011**, *23*, 2848–2859.
45. Hoang, K.; Johannes, M. *Chem. Mater.* **2011**, *23*, 3003–3013.
46. Axmann, P.; Stinner, C.; Wohlfahrt-Mehrens, M.; Mauger, A.; Gendron, F.; Julien, C. M. *Chem. Mater.* **2009**, *21*, 1636–1644.
47. Chen, M.; Hallstedt, B.; Gauckler, L. J. *J. Phase Equilib.* **2003**, *24*, 212–227.
48. Zaghib, K.; Mauger, A.; Kopec, M.; Gendron, F.; Julien, C. M. *ECS Trans.* **2009**, *16*, 31–41.
49. Le Bacq, O.; Pasturel, A.; Bengone, O. *Phys. Rev. B* **2004**, *69*, 245107/1–10.
50. Le Bacq, O.; Pasturel, A. *Philos. Mag.* **2005**, *16*, 1747–1754.
51. Deniard, P.; Dulac, A. M.; Rocquefelte, X.; Grigorova, V.; Le Bacq, O.; Pasturel, A.; Jobic, S. *J. Phys. Chem. Solids* **2004**, *65*, 229–233.
52. Lin, Z.-P.; Zhao, Y.-M.; Zhao, Y.-J. *Chin. Phys. Lett.* **2009**, *26*, 038202.
53. Lin, Z.-P.; Zhao, Y.-J.; Zhao, Y.-M. *Chin. Phys. B* **2011**, *20*, 018201.
54. Amador, U.; Gallardo-Amores, J. M.; Heymann, G.; Huppertz, H.; Moran, E.; Arroyo de Dompablo, M. E. *Solid State Sci.* **2009**, *11*, 343–348.
55. Zhou, F.; Cococcioni, M.; Kang, K.; Ceder, G. *Electrochem. Commun.* **2004**, *6*, 1144–1148.
56. Kang, Y.-M.; Kim, Y.-I.; Oh, M.-W.; Yin, R.-Z.; Lee, Y.; Han, D.-W.; Kwon, H.-S.; Kim, J. H.; Ramanath, G. *Energy Environ. Sci.* **2011**, *4*, 4978–4983.
57. Shang, S. L.; Wang, Y.; Mei, Z. G.; Hui, X. D.; Liu, Z. K. *J. Mater. Chem.* **2012**, *22*, 1142–1149.
58. Tadanaga, K.; Mizuno, F.; Hayashi, A.; Minami, T.; Tatsumisago, M. *Electrochemistry* **2003**, *71*, 1192–1195.
59. Wolfenstine, J.; Lee, U.; Poese, B.; Allen, J. L. *J. Power Sources* **2005**, *144*, 226–230.
60. Wolfenstine, J. *J. Power Sources* **2006**, *158*, 1431–1435.
61. J. Wolfenstine, J.; Read, J.; Allen, J. L. *J. Power Sources* **2007**, *163*, 1070–1073.
62. Morgan, D.; Van der Ven, A.; Ceder, G. *Electrochem. Solid State Lett.* **2004**, *7*, A30–A32.
63. Prabu, M.; Selvasekarapanadian, S.; Kulkarni, A. R.; Karthikeyan, S.; Hirankumar, G.; Sanjeeviraja, C. *Solid State Sci.* **2011**, *13*, 1714–1718.
64. Wolfenstine, J.; Poese, B.; Allen, J. L. *J. Power Sources* **2004**, *138*, 281–282.
65. Nagata, K.; Nanno, T. *J. Power Sources* **2007**, *174*, 832–837.
66. Oh, S.-M.; Myung, S.-T.; Sun, Y.-K. *J. Mater. Sci.* **2012**, *22*, 14932–14937.
67. Grigorova, V.; Roussev, D.; Deniard, P.; Jobic, S. *J. Phys. Chem. Solids* **2005**, *66*, 1598–1608.
68. Bramnik, N. N.; Bramnik, K. G.; Baehtz, C.; Ehrenberg, H. *J. Power Sources* **2005**, *145*, 74–81.
69. Fuertes, A. B.; Sevilla, M.; Valdes-Solid, T.; Tartaj, P. *Chem. Mater.* **2007**, *19*, 5418–5423.

70. Bhuwaneswari, M. S.; Dimesso, L.; Jaegermann, W. *J. Sol-Gel. Sci. Technol.* **2010**, *56*, 320–326.
71. Schneider, J. J.; Khanderi, J.; Popp, A.; Engstler, J.; Tempel, H.; Sarapulova, A.; Bramnik, N. N.; Mikhailova, D.; Ehrenberg, H.; Schmitt, L. A.; Dimesso, L.; Forster, C.; Jaegermann, W. *Eur. J. Inorg. Chem.* **2011**, 4349–4359.
72. Dimesso, L.; Cherkashinin, G.; Spanheimer, C.; Jaegermann, W. *J. Alloys Compd.* **2012**, *516*, 119–125.
73. Dimesso, L.; Forster, C.; Jaegermann, W.; Khandori, J. P.; Tempel, H.; Popp, A.; Engstler, J.; Schenider, J. J.; Sarapulova, A.; Mikhailova, D.; Schmitt, L. A.; Oswald, S.; Ehrenberg, H. *Chem. Soc. Rev.* **2012**, *41*, 5068–5080.
74. Sarapulova, A.; Mikhailova, D.; Schmitt, L. A.; Oswald, S.; Bramnik, N. N.; Ehrenberg, H. *J. Sol-Gel. Sci. Technol.* **2012**, *62*, 98–110.
75. Hu, M.; Wei, J.; Xing, L.; Zhou, Z. *J. Appl. Electrochem.* **2012**, *42*, 291–296.
76. Xing, L. Y.; Hu, M.; Tang, Q.; Wei, J. P.; Qin, X.; Zhou, Z. *Electrochim. Acta* **2012**, *59*, 172–178.
77. Yang, J.; Xu, J.-J. *J. Electrochemical Soc.* **2006**, *153*, A716–A723.
78. Huang, X.; Ma, J.; Wu, P.; Hu, Y.; Dai, J.; Zhu, Z.; Chen, H.; Wang, H. *Mater. Lett.* **2005**, *59*, 578–582.
79. Markevich, E.; Sharabi, R.; Haik, O.; Borgel, V.; Salitra, G.; Aurbach, D.; Semrau, G.; Schmitt, M. A.; Schall, N.; Stinnerl, C. *J. Power Sources* **2011**, *196*, 6433–6439.
80. Wang, F.; Yang, J.; Nuli, Y.; Wang, J. *J. Power Sources* **2011**, *196*, 4806–4810.
81. Su, J.; Wei, B.-Q.; Rong, J.-P.; Yin, W.-Y.; Ye, Z.-X.; Tian, X.-Q.; Ren, L.; Cao, M.-H.; Hu, C.-W. *J. Solid State Chem.* **2011**, *184*, 2909–2912.
82. Sharabi, R.; Markevich, E.; Borgel, V.; Salitra, G.; Aurbach, D.; Semrau, G.; Schmitt, M. A.; Schall, N.; Stinner, C. *Electrochim. Commun.* **2011**, *13*, 800–802.
83. Li, M. *Ionics* **2012**, *18*, 507–511.
84. Sharabi, R.; Markevich, E.; Borgel, V.; Salitra, G.; Gerchincky, G.; Aurbach, D.; Semrau, G.; Schmitt, M. A.; Schall, N.; Stinner, C. *J. Power Sources* **2012**, *203*, 109–114.
85. Markevich, E.; Sharabi, R.; Gottlieb, H.; Borgel, V.; Fridman, K.; Salitra, G.; Aurbach, D.; Semrau, G.; Schmitt, M. A.; Schall, N.; Bruenig, C. *Electrochim. Commun.* **2012**, *15*, 22–25.
86. Brutti, S.; Reale, P.; Piciollo, E.; Bruce, P. G.; Scrosati, B.; Panero, S. *Prep. Pap., Am. Chem. Soc., Div. Fuel Chem.* **2012**, *57*, 737–739.
87. Long Doan, T. N.; Taniguchi, I. *J. Power Sources* **2011**, *196*, 5679–5684.
88. Saint-Martin, R.; Franger, S. *J. Crystal Growth* **2008**, *310*, 861–864.
89. Xie, J.; Imanishi, N.; Zhang, T.; Hirano, A.; Takeda, Y.; Yamamoto, O. *J. Power Sources* **2009**, *192*, 689–692.
90. Shui, J. L.; Yu, Y.; Yang, X. F.; Chen, C. H. *Electrochim. Commun.* **2006**, *8*, 1087–1089.
91. Li, H. H.; Jin, J.; Wei, J. P.; Zhou, Z.; Yan, J. *Electrochim. Commun.* **2009**, *11*, 95–97.

92. Dimesso, L.; Jacke, S.; Spanheimer, C.; Jeagermann, W. *J. Solid State Electrochem.* **2012**, *16*, 911–919.
93. Bramnik, N. N.; Bramnik, K. G.; Buhrmester, T.; Baehtz, C.; Ehrenberg, H.; Fuess, H. *J. Solid State Electrochem.* **2004**, *8*, 558–564.
94. Yang, S. M. G.; Aravindan, V.; Cho, W. I.; Chang, D. R.; Kim, H. S.; Lee, Y. S. *J. Electrochem. Soc.* **2012**, *159*, A1013–A1018.
95. Aurbach, D.; Markovsky, B.; Salitra, G.; Markevich, E.; Talyossef, Y.; Koltypin, M.; Nazar, L.; Ellis, B.; Kovacheva, D. *J. Power Sources* **2007**, *165*, 491–499.
96. Fu, L. J.; Liu, H.; Li, C.; Wu, Y. P.; Rahm, E.; Holze, R.; Wu, H. Q. *Solid State Sci.* **2006**, *8*, 113–128.
97. Eftekhari, A. *J. Electrochem. Soc.* **2004**, *151*, A1456–1460.

Chapter 5

Flexible Supercapacitors – Development of Bendable Carbon Architectures

Zhiqiang Niu,¹ Lili Liu,¹ Peter Sherrell,² Jun Chen,^{*,2}
and Xiaodong Chen^{*,1}

¹School of Materials Science and Engineering, Nanyang Technological University, 50 Nanyang Avenue, Singapore 639798

²Intelligent Polymer Research Institute, ARC Centre of Excellence for Electromaterials Science, Australian Institute of Innovative Materials, Innovation Campus, University of Wollongong, Northfields Avenue, Wollongong, NSW 2522, Australia

*E-mail: chenxd@ntu.edu.sg, junc@uow.edu.au

As energy storage devices, Supercapacitors (SCs), also known as electrochemical capacitors, possess high power densities, excellent reversibility and long cycle life. SCs could be applied to diverse fields including electric vehicles, pulse power applications and portable devices. Flexible SCs have attracted significant attention for powering recently developed portable, flexible and wearable electronics. During the past several years, a variety of bendable carbon-based electrode architectures and flexible SC devices with different designs have been successfully prepared. In this review, we will describe recent developments in the preparation of such bendable carbon-based electrode architectures and the subsequent design of flexible SC devices. Future development and prospects of flexible SCs are also discussed.

1. Introduction

As energy storage devices, Supercapacitors (SCs), also known as electrochemical capacitors, possess high power densities, excellent reversibility and long cycle life (1–4). SCs could be applied to diverse fields such as electric vehicles, pulse power applications and portable devices (1, 2). Generally, on the

basis of the energy storage mechanism, SCs can be classified into two categories (1). One is the electrical double layer capacitor (EDLC), wherein the capacitance is ascribed to the pure electrostatic charge accumulated at the electrode/electrolyte interface. This charge is strongly dependent on the ability of electrolyte ions to access the surface area of the electrode materials. The other category is the pseudo-capacitor, where fast and reversible faradic processes occur due to electro-active species.

Figure 1 depicts the typical structure of a conventional SC. A conventional SC consists of four main components, including current collector, electrode materials, separator, and electrolyte, which are packaged together. In contrast to batteries, most SCs use the same materials in both electrodes (positive and negative). Carbon-based materials such as activated carbons (ACs), CNTs (CNTs), graphene and graphene oxide (GO) derivatives, and carbon aerogels (CAGs) are the most widely used electrodes because of their accessibility, ease of processing, relatively low cost, non-toxicity, high chemical stability, and wide temperature range (1). According to the storage mechanism, pure carbon-based SCs are typically EDLCs, which depend on the specific surface area (SSA) of carbon-based electrodes. However, the major problem of high SSA carbon is that not all the BET surface area is electrochemically accessible when in contact with electrolyte, such that the gravimetric capacitance of various carbon materials does not increase linearly with the SSA, resulting in a low energy density (5).

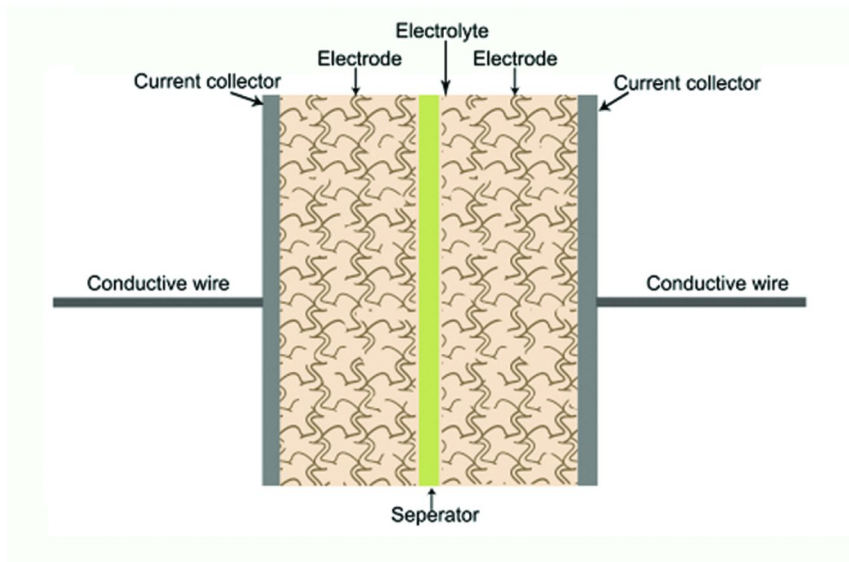


Figure 1. Schematic diagram of conventional SC

To improve their energy density, the pseudo-capacitance from quick and reversible faradic reactions such as electrosorption or from the oxidation-reduction of electroactive materials is often coupled with the EDLC to

enhance the overall capacitance of the electrode materials. Conductive polymers (CP), such as polypyrrole (PPy) or polyaniline (PANI), and metal oxides (MOs), are the most commonly studied species which provide pseudo-capacitance when combined with a carbon support material (2). The doped carbon electrodes display high energy density due to pseudo-capacitance originating from the CP or MO. However, their power density is dramatically reduced when compared to the pure carbon-based electrodes, due to the relatively poor electrical conductivity of CPs and MOs. Therefore, one of the most critical aspects in the development of carbon materials doped by CP or/and MOs is to optimize the energy density without causing a deterioration in their high power capability as the balance of these two parameters determine the ultimate performance of the SCs.

Energy storage systems are moving towards light, thin, low-cost, environmentally friendly, high-performance and often flexible devices due to the urgent demand of portable, flexible and wearable electronics (6). As such, developing high power, high energy, flexible SCs has attracted significant attention. CNTs and graphene possess high conductivity, SSA, and mechanical properties, which endow them with the capability of constructing flexible electrodes. In addition, in traditional SC devices, metallic foils or foams are used as current collectors for both the anode and cathode due to the poor conductivity of the active electrode materials. However, the use of such metallic current collectors add significant mass to the SC, resulting in devices that are too heavy, bulky or inflexible, limiting their use in applications where space and weight are constraints. Therefore, conventional SC configurations cannot meet the demand of flexible devices, and novel SC configurations with simplified designs and high flexibility should be considered. In the past several years, considerable attention has been paid to the fabrication of various forms of flexible SC electrodes and devices based on CNT and/or graphene. In this review, we will describe recent development in the preparation of bendable carbon architectures and the design of flexible SCs based on these electrodes. The further developments and prospects of flexible SCs in this exciting field are also discussed.

2. Carbon Materials-Based Flexible EDLCs

2.1. CNTs-Based Flexible EDLCs

Flexible EDLCs rely on large-surface-area, conductive electrodes with strong mechanical properties. CNTs, having a high electroactive surface area combined with high conductivity and durable mechanical properties, are attractive candidates for electrodes in flexible SC devices. Following the successful synthesis of CNT films, flexible CNT electrodes became significantly more viable.

Niu et al pioneered in fabricating the flexible multi-walled CNT (MWCNT) electrodes via three steps: 1) disassembling the MWCNT aggregates and introducing chemical functional groups on the surface of the MWCNTs by nitric acid treatment; 2) dispersing the functionalized hydrophilic nanotubes in water; 3) reassembling the individualized CNTs into an interconnected, entangled, freestanding film by filtration (7). These MWCNT film electrodes have smooth

surfaces, uniform thicknesses, acceptable mechanical strength and low electronic resistance ($1.6 \times 10^{-2} \Omega$). They are flexible and can be easily bent, rolled, and cut into different shapes and sizes. The measured density of the electrode is 0.8 g/cc, which can be controlled by varying the conditions of the nitric acid oxidation. Total pore volume is 0.79 cc/g with the micro-pore ($< 20 \text{ \AA}$) volume being negligible at 0.0016 cc/g. The average pore diameter is 92 \AA , which is accessible to the electrolyte. The specific surface area of these MWCNT films is 430 m^2/g . The combination of porous structure and high conductivity in the MWCNT film electrodes results in excellent electrochemical behaviour. The specific capacitance and power density of the MWCNT film electrodes are 104 F/g and 8 kW/kg respectively. The knee frequency is usually used to evaluate the frequency dependence of a capacitor and considered to be the critical frequency where supercapacitors begin to exhibit capacitive behavior. At a frequency higher than the “knee”, the real part of the impedance is frequency dependent and very small capacitance will be obtained. At a frequency below this value, the resistance changes weakly with frequency and the capacitor behavior tends to approach that of a pure capacitance. The knee frequency of most commercially available supercapacitors is less than 1 Hz. The knee frequency of such MWCNT electrodes is up to about 100 Hz. A very high “knee” frequency of 100 Hz suggests that most of the stored energy of the capacitor is accessible at frequencies as high as 100 Hz.

Similarly, by filtering DNA-dispersed double-walled CNTs (DWCNTs) into a thin film and thermally treating the film in argon, freestanding, thin, and bendable electrodes for SCs were fabricated (8). The DNA wrapped around the DWCNTs was converted to phosphorus-enriched carbon during thermal treatment of the film under an argon atmosphere, giving rise to strong redox peaks at around 0.4 V. The combination of the large capacitance (66.9 F/g) from the DNA-derived carbons and the high electrical conductivity of CNTs allow DWNT/DNA films to be used as a potential flexible electrode material for SCs.

Based on flexible polyethylene-terephthalate (PET) substrate, Cui and co-workers successfully prepared flexible single-walled CNT (SWCNT) film electrodes by utilizing spray coating technology, serving as both electrodes and charge collectors, as shown in Figure 2a and b (6). The demonstrated high current carrying capability together with the substantial mechanical strength of the SWCNT networks assists the creation of flexible robust devices. The use of solid gel or polymer electrolytes opens up automatable fabrication avenues for SCs, including printing. The use of a liquid electrolyte in an electrochemical device requires both robust encapsulation to prevent leakage and a separator to avoid electrical contact between the electrodes. Solid gel or polymer electrolytes offer dual functionality as they combine the separator and the electrolyte into a single layer. It also avoids potential leakages since the electrolyte is bound within the polymer matrix. The specific capacitance of SWCNT thin film supercapacitors obtained using the polymer electrolyte was about 110 F/g, which is comparable to examined aqueous electrolytes. The SCs also show very high energy (6 Wh/kg) and power densities (23 kW/kg). The simplified architecture and the sole use of printable materials may lead to a new class of entirely printable charge storage devices, allowing for full integration with the emerging field of printed electronics.

In addition, this group demonstrates that commercially available paper can also be made highly conductive with a sheet resistance ($1\ \Omega/\text{square}$) by using simple solution processes to achieve conformal coating of SWCNT and silver nanowire films, as shown in Figure 2c-h (9). Compared with plastics, paper substrates can remarkably improve film adhesion, simplify the coating process, and significantly lower the device cost. The combination of the flexibility of individual CNTs, the strong binding of the CNTs with the paper fibers, and the porous morphology of the paper endow the CNT-conductive paper with excellent mechanical properties (Figure 2g). The conductive paper with CNT thicknesses from 100 nm to 5 μm can be folded without any measurable change in electrical conductivity. Fatigue tests show that the conductive paper can be bent to a 2-mm radius 100 times with a resistance increase of less than 5%. Such flexibility could meet the demand of flexible SC electrodes, including various rolled-up devices. The SCs, in which the CNT-conductive paper acts as both the active electrode and current collector, show excellent electrochemical properties. A specific capacitance of 200 F/g (Figure 2h), a specific energy of 30-47 Wh/kg, a specific power of 200 kW/kg (considering only the mass of CNT), and a stable cycle life of over 40,000 cycles are achieved for a liquid electrolyte-based CNT-conductive paper SC. To make the SCs more compact and flexible, all-solid SCs based on CNT-conductive paper were prepared by using an ionic-liquid-based gel electrolyte (10). The specific capacitance of the all-solid-state SC was 135 F/g at a current density of 2 A/g (considering only the mass of active materials). The maximum power and energy densities of the all-solid-state SC were 164 kW/kg and 41 Wh/kg, respectively. More importantly, the all-solid-state SC was flexible, and could be repeatedly bent without any significant variation in the electrochemical properties including specific capacitance, power and energy density (<5%).

Apart from PET and commercially available paper, textiles such as cotton or polyester are also excellent support materials for the deposition of CNTs and nanowires, due to the flexibility and porosity inherent in textile fabrication techniques, such as weaving or pressing. Cui et al fabricated conductive textile through an extremely simple “dipping and drying” process using a SWCNT ink (11). The electrical conductivity of these conductive textiles improved from ~ 5 to $\sim 125\ \text{S}/\text{cm}$ with the decrease of the thickness of the cotton sheets from $\sim 2\ \text{mm}$ to $\sim 80\ \mu\text{m}$ under mechanical pressing. The sheet resistance of conductive textiles was less than $1\ \Omega/\text{square}$. The conductive textiles show outstanding mechanical properties, strong binding between SWCNTs and the textile, flexibility, and stretchability, making them an ideal candidate for flexible, stretchable SCs. SCs made from these conductive textiles show a high area capacitance, up to $0.48\text{F}/\text{cm}^2$, and high specific energy of 20 Wh/kg at a specific power of 10 kW/kg. These highly conductive textiles can provide new design opportunities for wearable electronics and energy storage applications. Based on the conductive cotton paper coated with SWCNTs, flexible solid-state SCs can be obtained by using poly (vinyl alcohol) (PVA)/phosphoric acid as the electrolyte (12). The as-prepared SC is very flexible and can be bent by more than 90° without showing any fracture. The SC is also very thin with a thickness of only 1.3 mm. The specific capacitance of the as-fabricated SC was 115.83 F/g, and specific energy was 48.86 Wh/kg.

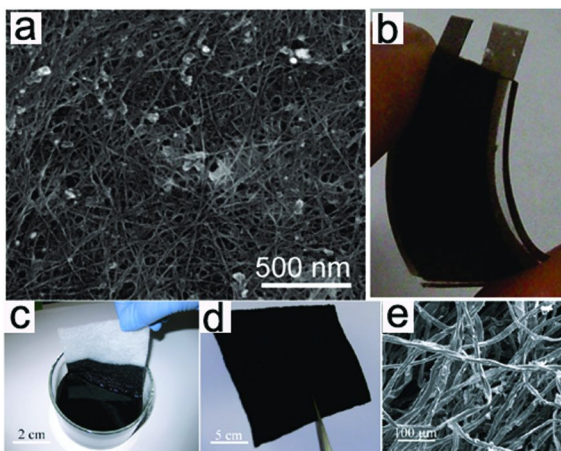


Figure 2. (a) Scanning electron microscopy image of as-deposited SWCNT networks. (b) Thin film SC using sprayed SWCNT films on PET as electrodes and a PVA/H₃PO₄ based polymer electrolyte as both electrolyte and separator.

Reproduced with permission from reference (6). Copyright 2009 American Chemical Society. (c) Conductive textiles are fabricated by dipping textile into an aqueous SWNT ink followed by drying in oven at 120 °C for 10 min. (d) A thin, 10 cm × 10 cm textile conductor based on a fabric sheet with 100% cotton and R_s of 4 Ω/square. (e) SEM image of coated cotton reveals the macroporous structure of the cotton sheet coated with SWNTs on the cotton fiber surface. Reproduced with permission from reference (11). Copyright 2010 American Chemical Society.

Integrated, flexible SC structures containing the three essential components (electrodes, spacer, and electrolyte) of the electrochemical device enable SCs to be embedded as various functional devices in a wide range of innovative products such as smart cards, displays, and implantable medical devices. By combining a CNT array, cellulose and a room temperature ionic liquid (RTIL), Ajayan et al integrated electrodes, spacer, and electrolyte into one single contiguous nanocomposite unit that can serve as a building block for a variety of mechanically flexible thin energy storage devices (13). The units are used to build various flexible SCs, batteries and hybrid dual-storage battery-in-SC devices. A specific capacitance of 22 F/g and a power density of 1.5 kW/kg were obtained at room temperature for the nanocomposite RTIL SC.

Freestanding and highly conductive SWCNT films with a continuous reticulate architecture were fabricated by improving the floating catalyst chemical vapor deposition technique (14, 15). Such films are different from conventional SWCNT films prepared by other post-deposition methods that produce short and randomly-oriented structures. A continuous reticulate architecture endows

directly synthesized films superior electrical conductivity (about 2000 S/cm) and better mechanical properties than that of post-deposited SWCNT films. Based on our directly synthesized SWCNT films (Figure 3b and c), we assembled compact-designed SCs using large-scaled free-standing and flexible SWCNT films as both anode and cathode, as shown in Figure 3. A prototype of the processing procedures was first developed to obtain uniform spreading of the SWCNT films onto the separators, serving as both electrodes and charge collectors, allowing for a device without metallic current collectors (Figure 3a and d), leading to a simplified and lightweight architecture (16). In ethanol, these SWCNT films can be easily spread out onto the separator end to end or/and layer by layer. When the SWCNT films were spread out onto the separator end to end, the ends of neighbouring SWCNT films overlap, as shown in Figure 3a. This can effectively avoid the presence of uncovered regions of the separator and ensure good connection between the SWCNT films. Relative to the size of the films, these short overlapping regions have little effect on the uniformity of the SWCNT films on the separator, however, if the overlapping is greater than 1mm, there is a loss of uniformity in the coating. The quantity and configuration of the SWCNT films on the separator can be adjusted, according to the practical demand. After uniformly spreading out SWCNT films onto the separator, ethanol was evaporated and the SWCNT films adhered firmly to the separator, as shown in Figure 3d. Subsequently, two pieces of separator coated with SWCNT films were stacked together and rolled up (Figure 3e), following which the SC was filled with 1 M LiClO₄ in a mixture of ethylene carbonate (EC), diethyl carbonate (DEC), and dimethylene carbonate (DMC) in a volume ratio of EC/DEC/DMC=1:1:1 as the electrolyte, as shown in Figure 3f. It is worth noting that the shape and size of the external shell of the resulting SC can be readily adjusted to various designs according to the practical applications.

In our case, the SWCNT films were directly used as both electrodes and charge collectors, which not only eliminated the metal/SWCNT film, namely charge collector/electrode interface, but also simplified the SC design with less weight. The SWCNT film-based roll-designed SC was powerful enough to light up a light-emitting diode (Figure 3g) when fully charged. The electrochemical characterization of the above roll-designed SC was investigated by cyclic voltammetry (CV) at different scan rates (Figure 3h), showing a typical rectangular shape. This shape indicates that the SWCNT film has excellent capacitance behaviour with a rapid current response on voltage reversal with low equivalent series resistance (ESR), which refers to the resistance that adds to the impedance due to imperfections within the capacitor's material.

The specific capacitance decreases continually with the increase of scan rate due to progressively less efficient infiltration of ions into the porous films at higher scan rates (Figure 3i), a typical characteristic of CNT film electrode due to diffusion limitations. At slower scan rates, the diffusion of ions from the electrolyte can gain access to almost all available pores of the film electrodes and penetration of electrolytic ions into the pores will be greatly deeper, leading to a high specific capacitance. However, when the scan rate is increased, efficient infiltration of ions into the porous films is progressively less due to a decreased time for this diffusion to occur, as a result, there is a reduction in capacitance.

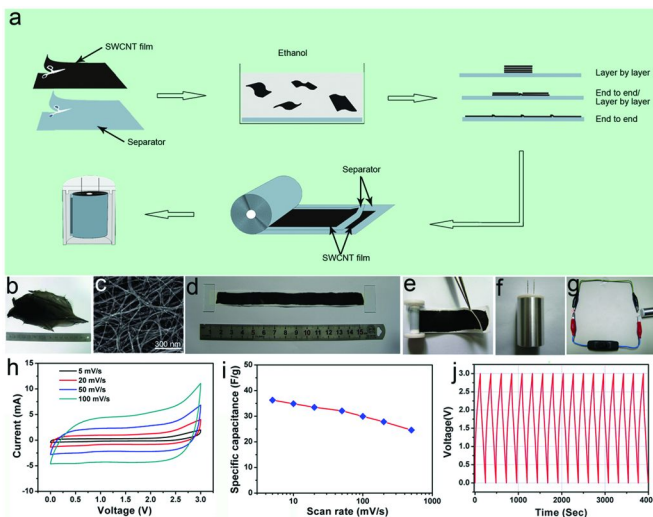


Figure 3. (a) Schematic diagram of assembling roll-designed SC using free-standing flexible SWCNT films. Optical image (b) and SEM image (c) of the directly grown SWCNT film. Optical image of (d) the SWCNT films spread out on a separator; (e) rolled design of the separator with SWCNT films and (f) the resulting roll-designed SC. (g) Optical image of the resulting roll-designed SC used to glow a red light-emitting diode (LED). (h) Typical CVs of a representative roll-designed SWCNT film SC at different scan rates. (i) The specific capacitance of the SWCNT film supercapacitor as a function of the scan rate. (j) Typical galvanostatic charge/discharge curves of the roll-designed SWCNT film SC.

Reproduced with permission from reference (16). Copyright 2011 Royal Society of Chemistry.

The specific capacitance calculated from charge/discharge curves (Figure 3j) of the compact SWCNT film SC is approximately 35 F/g for a two-electrode cell and corresponds to 140 F/g for a three-electrode cell, which is higher than those of a post-deposited CNT film or CNT array SCs, the energy density is 43.7 Wh/kg and the maximum power density of the resulting compact SWCNT film SC, is 197.3 kW/kg. The high conductivity of our SWCNT film electrode and the optimized architecture of SCs result in a low ESR and therefore a high power density of the SWCNT film-based SC. In addition, the coulombic efficiency of the compact SC reached ~95% with a knee frequency of approximately 17 Hz. These results clearly show the potential application of free-standing SWCNT film in compact SCs with enhanced performance and significantly improved energy and power densities.

Although directly grown SWCNT films are freestanding, highly conducting and transparent, the thickness of our freestanding SWCNT films could not be less than 100 nm otherwise the sample could not be removed, non-destructively, from the wall of the quartz tube. Thus, the transparency of as-prepared SWCNT

films could not exceed that of the SWCNT film with a thickness of 100 nm (70% at 550 nm) and is lower than that required for many applications, such as touch screens. As such, it is of great significance to reduce the thickness and increase the transparency of as-prepared, directly grown, SWCNT films for broad applications. To decrease the thickness and improve the transparency of directly grown SWCNT films, we report a fast, simple, and effective strategy for post-treatment of directly grown SWCNT films to fabricate ultrathin transparent and conductive films (TCFs) on a flexible and transparent substrate, as shown in Figure 4a (17). This strategy includes two processes. Firstly, an approach is put forward for processing free-standing SWCNT films to resolve the stickiness problem and spread them out onto various substrates uniformly. Then, a “repeated halving” approach based on electrostatic adsorption is presented to separate a directly grown thick SWCNT film quickly into many ultrathin SWCNT films with a thickness less than 100 nm, and down to a quasi-single layer of SWCNT bundle network. The “repeated halving” approach effectively improves the utilization rate of SWCNTs and can retain the uniformity of SWCNT films. Moreover, this method simplifies experimental procedures and conditions and provides a simple, rapid process to prepare ultrathin SWCNT TCFs with high efficiency and good reproducibility. The thickness of thinnest film can be up to about 13 nm (Figure 4b). The transmittance of the SWCNT film on the PET substrate obtained by “repeated halving” approach is greatly increased with decreasing film thickness, up to 90% transmittance (Figure 4c), which is of great significance for the practical applications.

To meet the design and power needs of fully flexible and transparent devices, flexible and transparent energy conversion and storage units or devices have to be considered. The ultrathin SWCNT films prepared by “repeated halving” approach possess high conductivity, transmittance and flexibility, making these suitable for transparent energy conversion and storage devices. As a proof-of-concept, the ultrathin SWCNT films prepared by “repeated halving” approach were fabricated into flexible and transparent symmetrical SCs (Figure 4d and e). The separator and electrolyte were sandwiched by the SWCNT films on the PET substrates. Nafion 117 membrane served as transparent separator and the electrolyte is 1 M non-aqueous LiClO₄ in a mixture of ethylene carbonate (EC), diethyl carbonate (DEC), and dimethylene carbonate (DMC) in a volume ratio of EC/DEC/DMC=1:1:1. The transmittance of the SCs using SWCNT films with different thicknesses as electrodes is shown in Figure 4c. The transmittance of SCs fabricated using SWCNT films of approximately 50 nm in thickness is about 60% at 550 nm (Figure 4f).

The calculated specific capacitance for the transparent SWCNT electrode material is 22.5 F/g (146 μ F/cm for SWCNT films of 50 nm). The energy density of the SWCNT film electrodes is 12.5 Wh/kg and the maximum power density is 13.9 kW/kg. In order to study the stability of flexible and transparent SWCNT film SCs, the prepared SCs were examined by galvanostatic charge/discharge measurements for 200 cycles under the same conditions, as shown in Figure 4f. After 10 cycles, there is a slight decrease in specific capacitance from 22.5 to 20 F/g. The specific capacitance then retains the same value with minimal capacitive loss up to 200 cycles.

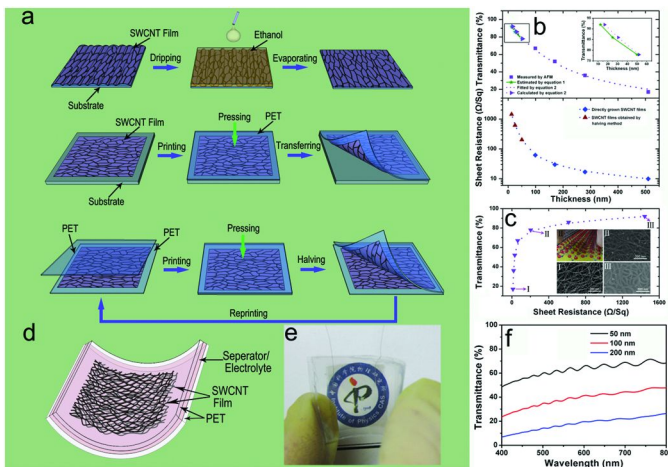


Figure 4. (a) Schematic diagram of preparing ultrathin SWCNT films by “repeated halving” approach: 1) spreading out a SWCNT film on to a substrate; 2) transferring SWCNT film from a substrate to PET substrate and 3) thinning thick SWCNT film to ultrathin SWNCT films by “repeated halving” approach. (b) Typical transmittance at 550 nm and sheet resistance curves of film as a function of SWCNT film thickness. Inset is the calculated thickness of halved thin SWCNT films by equation 1 and 2 as a function of transmittance at 550 nm. (c) Typical sheet transmittance-resistance curve. Insets are the SEM and optical images of the SWCNT films with different thicknesses on PET substrates (I: ~500 nm, II: ~50 nm, and III: ~13 nm). (d) The schematic diagram of the transparent SWNCT film SC. (e) The optical image of the transparent SWCNT film SC. (f) Transmittance curve of SCs based on SWCNT films with different thickness. Reproduced with permission from reference (17). Copyright 2012 Wiley-VCH.

Based on an organic iron catalyst, iron(III) *p*-toluenesulfonate (Fe(III)pTS), we modified CVD synthesis to grow CNT networks integrated into a conductive carbon layer (CL) on insulating quartz sheets (Figure 5) (18). This method was further adapted for growth on metallic substrates (e.g. aluminum or copper foil), and on structured carbons such as carbon fibre paper (19). In a typical experiment, a thin film of Fe(III)pTS catalyst was spin-coated onto quartz plates from organic solutions. After annealing, which facilitates solvent removal, the CVD process was initially carried out at 600 °C under Ar/H₂ gas flow to reduce the Fe³⁺ catalyst to iron nanoparticles. Then, a CNT growth phase carried out at 800 °C using C₂H₂ as the carbon source. The resultant CNT films (Figure 5a) were observed to be very much unlike those grown using conventional catalysts. During CNT growth, a reflective layer was formed beneath the carbon film (Figure 5b). The formed CNT/carbon layer (CNT/CL) paper appears as a matt-black layer on top of the quartz plate, while a flexible, shiny carbon layer forms the lower layer of the CNT/CL paper. The CNT/CL paper was easily removed from the substrate and the resulting freestanding film could be rolled around a glass rod without visible signs of degradation (Figure 5c). The size of the CNT/CL 3D networks is easily

scaled up to 100 cm² by using a larger CVD quartz tube, given that scale up is not limited by the CVD process itself. SEM confirmed the top layer indeed consisted of CNTs and a highly porous 3D structured CNT network grown on top of a dense CL with less than 1 μ m thickness (Figure 5d and e). The long nanotubes obtained in the network are MWCNTs with an external diameter of 20–40 nm, and the CL (Figure 5f) displays a uniformly dense continuous film. The resistance of CNT/CL paper is about 46 Ω /square is significantly lower than that of amorphous carbon ($> 1 \text{ k}\Omega/\text{square}$), which is often formed on top of CNTs during normal CVD based growth processes using inorganic iron(III) compounds. These networks possess a high surface area and superior electrochemical properties. The freestanding CNT/CL paper electrodes are lightweight, flexible. Furthermore, they exhibit high conductivity, high surface area and superior electrochemical properties, which make them promising as flexible electrodes.

Activated carbon (AC), which is widely used in commercial products, is a cheap electrode material with a high surface area yielding a moderate capacity for SCs. AC in powder form is difficult to handle as an electrode material. Thus, conductive agents (carbon black) and binder (poly(tetrafluoroethylene) (PTFE)) are always needed. Recently, Dai et al used CNTs to bind AC particles together to obtain a paper-like composite by filtration (20). The AC/CNT papers possess higher specific capacity, rate performance, and power density than the corresponding values for an AC/acetylene black electrode. The capacity reached a maximum value of 267.6 F/g with a CNT loading of 5 wt%, and the energy density and power density were 22.5 Wh/kg and 7.3 kW/kg, respectively, at a high current density of 20 A/g. The AC/CNT paper electrode also showed a good cycle performance, with 97.5% of the original capacity retained after 5000 cycles at a scan rate of 200 mV/s. This method affords not only a promising paper-like nanocomposite for use in low-cost and flexible SCs, but also a general way of fabricating multi-functional paper-like CNT-based nanocomposites for use in devices such as flexible lithium ion batteries and solar cells.

2.2. Graphene-Based Flexible EDLCs

Graphene is a monolayer of planar carbon structured in conjugated hexagonal lattices, in which the carbon bonds are sp^2 hybridized. Graphene has attracted increasing attention because of its unique structure and properties (21–49). For example, in graphene, electron-phonon scattering is so weak that the mobilities of charge carriers can be improved significantly, even up to 200 000 cm²/Vs under ambient conditions, if the extrinsic disorder is eliminated (50). This value exceeds the intrinsic mobility of any other semiconductor (50, 51). In addition, graphene possess a large theoretical specific surface area (2630 m²/g) (52), high Young's modulus (~1.0 TPa) (53), thermal conductivity (~5000 Wm/ K) (54), and good electrical conductivity (55). Its unique structure and properties make graphene promising for a EDLC electrodes (56). Although pure graphene sheets with high quality can be prepared by mechanical cleavage of graphite (57) or CVD method at high temperature (58–76), these methods suffer from high cost, high temperature, substrate limitation, and extremely low yield. In addition, the surface of pristine graphene is so hydrophobic that pristine graphene tend to agglomerate

in solvents, leading to the loss of excellent properties of monolayer graphene sheets. As a result, solution-based process in a large scale is not applicable for the graphene sheets obtained from above mentioned methods. Solution-phase exfoliation of graphite is an effective method for the mass production of graphene and its derivatives (77–81). Graphene derivatives such as graphene oxide (GO), an electrical insulator, and reduced graphene oxide (rGO), lose planarity and electrical conductivity through functionalization disrupting the conjugation of the basal plane. However, these materials become significantly easier to process into usable materials as a trade-off (82).

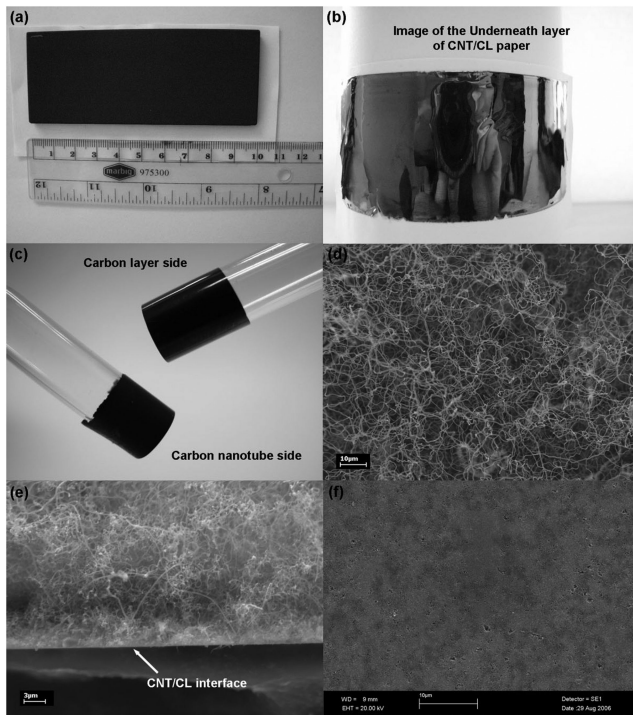


Figure 5. Scanning electron microscopy (SEM) and optical images of freestanding CNT/CL paper. a) Image of the upper surface of CNT/CL as grown on a 40 cm² quartz plate by a CVD process. b) Image of the underneath surface of the carbon layer when removed from the substrate. As is obvious from the image, this layer is highly reflective. c) Image of CNT/CL paper removed from the quartz substrate and rolled onto glass rods, indicating the flexibility and mechanical robustness of both sides of the CNT/CL composite paper. d) SEM image of the top surface of the film, showing a dense entanglement of CNTs. e) SEM image of the cross section of the CNT/CL paper, showing an obvious ‘intersection’ (indicated by the white arrow) between the carbon layer and the upper CNT network layer. f) SEM image of the underneath of the CL layer, showing densely packed but still porous morphology. Reproduced with permission from reference (18). Copyright 2008 Wiley-VCH.

Ruoff and co-workers first explored graphene-based EDLCs using rGO as electrode materials (52). Although these rGO-based electrodes exhibit excellent performance, these graphene-based electrodes have been achieved by mixing rGO with conductive binders and coating collector electrodes. The utilization of conductive binders and metal substrates would limit the flexibility of the SC electrodes. Therefore, the integration of graphene sheets, into flexible paper-like structures (e.g., layered films and porous scaffolds) is drawing much attention. However, in most cases, during the assembly process of nanoscale building blocks into paper-like structures, the large accessible surface area of 2D graphene sheets is lost. The reason for this loss is that the individual graphene sheets irreversibly aggregate and restack due to the strong π - π stacking and van der Waals force between the planar basal planes of graphene sheets. This affects the potential applications of graphene materials in electrochemical electrodes, composite materials, and so on. Therefore, preventing aggregation of graphene sheets in macroscopic porous structures, such that the properties of the individual graphene sheets are not compromised, is a critical challenge in constructing functional graphene-based macroscopic structures for SC electrodes.

Leavening is the process of adding gas to produce lighter, more easily chewable bread with the porous structures from compact dough before or during baking or steaming. Inspired from this, we fabricated paper-like, lightweight, and electrically conductive rGO foams with open porous and continuous cross-link structures by autoclaved leavening and steaming of GO layered films, as depicted in Figure 6a and 6b (83). We clearly observed the formation of foamed structures with \sim 50 times the volume expansion and \sim 30% of the mass loss in comparison with original GO film. The porous walls in the foams are continuously cross-linked and not simply and completely separated between different layers, as shown in Figure 6c. Such continuous cross-linked structures not only effectively overcome the re-stacking forces between graphene sheets, but also allow for better conductive contacts between the sheets to lower the resistance of foams (to less than $100\ \Omega/\text{square}$). Furthermore, the porous walls consisting of thin layers of stacked graphene sheets in these foams are not fully compact and there are still small gaps in the walls, allowing for electrolyte diffusion through the materials. The tensile strength of the rGO foams is about 3.2 MPa and the Young's modulus of the rGO foams were about 7 and 40 MPa at the first and last tensile stage, respectively. The tensile strain can be up to 10%, which is much larger than the case of the compact GO films ($< 0.6\%$). Since the free-standing rGO foams with continuous cross-linking porous structures overcome the re-stacking forces, it results in higher active electrochemical surface area and good conductivity. Our rGO foams possess a porous structure coupled with high mechanical strength and conductivity. These properties make our rGO foams an excellent candidate for flexible SC electrodes where neither an insulating binder nor a low capacitance conducting additive is required. In a proof-of-concept experiment, we built flexible rGO foam SCs using free-standing rGO foams as both current collectors and electrodes. The free-standing rGO foams were first uniformly spread out onto a PET substrate. Then, the separator and electrolyte were sandwiched by the rGO foams on the PET substrates, as shown in Figure 6d and e. Here, filter paper served as separator and the electrolyte was 1 M H_2SO_4 . CVs of the SC

were found to be rectangular in shape within a selected range of potential (Figure 6f), indicating an excellent capacitive behavior. The discharge curve is nearly linear (Figure 6g), indicating good electrical double layer performance. The calculated specific capacitance of the resulting rGO foam SC is about 110 F/g. The calculated specific capacitance of SC based on rGO foams is much larger than that of SCs using compact rGO films as electrodes (17 F/g). The knee frequency of rGO foam electrodes is 15 Hz (Figure 6h). CV curves of a representative rGO foam SC (device size: 3 cm \times 3 cm, rGO foam electrode size: 1.5 cm \times 1.5 cm) before and after bending demonstrated nearly no deviation (Figure 6f) when the distance between two sides of the SC was changed from 3 to 2 cm under bending (Figure 6i). This suggested that the rGO foam SCs are quite stable under bending, and the rGO foams are suitable for the flexible device applications.

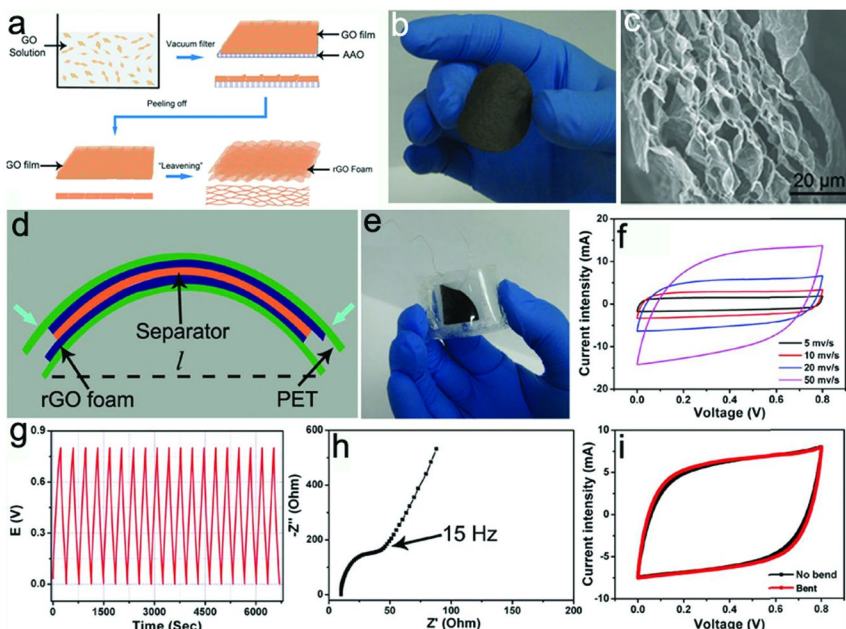


Figure 6. (a) Schematic drawings illustrating the leavening process to prepare rGO foams and (b) the photographs of free-standing paper-like rGO foams obtained by leavening method. (c) The cross-sectional SEM images of rGO foams formed at 90 °C for 10 hours in the autoclave with hydrazine monohydrate of 40 μL. (d) Schematic diagram of the flexible rGO foam SP, the distance (l) between two sides of the rGO foam SP characterize its bending degree, (e) optical image of the flexible rGO foam SP, (f) CV curves of a representative rGO foam SP at different scan rates, (g) charge and discharge curve of rGO foam SP at the current of 0.5 A/g, (h) the Nyquist impedance plot of the rGO foam SP with frequency ranging from 10 kHz to 1 Hz, and (i) the CV of the rGO foam SP before (l = 3 cm) and after (l = 2 cm) bending. Reproduced with permission from reference (83). Copyright 2012 Royal Society of Chemistry.

Li et al successfully fabricated stable aqueous rGO sheet colloids through electrostatic stabilization (82). Conductive rGO films can also be readily formed by vacuum filtration of the above rGO dispersions and subsequent drying procedures. However, if the rGO samples were not fully dried, the graphene sheets can remain largely separated in a solvated state, providing a highly open pore structure (Figure 7a), allowing the electrolyte solution to easily access to the surface of individual sheets. This has made it possible to combine ultrahigh power density and high energy density in graphene-based SCs and to allow the device operational at high rates (84). In an aqueous electrolyte, specific capacitance of rGO film is up to 215.0 F/g (Figure 7b). A capacitance of 156.5 F/g can be obtained even at an ultrafast charge/discharge rate of 1080 A/g. These RGO film can provide a maximum power density of 414.0 kW/kg at a discharge current of 108 A/g. The operating frequency of the rGO film is 75 Hz. In an ionic liquid electrolyte, rGO film-based SCs can offer a specific capacitance of up to 273.1 F/g and an energy density and maximum power density up to 150.9 Wh/kg and 776.8 kW/kg, respectively (Figure 7b). RGO films can be bonded on to shape-memory polyurethane (PU) film and forming a bi-layered composite film (85). Based on the good flexibility of graphene paper and the outstanding shape holding capacity of PU phase, the resulting composite film can be changed into various shapes. The rGO/PU composite film used as the supercapacitor electrode maintains a satisfactory electrochemical capacitance. Su et al prepared a 3D macroporous bubble rGO film through a novel hard template-directed ordered assembly by combining vacuum filtration and polymethyl methacrylate (PMMA) latex spheres (86). The as-prepared rGO film provides mediated 3D macropores for ion-buffering reservoirs and low-resistant channels for ion diffusion, which are promising characteristics for a high rate supercapacitor electrode. The supercapacitors based on 3D macroporous bubble rGO films exhibit extraordinary electrochemical capacitance with high rate capability.

Laser Irradiation of the GO film induces the reduction of GO into rGO with improving electrical conductivity. Ajayan et al demonstrated the ability to directly pattern various rGO geometries with micrometre resolution on a single piece of GO paper for the construction of both in-plane and conventional sandwich SC designs as shown in Figure 7d-g (87). The substantial amounts of trapped water in the GO makes GO simultaneously a good ionic conductor and an electrical insulator, serving as both an electrolyte and an electrode separator with ion transport characteristics. The in-plane SC structure (Figure 7d) with a circular geometry gives the highest capacitance of 0.51 mF/cm^2 , nearly twice that of the sandwich structure (Figure 7e). The energy density for in-plane SC device is calculated to be $\sim 4.3 \times 10^{-4}\text{ Wh/cm}^3$, with a power density of 1.7 W/cm^3 (Figure 7f). The sandwich device geometry shows a higher power density of $\sim 9.4\text{ W/cm}^3$ due to its lower ESR value, however, the energy density is lower ($1.9 \times 1024\text{ Wh/cm}^3$). The cyclic stability tests shows that, after 10,000 cycles, there is a $\sim 30\%$ drop in the capacitance of the in-plane circular device, whereas an $\sim 35\%$ drop for the sandwich devices. Based on a standard LightScribe DVD optical drive to do the direct laser reduction of graphite oxide films to graphene, as depicted in Figure 7h (88), Kaner and co-workers prepared a rGO film with an open network. The as-prepared films with open pores are mechanically robust,

show high electrical conductivity (1738 S/m) and specific surface area (1520 m³/g), indicating that the films can be used directly as EC electrodes without the need for binders or current collectors. The SCs based on laser-scribed rGO films are robust enough to be charged and discharged over a wide range of scan rates (from 100 to 10,000 mV/s) and still maintain its nearly ideal rectangular CV shape. The area capacitance of the laser-scribed rGO SC was 3.67 mF/cm² in polymer electrolyte and 4.04 mF/cm² in 1.0 M H₂SO₄ at 1A/g (Figure 7i). The area capacitance of the SC device is maintained at 1.84 mF/cm², even when the SC is operated at an ultrafast charge/discharge rate of 1000 A/g, indicating a very high rate capability. The laser-scribed rGO SC exhibits energy densities of up to 1.36 mWh/cm³ and power density of ~20 W/cm³.

Ruoff et al present a novel method to prepare highly conductive, free-standing, and flexible porous carbon thin films by chemical activation of rGO paper by KOH (89). First, 1 M KOH was dropwise added into 1 mg/mL of GO colloidal suspension. The water was evaporated by heating in an oil bath at 100 °C under constant stirring until it thickened into an “ink paste”. The paste consists of GO platelets dispersed with KOH in some remaining water. Films composed of stacked and overlapped GO platelets decorated with KOH were obtained through brief vacuum filtration under directional flow followed by drying, followed by an activation step, in which the dry film was placed in a quartz tube furnace under flowing argon at 800 °C for 1 h and a pressure of 1 atm. These flexible carbon thin films possess a very high specific surface area of 2400 m²/g with a high in-plane electrical conductivity of 5880 S/m. These rGO films demonstrated an excellent high-frequency response, an extremely low ESR, on the order of 0.1 Ohm, and a high-power delivery of about 500 kW/kg. The specific capacitances and energy densities of these rGO thin films are 120 F/g and 26 W/h kg, respectively. Free-standing thin films provide a route to simplify the electrode-manufacturing process by eliminating conducting additives and binders and are also compatible with roll-to-roll thin-film fabrication technologies.

A multilayered nano-architecture of variable sized graphene nanosheets was prepared by capillary force driven LBL self-assembly (90). A two-phase mixture was first formed by dispersing Graphene nanosheets in chloroform followed by the addition of a small amount of water. This two-phase mixture was then briefly sonicated to get the nanosheets adsorbed at the liquid-liquid interface. Once the nanosheets were adsorbed at the interface, they could not be brought back to the bulk phase even after vigorous shaking. However, upon shaking, numerous emulsion droplets with the nanosheets were formed still covering the interface between the two immiscible liquids. After these droplets reach the air-water interface, they spread in the form of a thin film. Following by the rapid evaporation of chloroform, a dry graphene film was obtained and floated at the air-water interface. This film can be easily transferred to other substrate. To remove the residual water, the film was then heated at 100 °C. Multilayer films were formed by successive depositions of these monolayer films on top of another. The multilayer graphene film exhibits very high electrical conductivity of 1.24×10^4 S/m. This multilayer graphene film exhibits a high-frequency capacitative response and a nearly rectangular cyclic voltammogram at a 1000 mV/s scan rate and possesses a rapid current response. The average specific

capacitance of the aligned composite configuration was close to 80 F/g at a high charge/discharge current 10 A/g. The SCs based on this multilayered film structure demonstrate long term stability with the retention of more than 98% of the specific capacitance at the end of 1000 electrochemical cycles. In addition, the resulting multilayer film exhibits superior high-frequency capacitative properties with a knee frequency close to 398 Hz.

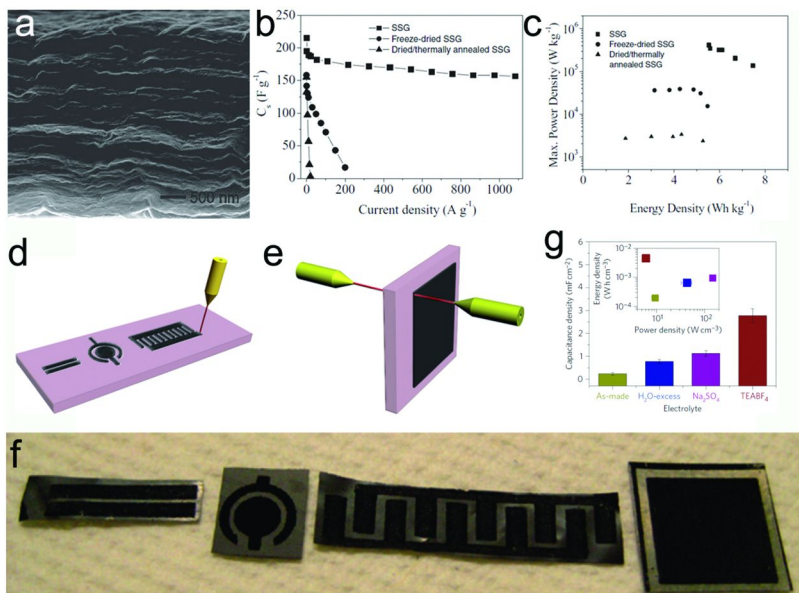


Figure 7. (a) SEM image of the solvated graphene film. (b) Gravimetric capacitances measured at various charge/discharge currents. (c) Ragone plots of the solvated graphene films-based SPs. The energy density and maximum peak power density are against the mass of the active materials in the electrodes. All the tests with a 1 V operation voltage were carried out in 1.0 M aqueous H₂SO₄ electrolyte. Reproduced with permission from reference (84). Copyright 2011 Wiley-VCH. Schematics of CO₂ laser-patterning of free-standing hydrated GO films to fabricate RGO-GO-RGO devices with in-plane (d) and sandwich geometries (e). The black contrast in the top schematics corresponds to RGO, and the light contrast to unmodified hydrated GO. (f) Photographs of patterned films with different styles. (g) Histogram comparison of area-based capacitance density of a sandwich device in different electrolyte. Inset: volumetric energy density versus power density data of the corresponding devices. (h) Schematic illustration of the fabrication of laser-scribed graphene-based electrochemical capacitors. (i) Energy and power densities of LSG-Ecs compared with commercially available AC-EC, aluminum electrolytic capacitors, and a lithium thin-film battery. Reproduced with permission from reference (87). Copyright 2011 Nature Publishing Group.

To overcome the self-agglomeration of graphene sheets in macroscale structures, we report a facile and scalable assembly strategy, the electrophoretic alternate deposition, to fabricate alternately multilayered films using graphene sheets and metal nanoparticles as building blocks, as depicted in Figure 8a and b (91). The conductivity of hybrid films can be up to 8375 S/m, which is larger than other porous rGO structure (0.5 S/m). In the multilayered rGO/AuNP hybrid nano-architecture, AuNP layers not only avoid the self-agglomeration of rGO sheets, but also connected the rGO layers well. This assembly strategy can effectively control the orientation of graphene nanosheets and metal NPs and the organization at the nanoscale. The obtained multilayered films on ITO substrates can easily be transferred to other flexible substrates, which is a fundamental requirement for flexible devices

Since these rGO/AuNP hybrid films have a higher electrical conductivity, the hybrid films are expected to be used as the electrodes of flexible SC devices. Here, neither an insulating binder nor a low capacitance conducting additive is required. We constructed and measured the performance of two-electrode symmetrical flexible SC cells based on the obtained multilayered rGO/AuNP hybrid films. The separator (Celgard 2325) and electrolyte were sandwiched by the rGO/AuNP films on the PET substrates (Figure 8c and d). To make SCs more flexible, directly grown SWCNT films were used as current collectors instead of metallic foils or foams, as directly fabricated SWCNT films have high conductivity, low mass density, large specific surface area and high mechanical strength. In traditional SC devices, metallic foils or foams are normally used as current collectors for both anode and cathode due to poor conductivity of active electrode materials. However, the use of metallic current collectors would make the SCs too heavy, bulky or inflexible, which limit their use in applications where space and weight are constraints. The mass density of SWCNT film is much smaller than that of metallic current collectors, leading to a lightweight architecture. In addition, the porosity of SWCNT films may be useful to improve the penetration of electrolytic ions into the electrodes, leading to a high specific capacitance. The calculated specific capacitance, energy and maximum power densities of the resulting multilayered hybrid film from CV (Figure 8c) and discharge curves (Figure 8 d) SC were 65 F/g, 36 Wh/kg and 49 kW/kg, respectively, which is higher than that of SCs based on compact RGO films (23 F/g, 13 Wh/kg and 27 kW/kg). These indicate that the addition of the spacer, AuNPs, in the multilayered film effectively improve the performance of the rGO SC electrodes. Furthermore, it is important to note that the specific capacitances of SCs based on the RGO/AuNP hybrid films is strongly related to the AuNP deposition time, as shown in Figure 8g. The optimal deposition time for AuNPs was determined to be 120s with deposition times on either side of this value resulting in a decreased capacitive response. The RGO/AuNP hybrid film SCs possess high knee frequency of 370 Hz, as shown in Figure 8h. It was found that there was nearly no obvious deviation in the CV curves (Figure 8i) when the distance between two sides of the supercapacitor was changed from 3 to 2 cm under bending. This suggested that the hybrid film supercapacitors are quite stable under bending, and the hybrid film are suitable for the flexible device applications.

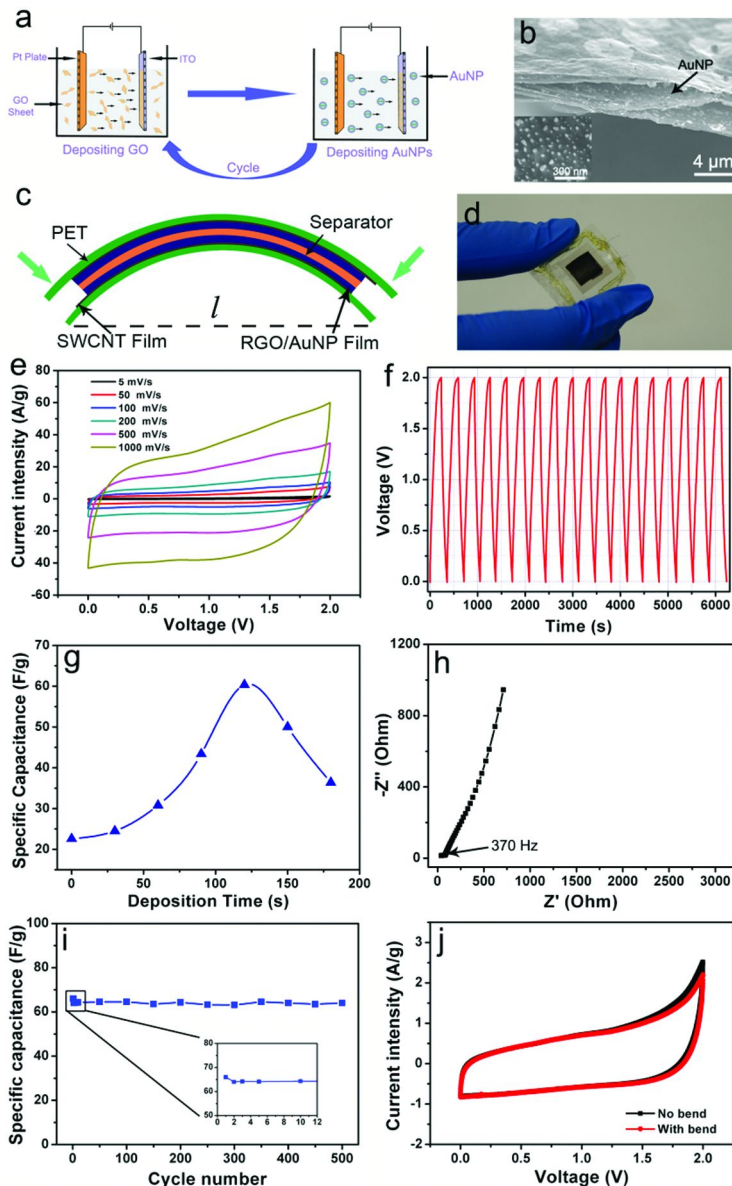


Figure 8. (a) Schematic process of constructing alternately multilayered GO/AuNP films on ITO surface cell. These two steps are the basic buildup sequence for the architecture of the multilayered GO/AuNP composite films. (b) The cross-section SEM image of multilayered RGO/AuNP hybrid film. Inset is the SEM image of AuNPs on the graphene sheet surface. The schematic diagram (c) and optical image (d) of the flexible multilayered RGO/AuNP hybrid film SP using SWCNT film as current collector. (e) The CV curves of a representative RGO/AuNP hybrid film (AuNP deposition time: 120s) SP at different scan rates. (f) Typical galvanostatic charge/discharge curves of the representative

multilayered hybrid film SP at 1 A g⁻¹. (g) Specific capacitance of RGO/AuNP film SPs as a function of AuNP deposition time. (h) The Nyquist impedance plot of the hybrid film SP with frequency ranging from 100 kHz to 1 Hz. (i) Variation of capacitance stability of the hybrid film SP with cycle number. (h) The CV of the hybrid film SP before ($l = 3$ cm) and after ($l = 2$ cm) bending.

Apart from Au NPs, carbon black (CB) NPs can also be used as “spacer” to prevent the restacking of graphene sheets in the graphene film (92). Flexible graphene paper (GP) pillared by CB NPs was produced using a simple vacuum filtration method. The pillared GP can be directly used as SC electrodes without binder, serving both as electrodes and current collectors, due to its intrinsic high electrical conductivity. The pillared GP-based SCs exhibit excellent electrochemical performances and cyclic stabilities, compared to GP without the addition of CB nanoparticles. The specific capacitance of the pillared GP is 138 F/g and 83.2 F/g in aqueous and organic electrolytes, respectively, at a scan rate of 10 mV/s. After 2000 cycles, a negligible amount of capacitance loss was observed in aqueous and organic electrolytes, 3.85% and 4.35%, respectively. At an extremely fast scan rate of 500 mV/s the specific capacitance can reach 80 F/g in aqueous electrolyte. The pillared GP has great potential in the development of promising flexible and ultralight-weight SCs for electrochemical energy storage.

To prepare flexible and transparent graphene EDLCs, Chen and co-workers fabricated flexible and transparent graphene films via vacuum filtering (93). The minimum thickness of the produced graphene films was up to 25 nm. At 550 nm the highest transmittance of approximately 70% was obtained for a 25 nm thick film. The conductivities of the films range from 800 to 1000 S/m. The film collected on a PET substrate can be readily bent to some degree without losing conductivity. The transparency, conductivity, and flexibility of graphene ultrathin films demonstrate it as a promising material for application where flexible coatings are required, such as flexible electrodes. At a scan rate of 10 mV/s, specific capacitances of 111 F/g, 105 F/g, 102 F/g, and 99 F/g were obtained for the 25 nm, 50 nm, 75 nm, and 100 nm films, respectively. There is a slight increase of 12 F/g in specific capacitance as the film thickness decreases from 100 to 10 nm. It is important to note that the graphene thin films retain 75%–80% of their capacitance when the scan rate is increased from 10 to 200 mV/s. This suggests that there is very good contact between the electrolyte and the active material allowing for excellent charge transfer kinetics. The 25 nm film shows the best performance with a high energy density of 15.4 Wh/kg at 554 W/kg which gradually reduces to 10 Wh/kg at 7200 W/kg.

Cotton cloth has been used to support SWCNT as flexible SC electrodes due to the flexible and porous structure made by weaving natural cotton fibers, which leads to a hierarchical network structure with a complicated surface morphology, functional groups such as hydroxyl groups, and high porosity. Yan et al prepared a flexible, processable, electrode via a simple “brush-coating and drying” process using everyday cotton cloth as the platform and a stable GO suspension as the ink (94). Following by annealing at 300 °C in argon atmosphere,

the graphene/cotton cloth composite fabric exhibits good electrical conductivity, outstanding flexibility, and strong adhesion between graphene nanosheets (GNSs) and cotton fibers. The SC based on graphene/cotton cloth composite fabric shows a specific capacitance of 81.7 F/g for a two-electrode system in aqueous electrolyte. In an ionic-liquid/organic electrolyte, the SC also exhibits satisfactory capacitance of 83.2 F/g. Using pure cotton cloth as separator and GNSs/cotton cloth composite fabric as electrode and current collector, an all-fabric SC was also fabricated. Such a conductive GNSs/cotton cloth composite fabric may provide new design opportunities for wearable electronics and energy storage applications. In addition, a flexible and freestanding carbon nanofiber/graphene nanosheet (CNF/GNS) composite paper was prepared via electrospinning followed by high-temperature annealing using a polyacrylonitrile/GNS/dimethylformamide mixture as electrospun precursor (95). The GNS/CNF composite paper exhibits the largest specific capacitance of 197 F/g, about 24% higher than that of pure CNF paper. Therefore, based on the above investigations, such GNS/CNF composite paper can be a potential candidate for high-performance flexible capacitors.

The introduction of an electric phase into a cellulose paper can make it electrically active for applications such as electrodes, electromagnetic shielding and sensors. High performance flexible cellulose electric papers can be used for the development of novel paper electronics and foldable energy storage devices. GNS coated cellulose composite papers can be fabricated via a simple paper-making process, dispersing chemically synthesized GNS into a cellulose pulp, followed by filtration (96). These composite papers are electrically conductive and electrochemically active. The GNS/cellulose paper is as flexible and mechanically tough as the pure cellulose paper. The electrical measurements show the composite paper has a sheet resistance of 1063 Ω/square and a conductivity of 11.6 S/m. As a flexible double layer SC electrode, the GNS/cellulose paper in an organic electrolyte (LiPF₆) displays a high capacity of 252 F/g at a current density of 1 A/g with respect to GNS.

2.3. CNT-Graphene Composites

As mentioned above two sections, pure rGO or CNTs can be directly used as SC electrodes. The SC electrodes based on CNTs possess high power density due to high conductivity of CNTs. The SC electrodes based on rGO sheets have high specific capacitance due to the high specific surface area of rGO sheets. The combination of CNTs and rGO sheets is a compromise between the high conductivity of CNTs and the high specific surface area of RGO. A transparent, conductive, and flexible MWCNT/rGO hybrid film with an interconnected network and a double-layer structure can be prepared by four steps: 1) vacuum-filtration of an aqueous MWCNT and GO solution onto a membrane; 2) transferring onto a PET sheet by dissolving the membrane in acetone; 3) chemically reducing graphene oxide to graphene by HI and repeatedly washing by ethanol; 4) HNO₃ treatment for the p-type doping and the removal of the surfactant (97). The thickness and transparency can be tuned by varying the CNT/rGO ratios and the volumes of the solution. Furthermore,

this MWCNT/rGO hybrid flexible film maintains an excellent stability of the conductivity (over 95%) after the repeated flexure over 120° more than 3000 times. This stability and performance of the MWCNT/rGO hybrid flexible films indicates a broad applicability for flexible optoelectronics. Interconnected MWCNT/rGO composites with a large surface area and high porosity show a maximum specific electrochemical capacitance of 150 F/g, which is much higher than that for only MWCNT (100 F/g). Importantly, the MWCNT/graphene exhibits a high rate capability of 141 F/g at high current density (10 A/g) with 96% retention. The outstanding performance of the MWCNT/rGO hybrid films results from a unique interconnected nanostructure with the highly porous flakes leading to a large surface area. This combination of nanostructure and surface area demonstrates a synergic effect that improves the penetration of electrolyte ions, and the ion transport within a short distance.

Similarly, flexible rGO/MWCNT films can be fabricated by flow-directed assembly from dispersions of GO and pristine MWCNTs followed by the use of gas-based hydrazine or heat-treatment to reduce the GO into RGO (98, 99). The MWCNTs in the hybrid films not only efficiently increase the basal spacing but also bridge the defects for electron transfer between RGO sheets, increasing electrolyte/electrode contact area and facilitating transportation of electrolyte ion and electrons to the inner region of electrodes. The rGO/MWCNT films possesses a specific capacitance of 265 F/g at 0.1 A/g and a good rate capability (49% capacity retention at 50 A/g), and displays an excellent specific capacitance retention of 97% after 2000 continuous charge/discharge cycles (98).

CNTs can form stable aqueous through charge stabilization after acid oxidation, leading to a negative charge on the backbone of the CNT. Stable aqueous dispersions of positively charged polymer-modified graphene sheets were obtained via the *in situ* reduction of exfoliated graphite oxides in the presence of cationic poly(ethyleneimine) (PEI) (100). The resulting water-soluble PEI-modified graphene sheets were then used for sequential self-assembly with acid-oxidized MWCNTs, forming multilayered RGO/CNT hybrid films with interconnected carbon structures of well-defined nanoscale pores. The hybrid films exhibited a nearly rectangular cyclic voltammogram even at a high scan rate of 1 V/s with an average specific capacitance of 120 F/g.

3. Carbon/Polymer Composite Flexible Pseudo-Capacitors

According to the storage mechanism, pure CNTs- and/or rGO-based SCs are ascribed to EDLCs, which depend on their SSA. However, the major problem of pure CNTs- and/or rGO-based electrodes is that not all their BET surface area is electrochemically accessible when in contact with electrolyte (5). As a result, their energy density is relatively low. To improve their energy density, the pseudo-capacitance from CP, such as PANI or PPy, and MOs is often coupled with the EDLC to enhance the overall capacitance of the electrode materials. The doped CNTs and/or rGO electrodes display high energy density due to pseudo-capacitance originating from the CP or MO.

3.1. CNTs/Conductive Polymer Flexible Pseudo-Capacitors

In section 2.1, it has been shown that pure SWCNT film SC electrodes are usually regarded as the material of choice for a high-power electrode because of their good electrical conductivity and readily accessible surface area (6, 16, 101). However, the specific surface area of the pure SWCNT film-based electrodes is generally low because SWCNTs exist in the form of bundles, leading to a low energy density (1, 102). Currently, many efforts have been made to improve the energy density of the SWCNT-based electrodes including the addition of CPs into the SWCNT-based electrodes (103–114). The SWCNT/CP electrodes display high energy density due to pseudo-capacitance originating from CP. Therefore, one of the most critical aspects in the development of SWCNT/CP SCs is to optimize the energy density without deteriorating their high power capability as both these parameters determine the ultimate performance of the SC.

PANI has been considered as one of the most promising electrode materials because of its relatively high conductivity and lower cost compared to other CPs (115–120). Utilizing a “skeleton/muscle” strategy, a free-standing thin and flexible SWCNT/PANI hybrid film was produced via a simple *in situ* electrochemical polymerization method (121). The films with a continuous reticulate structure were utilized as a template, as depicted in Figure 9a (121). *In situ* electrochemical polymerization effectively deposited PANI onto the surface of SWCNT bundles, and controlled the morphology and microstructure of the SWCNT/PANI hybrid film. In a SWCNT/PANI hybrid film, the directly grown SWCNT film with its continuous reticulate architecture acts as the skeleton and PANI layers act as muscles. This unique continuous “skeleton/muscle” structure (Figure 9b and c) ensures that these hybrid films have much higher conductivity compared to other methods of producing SWCNT/PANI composite films. Furthermore, the continuous “skeleton/muscle” architecture ensures that the SWCNT/PANI hybrid films possess high conductivity. The thin SWCNT/PANI hybrid films remain free-standing and can be bent, rolled up and even twisted without cracking (Figure 9d). As a promising carbon material for flexible SCs, the as-prepared thin SWCNT/PANI hybrid films combining the high conductivity from SWCNT film and the pseudo-capacitance from PANI are suitable for the electrodes of flexible SCs in which neither an insulating binder nor a low capacitance conducting additive is required. The flexible SCs have been fabricated directly using the SWCNT/PANI hybrid films as both electrodes and charge collectors without metallic current collectors (Figure 9e). The CV (Figure 9f) curve area of the SWCNT/PANI hybrid film is much larger than that of the pure SWCNT film, which indicates that the specific capacitance of the SWCNT/PANI hybrid film is much higher than that of the pure SWCNT film owing to its additional pseudo-capacitance. CVs of the SC maintain its shape within a selected range of potential and even at a high scan rate of 500 mV/s (Figure 9g), indicating that the SWCNT/PANI hybrid films have very rapid current response on voltage reversal. The discharge curves were not ideal straight line (Figure 9h), indicating the process of a faradic reaction. The specific capacitance of SWCNT/PANI hybrid film with 30s of PANI deposition time is 236 F/g, which is much larger than that of pure SWCNT film (23.5 F/g) (Figure 9i), indicating that

the specific capacitance of SWCNT film was remarkably improved due to the pseudo-capacitance contributed by PANI. High energy and power densities (131 Wh/kg and 62.5 kW/kg, respectively) have been achieved. The knee frequency of SWCNT/PANI hybrid film SCs is 25 Hz (Figure 9j), indicating that most of its stored energy is accessible at frequencies below 25 Hz for the SWCNT/PANI hybrid film SCs. The high electrical conductivity and flexibility, in combination with a continuous porous architecture, suggest that the as-prepared ultrathin free-standing SWCNT/PANI hybrid films have the significant potential to be the promising electrode materials for thin, lightweight and flexible energy storage devices with high performance.

Freestanding CNT Bucky paper can also be prepared by vacuum filtering. Based on the CNT Bucky paper, Liu et al fabricated the free-standing CNT/PANI hybrid films by chemical polymerization (105). Compared with the conventional brittle CNT/PANI composites, these paper-like composites were significantly thinner and more flexible. The paper-like CNT/PANI film can be rolled up, bent or twisted easily, and even folded without any cracking. These film electrodes showed superior electrochemical performance with a higher specific capacitance (424 F/g), lower internal resistivity, and greater stability under different current loads. To simplify the structure and improve the flexibility of SCs, this group developed a ultrathin all-solid-state SC configuration through an extremely simple process based on two slightly separated CNT/PANI electrodes embedded in the H₂SO₄-polyvinyl alcohol (PVA) gel electrolyte (105). The integrated device shows a high specific capacitance of 350 F/g for the electrode materials, excellent cycle stability after 1000 cycles and a leakage current as small as 17.2 μ A. Furthermore, due to its polymer-based component structure, it has a specific capacitance of as high as 31.4 F/g for the entire device, which is more than 6 times that of current high-level commercial SC products.

As mentioned above, flexible electrodes have been successfully prepared by uniformly coating SWCNT ink on cotton and other fabrics. However, their specific capacitance is relatively low. To improve the energy density of SWCNT/cloth electrodes, conducting PANI nanowire arrays are successfully deposited onto the surface of the SWCNT/cloth composite through dilute polymerization to obtain the PANI/SWCNT/cloth composite electrodes (122). The sheet resistance of the PANI/SWCNT/cloth electrode is 150 Ω /square. Using PANI/SWCNT/cloth composites as electrodes, flexible SCs were produced in a sandwich configuration. These flexible composites can be directly used as SC electrodes without using any insulator binder; which simplifies the assembly in practical applications. Bending the flexible SCs to an angle smaller than 90° did not noticeably affect their performance. The PANI/SWCNT/cloth electrodes display a large capacitance (410 F/g), high rate capability, and good stability, which may lead to its future application in high-performance flexible devices.

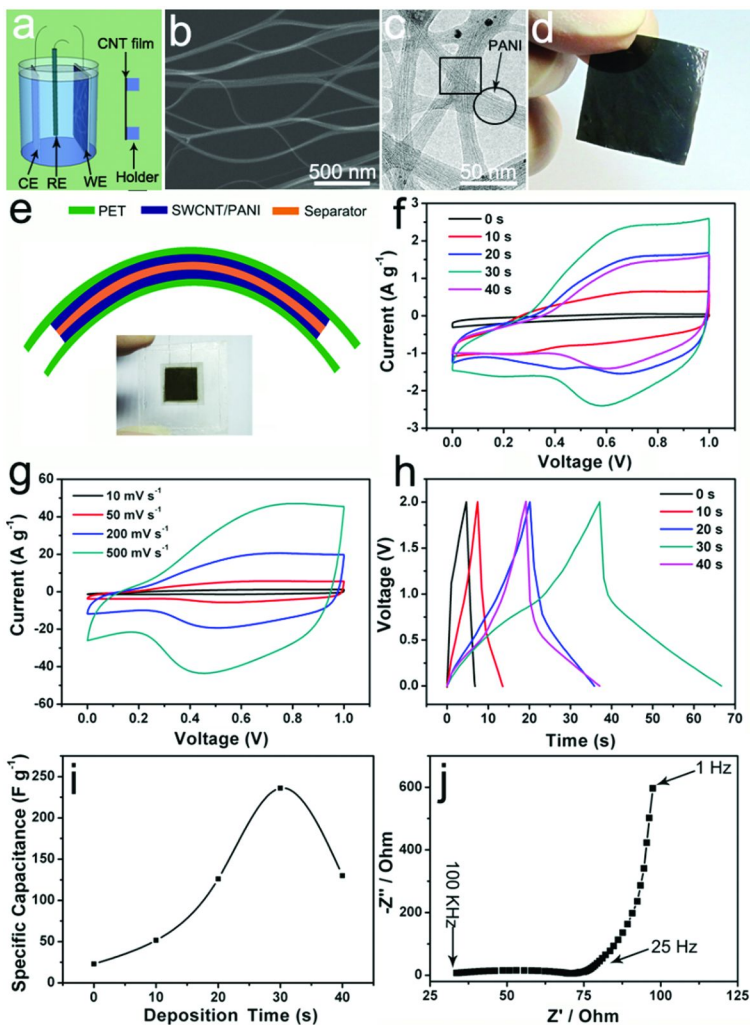


Figure 9. (a) Sketch of PANI electrodeposition using the directly grown SWCNT film as template. (CE: counter electrode, RE: reference electrode, WE: working electrodes) ((a) Schematic diagram and optical image of a flexible SWCNT/PANI hybrid film SP. (b) CV curves of SPs based on SWCNT/PANI hybrid film under different PANI deposition time, scan rate: 20 mV/s. (c) CVs of SWCNT/PANI hybrid film SPs at different scan rates. (d) Charge/discharge curves and (e) specific capacitance of SPs based on SWCNT/PANI hybrid film under different PANI deposition time. (f) Nyquist impedance plots of the SWCNT/PANI hybrid film SP with frequency ranging from 100 kHz to 1 Hz. Reproduced with permission from reference (91). Copyright 2012 Wiley-VCH.

To simplify the assembly, flexible sheets of SCs were prepared based on painting a sheet of flexible plastic electrolyte with a composite material made of a CP and CNTs (123). PVA and phosphoric acid (H_3PO_4 , 85%) films, 0.3mm thick, were formed by first casting a mixture of PVA and H_3PO_4 on a glass surface and then peeling film off the substrate once dry. A painting brush was used to transfer the PANI–CNT aqueous mixture on both sides of a PVA film to form the shape of the SC. Painted sheets were put in an oven at 40 °C to remove residual water. The specific capacitance of the flexible sheets was evaluated to be 16 F/g, consisting of pseudo-capacitance produced by the polymer and electrical double-layer capacitance produced by CNTs. The SC sheet has a maximum specific energy of 0.5 Wh/kg and a maximum specific power of 0.3 kW/kg. These values are much lower than those observed previously with other forms of flexible SCs (6, 13).

To improve the energy density of transparent CNT film SCs, Chen et al presents transparent and flexible SCs assembled from PANI/SWCNT hybrid films, which were prepared by electrochemical polymerization of PANI onto thin SWCNT films (109). The PANI/SWCNT hybrid films are optically homogeneous, transparent, electrically conducting and mechanically flexible. Owing to the double-layer capacitance from SWCNTs and pseudo-capacitance from PANI, The PANI/SWNT hybrid films show a large specific capacitance of 55.0 F/g at a current density of 2.6 A/g, indicating its possibility for transparent and flexible energy storage.

Apart from PANI, we prepared free-standing poly (3,4-ethylenedioxy-thiophene) (PEDOT) /poly(styrene sulfonate) (PSS)/SWCNT hybrid films with varying compositions of PEDOT/PSS (124). A comparison of results shows that having single walled nanotubes dispersed throughout the polymer matrix increase the capacitance by 65% and the energy density by a factor of 3 whilst achieving good capacity retention over 1000 cycles.

3.2. Graphene/Conductive Polymers for Flexible Pseudo-Supercapacitors

Although pure graphene macroscopic structures have been used as SC electrodes, their energy density is moderate. In order to improve the energy density of the graphene-based electrodes, CPs were added into the graphene-based electrodes (120, 125–129). Using a vacuum filtration method, RGO/PANI-nanofibers (NFs) films were prepared (120). RGO/PANI-NF film has a high conductivity of 5.5×10^2 S/m, which is about 10 times higher than that of pure PANI-NFs. These films can be cut into desired shape and directly used as SC electrodes without insulating binders or conducting additives due to the ability of these materials to support themselves mechanically, along with having a high amount of flexibility. The specific capacitance of RGO/PANI-NFs film SCs is 210 F/g, which is also much higher than the average value of PANI-NF and RGO films (145 F/g). The internal resistance of RGO/PANI-NFs film SCs is much smaller than that of pure PANI-NFs SCs. The high conductivity of RGO/PANI-NFs film accelerated the charge-transfer during the discharging process, the RGO/PANI-NFs film maintained a higher capacitance of 94% (197 F/g) as current was increased from 0.3 to 3 A/g as against that of the PANI-NF film (86%) in the same current range. However, when current was increased

beyond 6 A/g, the specific capacitance of the RGO/PANI-NFs film was measured to be slightly lower than that of the PANI-NF film due to the limitations of the electrolyte. The electrochemical stability of the RGO/PANI-NFs film was improved by the addition of RGO sheets, which act as the frameworks for sustaining PANI-NFs, preventing the fibers from severely swelling and shrinking during cycling. Flexible graphene/PANI-NFs hybrid paper can also be prepared via a facile and fast two-step route composed of electrostatic adsorption between negatively-charged poly(sodium 4-styrenesulfonate) (PSS) mediated graphene sheets (PSS-GS) and positively-charged PANI NFs and the follow-up vacuum filtration of the as-prepared PSS-GS/PANI NFs suspension (130). Highly ordered, layered, PSS-GS/PANI composite papers have been produced where the PANI NFs are coated by PSS-GS because of an electrostatic interaction. The highest specific capacitance of the composites reaches 301 F/g, owing to effective synergy between graphene and PANI NFs.

Based on LBL assembly, flexible multilayered RGO/PANI films can be obtained by alternate deposition of positively charged PANI and negatively charged GO nanosheets on a PET substrate, followed by chemical reduction of GO to RGO (131). The hybrid electrodes provide not only an improved electronic conductivity through the intimate contact with the rGO nanosheets, but also enhanced chemical stability during the charge-discharge process. A synergistic effect between an EDLC of rGO nanosheets and a pseudocapacitor of the CP PANI was exhibited for the flexible thin film SCs with excellent electrochemical performance. The electrochemical performance of the RGO/PANI hybrid film depends on the various parameters of the LBL assembly such as the number of bilayers and the post-thermal and chemical treatments that affect the degree of reduction of GO and PANI. RGO/PANI hybrid films possess an excellent gravimetric capacitance of 375.2 F/g at a discharge current density of 0.5 A/g. The hybrid SC maintained its capacity up to 90.7% over 500 cycles at a high current density of 3.0 A/g. This study opens up the possibility for the production of diverse graphene-based hybrid nanocomposites that are promising for future flexible SCs.

Based on an *in situ* anodic electropolymerization of PANI on graphene paper, Cheng and co-workers prepared freestanding and flexible graphene/PANI composite papers (127). These hybrid films show a high capacitance of 233 F/g, reaching a 58% enhancement in comparison with the graphene paper (147 F/g). These intriguing features make it quite a promising material as a freestanding electrode for flexible SCs.

PPy is another one of most promising conductive polymers used in SCs. Multilayered nanoarchitectures of rGO sheets and PPy nanowires was prepared by combining liquid-air interface assembly with capillary force driven LBL assembly (132). In these multilayered films, the fibrous network of PPy nanowires, possessing high ionic accessibility, was interspersed with electrically conductive monolayers of highly aligned large sized rGO sheets as a series of current collectors. These multilayer film electrodes exhibit a specific capacitance of 165 F/g at a 1A/g discharge current density even after 1000 electrochemical cycles. They maintain a high frequency capacitive response with a knee frequency close to 50 Hz.

Pulsed electrodeposition utilizing well-separated short potential pulses has been employed to create flexible, uniform rGO/PPy hybrid films (133). Pulsed electrodeposition allows pyrrole monomers to diffuse into the pore space of the rGO between deposition pulses, and demonstrated a significant improvement in the uniformity of PPy coatings on rGO sheets. The addition of PPy still maintains the inherent flexibility of rGO films. The flexible SC based on rGO/PPy hybrid films displays a specific capacitance as high as 237 F/g for a moderate total deposition time of only 120 s, which is approximately four times higher than the blank scaffold, rGO films, due to the pseudocapacitive contribution of conformal redox-active polypyrrole. Furthermore, this flexible SC exhibited very high energy and power densities of ~33 Wh/kg and ~1184 W/kg, respectively, at a scan rate of 10 mV/s. This increase was attributed to the favorable nucleation of new polymer chains at defects on the graphene surface, which become less favorable as defect sites are occupied by existing polymer nanoparticles.

3.3. Graphene/CNTs/Conductive Polymer for Flexible Pseudo-Capacitors

The excellent mechanical properties of flexible rGO sheets and rigid CNT can synergistically release the differential strain of polymer chains during doping/dedoping processes for CPs, leading to excellent cyclic stability (107, 134). Zhang et al distributed PPy/CNT composites between rGO sheets homogeneously by flow-assembly to prepare unique flexible films (135). rGO/PPy/CNT hybrid films exhibit good flexibility. In such a layered structure, the coaxial PPy/CNT nanocables can not only enlarge the space between rGO sheets but also provide pseudo-capacitance to enhance the total capacitance of electrodes. Multilayered rGO/PPy/CNT achieve high mass and volume specific capacitances of 211 F/g and 122 F/cm at a current density of 0.2 A/g, which is higher than those of the rGO film (73 F/g and 79 F/cm²) and PPy/CNT (164 F/g and 67 F/cm²). Significantly, the rGO/PPy/CNT electrode shows excellent cyclic stability (with only a 5% capacity loss after 5000 cycles) due to the flexible GN layer and the rigid CNT core synergistically releasing the intrinsic differential strain of PPy chains during long-term charge/discharge cycles.

4. Carbon/Metal Oxide Composite

In addition to conductive polymers, previous studies demonstrate that energy density of SCs can be effectively improved by utilizing nanostructured MOs, such as MnO₂ and RuO₂, as Faradic electrodes at the cost of electrochemical stability. The high surface area of rGO sheets and CNTs make them promising support for the deposition of MOs. Furthermore, the electrons from the reversible oxidation-reduction of MOs can be effectively transported through rGO or CNT structure due to the high conductivity of rGO sheets and CNTs, which benefit the improve the power density of hybrid electrode materials. The high mechanical properties of CNTs and rGO sheets endow the hybrid film electrodes with good flexibility.

4.1. CNT/Metal Oxide Composite Flexible Pseudo-Supercapacitors

Lee et al prepare flexible CNT/MnO_x hybrid sheets by electrodepositing MnO_x onto CNT sheets (Figure 10a and b), pulled directly from MWCNT forests (136). The morphology and microstructure of the CNT/MnO_x hybrid sheets varied substantially as the electrodeposition time was increased. Both the specific capacitances and rate capabilities depend on the average size of the MnO_x nanoparticles on the CNTs, as indicated in CV and charge/discharge curves (Figure 10c and d). The resulting CNT/MnO_x hybrid sheets have high specific capacitances of 1250 F/g, high charge/discharge rate capabilities, and excellent cyclic stability. These properties are ascribed to a synergistic combination of large surface area and good electron-transport capabilities of the MnO_x nanoparticles with the good conductivity of the CNT sheets. Flexible high frequency response SCs can be fabricated using freestanding SWCNT/MnO₂ electrodes, which was obtained by a facile and scalable asymmetric *in situ* deposition method to incorporate MnO₂ nanoparticles in vacuum filtrated SWCNT films. The as-prepared SCs showed a superior performance with specific capacitance of 529.8 F/g, energy density of 73.6 Wh/kg, power density of 14.6 Kw/kg, excellent capacitance retention (99.9%) after 2000 charge and discharge cycles, and high knee frequency of 1318 Hz.

More recently, coating MO, and/or CNT composites on textiles, sponges, and papers have also been reported as feasible methods to prepare flexible electrodes for SCs (11, 137–139). As mention in 3.1 section, highly conductive SWCNTs/cloth electrodes can be obtained by simple “dipping and drying” process using SWCNT ink (11). To improve the energy density of the SWCNTs/cloth electrodes, MnO₂ was uniformly electrodeposited on the SWCNTs (11). This was effective in significantly increasing the mass loading of the pseudocapacitor, while maintaining contact between SWNTs and providing a good electrical conduction path. The deposition is observed not only on the surfaces of the SWCNT/cotton but also inside the layers of cotton fibers. The capacitance with respect to the device increases by a factor of 24 after MnO₂ deposition, reaching 0.41 F/cm². The specific capacitance when including the masses of both CNT and MnO₂ increases by a factor of 4 with MnO₂ deposition. In addition, this group reports a new nanostructure based on a conductive CNT-textile fiber network, where MnO₂ nanoflowers were conformally electrodeposited onto CNT-enabled conductive textile fibers (137). Such a porous structure effectively decreases the ion diffusion and charge transport resistance in the electrodes and also allows a large mass loading, up to 8.3 mg/cm², which leads to a high areal capacitance of 2.8 F/cm² at a scan rate of 0.05 mV/s. In addition to the textile composite, this group also used sponges as support substrates to fabricate nanostructured MnO₂/CNT/sponge hybrid electrodes (138). The SCs based on these hybrid electrodes exhibited high specific power and energy densities of 63 kW/kg and 31 Wh/kg, respectively. The MnO₂/CNT/sponge SCs show only 4% of degradation after 10000 cycles at a charge-discharge specific current of 5 A/g. In addition, Kim et al reported that flexible paper-based SCs with increased specific capacitance and specific energy can be fabricated by depositing MnO₂ on CNT-coated papers. The MnO₂/CNT/paper SCs showed a high specific capacitance of 540 F/g (139).

Specific energy and specific power densities were determined to be 20 Wh/kg and 1.5 kW/kg, respectively at current density of 5 A/g

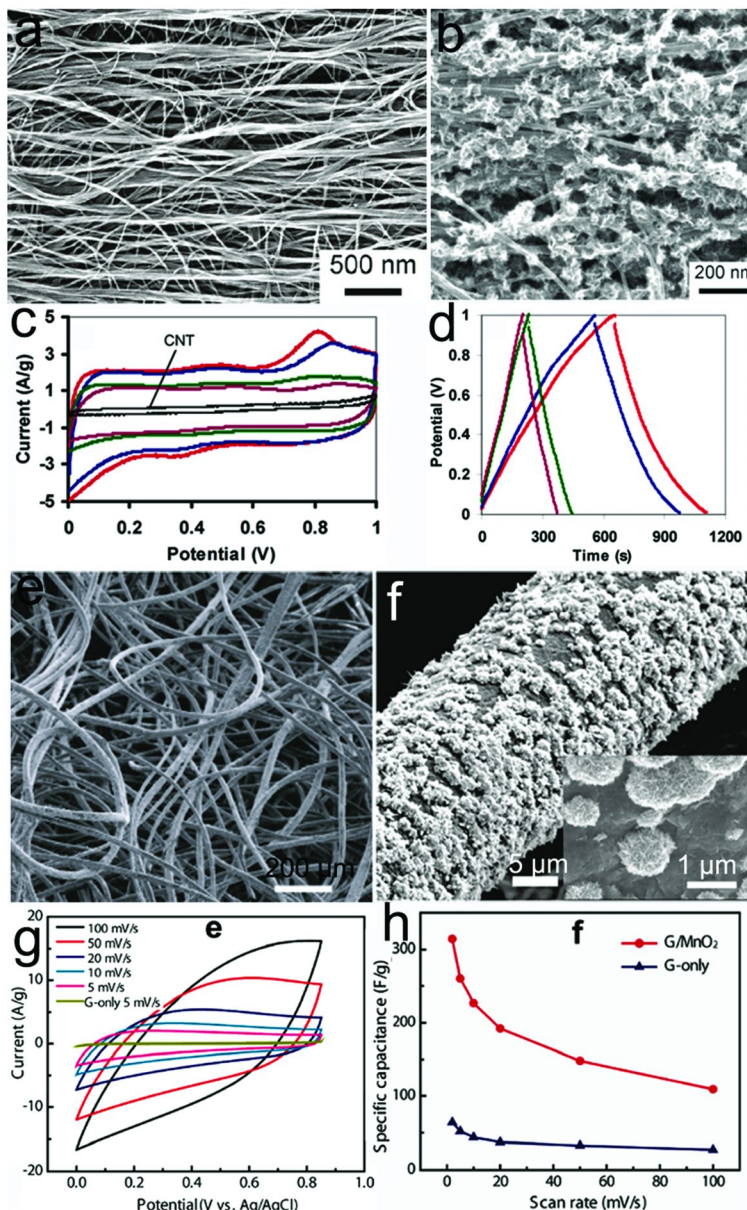


Figure 10. (a) CNT alignment in the electrode. (b) Morphology and microstructures of CNT sheet/MnO_x composites deposited for 5s. (c) CVs of the composites deposited for 15 (red), 30 (blue), 60 (green), and 180 s (brown) at 5 mV/s. (d) The charge/discharge curves for the composites at 1 A/g. Reproduced with permission from reference (136). Copyright 2010 American Chemical

Society. (e) SEM image of a sheet of graphene-coated textile after 60 min MnO_2 . (f) SEM image of a typical microfiber with conformal coating of MnO_2 nanostructures in the same textile. (Inset) High magnification SEM image showing the nanoflower structure of electrodeposited MnO_2 particles and a clear interface between MnO_2 nanoflower and underneath graphene nanosheets. (g) CVs for graphene/ MnO_2 -textile electrode at different scan rates in 0.5 M aqueous Na_2SO_4 electrolyte (CV curve for graphene-only textile at a scan rate of 5 mV/s included for comparison). (h) Comparison of specific capacitance values between graphene/ MnO_2 -textile and graphene nanosheets-only textile at different scan rates. Reproduced with permission from reference (148). Copyright 2010 American Chemical Society.

Using other CNT structures as templates, flexible CNT/ MnO_2 SC electrodes were also prepared. For example, flexible carbon fabric (CF)-CNT array (CNTA)/ MnO_2 hybrid electrodes with a 3D porous structure are prepared by the electrochemical deposition of MnO_2 onto CNTA (140). The maximum specific capacitance of CF-CNTA/ MnO_2 electrodes is up to 740 F/g at the scan rate of 2 mV/s. CF-CNTA/ MnO_2 achieved a high retention of 70% with a scan rate range of 2-200 mV/s due to the 3D structures.

Based on SWCNT inks and an off-the-shelf inkjet printer, Zhou et al successfully printed SWCNT thin film electrodes on flexible substrates and cloth fabrics with features of controlled pattern geometry, location, thickness, and tunable electrical conductivity (141). Then, RuO_2 in an isopropanol alcohol (IPA) suspension dispersed on the printed SWNT films until a reasonable nanowire density was achieved. The SWCNT/ RuO_2 hybrid films were then sandwiched together with a piece of printable polymer electrolyte to form flexible and wearable SCs. Owing to the addition of RuO_2 , the performance of the SWCNT/ RuO_2 hybrid film SC was significantly improved in terms of its specific capacitance of 138 F/g, power density of 96 kW/kg, and energy density of 18.8 Wh/kg. Furthermore, the knee frequency of the hybrid thin film electrodes can reach 1,500 Hz, which is much higher than the knee frequency of the bare SWCNT electrodes (~158 Hz).

Owing to the unique properties of MO nanowires, such as high aspect ratio and short diffusion path length for ions, they can provide high surface area, fast charge/discharge, and facial redox reactions, and thus can be one of good candidates for electrochemical capacitors. As is well known, In_2O_3 is a wide band gap material (3.57 eV), which has been widely applied in the transparent electronics. Zhou et al improved the conductivity of In_2O_3 electrodes by integrating In_2O_3 together with SWCNTs to form hybrid nanostructured films for flexible and transparent SCs (142). The In_2O_3 nanowire/CNT hybrid film SC exhibits high specific capacitance of 64 F/g, high power density of 7.48 kW/kg and a good retention of capacity (88% after 500 cycles). An alternative approach to improve energy density is to develop asymmetric SCs (ASCs). ASCs can make use of the different potential windows of the two electrodes to increase the maximum operation voltage of the aqueous electrolyte in the device. Zhou et al has developed an easy and efficient method to prepare hybrid nanostructured

thin film electrodes by using two different transition-metal-oxide nanowires, including MnO_2 nanowires and In_2O_3 nanowires, together with SWCNTs and fabricated hybrid nanostructured ASCs (143). In this asymmetric SC, a MnO_2 nanowire/SWCNT hybrid film served as the positive electrode, while a In_2O_3 nanowire/SWCNT hybrid film functioned as the negative electrode with a neutral electrolyte. These hybrid nanostructured films obtained from a filtration method possess mechanical flexibility, uniform layered structures, and mesoporous surface morphology. The mass balance between two electrodes has been optimized to obtain stable electrochemical behavior during charging-discharging cycles in a 2 V potential window. The optimized hybrid nanostructured ASCs exhibited a superior device performance with specific capacitance of 184 F/g, energy density of 25.5 Wh/kg, power density of 50.3 kW/kg and columbic efficiency of 90%.

In addition to MnO_2 and In_2O_3 , other MOs were also developed to improve the performance of the electrodes. Generally, vanadium oxides offer high pseudo-capacitance but limited electrical conductivity and specific surface area. To overcome this issue, smooth nanostructured vanadium oxide with various thicknesses can be coated uniformly on the surface of porous MWCNT electrodes by atomic layer deposition (144). The as-prepared binder-free flexible hybrid electrodes have controlled porosity, greatly improved electrical conductivity and cycle stability. Remarkable capacitance of up to ~ 1550 F/g per active mass of the vanadium oxide and up to ~ 600 F/g per mass of the composite electrode MWCNT/vanadium oxide electrodes were achieved, significantly exceeding specific capacitance of commercially used activated carbons (100–150 F/g). In addition, flexible CNT/TiO₂ hybrid electrodes can be obtained by coating CNT networks on the TiO₂ nanotubes (145). The specific capacitance of CNT/TiO₂ hybrid electrodes can be enhanced by about 30% as compared to pure carbon-nanotube electrodes.

4.2. Graphene/MO Composite Flexible Pseudo-Capacitors

3D macroporous RGO electrodes can be fabricated by replicating and embossing techniques using polystyrene colloidal particles as a sacrificial template (146). For further improvement of capacitance, a thin layer of MnO_2 was additionally deposited onto the RGO surface in the 3D structure. The macroporous hybrid structure endows a large surface area and facilitates fast ionic transport within the electrode while preserving decent electronic conductivity. These MnO_2 /RGO hybrid composite electrodes exhibit a high specific capacitance of 389 F/g at 1 A/g and 97.7% capacitance retention upon a current increase to 35 A/g. Moreover, when the MnO_2 /RGO composite electrode was asymmetrically assembled with an RGO macroporous electrode, the resulting SCs possess energy density of 44 Wh/kg, power density of 25 kW/kg, and excellent cycle life. Flexible RGO/ MnO_2 hybrid papers have successfully fabricated via a simple three-step route: preparation of GO/ MnO_2 composite dispersion, subsequent vacuum filtration of the composite dispersion to achieve GO/ MnO_2 hybrid paper, and finally thermal reduction of the GO/ MnO_2 to generate RGO/ MnO_2 hybrid

paper (147). These RGO/MnO₂ hybrid papers can be used as a binder-free and flexible electrode material for SCs. The specific capacitance of the hybrid paper with the MnO₂ weight ratio of 24% reaches 256 F/g at a current density of 500 mA/g and also shows good cycle stability.

Solution-based coating and printing techniques have been recently exploited to make conductive CNT-based papers and textiles as electrodes and/or current collectors for SCs (11). Using a similar concept, Bao et al demonstrate that rGO nanosheets can be conformably coated from solution on the fiber surfaces of 3D porous textile support structures, serving as a conductive support with large surface area for the subsequent deposition of nanoscale MnO₂ particles, as shown in Figure 10e and f (148). 3D porous textiles ensure the high loading of active electrode materials and facilitate the access of electrolytes to those materials. As the scan rate increases from 50 to 100 mV/s, the peak current increases and the shape of CV curves shows some distortions from an ideal capacitor, possibly due to increasing overpotentials from ion transport between the electrolyte and MnO₂, as shown in Figure 10g. The hybrid rGO/MnO₂-based textile possesses a high-capacitance performance with specific capacitance up to 315 F/g (Figure 10h). To improve the power density and cycling of graphene/MnO₂-based textile, this group developed a “conductive wrapping” method to greatly improve the SC performance of rGO/MnO₂-based nanostructured electrodes (149). Owing to 3D conductive wrapping of rGO/MnO₂ nanostructures with CNTs or CP, specific capacitance of the electrodes (considering total mass of active materials) has substantially increased by ~20% and ~45%, respectively, with values as high as~380 F/g achieved. Moreover, these ternary composite electrodes have also exhibited excellent cycling performance with > 95% capacitance retention over 3000 cycles.

Apart from MnO₂, other MOs also exhibit the capacity of improving the energy density of graphene-based SCs. Well-designed flexible and free-standing Co₃O₄/RGO/CNTs hybrid paper electrodes prepared by one-step hydrothermal method exhibit a specific capacitance of 378 F/g at 2 A/g and 297 F/g at 8 A/g with excellent electrochemical stability (150). Zhang et al prepared 3D graphene/NiO networks by electrochemically depositing NiO on the 3D graphene networks prepared by CVD with Ni foam as a sacrificial template. The graphene/NiO composite electrode exhibits a high specific capacitance of 816 F/g at 5 mV/s along with a good rate capability. Taking into account the easy hydrothermal growth of ZnO on various substrates, especially on graphene films, tailoring nanostructures, and its pseudo-capacitance behavior, Huang et al propose a 3D structure of vertical aligned ZnO nanorods sandwiched between RGO films as flexible SC electrodes. ZnO nanorods in the electrodes prevent aggregation of RGO sheets and help in forming a porous structure. A specific capacitance of 51.6 F/g at the scan rate of 10 mV/s is achieved for the RGO/ZnO nanorods/RGO sandwich. As a novel composite of one-atom-thick sheets, Co-Al layered double hydroxide nanosheets can be used as supercapacitors. Flexible multilayer hybrid films of Co-Al layered double hydroxide nanosheets (Co-Al LDH-NS) and GO were fabricated through LBL assembly. The Co Al LDH-NS/GO multilayer films exhibited a high specific capacitance of 880 F/g and area capacitance of 70 F/m² under the scan rate of 5 mV/s. In addition, the film exhibited good cycle stability

over 2000 cycles. After reduction of GO to RGO, the specific capacitance and area capacitance were largely increased up to 1204 F/g and 90 F/m².

4.3. Graphene/CNT/MO Composite Flexible Pseudo-Capacitors

Graphene has been widely considered as an ideal substrate for ultrathin coating of functional materials due to its unique structural and electrical properties, while the uniformly interconnected CNTs network is beneficial for electronic and ionic transport due to its high conductivity and porosity. While MnO₂ has attracted much attention in SC applications due to its high capacitance due to pseudo-capacitance, its low conductivity significantly reduces the overall power density of devices. To fully utilize their own advantages of graphene, CNTs and MnO₂, Liu and co-workers present a novel method to fabricate conductive, highly flexible, and robust film SC electrodes based on rGO/MnO₂/CNTs nanocomposites. Synergistic effects from both rGO and CNTs were utilised as the rGO provides a high-surface-area substrate for direct growth of MnO₂ nanoparticles and CNTs provide electron conductance and mechanical reinforcement. The synergistic effects from rGO, CNTs, and MnO₂ deliver outstanding mechanical properties (tensile strength of 48 MPa) and superior electrochemical activity that were not achieved by any of these components individually. These flexible electrodes allow for a high specific capacitance (372 F/g) with excellent rate capability for SCs without the need of current collectors and binders. The film can also be wound around 0.5 mm diameter rods for fabricating full cells with high performance, showing significant potential in flexible energy storage devices.

5. Perspectives

Although some great progresses have been achieved in both preparation of flexible SC electrodes and assembly of flexible SC based on these electrodes, much work remains to be done in the preparation of these electrodes. Further work is needed for controllable assembly of electrodes and devices, improvement of properties, and extended of practical applications.

Although various flexible SC electrodes have been successfully fabricated by different methods, such as vacuum filtration, solution-based coating and printing techniques, and high specific capacitance have been obtained, the overall capacitance is much smaller than the practical requirement due to the limited mass and area of electrodes. Preparation of flexible SC with high capacitance should be considered for the practical application of flexible supercapacitors. Currently various flexible functional devices have been reported. In future, flexible SCs with controlled design should be prepared to match and power these functional devices, even integrate the flexible SCs with these functional devices into fully flexible devices. The flexibility of SC electrodes should also be improved by controlling the structure of electrode materials. The measurement methods for the flexibility and electrochemical performance of flexible supercapacitors are not well

standardized and as a result it is difficult to assess the true performance reported in the literature. Test methods for flexible ultracapacitors should be well developed.

Graphene and CNT have high theoretical SSA. However, the practical SSA of pure graphene and/or CNT SC electrodes is much smaller than the theoretical value due to their structure, in which not all their surface area is electrochemically accessible when in contact with electrolyte. In further work, the SSA utilisation of graphene and CNT in the flexible electrodes should be improved by controlling their porous structure to increase the energy density of the electrodes. Graphene- and CNT-based hybrid electrodes would be optimized by controlling their compositions, morphology, micro-structure to enhance their power density.

Assembly of devices is another issue that affects the performance and flexibility of SCs. Conventional flexible SC devices, as shown in Figure 1, can not meet the requirement of highly flexible SCs. SCs with different design and structure should be explored. The SCs will move to compact, flexible, lightweight and low-cost direction.

References

1. Zhang, L. L.; Zhao, X. S. *Chem. Soc. Rev.* **2009**, *38*, 2520–2531.
2. Zhang, Y.; Feng, H.; Wu, X. B.; Wang, L. Z.; Zhang, A. Q.; Xia, T. C.; Dong, H. C.; Li, X. F.; Zhang, L. S. *Int. J. Hydrogen Energy* **2009**, *34*, 4889–4899.
3. Simon, P.; Gogotsi, Y. *Nat. Mater.* **2008**, *7*, 845–854.
4. Winter, M.; Brodd, R. *J. Chem. Rev.* **2004**, *104*, 4245–4269.
5. Talpone, J. I.; Puleston, P. F.; More, J. J.; Grino, R.; Cendoya, M. G. *Int. J. Hydrogen Energy* **2012**, *37*, 10346–10353.
6. Kaempgen, M.; Chan, C. K.; Ma, J.; Cui, Y.; Gruner, G. *Nano Lett.* **2009**, *9*, 1872–1876.
7. Niu, C. M.; Sichel, E. K.; Hoch, R.; Moy, D.; Tennent, H. *Appl. Phys. Lett.* **1997**, *70*, 1480–1482.
8. Frackowiak, E.; Metenier, K.; Bertagna, V.; Beguin, F. *Appl. Phys. Lett.* **2000**, *77*, 2421–2423.
9. Hu, L. B.; Choi, J. W.; Yang, Y.; Jeong, S.; La Mantia, F.; Cui, L. F.; Cui, Y. *Proc. Natl Acad. Sci. U.S.A.* **2009**, *106*, 21490–21494.
10. Kang, Y. J.; Chung, H.; Han, C. H.; Kim, W. *Nanotechnology* **2012**, *23*.
11. Hu, L. B.; Pasta, M.; La Mantia, F.; Cui, L. F.; Jeong, S.; Deshazer, H. D.; Choi, J. W.; Han, S. M.; Cui, Y. *Nano Lett.* **2010**, *10*, 708–714.
12. Hu, S.; Rajamani, R.; Yu, X. *Appl. Phys. Lett.* **2012**, *100*.
13. Pushparaj, V. L.; Shajumon, M. M.; Kumar, A.; Murugesan, S.; Ci, L.; Vajtai, R.; Linhardt, R. J.; Nalamasu, O.; Ajayan, P. M. *Proc. Natl Acad. Sci. U.S.A.* **2007**, *104*, 13574–13577.
14. Ma, W. J.; Song, L.; Yang, R.; Zhang, T. H.; Zhao, Y. C.; Sun, L. F.; Ren, Y.; Liu, D. F.; Liu, L. F.; Shen, J.; Zhang, Z. X.; Xiang, Y. J.; Zhou, W. Y.; Xie, S. S. *Nano Lett.* **2007**, *7*, 2307–2311.

15. Ma, W. J.; Liu, L. Q.; Zhang, Z.; Yang, R.; Liu, G.; Zhang, T. H.; An, X. F.; Yi, X. S.; Ren, Y.; Niu, Z. Q.; Li, J. Z.; Dong, H. B.; Zhou, W. Y.; Ajayan, P. M.; Xie, S. S. *Nano Lett.* **2009**, *9*, 2855–2861.
16. Niu, Z. Q.; Zhou, W. Y.; Chen, J.; Feng, G. X.; Li, H.; Ma, W. J.; Li, J. Z.; Dong, H. B.; Ren, Y.; Zhao, D.; Xie, S. S. *Energy Environ. Sci.* **2011**, *4*, 1440–1446.
17. Niu, Z. Q.; Zhou, W. Y.; Chen, J.; Feng, G. X.; Li, H.; Hu, Y. S.; Ma, W. J.; Dong, H. B.; Li, J. Z.; Xie, S. S. *Small* **2013**, *9*, 518–524.
18. Chen, J.; Minett, A. I.; Liu, Y.; Lynam, C.; Sherrell, P.; Wang, C.; Wallace, G. G. *Adv. Mater.* **2008**, *20*, 566–570.
19. Chen, J.; Wang, J. Z.; Minett, A. I.; Liu, Y.; Lynam, C.; Liu, H. K.; Wallace, G. G. *Energy Environ. Sci.* **2009**, *2*, 393–396.
20. Xu, G. H.; Zheng, C.; Zhang, Q.; Huang, J. Q.; Zhao, M. Q.; Nie, J. Q.; Wang, X. H.; Wei, F. *Nano Res.* **2011**, *4*, 870–881.
21. Bolotin, K. I.; Ghahari, F.; Shulman, M. D.; Stormer, H. L.; Kim, P. *Nature* **2009**, *462*, 196–199.
22. Chen, C. F.; Park, C. H.; Boudouris, B. W.; Horng, J.; Geng, B. S.; Girit, C.; Zettl, A.; Crommie, M. F.; Segalman, R. A.; Louie, S. G.; Wang, F. *Nature* **2011**, *471*, 617–620.
23. Du, X.; Skachko, I.; Duerr, F.; Luican, A.; Andrei, E. Y. *Nature* **2009**, *462*, 192–195.
24. Garaj, S.; Hubbard, W.; Reina, A.; Kong, J.; Branton, D.; Golovchenko, J. A. *Nature* **2010**, *467*, 190–U73.
25. Gomes, K. K.; Mar, W.; Ko, W.; Guinea, F.; Manoharan, H. C. *Nature* **2012**, *483*, 306–310.
26. Huang, P. Y.; Ruiz-Vargas, C. S.; van der Zande, A. M.; Whitney, W. S.; Levendorf, M. P.; Kevek, J. W.; Garg, S.; Alden, J. S.; Hustedt, C. J.; Zhu, Y.; Park, J.; McEuen, P. L.; Muller, D. A. *Nature* **2011**, *469*, 389–392.
27. Kim, K. S.; Zhao, Y.; Jang, H.; Lee, S. Y.; Kim, J. M.; Ahn, J. H.; Kim, P.; Choi, J. Y.; Hong, B. H. *Nature* **2009**, *457*, 706–710.
28. Lui, C. H.; Liu, L.; Mak, K. F.; Flynn, G. W.; Heinz, T. F. *Nature* **2009**, *462*, 339–341.
29. Meyer, J. C.; Geim, A. K.; Katsnelson, M. I.; Novoselov, K. S.; Booth, T. J.; Roth, S. *Nature* **2007**, *446*, 60–63.
30. Novoselov, K. S.; Geim, A. K.; Morozov, S. V.; Jiang, D.; Katsnelson, M. I.; Grigorieva, I. V.; Dubonos, S. V.; Firsov, A. A. *Nature* **2005**, *438*, 197–200.
31. Son, Y. W.; Cohen, M. L.; Louie, S. G. *Nature* **2006**, *444*, 347–349.
32. Stankovich, S.; Dikin, D. A.; Dommett, G. H. B.; Kohlhaas, K. M.; Zimney, E. J.; Stach, E. A.; Piner, R. D.; Nguyen, S. T.; Ruoff, R. S. *Nature* **2006**, *442*, 282–286.
33. Zhang, Y. B.; Tan, Y. W.; Stormer, H. L.; Kim, P. *Nature* **2005**, *438*, 201–204.
34. Berger, C.; Song, Z. M.; Li, X. B.; Wu, X. S.; Brown, N.; Naud, C.; Mayou, D.; Li, T. B.; Hass, J.; Marchenkov, A. N.; Conrad, E. H.; First, P. N.; de Heer, W. A. *Science* **2006**, *312*, 1191–1196.
35. Bostwick, A.; Speck, F.; Seyller, T.; Horn, K.; Polini, M.; Asgari, R.; MacDonald, A. H.; Rotenberg, E. *Science* **2010**, *328*, 999–1002.

36. Bunch, J. S.; van der Zande, A. M.; Verbridge, S. S.; Frank, I. W.; Tanenbaum, D. M.; Parpia, J. M.; Craighead, H. G.; McEuen, P. L. *Science* **2007**, *315*, 490–493.
37. Dimiev, A.; Kosynkin, D. V.; Sinitskii, A.; Slesarev, A.; Sun, Z. Z.; Tour, J. M. *Science* **2011**, *331*, 1168–1172.
38. Elias, D. C.; Nair, R. R.; Mohiuddin, T. M. G.; Morozov, S. V.; Blake, P.; Halsall, M. P.; Ferrari, A. C.; Boukhvalov, D. W.; Katsnelson, M. I.; Geim, A. K.; Novoselov, K. S. *Science* **2009**, *323*, 610–613.
39. Geim, A. K. *Science* **2009**, *324*, 1530–1534.
40. Girit, C. O.; Meyer, J. C.; Erni, R.; Rossell, M. D.; Kisielowski, C.; Yang, L.; Park, C. H.; Crommie, M. F.; Cohen, M. L.; Louie, S. G.; Zettl, A. *Science* **2009**, *323*, 1705–1708.
41. Lin, Y. M.; Valdes-Garcia, A.; Han, S. J.; Farmer, D. B.; Meric, I.; Sun, Y. N.; Wu, Y. Q.; Dimitrakopoulos, C.; Grill, A.; Avouris, P.; Jenkins, K. A. *Science* **2011**, *332*, 1294–1297.
42. Miller, J. R.; Outlaw, R. A.; Holloway, B. C. *Science* **2010**, *329*, 1637–1639.
43. Nair, R. R.; Blake, P.; Grigorenko, A. N.; Novoselov, K. S.; Booth, T. J.; Stauber, T.; Peres, N. M. R.; Geim, A. K. *Science* **2008**, *320*, 1308–1308.
44. Seol, J. H.; Jo, I.; Moore, A. L.; Lindsay, L.; Aitken, Z. H.; Pettes, M. T.; Li, X. S.; Yao, Z.; Huang, R.; Broido, D.; Mingo, N.; Ruoff, R. S.; Shi, L. *Science* **2010**, *328*, 213–216.
45. Wei, Z. Q.; Wang, D. B.; Kim, S.; Kim, S. Y.; Hu, Y. K.; Yakes, M. K.; Laracuente, A. R.; Dai, Z. T.; Marder, S. R.; Berger, C.; King, W. P.; de Heer, W. A.; Sheehan, P. E.; Riedo, E. *Science* **2010**, *328*, 1373–1376.
46. Westervelt, R. M. *Science* **2008**, *320*, 324–325.
47. Zhao, L. Y.; He, R.; Rim, K. T.; Schiros, T.; Kim, K. S.; Zhou, H.; Gutierrez, C.; Chockalingam, S. P.; Arguello, C. J.; Palova, L.; Nordlund, D.; Hybertsen, M. S.; Reichman, D. R.; Heinz, T. F.; Kim, P.; Pinczuk, A.; Flynn, G. W.; Pasupathy, A. N. *Science* **2011**, *333*, 999–1003.
48. Zhu, Y. W.; Murali, S.; Stoller, M. D.; Ganesh, K. J.; Cai, W. W.; Ferreira, P. J.; Pirkle, A.; Wallace, R. M.; Cyhlosz, K. A.; Thommes, M.; Su, D.; Stach, E. A.; Ruoff, R. S. *Science* **2011**, *332*, 1537–1541.
49. Geim, A. K.; Novoselov, K. S. *Nat. Mater.* **2007**, *6*, 183–191.
50. Morozov, S. V.; Novoselov, K. S.; Katsnelson, M. I.; Schedin, F.; Elias, D. C.; Jasdzak, J. A.; Geim, A. K. *Phys. Rev. Lett.* **2008**, *100*.
51. Durkop, T.; Getty, S. A.; Cobas, E.; Fuhrer, M. S. *Nano Lett.* **2004**, *4*, 35–39.
52. Stoller, M. D.; Park, S. J.; Zhu, Y. W.; An, J. H.; Ruoff, R. S. *Nano Lett.* **2008**, *8*, 3498–3502.
53. Lee, C.; Wei, X. D.; Kysar, J. W.; Hone, J. *Science* **2008**, *321*, 385–388.
54. Balandin, A. A.; Ghosh, S.; Bao, W. Z.; Calizo, I.; Teweldebrhan, D.; Miao, F.; Lau, C. N. *Nano Lett.* **2008**, *8*, 902–907.
55. Zhu, Y. W.; Murali, S.; Cai, W. W.; Li, X. S.; Suk, J. W.; Potts, J. R.; Ruoff, R. S. *Adv. Mater.* **2010**, *22*, 5226–5226.
56. Huang, Y.; Liang, J. J.; Chen, Y. S. *Small* **2012**, *8*, 1805–1834.
57. Novoselov, K. S.; Geim, A. K.; Morozov, S. V.; Jiang, D.; Zhang, Y.; Dubonos, S. V.; Grigorieva, I. V.; Firsov, A. A. *Science* **2004**, *306*, 666–669.

58. Li, X. S.; Cai, W. W.; An, J. H.; Kim, S.; Nah, J.; Yang, D. X.; Piner, R.; Velamakanni, A.; Jung, I.; Tutuc, E.; Banerjee, S. K.; Colombo, L.; Ruoff, R. S. *Science* **2009**, *324*, 1312–1314.
59. Zhang, B.; Lee, W. H.; Piner, R.; Kholmanov, I.; Wu, Y. P.; Li, H. F.; Ji, H. X.; Ruoff, R. S. *ACS Nano* **2012**, *6*, 2471–2476.
60. Wu, W.; Jauregui, L. A.; Su, Z. H.; Liu, Z. H.; Bao, J. M.; Chen, Y. P.; Yu, Q. K. *Adv. Mater.* **2011**, *23*, 4898–4903.
61. Wassei, J. K.; Mecklenburg, M.; Torres, J. A.; Fowler, J. D.; Regan, B. C.; Kaner, R. B.; Weiller, B. H. *Small* **2012**, *8*, 1415–1422.
62. Wang, Y.; Zheng, Y.; Xu, X. F.; Dubuisson, E.; Bao, Q. L.; Lu, J.; Loh, K. P. *ACS Nano* **2011**, *5*, 9927–9933.
63. Tao, L.; Lee, J.; Chou, H.; Holt, M.; Ruoff, R. S.; Akinwande, D. *ACS Nano* **2012**, *6*, 2319–2325.
64. Robertson, A. W.; Warner, J. H. *Nano Lett.* **2011**, *11*, 1182–1189.
65. Rasool, H. I.; Song, E. B.; Mecklenburg, M.; Regan, B. C.; Wang, K. L.; Weiller, B. H.; Gimzewski, J. K. *J. Am. Chem. Soc.* **2011**, *133*, 12536–12543.
66. Rasool, H. I.; Song, E. B.; Allen, M. J.; Wassei, J. K.; Kaner, R. B.; Wang, K. L.; Weiller, B. H.; Gimzewski, J. K. *Nano Lett.* **2011**, *11*, 251–256.
67. He, R.; Zhao, L. Y.; Petrone, N.; Kim, K. S.; Roth, M.; Hone, J.; Kim, P.; Pasupathy, A.; Pinczuk, A. *Nano Lett.* **2012**, *12*, 2408–2413.
68. Han, G. H.; Gunes, F.; Bae, J. J.; Kim, E. S.; Chae, S. J.; Shin, H. J.; Choi, J. Y.; Pribat, D.; Lee, Y. H. *Nano Lett.* **2011**, *11*, 4144–4148.
69. Gao, L. B.; Ren, W. C.; Zhao, J. P.; Ma, L. P.; Chen, Z. P.; Cheng, H. M. *Appl. Phys. Lett.* **2010**, *97*.
70. Gao, L.; Guest, J. R.; Guisinger, N. P. *Nano Lett.* **2010**, *10*, 3512–3516.
71. Reina, A.; Thiele, S.; Jia, X. T.; Bhaviripudi, S.; Dresselhaus, M. S.; Schaefer, J. A.; Kong, J. *Nano Res.* **2009**, *2*, 509–516.
72. Lahiri, J.; Miller, T.; Adamska, L.; Oleynik, II; Batzill, M. *Nano Lett.* **2011**, *11*, 518–522.
73. Addou, R.; Dahal, A.; Sutter, P.; Batzill, M. *Appl. Phys. Lett.* **2012**, *100*.
74. Li, X. S.; Cai, W. W.; Colombo, L.; Ruoff, R. S. *Nano Lett.* **2009**, *9*, 4268–4272.
75. Chen, S. S.; Cai, W. W.; Piner, R. D.; Suk, J. W.; Wu, Y. P.; Ren, Y. J.; Kang, J. Y.; Ruoff, R. S. *Nano Lett.* **2011**, *11*, 3519–3525.
76. Sutter, P. W.; Flege, J. I.; Sutter, E. A. *Nat. Mater.* **2008**, *7*, 406–411.
77. Cui, X.; Zhang, C. Z.; Hao, R.; Hou, Y. L. *Nanoscale* **2011**, *3*, 2118–2126.
78. Li, C.; Shi, G. Q. *Nanoscale* **2012**, *4*, 5549–5563.
79. Dikin, D. A.; Stankovich, S.; Zimney, E. J.; Piner, R. D.; Dommett, G. H. B.; Evmenenko, G.; Nguyen, S. T.; Ruoff, R. S. *Nature* **2007**, *448*, 457–460.
80. Chen, D.; Tang, L. H.; Li, J. H. *Chem. Soc. Rev.* **2010**, *39*, 3157–3180.
81. Dreyer, D. R.; Park, S.; Bielawski, C. W.; Ruoff, R. S. *Chem. Soc. Rev.* **2010**, *39*, 228–240.
82. Li, D.; Muller, M. B.; Gilje, S.; Kaner, R. B.; Wallace, G. G. *Nat. Nanotechnol.* **2008**, *3*, 101–105.
83. Niu, Z. Q.; Chen, J.; Hng, H. H.; Ma, J.; Chen, X. D. *Adv. Mater.* **2012**, *24*, 4144–4150.

84. Yang, X. W.; Zhu, J. W.; Qiu, L.; Li, D. *Adv. Mater.* **2011**, *23*, 2833–2838.
85. Tai, Z. X.; Yan, X. B.; Xue, Q. *J. Power Sources* **2012**, *213*, 350–357.
86. Chen, C. M.; Zhang, Q.; Huang, C. H.; Zhao, X. C.; Zhang, B. S.; Kong, Q. Q.; Wang, M. Z.; Yang, Y. G.; Cai, R.; Su, D. S. *Chem. Commun.* **2012**, *48*, 7149–7151.
87. Gao, W.; Singh, N.; Song, L.; Liu, Z.; Reddy, A. L. M.; Ci, L. J.; Vajtai, R.; Zhang, Q.; Wei, B. Q.; Ajayan, P. M. *Nat. Nanotechnol.* **2011**, *6*, 496–500.
88. El-Kady, M. F.; Strong, V.; Dubin, S.; Kaner, R. B. *Science* **2012**, *335*, 1326–1330.
89. Zhang, L. L.; Zhao, X.; Stoller, M. D.; Zhu, Y. W.; Ji, H. X.; Murali, S.; Wu, Y. P.; Perales, S.; Clevenger, B.; Ruoff, R. S. *Nano Lett.* **2012**, *12*, 1806–1812.
90. Biswas, S.; Drzal, L. T. *ACS Appl. Mater. Interfaces* **2010**, *2*, 2293–2300.
91. Niu, Z. Q.; Du, J. J.; B., C. X.; Sun, Y. H.; Zhou, W. Y.; Hng, H. H.; Ma, J.; Chen, X. D.; Xie, S. S. *Small* **2012**, *8*, 3201–3208.
92. Wang, G. K.; Sun, X.; Lu, F. Y.; Sun, H. T.; Yu, M. P.; Jiang, W. L.; Liu, C. S.; Lian, J. *Small* **2012**, *8*, 452–459.
93. Yu, A. P.; Roes, I.; Davies, A.; Chen, Z. W. *Appl. Phys. Lett.* **2010**, *96*.
94. Liu, W. W.; Yan, X. B.; Lang, J. W.; Peng, C.; Xue, Q. *J. Mater. Chem.* **2012**, *22*, 17245–17253.
95. Tai, Z. X.; Yan, X. B.; Lang, J. W.; Xue, Q. *J. Power Sources* **2012**, *199*, 373–378.
96. Kang, Y. R.; Li, Y. L.; Hou, F.; Wen, Y. Y.; Su, D. *Nanoscale* **2012**, *4*, 3248–3253.
97. Peng, L. W.; Feng, Y. Y.; Lv, P.; Lei, D.; Shen, Y. T.; Li, Y.; Feng, W. *J. Phys. Chem. C* **2012**, *116*, 4970–4978.
98. Lu, X. J.; Dou, H.; Gao, B.; Yuan, C. Z.; Yang, S. D.; Hao, L.; Shen, L. F.; Zhang, X. G. *Electrochim. Acta* **2011**, *56*, 5115–5121.
99. Li, Y. F.; Liu, Y. Z.; Yang, Y. G.; Wang, M. Z.; Wen, Y. F. *Appl. Phys. A* **2012**, *108*, 701–707.
100. Yu, D. S.; Dai, L. M. *J. Phys. Chem. Lett.* **2010**, *1*, 467–470.
101. Izadi-Najafabadi, A.; Yamada, T.; Futaba, D. N.; Yudasaka, M.; Takagi, H.; Hatori, H.; Iijima, S.; Hata, K. *ACS Nano* **2011**, *5*, 811–819.
102. Obreja, V. V. N. *Phys. E* **2008**, *40*, 2596–2605.
103. Hyder, M. N.; Lee, S. W.; Cebeci, F. C.; Schmidt, D. J.; Shao-Horn, Y.; Hammond, P. T. *ACS Nano* **2011**, *5*, 8552–8561.
104. Salvatierra, R. V.; Oliveira, M. M.; Zarbin, A. J. G. *Chem. Mater.* **2010**, *22*, 5222–5234.
105. Meng, C. Z.; Liu, C. H.; Fan, S. S. *Electrochem. Commun.* **2009**, *11*, 186–189.
106. Mikhaylova, A. A.; Tusseeva, E. K.; Mayorova, N. A.; Rychagov, A. Y.; Volkovich, Y. M.; Krestinin, A. V.; Khazova, O. A. *Electrochim. Acta* **2011**, *56*, 3656–3665.
107. Yan, J.; Wei, T.; Fan, Z. J.; Qian, W. Z.; Zhang, M. L.; Shen, X. D.; Wei, F. *J. Power Sources* **2010**, *195*, 3041–3045.
108. Wang, T.; Kiebele, A.; Ma, J.; Mhaisalkar, S.; Gruner, G. *J. Electrochem. Soc.* **2011**, *158*, A1–A5.

109. Ge, J.; Cheng, G. H.; Chen, L. W. *Nanoscale* **2011**, *3*, 3084–3088.
110. Liu, J. L.; Sun, J.; Gao, L. *Nanoscale* **2011**, *3*, 3616–3619.
111. Huang, J. E.; Li, X. H.; Xu, J. C.; Li, H. L. *Carbon* **2003**, *41*, 2731–2736.
112. Wu, T. M.; Lin, Y. W.; Liao, C. S. *Carbon* **2005**, *43*, 734–740.
113. Lee, J. A.; Shin, M. K.; Kim, S. H.; Kim, S. J.; Spinks, G. M.; Wallace, G. G.; Ovalle-Robles, R.; Lima, M. D.; Kozlov, M. E.; Baughman, R. H. *ACS Nano* **2012**, *6*, 327–334.
114. Yuan, L. Y.; Lu, X. H.; Xiao, X.; Zhai, T.; Dai, J. J.; Zhang, F. C.; Hu, B.; Wang, X.; Gong, L.; Chen, J.; Hu, C. G.; Tong, Y. X.; Zhou, J.; Wang, Z. L. *ACS Nano* **2012**, *6*, 656–661.
115. Peng, C.; Zhang, S. W.; Jewell, D.; Chen, G. Z. *Prog. Nat. Sci.* **2008**, *18*, 777–788.
116. Liao, Y. Z.; Zhang, C.; Zhang, Y.; Strong, V.; Tang, J. S.; Li, X. G.; Kalantazadeh, K.; Hoek, E. M. V.; Wang, K. L.; Kaner, R. B. *Nano Lett.* **2011**, *11*, 954–959.
117. Wang, H. L.; Hao, Q. L.; Yang, X. J.; Lu, L. D.; Wang, X. *Nanoscale* **2010**, *2*, 2164–2170.
118. Yan, X. B.; Tai, Z. X.; Chen, J. T.; Xue, Q. J. *Nanoscale* **2011**, *3*, 212–216.
119. Fan, H. S.; Wang, H.; Zhao, N.; Zhang, X. L.; Xu, J. *J. Mater. Chem.* **2012**, *22*, 2774–2780.
120. Wu, Q.; Xu, Y. X.; Yao, Z. Y.; Liu, A. R.; Shi, G. Q. *ACS Nano* **2010**, *4*, 1963–1970.
121. Niu, Z. Q.; Lu, P. S.; Shao, Q.; Dong, H. B.; Li, J. Z.; Chen, J.; Zhao, D.; Cai, L.; Zhou, W. Y.; Chen, X. D.; Xie, S. S. *Energy Environ. Sci.* **2012**, *5*, 8726–8733.
122. Wang, K.; Zhao, P.; Zhou, X. M.; Wu, H. P.; Wei, Z. X. *J. Mater. Chem.* **2011**, *21*, 16373–16378.
123. Liu, Q. A.; Nayfeh, M. H.; Yau, S. T. *J. Power Sources* **2010**, *195*, 7480–7483.
124. Antiohos, D.; Folkes, G.; Sherrell, P.; Ashraf, S.; Wallace, G. G.; Aitchison, P.; Harris, A. T.; Chen, J.; Minett, A. I. *J. Mater. Chem.* **2011**, *21*, 15987–15994.
125. Zhang, L. L.; Zhao, S. Y.; Tian, X. N.; Zhao, X. S. *Langmuir* **2010**, *26*, 17624–17628.
126. Xu, J. J.; Wang, K.; Zu, S. Z.; Han, B. H.; Wei, Z. X. *ACS Nano* **2010**, *4*, 5019–5026.
127. Wang, D. W.; Li, F.; Zhao, J. P.; Ren, W. C.; Chen, Z. G.; Tan, J.; Wu, Z. S.; Gentle, I.; Lu, G. Q.; Cheng, H. M. *ACS Nano* **2009**, *3*, 1745–1752.
128. Kumar, N. A.; Choi, H. J.; Shin, Y. R.; Chang, D. W.; Dai, L. M.; Baek, J. B. *ACS Nano* **2012**, *6*, 1715–1723.
129. Zhang, K.; Zhang, L. L.; Zhao, X. S.; Wu, J. S. *Chem. Mater.* **2010**, *22*, 1392–1401.
130. Liu, S.; Liu, X. H.; Li, Z. P.; Yang, S. R.; Wang, J. Q. *New J. Chem.* **2011**, *35*, 369–374.
131. Lee, T.; Yun, T.; Park, B.; Sharma, B.; Song, H. K.; Kim, B. S. *J. Mater. Chem.* **2012**, *22*, 21092–21099.
132. Biswas, S.; Drzal, L. T. *Chem. Mater.* **2010**, *22*, 5667–5671.

133. Davies, A.; Audette, P.; Farrow, B.; Hassan, F.; Chen, Z. W.; Choi, J. Y.; Yu, A. P. *J. Phys. Chem. C* **2011**, *115*, 17612–17620.
134. Kim, K. S.; Park, S. *J. Electrochim. Acta* **2011**, *56*, 1629–1635.
135. Lu, X. J.; Dou, H.; Yuan, C. Z.; Yang, S. D.; Hao, L.; Zhang, F.; Shen, L. F.; Zhang, L. J.; Zhang, X. G. *J. Power Sources* **2012**, *197*, 319–324.
136. Kim, J. H.; Lee, K. H.; Overzet, L. J.; Lee, G. S. *Nano Lett.* **2011**, *11*, 2611–2617.
137. Hu, L. B.; Chen, W.; Xie, X.; Liu, N. A.; Yang, Y.; Wu, H.; Yao, Y.; Pasta, M.; Alshareef, H. N.; Cui, Y. *ACS Nano* **2011**, *5*, 8904–8913.
138. Chen, W.; Rakhi, R. B.; Hu, L. B.; Xie, X.; Cui, Y.; Alshareef, H. N. *Nano Lett.* **2011**, *11*, 5165–5172.
139. Kang, Y. J.; Kim, B.; Chung, H.; Kim, W. *Synth. Met.* **2010**, *160*, 2510–2514.
140. Lv, P.; Zhang, P.; Feng, Y. Y.; Li, Y.; Feng, W. *Electrochim. Acta* **2012**, *78*, 515–523.
141. Chen, P. C.; Chen, H. T.; Qiu, J.; Zhou, C. W. *Nano Research* **2010**, *3*, 594–603.
142. Chen, P. C.; Shen, G.; Sukcharoenchoke, S.; Zhou, C. *Appl. Phys. Lett.* **2009**, *94*, 233104.
143. Chen, P. C.; Shen, G. Z.; Shi, Y.; Chen, H. T.; Zhou, C. W. *ACS Nano* **2010**, *4*, 4403–4411.
144. Boukhalfa, S.; Evanoff, K.; Yushin, G. *Energy Environ. Sci.* **2012**, *5*, 6872–6879.
145. Chien, C. J.; Deora, S. S.; Chang, P. C.; Li, D. D.; Lu, J. G. *IEEE Trans. Nanotechnol.* **2011**, *10*, 706–709.
146. Choi, B. G.; Yang, M.; Hong, W. H.; Choi, J. W.; Huh, Y. S. *ACS Nano* **2012**, *6*, 4020–4028.
147. Li, Z. P.; Mi, Y. J.; Liu, X. H.; Liu, S.; Yang, S. R.; Wang, J. Q. *J. Mater. Chem.* **2011**, *21*, 14706–14711.
148. Yu, G. H.; Hu, L. B.; Vosgueritchian, M.; Wang, H. L.; Xie, X.; McDonough, J. R.; Cui, X.; Cui, Y.; Bao, Z. N. *Nano Lett.* **2011**, *11*, 2905–2911.
149. Yu, G. H.; Hu, L. B.; Liu, N. A.; Wang, H. L.; Vosgueritchian, M.; Yang, Y.; Cui, Y.; Bao, Z. N. *Nano Lett.* **2011**, *11*, 4438–4442.
150. Yuan, C. Z.; Yang, L.; Hou, L. R.; Li, J. Y.; Sun, Y. X.; Zhang, X. G.; Shen, L. F.; Lu, X. J.; Xiong, S. L.; Lou, X. W. *Adv. Funct. Mater.* **2012**, *22*, 2560–2566.

Chapter 6

Low Temperature Preparation Routes of Nanoporous Semi-Conducting Films for Flexible Dye-Sensitized Solar Cells

Tamez Uddin, Yohann Nicolas, Céline Olivier, and Thierry Toupance*

Université de Bordeaux 1, Institut des Sciences Moléculaires, Groupe C2M,
UMR 5255 CNRS, 351 Cours de la Libération, F-33405 Talence Cedex,
France

*E-mail: t.toupance@ism.u-bordeaux1.fr

Various methods for the low temperature processing of mesoporous nanocrystalline metal oxide semiconductor (TiO₂, ZnO and SnO₂) have been reviewed. These routes mainly associate a deposition technique (“spin-coating”, “doctor-blading”, “dip-coating”, electrophoretic deposition, screen-printing) of metal oxide layers with a suitable low-temperature post-treatment (drying, compression, hydrothermal, microwave, UV, Chemical vapor deposition...) to yield adherent metal oxide films on plastics. After sensitization with a ruthenium dye, these films lead to rather good efficiencies in dye-sensitized solar cells (DSCs). The efficiencies of the corresponding DSCs are then discussed on the basis of the texture, the structure and the crystallinity of the metal oxide photoanodes obtained. So far, the compression method applied to anatase TiO₂ photoelectrodes gave the highest efficiencies, i.e. 6 to 7.4%, which is yet far away from the efficiency of classical high temperature sintered layers. Further advances are expected from the combination of a suitable deposition method (as screen-printing) with several post-treatments (compression, UV...) at low-temperature, the UV-processing being known to enhance both FF and VOC.

1. Introduction

The dependence on oil and electricity has made energy a vital component of our everyday needs. In the 20th century, the population quadrupled and our energy demand went up 16 times. About 15 terawatts (TW) of energy is currently needed to sustain the lifestyle of 7 billion people worldwide (1). By year 2050, we will need an additional 10 TW of clean energy to maintain the current lifestyle. The exponential energy demand is exhausting our fossil fuel supply at an alarming rate. Another important consideration of increasing the energy production based on fossil fuels is its impact on the environment. Global warming from the fossil fuel greenhouse gases which contributes to the climate changes is becoming a major concern. In order to meet the increasing energy demand in the near future, we will be forced to seek environmentally clean alternative renewable energy resources. There is a wide variety of renewable energy sources: solar, wind, geothermal, biomass and hydro. Among these renewable energy sources, solar cell is a promising energy conversion system that can directly convert solar energy into electricity (2). However, the present cost of electricity from standard silicon-based photovoltaic cells is much higher than the current commercial prices of electricity generated by hydraulic power and nuclear and fossil fuels. Therefore, it is desirable to develop highly efficient solar cells with a low production cost. Organic solar cells have the potential for fulfilling these requirements. Moreover, they show considerable advantages over inorganic solar cells in terms of flexibility, lightness, and colorfulness. In this context, dye-sensitized solar cells (DSCs) have been investigated extensively as potential alternatives to traditional photovoltaic devices because of their high conversion efficiency and low cost (3). Conversion efficiencies reaching 11-13% have been reported for these solar cells which can compete with those reported by amorphous silicon solar cells (4-9). The operating principle of a typical dye sensitized solar cell is illustrated in Figure 1. In DSCs, sunlight is harvested by a sensitizer (dye) that is attached to the surface of nanocrystalline and mesoporous network of a wide band gap semiconductor (usually titanium dioxide, i.e. TiO_2 , for the most efficient system). The dye-coated semiconductors are supported on transparent conducting oxide (TCO) glass electrode, through which the cell is illuminated. The pores of the nanocrystalline TiO_2 film are filled with a liquid electrolyte which acts as an electron donor (10). When a DSC is illuminated by sunlight, the dye molecules adsorbed on the surface of the semiconductor absorb light and become excited. The photo-excitation of dye molecules results in the injection of electrons from the excited state of the dye to the conduction band of the semiconductor. The electron passes through the TiO_2 semiconductor and is taken out into the external circuit by the transparent conducting oxide (TCO) glass electrode (3, 4). The dye is regenerated by the electron donor present in the liquid electrolyte, which is usually the iodide/triiodide couple dissolved in a non-volatile solvent as acetonitrile or an ionic liquid. At the counter electrode, the oxidized donor is reduced by metallic platinum under uptake of electrons from the external circuit. More recently, the redox electrolyte has been replaced by an organic hole transporter to furnish solid state DSCs showing energy conversion efficiencies up to 7% (11). The porous nanocrystalline TiO_2

photoelectrode films are traditionally prepared by depositing a suspension or paste containing TiO_2 nanoparticles of desired size and organic additives onto a substrate by doctor-blading or by spin-coating (12). The organic additives are essential to suppress agglomeration of the particles and to reduce stress during sintering, in order to obtain crack-free and well-adherent films with the optimal mesoporous structure. The organic additives are removed by sintering the bladed or spin-coated nanocrystalline TiO_2 electrodes at high temperature (450 °C). The sintering also promotes chemical interconnection between the particles to establish an electrically connected network. The use of plastic substrates restricts the choice of the TiO_2 suspension media and additives to those volatile at temperatures below the upper limit of the substrate material, which is about 150 °C for the commonly used polyethylene terephthalate (PET). Modern portable electronic devices, i.e. mobile phones, laptops, pocket calculators or watches, require the development of renewable power sources, such as solar cells, on lightweight flexible substrates such as plastic. Flexible substrates are also a prerequisite for roll-to-roll production techniques that are considered promising for cost-effective mass production of thin film solar cells. The use of flexible substrates also opens to design the prototypes in different shapes to be applied at different surfaces. The transparent conductive flexible films are obtained by coating indium-tin-oxide (ITO) on plastic supports such as polyethylene terephthalate (PET) film. The glass transition temperature (T_g) of PET is 75 °C and surface electric resistance of ITO–PET is regarded only sustainable at temperatures below 150 °C. Therefore, the use of such plastic substrates requires that all processes needed for the fabrication of DSC, including the formation of TiO_2 nanocrystalline films, to be designed at temperatures lower than 150°C.

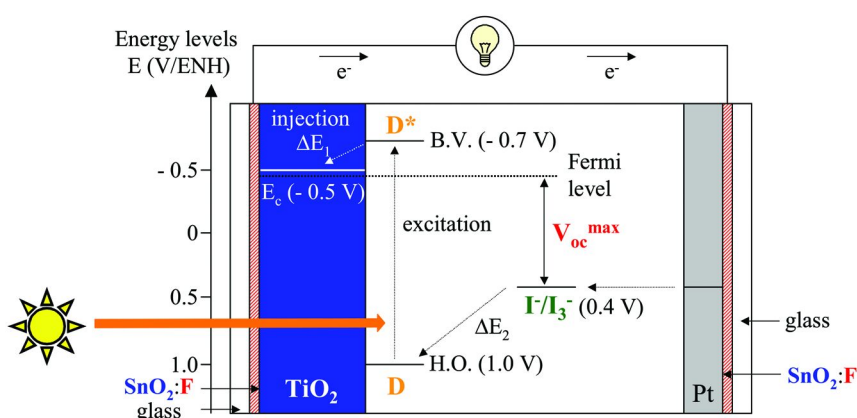
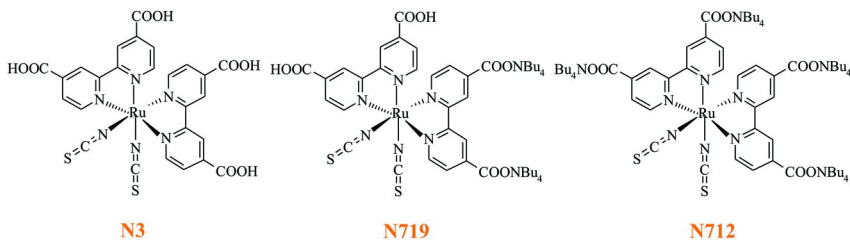


Figure 1. Schematic representation of a DSC based on a nanoporous TiO_2 layer sensitized with a Ru-complex dye in contact with a iodine-iodide redox mediator that illustrates its operating principle.

Many efforts, however, have already been made to investigate the preparation of mesoporous TiO_2 film at low temperature on glass or flexible polymer substrates for DSC cell. The mesoporous TiO_2 thin films prepared at low temperature should have high surface area for dye adsorption and a high degree of crystallinity for fast transport of electrons. The incomplete necking of the particles and the presence of residual organic in the film prepared at low temperature causes lower electron diffusion coefficients and electron lifetimes. Therefore, enhancing the electron transport rate and electron lifetime is compulsory for low-temperature fabrication processes. Several deposition methods of preparation of mesoporous TiO_2 films have been reported in the literature. Among them, the mostly used methods include spin coating, doctor blading, electrophoretical, deposition, chemical vapor deposition, screen printing and spraying. Methods developed for the post treatment of the nanocrystalline TiO_2 films include low temperature sintering (13–31), mechanical compression (32–45), hydrothermal necking (46–49), microwave irradiation (50, 51), UV light assisted chemical vapor deposition (52–54), UV light irradiation (17, 55–57), and spraying (58–60).

Other cheap and wide band gap semiconductor materials for photoanodes of DSC are zinc oxide (ZnO), tin dioxide (SnO_2), and niobium oxide (Nb_2O_5). Specifically, zinc oxide has received much attention due to its similar band-gap to that of TiO_2 (61). ZnO nanoparticle based DSCs have shown the second highest efficiencies after TiO_2 . Moreover, ZnO , as an n-type semiconductor, has many unique properties, such as transparency in the visible and high infrared reflectivity, acoustic characteristics, high electrochemical stability and excellent electronic properties. Both TiO_2 and ZnO exhibit a similar electron injection process from excited dyes in DSCs (62). A lot of works have already reported in the literature of using the ZnO thin film for DSCs (63–73). In most of the works, the ZnO film after deposition on substrate is annealed at high temperature (74, 75). Very few researchers have reported the preparation of ZnO film for DSCs at low temperature (76–80). Another alternative to TiO_2 for photoelectrode of DSCs is SnO_2 that is a high band gap ($E_g = 3.6$ eV) semiconductor and has a conduction band potential more positive than TiO_2 . As the conduction band potential of SnO_2 is approximately 0.5V more positive than that of TiO_2 , SnO_2 is a better electron acceptor than that of TiO_2 (81).

In the present contribution, various methods for the low temperature preparation of mesoporous nanocrystalline metal oxide semiconductor films (particularly, TiO_2 , ZnO and SnO_2) are reviewed. Specific emphasis will be given to use these low temperature processed semiconductors film as photoanodes for DSCs. The photon-to-current conversion efficiencies of the DSCs built from these photoanodes, sensitized with various ruthenium dyes (Scheme 1), will also be investigated and compared. Before going to detail, different deposition methods of metal oxide semiconductors on the glass or plastic substrates will be described briefly. Then, different post-treatment method for necking reported in the literature will be discussed.



Scheme 1. Chemical formula of the different dyes employed to sensitize the low-temperature processed semiconducting metal oxide photoanodes.

2. Theory of Photovoltaic Device Characterization

In order to investigate the PV performance of a cell, as well as its electric behavior, the current-voltage (I-V) characteristics in the dark and under white light illumination of different intensities are considered. The I-V curve of an illuminated PV cell has the shape shown in Figure 2 as the voltage across the measuring load is swept from zero to V_{OC} , and different performance parameters for the cell can be determined from this data, as described in the sections below. Analysis of the photocurrent-voltage curves includes the determination of the following parameters.

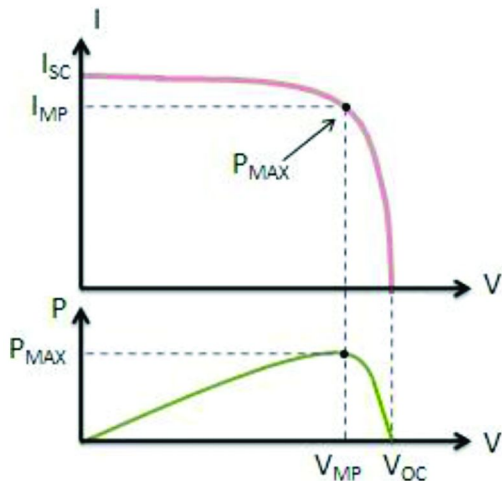


Figure 2. Illuminated I-V sweep curve of PV cells explaining maximum power and fill factor.

2.1. Short-Circuit Current (I_{SC})

The maximum current that can run through the cell at zero applied voltage is called the short-circuit current, I_{SC} . I_{SC} occurs at the beginning of the forward-bias sweep and is the maximum current value in the power quadrant. For an ideal cell, this maximum current value is the total current produced in the solar cell by photon excitation.

2.2. The Open-Circuit Voltage (V_{OC})

The open-circuit voltage, V_{OC} , is the maximum photovoltage that can be generated in the cell and corresponds to the voltage where current under illumination is zero.

2.3. Maximum Power (P_{max})

The maximum of the obtained electrical power P_{max} is located in the fourth quadrant where the product of current density J and voltage V reached its maximum value. At the I_{SC} and V_{OC} points, the power will be zero and the maximum value for power will occur between the two. The voltage and current at this maximum power point are denoted as V_{MP} and I_{MP} respectively. The maximum power corresponds visually to the area of the largest rectangle, which can fit inside the current voltage curve as shown in Figure 2.

2.4. Fill Factor (FF)

Fill factor is defined as the ratio of the maximum power to the theoretical power (PT) that would be output at both the open circuit voltage and short circuit current together. FF can also be interpreted graphically as the ratio of the rectangular areas depicted in Figure 2.

$$FF = \frac{I_{MP} \cdot V_{MP}}{I_{SC} \cdot V_{OC}} \quad (1)$$

This parameter indicates the deflection of the current-voltage characteristic from a square like curve and is therefore dependent on series and shunt resistance. A larger fill factor is desirable, and corresponds to an I - V sweep that is more square-like. To obtain high fill factors series resistance has to be as small as possible, while and shunt resistance needs to be as high as possible.

2.5. Efficiency (η)

The efficiency is defined as the ratio of maximum electric power output to the radiation power incident on the solar cell surface.

$$\eta = \frac{P_{Max}}{P_{in}} = \frac{I_{MP} \cdot V_{MP}}{P_{in}} = \frac{I_{SC} \cdot V_{OC} \cdot FF}{P_{in}} \quad (2)$$

P_{in} is taken as the product of the irradiance of the incident light, measured in $\text{W} \cdot \text{m}^{-2}$ or in suns (1000 $\text{W} \cdot \text{m}^{-2}$), with the surface area of the solar cell (m^2).

The efficiency of photovoltaic cells are measured under a set of standard test condition, at temperature of 25°C, the solar radiation incident on the cell should have a total power density of 1000 $\text{W} \cdot \text{m}^{-2}$, with a spectral power distribution characterized as AM 1.5G.

3. Deposition Techniques

The role of porous TiO_2 film is crucial and the overall energy conversion efficiency of the cells strongly depends on the surface and electronic properties of the electrode with thickness varying from several hundred nanometers up to 8–10 μm . Many efforts have been undertaken in order to deposit TiO_2 on the substrates. Generally, a doctor-blade technique is used to fabricate such porous TiO_2 film by coating TiO_2 paste onto a conductive glass or plastic substrates. Other deposition techniques currently used for DSCs are spin coating, dip coating, electrophoretic deposition, screen printing, chemical vapor deposition and spraying. In this section, mostly used techniques will be described briefly.

3.1. Spin Coating

Spin coating has been used for several decades for thin film processing. A typical spin coating process, as shown in Figure 3, involves depositing a small volume of a suspension containing TiO_2 nanoparticles and a binder onto the center of a substrate and then spinning the substrate at high speed (typically > 1000 rpm). The centripetal force during the rotation will cause the liquid to spread to the edge of the substrate leaving a thin layer of liquid. After evaporation or solidification occurs on the surface, this liquid layer becomes a thin film. Final film thickness depends on the nature of the liquid such as the viscosity, drying rate, percent solids, surface tension, and so on, and the spinning parameters. By this way, rather regular and homogenous films are obtained but the film thickness is limited to 1–3 μm . Some of the researchers have used spin coating method for the low temperature preparation of TiO_2 photoelectrode for DSCs (13, 18, 26).

3.2. Doctor Blading

The most used TiO_2 film forming technique for DSCs is doctor blading. The special feature of the doctor blade is that it produces a very uniform thickness. A typical doctor blade assembly is shown in Figure 4 (82). In general, the working principle of this technique is to place a sharp blade at a fixed distance from the substrate surface that is to be coated. The coating solution (slurry) containing a TiO_2 together with a complex mixture of solvents and binders is then placed in front of the blade that is then moved linearly across the substrate leaving a thin

wet film after the blade. The thickness of the deposited layer is determined by the height of the doctor blade. The final wet thickness of the film on the surface energy of the substrate, the surface tension of the coating solution and the viscosity of the coating solution. The suspensions are prepared by adding TiO_2 powder to water or spectrograde ethanol. The ethanol is mostly used as suspending agent because of its low surface tension resulted in a smooth film deposition. The TiO_2 powder usually used is anatase TiO_2 . The suspension is then stirred with a magnetic stirrer for a period of time before deposition on the substrates. Many works have already been reported in the literature for the deposition of TiO_2 using doctor blading technique (15, 19, 21, 23, 25–28, 32–36, 41–45). The main drawbacks of this process are that it is a relatively slow process and sometimes dissolved materials have high tendency to aggregate or crystallize at high concentration during doctor blading.

3.3. Electrophoretic Deposition (EPD)

Electrophoresis is the movement of charged particles through a liquid under the influence of an external electric field. EPD represents a material processing technique in which charged particles in a suspension including an electrolyte, particles, additives and solvent are moved toward an oppositely charged electrode and are then deposited onto a substrate under an applied DC electric field. EPD is, therefore, a combination of electrophoresis and deposition (Figure 5). The substrate forms one of the electrodes in an electrochemical cell. Successful EPD requires the development of stable suspensions composed of electrostatically charged particles suspended in a suitable solvent where specific mechanisms active keeping the particle from flocculating or agglomerating. The particles that will form the coating are suspended in a liquid, which produces a surface charge on the particles by selective adsorption of ions (for example, proton) from the solvent. When this charged particle is placed in an electric field it experiences a force, this force accelerates the particle toward the oppositely charged electrode. Some photoelectrodes of TiO_2 have been prepared by using EPD method (39, 49, 52–54).

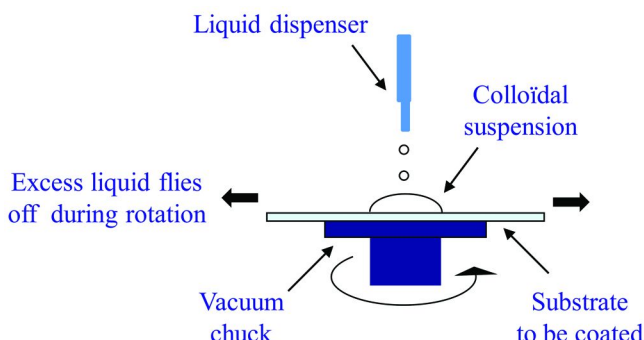


Figure 3. A schematic representation of the spin-coating process

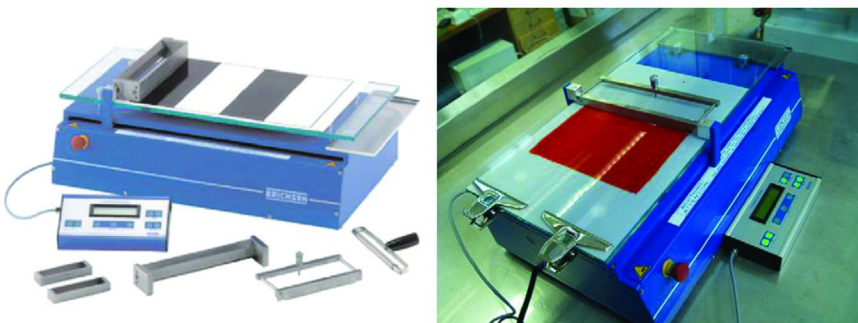


Figure 4. A picture of the Erichsen Coatmaster 509 MC-I that can be used for doctor blading (left) and a photograph showing doctor blading of MEHPPV (right). (Reproduced with permission from reference (82). Copyright 2009 Elsevier)

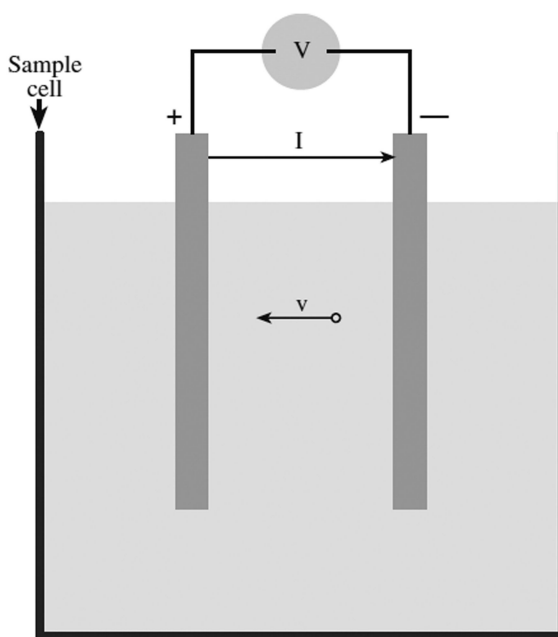


Figure 5. Schematic diagram of a particle electrophoresis cell.

3.4. Dip Coating

The TiO_2 film for DSCs photoelectrode can be produced without further treatment by dip coating. This is an easy method for producing surfactant-free films of nanocrystalline TiO_2 at room temperature with excellent mechanical

stability when deposited on glass or plastic substrates for DSCs (Figure 6). The starting material usually consists of metal alkoxides, but solutions of metal salts, such as nitrates, may be used instead. The substrate, or object to be coated, is lowered into the solution and withdrawn at specified rates (between 10 and 30 $\text{cm} \cdot \text{min}^{-1}$). It is necessary that the solution wets and spreads over the surface of the substrate and so the contact angle must be low. According to this procedure, for the deposition of TiO_2 nanoparticles, a small amount of titanium isopropoxide (TTIP) is added to an alcoholic dispersion of commercially available P25- TiO_2 powder. The hydrolysis of the alkoxide after its addition helps to the chemical connection between titania particles and their stable adhesion on plastic or glass substrate without sacrificing the desired electrical and mechanical properties of the film.

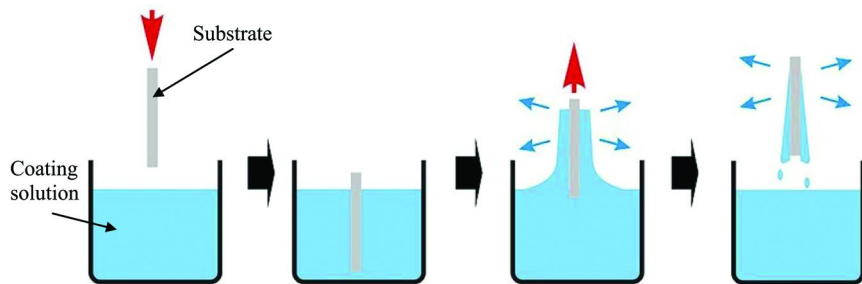


Figure 6. Schematic representation of a simple dip coating process.

3.5. Screen Printing

Screen printing is a reliable and cost-effective method that can be used to print on a wide size variety of substrates (Figure 7) (83). This technique consists of three elements, as shown in Figure 7: the screen, which is the image carrier, the squeegee and the TiO_2 paste. The screen uses a porous mesh, made of porous fabric or stainless steel stretched tightly over a frame made of metal. Proper tension is essential to accurate printing. A stencil that defines the image to be printed is photochemically produced on the screen. The titanium dioxide paste is placed on top of the screen. The paste is then forced through the fine mesh openings using a squeegee that is drawn across the screen, applying pressure and thereby forcing the paste through the open areas of the screen. The paste will pass through, only in areas where no stencil is applied, thus forming an image on the printing substrate. On the aspect of screen-printing film, many conditions, such as paste composition, particle size, mesh-opening and tension of screen, squeegee angle, pressure and printing speed, film layer and distance between screen and substrate, will affect the printing quality of the porous TiO_2 films.

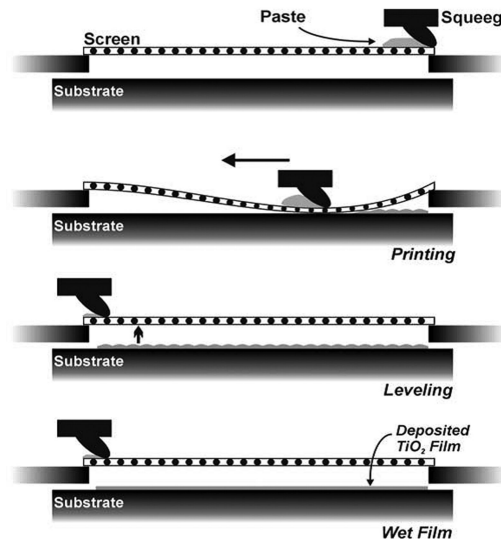


Figure 7. Schematic representation of the screen-printing process. (Reproduced with permission from reference (83). Copyright 2005 Elsevier)

4. Post Treatment Methods

4.1. Low Temperature Sintering

A first method to process nanocrystalline oxide electrodes for DSSCs on plastic substrate is the low temperature sintering. Low temperature sintering may be defined as the sintering of TiO_2 film at a temperature below 150 °C. Although, low-temperature sintering is a challenging route due to the lower performance of the electrode than that of the electrodes prepared via a high-temperature route, a lot of researchers have investigated the performance of photoelectrode prepared at low temperature. The efficiencies of the photoelectrodes sintered/dried at low temperature reported in the literature are shown in Table 1. As there are many studies, only three articles describing the best efficiencies will be commented in this section. From Table 1, it is obvious that the highest efficiency, 5.8% was obtained by Kijitora *et. al.* (21). A mesoporous binder free TiO_2 film was prepared by using doctor blading technique on the Indium-tin-oxide (ITO)-coated polyethylene naphthalate (PEN) followed by drying at 110–125 °C. The binder-free TiO_2 paste was produced by dispersing the TiO_2 nanoparticles of various average sizes of 30–150 nm in a mixed solvent of water and *t*-butanol where large TiO_2 particles were used to enhance the light harvesting by scattering and *t*-butanol reduced the surface tension of the liquid paste to improve its adhesion to the hydrophobic ITO-PEN surface. Depending on the dye nature and the electrolyte composition, the energy conversion efficiency varies from 4.6 to 5.8%. The best results were obtained with N712 dye and an electrolyte containing the composition of electrolyte was 0.4M LiI, 0.4M tetrabutylammonium iodide (TBAI), 0.04M, *tert*-butylpyridine (TBP) in a solvent of 3-methoxypropionitrile

(MPN). Lee *et. al* (24) have studied the efficiency of the photoelectrode made of TiO_2 nanoparticles mixed with acid treated multi-walled carbon nanotubes (MWCNTs) deposited on FTO glass electrode sintered at 150 °C. The result showed that cell conversion efficiency based on bare TiO_2 film was 4.15 % where as the efficiency of the cell with the TiO_2 electrode containing 0.1wt% of MWCNT was 5.02%. The J_{sc} of the TiO_2 electrode containing 0.1wt% of MWCNT increased from 7.96 to 9.08 mA.cm^{-2} compared to the as prepared TiO_2 electrode due the enhancement of the collection and transport of electrons.

The addition of MWCNT also increased the fill factor from 0.68 to 0.71, due to the increase in the conductivity of the TiO_2 electrode. The effect of the Li^+ free electrolyte on the efficiency based on TiO_2 electrode containing 0.1wt% of MWCNT was studied and result showed that using electrolyte containing triethylamine hydroiodide (THI) increased the efficiency from 5.02% to 5.15% compared to the electrolyte containing LiI. In another experiment, the power conversion efficiency of a binder free TiO_2 films based on nanocrystalline P-25 TiO_2 slurries developed using ball milling was studied (26). TiO_2 slurries developed by ball milling were deposited on ITO-PEN substrate by the doctor blading or spin coating techniques followed by heating at 150 °C. The result showed the conversion efficiency of 4.2% for the cell prepared using the TiO_2 slurry milled for 20 h which showed 30% increment compared to the 3.2% efficiency reported for the non-milled electrodes. This increase in power conversion efficiency was due to deagglomeration by milling and the subsequent increase of surface area leading to higher dye adsorption onto the titania film.

4.2. Compression Method

Compression method for the preparation of nanostructured TiO_2 films at room temperature involves the compression of a TiO_2 powder film at pressures ranging from 100 to 2000 kg.cm^{-2} . The resulting films are porous and mechanically stable, even without heat treatment. Recently, a lot of studies for the preparation of nanostructured TiO_2 films by compression on conducting plastic and glass substrates for use in dye-sensitized solar cells have been reported in the literature. Homogeneous and crack-free nanoparticulate TiO_2 films were thus obtained as depicted in Figure 8. Table 2 shows the efficiency and other parameters of the TiO_2 photoelectrodes prepared by the compression method.

A 6% efficiency of a plastic substrate DSC using the compression method for the preparation of TiO_2 photoelectrodes was obtained by Yamaguchi *et al.* (43). The photoelectrode was prepared by applying the TiO_2 paste composed of a mixture of TiO_2 powder and ethanol at a concentration of 20 wt% onto ITO-PEN film by doctor blading followed by compression at a pressure of 100 MPa. It was shown that the efficiency (6%) of the photoelectrode prepared by only compression was higher than that (5.3–5.6%) of the photoelectrode prepared by compression method followed by heat treatment. This was because the adhesive force between the TiO_2 nanoparticles and the conducting plastic substrate was decreased by heat treatment. The author also reported that the TiO_2 paste using water solvent was better than that using organic solvent for making a plastic substrate DSC. The performance of the solar cell with photoelectrode prepared from TiO_2 -water paste

was $\eta = 7.1\%$, $J_{SC} = 12.4 \text{ mA.cm}^{-2}$, $V_{OC} = 0.75 \text{ V}$ and $FF = 0.76$ where as that of the solar cell prepared from the TiO_2 paste using ethanol solvent was $\eta = 6.5\%$, $J_{SC} = 11.6 \text{ mA.cm}^{-2}$, $V_{OC} = 0.76 \text{ V}$ and $FF = 0.73$. This attributed the influence of the organic solvent in the TiO_2 paste to the stability of the conducting plastic substrate. UV-O_3 treatment of the ITO-PEN film before TiO_2 paste application also improved the cell efficiency to 7.4%.

In another experiment, Boschloo *et al.* (34) prepared nanostructured TiO_2 films by depositing onto flexible conducting plastic substrates (ITO-PET) using a compression technique. TiO_2 suspension in ethanol was applied onto the substrate by doctor blading using scotch tape as frame and spacer. After evaporation of the ethanol, the substrate with the attached powder film was put between two planar steel press plates and a pressure of 1500 kg.cm^{-2} was applied by using a hydraulic press. The result showed the overall efficiency up to 5.5% under 10 mW.cm^{-2} solar illumination. Preparation of nanocrystalline porous titanium dioxide (TiO_2) films with roll-to-roll compatible methods was studied by Nokki *et al.* (41). Titanium dioxide (TiO_2) paste was spread onto ITO-coated polyethylene terephthalate (PET) by doctor blading followed by drying in air for few minutes. Then the nanoparticulate TiO_2 film was pressed using two pressure methods: (1) applying static pressure of 10 kN.cm^{-2} and (2) calendering at a linear load of 300 kN.m^{-1} , a speed of 10 m/min and a temperature of $30 \text{ }^\circ\text{C}$. The DSC with doctor-bladed and calendered TiO_2 film exhibited efficiency as high as 4.7%. On the other hand the efficiency of the DSC based on statically pressed TiO_2 film was 5.1%. The author also used gravure printing to spread TiO_2 paste on the substrate followed by calendering to compress the film but the efficiency of cells with gravure printed TiO_2 film only reached 1.7%.

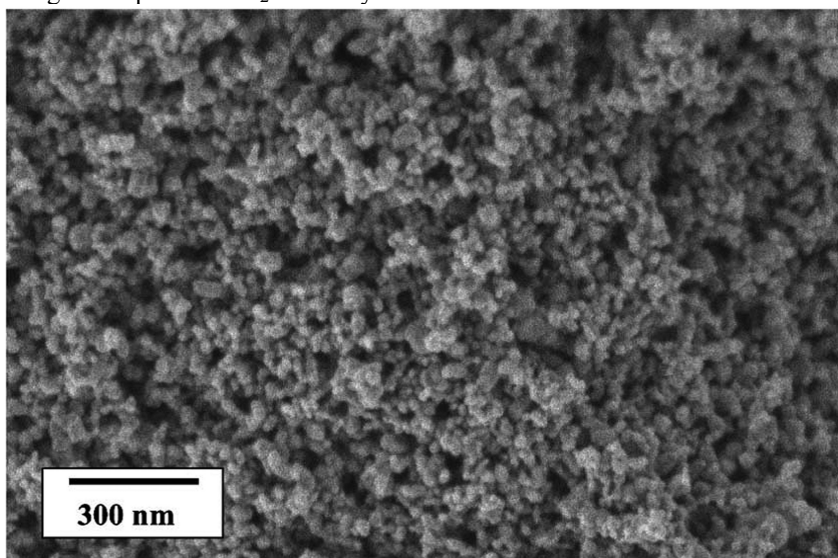


Figure 8. SEM image of a nanoparticulate TiO_2 porous film processed by compression. (Reproduced with permission from reference (33). Copyright 2002 Elsevier)

Table 1. Efficiency (η), short-circuit current density (J_{SC}), open circuit voltage (V_{OC}), fill factor (FF), sintering/drying temperature of photoelectrode sintered at low temperature.

Substrate	Deposition method	Sintering temperature (°C)	Power intensity (mWcm ⁻²)	J_{SC} (mA.cm ⁻²)	V_{OC} (V)	FF	Efficiency η (%)	Reference
FTO-glass	Spin coating	100	100	2.05	0.64	0.69	1.22	(13)
ITO-PET	Doctor blading	140	100	0.19	0.83	0.56	0.09	(15)
ITO-PET	Spreading by glass rod	130	100	0.40	0.72	0.42	0.12	(16)
ITO-PET	Spreading by glass rod	140	100	0.54	—	—	0.23	(17)
ITO-glass	Spin-coating	150	100	9.79	0.75	0.52	3.69	(18)
FTO-glass	Immersion at 60 °C	RT	46–59	1.1 – 1.4	0.63	0.53	0.92	(19)
FTO-glass	Doctor blading	100	46–59	6.3	0.63	0.65	4.40	(19)
ITO-PEN	Doctor blading	110–125	100	12.0	0.75	0.65	5.80	(21)
FTO-glass	Spreading by glass rod	150	100	8.81			4.20	(22)
ITO-PEN	Doctor blading	150	100	7.5	0.69	0.59	3.05	(23)
ITO-glass	Doctor blading	150	100	9.1	0.71	0.64	4.10	(23)
FTO-glass	Spreading by glass rod	150	100	9.96	0.76	0.68	5.15	(24)
ITO-PEN	Doctor blading	150	100	6.7	0.78	0.62	3.70	(25)

<i>Substrate</i>	<i>Deposition method</i>	<i>Sintering temperature (°C)</i>	<i>Power intensity (mWcm⁻²)</i>	<i>J_{SC} (mA.cm⁻²)</i>	<i>V_{OC} (V)</i>	<i>FF</i>	<i>Efficiency η (%)</i>	<i>Reference</i>
ITO-PEN	Doctor blading/ spin coating	150	100	9.7	0.64	0.63	4.20	(26)
FTO-glass	Doctor blading	150	—	8.77	0.70	0.67	4.18	(27)
ITO-PEN	Doctor blading	150	100	10.84	0.63	0.49	3.30	(28)
ITO-PET	Dip coating	100	100	6.95	0.75	0.6	3.20	(30)

Table 2. Efficiency (η), short-circuit current density (J_{SC}), open circuit voltage (V_{OC}), fill factor (FF) of TiO_2 photoelectrodes prepared by the compression method.

Substrate	Deposition method	Pressure (kg.cm^{-2})	Power intensity (mW.cm^{-2})	J_{SC} (mA.cm^{-2})	V_{OC} (V)	FF	Efficiency η (%)	Reference
ITO-PET	Doctor blading	100	10	0.91	0.67	0.66	4.0	(32)
ITO-PET	Doctor blading	1000	10	1.10	0.65	0.68	4.9	(33)
FTO-glass	Doctor blading	1000	100	8.6	0.73	0.47	3.0	(33)
ITO-PET	Doctor blading	1500	10	1.40	0.63	0.64	5.5	(34)
FTO-glass	Doctor blading	2000	10	1.00	0.66	0.67	4.5	(35)
ITO-PET	Doctor blading	700	100	6.10	0.80	0.53	2.5	(36)
ITO-PET	EPD	204	100	3.84	0.76	0.56	1.7	(39)
ITO-PET	Spraying	1530	100	7.10	0.74	0.53	2.8	(40)
ITO-PET	Doctor blading	1020	10	1.24	0.68	0.60	5.1	(41)
ITO-PEN	Doctor blading	1020	100	13.4	0.75	0.74	7.4	(43)
ITO-PET	Doctor blading	700	10	1.30	0.68	0.60	5.3	(45)

4.3. Hydrothermal Necking

The term *hydrothermal* can be defined as any homogeneous or heterogeneous chemical reaction in the presence of a solvent (whether aqueous or non-aqueous) above the room temperature and at pressure greater than 1 atm in a closed system. The basic principle used in the hydrothermal synthesis of nanoparticles is that the solute raw material or the precursor material along with the appropriate solvent are taken in an autoclave which is maintained at a high temperature either below or above the critical temperature of the solvent over a period of time, which allows the solute to dissolve and recrystallize to the desired product. For the preparation of TiO_2 film for DSC, titanium monomers such as $TiCl_4$, $TiOSO_4$, and $Ti(IV)$ -tetraisopropoxide (TTIP) are mixed with nanocrystalline TiO_2 powder. Upon hydrolysis by hot steam, the above mentioned precursors are crystallized into TiO_2 which acts as “interconnects” of the TiO_2 particles as well as that between the film and the substrate (Figure 9) (47). Very few studies have been performed for the preparation of TiO_2 photoelectrode for DSCs by hydrothermal process. Zhang *et al.* (46) prepared porous nanocrystalline TiO_2 thick film for DSCs by hydrothermal crystallization. The film was produced by spreading a paste of pure $TiCl_4$ and TiO_2 on an F-doped SnO_2 -coated conductive glass by a glass rod followed by hydrothermal treatment in an autoclave and drying at 100 °C for 12 h. The result showed that under white light illumination (100 $mW.cm^{-2}$), the film prepared by hydrothermal process and sensitized with the N3 dye exhibited I_{SC} , V_{OC} , FF and η of 16 $mA.cm^{-2}$, 0.73 V, 0.54 and 6.23%, respectively whereas the film prepared by low temperature sintering gave I_{SC} , V_{OC} , FF and η of 13.1 $mA.cm^{-2}$, 0.65 V, 0.52 and 4.4%, respectively. The TiO_2 film prepared by hydrothermal method improved the cell efficiency by almost 50%.

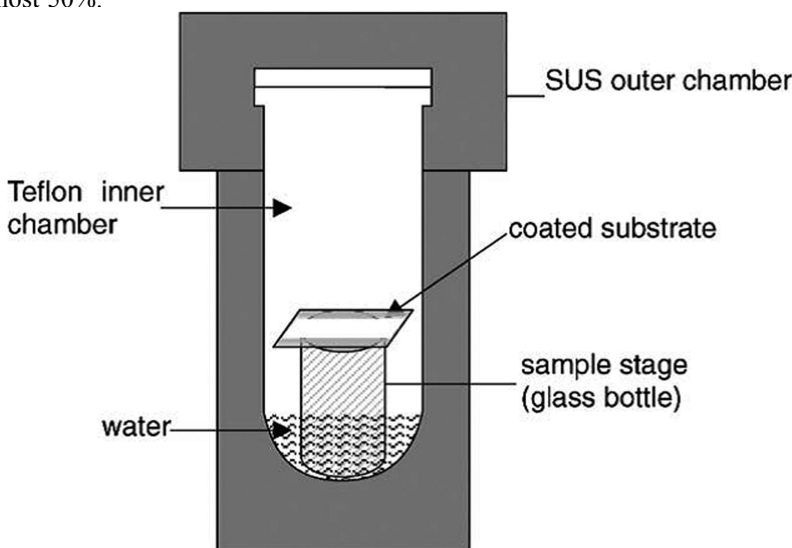


Figure 9. Experimental set-up for hydrothermal treatment of the films.
(Reproduced with permission from reference (47). Copyright 2004 Elsevier)

In another report, Zhang *et al.* (47) studied the preparation of porous nano-crystalline TiO_2 film on indium tin oxide (ITO)-coated poly (ethylene terephthalate) (PET) for flexible solar cells by hydrothermal process. The same preparation method described elsewhere (43) was applied. But, Ti(IV) -tetraisopropoxide (TTIP) precursor was used instead of TiCl_4 and TiOSO_4 for ITO-PET film as these acidic precursors damage the ITO layer. The overall energy conversion efficiency of the cell made by this film was 2.5 % under illumination with AM 1.5 simulated sunlight (100 mW.cm^{-2}). The value of I_{SC} , V_{OC} , FF were 6.1 mA.cm^{-2} , 0.7 V, and 0.61, respectively. On the other hand, the film prepared on the FTO conducting glass exhibited the efficiency of 4.2%. Tan *et al.* (49) investigated the TiO_2 thin film electrode prepared by electrophoretic deposition combined with common pressure hydrothermal treatment. Thin film of TiO_2 was deposited on FTO glass by electrophoretic deposition process followed by heat treatment in a non-sealed container full of water (common pressure hydrothermal process) or in an oven at 100°C for 4 h. The yielded conversion efficiency of the cell with TiO_2 thin film that underwent hydrothermal treatment after the electrophoretic deposition process was 6.12%. The higher light-to-electricity conversion efficiency was attributed to the improvement of particle connection and reduction of surface states due to hydrolysis of tetra-n-butyl titanate followed by crystallization of amorphous TiO_2 during hydrothermal treatment.

4.4. Microwave Irradiation Process

Microwave processing of inorganic compounds is an attractive field in modern material science. Various inorganic phases have been synthesized using microwave ovens operating at a frequency of 2.45GHz. This technique can be applied to the preparation of TiO_2 film for dye sensitized solar cell. So far, only two articles have been found in the literature on the preparation of TiO_2 photoelectrode for DSCs by microwave irradiation. Uchida *et al.* (50) studied the preparation of TiO_2 film deposited on FTO conducting glass by microwave operating at a frequency of 28GHz. Solar cell prepared with this exhibited photoelectron energy conversion efficiency of 5.51% which is almost equivalent to the efficiency (5.88%) of the cell with TiO_2 photoelectrode fabricated by conventional electric furnace heating at 480°C for 50 min. In another paper, Uchida *et al.* (51) reported the preparation of TiO_2 film by microwave on ITO-PET. The result showed that under condition of 100 mW.cm^{-2} , the cell prepared with the film exhibited I_{SC} , V_{OC} , FF , and h of 4.91 mA.cm^{-2} , 0.68 V, 0.64 and 2.16%, respectively.

4.5. UV-Assisted Chemical Vapor Deposition Method (CVD)

The formation of TiO_2 by chemical vapor deposition (CVD) is a well-established reaction. In this process the TiO_2 is formed by introducing

gaseous precursors between existing particles developing a necking structure that promotes interparticle electron conduction. UV irradiation, however, is regarded nothing to do with chemical necking as far as UV is solely employed. It can be understood that the some impurities of insulation adsorbed on TiO_2 surfaces were decomposed by UV irradiation and photocatalytic reaction of TiO_2 . Very few studies have been performed so far for the preparation of TiO_2 photoelectrode by CVD. Murakami *et al.* (52) studied the preparation of TiO_2 photoelectrode on indium-tin-oxide (ITO)-coated polyethylene terephthalate (PET) for DSCs by chemical vapor deposition combined with UV light irradiation. Binder-free TiO_2 nanoparticle layers were formed on the ITO-PET electrode by electrophoretic deposition method followed by CVD and/or UV light irradiation treatments. The CVD treatment was performed by exposure of the TiO_2 nanoparticle layer to gaseous $[(\text{CH}_3)_2\text{CHO}]_4\text{Ti}$ at 80 °C in a closed chamber for varied time of < 20 min. UV treatment was carried out independently or combined with the above CVD process as a post-CVD process by irradiating the TiO_2 layer with 254 nm light supplied by a 13W low-pressure mercury lamp at 110 °C. CVD/UV treated, dye-sensitized TiO_2 -ITO-PET film electrode exhibited conversion efficiency of 3.8% whereas CVD-treated cell showed an efficiency of 2.7% under incident power condition of 85 mW.cm^{-2} . The result also showed the values of J_{SC} , V_{OC} and FF of 7.0 mA.cm^{-2} , 0.75 V, and 0.61, respectively, for CVD/UV treated film. In another experiment, Murakami *et al.* (53) investigated the preparation of TiO_2 photoelectrode by CVD followed by UV treatment. The results were similar as that described elsewhere (52). Miyasaka *et al.* (54) investigated the performance of the DSC with the TiO_2 photoelectrode prepared by depositing TiO_2 on the electrode by electrophoretic deposition method combined with chemical vapor deposition of Ti-alkoxide followed by UV treatment. The F-doped SnO_2 transparent conductive glass or ITO-coated PET (polyethylene terephthalate) plastic film were used as substrates. The result showed that the conversion efficiency of the F/ SnO_2 glass-based photoelectrode post treated by CVD followed by UV radiation was 3.7% with J_{SC} , V_{OC} and FF of 7.7 mA.cm^{-2} , 0.74 V, and 0.65, respectively, which was more than half that of the photocell (6%) made by high-temperature sintering at 550 °C. The ITO-PET based solar cell therefore showed the lower performance.

4.6. UV Light Irradiation Method

Another alternative method for low temperature preparation of TiO_2 photoelectrode for DSCs is the irradiation of the TiO_2 film by UV radiation. Few efforts have already been devoted for the preparation of TiO_2 photoelectrode by simple UV irradiation. Some interesting results have been reported for thin TiO_2 films, i.e. 1 μm , used as active layer in flexible electrochromic devices (84). Nonetheless, the efficiency of the most cells fabricated from photoanodes prepared by UV irradiation is not appreciable as shown in Table 3.

Table 3. Efficiency (η), short-circuit current density (J_{SC}), open circuit voltage (V_{oc}), fill factor (FF) of TiO_2 photoelectrodes prepared by UV light irradiation method.

<i>Substrate</i>	<i>Deposition method</i>	<i>Power intensity (mWcm⁻²)</i>	<i>J_{SC} (mA cm⁻²)</i>	<i>V_{oc} (V)</i>	<i>FF</i>	<i>Efficiency η (%)</i>	<i>Reference</i>
ITO-PET	Spreading by glass rod	140	7.2	0.77	0.62	2.5	(55)
ITO-PET	Spreading by glass rod	100	4.42	0.64	0.65	1.84	(56)
ITO-PET	Spreading by glass rod	10	-	0.72	-	0.32	(17)
ITO-PET	Spreading by glass rod	100	-	-	-	0.23	(17)

Tebby *et al.* (55) studied the preparation of TiO_2 photoelectrode on ITO-PET by direct UV irradiation method without subsequent thermal treatment. The colloids containing TiO_2 nanoparticles were spread over the conductive substrates with a glass rod followed UV-irradiation treatment for 3 h (Figure 10). The result showed the overall efficiency of 2.5% under the illumination of 140 mW.cm^{-2} for a film thickness of $3.8 \mu\text{m}$. The fabrication of nanocrystalline TiO_2 electrodes using a UV laser sintering technique was also performed by Kim *et al* (56). The porous nc- TiO_2 electrodes were deposited onto ITO-PET from a colloidal TiO_2 paste using a laser direct-write (LDW) technique followed by drying the film at 100°C for about 12 h and then sintered by irradiating the film with UV radiation ($\lambda = 355 \text{ nm}$). The result showed that the overall conversion efficiency of the device based on the UV laser-sintered TiO_2 electrode was $\eta = 1.84\%$, which was more than a two-fold improvement from that of the device based on a non laser-sintered TiO_2 electrode ($\eta = 0.71\%$).

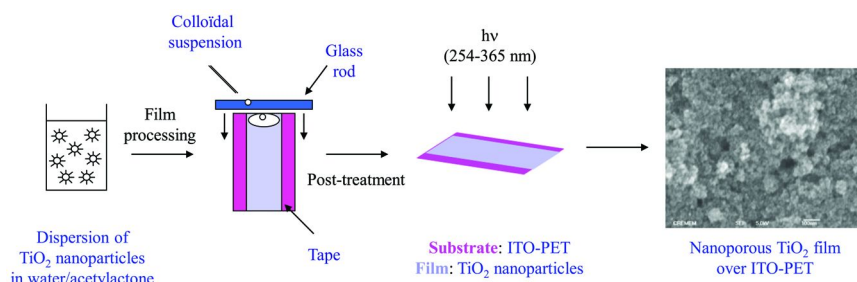


Figure 10. Schematic representation of the UV-treatment route towards flexible TiO_2 nanoparticulate films developed by Tebby *et al.* (55).

4.7. Spraying

A few studies have been found in the literature of preparing TiO_2 photoelectrode by spraying. In most of the articles, the spraying method followed other low temperature necking methods such as compression, low temperature sintering. Here two articles where vacuum cold spraying and only spraying without any post treatment are commented. Vacuum cold spraying (VCS) is an alternative way for low temperature preparation of TiO_2 photoelectrode on flexible plastic substrate. In VCS, dry TiO_2 powder is directly deposited on the substrate to form a uniform coating under a reduced-pressure atmosphere at room temperature (Figure 11) (85). TiO_2 coatings can also be deposited through solid particle impact of high velocity achieved by high pressure gas. The high dynamic pressure on impact makes it possible to form TiO_2 coatings with “good” mechanical stability and contact between particles even without any post-treatment. The VCS TiO_2 coatings can be deposited using nano- TiO_2 powder to a thickness from several micrometers to several tens of micrometers through controlling deposition parameters. Fan *et al.* (58) studied the porous nano- TiO_2

coating deposited by vacuum cold spraying (VCS) at room temperature on a FTO conducting glass substrate using commercial P25 nanocrystalline TiO_2 powder. The result showed that the overall conversion efficiency of the DSC assembled using this film was 2.4% which was comparable to that of the cells assembled using TiO_2 coatings prepared by other methods at low temperature. This result indicated that vacuum cold spraying was an effective low-temperature deposition method for nanocrystalline TiO_2 coating applied to DSC. A short-circuit current density of 7.3 mA.cm^{-2} and an open circuit voltage of 0.54 V were also obtained by the cell. Nanu *et al.* (59) studied the low-cost preparation of thin film $\text{TiO}_2|\text{CuInS}_2$ nanocomposite three-dimensional (3D) solar cells. A 100 nm thin film of anatase TiO_2 on FTO-glass was prepared by spray deposition followed by a nanocrystalline anatase TiO_2 coating using doctor blading resulting $2 \mu\text{m}$ thick film. The CuInS_2 was then deposited inside the porous nanocrystalline TiO_2 film by spraying. The results exhibited an open circuit voltage V_{OC} of 0.53 V , a short-circuit current I_{SC} of 17 mA.cm^{-2} and a fill factor FF of 0.55. The energy conversion efficiency of the cell was around 5%.

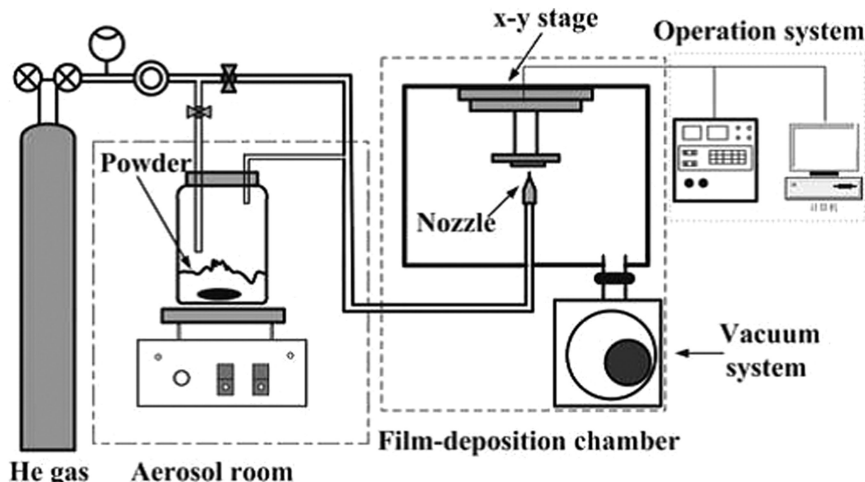


Figure 11. Schematic representation of the Vacuum Cold Spraying (VCS) system. (Reproduced with permission from reference (85). Copyright 2006 Springer)

5. Low Temperature Preparation of ZnO and SnO_2 Photoanodes for DSCs

It has already been mentioned in the introduction that the most of the researchers cited in the literature used the ZnO photoelectrodes for DSCs which were post treated by high temperature annealing that is not suitable for flexible plastic substrates. The performances of some of the DSCs cited in the literature with ZnO photoelectrode fabricated at low temperature are shown in Table 4.

Table 4. Efficiency (η), short-circuit current density (J_{SC}), open circuit voltage (V_{oc}), fill factor (FF) of ZnO photoelectrodes.

<i>Substrate</i>	<i>Deposition method</i>	<i>Drying conditions</i>	<i>Power intensity (mW.cm⁻²)</i>	<i>J_{SC} (mA.cm⁻²)</i>	<i>V_{oc} (V)</i>	<i>FF</i>	<i>Efficiency η (%)</i>	<i>Reference</i>
FTO-glass	Doctor blading	Drying in vacuum at RT	100	9.71	0.61	0.55	3.27	(76)
ITO-plastic	Doctor blading	-	20	0.49	0.72	0.69	1.21	(77)
ITO-PET	-	100°C	100	6.22	0.53	0.59	1.94	(78)
ITO-glass	Spin coating	Air drying	-	0.30	0.67	0.52	0.12	(79)
FTO-glass	Doctor blading	Air drying and compression	10	1.3	0.56	0.68	5.0	(80)

Here the performances of three cells with the highest performance will be illustrated briefly. Keis *et al.* (80) have described an efficient photoelectrochemical solar cell based on nanostructured ZnO electrodes. The electrode was prepared by spreading a suspension of ZnO on FTO coated glass by doctor blading followed by post treatment using compression with an applied pressure of 1000 kg.cm⁻². The overall conversion efficiency of the ZnO photoelectrode was 5% under the illumination of 10 mW.cm⁻². The results also exhibited fill factors of 0.68, V_{OC} of 0.56 V, I_{SC} of 1.3 mA.cm⁻². Chen *et al.* (76) also observed a new photoanode architecture based on ZnO nanotetrapods integrated to a DSC system. A paste of ZnO nanotetrapod was spread onto FTO-glass by doctor blading followed by drying in a vacuum oven at room temperature. The result exhibited an overall solar electric conversion efficiency of 3.27% under illumination of 100 mW.cm⁻². A short-circuit current density of 9.71 mA.cm⁻², open circuit voltage of 0.61 V and fill factor of 0.55 was also obtained by the cell with the ZnO photoelectrode. In another experiment, Dentani *et al.* (78) studied the conversion efficiency of flexible zinc oxide solar cells where ZnO was deposited on ITO-PET. The, maximum short-circuit photocurrent density (J_{SC}), open-circuit photovoltage (V_{OC}), fill factor (FF), and solar-light-to-electricity conversion efficiency (η) were observed to be 6.22 mA cm⁻², 0.53 V, 0.59, and 1.94%, respectively.

Finally, the low-temperature processing of SnO₂ photoanodes has been scarcely investigated (55, 86). The best results were reached by employing a connection of SnO₂ particles by simple UV-irradiation in air that led to homogeneous cassiterite SnO₂ porous films without any further thermal post-treatment. After dye-sensitization with the N3 dye, the 3.6 to 5 μ m thick SnO₂ films showed excellent photovoltaic responses with an energy conversion yield reaching 2.27% under AM1.5G illumination (100 mW.cm⁻²) with a J_{SC} of 10.5 mA cm⁻², a V_{OC} of 0.45 V, and a FF of 0.48. These performances outperformed those of similar layers annealed at 450°C mostly due to higher V_{OC} and FF . These findings were rationalized in terms of slower recombination rates for the UV-processed films on the basis of dark current analysis, photovoltage decay, and electrical impedance spectroscopy studies.

6. Concluding Remarks

Most of the studies dealing with the low-temperature processing of porous semi-conducting metal oxide electrodes for DSC's applications have concerned anatase TiO₂-based systems. In this case the TiO₂ film, which serves as support for dye molecules for light adsorption and electrons acceptor/transporter, requires a high-surface area, porosity, and good connections between TiO₂ nanoparticles. A high-surface area and porosity can allow a large quantity of dye to be chemisorbed, which favors the harvesting of a large quantity of photons. Moreover, good connections such as necking and chemical bonds between TiO₂ particles are necessary to ensure the fast electron transport through the TiO₂ film towards the front electrode. In this context, several studies have reported crack-free and

homogeneous porous TiO_2 photoanodes processed at low-temperature on flexible substrates as shown in Figure 12 (87).



Figure 12. Image of a TiO_2 -coated ITO-PEN substrate for flexible DSC. (Reproduced with permission from reference (87). Copyright 2007 The Electrochemical Society.)

However, according to the present review concerning the various low temperature preparation methods of TiO_2 photoelectrodes, it can be concluded that the energy conversion efficiency of the photoelectrode sintered at low temperature is lower than that of the electrode sintered at high temperature. This is due to the fact that low temperature treatment results in poor connections, which slow down the transport of photo-induced electrons in the film and give rise to much more electron recombination. Furthermore, the mechanical strength of the film treated at a low temperature is very poor. Another reason is the reduction of adhesion of the particles. Comparing the different low temperature preparation methods of the TiO_2 photoelectrode for DSCs, the DSCs fabricated with photoanodes prepared by the compression method lead to the better efficiencies. Thus, DSCs including photoelectrodes prepared by compression have yielded the best efficiency (7.4%) reported so far on plastic and showed a photocurrent–voltage curve typical of a photovoltaic cell (Figure 13) (43). More recently, a 6.2% efficiency of a plastic-based DSC has been reported, where the photoelectrode was prepared by depositing the TiO_2 on plastic substrate by electrophoretic deposition method followed by heating at 150 °C and then compression by applying pressure (88). These rather good performances have been related to the fact that the films became more transparent and more adherent to the transparent and conductive substrates after compression. The mechanical stability of pressed films was thus improved, while irregular large pores and pronounced agglomerates have been eliminated. Consequently, the compression route provides a method to systematically increase the connection between particles and increase the effective electron diffusion coefficient in the film. Nonetheless, the reduction in porosity decreases the amount of dye to be adsorbed on the particles resulting lower

absorption of photons. However, this effect is compensated by swift electron transfer resulting from better connection. Besides, the main drawback of this method is that it always needs other deposition technique, such as electrophoretic deposition method, to deposit the TiO_2 on the substrate.

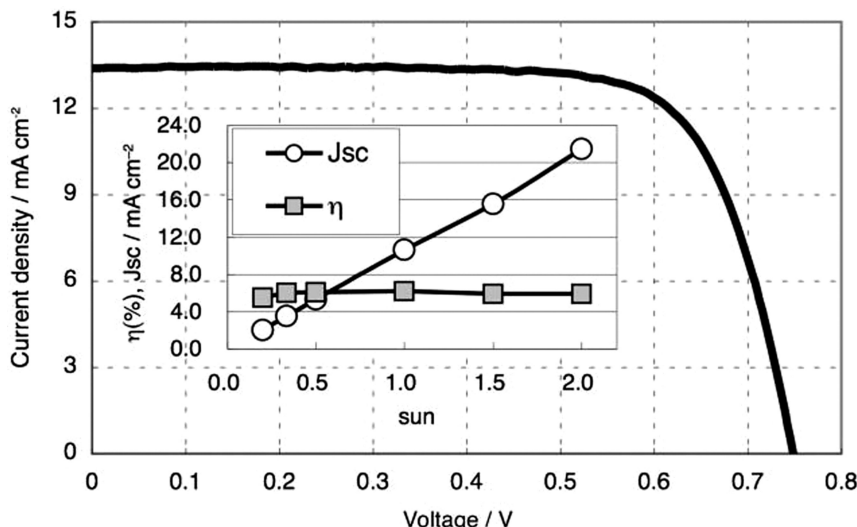


Figure 13. Photocurrent–voltage curve of the optimized plastic based DSSC. Solar energy to electricity conversion efficiency $\eta = 7.4\%$ with $J_{\text{SC}} = 13.4 \text{ mA.cm}^{-2}$, $V_{\text{OC}} = 0.75 \text{ V}$ and $FF = 0.74$. Light intensity = 100 mW.cm^{-2} (1 sun). The inset shows the dependence of J_{SC} and η on light intensity from 0.2 to 2 sun.
(Reproduced with permission from reference (43). Copyright 2007 RSC)

In summary, the low-temperature preparation of metal oxide, such as TiO_2 , ZnO or SnO_2 , photoelectrodes for DSCs is still challenging. The different deposition methods and post-treatment operation for the low temperature preparation of metal oxide photoelectrodes for DSCs reported in the literature have been discussed that showed that TiO_2 film on plastic substrate for DSCs can be processed in the absence of organic additives. Among the various low temperature preparation methods reported, the highest efficiency (6-7.4%) has been obtained by the anatase TiO_2 photoelectrode fabricated by compression method that is still far away from the efficiency of classic high temperature films. However, the films prepared at low temperature have a larger internal surface area and can therefore adsorb more dye for an equivalent film thickness resulting compensation somewhat for the efficiency loss by absorbing more light. More recently, very promising reports have concerned UV-processed SnO_2 photoanodes, the efficiencies of the corresponding DSCs competing with those measured for the same electrodes annealed at high temperature. A suitable deposition method combined with different post-treatment (compression, UV...) at low temperature should allow increasing the efficiency of the photoelectrode in the next future. For instance, using a paste of suitable viscosity including

TiO₂ particles and low molecular weight additives, the screen printing deposition technique combined with low temperature sintering method should offer the possibility to work on flexible substrates and to reach good efficiencies in DSCs.

References

1. International Energy Agency (IEA). Key world energy statistics, 2011.
2. Lewis, N. A global energy perspective. <http://www.its.caltech.edu/mmrc/nsl/energy.html>, 2004.
3. O'Regan, B.; Grätzel, M. *Nature* **1991**, *353*, 737.
4. Grätzel, M. *Nature* **2001**, *414*, 338.
5. Grätzel, M. *Acc. Chem. Res.* **2009**, *42*, 1788.
6. Hagfeldt, A.; Boschloo, G.; Sun, L.; Kloo, L.; Pettersson, H. *Chem. Rev.* **2010**, *110*, 6595.
7. Yu, Q. J.; Wang, Y. H.; Yi, Z. H.; Zu, N. N.; Zhang, J.; Zhang, M.; Wang, P. *ACS Nano* **2010**, *4*, 6032.
8. Yella, A.; Lee, H. W.; Tsao, H. N.; Yi, C.; Chandiran, A. K.; Nazeeruddin, Md. K.; Diau, E. W. G.; Yeh, C. Y.; Zakeeruddin, S. M.; Grätzel, M. *Science* **2011**, *434*, 629.
9. Hardin, B. E.; Snaith, H. J.; Mc Gehee, M. D. *Nat. Photonics* **2012**, *6*, 162.
10. Grätzel, M. *J. Photochem. Photobiol. A: Chem.* **2004**, *164*, 3.
11. Burschka, J.; Dualeh, A.; Kessler, F.; Baranoff, E.; Cevey-Ha, N.-L.; Yi, C.; Nazeeruddin, M. K.; Grätzel, M. *J. Am. Chem. Soc.* **2011**, *133*, 18042.
12. Kalyanasundaram, K.; Grätzel, M. *Coord. Chem. Rev.* **1998**, *177*, 347.
13. Pichot, F.; Pitts, R. J.; Gregg, B. A. *Langmuir* **2000**, *16*, 5626.
14. Pichot, F.; Ferrere, S.; Pitts, R. J.; Gregg, B. A. *J. Electrochem. Soc.* **1999**, *146*, 4324.
15. Paoli, M. A. D.; Nogueira, A. F.; Machado, D. A.; Longo, C. *Electrochim. Acta* **2001**, *46*, 4243.
16. Longo, C.; Nogueira, A. F.; Paoli, M. A. D. *J. Phys. Chem. B* **2002**, *106*, 5925.
17. Longo, C.; Freitas, J.; Paoli, M. A. D. *J. Photochem. Photobiol. A: Chem.* **2003**, *159*, 33.
18. Ito, S.; Takeuchi, T.; Katayama, T.; Sugiyama, M.; Matsuda, M.; Kitamura, T.; Wada, Y.; Yanagida, S. *Chem. Mater.* **2003**, *15*, 2824.
19. Watanabe, T.; Hayashi, H.; Imai, H. *Sol. Energy Mater. Sol. Cells* **2006**, *90*, 640.
20. Pasquier, A. D. *Electrochim. Acta* **2007**, *52*, 7469.
21. Kijitora, Y.; Ikegami, M.; Miyasaka, T. *Chem. Lett.* **2007**, *36*, 190.
22. Hsu, C. P.; Lee, K. M.; Huang, J. T. M.; Lin, C. Y.; Lee, C. H.; Wang, L. P.; Tsai, S. Y.; Ho, K. C. *Electrochim. Acta* **2008**, *53*, 7514.
23. Li, X.; Lin, H.; Li, J.; Wang, N.; Lin, C.; Zhang, L. *J. Photochem. Photobiol. A: Chem.* **2008**, *195*, 247.
24. Lee, K. M.; Hu, C. W.; Chen, H. W.; Ho, K. C. *Sol. Energy Mater. Sol. Cells* **2008**, *92*, 1628.

25. Ikegami, M.; Suzuki, J.; Teshima, K.; Kawaraya, M.; Miyasaka, T. *Sol. Energy Mater. Sol. Cells* **2009**, *93*, 836.
26. Weerasinghe, H. C.; Sirimanne, P. M.; Simon, G. P.; Cheng, Y. B. *J. Photochem. Photobiol. A: Chem.* **2009**, *206*, 64.
27. Kim, K.; Lee, G. W.; Yoo, K.; Kim, D. Y.; Kim, J. K.; Park, N. G. *J. Photochem. Photobiol. A: Chem.* **2009**, *204*, 144.
28. Pasquier, A. D.; Stewart, M.; Spitler, T.; Coleman, M. *Sol. Energy Mater. Sol. Cells* **2009**, *93*, 528.
29. Nakade, S.; Matsuda, M.; Kambe, S.; Saito, Y.; Kitamura, T.; Sakata, T.; Wada, Y.; Mori, H.; Yanagida, S. *J. Phys. Chem. B* **2002**, *106*, 10004.
30. Stathatos, E.; Chen, Y.; Dionysiou, D. D. *Sol. Energy Mater. Sol. Cells* **2008**, *92*, 1358.
31. Fan, K.; Peng, T.; Chen, J.; Dai, K. *J. Power Sources* **2011**, *196*, 2939.
32. Lindström, H.; Holmberg, A.; Magnusson, E.; Lindquist, S. E.; Malmqvist, L.; Hagfeldt, A. *Nano Lett.* **2001**, *1*, 97.
33. Lindström, H.; Holmberg, A.; Magnusson, E.; Malmqvist, L.; Hagfeldt, A. *J. Photochem. Photobiol. A: Chem.* **2001**, *145*, 107.
34. Boschloo, G.; Lindström, H.; Magnusson, E.; Holmberg, A.; Hagfeldt, A. *J. Photochem. Photobiol. A: Chem.* **2002**, *148*, 11.
35. Lindström, H.; Magnusson, E.; Holmberg, A.; Södergren, S.; Lindquist, S. E.; Hagfeldt, A. *Sol. Energy Mater. Sol. Cells* **2002**, *73*, 91.
36. Haque, S. A.; Palomares, E.; Upadhyaya, H. M.; Otley, L. R.; Potter, J.; Holmes, A. B.; Durrant, J. R. *Chem. Commun.* **2003**, *24*, 3008.
37. Hagfeldt, A.; Boschloo, G.; Lindström, H.; Figgemeier, E.; Holmberg, A.; Aranyos, V.; Magnusson, E.; Malmqvist, L. *Coord. Chem. Rev.* **2004**, *248*, 1501.
38. Almeida, P. D.; Deelen, J. V.; Catry, C.; Sneyers, H.; Pataki1, T.; Andriessen, R.; Roost, C. V.; Kroon, J. M. *Appl. Phys. A* **2004**, *79*, 1819.
39. Yuma, J. H.; Kima, S. S.; Kima, D. Y.; Sung, Y. E. *J. Photochem. Photobiol. A: Chem.* **2005**, *173*, 1.
40. Halme, J.; Saarinen, J.; Lund, P. *Sol. Energy Mater. Sol. Cells* **2006**, *90*, 887.
41. Nokki, H. S.; Kallioinen, J.; Kololuoma, T.; Tuboltsev, V.; Tommolaa, J. K. *J. Photochem. Photobiol. A: Chem.* **2006**, *182*, 187.
42. Halme, J.; Toivola, M.; Tolvanen, A.; Lund, P. *Sol. Energy Mater. Sol. Cells* **2006**, *90*, 872.
43. Yamaguchi, T.; Tobe, N.; Matsumoto, D.; Arakawa, H. *Chem. Commun.* **2007**, *45*, 4767.
44. Halme, J.; Boschloo, G.; Hagfeldt, A.; Lund, P. *J. Phys. Chem. C* **2008**, *112*, 5623.
45. Haque, S. A.; Palomares, E.; Upadhyaya, H. M.; Otley, L.; Potter, R. J.; Holmes, A. B.; Durrant, J. R. *Chem. Commun.* **2003**, *24*, 3008.
46. Zhang, D.; Yoshida, T.; Minoura, H. *Chem. Lett.* **2002**, *31*, 874.
47. Zhang, D.; Yoshida, T.; Furuta, K.; Minoura, H. *J. Photochem. Photobiol. A: Chem.* **2004**, *164*, 159.
48. Oekermann, T.; Zhang, D.; Yoshida, T.; Minoura, H. *J. Phys. Chem. B* **2004**, *108*, 2227.

49. Tan, W.; Chen, J.; Zhou, X.; Zhang, J.; Lin, Y.; Li, X.; Xiao, X. *J. Solid State Electrochem.* **2009**, *13*, 651.
50. Uchida, S.; Tomiha, M.; Masaki, N.; Miyazawa, A.; Takizawa, H. *Sol. Energy Mater. Sol. Cells* **2004**, *81*, 135.
51. Uchida, S.; Tomiha, M.; Takizawa, H.; Kawaraya, M. *J. Photochem. Photobiol. A: Chem.* **2004**, *164*, 93.
52. Murakami, T. N.; Kijitora, Y.; Kawashima, N.; Miyasaka, T. *J. Photochem. Photobiol. A: Chem.* **2004**, *164*, 187.
53. Murakami, T. N.; Kijitora, Y.; Kawashima, N.; Miyasaka, T. *Chem. Lett.* **2003**, *32*, 1076.
54. Miyasaka, T.; Kijitora, Y.; Murakami, T. N.; Kimura, M.; Uegusa, S. *Chem. Lett.* **2002**, *31*, 1250.
55. Tebby, Z.; Babot, O.; Michau, B.; Hirsch, L.; Carlos, L.; Toupane, T. *J. Photochem. Photobiol. A: Chem.* **2009**, *205*, 70.
56. Kim, H.; Auyeung, R. C. Y.; Ollinger, M.; Kushto, G. P.; Kafafi, Z. H.; Piqué, A. *Appl. Phys. A* **2006**, *83*, 73.
57. Gutiérrez-Tauste, D.; Zumeta, I.; Vigil, E.; Fenollosa, M. A. H.; Doménech, X.; Ayllón, J. A. *J. Photochem. Photobiol. A: Chem.* **2005**, *175*, 165.
58. Fan, S. Q.; Li, C. J.; Yang, G. J.; Zhang, L. Z.; Gao, J. C.; Xi, Y. X. *J. Therm. Spray Technol.* **2007**, *16*, 893.
59. Nanu, M.; Schoonman, J.; Goossens, A. *Nano Lett.* **2005**, *5*, 1716.
60. Halme, J.; Toivola, M.; Tolvanen, A.; Lund, P. *Sol. Energy Mater. Sol. Cells* **2006**, *90*, 872.
61. Quintana, M.; Edvinsson, T.; Hagfeldt, A.; Boschloo, G. *J. Phys. Chem. C* **2007**, *111*, 1035.
62. Katoh, R.; Furube, A.; Yoshihara, T.; Hara, K.; Fujihashi, G.; Takako, S.; Murata, S.; Arakawa, H.; Tachiya, M. *J. Phys. Chem. B* **2004**, *108*, 4818.
63. Rensmo, H.; Keis, K.; Lindström, H.; Södergren, S.; Solbrand, A.; Hagfeldt, A.; Lindquist, S. E. *J. Phys. Chem. B* **1997**, *101*, 2598.
64. Keis, K.; Bauer, C.; Boschloo, G.; Hagfeldt, A.; Westermark, K.; Rensmo, H.; Siegbahn, H. *J. Photochem. Photobiol. A: Chem.* **2002**, *148*, 57.
65. Kashyout, A. B.; Soliman, M.; Gamal, M. E.; Fathy, M. *Mater. Chem. Phys.* **2005**, *90*, 230.
66. Baxter, J. B.; Aydil, E. S. *Sol. Energy Mater. Sol. Cells* **2006**, *90*, 607.
67. Kakiuchi, K.; Hosono, E.; Fujihara, S. *J. Photochem. Photobiol. A: Chem.* **2006**, *179*, 81.
68. Suri, P.; Mehra, R. M. *Sol. Energy Mater. Sol. Cells* **2007**, *91*, 518.
69. Suliman, A. E.; Tang, Y.; Xu, L. *Sol. Energy Mater. Sol. Cells* **2007**, *91*, 1658.
70. Choopun, S.; Tubtimtae, A.; Santhaveesuk, T.; Nilphai, S.; Wongrat, E.; Hongsith, N. *Appl. Surf. Sci.* **2009**, *256*, 998.
71. Guillen, E.; Lorenzo, C. F.; Alcantara, R.; Martin-Calleja, J.; Anta, J. A. *Sol. Energy Mater. Sol. Cells* **2009**, *93*, 1846.
72. Hajry, A. A.; Umar, A.; Hahn, Y. B.; Kim, D. H. *Superlattices Microstruct.* **2009**, *45*, 529.

73. Liu, Z.; Liu, C.; Ya, J. *Solid State Sci.* **2010**, *12*, 111.

74. Saito, H.; Fujihara, S. *Energy Environ. Sci.* **2008**, *1*, 280.

75. Nemarian, N.; Concina, I.; Braga, A.; Rozati, S. Md.; Vomiero, A.; Sberveglieri, G. *Angew. Chem., Int. Ed.* **2011**, *50*, 12321.

76. Chen, W.; Zhang, H.; Hsing, I. M.; Yang, S. *Electrochem. Commun.* **2009**, *11*, 1057.

77. Kim, S.; Yum, J. H.; Sung, Y. E. *J. Photochem. Photobiol. A: Chem.* **2005**, *171*, 269.

78. Dentani, T.; Nagasaka, K.; Funabiki, K.; Jin, J. Y. *Dyes Pigm.* **2008**, *77*, 59.

79. Suresh, P.; Balaraju, P.; Sharma, S. K.; Roy, M. S.; Sharma, G. D. *Sol. Energy Mater. Sol. Cells* **2008**, *92*, 900.

80. Keis, K.; Magnusson, E.; Lindström, H.; Lindquist, S. E.; Hagfeldt, A. *Sol. Energy Mater. Sol. Cells* **2002**, *73*, 51.

81. Bedja, I.; Hotchandani, S.; Kamat, P. *J. Phys. Chem.* **1994**, *98*, 4133.

82. Krebs, F. *Sol. Energy Mater. Sol. Cells* **2009**, *93*, 394.

83. Tsoukleris, D. S.; Arabatzis, I. M.; Chatzivasiloglou, E.; Kontos, A. I.; Belessi, V.; Bernard, M. C.; Falaras, P. *Sol. Energy* **2005**, *79*, 422.

84. Tebby, Z.; Babot, O.; Toupance, T.; Park, D.-H.; Campet, G.; Delville, M.-H. *Chem. Mater.* **2008**, *20*, 7260.

85. Fan, S. Q.; Yang, G. J.; Li, C. J.; Liu, G. J.; Li, C. X.; Zhang, L. *J. Therm. Spray Technol.* **2006**, *15*, 513.

86. Tebby, Z.; Uddin, T.; Olivier, C.; Nicolas, Y.; Toupance, T.; Hirsch, L. *ACS Appl. Mater. Interfaces* **2011**, *3*, 1485.

87. Miyasaka, T.; Ikegami, M.; Kijitora, Y. *J. Electrochem. Soc.* **2007**, *154*, A455.

88. Grinis, L.; Kotlyar, S.; Rühle, S.; Grinblat, J.; Zaban, A. *Adv. Funct. Mater.* **2010**, *20*, 282.

Chapter 7

Anions vs. Cations of $\text{Pt}_{13}\text{H}_{24}$ Cluster Models: *Ab Initio* Molecular Dynamics Investigation of Electronic Properties and Photocatalytic Activity

Qingguo Meng, Hugo Yao, and Dmitri Kilin*

Department of chemistry, University of South Dakota, Vermillion,
South Dakota 57069, United States
*E-mail: Dmitri.Kilin@usd.edu

Platinum is one of the most valuable catalysts that have been used in the catalytic fields of hydrogenation, fuel-cell technologies, and water splitting photo-catalytically. In this work, an extension of one of our previous paper (1), using first-principles density functional theory (DFT) calculation the dissociation of hydrogen in molecule form from neutral and both negatively and positively charged $\text{Pt}_{13}\text{H}_{24}^{n\pm}$ ($n = 0, 1$ and 2) clusters is investigated by *ab initio* molecular dynamics (AIMD). $\text{Pt}_{13}\text{H}_{24}^{2-}$ model shows the highest catalytic activity on H_2 dissociation among all the investigated models, whose electronic and catalytic properties are specifically investigated in this work. Heat treatment at elevated temperature is applied on cluster models, in order to simulate the experimental reaction of hydrogen on the $\text{Pt}_{13}\text{H}_{24}$ cluster surface, followed by the AIMD process to compare the H_2 desorption rate on different models. Electronic properties, e.g., spinful and spinless density of state (DOS), linear absorption spectrum, and radiative lifetime on all the models are also calculated.

Introduction

Platinum structures have been used to catalyze the dissociative chemisorption of hydrogen in a molecular form, and the generated hydrogen molecules undergo a dissociative chemisorption process on a Pt catalyst, which supplies hydrogen since hydrogenated products could also be formed after the hydrogen atoms desorb from the Pt surfaces (2, 3). Theoretical studies on the chemisorption of hydrogen on the Pt surface have been performed for a long time (4). For example, the electronic structures of Pt_{13} clusters in icosahedral and cubic symmetry were studied by the first principle calculations, and the calculated energies were in good agreement with experimental hydrogen-metal binding energies (5). In the meanwhile, when the transition metal clusters are deposited on electrodes or in a course of photo-induced charge transfer from a substrate, charging on the clusters can modify the catalytic properties (6–10).

A $\text{Pt}_{13}\text{H}_{24}$ cluster model is used in our research to describe the interaction between hydrogen atoms and Pt catalyst, assuming that Pt cluster with an appropriate size would be an excellent representation of Pt nanoparticles (11). The 13-atom Pt clusters have drawn much attention because it can form closed-shell icosahedral structure and is considered as being representative of highly dispersed platinum catalysts (12–14). Catalytic reactions present a challenge to computational studies since the electronic structure and thus the bonding pattern changes qualitatively in the course of the simulation. In the previous work (1) we established a $\text{Pt}_{13}\text{H}_{24}$ cluster model to investigate the interaction between hydrogen atoms and Pt cluster catalyst, using *ab initio* molecular dynamics (AIMD). It was observed that increasing the negative charges of the anion cluster model higher than two inhibited the H_2 molecules desorption reaction. In an extension of the previous study, the $\text{Pt}_{13}\text{H}_{24}^{2-}$ anion cluster model, which presented the highest desorption rate and the lowest activation energy, was systematically investigated on the electronic and catalytic properties. Furthermore, the effect of removing electrons from Pt cluster, e.g. positive charged cation models $\text{Pt}_{13}\text{H}_{24}^{n+}$ ($n = 1$ and 2), on the electric and catalytic properties is still unknown.

Methodology

The $\text{Pt}_{13}\text{H}_{24}$ cluster structure in this work is the same as the models that have been used in our previous paper (1). Platinum has an electronic configuration of $[\text{Xe}] 4\text{f}^{14}5\text{d}^96\text{s}^1$, and the unsaturated bonds were hydrogenated by two hydrogen atoms and the ground electronic state geometry of the atomic model was optimized with DFT using the Vienna Ab initio Simulation Package (VASP) and PBE exchange-correlation functional (15–17). The atomic structure determines the initial positions of each ion $\{R_j\}$ in the $\text{Pt}_{13}\text{H}_{24}$ cluster model. The main equation to solve is a fictitious one-electron Kohn-Sham equation (15). The central quantity of the density functional theory for the electron-electron interaction energy was chosen according to *Perdew-Burke-Ernzerhof* procedure (PBE functional) (18).

This functional follows generalized gradient approximation (GGA) and provides higher precision than functional based on local density approximation (LDA). In VASP software, valence electrons are treated explicitly while core electrons are described with pseudopotentials (19). All calculations are done in the basis of plane waves. A cutoff energy of 200 eV is used throughout and the electronic structures are considered self-consistent if two consecutive energies and forces differ by less than 0.01 meV and 0.01 eV/Å.

The spectral density of absorption was calculated analogously to the density of states,

$$\alpha(\omega) = \sum_{ij} f_{ij} \delta(\hbar\omega - \Delta\epsilon_{ij}) \quad (1)$$

With the sum running over each transition $\Delta\epsilon_{ij} = |\epsilon_i - \epsilon_j|$, weighted by the relevant oscillator strength, $f_{ij} = |\mathbf{D}_{ij}|^2 \frac{2m_e \Delta\epsilon_{ij}}{3\hbar^2 e^2}$, composed of transition dipole matrix elements D_{ij} and fundamental constants (20).

For more details about methodology on density of states (DOS), molecular dynamics (MD), Pt-H distance for pairs of atoms as a function of time, H₂ desorption rate, etc, please refer to our previous paper (1). Charge is defined as difference between total charge component contributed by ions $Z_{ion} = \sum_{I=1}^{N_{ions}} Z_I$ and total charge contributed by electrons $Z_{elec} = eN_{elec}$ in units of elementary charge, $n = Z_{ion} - Z_{elec}$. Here in our work, $n = 0, \pm 1$, and ± 2 , corresponds to neutral, positively or negatively charged model, respectively. The variation of the total charge changes the total electron density and effective potential. This change systematically affects all observables, such as DOS, absorption spectra, MD trajectory pattern, desorption rate $R(T) = R(T, n)$, and activation energy $E_a = E_a(n)$.

Results and Discussion

Electronic Properties of the Pt₁₃H₂₄ Cluster Model

The geometry optimization of neutral Pt₁₃H₂₄ cluster model has been conducted previously (1). The bond length between the side and the central Pt atoms is elongated up to 2.735 ~ 2.808 Å, and the side Pt atoms bond distance is elongated to ~ 2.795 Å. These bond distances are longer than the naked Pt₁₃ cluster (21), which is due to the adsorbed hydrogen atoms, altering the electronic properties of Pt atoms. The electron density between Pt atoms decreases after the adsorption of H atoms, leading to the increase of Pt–Pt bond length.

Density of states (DOS) of electronic structures of the structural optimized Pt₁₃H₂₄^{±n} ($n = 0, 1$ and 2) clusters were computed and the results are shown in the left panel of Figure 1. For each model, the part of the curve under which the area is filled represents the occupied orbitals, HOMO (Highest Occupied Molecular Orbital). The part of the curve with unfilled area represents the unoccupied orbitals, LUMO (Lowest Unoccupied Molecular Orbital). A very small band gap

between HOMO and LUMO is observed for all the investigated cluster models, indicating a metal character of $\text{Pt}_{13}\text{H}_{24}$ cluster. It will take very small energy for the electrons being excited from HOMO to LUMO. After the cluster is charged by one electron, $\text{Pt}_{13}\text{H}_{24}^-$ anion, DOS (Figure 1-A4) of HOMO presents some new electronic states at higher energy, compared to that of the neutral model (Figure 1-A3). Adding two electrons on the cluster, $\text{Pt}_{13}\text{H}_{24}^{2-}$ anion, increases the orbital energy of HOMO dramatically (Figure 1-A5), which is in favor of a high intrinsic reactivity of the metallic sites (22). For the positive charged models (cations), the orbital energy of HOMO decreases with charge numbers (Figure 1-A2) and the Fermi level shifts to -7.5 eV after two electrons are removed (Figure 1-A1).

The corresponding linear absorption spectra and radiative lifetimes are also calculated and displayed in the middle and right panel of Figure 1. The neutral $\text{Pt}_{13}\text{H}_{24}$ cluster model displayed some absorption bands between 0.8 and 3.0 eV. After adding one electron, $\text{Pt}_{13}\text{H}_{24}^-$ model, all the absorption bands turns sharp and $\text{Pt}_{13}\text{H}_{24}^{2-}$ anion shows an identical absorption spectrum to $\text{Pt}_{13}\text{H}_{24}^-$. In contrast to this, the absorption spectra of $\text{Pt}_{13}\text{H}_{24}^+$ and $\text{Pt}_{13}\text{H}_{24}^{2+}$ cations become much broader, which can be due to the contributions of some new absorption bands. It is also interesting to note that a new absorption band appears at the low energy range (~ 0.5 eV) in the positively charged $\text{Pt}_{13}\text{H}_{24}^+$ cation, corresponding to the adsorption in the NIR range. The radiative lifetime calculation indicates that in the neutral model the longest lifetime is obtained under the excitation energy at ~ 0.65 eV, and decrease almost linearly with increase of excitation energy. But in the $\text{Pt}_{13}\text{H}_{24}^-$ and $\text{Pt}_{13}\text{H}_{24}^{2-}$ models the longest radiative decay are observed at much lower excitation energy, 0.2 eV for $\text{Pt}_{13}\text{H}_{24}^+$ and 0.3 eV for $\text{Pt}_{13}\text{H}_{24}^{2+}$ model, respectively.

Spin-polarized DOS of various $\text{Pt}_{13}\text{H}_{24}$ clusters are also computed and plotted in Figure 2. The curve above zero is spin-up DOS and below zero is spin-down DOS. The spin-up and spin-down DOS of cluster models with even number of electrons, e.g neutral $\text{Pt}_{13}\text{H}_{24}$ and $\text{Pt}_{13}\text{H}_{24}^{2-}$ models presents symmetrical character. Whereas the models with odd numbers, e.g $\text{Pt}_{13}\text{H}_{24}^-$ and $\text{Pt}_{13}\text{H}_{24}^+$ clusters, present asymmetric spin-up and spin-down density of states, representing a doublet ground state.

The images of partial charge density of HOMO and LUMO for $\text{Pt}_{13}\text{H}_{24}^{n\pm}$ ($n = 0, 1$ and 2) cluster models are given in Figure 3. In the neutral model, all the charges are localized around Pt atoms in the HOMO, and evidence of charges are also observed around H atoms in the LUMO. The binding of hydrogen atoms to the Pt cluster surface causes a partial electron transfer from the cluster to the hydrogen. In the HOMO of anion models, more charges are localized around the Pt atoms (from C1 to E1), whereas in the cation models it becomes less (from C1 to A1). In the LUMO of all the models, charges are consistently observed around the H atoms.

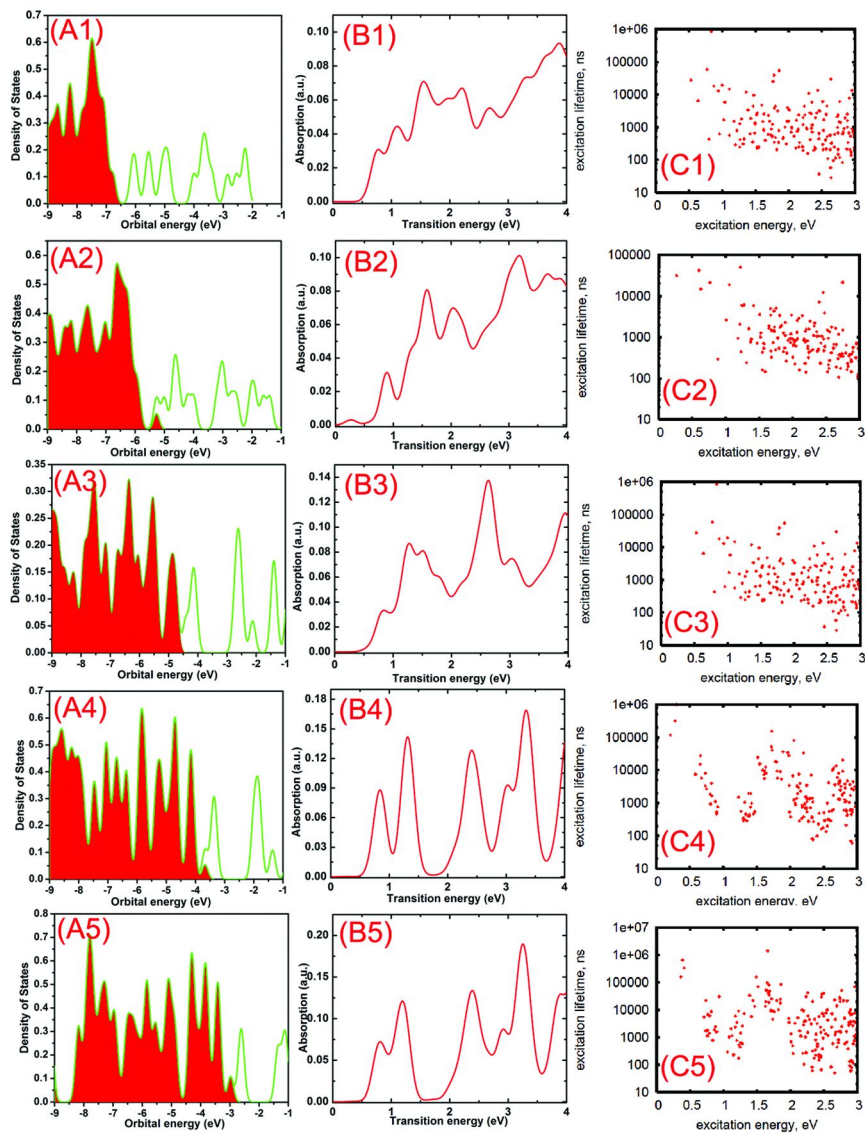


Figure 1. Left column: the density of states of $Pt_{13}H_{24}^{2+}$, $Pt_{13}H_{24}^+$, $Pt_{13}H_{24}$, $Pt_{13}H_{24}^-$ and $Pt_{13}H_{24}^{2-}$ models (from top to bottom). Filled area symbolizes filled orbitals. **Middle column:** computed linear absorption spectra for the same models. **Right column:** computed radiative lifetime for the same models. The DOS and absorption spectra results of $Pt_{13}H_{24}$, $Pt_{13}H_{24}^-$ and $Pt_{13}H_{24}^{2-}$ models are reproduced with the permission from reference DOI: 10.1002/qua.24301.

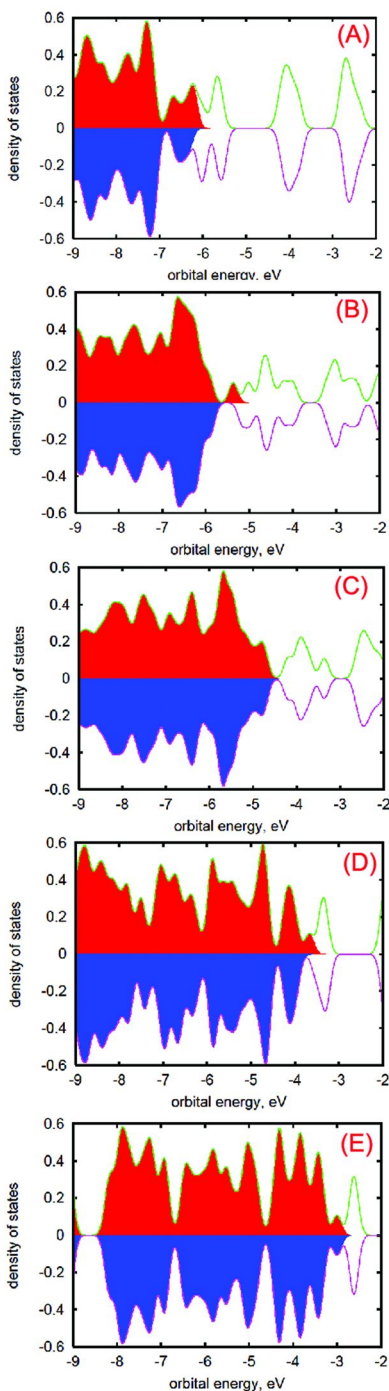


Figure 2. Spin-up and spin-down DOS of $Pt_{13}H_{24}^{2+}$ (A), $Pt_{13}H_{24}^+$ (B), $Pt_{13}H_{24}$ (C), $Pt_{13}H_{24}^-$ (D), $Pt_{13}H_{24}^{2-}$ (E) cluster models.

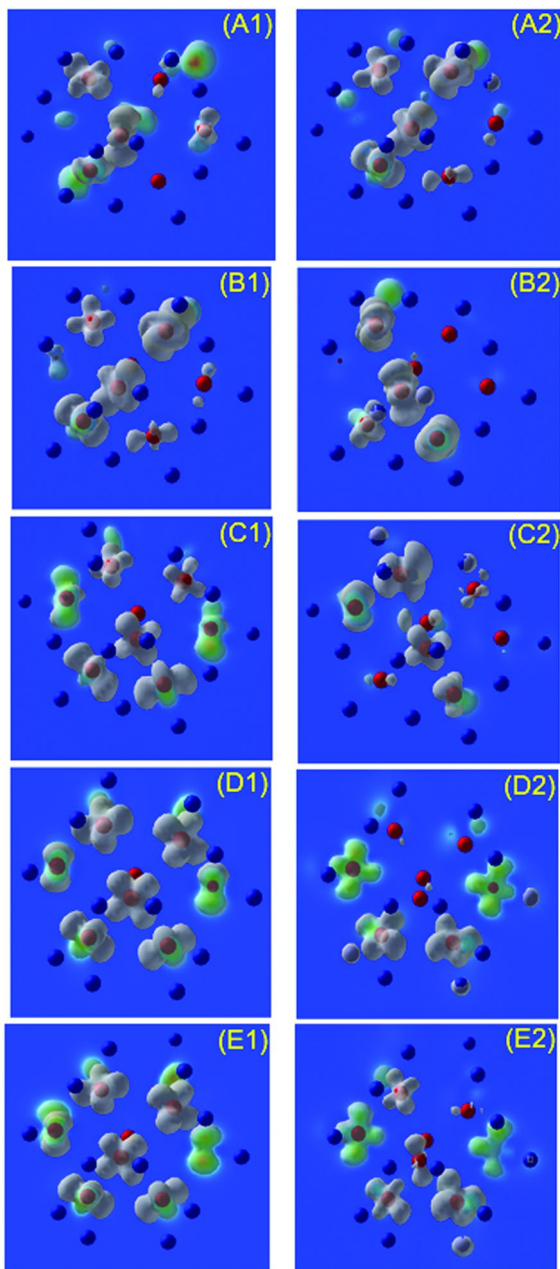


Figure 3. Partial charge density of $Pt_{13}H_{24}^{2+}$ (A), $Pt_{13}H_{24}^+$ (B), $Pt_{13}H_{24}$ (C), $Pt_{13}H_{24}^-$ (D), $Pt_{13}H_{24}^{2-}$ (E) cluster models. The left panel is HOMO and the right panel is LUMO. The isosurfaces value is 70.

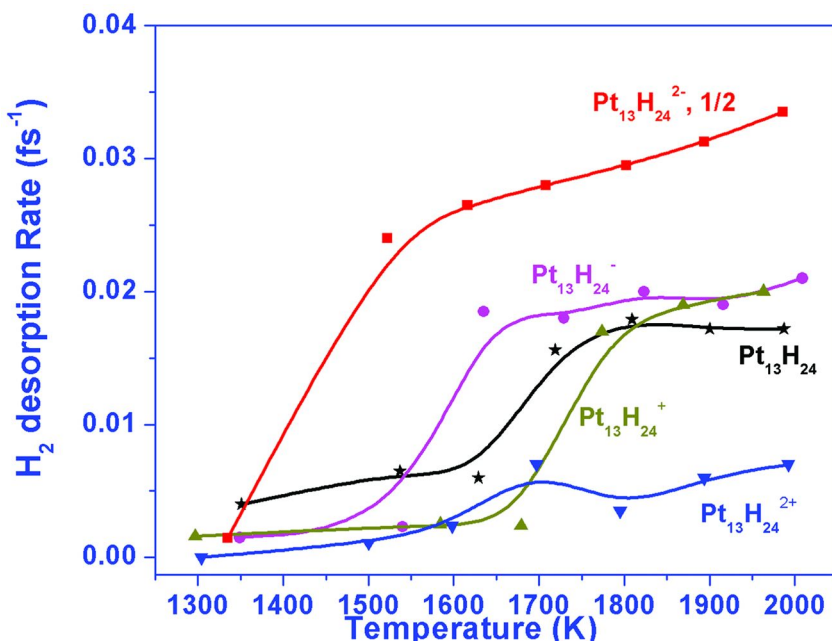


Figure 4. Heat treatment temperature dependence on the H_2 desorption rate for various kinds of $\text{Pt}_{13}\text{H}_{24}^{n\pm}$ cluster models. The 1/2 means that the H_2 desorption rate of $\text{Pt}_{13}\text{H}_{24}^{2-}$ is reduced to half for clarification. The H_2 desorption rate data of $\text{Pt}_{13}\text{H}_{24}$, $\text{Pt}_{13}\text{H}_{24}^{-}$ and $\text{Pt}_{13}\text{H}_{24}^{2-}$ models are reproduced with the permission from reference DOI: 10.1002/qua.24301.

Catalytic Properties of the $\text{Pt}_{13}\text{H}_{24}$ Cluster Model

Many catalytic reactions are carried out under elevated temperature. So it is interesting to investigate the electrical and structural changes of the $\text{Pt}_{13}\text{H}_{24}$ anion and cation cluster during heat treatment, which gives the information about thermal stability. Furthermore, all the atoms gain certain velocities transferred from their potentials during heating, and the forces that the atoms have can be derived based on their individual velocities and they depend on the electronic density only. So the ab initio molecular dynamics (AIMD) process was simulated to model the change of the position of the atoms in $\text{Pt}_{13}\text{H}_{24}$ anion and cation cluster after heating. In our previous work (1) it was interestingly observed that after around 60 fs two hydrogen atoms bonded together before they desorbed from the surface of the neutral Pt cluster in a molecular form. After adding one electron to the cluster, it took around 45 fs for the H_2 molecule desorption, whereas in the current research on cation models the H_2 molecule desorption takes 51 and 148 fs for $\text{Pt}_{13}\text{H}_{24}^{+}$ and $\text{Pt}_{13}\text{H}_{24}^{2+}$ cluster models, respectively. It has been concluded that adding electrons benefit the H_2 desorption, but charges higher than two inhibited desorption reaction, which might be due to unstable structure (1). When removing electrons, $\text{Pt}_{13}\text{H}_{24}^{n+}$ cations, a lower surface catalytic activity was observed. The desorption rates on all the $\text{Pt}_{13}\text{H}_{24}^{n\pm}$ cluster models as a function

of heating temperature were computed and compared in Figure 4. It can be seen that heating temperature lower than 1000 K doesn't cause any H₂ desorption, and after 1300 K H₂ desorption become evidence. Increasing the heating temperature benefits desorption rate on all the models. All the profiles are characterized by a sharp increase of desorption rate at 1500 K, after which only a slight increase of desorption rate is expected. The temperature, at which the sharp increase of desorption rate is observed, is denoted as T_a, and the lower the T_a, the higher catalytic activity of the cluster. Pt₁₃H₂₄²⁻ has the lowest T_a at around 1450 K and increase to 1600 K, 1700 K, and 1750 K for Pt₁₃H₂₄⁻, Pt₁₃H₂₄, and Pt₁₃H₂₄⁺ model, respectively, indicating a sequence of catalytic activity Pt₁₃H₂₄²⁻ > Pt₁₃H₂₄⁻ > Pt₁₃H₂₄ > Pt₁₃H₂₄⁺ > Pt₁₃H₂₄⁺. The desorption rate of Pt₁₃H₂₄²⁺ cation is even much lower that no apparent T_a can be identified. Removing electrons one or two from the cluster models is concluded not to benefit the H₂ desorption rate. Removing more electrons, e.g. Pt₁₃H₂₄⁶⁺ anion, doesn't cause any H₂ desorption after up to 1000 fs of MD steps. The maximum H₂ desorption rate found on Pt₁₃H₂₄²⁻ model at 1986 K is around 0.067 fs⁻¹, approximately corresponding to 0.61 ml/h per cluster, which is comparable to the experimental result of around 0.1~1.5 ml/h on Pt and RuO₂ co-deposited TiO₂ photocatalysts (23).

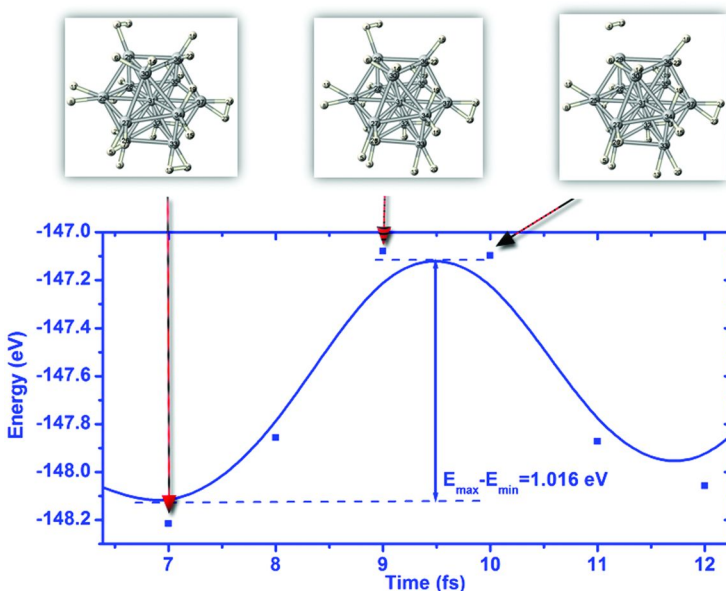


Figure 5. H₂ desorption pathway with time during MD process for Pt₁₃H₂₄²⁻ cluster model. The structures of the initial, intermediate, and final configurations are shown in the top panel. The bottom panel plots the energy change along the reaction pathway. The activation energy E is estimated as 1.016 eV as maximal fluctuation of total energy during desorptive MD trajectory. Note that the energy versus time plot and displayed value of the activation barrier are found for one specific desorption event along one specific trajectory.

An important issue for the surface catalysis is the energy required for the H₂ molecules to be dissociated from metal catalyst surface. Pt₁₃H₂₄²⁻ cluster has been concluded the most active model, so in Figure 5 the curve on the bottom shows the time dependence on total energy of Pt₁₃H₂₄²⁻ cluster in the step ranges when one H₂ molecule is leaving. On the top panel, the image of initial configuration of the cluster is shown in the leftmost, together with the image of intermediate structure in the middle. The rightmost frame is the final configuration of the cluster where one H₂ molecule has desorbed. In our calculation, the geometry of intermediate state is determined by the configuration who has the maximum total energy during the dissociation steps. Then the instant activation energy can be obtained by the difference of energy between initial and intermediate state, for example, as shown in Figure 5, which is determined to be around 1.016 eV. The actual activation energies for comparison were calculated by the energy difference between the reactant state and the intermediate state. All the energy data and desorption rate comparison are concluded in Table 1. By comparison the Pt₁₃H₂₄²⁻ model shows again the highest desorption rate and correspondingly the lowest activation energy. Accordingly, the 1st ionization energy of the Pt₁₃H₂₄ cluster is estimated to be 5.26 eV and the 2nd ionization energy is 10.43 eV. The electron affinity of the Pt₁₃H₂₄ cluster is determined as 1.32 eV.

Table 1. Total energy, desorption rate and activation energy of different Pt₁₃H₂₄^{n±} models (n = 0, 1, and 2). The actual activation energies are calculated by the energy difference between the reactant state and the intermediate state.

Model	Charge	<i>E_{tot}</i> (spinless, eV)	<i>E_{tot}</i> (spinful, eV)	Desorption rate at ~2000 K (fs⁻¹)	Activation energy, <i>E_a</i> (eV)
Pt ₁₃ H ₂₄ ²⁺	+2	-138.33	-138.33	0.007	2.33
Pt ₁₃ H ₂₄ ⁺	+1	-143.50	-143.54	0.020	2.57
Pt ₁₃ H ₂₄	0	-148.76	-148.72	0.017	2.23
Pt ₁₃ H ₂₄ ⁻	-1	-150.08	-150.11	0.021	2.72
Pt ₁₃ H ₂₄ ²⁻	-2	-153.37	-153.37	0.067	1.02

Conclusion

In the extension of our previous work, the electronic and catalytic properties of the Pt₁₃H₂₄^{n±} cluster models (n = 0, 1, and 2) was investigated in this study. DOS results reveal that after Pt₁₃H₂₄ cluster is negatively charged some new electronic states at higher energy is observed, and adding more electrons on the cluster increases the orbital energy of HOMO dramatically, which is in favor of a high intrinsic reactivity of the metallic site. Partial charge density images indicate that in the Pt₁₃H₂₄ anions, more charges are seen localized around Pt atoms and it becomes less in the cation models. There is a sharp increase of desorption rate

at different heating temperature for different models and levels off afterwards. The catalytic activity has a sequence of $\text{Pt}_{13}\text{H}_{24}^{2-} > \text{Pt}_{13}\text{H}_{24}^- > \text{Pt}_{13}\text{H}_{24} > \text{Pt}_{13}\text{H}_{24}^+$ $> \text{Pt}_{13}\text{H}_{24}^{2+}$. The maximum H_2 desorption rate found on $\text{Pt}_{13}\text{H}_{24}^{2-}$ anion at heating temperature of 1986 K is around 0.067 fs^{-1} , approximately corresponding to 0.61 ml/h per cluster. The lowest activation energy activation energy of $\text{Pt}_{13}\text{H}_{24}^{2-}$ model is consistent with the conclusion of its highest desorption rate result. In the future work we expect the modification of the activation energy upon using van der Waals enabled functions (24). Combining together simulation of photon absorption (25, 26), and charge transfer from a substrate to the surface of nanocatalyst (27–29) and charge-facilitated surface reaction (1), one is able to complete the pathways of subsequent elementary processes contributing to the photocatalytic water splitting.

Acknowledgments

We thank the NSF/EPSCoR (grant No. 0554609), NSF award EPS0903804, and the State of South Dakota, governor's Office of Economic Development, DOE, BES – Chemical Sciences, NERSC Contract No. DE-AC02-05CH11231, allocation Award 85213 “Computational Modeling of Photo-catalysis and Photoinduced Charge Transfer Dynamics on Surfaces”, for support. Computational resources of USD High Performance Computing facilities maintained by Doug Jenevin are gratefully acknowledged. DK thanks Sergei Tretiak for hosting the visit to Los Alamos National Laboratory, New Mexico during manuscript preparation. Inspiring discussions with James Hoefelmeyer on open problems in photocatalysis are gratefully acknowledged. Discussions with Sergei Ivanov (Sandia National Lab, New Mexico) on computation of charged nanoclusters are acknowledged.

References

1. Meng, Q. G.; May, P. S.; Berry, M. T.; Kilin, D. *Int. J. Quantum Chem.* **2012**, *112* (24), 3896–3903.
2. Khoobiar, S. Particle to Particle Migration of Hydrogen Atoms on Platinum-Alumina Catalysts from Particle to Neighbouring Particles. *J. Phys. Chem.* **1964**, *68*, 411–412.
3. Kyriakou, G.; Boucher, M. B.; Jewell, A. D.; Lewis, E. A.; Lawton, T. J.; Baber, A. E.; Tierney, H. L.; Flytzani-Stephanopoulos, M.; Sykes, E. C. H. Isolated Metal Atom Geometries as a Strategy for Selective Heterogeneous Hydrogenations. *Science* **2012**, *335*, 1209–1212.
4. Christmann, K. Interaction of Hydrogen with Solid Surfaces. *Surf. Sci. Rep.* **1988**, *9*, 1–163.
5. Watari, N.; Ohnishi, S. Electronic Structure of H Adsorbed on Pt_{13} Clusters. *J. Chem. Phys.* **1997**, *106* (18), 7531–7540.
6. Chen, S. W.; Murray, R. W.; Feldberg, S. W. Quantized Capacitance Charging of Monolayer-Protected Au Clusters. *J. Phys. Chem. B* **1998**, *102*, 9898–9907.

7. Mertens, S. F. L.; Voller, C.; Held, A.; Aguirre, M. H.; Walter, M.; Janiak, C.; Wandlowski, T. "Ligand-Free" Cluster Quantized Charging in an Ionic Liquid. *Angew. Chem., Int. Ed.* **2011**, *50* (41), 9735–9738.
8. Anpo, M.; Takeuchi, M. The Design and Development of Highly Reactive Titanium Oxide Photocatalysts under Visible Light Irradiation. *J. Catal.* **2003**, *216*, 505–516.
9. Roth, J. D.; Lewis, G. J.; Safford, L. K.; Jiang, X.; Dahl, L. F.; Weaver, M. J. Exploration of the Ionizable Metal Cluster-Electrode Surface Analogy: Infrared Spectroelectrochemistry of $[\text{Pt}_{24}(\text{CO})_{30}]^n$, $[\text{Pt}_{26}(\text{CO})_{32}]^n$, and $[\text{Pt}_{38}(\text{CO})_{44}]^n$ ($n=0$ to -10) and Comparisons with Potential-Dependent Spectra of CO Adlayers on Platinum Surfaces. *J. Am. Chem. Soc.* **1992**, *114* (15), 6159–6169.
10. Rabilloud, F.; Harb, M.; Ndome, H.; Archirel, P. UV-Visible Absorption Spectra of Small Platinum Carbonyl Complexes and Particles: A Density Functional Theory Study. *J. Phys. Chem. A* **2010**, *114* (23), 6451–6462.
11. Barrio, L.; Liu, P.; Rodríguez, J. A.; Campos-Martín, J. M.; Fierro, J. *J. Chem. Phys.* **2006**, *125*, 164715–164719.
12. Sun, Y.; Zhang, M.; Fournier, R. *Phys. Rev. B* **2008**, *77*, 075435–075442.
13. Kang, J. H.; Menard, L. D.; Nuzzo, R. G.; Frenkel, A. I. *J. Am. Chem. Soc.* **2006**, *128*, 12068–12069.
14. Singh, J.; Nelson, R. C.; Vicente, B. C.; Scott, S. L.; van Bokhoven, J. A. *Phys. Chem. Chem. Phys.* **2010**, *12*, 5668–5677.
15. Car, R.; Parrinello, M. *Phys. Rev. Lett.* **1985**, *55*, 2471–2474.
16. Kresse, G.; Furthmüller, J. Efficient Iterative Schemes for *ab initio* Total-Energy Calculations Using a Plane-Wave Basis Set. *Phys. Rev. B* **1996**, *54* (16), 11169–11186.
17. Hafner, J. *Ab-initio* Simulations of Materials using VASP: Density-Functional Theory and Beyond. *J. Comput. Chem.* **2008**, *29*, 2044–2078.
18. Feynman, R. P. *Phys. Rev.* **1939**, *56*, 340–343.
19. Vanderbilt, D. Soft Self-Consistent Pseudopotentials in a Generalized Eigenvalue Formalism. *Phys. Rev. B* **1990**, *41*, 7892–7895.
20. Kilin, D.; Tsemekhman, K.; Kilina, S.; Balatski, A.; Prezhdo, O. Photoinduced Conductivity of a Porphyrin-Gold Composite Nanowire. *J. Phys. Chem. A* **2009**, *113*, 4549–4556.
21. Okamoto, Y. *Chem. Phys. Lett.* **2006**, *429*, 209–216.
22. Mager-Maury, C.; Bonnard, G.; Chizallet, C.; Sautet, P.; Raybaud, P. H₂-Induced reconstruction of Supported Pt Clusters: Metal-Support Interaction versus Surface Hydride. *ChemCatChem* **2011**, *3* (1), 200–207.
23. Borgarello, E.; Kiwi, J.; Pelizzetti, E.; Visca, M.; Grätzel, M. Photochemical Cleavage of Water by Photocatalysis. *Nature* **1981**, *289*, 158–160.
24. Wang, J.; Román-Pérez, G.; Soler, J. M.; Artacho, E.; Fernández-Serra, M. V. Density, Structure, and Dynamics of Water: The Effect of van der Waals Interactions. *J. Chem. Phys.* **2011**, *134*, 024516–024525.
25. Jensen, S.; Kilin, D. Anatase (100) Thin Film Surface Computational Model for Photoelectrochemical Cell. *Int. J. Quantum Chem.* **2012**, *112* (24), 3874–3878.

26. Zhang, Y.; Kilin, D. Computational Modeling of Wet TiO₂ (001) Anatase Surfaces Functionalized by Transition Metal Doping. *Int. J. Quantum Chem.* **2012**, *112* (24), 3867–3873.
27. Inerbaev, T. M.; Hoefelmeyer, J. D.; Kilin, D. S. Atomistic Simulation of Dissipative Charge Carrier Dynamics for Photocatalysis. *MRS Proc.* **2012**, *1390* (mrsf11), mrsf11-1390-i03-03.
28. Inerbaev, T. M.; Hoefelmeyer, J. D.; Kilin, D. S. Photoinduced Charge Transfer from Titania to Surface Doping Site. *J. Phys. Chem. C* **2013**, *117* (19), 9673–9692.
29. Chen, J. C.; Schmitz, A.; Kilin, D. Computational simulation of the p-n doped silicon quantum dot. *Int. J. Quantum Chem.* **2012**, *112*, 3879.

Chapter 8

Electronic Properties of Silver Doped TiO_2 Anatase (100) Surface

Stephanie Jensen and Dmitri Kilin*

Department of Chemistry, The University of South Dakota, Vermillion,
South Dakota 57069, United States

*E-mail: Dmitri.Kilin@usd.edu

Using computational approaches, one is able to better understand electron transfer and specific atomistic behaviors in semiconductor materials; it is also more cost and time effective than experimental methods. If computed characteristics of a material show promise, experimentalists can synthesize and further examine the structure of such material. In this letter, we dope TiO_2 thin film surfaces with silver, which has been shown to increase photoelectric properties to induce H_2 production. In the computational study, TiO_2 anatase thin film (100) surface is doped with silver. The formulas used are $\text{Ti}_{32}\text{O}_{72}\text{H}_{16}$ and $\text{Ag}_2\text{Ti}_{30}\text{O}_{72}\text{H}_{16}$ with the (100) crystallographic surface exposed and covered with a monolayer of water. Optimization is completed by DFT and PBE functional in VASP software. The density of states, absorption spectra, partial density of states, partial charge densities, molecular dynamics, and non adiabatic couplings are compared between doped and un-doped as the standard. According to our calculations, holes relax faster than electrons. The information can be used to show the mechanism of how doping the titanium dioxide nanocrystals facilitates photo induced charge transfer at the surfaces, which is useful in understanding photoelectrochemical water splitting.

Introduction

Computational methods and software allow an extremely cost effective solution to the search for a solar energy material that can turn absorbed photons into usable electrical or chemical energy (1, 2). VASP (3, 4) software allows one to obtain the properties of prospective materials without the cost of chemicals, lab equipment, and valuable time. Doped titanium dioxide (TiO_2) (2, 5) is known to convert and store solar energy by dye sensitizing for photo induced charge separation (6, 7). Specifically, concentration will be made on the chemical energy possibly created by the aforementioned processes in which water is reduced to form hydrogen and oxidized to form oxygen gases (2, 8, 9).

Due to TiO_2 's inexpensiveness, non toxicity, and high photo-stability, it has become well studied as a material base for solar cells (8). Metal oxide crystal shape, size and structure effect how the material will perform as an energy conversion material (10). It is known that each phase and, further, surface of TiO_2 will act differently as a solar energy converter. Rutile has long been touted as the most stable polymorph (11), but due to recent studies, it is suggested anatase at the nano scale (50 nm or less) is more stable (12). Anatase exhibits a substantial lifetime of photo excitations. The structure of the anatase polymorph is stable up to 973 K. At 973K, anatase transforms to rutile (13, 14).

The (100) surface of TiO_2 is not found in natural crystal form and therefore not studied often; however, the surface can be found in powder form and is predicted to be very stable (15). Therefore, this letter focuses on the properties of the (100) surface through computational methods to determine whether experimental time and money would be worth the effort.

One disadvantage of TiO_2 is its band gap size of 3.2 eV (16). It is necessary to have a band gap of 1.23 eV in order to split water (17). In order to overcome the band gap obstacle, titanium dioxide is doped to increase photocatalytic activity (18–23). Silver doped titanium oxide material has many uses ranging from an antimicrobial material (24), humidity sensor (25), and increased light absorption (26). The synthesis for silver doped titanium dioxide is also known (27).

Born-Oppenheimer approximation does not work efficiently to calculate the hot carrier relaxation in molecules and nanostructures, which is due to energy flow between electronic part and nuclear part (28, 29). The electronic relaxation process based on the concept of surface hopping between potential energy surfaces has been done successively by several groups (30). Various methods ranging from DFT (31–33) to high-precision non-adiabatic excited state molecular dynamics approach (34–37) have been implemented to model this process. The utility of molecular dynamics trajectory for determining the electron-to-lattice coupling in semiconductors seems very efficient (38, 39). The integration of TDDFT and molecular dynamics methods was recently proven to be an efficient approach (40, 41).

According to Egorova et al. (43), multilevel Redfield theory is considered as a useful and practical approach for electronic relaxation. This theory is efficient in the limits of long time dynamics, low couplings, and multiple electronic states (42–50). The choice of this theory is rationalized by a compromise between precision and practical efficiency. The balance between the following

benefits, shortcomings, and features of Redfield theory is taken into account while selecting a method for this work: (i) Redfield theory is one of the specific implementations of the density matrix equation of motion and, therefore it does describe broader range of phenomena than wavefunction or surface hopping or Pauli Master equation approaches: (ii) Redfield theory can be easily combined with ab initio computation. It is clear which parameters need to be computed and used, with an efficient algorithm for computation. (iii) Redfield theory might not be the most precise: for example a method of non-equilibrium Green's function is more general and potentially precise but much less practical (51). There is an attempt to combine Redfield theory with electrons-to-lattice coupling to achieve on-the-fly electron and hole relaxation (52, 53). Optimum results are expected in the following conditions: ions are considered as point charges, lattice vibrations instantaneously equilibrate with a thermostat, coupling autocorrelation function decays abruptly leading to Markov approximation, vibrational reorganization is neglected, and excited state potential energy surfaces are assumed to have the same shape as the ground state.

In this work, we explore silver as a possible dopant to the anatase (100) titanium dioxide photoelectrochemical cell by analyzing and interpreting electronic properties such as density of states, visible light absorption spectrum, partial charge densities, along with non-adiabatic molecular dynamics, energy fluctuations, and couplings by heat based excitation. Finally, using the above computations, the relaxation rates of likely electron and hole pairs are calculated for probable excitation pairs. The studied model and typical photo excited processes are schematically represented in Figure 1(b, c). One of the goals of the present work is to identify the dependence of the relaxation rates on presence of orbitals contributed by doping in the band gap. The relaxation rates are symbolically partitioned on cooling of electron (K_e), cooling of hole (K_h), hole, and recombination (K_r). The computations are used to test the hypothetical relations between such rates for doped (^{dop}) and un-doped (^{un}) surfaces

$$K_e^{\text{un}} \geq K_e^{\text{dop}}$$

$$K_h^{\text{un}} \geq K_h^{\text{dop}}$$

$$K_r^{\text{un}} \ll K_r^{\text{dop}}$$

$$K_e^{\text{un}} + K_h^{\text{un}} + K_r^{\text{un}} < K_e^{\text{dop}} + K_h^{\text{dop}} + K_r^{\text{dop}}$$

The computed values for the rates of relaxation are tested to follow these hypothetical inequalities. The computed rates are found to depend on the density of states.

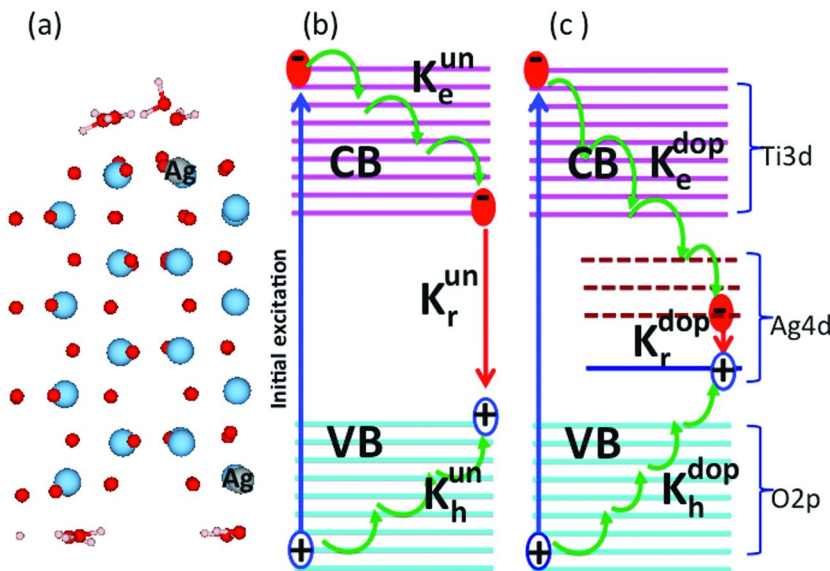


Figure 1. Optimized geometry (a) and schematic of relaxation (b)-(c). Optimized simulation cell is shown in panel (a). Addition of silver doping (Ag, grey sphere) induces little corrugation and buckling of the surface. Optimization of the geometry was complete with fixed size of the simulation cell. We hypothesize that increasing the lattice constant for a given concentration may reduce buckling.

Surface water molecules have shorter distance to Ag than to Ti. Schematic energy diagram is sketched for un-doped (b) and doped (c) models. Both models contain unfilled Ti3d orbitals, and both models contain filled O2P orbital. Only doped model contains Ag4d orbitals with some being occupied and some being unoccupied. In each model a photo excitation (blue arrow) is followed by cooling of electron (K_e), cooling of hole (K_h), and recombination (K_r , red arrow). One of the goals of the present work is to identify the dependence of the cooling rates on presence of doping orbitals in the band gap. Note that one can compare only processes induced by light of the same transition energy.

Methods

Consider the fictitious one electron Kohn-Sham (54, 55) equation

$$(1) \quad \left(\frac{-\hbar^2}{2m} \nabla^2 + v[\vec{r}, \{\vec{R}_I\}, \rho(\vec{r})] \right) \psi_i^{KS}(\vec{r}, \{\vec{R}_I\}) = \varepsilon_i(\{\vec{R}_I\}) \psi_i^{KS}(\vec{r}, \{\vec{R}_I\}).$$

Where the first term corresponds to kinetic energy T and uses symbol of gradient $\nabla = (\frac{\partial}{\partial x}, \frac{\partial}{\partial y}, \frac{\partial}{\partial z})$. In equation (1), one finds the set of one-electron orbitals $\varphi_i^{KS}(r, \{\vec{R}_I\})$ and the respective orbital energy levels $\varepsilon_i(\{\vec{R}_I\})$. The orbitals are combined with the orbital occupation function f_i for constructing the total density of electrons

$$(2) \quad \rho(\vec{r}) = \sum_{i \leq HOMO} \rho_{ij} \rho_i^{KS}(\vec{r}) , \rho_{ij} = \delta_{ij} \rho_{ii} , \rho_{ii} = f_i$$

and rests on partial charge density $\rho_i^{KS}(\vec{r})$ of orbital number i . In order to account for dynamical changes of occupation function of f_i , we use density matrix approach as introduced below.

$$(3a) \quad \rho_i^{KS}(\vec{r}) = \psi_i^{KS*}(\vec{r}) \psi_i^{KS}(\vec{r})$$

$$(3b) \quad \rho_i^{KS}(z) = \iint dx dy \rho_i^{KS}(\vec{r})$$

The total density determines the total energy, $E_{total} = E_{total}[\rho]$, and potential

$$(4) \quad v[\vec{r}, \rho(\vec{r})] = \frac{\delta}{\delta \rho} (E^{tot}[\rho] - T)$$

defined as the functional derivative of the total energy in respect to variation of the total density. It includes interactions of electrons with ions and three electron iterations: Coulomb, correlation, and exchange. The rectangular brackets symbolize a functional. Equations (1)-(4) are solved in the iterative, self-consistent manner using VASP software with PBE functional (56, 57) method to solve equations (1)-(4). Positions of ions $\{\vec{R}_I\}$ enter these equations as parameters. The following were computed and analyzed for silver doped titanium dioxide nanocrystals: band energies, density of states, absorption spectra, partial charge densities, molecular dynamic fluctuations, and non adiabatic couplings.

Geometry Optimization

Geometries of all studied models are optimized by finding such positions of ions $\{\vec{R}_I\}$, which provide minimal total energy of the model, according to DFT procedure.

Density of States

The density of states is calculated by taking the sum total of the energy level differences and applying the Dirac delta function.

$$(5a) \quad n(\varepsilon) = \sum_i \delta(\varepsilon - \varepsilon_i)$$

$$(5b) \quad n'(\varepsilon) = \sum_i f_i \delta(\varepsilon - \varepsilon_i)$$

Occupied orbitals $n'(\varepsilon)$ are filled in with red while unoccupied orbitals $n(\varepsilon)$ have no fill. The valence band (VB) includes all orbitals with index less than and including HOMO, where $f_i \leq 1/2$, $i \leq HOMO$, while the conduction band (CB) includes orbitals with index greater than and including LUMO, where $f_i \geq 1/2$, $i \geq LUMO$. Here HOMO and LUMO abbreviate for highest occupied molecular orbital and lowest unoccupied molecular orbital, respectively. The band gap is defined as $band\ gap = |\varepsilon_{LUMO} - \varepsilon_{HOMO}|$. The density of states allows for the determination

of whether the dopant will act as an acceptor or donor purely based on energy differences as follows

$$(6) \quad E_a = \varepsilon_{LUMO, Ag \text{ doped}} - \varepsilon_{HOMO, un-doped},$$

$$(7) \quad E_d = \varepsilon_{LUMO, un-doped} - \varepsilon_{HOMO, Ag \text{ doped}}.$$

Here, E_a and E_d are referred to as charge carrier activation energy for acceptor and donor.

Optical Properties

The transition dipole moment (8) is the electric dipole moment matrix element for the transition between the initial state i and final state j .

$$(8) \quad \vec{D}_{ij} = e \int \psi_i^* \vec{r} \psi_j d\vec{r}$$

It uses the summation of the position of all electrons in the system (\vec{r}) and elementary charge e . The transition dipole moment is then used as a weight when calculating oscillator strength (9).

$$(9) \quad f_{ij} = \left| \vec{D}_{ij} \right|^2 \frac{4\pi m_e v_{ij}}{3\hbar e^2}$$

In (9), m_e is the mass of an electron, \hbar is Planck's reduced constant, v_{ij} is resonant frequency, and e is the charge of the electron. The oscillator strength gives the probability of absorbing light between the i and j transition, which is then used as a weight to calculate absorption in (10).

$$(10) \quad a(\varepsilon) = \sum_{ij} f_{ij} \delta(\varepsilon - \Delta\varepsilon_{ij})$$

The summation of energy differences with the Dirac delta function applied multiplied by the oscillator strength gives a direct relationship between absorption and oscillator strength. Note that absorption of light can modify occupation function as in equation (2).

Partial Charge Density

The individual charge densities for the atoms in the system can be calculated to locate where the charge is for each individual Kohn-Sham orbital i defined in equation (2). Partial charge uses the summation over all orbitals contributing to the electron density in the vicinity of atom I

$$(11) \quad q_I = \sum_{i \leq HOMO} \sum_{nlm} \left| C_{nlm,I}^i \right|^2$$

where $N=HOMO$ represents the number of electrons and $C_{nlm,I}^i$ is the linear combination of atomic orbitals (LCAO) weighting contributions of Kohn-Sham

orbitals. Since VASP provides $\psi_i^{KS}(\vec{r})$ as in equation 1, $C_{nlm,I}^i$ is calculated as follows:

$$(12a) \quad C_{nlm,I}^i = \int \Psi_{nlm}(\vec{R}_I - \vec{r}) \psi_i^{KS}(\vec{r}) dr^3$$

$$(12b) \quad \sum_{nlm,I} |C_{nlm,I}^i|^2 = 1$$

Here $\Psi_{nlm}(\vec{R}_I - \vec{r})$ is the atomic orbital centered at ion # I , i is the index of Kohn-Sham orbital, and n,l,m are principle, orbital, and magnetic quantum numbers. In what follows we analyze relative contribution of atomic orbitals with given orbital quantum numbers $l=0,1,2$ of s,p,d character into given Kohn-Sham orbital.

$$(12c) \quad P_l^i = \sum_{nlm,I} |C_{nlm,I}^i|^2$$

Note that for each Kohn-Sham orbital, relative contributions add to one $P_{l=0}^i + P_{l=1}^i + P_{l=2}^i + \dots = 1$.

Molecular Dynamics, Fluctuations, and Non-Adiabatic Couplings

Electronic structure of atomic models was explored at equilibrium-optimized geometry and along nuclear trajectory $\{\vec{R}_I(t)\}$ modeling system interfacing a thermostat. Positions of ions enter DFT equations as parameters as in equation (1).

Electronic dissipative transitions $\left(\frac{d\rho_{jk}}{dt}\right)_{diss}$ are computed along molecular dynamics trajectory for positions of ions $\{\vec{R}_I(t)\}$ with initial conditions for positions $\{\vec{R}_I(t=0)\}$ and velocities $\left\{\frac{d}{dt}\vec{R}_I(t=0)\right\}$ representing ambient temperature. On-the-fly nonadiabatic couplings are computed along nuclear trajectory as

$$(13) \quad V_{ij}(t) = \frac{1}{\Delta t} \int d\vec{r} \varphi_i^{KS*}(\{\vec{R}_I(t)\}, \vec{r}) \varphi_j^{KS}(\{\vec{R}_I(t + \Delta t)\}, \vec{r}).$$

Then, we process autocorrelation function of these couplings

$$(14) \quad M_{ijkl}(\tau) = \frac{1}{T} \int_0^T dt V_{ij}(t + \tau) V_{kl}(t).$$

A Fourier transform of coupling autocorrelation function provides components of Redfield tensor, which control dynamics of density matrix

$$(15) \quad \left(\frac{d\rho_{jk}}{dt}\right)_{diss} = \sum_{lm} R_{jklm} \rho_{lm}.$$

Specific initial excitations by a photon, $\hbar\Omega_{AB} = \varepsilon_B - \varepsilon_A$, occur between orbitals A and B. This excitation is described by density matrix at time $t=0$.

$$(16a) \quad \rho_{ij}(0) = \delta_{ij} (f_i - \delta_{iA} + \delta_{iB}).$$

Time evolution of electronic state is calculated by solving the equation of motion as follows:

$$(16b) \quad \dot{\rho}_{ij} = -\frac{i}{\hbar} \sum_k (F_{ik}\rho_{kj} - \rho_{jk}F_{ki}) + \left(\frac{d\rho_{ij}}{dt}\right)_{diss}.$$

Electronic transitions are facilitated by thermal fluctuations of ions. Solution of equation 16b provides time dependent elements of density matrix $\rho_{kj}(t)$. Of Special importance are diagonal elements $\rho_{jj}(t)$, which determine time-dependent occupations of Kohn-Sham orbitals. With the above information, charge density distribution, rate of energy dissipation, and rate of charge transfer can be calculated. Specifically, the distribution of charge as function of energy reads

$$(16c) \quad n''(\varepsilon, t) = \sum_i \rho_{ii}(t) \delta(\varepsilon - \varepsilon_i).$$

The difference of non-equilibrium distribution presented in equation 16c and the equilibrium distribution presented in equation 5b provides the comprehensive explanation of electron and hole dynamics, as function of energy and time. The change of population with respect to the equilibrium distribution is then expressed as

$$(16d) \quad \Delta n(\varepsilon, t) = n''(\varepsilon, t) - n'(\varepsilon).$$

This equation describes dynamics of a population gain when $\Delta n > 0$ and a population loss when $\Delta n < 0$ at energy ε , which corresponds to the electron and the hole parts of an excitation.

Results

Model Creation and Geometry Optimization

The models were created by taking bulk titanium dioxide crystal and then cutting it along the (100) direction to expose the surfaces. For the doped model, a titanium atom at each top and bottom surface was replaced with a silver atom creating a 6.25% doping. Four water molecules were then placed on each (100) surface, representing a monolayer and providing an octahedral coordination to each surface metal ion. Additional layers of water are neglected for minimizing computational expenses. Each model was optimized geometrically in VASP software by calculating the lowest total energy using DFT method. Ground state geometry of the resulting doped model is shown in Figure 1(a).

Distances between surface metal and oxygen atoms are found for doped and un-doped models. The distances are 1.85 and 2 angstroms, respectively. Therefore, one can assume the titanium binds to oxygen slightly more strongly than the silver to oxygen at the surface.

Both models are optimized geometrically in VASP according to the lowest total energy, found in Table 1.

Table 1. Energies and properties of un-doped and silver doped anatase (100) surface are above. Ag increases the number of electrons and lowered the total energy along with the band gap. Also, the acceptor energy and donor energy are calculated as in equations 6 and 7.

Dopant	# Electrons	Total Energy	Fermi Energy	HOMO	HOMO Energy	LUMO	LUMO Energy	Band Gap	# Added States (BG)	Group #	Aufbau	E_{acceptor}	E_{donor}	P dopant	n dopant
Standard	576	-974.39	-2.0039	288	-1.9324	289	0.157	2.0894	N/A	4	[Ar] 4s ² 3d ²	N/A	N/A	Not Applicable	
Ag	590	-941.63	-1.4776	295	-1.2983	296	-1.2791	0.0192	6	9	[Kr] 5s ¹ 4d ¹⁰	1.2917	0.8506		X

Density of States

The density of states (DOS) images of un-doped TiO_2 and silver doped TiO_2 are shown in Figure 2. The un-doped DOS has a band gap of 2.0894 eV as seen in Table 1. The HOMO is at energy level -1.93 eV with LUMO at 0.16 eV. The known band gap of un-doped TiO_2 is 3.2 eV; however, the shorter band gap is a known expense of DFT method due to approximations which can be corrected by GW and BSE methods (58). It is noted that the valence band is completely full while the conduction band is empty.

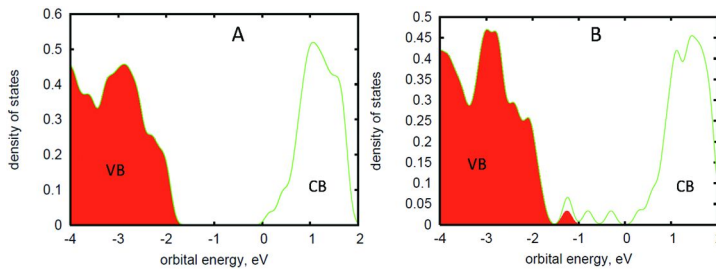


Figure 2. Density of states of un-doped (A), originally in (61), and silver doped (B) anatase (100) surface TiO_2 photoelectrochemical thin film crystal is shown. The added states due to the dopant are clearly seen at $-2 < \epsilon < 0$. The much smaller band gap is also noted. For un-doped model, DOS at the edges of VB and CB have different values: $\text{DOS}(E_{VB} \cong -2 \text{ eV}) \cong 0.25 \text{ eV}^{-1}$ and $\text{DOS}(E_{CB} \cong 0 \text{ eV}) \cong 0.05 \text{ eV}^{-1}$. Absolute value of VB edges is about 3-5 times greater than that of CB edge. According to the aforementioned data, one expects that the holes should relax 3-5 times faster than the electrons.

The silver doped DOS clearly shows added states in the original band gap compared to the un-doped DOS. In Table 1, it is shown that 6 states are added and the band gap has decreased to 0.0192 eV in comparison with the un-doped simulation. With the energy values of HOMO' and LUMO', one can try to predict if the dopant will act as either a donor or acceptor by using equations 6 and 7.

According to the calculations of E_a and E_d in Table 1, it is theorized that this thin film crystal would act as a p-dopant, or donor, since $E_a > E_d$. This states that the LUMO of the un-doped crystal is closer in energy to the HOMO' of the Ag doped crystal than the LUMO' of doped to HOMO of un-doped.

Optical Absorption Spectrum

Figure 3 shows the optical absorption spectra for the un-doped and Ag doped model as a function of transition energy (eV) on the left and wavelength (nm) on the right. It is noted that the un-doped model absorbs light in the 2.1-3 eV range. The doped model also has strong absorption in 2.1-3 eV region. Several electron-hole pairs are needed to fully describe an optical transition at given energy (59). At each transition energy, an excitation is represented by a superposition of multiple electron hole pairs. However, partial contributions of those are unequal. For each transition energy, one can identify a specific electron-hole pair providing leading contribution to optical absorption.

The most probable transitions contributing to the absorption in this range are indicated in Table 2, and they primarily correspond to oxygen 2p to Titanium 3d transitions. In addition to the main absorption band, the dopant contributes additional absorption features at lower transition energies. It is clear that the silver doped crystal increases the range of absorption.

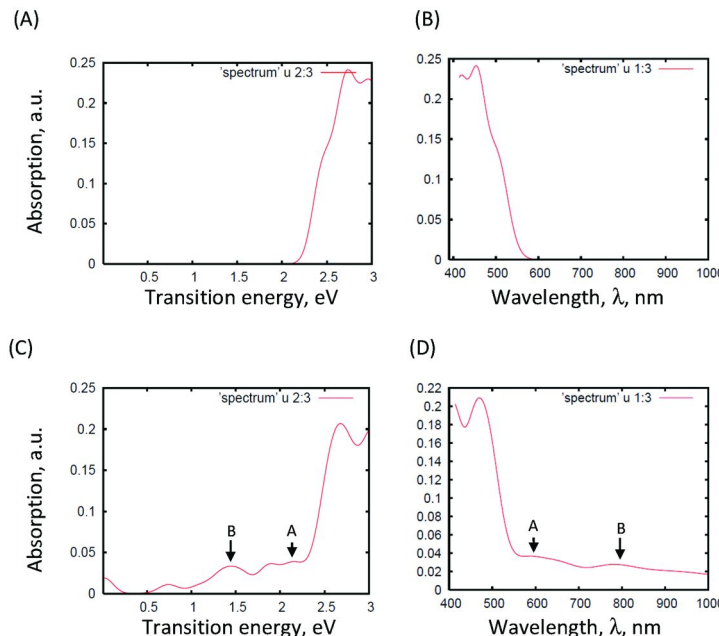


Figure 3. The optical absorption spectra of un-doped (A),(B) and silver doped (C),(D) anatase (100) surface TiO_2 photoelectrochemical thin film as function of transition energy (A),(C) and wavelength (B),(D). It is very clear that doping increases the range of absorption. Also, two broad peaks are noted in the added absorption due to Ag labeled as A at 582.74 nm and B at 806.93 nm. It is found that both of these are likely p to d transitions.

Table 2. Table 2 presents the important aspects in the likely transitions for electron-hole relaxation rates for probable excitation pairs in Ag doped (Figure 8) and un-doped (Figure 9) anatase (100) surface. A large oscillator strength value is wanted as well as a small enough transition energy. The electron relaxation and hole cooling rates are also shown. For all transitions with the Ag doped model (excluding HOMO' and LUMO'), the hole cools faster than the electron relaxes due to smaller energy gaps as seen in Figure 9. Interestingly, excitations of lower energies relax slightly faster. The un-doped model also has all holes relaxing faster.

Figure Identification	Oscillator Strength	$\varepsilon_{\text{transition}}$ (eV)	Occupied Orbital	$\varepsilon_{\text{occupied}}$ (eV)	Unoccupied Orbital	$\varepsilon_{\text{unoccupied}}$ (eV)	K_e ps ⁻¹	K_h ps ⁻¹	$K_e + K_h$ ps ⁻¹
Un-doped	8. A	2.34	2.42	281	-2.2781	289	0.1080	0	3.2868
	8. B	1.57	2.43	280	-2.2877	289	0.1080	0	3.0638
	8. C	1.40	2.72	280	-2.2877	291	0.3526	0.7282	3.0638
	8. D	1.38	2.66	284	-2.1455	292	0.4811	0.7248	4.6221
	8. E	1.27	2.54	284	-2.1455	290	0.3229	0.7005	4.6221
Doped	9. A	2.54	2.55	290	-2.0041	300	0.5487	0.4550	2.6782
	9. B	2.11	2.46	285	-2.1471	299	0.3108	0.7131	1.4763
	9. C	1.62	2.64	280	-2.3303	299	0.3108	0.7131	1.2853
	9. D	0.94	2.70	287	-2.0871	301	0.6115	0.4474	1.6185
	9. E	0.621	0.03	295	-1.2583	296	-1.2294	0	0.0000

Two additional peaks at 582.74 nm and 806.93 nm are noted as “A” and “B” on the silver doped spectra. By investigating the computed oscillator strength values as in equation 9, the transitions are known to be between the states of A) HOMO'-45 to LUMO'+1 and B) HOMO-16 to LUMO+1. By inspecting Figure 4, the states of HOMO'-45, LUMO'+1, and HOMO'-16 are found along with which type of orbital is mostly occupied: s, p, or d. The PDOS confirms that the transition of A is most likely a mix of p-to-p and p-to-d orbital transitions confirmed by the partial density of states images. The transition of B at 806.93 nm is found to also be likely a mix of p-to-p and p-to-d orbital transitions. It is almost certain the initial orbital is a p orbital; however, the accepting orbital is less convincing as the PDOS shows a 0.528 density of electrons in the p orbitals and 0.289 in the d orbital. Two scenarios are possible: a hybrid orbital is the accepting orbital which would be the d orbital of Ag and p orbitals of surrounding oxygen atoms or a p to d transition, in which Figure 5 shows the d orbital would be that of the Ag dopant on the top surface.

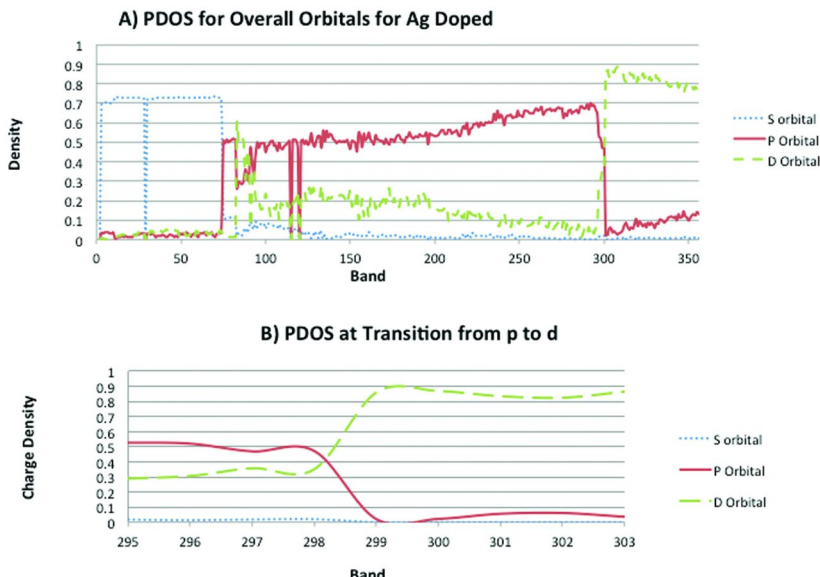
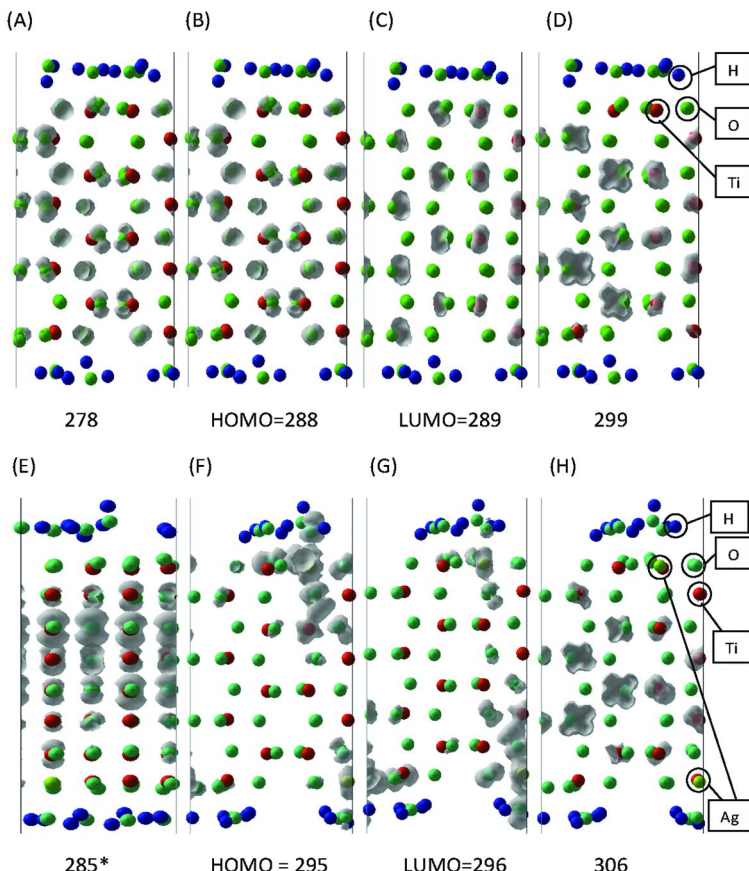


Figure 4. The partial density of states for the silver doped model. It is easy to see the dominant orbitals transition from s, p, to d in panel (A). The states that have mainly s orbital occupations are from 1-74, mainly p from 75-295, and mainly d from 301-356. Some d character does show in the early p dominance states. Inspection of the partial charge densities show the s character is of that of the oxygen atoms, the p character is also of oxygen atoms, and the lower state d character is from titanium and not silver. The states from 296-300, seen in panel (B), are a transition from p orbitals of oxygen to d orbitals. Figure 6 shows this is the period where the charge density is among the Ag dopant and surrounding oxygen atoms. The predominant d orbital character at states 301-356 are due to titanium atoms.

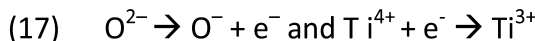
Partial Charge Densities

Figures 5 and 6 give the partial charge density images of the un-doped and Ag doped thin films. The partial charge densities of the un-doped crystal exhibit a straightforward trend. Specifically, occupied orbitals have charge on the p orbitals of oxygen while unoccupied orbitals have charge concentrated on the d orbitals of titanium. The charge density of Ag doped starts on the p orbitals of oxygen as in the un-doped model and stays consistent for the orbitals far below HOMO'. As HOMO' approaches, the charge is observed in the vicinity of the Ag dopant. Once at HOMO', hybrid orbitals including Ag, surrounding atoms, and water molecules are formed. LUMO' and orbitals close to it also show the Ag centered hybrid orbitals. The states far above HOMO' are composed of the d orbitals of the titanium atoms.



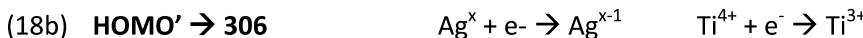
*Figure 5. Partial charge densities $\rho_i(\vec{r})$ of representative orbitals for un-doped (A)-(D) and silver doped (E)-(H) models of TiO_2 anatase (100) surface are shown in Figure 5. In panels (A)-(D) atoms are color-coded as Blue (black) = Hydrogen, Green (light grey) = Oxygen, Red (medium grey) = Titanium. In panels (E)-(H) atoms are color coded as Blue (black) = Hydrogen, Aqua (light grey) = Oxygen, Red (medium grey) = Titanium, Lime Green (medium grey) = Silver. Grey clouds represent the charge density at isosurfaces $\rho_i(\vec{r}) = 20$. The un-doped crystal has a very disperse charge density at HOMO-20, HOMO, LUMO, and LUMO+20. The charge transfers from p orbitals of oxygen to d orbitals of titanium when applying excitation from occupied to unoccupied states. The Ag doped shows a different case. HOMO'-20 shows the charge on the p orbitals of oxygen concentrated in the middle of the crystal. At HOMO', the charge centers around the Ag dopant at the top surface with a hybrid orbital of surrounding atoms; LUMO 'shows almost the exact same thing but the charge is concentrated at the bottom surface. LUMO'+20 has charge concentrated at the center in the d orbitals of titanium atoms. * Star symbol indicate states which are exposed at a 90 degree angle to better see the p orbitals around the oxygen atoms.*

For the un-doped cell, the proposed reaction when going from unoccupied to occupied states is



The charge is dispersed with no localization on the surfaces. Also, no mixing of the orbitals is noted with the surface water.

The partial charge densities show a very different story for the Ag doped thin film photoelectrochemical cell. At HOMO' and LUMO', most of the charge is located at the surface. The proposed reactions are (where $x > 0$):



At HOMO'-10 and LUMO'+10, the charge is localized in the center of the crystal on oxygen and titanium respectively. The charge at HOMO' and LUMO' is centered at the dopants with one surface being favored in each case. Also, the orbital mixing with the surface water molecules suggests that if the cell were excited by a photon, the charge would reach the surface molecules and induce the redox reaction on water to form hydrogen and oxygen.

Molecular Dynamics

Here we model why and how occupation function f_i of a given orbital evolves in time. The electronic energy changes $\varepsilon_i(\{\vec{R}_I(t)\})$ with time for individual orbitals in the interval of $i = [HOMO-20, HOMO, LUMO, & LUMO+20]$ for both cells are shown in Figure 7. The added states from silver into the original band gap are easily seen between the empty space of the un-doped molecular dynamics image. It is also noted that the silver doped states tend to have larger amplitudes of orbital energy variation compared to that of the un-doped cell. The energy of an orbital and its fluctuation is related to the delocalization of orbital. For the states contributed by Ag doping, it is noted in Figure 6B that the states are concentrated around few atoms. Therefore, it is expected that these states will have much larger fluctuations. In the un-doped model, Figure 6A, the orbitals are very disperse and show smaller fluctuations.

One offers a hypothetic explanation of this effect as follows. The Energy of an orbital ε_i is perturbed by motion of a given ion \vec{R}_I only in case spatial distribution of this orbital is large enough in the vicinity of this ion $|\varphi_i^{KS}|^2_{\vec{r}=\vec{R}_I} > 0$. Delocalized orbitals are nonzero at any area inside the slab; therefore, random distortions of different ions from their equilibrium provide contributions of a different sign into the energy of an orbital. An average of such contributions adds up in a destructive interference pattern and hence is close to zero. The situation is different for localized orbitals: being dependent on distortion of only one or few ions, the relevant orbital energies get substantial fluctuations.

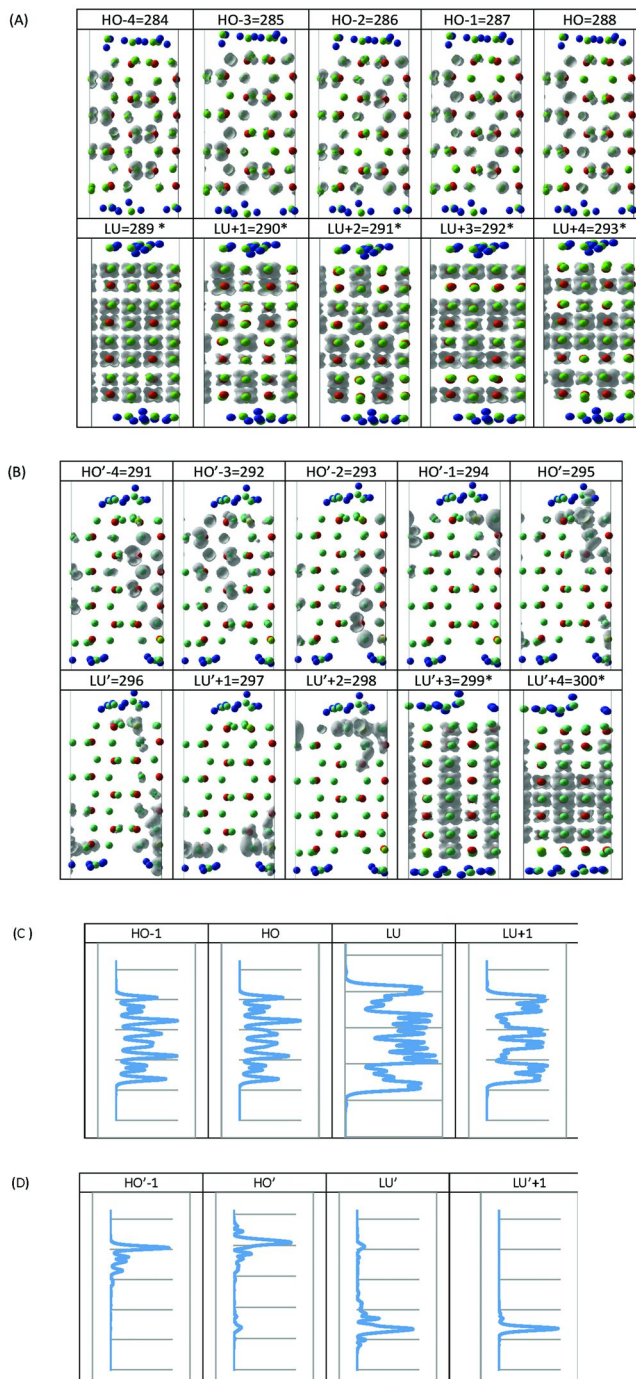


Figure 6. The partial charge densities of un-doped (A) and silver doped (B) models for orbitals in the interval from HOMO-4 to LUMO+4. Note that for

un-doped model $HOMO=288$ and for Ag doped model $HOMO'=295$. * Star symbol indicate states which are exposed at a 90 degree angle to better see the p orbitals around the oxygen atoms. (C, D) Shown are integrated charge densities represented as 1-D distributions for orbitals $HOMO-1$, $HOMO$, $LUMO$, and $LUMO+1$ for un-doped (C) and Ag-doped (D) models, defined in Eq. 3a. Note that for un-doped model $HOMO=288$ and for Ag doped model $HOMO'=295$. The integrated charge density represented as 1-D distributions show how isolated the charge is for specific orbitals around HO and LU. The Ag doped model has much higher charge density at the Ag dopant compared to that of the un-doped model.

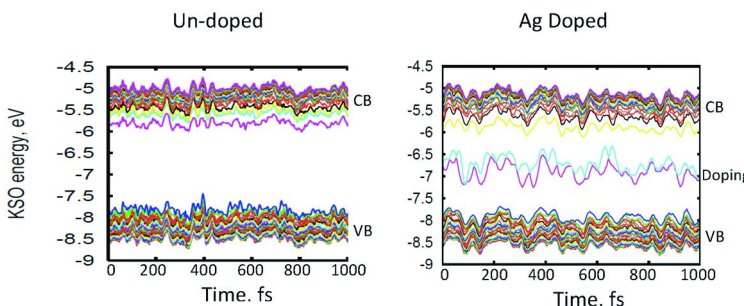


Figure 7. Thermal fluctuations of energy of orbitals along molecular dynamics trajectory for un-doped and silver doped models are shown for the orbitals in the range from $HOMO-10$ to $LUMO+10$. The orbital energy changes with time for individual orbitals of $HOMO-20$, $HOMO$, $LUMO$, & $LUMO+20$ as can be seen by the individual bands. Compared to the un-doped molecular dynamics image, added states are noted in the original band gap and exhibit substantial fluctuations in energy.

While the band gap size for both models stays consistent, it is noted that the valence band ends at about -8 eV while the conduction band starts at about -8 eV in Figure 7. In the DOS images of Figure 2, the VB ends at -2 eV and the CB begins at 0 eV. Please see supplemental section for the detailed explanation.

Non-Adiabatic Relaxation Dynamics

For the Ag doped and un-doped models, probable photo-excitations and their relaxation dynamics are studied. The excitations are single unoccupied to occupied state excitations. Due to the large oscillator strength values and low transition energies, initial photo-excitations A and B are most likely to occur. The un-doped model has likely initial photo-excitations depicted in Figure 8. Each photo-excitation is followed by a certain relaxation pathway. Specifically, electron relaxes to LUMO, hole relaxes to HOMO. For each case, the hole is cooling faster than the electron, as seen in the rates summarized in Table 2. This

is due to the differences in the VB and CB edges. DOS, Figure 2, at the edges of VB and CB have different values: $DOS(E_{VB} \cong -2 \text{ eV}) \cong 0.25 \text{ eV}^{-1}$ and $DOS(E_{CB} \cong 0 \text{ eV}) \cong 0.05 \text{ eV}^{-1}$. Absolute value of VB edges is about 3-5 times greater than that of CB edge. According to the aforementioned data, one expects that the holes should relax 3-5 times faster than the electrons.

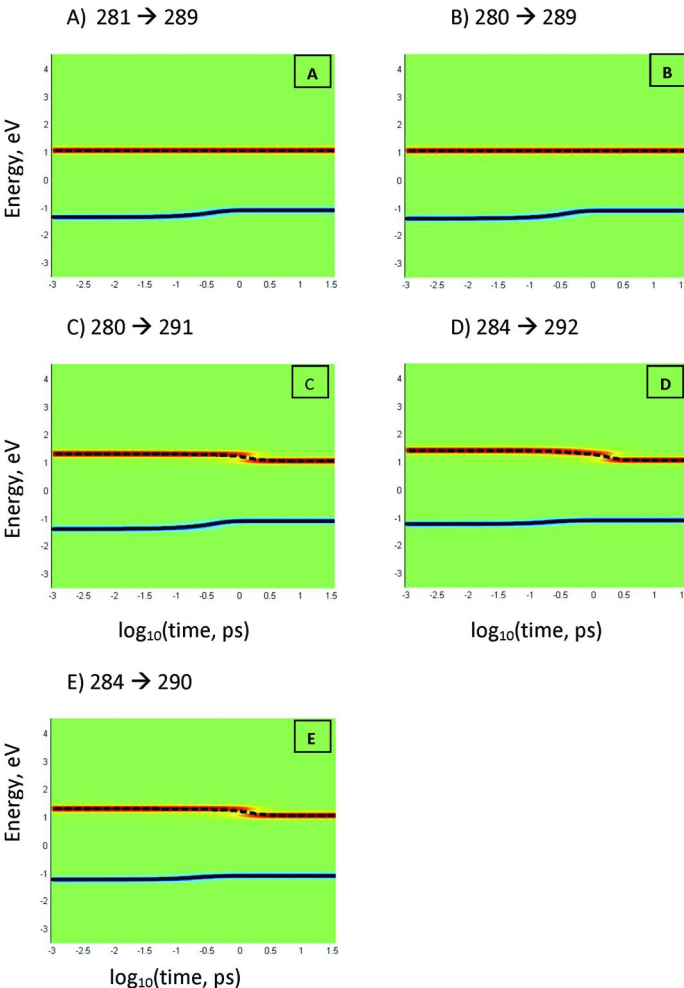


Figure 8. Figure 8 shows non adiabatic relaxation dynamics of likely initial photo-excitations of electron-hole pairs for the un-doped model. They are ordered in likelihood of occurrence according to the oscillator strength as seen in Table 2 with A being most likely and E least. In reference to excitation energies, the following correlation is found: $\varepsilon_A < \varepsilon_B < \varepsilon_E < \varepsilon_D < \varepsilon_C$. Each initial excitation evolves in time as illustrated by color code where red represents gain, blue represents loss, and green is no change in charge density distribution.

In the case of the silver doped model, five probable transitions are found; however, the HOMO' to LUMO' transition shows no effective relaxation rates for electron or hole cooling due to the fact that there is nowhere to relax or cool to. The transition was included due to the extremely low transition energy as seen in Table 2. Figure 9 shows the likely initial photo-excitations. The electron-hole relaxation rates are depicted in Table 2 for each transition. For each transition, the hole is relaxing faster than the electron just as in the un-doped model.

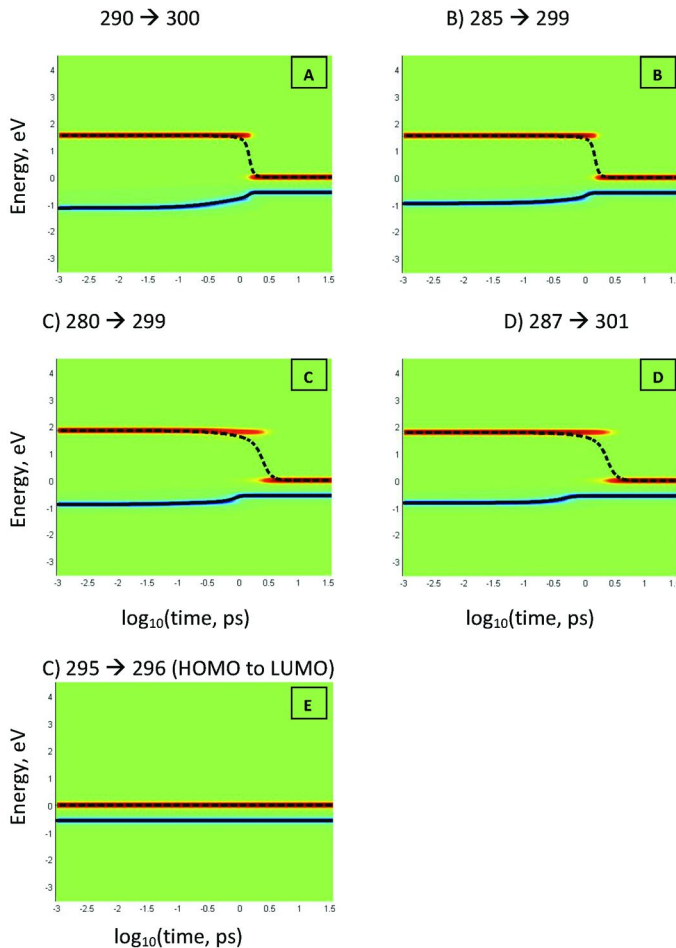


Figure 9. Figure 9 shows non adiabatic relaxation dynamics of likely initial excitation electron-hole pairs for the silver doped model. They are ordered in likelihood of occurrence according to the oscillator strength as seen in Table 2 with A being most likely and D least. In reference to excitation energies, the following correlation is found: $\varepsilon_E < \varepsilon_B < \varepsilon_A < \varepsilon_C < \varepsilon_D$. The color code is the same as that in Figure 8.

Silver doping affects the rate of both electron and hole cooling to HOMO and LUMO respectively, as seen in Table 2. It is also expected that doping will affect recombination rates which will be analyzed and calculated in the future.

Also, rather unusually, the holes of the un-doped model are relaxing twice as fast as those of the doped model while the electron relaxation remains about the same. Usually, a large or small energy sub gap would explain the relaxation differences; however, the energy gaps do not explain a twice as fast relaxation time for holes and equal relaxation times for the electrons. Therefore, it is indicative that the symmetry of the un-doped and doped states vary when involved in hole relaxation but are similar when involved with electron relaxation. For hole relaxation in the un-doped model, the holes are located in the 2p orbitals of oxygen while the Ag doped model has holes located in 2p orbitals of oxygen in 285 and 290, both 2p orbitals of oxygen and slight 4d orbitals of Ag in 280 and 287, and a mixed orbital of Ag 4d and surrounding oxygen 2p orbitals in 295 (HOMO'), which is visualized in Figure A1(a, b). It is theorized that the difference in symmetry explains the difference in hole relaxation rates, but the exact explanation should be researched further. Electron relaxation is involved in titanium 3d orbitals of both un-doped and silver doped structure, which is visualized in Figure A2 (a, b). This explains the similarity of electron relaxation times.

Water molecules are adsorbed to the surface with the binding energy of about .2 eV. During thermal molecular dynamics, the motion of water molecules contributes to the violation of orthogonality of KS orbitals. Therefore, motion of water molecules influences the rate of relaxation. According to Figure 6B, several orbitals contributed by Ag doping are hybridized with all six nearby oxygen orbitals forming octahedral coordination. For example, orbital HOMO' exhibits noticeable charge density of the oxygen belonging to the surface water molecule adsorbed to the Ag doping. The same pattern is observed for other Ag orbitals. The penetration of the charge to the surface water is an interesting and important trait related to photocatalysis. Adding or removing charge to the adsorbed molecules may lead to oxidation/reduction of surface molecules.

When examining Figure A3 and A4, all relevant initial transitions show the hole has much smaller energy difference between states to cool to while the electron in comparison has very large energy steps to overcome when relaxing. For lower energy differences, available low energy vibrations are ready to accommodate the excess energy (60). This explains why the hole is cooling much faster than the electron relaxing in all cases of transition.

Figure 10 shows comparison of relaxation rate for holes. According to computed data, hole cooling rate in both models follows the same trend: the hole excitations deep in the valence band take longer to relax to the HOMO or HOMO'. It supports subsequent mechanism of relaxation as bigger number of elementary relaxation steps take longer time. The K_h rate for un-doped model has systematically bigger values.

The rates of electron relaxation presented in Table 2 show another interesting result: the K_e rates are of the order of $.7 \text{ ps}^{-1}$ for both doped and un-doped models. This effect looks counterintuitive. According to "band gap law" one expects that the electron relaxation towards LUMO' is associated with instantaneous

dissipation of the electronic energy equal to the difference between Ti3d and Ag4d orbitals near the gap. This amount of energy is big enough. The Vibrational modes of the model need to have a frequency in a resonance with such transitions. One hypothesizes that the presence of surface adsorbed water molecules adds additional normal modes of higher frequency. Such modes could be responsible for accommodating the energy dissipating by electrons. In addition, this effect is recorded for very few initial states with approximately equal excitation energy. One may want to check if this conservation of electron relaxation rate sustains other initial conditions.

Additional insights of carrier dynamics in transition metal doped surfaces can be achieved by a detailed analysis of spin-polarization effects. Exploration of time dependent magnetization induced by light, probability of change of spin multiplicity of the doping ion might bring additional selection rules allowing for excitations with longer lifetime.

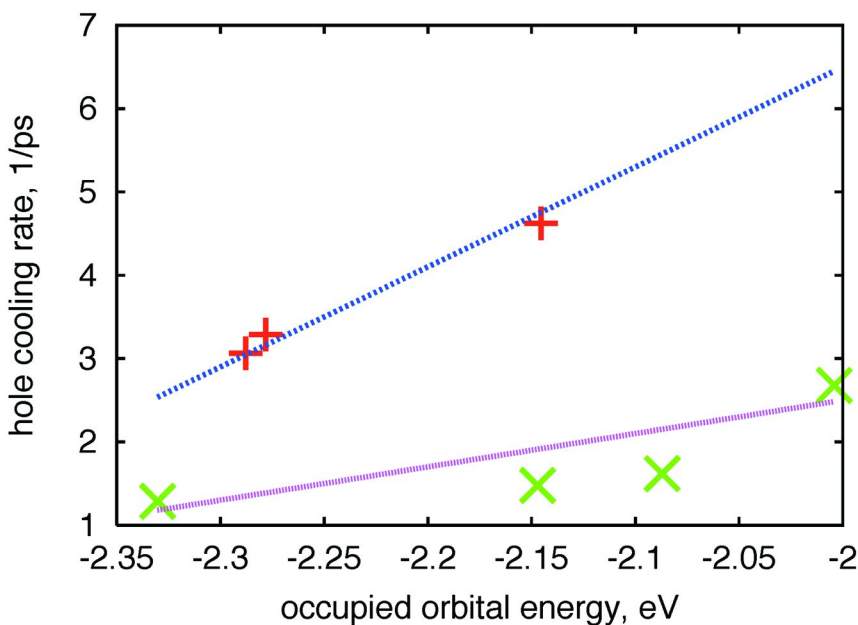


Figure 10. Hole cooling rate K_h as function of energy $\epsilon_{occupied}$ of occupied orbital perturbed by light at $t=0$, according to Table 2 for doped (+) and un-doped (x) models. Hole cooling rate in both models follows the same trend: the hole excitations deep in the valence band takes longer to relax to the HOMO or HOMO'. It supports subsequent mechanism of relaxation as bigger number of elementary relaxation steps take longer time. The K_h rate for un-doped model has systematically bigger values.

Conclusions

Ag doped TiO₂ anatase (100) surface thin film properties are modified in comparison to that of the un-doped thin film surface. Generally, doping of semiconductors provide an opportunity to tune the band gap, Fermi energy, and, hence controls the direction and rate of charge transfer.

In present work, Ag-doping of titania reduces the band gap, increases the Fermi energy, providing an opportunity to use Ag:TiO₂ as a catalytic site. According to presented results, both cooled electron and hole states are localized on the surface before they recombine. However, the hole is arriving to the surface earlier than electron. The period of time between these two events corresponds to the increased concentration of positive charge on the surface, which is expected to create preferential conditions for the oxidizing of the adsorbed water molecules. This feature makes Ag-doped titania worth of studying experimentally as a possible photo-activated oxidizer.

The six added states in the original band gap provide a lower energy difference between the conduction and valence band. The absorption spectra provide an increased range of absorption within the solar energy in the IR region and added predicted p to d transition peaks at 583 and 807 nm. The projected density of states shows the transition intervals of s, p, and d orbitals by each state, 1-356. Partial charge density images show how the charge distributes through the cells at each state. In the un-doped cell, the charge stays relatively dispersed at each state. The Ag doped, however, shows concentrated charge around Ag ions for HOMO, LUMO, and a few other orbitals. Further, it shows hybrid orbitals with the surface water, which could lead to the catalysis of the redox reaction of water to form hydrogen and oxygen. The images also lead to the suggested chemical reactions seen in equations 17 and 18 of how excitation charge transfer occurs from occupied to unoccupied states.

The more advanced calculations of molecular dynamics and non-adiabatic coupling provide insight into the opto-electrical properties of the crystals. Thermal motions of the lattice induce random changes (fluctuations) of electronic states and their energies. Such changes are stronger for dopant states. These changes are responsible for irreversible character of electron dynamics. The likely excitations are found based on maximal oscillator strength for given spectral region. The computed electron and hole relaxation was analyzed for each of such possible excitations, with rates summarized in Table 2. It is quite surprising that in all four excitations of the silver doped model (excluding the HOMO' and LUMO' transition), the hole is relaxing faster than the electron. It is hypothesized this is due to denser spacing of hole levels. Relaxation dynamics of each carrier, e⁻ and h⁺, starts at a dispersed slab orbital and ends at a concentrated orbital at the surface. Based on the calculations, positive charge appears on surface first and then a negative charge appears. The surface exists in charged state between these events.

Barring shortcomings or artifacts of the methodology, this result could indicate that relaxation mechanism is deviating from linear electron-phonon interaction. A multi-phonon relaxation steps could be involved. Also these results

could prompt that mechanism of hole relaxation goes beyond subsequent stepwise fashion and may include several relaxation channels activated in parallel.

The above characteristics suggest the Ag doped TiO_2 anatase (100) crystal warrants experimental investigation as a possible photo activated oxidizer, which can be a part of a photoelectrochemical cell. Combining together simulation of photon absorption (61, 62), and charge transfer from a substrate to the surface of nanocatalyst (53, 63) and charge-facilitated surface reaction (64), one is able to complete the pathways of subsequent elementary processes contributing to the photocatalytic water splitting.

Acknowledgments

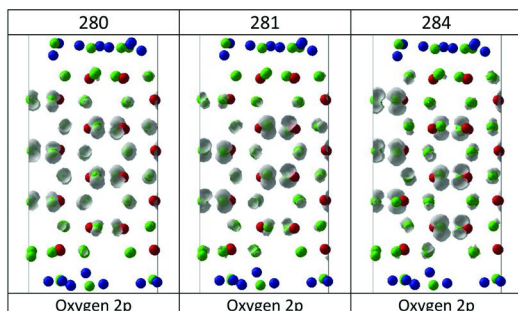
This research was supported by South Dakota Governor's Office of Economic Development, NSF award EPS0903804, and by DOE, BES - Chemical Sciences, NERSC Contract No. DE-AC02-05CH11231, allocation Awards 85213 and 86185 "Computational Modeling of Photo-catalysis and Photo-induced Charge Transfer Dynamics on Surfaces". The authors acknowledge computational resources of USD High Performance computational facilities co-sponsored by South Dakota IDeA Networks of Biomedical Research Excellence NIH 2 P20RR016479 and operated by Douglas Jennewein. DK thanks Sergei Tretiak for hosting the visit at the Los Alamos National Lab during manuscript preparation. Inspiring discussions with James Hoefelmeyer on open problems in photocatalysis are gratefully acknowledged.

Appendix

The consistent shift of all orbital energies is a technical artifact of post processing the output of VASP software. Specifically, the OUTCAR file for un-doped model contains the following record in front of list of orbital energies, quote begins "*E-fermi : -1.8734 XC(G=0): -7.1912 alpha+bet : -5.9443 add alpha+bet to get absolut eigen values*", end of quote. While this procedure was followed for computing data in Figure 7 and not for Figure 3, the VB edge energy is at about -7.8 and -1.8, respectively. A possible physical effect related to orbital energy modification is explained in (65). When heating the simulated structures to study the initial excitations, the vibrational thermal motion has an effect on the room temperature geometry. Thermal distortions then increase the energies of the system, causing the inconsistency in the VB and CB specific energies. The band gap size is not changed due to the displacement of the Ti atoms throughout the model, while the added dopant states change in energy due to the isolation within the models.

Consider photons of a given energy bombarding the doped and un-doped model. In the un-doped model, photo excitation will take T_{undop} picoseconds while the doped model with take T_{dop} picoseconds to completely recombine into ground state. However, this could be different for each partial rate of cooling for a carrier to the band gap edge.

A)



B)

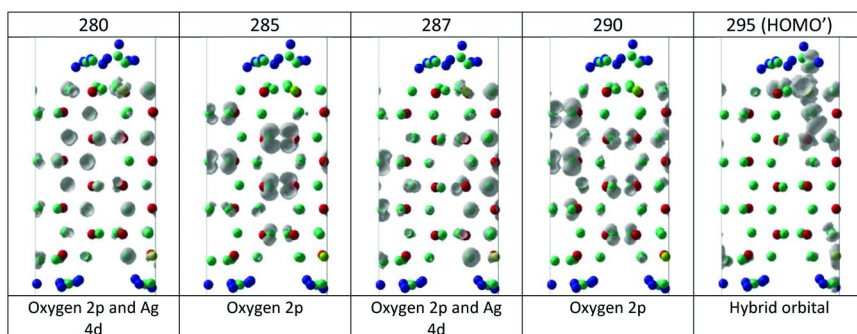
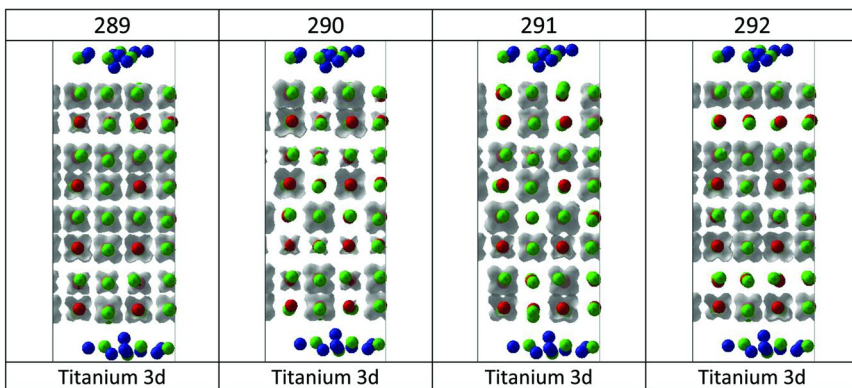


Figure A1. (A) The partial charge density images for the holes of the un-doped model. It is noted that all states have only oxygen 2p orbitals. (B) The partial charge density images for the holes of the Ag doped model. It is noted that states 285 & 290 show only 2p orbitals on the oxygen atoms, states 280 & 287 show 2p orbitals of oxygen and 4d orbitals of silver , while the 295 (HOMO') shows a hybrid orbital of 4d character from silver, 3d from nearby titanium, and surrounding oxygen 2p orbitals along with orbitals from an absorbed water molecule.

A)



B)

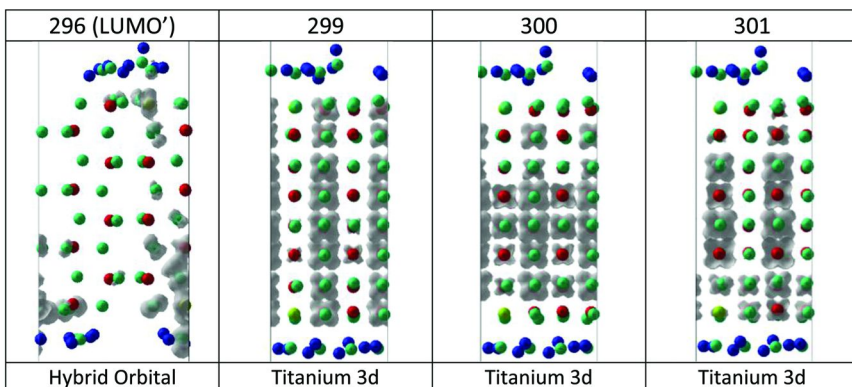


Figure A2. (A) The partial charge images for electron states of the un-doped model. It is noted that all states have only titanium 3d orbitals. (B) The partial charge images for electron states of the Ag doped model. All states but LUMO' show only titanium 3d orbitals.

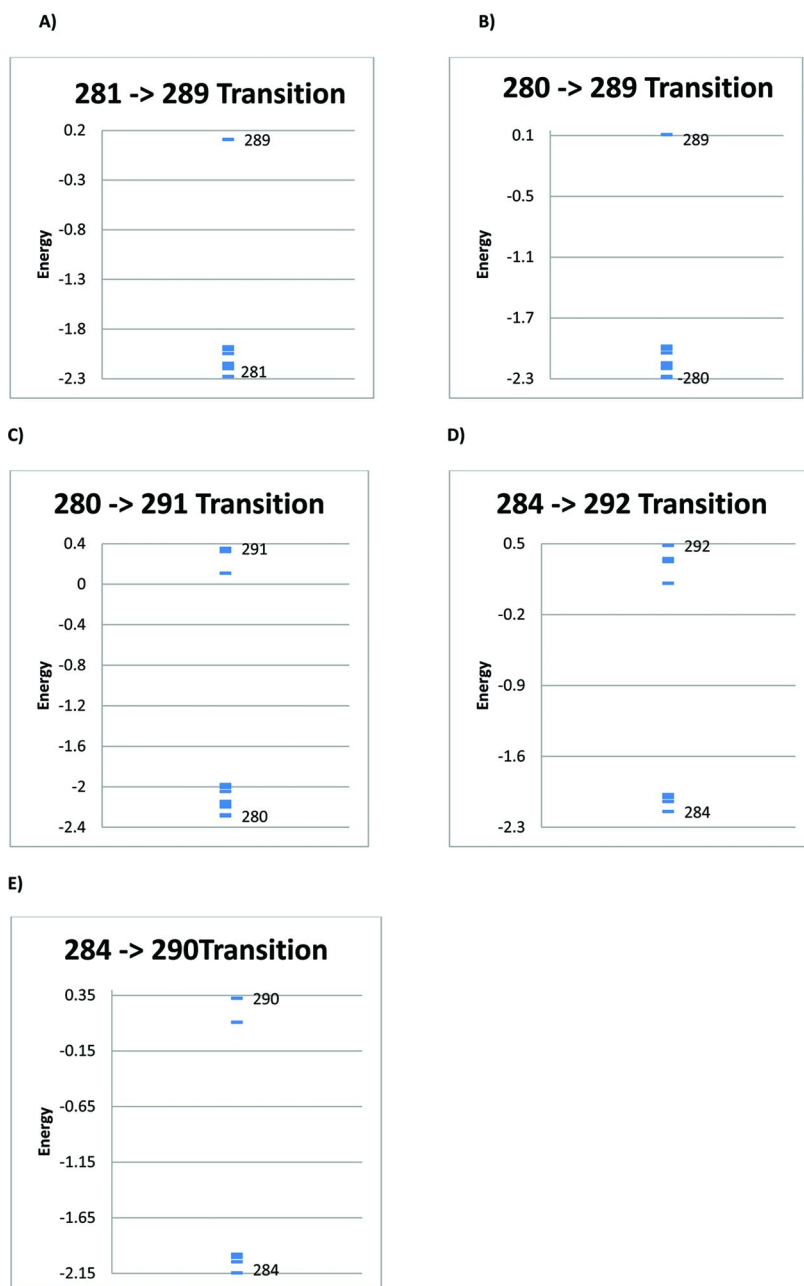


Figure A3. Orbital Energy levels for likely excitations and relaxations for the un-doped model. It is clearly seen in all initial excitations that the lower energy states, where holes are located, are much more closely stacked than those for the electron when excitation occurs.

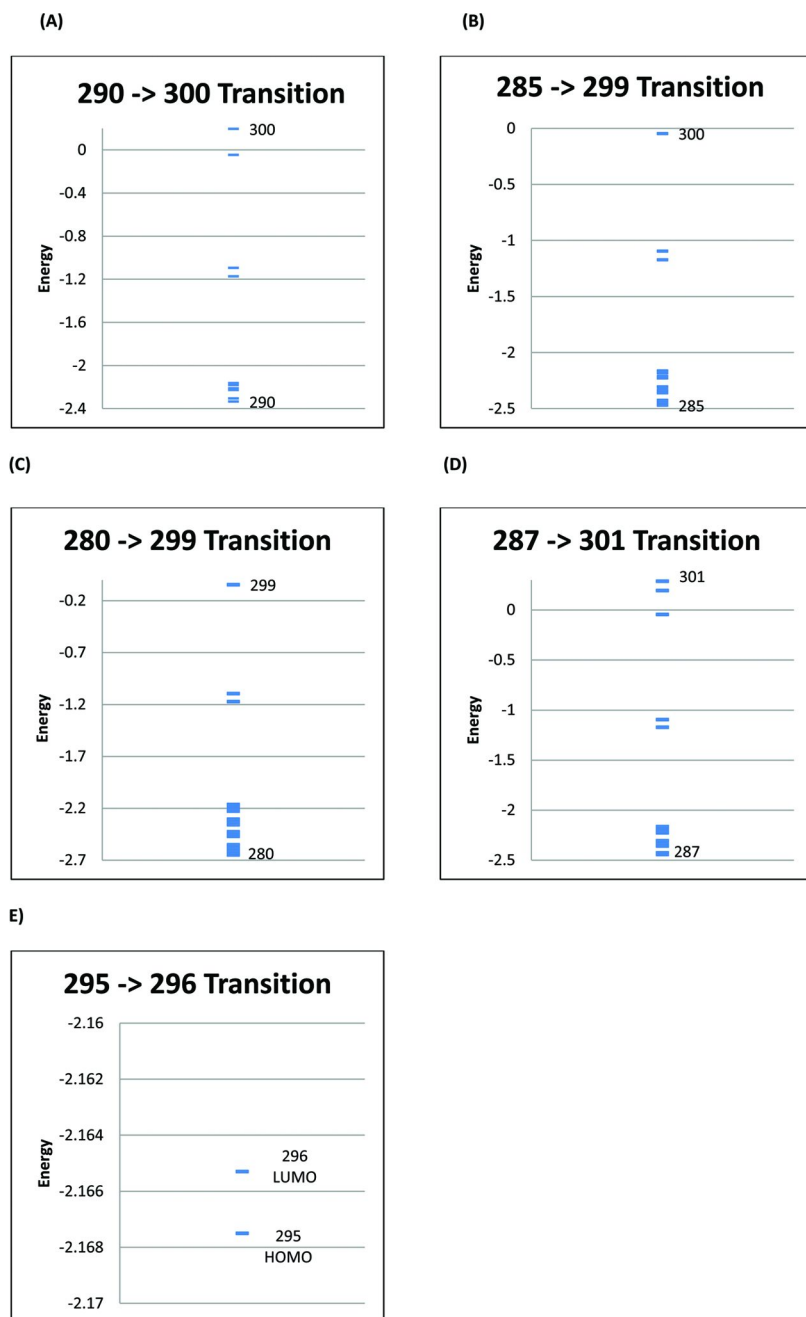


Figure A4. Orbital Energy levels for likely excitations and relaxations for the Ag doped model. It is clearly seen in A-D that the lower energy states, where holes are located, are much more closely stacked than those for the electron when excitation occurs.

References

1. Hafner, J. Ab-initio simulations of materials using VASP: Density-functional theory and beyond. *J Comput. Chem.* **2008**, *29* (13), 2044–2078.
2. Duncan, W. R.; Prezhdo, O. V. Theoretical Studies of Photoinduced Electron Transfer in Dye-Sensitized TiO₂. *Annu. Rev. Phys. Chem.* **2007**, *58* (1), 143–184.
3. Kresse, G.; Furthmüller, J. Efficiency of ab-initio total energy calculations for metals and semiconductors using a plane-wave basis set. *Comput. Mater. Sci.* **1996**, *6*, 15.
4. Kresse, G.; Furthmüller, J. Efficient iterative schemes for ab initio total-energy calculations using a plane-wave basis set. *Phys. Rev. B* **1996**, *54*, 11169.
5. Fujishima, A. Electrochemical Photolysis of Water at a Semiconductor Electrode. *Nature* **1972**, *238* (5358), 37–38.
6. O'Regan, B.; Grätzel, M. A low-cost, high-efficiency solar cell based on dye-sensitized colloidal TiO₂ films. *Nature* **1991**, *353* (6346), 737–740.
7. Xiaobo, C.; Burda, C. The Electronic Origin of the Visible-Light Absorption Properties of C-, N- and S-Doped TiO₂ Nanomaterials. *J. Am. Chem. Soc.* **2008**, *130* (15), 5018–5019.
8. Walter, M. G.; Warren, E. L.; McKone, J. R.; Boettcher, S. W.; Mi, Q.; Santori, E. A.; Lewis, N. S. Solar water splitting cells. *Chem. Rev.* **2010**, *110* (11), 6446–73.
9. Bachmann, J.; Nocera, D. G. Structural Tuning of Ligand-Based Two-Electron Intervalence Charge Transfer. *Inorg. Chem.* **2005**, *44* (20), 6930–6932.
10. Hagfeldt, A.; Graetzel, M. Light-Induced Redox Reactions in Nanocrystalline Systems. *Chem. Rev.* **1995**, *95* (1), 49–68.
11. Ramamoorthy, M.; Vanderbilt, D.; King-Smith, R. First-principles calculations of the energetics of stoichiometric TiO₂ surfaces. *Phys. Rev. B* **1994**, *49* (23), 16721.
12. Grätzel, M. Dye-sensitized solar cells. *J. Photochem. Photobiol., C* **2003**, *4* (2), 145–153.
13. Zhang, H.; Banfield, J. F. Kinetics of crystallization and crystal growth of nanocrystalline anatase in nanometer-sized amorphous titania. *Chem. Mater.* **2002**, *14* (10), 4145–4154.
14. Gribb, A. A.; Banfield, J. F. Particle size effects on transformation kinetics and phase stability in nanocrystalline TiO₂. *Am. Mineral.* **1997**, *82* (7), 717–728.
15. Lazzeri, M.; Vittadini, A.; Selloni, A. Structure and energetics of stoichiometric TiO₂ anatase surfaces. *Phys. Rev. B* **2001**, *63* (15), 155409.
16. Litter, M. I. Heterogeneous photocatalysis: transition metal ions in photocatalytic systems. *Appl. Catal., B* **1999**, *23* (2), 89–114.
17. Nowotny, J.; Bak, T.; Nowotny, M. K.; Sheppard, L. R. Titanium dioxide for solar-hydrogen I. Functional properties. *Int. J. Hydrogen Energy* **2007**, *32* (14), 2609–2629.

18. Navio, J.; Macias, M.; Gonzalez-Catalan, M.; Justo, A. Bulk and surface characterization of powder iron-doped titania photocatalysts. *J. Mater. Sci.* **1992**, *27* (11), 3036–3042.
19. Bickley, R. I.; Lees, J. S.; Tilley, R. J. D.; Palmisano, L.; Schiavello, M. Characterisation of iron/titanium oxide photocatalysts. Part 1.—Structural and magnetic studies. *J. Chem. Soc., Faraday Trans.* **1992**, *88* (3), 377–383.
20. Kominami, H.; Murakami, S.; Kohno, M.; Kera, Y.; Okada, K.; Ohtani, B. Stoichiometric decomposition of water by titanium (IV) oxide photocatalyst synthesized in organic media: Effect of synthesis and irradiation conditions on photocatalytic activity. *Phys. Chem. Chem. Phys.* **2001**, *3* (18), 4102–4106.
21. Nair, M.; Rao, K.; Nair, C. Investigation of the mixed oxide materials: $\text{TiO}_2\text{-SiO}_2$, $\text{TiO}_2\text{-SiO}_2\text{-Al}_2\text{O}_3$, $\text{TiO}_2\text{-SiO}_2\text{-In}_2\text{O}_3$ and $\text{TiO}_2\text{-SiO}_2\text{-RuO}_2$ -in regard to the photoelectrolysis of water. *Int. J. Hydrogen Energy* **1991**, *16* (7), 449–459.
22. Wang, M. H.; Guo, R. J.; Tso, T. L.; Perng, T. P. Effects of sintering on the photoelectrochemical properties of Nb-doped TiO_2 electrodes. *Int. J. Hydrogen Energy* **1995**, *20* (7), 555–560.
23. Sakata, T.; Hashimoto, K.; Kawai, T. Catalytic properties of ruthenium oxide on n-type semiconductors under illumination. *J. Phys. Chem.* **1984**, *88* (22), 5214–5221.
24. Zhang, H.; Chen, G. Potent Antibacterial Activities of Ag/TiO₂ Nanocomposite Powders Synthesized by a One-Pot Sol-Gel Method. *Environ. Sci. Technol.* **2009**, *43* (8), 2905–2910.
25. Wang, G.; Wang, Q.; Lu, W.; Li, J. Photoelectrochemical Study on Charge Transfer Properties of $\text{TiO}_2\text{-B}$ Nanowires with an Application as Humidity Sensors. *J. Phys. Chem. B* **2006**, *110* (43), 22029–22034.
26. Yang, L.; Jiang, X.; Ruan, W.; Yang, J.; Zhao, B.; Xu, W.; Lombardi, J. R. Charge-Transfer-Induced Surface-Enhanced Raman Scattering on Ag-TiO₂ Nanocomposites. *J. Phys. Chem. C* **2009**, *113* (36), 16226–16231.
27. Epifani, M.; Giannini, C.; Tapfer, T.; Vasanelli, L. Sol-gel synthesis and characterization of Ag and Au nanoparticles in SiO_2 , TiO_2 , and ZrO_2 thin films. *J. Am. Ceram. Soc.* **2000**, *83* (10), 2385–2393.
28. Webb, S. P.; Iordanov, T.; Hammes-Schiffer, S. Multiconfigurational nuclear-electronic orbital approach: Incorporation of nuclear quantum effects in electronic structure calculations. *J. Chem. Phys.* **2002**, *117* (9), 4106–4118.
29. Hammes-Schiffer, S. Avoiding the Born-Oppenheimer separation between electrons and nuclei: Explicitly correlated wavefunctions and multicomponent density functional theory. *Abstracts of Papers of the American Chemical Society* **2011**, 242.
30. Tully, J. C. Molecular dynamics with electronic transitions. *J. Chem. Phys.* **1990**, *93* (2), 1061–1071.
31. Kilina, S. V.; Craig, C.; Kilin, D. S.; Prezhdo, O. V. Ab initio time-domain study of phonon-assisted relaxation of charge carriers in a PbSe quantum dot. *J. Phys. Chem. C* **2007**, *111* (12), 4871–4878.

32. Kilina, S. V.; Kilin, D. S.; Prezhdo, O. V. Breaking the Phonon Bottleneck in PbSe and CdSe Quantum Dots: Time-Domain Density Functional Theory of Charge Carrier Relaxation. *ACS Nano* **2009**, *3* (1), 93–99.
33. Kilina, S. V.; Kilin, D. S.; Prezhdo, V.; Prezhdo, O. V. Theoretical Study of Electron-Phonon Relaxation in PbSe and CdSe Quantum Dots: Evidence for Phonon Memory. *J. Phys. Chem. C* **2011**, *115* (44), 21641–21651.
34. Fernandez-Alberti, S.; Kleinman, V. D.; Tretiak, S.; Roitberg, A. E. Nonadiabatic Molecular Dynamics Simulations of the Energy Transfer between Building Blocks in a Phenylene Ethynylene Dendrimer. *J. Phys. Chem. A* **2009**, *113* (26), 7535–7542.
35. Fernandez-Alberti, S.; Kleinman, V. D.; Tretiak, S.; Roitberg, A. E. Unidirectional Energy Transfer in Conjugated Molecules: The Crucial Role of High-Frequency C C Bonds. *J. Phys. Chem. Lett.* **2010**, *1* (18), 2699–2704.
36. Nelson, T.; Fernandez-Alberti, S.; Kleinman, V. D.; Roitberg, A. E.; Tretiak, S. Nonadiabatic Excited-State Molecular Dynamics Modeling of Photoinduced Dynamics in Conjugated Molecules. *J. Phys. Chem. B* **2011**, *115* (18), 5402–5414.
37. Nelson, T.; Fernandez-Alberti, S.; Chernyak, V.; Roitberg, A. E.; Tretiak, S. Nonadiabatic excited-state molecular dynamics: Numerical tests of convergence and parameters. *J. Chem. Phys.* **2012**, *136* (5), 054108.
38. Rego, L. G. C.; Batista, V. S. Quantum dynamics simulations of interfacial electron transfer in sensitized TiO₂ semiconductors. *J. Am. Chem. Soc.* **2003**, *125* (26), 7989–7997.
39. Craig, C. F.; Duncan, W. R.; Prezhdo, O. V. Trajectory surface hopping in the time-dependent Kohn-Sham approach for electron-nuclear dynamics. *Phys. Rev. Lett.* **2005**, *95* (16), 163001.
40. Tempel, D. G.; Aspuru-Guzik, A. Relaxation and dephasing in open quantum systems time-dependent density functional theory: Properties of exact functionals from an exactly-solvable model system. *Chem. Phys.* **2011**, *391* (1), 130–142.
41. Parkhill, J. A.; Tempel, D. G.; Aspuru-Guzik, A. Exciton coherence lifetimes from electronic structure. *J. Chem. Phys.* **2012**, *136* (10), 104510.
42. Redfield, A. G. On the theory of relaxation processes. *IBM J. Res. Dev.* **1957**, *1* (1), 19–31.
43. Egorova, D.; Thoss, M.; Domcke, W.; Wang, H. Modeling of ultrafast electron-transfer processes: Validity of multilevel Redfield theory. *J. Chem. Phys.* **2003**, *119* (5), 2761–2773.
44. Pollard, W. T.; Friesner, R. A. Solution of the Redfield equation for the dissipative quantum dynamics of multilevel systems. *J. Chem. Phys.* **1994**, *100* (7), 5054–5065.
45. Pollard, W. T.; Felts, A. K.; Friesner, R. A. The Redfield equation in condensed-phase quantum dynamics. *Advances in Chemical Physics*, Vol *XCIII* **1996**, *93*, 77–134.
46. Jean, J. M.; Friesner, R. A.; Fleming, G. R. Application of A multilevel Redfield theory to electron transfer in condensed phases. *J. Chem. Phys.* **1992**, *96* (8), 5827–5842.

47. Sundstrom, V.; Pullerits, T.; van Grondelle, R. Photosynthetic light-harvesting: Reconciling dynamics and structure of purple bacterial LH2 reveals function of photosynthetic unit. *J. Phys. Chem. B* **1999**, *103* (13), 2327–2346.
48. Kuhn, O.; May, V.; Schreiber, M. Dissipative vibrational dynamics in a curve-crossing system. *J. Chem. Phys.* **1994**, *101* (12), 10404–10415.
49. Davis, W. B.; Wasielewski, M. R.; Ratner, M. A. Electron transfer rates in bridged molecular systems: A phenomenological approach to relaxation. *J. Phys. Chem. A* **1997**, *101* (35), 6158–6164.
50. Apanasevich, P. A.; Kilin, S. Ya.; Nizovtsev, A. P.; Onischenko, N. S. Statistics of Dephasing perturbations and relaxation processes in a high-power optical field -- application to free-induction decay. *J. Opt. Soc. Am. B, Opt. Phys.* **1986**, *3* (4), 587–594.
51. Kolesov, G.; Dahnovsky, Y. Correlated electron dynamics in quantum-dot sensitized solar cell: Kadanoff-Baym versus Markovian approach. *Phys. Rev. B* **2012**, *85* (24), 241309.
52. Kilin, D. S.; Micha, D. A. Relaxation of Photoexcited Electrons at a Nanostructured Si(111) Surface. *J. Phys. Chem. Lett.* **2010**, *1* (7), 1073–1077.
53. Chen, J.; Schmitz, A.; Kilin, D. S. Computational simulation of the p-n doped silicon quantum dot. *International Journal of Quantum Chemistry* **2012**, *112*, 3879.
54. Kohn, W.; Sham, L. J. Self-Consistent Equations Including Exchange and Correlation Effects. *Phys. Rev.* **1965**, *140* (4A), 1133–1138.
55. Parr, R. G.; Yang, W. *Density-Functional Theory of Atoms and Molecules*; Oxford University Press: 1994.
56. Perdew, J. P.; Burke, K.; Ernzerhof, M. Generalized gradient approximation made simple. *Phys. Rev. Lett.* **1996**, *77*, 3865.
57. Perdew, J. P.; Burke, K.; Ernzerhof, M. Erratum: Generalized gradient approximation made simple. *Phys. Rev. Lett.* **1997**, *78*, 1396.
58. Chiodo, L.; Garcia-Lastra, J. M.; Iakomino, A.; Ossicini, S.; Zhao, J.; Petek, H.; Rubio, A. Self-energy and excitonic effects in the electronic and optical properties of TiO₂ crystalline phases. *Phys. Rev. B* **2010**, *82* (4), 045207.
59. Inerbaev, T. M.; Hoefelmeyer, J. D.; Kilin, D. S. Photoinduced Charge Transfer from Titania to Surface Doping Site. *J. Phys. Chem. C* **2013**, *117*, 9673–9692.
60. Chaban, V. V.; Prezhdo, V. V.; Prezhdo, O. V. Covalent Linking Greatly Enhances Photoinduced Electron Transfer in Fullerene-Quantum Dot Nanocomposites: Time-Domain Ab Initio Study. *J. Phys. Chem. Lett.* **2013**, *4*, 1–6.
61. Jensen, S.; Kilin, D. Anatase (100) thin film surface computational model for photoelectrochemical cell. *Int. J. Quantum Chem.* **2012**, *112*, 3874–3878.
62. Zhang, Y.; Kilin, D. S. Computational modeling of wet TiO₂ (001) anatase surfaces functionalized by transition metal doping. *Int. J. Quantum Chem.* **2012**, *112*, 3867.

63. Inerbaev, T. M.; Kilin, D. S.; Hoefelmeyer, J. Atomistic Simulation of Dissipative Charge Carrier Dynamics for Photocatalysis. *MRS Proc.* **2012**, *1390* (mrsf11), mrsf11-1390-i03-03.
64. Meng, Q.; et al. Sequential hydrogen dissociation from a charged Pt₁₃H₂₄ cluster modeled by ab initio molecular dynamics. *Int. J. Quantum Chem.* **2012**, *112*, 3896.
65. Duncan, W. R.; Craig, C. F.; Prezhdo, O. V. Time-domain ab initio study of charge relaxation and recombination in dye-sensitized TiO₂. *J. Am. Chem. Soc.* **2007**, *129* (27), 8528–8543.

Chapter 9

CdS-Based Semiconductor Photocatalysts for Hydrogen Production from Water Splitting under Solar Light

Sheng Huang, Yu Lin, Jian-Hua Yang, and Ying Yu*

College of Physical Science and Technology,
Central China Normal University, Wuhan 430079, China
*E-mail: yuying@phy.ccnu.edu.cn. Fax: 86-27-67861185.

Energy crisis around the world pushes people to take advantage of renewable energy. As one kind of photosynthesis, H₂ evolution from water splitting through solar light attracts a lot of interest. Herein, this article will introduce recently published CdS-based semiconductors for photocatalytic hydrogen evolution from water splitting under solar light. The activity and stability of different CdS-based photocatalysts including CdS with different nanostructures, CdS composites with other semiconductor, polymer or high surface area materials will be described and compared. The function of deposited cocatalysts and sacrificial reagents will be also introduced for the improvement of activity and stability for CdS. The prospective trend in this research area will be proposed as well. Summarily, by means of the nanostructure change and hybridization modification, the activity of CdS for hydrogen production and the corresponding quantum efficiency can be enhanced intensely and the stability can be improved as well. We hope the review will inspire people new good ideas and thus facilitate CdS-based photocatalysts moving forward to practical application in future.

1. Introduction

Conventional fossil fuel as non-renewable energy can not meet the growing energy demand of human beings. What's worse, environmental contamination is unavoidable for the use of non-renewable fossil fuel. The two challenges, energy crises and environment problem, have seriously restricted the development of our society. As a new renewable energy, hydrogen with high fuel value is abundant, environmentally friendly and has been used in fuel cell. Conventional methods for hydrogen production from water gas, cracking petroleum gas, water electrolysis etc. are not only high-energy consumed but also have troubles in environment and renewable aspects, which conventional fossil fuel is facing now. Splitting water into hydrogen and oxygen under the irradiation of solar light with the presence of photocatalysts can address the issues which the conventional methods for hydrogen production result in. Therefore, hydrogen may be the most promising substitute for traditional energy sources.

Since the discovery of photoelectrochemical water splitting into H_2 and O_2 over TiO_2 electrode (1), many efforts have been taken to improve the activity of hydrogen evolution and quantum efficiency (QE) of semiconductor photocatalyst. The main mechanism for photocatalytic hydrogen evolution is as follows. Firstly, semiconductor photocatalyst is irradiated by solar light and absorbs photon with energy equal to or higher than that of band gap for the semiconductor. Then, photogenerated electron–hole pairs are produced. Photogenerated hole is oxidative while photogenerated electron is reductive. Secondly, the energy band level should be at appropriate position. The top of valence band should be lower (or more positive) than the oxidation potential of O_2/H_2O (1.23 V vs normal hydrogen electrode (NHE)) (2), together with the bottom of conduction band to be higher (or more negative) than reduction potential of H^+/H_2 (0 V) (2). The related scheme is illustrated in Figure 1. Besides the two main reasons of photon absorption and the suitable position of energy band edge for a semiconductor, there are some other factors which will affect photocatalytic activity, such as the recombination possibility of photogenerated holes and electrons and the migration rate of photogenerated holes and electrons to the surface. In photocatalytic hydrogen evolution system, although equipment, photocatalyst mass, light source etc are different, we can compare hydrogen evolution efficiency by H_2 evolution rate ($\mu\text{mol h}^{-1}\text{g}^{-1}$) and QE. The QE is calculated based on the following equation (3).

$$QE [\%] = \text{number of reacted electrons} / \text{number of incident photons} \times 100\%$$

$$= (\text{number of evolved } H_2 \text{ molecules} \times 2) / \text{number of incident photons} \times 100\%.$$

At present, the synthesis of narrow band gap semiconductor that can absorb visible light is the main trend for hydrogen production since about 43% of solar energy lies in visible light region, which is far more abundant than UV light of only 5%.

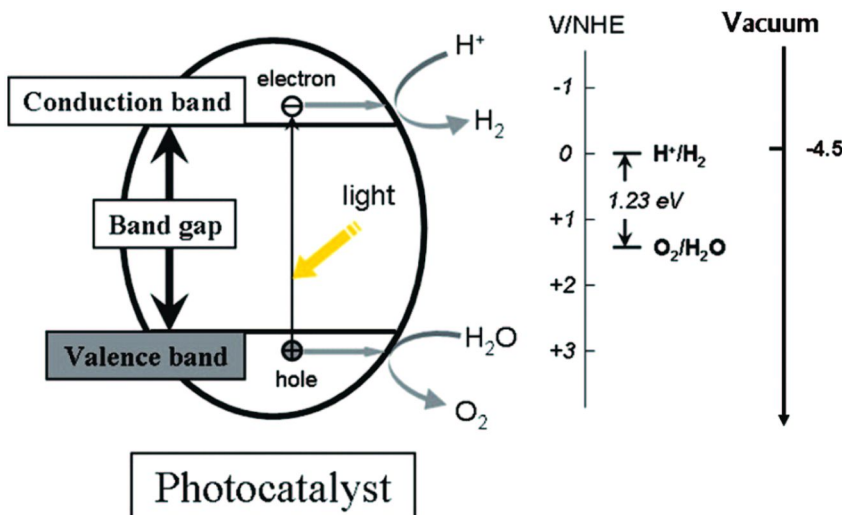


Figure 1. Fundamental principle of semiconductor-based photocatalytic water splitting for hydrogen production. Reprinted with permission from Ref. (2) Copyright 2010 American Chemical Society.

CdS is a visible-light-driven photocatalyst with narrow band gap of 2.42 eV (4) and its energy band edge matches hydrogen evolution potential (5, 6) as Figure 1 described. Due to the above dominant advantages, CdS becomes an attractive candidate for hydrogen evolution under solar light. It is well known that CdS has two main inherent shortcomings, low QE and photocorrosion (7, 8). So, many efforts have been taken to solve the problems. The improvement of the photocatalytic activity and stability of CdS for H₂ production has been achieved by the preparation of CdS with different morphologies, the hybridization with other semiconductor, polymer or high surface area materials, cocatalyst deposition and sacrificial reagent introduction. Although great progress has been made to overcome the shortcomings, there is almost no related summary. From this point of view, the visible-light-driven CdS-based semiconductors have been overviewed in this article for H₂ production from water splitting. The QE and H₂ evolution rate by using different CdS-based semiconductors have been compared in this review as well. Furthermore, the different kinds of CdS modification routes will be introduced. More specifically, the preparation of CdS with different nanostructures will be included in section 2. The hybridization of CdS with other materials such as sulfides, TiO₂, other semiconductors and high surface area matrix will be mentioned in section 3. In section 4, we will introduce cocatalyst effect. The function and mechanism of sacrificial reagents will be shown in section 5. Additionally, other modification methods will be briefly presented in section 6. Finally, in section 7, the important CdS-based photocatalysts for hydrogen evolution under visible light will be listed and compared in Table 1 and we will also put forward the problems and prospects in this section. We hope that researchers engaged in H₂ production under solar light can gain any inspiration based on the analysis and summary here.

2. CdS with Different Nanostructures

It is well known that specific surface area or particle size (9–11), crystallinity (9, 12, 13), crystalline phase (10) and morphology (14) have influence on photocatalytic activity of semiconductors. CdS with different size may have different activity for hydrogen evolution as well. The advantages of nanostructured CdS are as follow. First, it is well known that smaller grain size will lead to larger surface area, more active centers and more quickly migration of photogenerated electrons and holes to semiconductor surface. As a result, CdS with the smaller grain size may have higher activity. Second, when particle size decreases to nano level, the transfer of photogenerated electrons may be too quick to recombine with hole. Third, quantum size effect will happen. Tiny particle will result in the blue shift of light absorption and the increase of band gap. The enlarged energy level may lead to higher CB and lower VB of semiconductor (8). Ultimate result is the enhanced reductive and oxidative power of the photogenerated electrons and holes respectively (15, 16).

Bao et al. (11) designed nanoporous CdS with special hollow and sheetlike nanostructure, which possessed large specific area. Since the bulk-to-surface migration distance of electrons and holes was shortened, thoroughly improved photocatalytic activity was achieved. Sathish et al. (10) reported mesoporous CdS nanoparticle with small particle size and high surface area, which had the better photocatalytic activity of hydrogen evolution as well. As the examples listed above, the different morphologies of CdS will often result in different specific surface area and the different amount of active centers on surface. Nevertheless, Muruganandham et al. (14) found that the difference in morphology resulted in the different absorption of light and thus the final photocatalytic activity of hydrogen evolution.

Crystallinity can affect the hydrogen activity by tuning defects. The samples with high calcined temperature have few defects because calcination can eliminate lattice stress (17). CdS with high crystallinity has enhanced photocatalytic activity of hydrogen production. Fan et al. (12) demonstrated that for the calcined hexagonal CdS, the trap emission became more and more weak so that the trap states were reduced, which would decrease the recombination of photogenerated charge carriers and result in enhanced photocatalytic activity. Furthermore, Jang et al. (13) prepared CdS nanowires with higher crystallinity, which showed a higher hydrogen evolution rate under visible light.

Semiconductor with different crystalline phase will have different photocatalytic activity. Sathish et al. (10) synthesized two mesoporous CdS nanoparticles with the same particle size and surface area. The two samples showed different activity, which was because of different crystalline phase. They also found that hexagonal crystalline phase was more photoactive than the cubic, which is in accordance with other reported articles (5, 12).

3. Hybridization of CdS with Other Materials

Although CdS with narrow band gap can absorb solar light with long wavelength, the photogenerated carriers can be recombined easily since the

recombination possibility is inverse ratio to energy band gap. What's more, CdS has the other intrinsic shortcoming of photocorrosion, which means that CdS is not stable under solar light irradiation. So, many composites have been prepared to solve the two drawbacks. Here, we take the semiconductor-semiconductor heterojunction for example to elucidate the advantage of CdS hybridization with other materials. The hybridization of two semiconductors will lead to the formation of heterojunction, which will improve the transfer of photogenerated carriers, decrease the probability of carrier recombination, increase quantum yield and finally enhance the photocatalytic activity. The reason for the improved carrier separation effect is that photogenerated electrons and holes can be moved out due to the matched energy level between the different semiconductors, which will be discussed in detail below.

3.1. Hybridization of CdS with Sulfides

The publications about CdS composition with other sulfides (18–34), or the formation of solid solutions (3, 18, 23, 30–34) are enormous. The reason for CdS hybridization with sulfides is as follows. The first is that CdS hybridization with sulfides definitely improves the separation of photogenerated carriers, leading to the enhanced photocatalytic activity of hydrogen evolution (3, 19–34) since all of the listed articles about hybridization of CdS show enhanced activity of hydrogen evolution under visible light. The second may be the easy preparation for this kind of photocatalysts and one step method can make it (3, 20, 23, 26). The third is that only S ion acting as an anion among the CdS hybrid makes sample analysis easy. Actually, when we add other metal ions to modify CdS for activity improvement, no other materials but composites or solid solutions can be formed for final resultants.

The articles about CdS hybridization with zinc sulfide or the formation of Zn-Cd-S solid solution (3, 23, 30–34) is especially in large amount. We contribute it to the congeners of Zn and Cd, the small difference of atom radius (18) and the similar electronic structure for the two elements. In addition, the tight contact and the same hexagonal phase of CdS and ZnS make the crystal lattice of the two sulfides matched for the formation of composite or solid solution. In the work by Deshpande et al. (19), it was found that the small size of CdS crystallites and certain microstructural defects at the interface of CdS/ZnS nanocomposite photocatalysts provided a larger active surface area and the augmented number of reaction sites, which enabled a more efficient utilization of photogenerated e^-/h^+ pair for the dissociation of water molecules at the catalyst surface. Shen et al. (26) also reported that the transfer of photogenerated electrons and the unique nanostructure for CdS/ZnS nanocrystals were responsible for the highly efficient photocatalytic activity. While Yu et al. (3) indicated that high visible-light photocatalytic H₂-production activity was attributed to the quantum size effect of CdS, which altered the energy levels of the conduction and valence bands in coupled semiconductor system.

Some other solid solution systems of CdS have also been reported. Based on experiment data and DFT calculation, Ren et al. (35) attributed the high activity of $(\text{CuIn})_x\text{Cd}_{2(1-x)}\text{S}_2$ to the new energy levels presented near the top of valence band

because of Cu and In codoping. Liu et al. (30) assigned the improved activity of H₂ evolution to Mn²⁺ serving as shallow trapping sites, which could separate e⁻/h⁺ pairs at the surface of nanosized CdS. Moreover, Sasikala (31) demonstrated that the improved optical absorption was due to In doping for CdS.

CdSe (21), SrS (20), MoS₂ (22), AgGaS₂ (27) were also used to hybridize with CdS and all of them can efficiently improve charge separation. The formation of microstructural defect (19), the passivation of surface-deep traps (21), improved light absorption (28) are all the reasons to enhance the activity of H₂ production from water splitting.

3.2. Hybridization of CdS with Other Semiconductor

Except for the composition between sulfides, CdS hybridization with various non-sulfides has been reported as well, especially TiO₂-based semiconductors (36–45). TiO₂ is the most studied photocatalyst and has a number of advantages. There is an obvious advantage when CdS is hybridized with TiO₂. The main mechanism is shown in Figure 2.

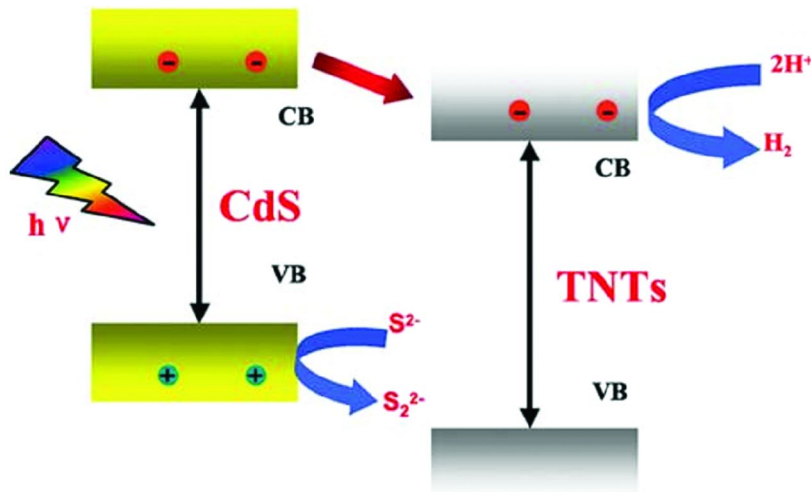


Figure 2. Schematic illustration of charge-separation between CdS and titanate nanotubes or nanoparticles from Ref. (38). Reproduced by permission of The Royal Society of Chemistry.

Under the irradiation of visible light, photon is absorbed by CdS. Meanwhile, electron is excited and injected from valence band to conduction band and the photogenerated electron and hole are generated. Although TiO₂ can not respond to visible light (46), the relative low position of conduction band makes TiO₂ a good trap for the electron generated by photoexcited CdS, which facilitates the free flow of photogenerated electron from CdS to TiO₂. At the same time, the holes remain in the valence band to oxidize sacrifice agents. Additionally, there are other reasons for the improved photocatalytic activity, which includes heterojunction (39), the formation of the potential gradient at the interface between CdS and TiO₂ (36, 41, 44), the enhanced charge separation and reduced distance that holes and electrons should travel to reach the electrolyte due to one-dimensional TiO₂ nanotube structure (37, 38, 40, 41), the homogeneous distribution of CdS nanoparticles and the difference in the positions of conduction bands (43–45).

In Park's work (36), the potential gradient formation at the interface between CdS and TiO₂ was necessary to achieve efficient charge separation and transfer. The unique nanoparticles enwrapped with titanate nanotubes (TNTs) resulted in the appropriate dispersion of CdS nanoparticles and the intimate multipoint contact between CdS nanoparticle and TNTs, which led to the intensive enhancement of charge separation in CdS/TNTs. In addition, highly crystalline hexagonal CdS in CdS/TNTs by one-step hydrothermal method was also essential for the enhanced photocatalytic performance (38). CdS/TNTs coaxial nanostructured array electrodes reported by Zhu et al. (40) could overcome the shortages of poor absorption and high charge-carrier recombination observed in nanoparticle films. The coaxial heterogeneous structure prepared by new electrochemical method possessed the intensively enhanced contact areas both between CdS and TiO₂, and CdS and electrolyte, which shortened the distance that holes and electrons should travel to reach the electrolyte or conducting substrate.

Furthermore, different kinds of semiconductors such as salt (47–52), oxide (53–56), hydroxide (57), have been hybridized with CdS. The prepared composites also have matched energy band level, which are almost the same as CdS/TiO₂ composite. So, we can conclude that the potential gradient resulted from matched energy level at the composite interface is the main reason for the effective separation of photogenerated electrons and holes, and thereafter the enhanced photocatalytic activity for hydrogen production from water splitting.

3.3. Hybridization of CdS with Inorganic or Organic Matrix Materials

The stability for CdS is poor and the photocorrosion restricts its practical application. CdS grown on the matrix with framework structures can have improved stability under visible light and is in favor of recycle as well. If the matrix has large surface area, uniform pore distribution, high thermal stability, and controllable mesoporous size, it leads to the good photocatalytic activity for hydrogen evolution simultaneously. In Zhang's work (58), the nanosized CdS particles inside the aluminum-substituted mesoporous silica (Al-HMS) channels with high surface area had dangling bonds, defect sites and traps in small particles. Wormhole-like mesoporous structure of Al-HMS retained the uniform dispersion of CdS inside the channels. The incorporation of CdS nanoparticles into the

wormhole-like channels of Al-HMS protected CdS from exposure to air and reduced the amount of light absorption. He also reported (59) Al-HMS molecular sieve with large surface area, uniform pore distribution and high thermal stability coupled with CdS. The wormhole-like framework structure of Al-HMS serving as the matrix for embedded CdS nanoparticles under ambient conditions was the main reason for the photostability. The enhanced hydrogen evolution activity for CdS immobilized in silica matrix can be attributed to high crystallinity and well-fabricated mesostructures (60), diffusion velocity of the reactants and resultants (61). Except silica matrix, there are other matrix materials (62–64) to immobilize CdS. Ryu et al. (62) prepared packaged CdS in zeolite-Y and found that the quantum confinement of hydrated CdS increased the reduction potential for bound proton to hydrogen atom with electron transfer ($\text{CdOH}_2^{++} + \text{e}^- \rightarrow \text{CdOH}^+ + \text{H}^-$) and the confined CdS supercluster was a more efficient chromophore in the visible portion of spectrum. In Hirai's work (63) about the immobilization of CdS nanoparticles onto aluminosilicate in reverse micelles, the chemical properties of the aluminosilicate, such as affinity for water and other reactants, were found to affect the photocatalytic activity of the immobilized CdS nanoparticles.

CdS incorporated into inorganic matrix can improve the hydrogen evolution activity and stability as described above. However, the above inorganic compounds used as the matrix may keep visible light from CdS (65). Therefore, the use of organic porous films in the synthesis of heteromatrices has been the subject of immense interest due to their distinctive optical and convenient reactivating properties (66). The hybridization with most commonly used organic polymer, polyaniline (PANI) (67, 68), can improve not only activity but also stability of CdS. He et al. (67) pointed out that there were two reasons for the better activity after PANI hybridization. On one hand, the coordination bond was formed between CdS and PANI, which might benefit the transfer of electrons and thus the improved activity for hydrogen evolution was achieved. On the other hand, the interaction between PANI and CdS prevented the agglomeration of CdS particles in a certain extent. Zhang et al. (68) also reported that PANI was helpful for the separation of photogenerated carriers. While in Ke's work (69) about CdS/regenerated cellulose nanocomposite, CdS nanoparticles dispersed in the nanocomposites could efficiently restrain the agglomeration among CdS nanoparticles. Thus, both of the activity and stability were improved. Lunawat et al. (70) demonstrated that CdS nanocrystallites immobilized onto water-repellant polymeric surface had long and active life because of its hydrophobic nature. These observations conform to the large surface area and hence the large number of reaction sites associated with nanosized CdS crystallites. While Lau et al. (71) analyzed improved activity for the composite in other aspects. They found that it was because of the interaction between CdS and organic solvent. As a result, CdS with different exposed active crystal face was prepared in special solvents and the activity was closely related to the exposed active crystal face.

The most effective matrix materials not only can inhibit the aggregation of semiconductor particle but also facilitate the migration of photogenerated carriers. Carbon nanotubes (72, 73), graphene (GR) (74, 75) and graphene oxide (GO) (49, 76, 77) have such advantages. For example, after CdS was hybridized with graphene, the aggregation of CdS was avoided and the particle size decreased as

shown in Figure 3. The main mechanism of enhanced photocatalytic activity for graphite-based materials can be defined in Figure 4.

As shown in Figure 4, GO was also used as matrix materials to immobilize CdS so that the dispersive and non-aggregated CdS could be obtained. In addition, the presence of GO can function as an electron collector and transporter to efficiently prolong the lifetime of the photogenerated carriers (76).

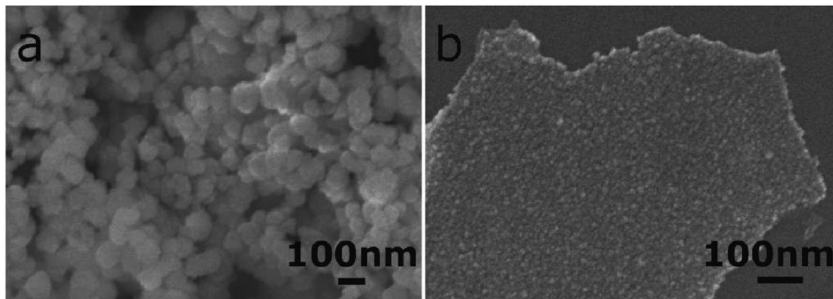


Figure 3. SEM images of (a) sample CdS and (b) sample CdS-GR. Reprinted with permission from Ref. (74). Copyright 2011 American Chemical Society.

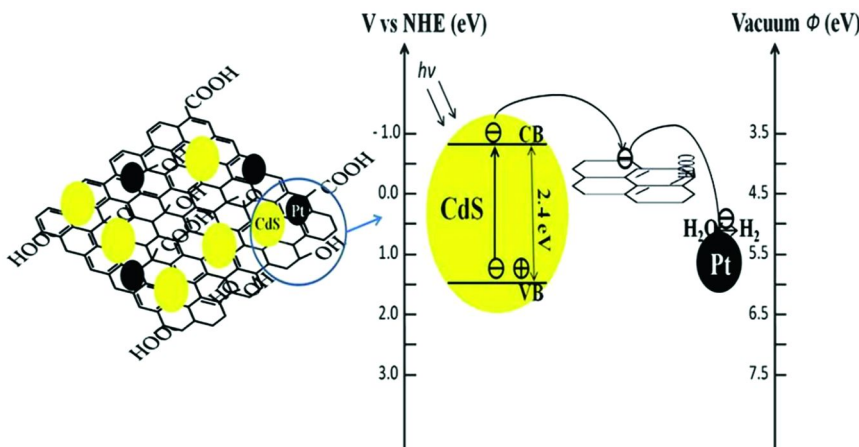


Figure 4. Schematic illustration of the charge separation and transfer in the organic matrix from Ref. (76). Reproduced by permission of The Royal Society of Chemistry.

4. Cocatalysts

Since the activity of pure CdS is not high enough, cocatalysts have been also tried to be deposited onto CdS surface for the improvement of hydrogen production from water splitting under solar light. With the presence of suitable cocatalysts, the photocatalytic activity for hydrogen evolution increases prominently. The rate with and without cocatalyst can be different with at least one order of magnitude. Taking cocatalyst Pt as an example, the mechanism of the enhanced hydrogen activity for CdS is illustrated as follows (78, 79): Under the irradiation of solar light, charge carriers can be separated in the heterojunction between CdS and Pt. The obvious separation of the charge carriers can be attributed to the higher work function and lower Fermi level of Pt than CdS. So, the electrons can be transferred from CdS with high Fermi level to Pt nanoparticles. At the same time, a thin depletion layer is formed when the bending of CdS conduction band occurs. Electrons transfer because of Fermi level difference between CdS and Pt will lead to the electron enrichment (negative charge) in Pt and the electron lack (positive charge) in CdS (i.e. holes enrichment in CdS). The separation of electrons and holes will result in the formation of contact potential and opposite transfer of electrons (i.e. electrons can be transferred from Pt nanoparticles to CdS), which is so-called drift current. The electron transfer will reach a dynamic balance when current (flow from CdS to Pt nanoparticles) resulted from different Fermi level is equal to drift current (flow from Pt nanoparticles to CdS). That is, under the irradiation of solar light, the photogenerated electron possesses higher energy. Thus, the Fermi level for CdS will continually increase and the aforementioned balance before light irradiation is broken. The electron transfer between the CdS and Pt will continue until it reaches a new balance. The transfer of photogenerated electrons and holes between CdS and Pt-cocatalyst can be described in Figure 5.

We can also apply this mechanism to composite system. The usage of Pt in photocatalytic hydrogen evolution system is so common that Pt deposition is acquiescent as a part of photocatalyst. It is well known that the deposited particle size (81, 82) and the amount (12) of cocatalyst can affect hydrogen evolution activity greatly. Huang (81) reported that the activity of as prepared photocatalysts was dependent on the size and distribution of Pt in Pt/CdS system in a large extent. Berr (82) demonstrated that CdS nanorods decorated with subnanometer size (<1 nm) Pt cluster would hold the same activity as those with nanosize while the amount of Pt used could decrease plentifully. The other reason for the deposition of noble metal was to decrease the activation energy of water splitting and the overpotential for hydrogen evolution (83, 84).

There are some other cocatalysts used except Pt but the activity of Pt deposited CdS is better than that of any others. As Sathish (85) reported, among noble metals of Pt, Pd, Rh and Ru, Pt with higher redox potential and work function, and lower metal hydrogen bond strength was found to be more favorable for hydrogen production. However, there is an exception. As Navarro (54) reported, the photocatalyst deposited with Ru had better hydrogen production activity than that with Pt, which might be attributed to a higher surface exposure of noble metal oxide species in the case of Ru/CdS–ZnO–CdO catalyst. As a

result, the presence of Ru oxide was endowed of high intrinsic activity by good surface coordination with CdS particles, which could facilitate electron transfer.

The cost of noble metal is so high that people are dedicate to develop cheap cocatalysts, for example, tungsten carbide (80), PdS (86), MoS₂ (87), graphene (88), Ag₂S (89) and so on. In relative articles, tungsten carbide, MoS₂ and graphene deposited CdS all have good activity for hydrogen production or even better than Pt/CdS. The reason for the better activity can be assigned to better coupling and hybrid effect, faster diffusion of photogenerated electrons between CdS and cocatalyst, together with more active site provision for proton reduction. Although PdS and Ag₂S act as oxidation cocatalyst to facilitate hole transfer, the transfer of photogenerated holes to the oxidation cocatalyst was beneficial for charge transfer between cocatalysts and CdS as well.

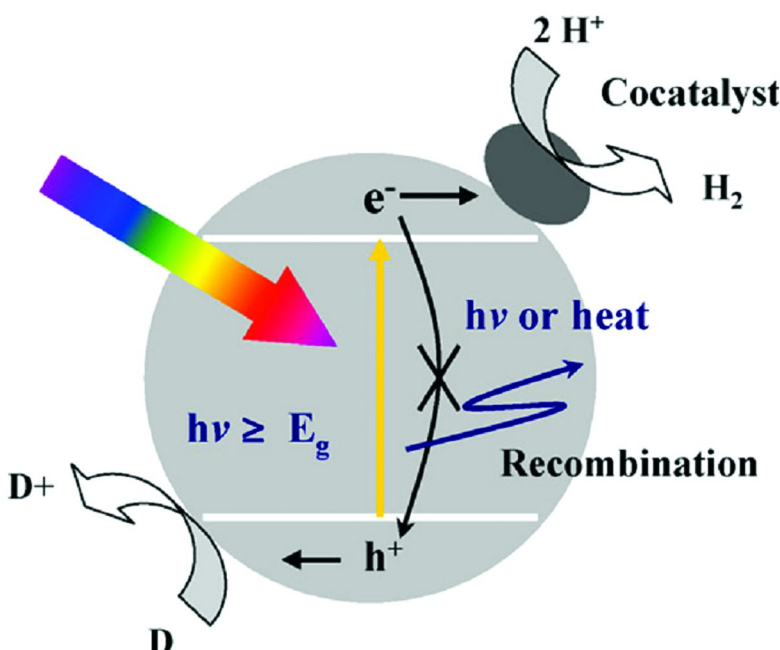


Figure 5. The function of cocatalyst. D and D+ represent an electron donor and its oxidized form, respectively, which is from Ref. (80). Reprinted with permission from Elsevier.

In summary, no matter what cocatalysts are used, the final goal is to enhance the transfer of photogenerated carriers. In a word, the Fermi level (relative to noble metal) or bottom of CB (relative to cocatalyst semiconductor) must be lower than the CB bottom of CdS. Generally speaking, for the deposition of cocatalysts, the lower of Fermi level for noble metal or CB bottom of semiconductor is, the more beneficial for the transfer of photogenerated carriers produced by CdS. However, the too low position of Fermi level or CB bottom of cocatalysts will lead to the low energy of photogenerated electrons and the hydrogen evolution from water splitting may be not so effective. For example (88), the photocatalytic hydrogen evolution activity was greatly enhanced for N-graphene/CdS, which was much better than graphene/CdS. The flow of photogenerated electron to the low Fermi level of graphene (0 eV relative to the normal hydrogen electrode) (90) might make the activity of graphene/CdS decrease, compared with that of N-graphene.

5. Sacrificial Reagents

With the presence of electron donor (sacrificial reagent), photogenerated hole will oxidize the electron donor instead of water (91, 92) or CdS itself. As a result, the reduction of water is accelerated by photogenerated electron. Currently, the often used sacrificial reagents include S^{2-}/SO_3^{2-} , lactic acid (60, 74, 87), formic acid (58, 59, 76), ethanol (62), isopropanol (50, 63), glycerol (22), glycol (22) triethanolamine (61). Many other organics have been used as sacrificial reagents as well in some experiments. The mechanism for the presence of the organic sacrificial reagents is similar to the photodegradation of organic contaminant, that is, organics are oxidized by photogenerated holes. The detail is shown in Figure 6.

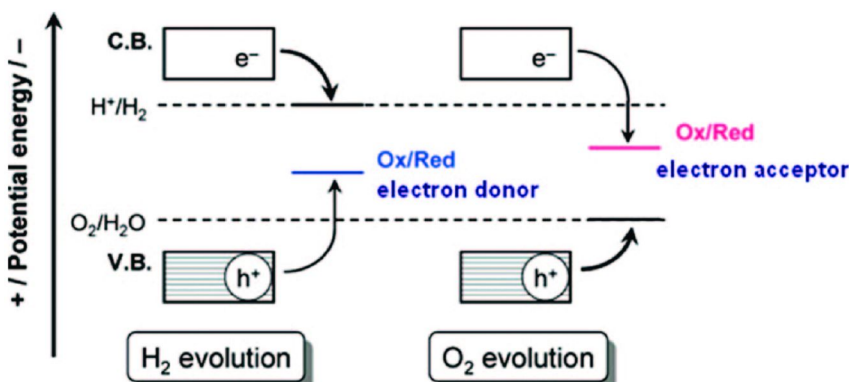
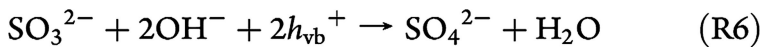
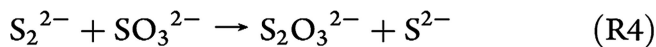
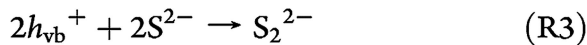
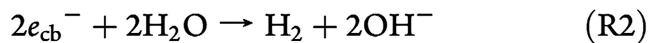
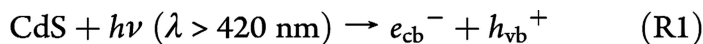


Figure 6. Basic principle of photocatalytic reactions in the presence of sacrificial reagents. Reprinted with permission from Ref. (93) Copyright 2007 American Chemical Society.

Harada (94) reported that CdS showed different oxidation ability for different sacrificial reagents and not all sacrificial reagents was able to be oxidized. For example, lactic acid can not be decomposed since CdS may oxidize the organic compound by •OH group but not photogenerated holes. So, the oxidation potential of sacrificial reagent must be located more positively than the valence band of CdS. The more positive of the oxidation potential of sacrificial reagent is, the easier of the sacrificial reagent is to be decomposed. Zong (22) reported MoS₂/CdS for H₂ evolution with different sacrificial reagents and found that the activity was in the order of lactic acid > glycerol > glycol > ethanol > methanol. The reason might be that CdS demonstrated diverse ability for the oxidation of different sacrificial reagents under visible light, which is consistent with Harada's report (54). Among all of the sacrificial reagents, S²⁻/SO₃²⁻ is the most commonly used one since S ion possesses relatively high reductive ability. It is easy for the reaction between photogenerated hole and S²⁻/SO₃²⁻ to happen. The detailed reactions are as follows (45, 91):



S²⁻ combines with two holes, which generates S elementary substance. Then, SO₃²⁻ reacts with S to generate S₂O₃²⁻. The removal of holes not only protects CdS from photocorrosion but also avoids the recombination with photogenerated electrons.

Besides the above mentioned sacrificial reagents, some inorganic sacrifice agents such as Fe^{2+} , Ce^{3+} and I^- , have been also used in H_2 production system with CdS photocatalysts. The detailed introduction and mechanism can be found in the review by Chen et al. (2). To keep photocatalytic reaction successive going, it is necessary for sacrificial reagents to be added to reaction system constantly. However, continuously addition of sacrificial reagents is inconvenient and what's worse, increases the cost. So, inorganic sacrifice agents will be replaced by organic ones in future since it is a beautiful dream to produce H_2 under solar light while to accomplish organic pollutant degradation.

6. Other Factors

PH can affect photocatalytic activity of hydrogen evolution, which might be inferred from the above equation R2 and R6. Relative low pH is a positive factor for hydrogen evolution. On the contrary, high pH is in favor of the capture of photogenerated holes. While Silva (95) reported that C-CdS/Pt/hex-CdS composite showed much higher activity at pH 14 with the mixed sulfide/sulfite $\text{S}^{2-}/\text{SO}_3^{2-}$ electron donor system. In that case, Pt (II) could be reduced back to Pt(0) at high pH and thus the activity increase was obtained at high pH compared with pH 7. The research about pH effect is so few that it is hard to say which pH is suitable for one particular photocatalytic system. Based on the principle of chemical reaction equilibrium of $\text{H}_2\text{O} = \text{H}_2 + \text{O}_2$, we can know that the removal of oxygen before photocatalytic reaction and the output of the photocatalytic resultant H_2 are the common used ways to promote positive reaction of H_2 evolution.

7. Summary and Prospects

To roundly study the photocatalytic activity for hydrogen production from water splitting over the above-mentioned CdS -based semiconductors, we list the reported CdS -based photocatalysts, their rate and QE for hydrogen evolution and some important parameters in photocatalytic reaction in Table 1. Because the equipment, photocatalyst mass, light source etc are different in different photocatalytic systems, we can only compare the samples with calculated quantum efficiency.

Table 1. Main CdS-based semiconductor photocatalysts for hydrogen evolution from water splitting under visible light.

Photocatalyst	Mass (g)/Volume (ml)	Light source (W/nm)	Sacrificial agent	Co catalyst	Rate ($\mu\text{mol}/(\text{h. 0.1g})$)	QE(%) 420 nm	Reference
Pt-PbS-CdS	0.3/200	300Xe ≥420	Na ₂ S Na ₂ SO ₃	Pt	2923	93	(86, 96)
Nanoporous CdS	0.15/200	300Xe ≥420	Na ₂ S Na ₂ SO ₃	Pt	-	60.34	(11)
CdS/TiO ₂ nanotube	0.15/300	300Xe ≥420	Na ₂ S Na ₂ SO ₃	Pt	208	43.4	(41)
CdS/ZnS/In ₂ S ₃	0.015/320	300Xe ≥400	Na ₂ S Na ₂ SO ₃	-	810	40.9	(26)
CdS/TaON	0.2/200	300Xe =420	Na ₂ S Na ₂ SO ₃	Pt	316.5	31	(49)
Ni(OH) ₂ /CdS	0.05/80	300Xe ≥420	triethylamine	Pt	508.4	28	(57)
CdS/TNT	0.2/190	500Xe ≥430	Na ₂ S Na ₂ SO ₃	Pt	176.7	25.5	(38)
Reduced GO-Zn _{1-x} Cd _x S	0.05/80	Solar simulator	Na ₂ S Na ₂ SO ₃	-	182.4	23.4	(77)
CdS/GR	0.02/80	350Xe ≥420	Lactic acid	Pt	5600	22.5	(75)
CdS-AgGaS ₂	0.1	450Hg ≥420	Na ₂ S Na ₂ SO ₃	Pt	296	19.7	(26)

Continued on next page.

Table 1. (Continued). Main CdS-based semiconductor photocatalysts for hydrogen evolution from water splitting under visible light.

Photocatalyst	Mass (g)/Volume (ml)	Light source (W/nm)	Sacrificial agent	Co catalyst	Rate ($\mu\text{mol}/(\text{h. 0.1g})$)	QE(%) 420 nm	Reference
Sr/CdS	0.2/50	350Xe	Na ₂ S Na ₂ SO ₃	-	123	10	(24)
CdS/TiO ₂	0.1/50	350Xe ≥400	Na ₂ S Na ₂ SO ₃	-	-	8.9	(43)
MoS ₂ /CdS	0.1/200	300Xe ≥420	Organic reagents	-	533	7.3	(21)
CdS-Zn _{1-x} Cd _x S	0.05/80	350Xe ≥400	Na ₂ S Na ₂ SO ₃	-	≈230	6.3	(8)
NiO-CdS	0.2/50	500 halogen	Na ₂ S Na ₂ SO ₃	-	74.5	6	(55)
CdS/TiO ₂	0.0125/25	450Xe ≥420	Na ₂ S Na ₂ SO ₃	Pt	672	4.5	(36)
SrS/CdS	0.2/200	350Xe ≥430	Na ₂ S Na ₂ SO ₃	-	-	2.85	(19)
Z-CdS-Cd	0.1/300	300Xe	Na ₂ S Na ₂ SO ₃	Pt	1920	-	(56)
PANI-PbS- CdS	0.2/200	300Xe ≥430	Na ₂ S Na ₂ SO ₃	-	1660	-	(68)
CeO ₂ /CdS	0.05/100	300Xe	Na ₂ S Na ₂ SO ₃	-	1564	-	(53)

Photocatalyst	Mass (g) /Volume (ml)	Light source (W/nm)	Sacrificial agent	Co catalyst	Rate ($\mu\text{mol}/(\text{h. } 0.1\text{g})$)	QE(%) 420 nm	Reference
Mesoporous CdS	0.1/50	400Hg	Na ₂ S Na ₂ SO ₃	Pt	1415	-	(10)
CdS/Ta ₂ O ₅	0.05/50	Xe 400-800	Lactic acid	-	≈900	-	(60)
Z-CdS	0.2/200	300Xe	Na ₂ S Na ₂ SO ₃	RuO ₂	≈630	-	(24)
CdS/Zeolite	0.1/50	400Hg UV	Na ₂ S Na ₂ SO ₃	Pt	600	-	(85)
MoS ₂ /CdS	0.1/200	300Xe	Lactic Acid	MoS ₂	≈530	-	(87)
MWCNTS/CdS	0.035/100	300Xe ≥420	Na ₂ S Na ₂ SO ₃	-	498	-	(72)
CdS Microcrystal	0.03/40	500Xe ≥400	Na ₂ S Na ₂ SO ₃	Pt	460	-	(14)
CdS/CdWO ₄	0.05/200	500Xe	Na ₂ S Na ₂ SO ₃	-	180.5	-	(51)
hexagonal CdS	0.3/200	300Xe ≥420	Na ₂ S Na ₂ SO ₃	Pt	160	-	(9)
CdS	0.1/100	500Hg ≥420	Na ₂ S Na ₂ SO ₃	WC	≈136	-	(80)
CdS/Re-Cellulose	0.05/100	250Xe ≥420	Na ₂ S Na ₂ SO ₃	Pt	132.3	-	(69)

Continued on next page.

Table 1. (Continued). Main CdS-based semiconductor photocatalysts for hydrogen evolution from water splitting under visible light.

Photocatalyst	Mass (g)/Volume (ml)	Light source (W/nm)	Sacrificial agent	Co catalyst	Rate ($\mu\text{mol}/(\text{h. 0.1g})$)	QE(%) 420 nm	Reference
N-GR/CdS	0.2/300	300Xe >420	Na ₂ S Na ₂ SO ₃	-	105	-	(88)
Ag ₂ S/CdS	0.1/120	Hg-Xe >400	Na ₂ S Na ₂ SO ₃	Ag ₂ S and Pt	87.4	-	(89)
Hexagonal CdS	0.1/200	300Xe ≥ 420	Lactic acid	Pt	74.9	-	(12)
Sr-CdS-ZnS	0.2/200	500Xe >430	Na ₂ S Na ₂ SO ₃	-	≈ 51	-	(23)
LaMnO ₃ /CdS	0.1/60	300Xe Visible light	Na ₂ S Na ₂ SO ₃	-	37.5	-	(47)
PANI-CdS	0.2/180	400Xe >420	Na ₂ S Na ₂ SO ₃	-	29.91	-	(67)
CdS/TiO ₂	0.1/100	450Hg ≥ 420	Na ₂ S Na ₂ SO ₃	Pt	≈ 11	-	(42)
CdS Nanowire	0.1/100	500Hg <400	Na ₂ S Na ₂ SO ₃	Pt	≈ 6	-	(13)
CdS/ZnS	0.1/10	00Ha UV	Na ₂ S Na ₂ SO ₃	-	≈ 4.5	-	(19)

By the analysis of various methods for CdS modification and the data shown in Table 1, we can draw some conclusions. In current systems of hydrogen production from water splitting over CdS-based photocatalysts under solar light, sacrificial reagents are essential, among which S^{2-}/SO_3^{2-} is the most commonly used one and the activity of hydrogen evolution for CdS with this sacrificial reagent is acceptable as well. In order to improve the activity for hydrogen evolution, cocatalysts are also necessary to be deposited onto the surface of photocatalysts. Although some low cost cocatalysts with high activity have been prepared (in part of 2.3), Pt as a highly efficient cocatalyst can not be substituted currently. With the presence of Pt on the surface of CdS, the materials can have the activity with remarkable enhancement. In some articles, the materials used to hybridize CdS such as TiO_2 , $Ni(OH)_2$, GR and so on can effectively separate photogenerated electrons and holes, the function of which is similar to that of reductive cocatalyst. Among all the modified materials of CdS, Pt–PdS/CdS (86, 96) has the highest quantum efficiency (93%) for hydrogen evolution and the materials process good photostability as well. The simultaneous presence of both PdS as an oxidation cocatalyst and Pt (or Pd) as a reduction cocatalyst is supposed to be beneficial for the efficient separation of the photogenerated electrons and holes, which contributes to the extremely high QE. So, the synergetic effect is far more important than simple one factor, which can be resulted from multiple function cocatalysts, both oxidation and reduction cocatalysts, material hybridization and reduction cocatalyst, etc. However, the complexity of multiple modified methods to achieve the synergetic effect hampers people to study it in detail. For example, in Li et al.'s report (96), the highest quantum effect of hydrogen evolution can be obtained with co-loading 0.30 wt% Pt and 0.13 wt% PdS onto CdS surface. However, CdS with loading of 0.65 wt% single Pt can reach the highest activity for Pt–CdS system. So, it is hard to say 0.30 wt% Pt and 0.13 wt% PdS is the most optimum deposition amount onto CdS. In many articles, people only concentrate on the study of the factors such as the kind of composite and the molar ratio of the composite. However, they ignore the other important factor such as the amount of deposited Pt. There should be an optimal amount for different composites.

For future application, the hydrogen evolution from water splitting through photocatalysis under solar light should be as simple as possible, be able to keep going consecutively for a long time and the most important, be low cost. For this purpose, the overall water-splitting systems have been developed (97–99). Nevertheless, with regard to CdS photocatalyst, overall water splitting reaction can not be achieved until the photostability of CdS can be improved greatly. Since sacrificial reagent is necessary to protect CdS from photocorrosion and thus the sacrificial reagent must be added to replenish the consumed part. As a result, the cost increases and the reaction procedure is not continuous. In order to overcome the shortage, a new experiment system has been designed and developed (82), in which the sacrificial reagent can be circulatory utilized.

Above all, great progress has been made for the hydrogen evolution by CdS-based photocatalysts but there is still a long way to go before practical application. The photocatalytic hydrogen production will keep in the laboratory stage for a while until the energy conversion efficiency reaches 10%. We propose

that multiply modified methods to achieve synergetic effect may be an effective way to obtain new CdS-based photocatalysts for highly efficient hydrogen production from water splitting under solar light in future.

Acknowledgments

This work was financially supported by the National Natural Science Foundation of China (No. 20973070), the National Basic Research Program of China (No. 2009CB939704) and the Key Project of Natural Science Foundation of Hubei Province (No. 2011CDA092).

References

1. Fujishima, A.; Honda, K. *Nature* **1972**, *238*, 37.
2. Chen, X. B.; Shen, S. H.; Guo, L. J.; Mao, S. S. *Chem. Rev.* **2010**, *110*, 6503.
3. Yu, J. G.; Zhang, J.; Jaroniec, M. *Green Chem.* **2010**, *12*, 1611.
4. Cao, J.; Sun, J. Z.; Hong, J.; Li, H. Y.; Chen, H. Z.; Wang, M. *Adv. Mater.* **2004**, *16*, 84.
5. Matsumura, M.; Furukawa, S.; Saho, Y.; Tsubomura, H. *J. Phys. Chem.* **1985**, *89*, 1327.
6. Reber, J. F.; Meier, K. *J. Phys. Chem.* **1986**, *90*, 824.
7. Li, W. J.; Li, D. Z.; Chen, Z. X.; Huang, H. J.; Sun, M.; He, Y. H.; Fu, X. Z. *J. Phys. Chem. C* **2008**, *112*, 14943.
8. De, G. C.; Roy, A. M.; Bhattacharya, S. S. *Int. J. Hydrogen Energy* **1995**, *20*, 127.
9. Bao, N. Z.; Shen, L.; Takata, T.; Domen, K.; Gupta, A.; Yanagisawa, K.; Grimes, G. A. *J. Phys. Chem. C* **2007**, *111*, 17527.
10. Sathish, M.; Viswanath, R. P. *Catal. Today* **2007**, *29*, 421.
11. Bao, N. Z.; Shen, L.; Takata, T.; Domen, K. *Chem. Mater.* **2008**, *20*, 110.
12. Fan, Y. Z.; Chen, G. P.; Li, D. M.; Li, F.; Luo, Y. H.; Meng, Q. B. *Mater. Res. Bull.* **2011**, *46*, 2338.
13. Jang, J. S.; Joshi, U. A.; Lee, J. S. *J. Phys. Chem. C* **2007**, *111*, 13280.
14. Muruganandham, M.; Kusumoto, Y.; Okamoto, C.; Muruganandham, A.; Abdulla-Al-Mamun, M.; Ahmmad, B. *J. Phys. Chem. C* **2009**, *113*, 19506.
15. Daskalaki, V. M.; Antoniadou, M.; Puma, G. L.; Kondarides, D. I.; Lianos, P. *Environ. Sci. Technol.* **2010**, *44*, 7200.
16. Qiu, X.; Miyauchi, M.; Yu, H.; Irie, H.; Hashimoto, K. *J. Am. Chem. Soc.* **2010**, *132*, 15259.
17. Kong, M.; Li, Y. Z.; Chen, X.; Tian, T. T.; Fang, P. F.; Zheng, F.; Zhao, X. J. *J. Am. Chem. Soc.* **2011**, *133*, 16414.
18. Yang, F.; Yan, N. N.; Huang, S.; Sun, Q.; Zhang, L. Z.; Yu, Y. *J. Phys. Chem. C* **2012**, *116*, 9078.
19. Deshpande, A.; Shah, P.; Gholap, R. S.; Gupta, M. N. *J. Colloid Interface Sci.* **2009**, *333*, 263.
20. Liu, H. P.; Zhang, K.; Jing, D. W.; Liu, G. J.; Guo, L. J. *Int. J. Hydrogen Energy* **2010**, *35*, 7080.

21. Thibert, A.; Frame, F. A.; Busby, E.; Holmes, M. A.; Osterloh, F. E.; Larsen, D. S. *J. Phys. Chem. Lett.* **2011**, *2*, 2688.
22. Zong, X.; Wu, G. P.; Yan, H. J.; Ma, G. J.; Shi, J. Y.; Wen, F. Y.; Wang, L.; Li, C. *J. Phys. Chem. C* **2010**, *114*, 1963.
23. Zhang, K.; Jing, D. W.; Chen, Q. Y.; Guo, L. J. *Int. J. Hydrogen Energy* **2010**, *35*, 2048.
24. Wang, X. W.; Liu, G.; Lu, G. Q.; Cheng, H. M. *Int. J. Hydrogen Energy* **2010**, *35*, 8199.
25. Khan, Z.; Chetia, T. R.; Qureshi, M. *Nanoscale* **2012**, *4*, 3543.
26. Shen, Z. Y.; Chen, G.; Wang, Q.; Yu, Y. G.; Zhou, C.; Wang, Y. *Nanoscale* **2012**, *4*, 2010.
27. Jang, J. S.; Hwang, D. W.; Lee, J. S. *Catal. Today* **2007**, *120*, 174.
28. Liu, M. C.; Du, Y. C.; Ma, L. J.; Jing, D. W.; Guo, L. J. *Int. J. Hydrogen Energy* **2012**, *37*, 730.
29. Sasikala, R.; Shirole, A. R.; Sudarsan, V.; Girija, K. G.; Rao, R.; Sudakar, C.; Bharadwaj, S. R. *J. Mater. Chem.* **2011**, *21*, 16566.
30. Zhang, W.; Zhong, Z. Y.; Wang, Y. S.; Xu, R. *J. Phys. Chem. C* **2008**, *112*, 17635.
31. Zhang, K.; Zhou, Z. H.; Guo, L. *Int. J. Hydrogen Energy* **2011**, *36*, 9469.
32. Peng, S. Q.; An, R.; Li, Y. X.; Lu, G. X.; Li, S. B. *Int. J. Hydrogen Energy* **2012**, *37*, 1366.
33. Wang, Y. B.; Wu, J. C.; Zheng, J. W.; Jiang, R. R.; Xu, R. *Catal. Sci. Technol.* **2012**, *2*, 581.
34. Zhang, X. H.; Jing, D. W.; Liu, M. C.; Guo, L. J. *Catal. Commun.* **2008**, *9*, 1720.
35. Ren, L.; Yang, F.; Deng, Y. R.; Yan, N. N.; Huang, S.; Lei, D.; Sun, Q.; Yu, Y. *Int. J. Hydrogen Energy* **2010**, *35*, 3297.
36. Park, H.; Choi, W.; Hoffmann, M. R. *J. Mater. Chem.* **2008**, *18*, 2379.
37. Xing, C. J.; Jing, D. W.; Liu, M. C.; Guo, L. J. *Mater. Res. Bull.* **2009**, *44*, 442.
38. Chen, Y. B.; Wang, L. Z.; Lu, G. Q.; Yao, X. D.; Guo, L. J. *J. Mater. Chem.* **2011**, *21*, 5134.
39. Zhang, Y. J.; Yan, W.; Wu, Y. P.; Wang, Z. H. *Mater. Lett.* **2008**, *62*, 3846.
40. Zhu, W.; Liu, X.; Liu, H. Q.; Tong, D. L.; Yang, J. Y.; Peng, J. Y. *J. Am. Chem. Soc.* **2010**, *132*, 12619.
41. Li, C. L.; Yuan, J.; Han, B. Y.; Jiang, L.; Shangguan, W. F. *Int. J. Hydrogen Energy* **2010**, *35*, 7073.
42. Jang, J. S.; Kim, H. G.; Joshi, U. A.; Jang, J. W.; Lee, J. S. *Int. J. Hydrogen Energy* **2008**, *33*, 5975.
43. He, D. L.; Chen, M. D.; Teng, F.; Li, G. Q.; Shi, H. X.; Wang, J.; Xu, M. J.; Lu, T. Y.; Ji, X. Q.; Lv, Y. J.; Zhu, Y. F. *Superlattices Microstruct.* **2012**, *51*, 799.
44. Shen, J.; Meng, Y. L.; Xin, G. *Rare Met.* **2011**, *30* (Supplement), 280.
45. Park, H.; Kim, Y. K.; Choi, W. Y. *J. Phys. Chem. C* **2011**, *115*, 6141.
46. Li, Y. F.; Xu, D. H.; Oh, J. I.; Shen, W. Z.; Li, X.; Yu, Y. *ACS Catal.* **2012**, *2*, 391.
47. Kida, T.; Guan, G. Q.; Yoshida, A. *Chem. Phys. Lett.* **2003**, *371*, 563.

48. Cui, W. Q.; Ma, S. S.; Liu, L.; Hu, J. S.; Liang, Y. H. *J. Mole. Catal. A: Chem.* **2012**, *359*, 35.
49. Hou, J. G.; Wang, Z.; Kan, W. B.; Jiao, S. Q.; Zhu, H. M.; Kumar, R. V. *J. Mater. Chem.* **2012**, *22*, 7291.
50. Choi, J.; Ryu, S. Y.; Balcerksi, W.; Lee, T. K.; Hoffmann, M. R. *J. Mater. Chem.* **2008**, *18*, 2371.
51. Wang, L.; Wang, W. Z. *CrystEngComm* **2012**, *14*, 3315.
52. Cui, W. Q.; Liu, Y. F.; Liu, L.; Hu, J. S.; Liang, Y. H. *Appl. Catal. A: Gen.* **2012**, *417*, 111.
53. Lu, X. H.; Xie, S. L.; Zhai, T.; Zhao, Y. F.; Zhang, P.; Zhang, Y. L.; Tong, Y. X. *RSC Adv.* **2011**, *1*, 1207.
54. Navarro, R. M.; Valle, F. D.; Fierro, J. L. G. *Int. J. Hydrogen Energy* **2008**, *33*, 4265.
55. Ziyauddin Khan, Z.; Khannam, M.; Vinothkumar, N.; De, M.; Qureshi, M. *J. Mater. Chem.* **2012**, *22*, 12090.
56. Wang, X. W.; Liu, G.; Wang, L. Z.; Chen, Z. G.; Lu, G. Q.; Cheng, H. M. *Adv. Energy Mater.* **2012**, *2*, 42.
57. Ran, J. R.; Yu, J. G.; Jaroniec, M. *Green Chem.* **2011**, *13*, 2708.
58. Zhang, Y. J.; Zhang, L. *Desalination* **2009**, *249*, 1017.
59. Zhang, Y. J.; Zhang, L.; Li, S. *Int. J. Hydrogen Energy* **2010**, *35*, 438.
60. Xu, L. L.; Shi, W. D.; Guan, J. G. *Catal. Commun.* **2012**, *25*, 54.
61. Liu, Z.; Shen, S. H.; Guo, L. J. *Int. J. Hydrogen Energy* **2012**, *37*, 816.
62. Ryu, S. Y.; Balcerksi, W.; Lee, T. K.; Hoffmann, M. R. *J. Phys. Chem. C* **2007**, *111*, 18195.
63. Hirai, T.; Bando, Y. *J. Colloid Interface Sci.* **2005**, *288*, 513.
64. Tambwekar, S. V.; Subrahmanyam, M. *Int. J. Hydrogen Energy* **1998**, *23*, 741.
65. Arora, K.; Sahu, N.; Upadhyay, S. N.; Sinha, A. S. K. *Ind. Eng. Chem. Res.* **1999**, *38*, 4694.
66. Kanade, K. G.; Baeg, J.; Mulik, U. P.; Amalnerkar, D. P.; Kale, B. B. *Mater. Res. Bull.* **2006**, *41*, 2219.
67. He, K.; Li, M. T.; Guo, L. J. *Int. J. Hydrogen Energy* **2012**, *37*, 755.
68. Zhang, S.; Chen, Q. Y.; Jing, D. W.; Wang, Y. H.; Guo, L. J. *Int. J. Hydrogen Energy* **2012**, *37*, 791.
69. Ke, D. N.; Liu, S. L.; Dai, K.; Zhou, J. P.; Zhang, L. N.; Peng, T. Y. *J. Phys. Chem. C* **2009**, *113*, 16021.
70. Lunawat, P. S.; Senapati, S.; Kumar, R.; Gupta, N. M. *Int. J. Hydrogen Energy* **2007**, *32*, 2784.
71. Lau, V. W.; Water, L. G. A.; Masters, A. F.; Maschmeyer, T. *Chem. Eur. J.* **2012**, *18*, 2923.
72. Peng, T. Y.; Zeng, P.; Ke, D. N.; Liu, X. J.; Zhang, X. H. *Energy Fuels* **2011**, *25*, 2203.
73. Yu, J. G.; Yang, B.; Cheng, B. *Nanoscale* **2012**, *4*, 2670.
74. Li, Q.; Guo, B. D.; Yu, J. G.; Ran, J. R.; Zhang, B. H.; Yan, H. J.; Gong, J. R. *J. Am. Chem. Soc.* **2011**, *133*, 10878.
75. Ye, A.; Fan, W. Q.; Zhang, Q. H.; Deng, W. P.; Wang, Y. *Catal. Sci. Technol.* **2012**, *2*, 969.

76. Gao, P.; Liu, J. C.; Lee, S.; Zhang, T.; Sun, D. D. *J. Mater. Chem.* **2012**, *22*, 2292.
77. Zhang, J.; Yu, J. G.; Jaroniec, M.; Gong, J. R. *Nano Lett.* **2012**, *12*, 4584.
78. Xiong, L. B.; Huang, S.; Yang, X.; Qiu, M. Q.; Chen, Z. H.; Yu, Y. *Electrochim. Acta* **2011**, *56*, 2735.
79. Huang, K.; Han, R. Q. *Solid State Physics*; Higher Education Press: Beijing, 1985; pp 286–290.
80. Jang, J. S.; Ham, D. J.; Lakshminarasimhan, N.; Choi, W. Y.; Lee, J. S. *Appl. Catal. A: Gen.* **2008**, *346*, 149.
81. Huang, C.; Illiassou, B.; T-Raissi, A.; Muradov, N. *Proc. SPIE* **2007**, *6650*, 665010.
82. Berr, M.; Vaneski, A.; Susha, A. S.; Rodríguez-Fernández, J.; Döblinger, M.; Jäckel, F.; Rogach, A. L.; Feldmann, J. *Appl. Phys. Lett.* **2010**, *97*, 093108.
83. Lin, Y. J.; Xu, Y.; Mayer, M. T.; Simpson, Z. I.; McMahon, G.; Zhou, S.; Wang, D. *J. Am. Chem. Soc.* **2012**, *134*, 5508.
84. Zhong, D. K.; Cornuz, M.; Sivula, K.; Gratzel, M.; Gamelin, D. R. *Energy Environ. Sci.* **2011**, *4*, 1759.
85. Sathish, M.; Viswanathan, B.; Viswanath, R. P. *Int. J. Hydrogen Energy* **2006**, *31*, 891.
86. Yang, J. H.; Yan, H. J.; Wang, X. L.; Wen, F. Y.; Wang, Z. J.; Fan, D. Y.; Shi, J. Y.; Li, C. *J. Catal.* **2012**, *290*, 151.
87. Zong, X.; Yan, H. J.; Wu, G. P.; Ma, G. J.; Wen, F. Y.; Wang, L.; Li, C. *J. Am. Chem. Soc.* **2008**, *130*, 7176.
88. Jia, L.; Wang, D. H.; Huang, Y. X.; Xu, A. W.; Yu, H. Q. *J. Phys. Chem. C* **2011**, *115*, 11466.
89. Shen, S. H.; Guo, L. J.; Chen, X. B.; Ren, F.; Mao, S. S. *Int. J. Hydrogen Energy* **2010**, *35*, 7110.
90. Yu, H. T.; Chen, S.; Fan, X. F.; Quan, X.; Zhao, H. M.; Li, X. Y.; Zhang, Y. B. *Angew. Chem., Int. Ed.* **2010**, *49*, 5106.
91. Xu, Z. D.; Li, Y. X. Doctoral Dissertation. Nan Chang University, 2011; p 13.
92. Zhang, J.; Yu, J. G. Doctoral Dissertation. Wuhan University of Technology, 2010; p 20.
93. Maeda, K.; Domen, K. *J. Phys. Chem. C* **2007**, *111*, 7851.
94. Harada, H.; Sakata, T.; Ueda, T. *J. Am. Chem. Soc.* **1985**, *107*, 1773.
95. Silva, L. A.; Ryu, S. Y.; Choi, J.; Choi, W. Y.; Hoffmann, M. R. *J. Phys. Chem. C* **2008**, *112*, 12069.
96. Yan, H. J.; Yang, J. H.; Ma, G. J.; Wu, G. P.; Zong, X.; Lei, Z. B.; Shi, J. Y.; Li, L. *J. Catal.* **2009**, *266*, 165.
97. Takata, T.; Tanaka, A.; Hara, M.; Kondo, J. N.; Domen, K. *Catal Today* **1998**, *44*, 17.
98. Zou, Z.; Ye, J.; Sayama, K.; Arakawa, H. *Nature* **2001**, *414*, 625.
99. Wang, D. G.; Li, R. G.; Zhu, J.; Shi, J. Y.; Han, J. F.; Zong, X.; Li, C. *J. Phys. Chem. C* **2012**, *116*, 5082.

Chapter 10

Self-Assembly of Nanostructured Proton Exchange Membranes for Fuel Cells

Haolin Tang,^{*,1} Junrui Li,^{1,2} Zhao Wang,¹ Huijie Zhang,¹ Mu Pan,¹ and San Ping Jiang^{*,3}

¹State Key Laboratory of Advanced Technology for Materials Synthesis and Processing, Wuhan University of Technology, Wuhan 430070, People's Republic of China

²Department of Chemistry, School of Science, Wuhan University of Technology, Wuhan 430070, People's Republic of China

³Fuels and Energy Technology Institute and Department of Chemical Engineering, Curtin University, Perth, WA 6102, Australia

*E-mail: tanghaolin2005@yahoo.com.cn (H.T.); s.jiang@curtin.edu.au (S.P.J.)

Research interest for the synthesis and fabrication of novel proton conducting electrolytes which can be operated under the elevated temperatures and low relative humidification (RH) conditions has been increased extensively in recent years. Self-assembly is a powerful, efficient and environment-friendly technical tool to create highly ordered nano-structures with unique properties and has been extensively investigated and applied to the development of highly efficient proton conductive electrolyte materials for fuel cells. For instance, nano-structured Nafion membranes via self-assembly approaches can achieve significantly enhanced proton conductivity under reduced humidity, as compared to pristine Nafion membranes. In this Chapter, an overview of the application of self-assembly technique in the synthesis and development of novel nano-structured proton exchange membranes and their electrochemical performance for fuel cells is presented. New opportunities for highly ordered and low humidity or anhydrous-operating proton exchange membranes are critically reviewed and discussed.

Keywords: fuel cells; self-assembly; hybrid composite membrane; Nano-structured proton exchange membranes; proton conductivity

Introduction

Fuel cells are electrochemical devices to convert the chemical energy of fuels such as hydrogen, methanol and natural gas into electricity without combustion route. Thus fuel cells are inherently highly efficient and emit much low greenhouse gases as compared to conventional energy conversion technologies such as internal combustion engine (ICE). Fuel cells are also versatile devices ranging from room temperature fuel cells such as proton exchange membrane fuel cells (PEMFCs), medium temperature (650-700 °C) molten carbonate fuel cells (MCFCs) to high temperature (700 - 1000 °C) solid oxide fuel cells (SOFCs). As one of the key members in fuel cells, PEMFCs are considered to be the most promising power sources for applications from portable electronic devices, vehicle transportation to stationary power generation (1-5).

The core component of a PEMFC is a membrane-electrode-assembly (MEA) with the electrocatalytic anode and cathode separated by a proton exchange membrane (PEM). The PEM has an essential function of a proton conducting medium as well as a barrier to prevent the mixing between fuel and oxidant. Perfluorosulfonic acid based polymer such as Nafion is the most popular PEM due to its high proton conductivity when fully hydrated and high chemical stability (6, 7). However, Nafion is expensive and its proton conductivity is very sensitive to the the water uptake (8, 9), which requires the complicated water managmenet units to maintain the adequate humidity level for the practical applications. In the case of PEMFCs using liquid fuels such as methanol, methanol readily migrates from the anode, through the Nafion membrane, to the cathode, reducing the open-circuit potential (OCP) by as much as 0.15 – 0.2 V and poisoning the electrocatalysts at the cathode (10). The methanol crossover of Nafion based membrane can be suppressed by conventional hybrid composite or surface modification techniques such as deposition with Pd-based thin film (11), formation of multilayered Nafion/sulfonated poly(etheretherketone) (SPEEK) (12), and Nafion-silica or Nafion-heteropolyacids hybrid composites (13, 14). The modification of Nafion membrane in general reduces the methanol crossover. However, the incorporation of inorganic nanoparticles such as silica inevitably alters the microstructure of Nafion, resulting in the deterioration in mechanical strength and proton conductivity particularly in the case of non-conducting inorganic particles.

Layer-by-layer (LbL) self-assembly is a powerful and emerging tool for the synthesis of the highly ordered nanostuctures with unique properties (15-18). Self-assembly is a spontaneous process and is essentially driven by inter-molecular forces such as electrostatic, dispersive, hydrogen bonding, and coordinations without the disruption of the exisiting bonds within the organic or inorganic molecular building blocks. The method is environmentally friendly and low cost for constructing highly ordered nanostructures in molecular scale

without use of toxic chemicals. LbL self-assembly technique has been applied for the development of highly catalytically active and nano-structured materials for solar cells (19–22), lithium-ion batteries (23–25), fuel cells (26–29) and supercapacitors (30–32). Most recently Xiang et al presented an extensive review on the application of LbL self-assembly in electrochemical energy conversion devices such as fuel cells and supercapacitors (33).

Owing to its unique advantages, LbL self-assembly has been increasingly applied to the development of novel proton conducting membranes for fuel cells (34–39). This Chapter will start with the modification and enhancement of the state-of-the-art Nafion membranes *via* LbL self-assembly techniques and then its application in building nanostructured proton conducting electrolyte for fuel cells will be critically reviewed and discussed.

Enhancing Nafion Membrane by Self-Assembly

Modification of Nafion by LbL Self-Assembly Technique

Direct methanol fuel cells (DMFCs) show the most promising potential as power sources for microelectronic and portable electronic devices due to high theoretical power density and easy storage and accessibility of liquid fuels. However, methanol crossover from the anode side to the cathode side is a significant issue of Nafion membrane based DMFCs. Early reports show that charged Pt (40–42), Pd (43–45) or Au (46, 47) nanoparticles can be self-assembled onto the surface of Nafion membranes and such surface modified Nafion membranes show the significantly reduced methanol permeability for DMFCs. The charged metal nanoparticles are prepared by alcoholic reduction of the metallic ions in the presence of positively charged polyelectrolyte such as poly(diallyldimethylammonium chloride) (PDDA). The function of PDDA is to stabilize synthesized metal nanoparticles and to make the metal nanoparticles positively charged. In this case, self-assembly occurs due to the electrostatic forces between the positively charged metallic nanoparticle and the negatively charged sulfonic acid function groups on Nafion membrane surface, via the classic Coulomb law:

$$E = (Z_1 e)(Z_2 e) / 4\pi\epsilon_0\chi \quad (1)$$

in which E is the interaction energy, Z_1 and Z_2 stand for the charge number of the cation and the anion, e is the unit charge, ϵ_0 and χ represent the vacuum electric constant and the distance between the two ions, respectively. The electrostatic self-assembly of positively charged metallic nanoparticles reverse the surface charge of Nafion membrane, inhibiting the further assembly or packaging of charged particles. Consequently, a molecular monolayer structure is obtained. Such surface modified Nafion membrane shows a dramatically reduced methanol permeability to $\sim 1.3 \times 10^{-15}$ mol cm $^{-2}$ s $^{-1}$, as compared to that of pristine Nafion membranes (45). On the other hand, the blocking effect of the self-assembled metal nanoparticles on the proton conductivity is relatively small.

LbL self-assembly of polyelectrolyte multilayer films has been shown to be effective to enhance the resistance of Nafion membranes to methanol permeability (48). Very different from the conventional approaches to incorporate hygroscopic metal oxide particles such as SiO_2 , TiO_2 and zirconium phosphate into the hydrophilic domains of the Nafion-based membranes to reduce the methanol permeation with the cost of the deteriorated durability (6, 49–51), the LbL self-assembled polyelectrolyte multilayer films on Nafion has no detrimental effect on its thermal and chemical stability. Figure 1 shows the methanol crossover current and the power output of modified Nafion membrane cells in methanol fuel as a function of LbL self-assembled multilayers (48).

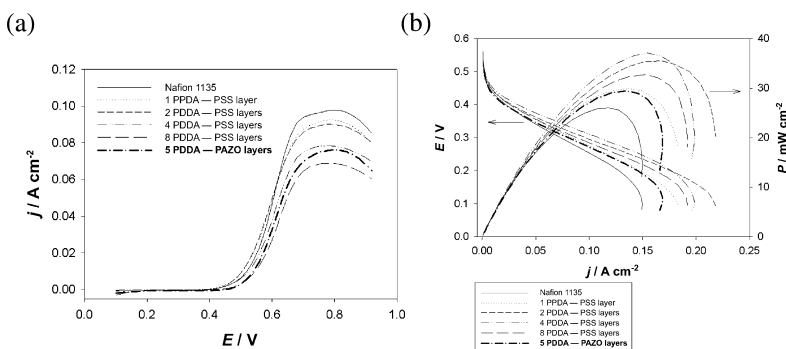


Figure 1. (a) Methanol-crossover current of an MEA with LbL self-assembly of PDDA-PSS and PDDA-PAZO bilayers on N1135 membranes, measured at 30 °C. (b) Polarization curves and power output of a DMFC using an unmodified Nafion1135 membrane, and N1135 membranes modified with self-assembled PDDA-PSS and PDDA-PAZO bilayers, measured at 30 °C. Operating conditions: 2 M CH_3OH , 0 psi; cathode, oxygen, 10 psi. (Reproduced with permission from ref. (48) ©2006, John Wiley and Sons)

The methanol-crossover limiting current decreases with the increase in the number of LbL self-assembled PDDA-PSS (poly(sodium styrene sulfonate) polyelectrolyte bilayer (Fig.1a), indicating that the LbL self-assembly of the PDDA-PSS bilayer reduces the methanol crossover. With eight self-assembled PDDA-PSS bilayers, the limiting methanol-crossover current density is 69 mA cm^{-2} , a decrease of 30% in methanol permeability in comparison to 98 mA cm^{-2} measured for an unmodified Nafion1135 membrane. With an increasing number of PDDA-PSS bilayers, the OCP increased slightly to 0.56 V, most likely owing to a reduction of the methanol crossover (Fig.1b). The best performance was observed for the DMFC that used an N1135 membrane with four self-assembled PDDA-PSS bilayers, achieving a power density of 37 mW cm^{-2} , an increase of 42% in power output when compared to the cell using an unmodified N1135 membrane (26 mW cm^{-2}). However, on further increasing the number of polyelectrolyte bilayers, the maximum power density decreases, indicating that excessive polyelectrolyte bilayers also decrease the proton conductivity of the Nafion membranes.

The effectiveness of the LBL self-assembly technique for enhancing the methanol crossover resistance of proton exchange membranes has also been confirmed by others (36, 52–56). Assembly of a multi-layered film on the surface of Nafion membranes can be carried by immersing the membrane alternatively in solutions with positively and negatively charged polyelectrolytes or nanoparticles (see Fig.2). The self-assembled PDDA-PSS multilayer modified Nafion membrane, Nafion/[PPDA-PSS]_n showed slightly higher open circuit voltage (OCV) and better cell performance than the pristine Nafion membrane (as shown in Fig.2b). Poly (allylaminehydrochloride) (PAH) has been found to be a good substitute for PPDA with amidogen function groups contained in the side chain of the polymer backbones (57). Nafion membrane assembled with 20 PAH/PSS bi-layers showed little reduction in the proton conductivity. The addition of salt ions has been found to enhance the proton conductivity and reduce the methanol crossover compared to the pristine Nafion membrane. Ion exchange with 0.1M and 1.0M NaCl solutions of (PAH/PSS)₅–H⁺ form membrane results in the proton conductivity of 87.91 and 74.69 mS cm⁻¹ which are 2–3 times higher than that of untreated Nafion117 (57). Transforming the morphology of the LBL film to a porous matrix can also increase the proton conductivity of LBL self-assembled membranes (58). Self-assembled PDDA-PSS multilayers on the Nafion membranes are also shown to be effective to suppress vanadium ion crossover for vanadium redox flow batteries (59).

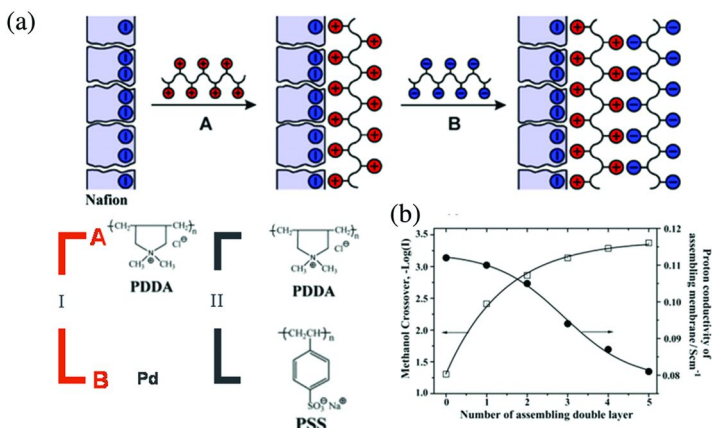


Figure 2. (a) Self-assembly of A and B on the surface of Nafion membrane (I. A. PPDA and B. Pd, II. A. Positively charged PAH, B. negatively charged PSS) and (b) methanol permeability as a function of assembled layers. (Reproduced with permission from ref. (43, 57) ©2005,2009 Elsevier).

Besides polyelectrolytes, heteropolyacids and some proteins can also be assembled on the membrane surface as effective methanol-blocking agent (60, 61). Xiang *et al* (61) first studied the effects of self-assembled purple membrane (PM) on the conductivity and cell performance of Nafion 212 and reported a substantial reduction in methanol crossover up to 73.4 %. Cell performance with

PM single-layer modified Nafion membrane has been improved by 48.4 % and performance stability over 400 h operation time has been demonstrated with this biological composite membrane for use in fuel cells. Similar results were also reported by Saab et al (62, 63). In addition to PM, chitosan (CS), together with sulfonated poly(aryl ether ketone) bearing carboxyl groups (SPAEK-C) has been assembled as an effective methanol blocking agents on the Nafion surface (64, 65). Cross-linking between ammonium groups of CS and carbon groups of SPAEK-C occurs by formation of an amide bond, which results in the significant reduction in the water swelling and methanol permeability as compared to the PEC-coated and Nafion membrane.

Mesoporous Nafion Membranes Synthesized by Self-Assembly Route

Nafion is still not an ideal PEM for fuel cells despite the fact that Nafion possesses many unique characteristics such as high intrinsic conductivity when hydrated, good chemical and thermal stability. Nafion exhibits high proton conductivity ($\sim 0.1 \text{ Scm}^{-1}$) when fully saturated with water, but its proton conductivity depends strongly on the relative humidity (RH) and water content in the membrane structure (66–69). The proton conductivity decreases dramatically by orders of magnitude with reduced RH, and the acceptable conductivity can only be obtained in well-saturated environment (66, 70–72). The inherent limitation is primarily the result of the lack of long-range and ordered nano- or mesoporous structures in Nafion (73). Thus, the Nafion membranes-based fuel cells rely on complicated water management system for the humidification of gas streams prior to the entry of the cell.

A study by Li et al clearly showed that nano-structured catalysts can substantially increase their electrocatalytic activity (74). The unique aspect of capillary condensation is that the vapor condensation occurs below the saturation vapor pressure of the pure liquid due to an increased number of van der Waals interactions between the vapor phase molecules within the confined space of a capillary (75, 76). Park et al showed that a mesoporous block copolymer based on the sulfonated polystyrenesulfonate-*block*-polymethylbutylene (PSS-*b*-PMB) copolymer can significantly enhance water condensation and retention properties of the copolymer, particularly at elevated temperatures as compared to conventional Nafion membranes (77). Thus, it is expected that the introduction of long-range mesoporous structural orders into the Nafion would significantly enhance the water retention ability and thus the proton conductivity properties without diminishing the intrinsic mechanical, thermal and chemical properties of the Nafion membranes.

We recently developed a soft template method using surfactant or diblock copolymers for the synthesis of highly ordered mesoporous Nafion membranes (38, 78). In this method, nonionic surfactant, PEO₁₂₇-PPO₄₈-PEO₁₂₇ (Pluronic F108) is used to control the micelle size in the polymer mixture. The microscopic phase separation on a nanometer scale is developed through self-assembly due to the interaction between hydrophilic portion of Nafion ionomer and the hydrophilic PEO groups of Pluronic F108 surfactant, which lead to the ordered arrangement of the micelle templates with self-assembled surfactant. After the heating treatment,

the membranes are immersed in de-ionized water, and the surfactant embedded in the synthesized micelle/Nafion precursor is then removed by reflux with hot water, forming ordered mesoporous structures in Nafion. Figure 3 shows schematic of the formation of mesoporous structures in Nafion membranes via the soft template method.

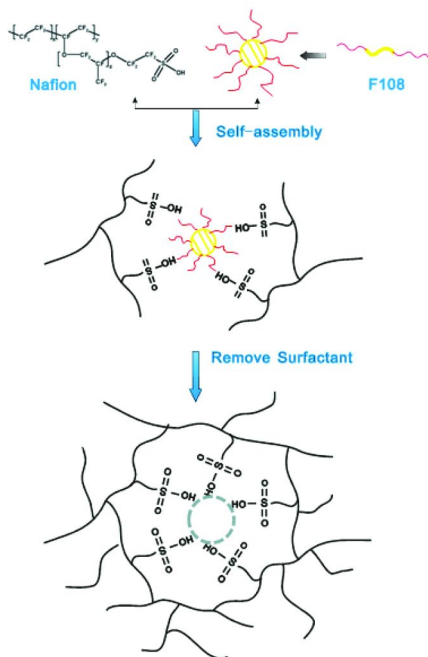


Figure 3. Synthesis principle of formation of mesoporous structures in Nafion via a surfactant-directed self-assembly process. The dotted circle refers to the ordered mesopores formed after the removal of the F108 surfactant. (Reproduced with permission from ref. (38) ©2012 The Royal Society of Chemistry)

Introducing mesoporous structure substantially enhances the water retention and proton conductivity properties of Nafion membranes. Figure 4a is the Arrhenius plots of the proton conductivity of the *meso*-Nafion and Nafion 115 membranes measured under 100%RH. The conductivities of the *meso*-Nafion are higher than that of the pristine Nafion 115 and the best conductivity has been obtained on the 10%-*meso*-Nafion (which was prepared by adding 10wt% F108 surfactant during the synthesis of *meso*-Nafion); 0.11 Scm⁻¹ at 100%RH and 100 °C, which is higher than 0.083 Scm⁻¹ measured on pristine Nafion 115 under the identical conditions. In the case of Nafion 115, the conductivity reduced dramatically to 0.013 Scm⁻¹ when the RH was decreased to 40%, an 84% reduction in conductivity (Fig.4b). In the case of Nafion 117, it has been reported that the proton conductivity changed from 0.08 Scm⁻¹ at 30°C and 90%RH to 0.0045 Scm⁻¹ when the RH was reduced to 30%, the reduction in conductivity is 94.4% (79). In the case of 10%-*meso*-Nafion, conductivity is 0.07 Scm⁻¹ at

40%RH, which is more than five times better than pristine Nafion 115. This clearly indicates that *meso*-Nafion has a much better conductivity at low RH and is much less sensitive to the change in RH, a very important property for practical operation of PEMFC systems. The cells with *meso*-Nafion membranes also demonstrate a much better power output at elevated temperature of 120 °C and reduced humidity (38).

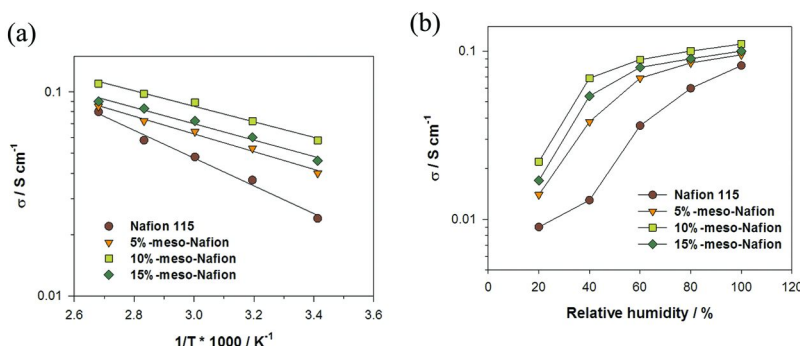


Figure 4. Conductivity plots of Nafion 115 and meso-Nafion membranes synthesized with different F108 contents, measured (a) in 100% RH and different temperatures and (b) at 80°C and different RH. (Reproduced with permission from ref. (38) ©2012 Royal Society of Chemistry)

Further study shows that heteropolyacids such as phosphotungstic acid (HPW) can be effectively impregnated into *meso*-Nafion membranes, forming hybrid multilayer HPW-Nafion membranes (80). The results indicate that the HPW-impregnated multilayer Nafion membrane shows a much higher conductivity and performance, particularly under reduced humidities and elevated temperatures as compared to pristine Nafion membranes. The improvements have been attributed to the significantly enhanced water retention ability and the uniformly dispersed HPW molecules. The higher conductivity and higher water retention ability significantly improve the cell stability and enhance the tolerance to humidity variation.

PEMs Based on Self-Assembled Block Copolymers

There are significant efforts in the synthesis of novel and alternative proton conducting polymers for PEM fuel cells over the past decade (81–83). Among them, aromatic block copolymers show the most promising potential due to its high self-assembly capabilities to form well-ordered nanostructures with tunable morphology and structure (84–88). Sulfonic groups are generally introduced into the aromatic block copolymers through sulfonation (89). The thermodynamic incompatibility among chemically different blocks gives rise to a phase separation, resulting in the formation of ordered nanostructures such as lamellar, spheres, hexagonal packed cylinders and bicontinuous gyroids, etc. (90, 91).

An accurate prediction of the phase separation behaviors in a wide range of block copolymers has been presented in Flory-Huggins theory and models (92, 93). Recently, Komarov et al (85) successfully predicted the self-assembled morphologies of the amphiphilic block copolymer, sulfonated poly (ether ether ketone) (SPEEK), by a statistical mechanical approach. These models and simulations provide theoretical background for building nanostructures in block copolymers for fuel cells.

Sisbandini et al (94) studied the spontaneous alignment of two partially sulfonated copolymers of poly(p-phenyleneterephthalamide) (PPTA) using X-ray diffraction. The combination of mechanically solid backbones like PPTA and the proton exchange competence of ionic moieties like a sulfonated counterpart is expected to form a stable polyelectrolyte membrane. Cylindrical aggregates and the consequently nematic liquid-crystalline arrays have been further proved by the X-ray scattering characterization. A side view of the SEM image also exhibited a lamellar-within-lamellar morphology. The proton conductivity of the copolymer with lamellar structure is in the order of 10^{-3} to 10^{-2} S cm $^{-1}$ between 20 and 90°C. A systematic synthesis of a range of poly(vinylidene fluoride)-g-sulfonated polystyrene (PVDF-g-SPS) graft copolymers has been reported by Zhang et al (81). In a series of well-designed PVDF-g-SPS graft copolymers, PVDF-g-SPS graft copolymer with low graft density (0.3–0.8 mol%) and long SPS graft length was prepared to form lamellar structures. Different mole ratios of the reactants lead to various graft density and length, ion exchange capacity (IEC), and the consequently water uptake capabilities. A higher proton conductivity than Nafion 112 membrane was reported.

Further study on the synthesis of block polymers with various ordered structures are presented by Rubatet et al (95). Highly ordered structures such as isotropic phase (ISO), lamellar phases (LAM), cylindrical hexagonal phase (HEX) and hexagonally perforated lamellae (HPL) have been formed from polystyrene-block-poly (methyl methacrylate) block copolymers with various volume fractions. At the same sulfonation degree, the LAM structure displayed the highest proton conductivity (see Figure 5). The results indicate the effect of controlled addition of proton donating sulfonated fraction in the self-assembly of block copolymers on the proton conductivity.

Other than the diblock copolymers as discussed above, Xu et al (89) synthesized a novel nonionic triblock copolymer sulfonated poly(styrene-b-vinylidene fluoride-b-styrene). An increase in both water uptake and proton conductivity with the coalesce of ionic clusters into larger channels was observed. At 95% RH, 30°C and a 49% degree of sulfonation, the maximum proton conductivity is 0.091 S cm $^{-1}$, slightly higher than that of Nafion (0.072 S cm $^{-1}$). Different from the aromatic copolymers containing sulfonated benzene rings, sulfonic groups could also be interlinked on alkyl chains as pedant in a novel sulfonated block copolymer (96). TEM images showed various unique structures, ranging from the lamellae morphology with a periodicity as long as 300 nm, to a lamellae-like morphology with parallel-aligned alternative dark and bright strips. The methanol permeability of the membranes made from the alkylsulfonic acids contained copolymer has been observed to be much smaller than that of Nafion. The high sequential microdomains of ionic moieties and the organized

orientation due to self-assembly of block copolymers significantly enhance the proton conductivity as compared to that of random analogs.

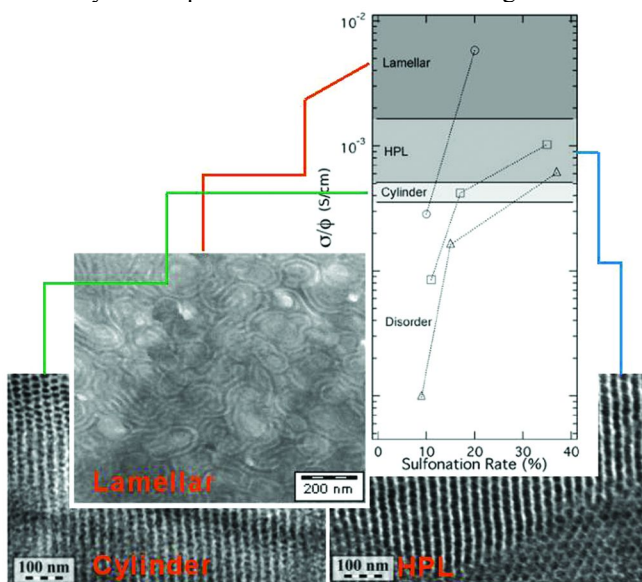


Figure 5. TEM images of samples with different structures and the normalized proton conductivity σ/ϕ as a function of the sulfonation degree. (Reproduced with permission from ref. (95) ©2008, American Chemical Society).

Hybrid Nanocomposite PEMs via Self-Assembly

Increase of the operation temperatures of PEM fuel cells can bring significant benefits and advantages such as reduced poisoning of anode catalysts by trace amounts of CO, simplified water management, higher catalytic performance and enhanced electrodes kinetics, etc (1, 97). Thus there are extensive research activities in the development of novel proton exchange membranes which can operate at elevated high temperatures and low humidities (49, 98–100).

Incorporating hydrophilic inorganic oxides with good water retention ability into the pristine Nafion membranes has been pursued intensively and recognized as an efficient method to maintain the high conductivity properties of Nafion under low relative humidity conditions. The key challenge here is to combine the hydrophilic inorganic oxides and Nafion membrane with intimate interfacial contact. Stable inorganic $\text{P}_2\text{O}_5\text{-SiO}_2$ glass membranes derived from sol-gel method has been demonstrated to be useful as a fuel cell electrolyte (37). The conductivity of $\text{P}_2\text{O}_5\text{-SiO}_2$ glasses was found to be better than that of Nafion membrane when the temperature is above 40 °C. Porous glass structures with water-sensitive hydroxyl groups bonded inside, as evidenced by nuclear magnetic resonance (NMR) and infrared (IR) spectroscopies, may be responsible for the reported conductivity behavior.

By employing water-retention inorganic oxides and the sol-gel technique, we have developed a novel self-assembly process to synthesize the stable and high water-retention Nafion/SiO₂ hybrid nanocomposite membranes (34, 101). Figure 6 shows the self-assembly process for the synthesis of Nafion-silica nanoparticles (34). Increasing the acidity of the TEOS solution will significantly increase the proton adsorption reaction of SiOH, leading to the formation of positively charged SiOH₂⁺ (102, 103). In the presence of Nafion ionomers self-assembly occurs between the silica with positively charged surface groups and Nafion with the negatively charged sulfonated (SO₃⁻) group. The Nafion assembled on the silica surface stabilizes the silica nanoparticle, preventing the grain growth and agglomeration of silica nanoparticles.

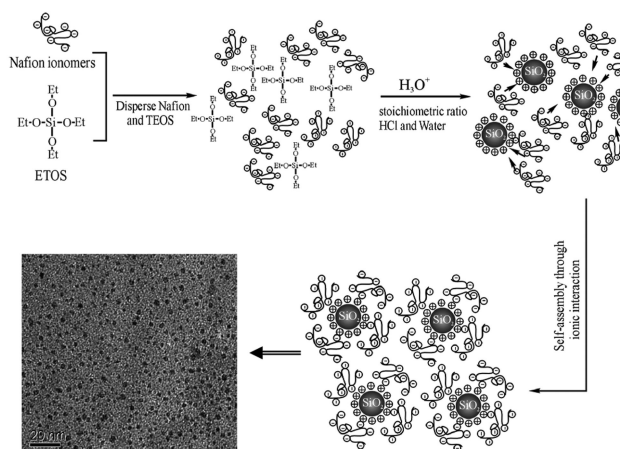


Figure 6. Scheme for the formation of the Nafion–SiO₂ nanoparticles by self-assembly method. The inset shows the TEM micrograph of the self-assembled Nafion–SiO₂ nanoparticles. (Reproduced with permission from ref. (34) ©2007, Elsevier)

The Nafion-silica hybrid membranes prepared from the self-assembled silica nanoparticles show exceptional durability and good electrochemical performance as compared to conventional pristine Nafion membrane cells (see Fig.7) (34). At cell/humidifying temperatures of 60°C/60°C, the cell performance with Nafion 212 and self-assembled Nafion/SiO₂ nanocomposite membrane is stable. However, the voltage of the cell with Nafion 212 decreases rapidly when the cell temperature is higher than humidified temperature (Fig.7a). The rapid decay in the cell stability is clearly due to the dehydration of the Nafion-based MEA (104). In contrast, PEM fuel cell with the self-assembled Nafion/SiO₂ nanocomposite shows a very stable performance with a much slow reduction in power output (Fig.7b). The self-assembled Nafion/SiO₂ composite membrane shows a promising prospect for the development of PEMFCs which can be operated at elevated high temperatures.

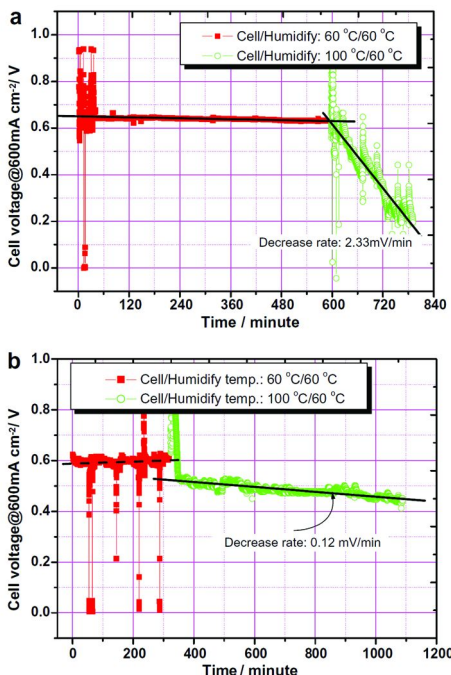


Figure 7. Stability of single cells with (a) Nafion 212 and (b) self-assembled Nafion/SiO₂nanocomposite membranes under a constant current density of 600 mA cm^{-2} at different cell/humidifying temperatures in H₂/air. (Reproduced with permission from ref. (34). ©2007, Elsevier)

Not only can silica nanoparticles be incorporated into Nafion membrane, but also other nano-sized organics such as TiO₂ nanowires (105) and metal oxides nanoparticles (35) have been demonstrated as effective additives to promote the high temperature capability of Nafion-based electrolyte. Pan et al self-assembled zirconium dioxide nanoparticle with Nafion, formed via in situ hydrolysis (106). In the Nafion/ZrO₂ composites, the addition of ZrO₂ increased water uptake in a wide range of temperatures without influencing the structures and crystallinity of Nafion significantly.

As a potential alternative for Nafion-based electrolyte, inorganic heteropoly acids, for instance phosphotungstic acids (HPW), has a remarkable proton conductivity, $\sim 7.9 \times 10^{-2} \text{ S cm}^{-1}$ at room temperature. However, heteropolyacids themselves cannot be used as PEMs due to their high solubility in water. Mesoporous materials have been studied as versatile supports for HPW molecules due to its high porosity, highly ordered nanochannels and high specific surface area (107, 108). We recently developed a novel inorganic proton exchange membrane using a novel one-step self-assembly synthesis strategy (109, 110). Mesoporous silica offers highly ordered nanochannels for anchoring HPW, providing conducting paths for protons, as illustrated in Figure 8c. The formation of ordered structure is supported by the SAXRD and TEM image (see Fig.8a).

N_2 adsorption-desorption isotherms of HPW/meso-SiO₂ show typical type IV curves with a sharp capillary condensation step at relative pressure (p/p_0) of ~ 0.6 (Fig. 8b), suggesting a narrow pore size distribution.

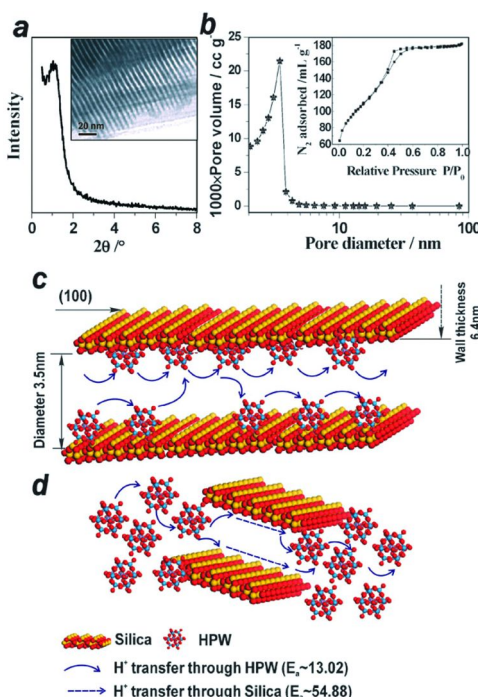


Figure 8. (a) small angle XRD pattern and (b) N_2 adsorption/desorption isotherm of the self-assembled 25 wt.% HPW/meso-silica electrolyte membrane. (c) and (d) are the proposed proton transportation pathways of the self-assembled HPW/meso-silica electrolyte membrane and the mixed HPW/meso-silica composite electrolyte membrane, respectively. The insert in (a) is the HRTEM micrograph of the self-assembled 25 wt.% HPW/meso-silica electrolyte membrane. (Reproduced by permission from ref. (109) ©2010, The Royal Society of Chemistry)

Further work has showed that a fuel cell within a 165 mm thick self-assembled HPW–silica nanocomposite membrane produced a peak power output of 128.5 and 112.0 mW cm⁻² for methanol and ethanol fuels, respectively, at 200°C without external humidification (111). A noticeably high proton conductivity of 0.05 S cm⁻¹ for 25 wt% HPW mesoporous membrane at 200 °C has bee reported. The cell performance is reasonably stable for direct alcohol fuel cells (DAFCs) tested at 200 °C. This demonstrates that such novel self-assembled HPW-silica mesoporous composites are promising candidates for high temperature PEM fuel cells.

Such highly ordered porous structures can also act as the anchor site for functional groups through a self-assembly process (112, 113). Due to the strong

Brønsted acidity at the border between strong acids and its unique Keggin-type structures, heteropolyacids, especially 12-phosphotungstic acid can act as proton donor not only in the acid-base composite but also in the acid-acid composite materials, which are composed of strong-acidic and acidic composite materials (114). Heteropolyacid-encapsulated materials and complexes based on its supramolecular polychains through self-assembly have shown as promising candidates for anhydrous proton conductive electrolytes (115–118). Table 1 lists some representative inorganic proton conductors which are promising candidates for high-temperature PEM fuel cells.

Table 1. High temperature inorganic proton conducting materials.

Inorganic proton conductors	Proton conductivity	Activation energy	Ref.
phosphoric acid doped polybenzimidazole (PBI)	7.9×10^{-2} S/cm at 200 °C and 5%RH	8.0 kJ/mol	119,120
phosphonic acid functionalized porous silica	0.015 S/cm at 130 °C and 20%RH	—	121
KH_2PO_4 (KDP)	up to 10^{-2} S cm ⁻¹ in the form of superprotic phase	0.32 eV	122
CsH_2PO_4 , and other derived solid acids in general formula $\text{MH}(\text{PO}_3\text{H})$	2.3×10^{-2} S/cm at 230 °C	0.32 eV	123
P_2O_5 SiO_2 glasses	$\sim 2 \times 10^{-2}$ S/cm at 30 °C	4.3 kJ/mol	124
$\alpha\text{-Fe}_2\text{O}_3$ ceramic membrane	2.76×10^{-3} S cm ⁻¹ at 90 °C and 81%RH.	—	125
heptadecatungstovanadodiphosphoric heteropoly acid $\text{H}_7\text{P}_2\text{W}_{17}\text{VO}_{62} \cdot 28\text{H}_2\text{O}$	3.10×10^{-2} S/cm at 26 °C and 75%RH	32.23 kJ/mol	126
Phosphotungstic acid functionalized mesoporous silica	7×10^{-2} S/cm at 25 °C and 100%RH	14 kJ/mol	127

Acid-Base Composite Proton Conducting Electrolyte Materials

Development of acid-base composite proton conducting materials has been inspired by the mechanism of biological system with acid as the proton donor and bases as the proton acceptor. Recently, acid-base composite polymer electrolytes

have been considered as alternatives for intermediate-temperature and anhydrous fuel cells due to the novel proton conducting pathway via a “hop-and-turn” or the Grotthuss mechanism offered by the self-organized electrostatic acid-base framework (128, 129).

Self-organized acid-base pairs possess a well-arranged proton assembly along the head functional groups of acid-base polymers through the self-assembly process driven by hydrogen-bonding (Fig.9a) (130), which offers a transporting path for protons with no water molecules involved. Self-assembled hybrid composites of acidic surfactant monododecyl phosphate (MDP) and basic surfactant 2-undecylimidazole (UI) molecules (Fig.9a) has been reported to exhibit a conductivity 1×10^{-3} S cm $^{-1}$ at 150 °C under the anhydrous condition (130). The proton transporting performance depends not only on the concentration of functional groups, but also on the ordered structures of acid-base bilayer arrays. Several new polymers containing functional groups, such as imidazole, hydroxyl and sulfonic groups are given in Fig.9b. An slight enhancement in anhydrous proton conductivity of 1.3×10^{-3} S cm $^{-1}$ at 200 °C is observed in supramolecular nanochannels formed by comb polymers with heterocyclic functionality benzotriazole (84). A complex synthesis process was involved in this work. Similarly to that of acid-base pairs, this self-assembly process is also driven by the hydrogen-bonding forces in imidazole groups (as shown in Fig.9c).

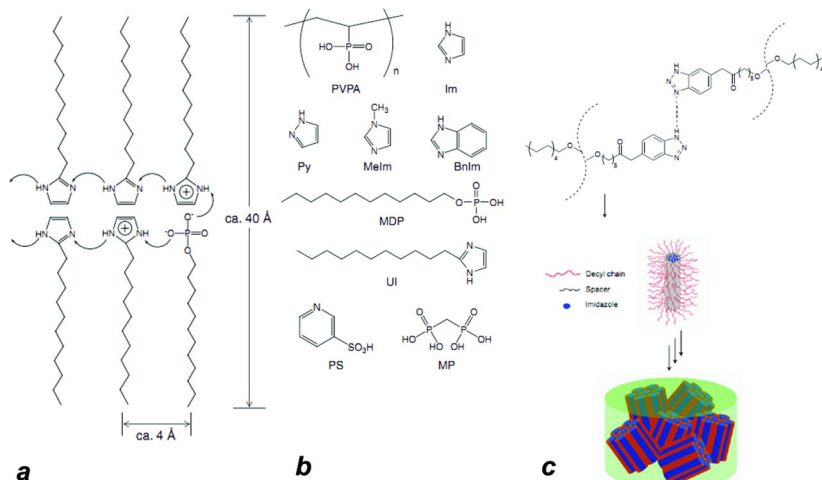


Figure 9. (a) Mechanistic mode for protonic conduction of UI-MDP composite materials and the calculated distance of acid-base pairs. (b) Molecular structures of acid-base composite materials. (c) An illustration of the proposed hydrogen-bonded interactions and self-assembly process to form supramolecular nanochannels. (Reproduced with permission from ref. (130) ©2004, American Chemical Society; Reproduced with permission from ref. (84) ©2010, Nature)

A common feature of this type of anhydrous proton conductors is that the self-assembled functionalized polymers are driven by hydrogen bonding forces (131) and along the acid-base pairs to give head-to-head transport nanochannels in lamellar structures. Other space structures are rarely reported to the best of our knowledge and the two-dimensional lamellar stacking are supposed to offer a short-distance jumping for proton translocation (132). The results show the importance of the space factors for proton conduction and the proper design of molecular structures to utilize the self-assembly process to achieve efficient proton conductivity.

Summary and Outlook

LbL self-assembly process is a powerful and versatile tool to synthesize and develop various nanostructured PEMs with high proton conductivity, high resistance to methanol crossover, high electrochemical performance, and enhanced durability. There is wide range of LbL self-assembly synthetic strategies for development of novel proton conductors as shown in this Chapter. However, LbL self-assembly approach largely remains experimental and thus to advance this research field, further research and development in the computational modeling and theoretical understanding on the nanostructures formation would be essential. Since the well-organized nanostructure has been shown to be closely related to the high proton conductivity and excellent performance, development of highly ordered and three-dimensional nanostructures is desirable for PEMs. Self-assembled proton conducting materials that combine the aspects of well-controlled morphologies, tunable and ordered nanochannels and operating capabilities under elevated temperature and low humidity conditions will be the most promising candidate for the next generation proton exchange membrane of fuel cells.

References

1. Zhang, J.; Xie, Z.; Zhang, J.; Tang, Y.; Song, C.; Navessin, T.; Shi, Z.; Song, D.; Wang, H.; Wilkinson, D. P.; Liu, Z.-S.; Holdcroft, S. *J. Power Sources* **2006**, *160*, 872–91.
2. Baniasadi, E.; Alemrajabi, A. A. *Int. J. Hydrogen Energy* **2010**, *35*, 9460–67.
3. Bernay, C.; Marchand, M.; Cassir, M. *J. Power Sources* **2002**, *108*, 139–52.
4. Ashley, S. *Sci. Am.* **2001**, *285*, 25–25.
5. Zenith, F.; Krewer, U. *J. Process Control* **2010**, *20*, 630–42.
6. Ramani, V.; Kunz, H. R.; Fenton, J. M. *J. Membr. Sci.* **2004**, *232*, 31–44.
7. Zhang, H. W.; Shen, P. K. *Chem. Rev.* **2012**, *112*, 2780–832.
8. Damay, F.; Klein, L. C. *Solid State Ionics* **2003**, *162–163*, 261–67.
9. Schmidt-Rohr, K.; Chen, Q. *Nat. Mater.* **2008**, *7*, 75–83.
10. Arico, A. S.; Srinivasan, S.; Antonucci, V. *Fuel Cells* **2001**, *1*, 133–61.
11. Prabhuram, J.; Zhao, T. S.; Liang, Z. X.; Yang, H.; Wong, C. W. *J. Electrochem. Soc.* **2005**, *152*, A1390–A97.
12. Yang, B.; Manthiram, A. *Electrochem. Commun.* **2004**, *6*, 231–36.

13. Miyake, N.; Wainright, J. S.; Savinell, R. F. *J. Electrochem. Soc.* **2001**, *148*, A905–A09.
14. Xiang, Y.; Yang, M.; Zhang, J.; Lan, F.; Lu, S. F. *J. Membr. Sci.* **2011**, *368*, 241–45.
15. Decher, G. *Science* **1997**, *277*, 1232–37.
16. Travasset, A. *Science* **2011**, *334*, 183–84.
17. Arora, H.; Du, P.; Tan, K. W.; Hyun, J. K.; Grazul, J.; Xin, H. L.; Muller, D. A.; Thompson, M. O.; Wiesner, U. *Science* **2010**, *330*, 214–19.
18. Gazit, E. *Nat. Chem.* **2010**, *2*, 1010–11.
19. Nedelcu, M.; Guldin, S.; Orilall, M. C.; Lee, J.; Huttner, S.; Crossland, E. J. W.; Warren, S. C.; Ducati, C.; Laity, P. R.; Eder, D.; Wiesner, U.; Steiner, U.; Snaith, H. J. *J. Mater. Chem.* **2010**, *20*, 1261–68.
20. Crossland, E. J. W.; Nedelcu, M.; Ducati, C.; Ludwigs, S.; Hillmyer, M. A.; Steiner, U.; Snaith, H. J. *Nano Lett.* **2009**, *9*, 2813–19.
21. Tang, B.; Hu, G. X. *J. Power Sources* **2012**, *220*, 95–102.
22. Zhang, W. F.; Wang, H. T.; Chen, B. X.; Bi, X. H.; Venkatesan, S.; Qiao, Q. Q.; Yang, S. F. *J. Mater. Chem.* **2012**, *22*, 24067–74.
23. Kim, J. M.; Lee, G.; Kim, B. H.; Huh, Y. S.; Lee, G. W.; Kim, H. J. *Ultrason. Sonochem.* **2012**, *19*, 627–31.
24. Huang, Y.; Huang, X. L.; Lian, J. S.; Xu, D.; Wang, L. M.; Zhang, X. B. *J. Mater. Chem.* **2012**, *22*, 2844–47.
25. Kang, E.; Jung, Y. S.; Kim, G. H.; Chun, J.; Wiesner, U.; Dillon, A. C.; Kim, J. K.; Lee, J. *Adv. Funct. Mater.* **2011**, *21*, 4349–57.
26. Yılmaztürk, S.; Gümüşoğlu, T.; Ari, G. A.; Öksüzömer, F.; Deligöz, H. J. *Power Sources* **2012**, *201*, 88–94.
27. Liu, H. J.; Wang, X. M.; Cui, W. J.; Dou, Y. Q.; Zhao, D. Y.; Xia, Y. Y. *J. Mater. Chem.* **2010**, *20*, 4223–30.
28. Ji, J. Y.; Jia, Y. J.; Wu, W. G.; Bai, L. L.; Ge, L. Q.; Gu, Z. Z. *Colloids Surf. A* **2011**, *390*, 56–61.
29. Wang, D. L.; Lu, S. F.; Xiang, Y.; Jiang, S. P. *Appl. Catal. B* **2011**, *103*, 311–17.
30. Guo, C. X.; Li, C. M. *Energy Environ. Sci.* **2011**, *4*, 4504–07.
31. Balach, J.; Bruno, M. M.; Cotella, N. G.; Acevedo, D. F.; Barbero, C. A. *J. Power Sources* **2012**, *199*, 386–94.
32. Jiang, H.; Zhao, T.; Li, C. Z.; Ma, J. *J. Mater. Chem.* **2011**, *21*, 3818–23.
33. Xiang, Y.; Lu, S.; Jiang, S. P. *Chem. Soc. Rev.* **2012**, *41*, 7291–321.
34. Tang, H.; Wan, Z.; Pan, M.; Jiang, S. P. *Electrochem. Commun.* **2007**, *9*, 2003–08.
35. Li, K.; Ye, G. B.; Pan, J. J.; Zhang, H. N.; Pan, M. *J. Membr. Sci.* **2010**, *347*, 26–31.
36. Farhat, T. R.; Hammond, P. T. *Adv. Funct. Mater.* **2005**, *15*, 945–54.
37. Nogami, M.; Matsushita, H.; Goto, Y.; Kasuga, T. *Adv. Mater.* **2000**, *12*, 1370–72.
38. Lu, J.; Tang, H.; Xu, C.; Jiang, S. P. *J. Mater. Chem.* **2012**, *22*, 5810–19.
39. Gröschel, A. H.; Schacher, F. H.; Schmalz, H.; Borisov, O. V.; Zhulina, E. B.; Walther, A.; Müller, A. H. E. *Nat. Commun.* **2012**, *3*, 710.

40. Tang, H. L.; Pan, M.; Mu, S. C.; Yuan, R. Z. *Chin. J. Inorg. Chem.* **2004**, *20*, 128–32.
41. Tang, H. L.; Luo, Z. P.; Pan, M.; Jiang, S. P.; Liu, Z. C. *J. Chem. Res., Synop.* **2005**, 449–51.
42. Tang, H. L.; Pan, M.; Mu, S. C.; Yuan, R. Z. *Acta Chim. Sin.* **2004**, *62*, 127–30.
43. Tang, H. L.; Pan, M.; Jiang, S. P.; Wan, Z. H.; Yuan, R. Z. *Colloids Surf., A* **2005**, *262*, 65–70.
44. Tang, H. L.; Pan, M.; Wan, Z. H. *J. Appl. Polym. Sci.* **2008**, *110*, 2227–33.
45. Tang, H. L.; Pan, M.; Jiang, S. P.; Yuan, R. Z. *Mater. Lett.* **2005**, *59*, 3766–70.
46. Mu, S. C.; Tang, H. L.; Wan, Z. H.; Pan, M.; Yuan, R. Z. *Electrochem. Commun.* **2005**, *7*, 1143–47.
47. Wan, Z. H.; Tang, H. L.; Pan, M.; Mu, S. C.; Yuan, R. Z. *Rare Met. Mater. Eng.* **2007**, *36*, 134–37.
48. Jiang, S. P.; Liu, Z. C.; Tian, Z. Q. *Adv. Mater.* **2006**, *18*, 1068+.
49. Shao, Z. G.; Xu, H. F.; Li, M. Q.; Hsing, I. M. *Solid State Ionics* **2006**, *177*, 779–85.
50. Li, Q. F.; He, R. H.; Jensen, J. O.; Bjerrum, N. J. *Chem. Mater.* **2003**, *15*, 4896–915.
51. Jia, N. Y.; Lefebvre, M. C.; Halfyard, J.; Qi, Z. G.; Pickup, P. G. *Electrochem. Solid-State Lett.* **2000**, *3*, 529–31.
52. Yilmazturk, S.; Deligoz, H.; Yilmazoglu, M.; Damyan, H.; Oksuzomer, F.; Koc, S. N.; Durmus, A.; Gurkaynak, M. A. *J. Membr. Sci.* **2009**, *343*, 137–46.
53. Yilmazt  rk, S.; Ercan, N.; Delig  z, H. *Appl. Surf. Sci.* **2012**, *258*, 3139–46.
54. Kharlampieva, E.; Kozlovskaya, V.; Sukhishvili, S. A. *Adv. Mater.* **2009**, *21*, 3053–65.
55. Lin, H. D.; Zhao, C. J.; Ma, W. J.; Li, H. T.; Na, H. *Int. J. Hydrogen Energy* **2009**, *34*, 9795–801.
56. Zhao, C. J.; Lin, H. D.; Zhang, Q. A.; Na, H. *Int. J. Hydrogen Energy* **2010**, *35*, 10482–88.
57. Deligoz, H.; Yilmazturk, S.; Karaca, T.; Ozdemir, H.; Koc, S. N.; Oksuzomer, F.; Durmus, A.; Gurkaynak, M. A. *J. Membr. Sci.* **2009**, *326*, 643–49.
58. Lutkenhaus, J. L.; Hammond, P. T. *Soft Matter* **2007**, *3*, 804–16.
59. Xi, J. Y.; Wu, Z. H.; Teng, X. G.; Zhao, Y. T.; Chen, L. Q.; Qiu, X. P. *J. Mater. Chem.* **2008**, *18*, 1232–38.
60. Yang, M.; Lu, S. F.; Lu, J. L.; Jiang, S. P.; Xiang, Y. *Chem. Commun.* **2010**, *46*, 1434–36.
61. Xiang, Y.; Hang, J.; Liu, Y.; Guo, Z. B.; Lu, S. F. *J. Membr. Sci.* **2011**, *367*, 325–31.
62. Zhang, J.; Lan, F.; Liang, D. W.; Xiao, Y. X.; Lu, S. F.; Xiang, Y. *J. Membr. Sci.* **2011**, *382*, 350–54.
63. Saab, M. B.; Estephan, E.; Cloitre, T.; Legros, R.; Cuisinier, F. J. G.; Zimanyi, L.; Gergely, C. *Langmuir* **2009**, *25*, 5159–67.
64. Lin, H. D.; Zhao, C. J.; Ma, W. J.; Li, H. T.; Na, H. *J. Membr. Sci.* **2009**, *345*, 242–48.

65. Zhang, H. W.; Huang, H. P.; Shen, P. K. *Int. J. Hydrogen Energy* **2012**, *37*, 6875–79.
66. Zawodzinski, T. A.; Springer, T. E.; Davey, J.; Jestel, R.; Lopez, C.; Valerio, J.; Gottesfeld, S. *J. Electrochem. Soc.* **1993**, *140*, 1981–85.
67. Buchi, F. N.; Scherer, G. G. *J. Electrochem. Soc.* **2001**, *148*, A183–A88.
68. Buchi, F. N.; Scherer, G. G. *J. Electroanal. Chem.* **1996**, *404*, 37–43.
69. Motupally, S.; Becker, A. J.; Weidner, J. W. *J. Electrochem. Soc.* **2000**, *147*, 3171–77.
70. Sone, Y.; Ekdunge, P.; Simonsson, D. *J. Electrochem. Soc.* **1996**, *143*, 1254–59.
71. Cappadonia, M.; Erning, J. W.; Niaki, S. M. S.; Stimming, U. *Solid State Ionics* **1995**, *77*, 65–69.
72. Ciureanu, M. *J. Appl. Electrochem.* **2004**, *34*, 705–14.
73. Diat, O.; Gebel, G. *Nat. Mater.* **2008**, *7*, 13–14.
74. Lashtabeg, A.; Bradley, J. L.; Vives, G.; Drennan, J. *Ceram. Int.* **2010**, *36*, 653–59.
75. Armatas, G. S.; Salmas, C. E.; Louloudi, M.; Androutsopoulos, G. P.; Pomonis, P. *J. Langmuir* **2003**, *19*, 3128–36.
76. Dourdain, S.; Gibaud, A. *Appl. Phys. Lett.* **2005**, *87*.
77. Park, M. J.; Downing, K. H.; Jackson, A.; Gomez, E. D.; Minor, A. M.; Cookson, D.; Weber, A. Z.; Balsara, N. P. *Nano Lett.* **2007**, *7*, 3547–52.
78. Lu, J. L.; Lu, S. F.; Jiang, S. P. *Chem. Commun.* **2011**, *47*, 3216–18.
79. Marina, O. A.; Pederson, L. R.; Thomsen, E. C.; Coyle, C. A.; Yoon, K. J. *J. Power Sources* **2010**, *195*, 7033–37.
80. Lu, J. L.; Fang, Q. H.; Li, S. L.; Jiang, S. P. *J. Membr. Sci.* **2013**, *427*, 101–07.
81. Zhang, Z. C.; Chalkova, E.; Fedkin, M.; Wang, C. M.; Lvov, S. N.; Komarneni, S.; Chung, T. C. Synthesis and Characterization of Poly(vinylidene fluoride)-g-Sulfonated Polystyrene Graft Copolymers for Proton Exchange Membrane. In *Fuel Cell Chemistry and Operation*; ACS Symposium Series; Herring, A. M., Zawodzinski, T. A., Hamrock, S. J., Eds.; American Chemical Society: Washington, DC, 2010; Vol. 1040 pp 31–48.
82. Deluca, N. W.; Elabd, Y. A. *J. Polym. Sci., Part B: Polym. Phys.* **2006**, *44*, 2201–25.
83. Hickner, M. A.; Ghassemi, H.; Kim, Y. S.; Einsla, B. R.; McGrath, J. E. *Chem. Rev.* **2004**, *104*, 4587–611.
84. Chen, Y. B.; Thorn, M.; Christensen, S.; Versek, C.; Poe, A.; Hayward, R. C.; Tuominen, M. T.; Thayumanavan, S. *Nat. Chem.* **2010**, *2*, 503–08.
85. Komarov, P. V.; Veselov, I. N.; Chu, P. P.; Khalatur, P. G. *Soft Matter* **2010**, *6*, 3939–56.
86. Yu, X.; Roy, A.; Dunn, S.; Badami, A. S.; Yang, J.; Good, A. S.; McGrath, J. E. *J. Polym. Sci., Polym. Chem.* **2009**, *47*, 1038–51.
87. Goseki, R.; Hayakawa, T.; Kakimoto, M. A.; Tokita, M.; Watanabe, J. *J. Photopolym. Sci. Technol.* **2007**, *20*, 771–76.
88. Ingratta, M.; Jutemar, E. P.; Jannasch, P. *Macromolecules* **2011**, *44*, 2074–83.
89. Xu, K.; Li, K.; Khanchaitit, P.; Wang, Q. *Chem. Mater.* **2007**, *19*, 5937–45.

90. Izzo, J. R.; Grew, K. N.; Chiu, W. K. S. *Proceedings of the 7th International Conference on Fuel Cell Science, Engineering, and Technology* **2009**, 625–29.

91. Choi, W. H.; Jo, W. H. *J. Power Sources* **2009**, *188*, 127–31.

92. Helfand, E.; Wasserman, Z. R. *Macromolecules* **1976**, *9*, 879–88.

93. Matsen, M. W.; Bates, F. S. *Macromolecules* **1996**, *29*, 1091–98.

94. Sisbandini, C.; Every, H. A.; Viale, S.; Mendes, E.; Picken, S. J. *J. Polym. Sci., Part B: Polym. Phys.* **2007**, *45*, 666–76.

95. Rubatat, L.; Li, C. X.; Dietsch, H.; Nykanen, A.; Ruokolainen, J.; Mezzenga, R. *Macromolecules* **2008**, *41*, 8130–37.

96. Lee, H. C.; Lim, H.; Su, W. F.; Chao, C. Y. *J. Polym. Sci., Part A: Polym. Chem.* **2011**, *49*, 2325–38.

97. Garland, N. L.; Kopasz, J. P. *J. Power Sources* **2007**, *172*, 94–99.

98. Asensio, J. A.; Gomez-Romero, P. *Fuel Cells* **2005**, *5*, 336–43.

99. Hogarth, W. H. J.; da Costa, J. C. D.; Lu, G. Q. *J. Power Sources* **2005**, *142*, 223–37.

100. Zhang, J. L.; Xie, Z.; Zhang, J. J.; Tanga, Y. H.; Song, C. J.; Navessin, T.; Shi, Z. Q.; Song, D. T.; Wang, H. J.; Wilkinson, D. P.; Liu, Z. S.; Holdcroft, S. *J. Power Sources* **2006**, *160*, 872–91.

101. Tang, H. L.; Pan, M. *J. Phys. Chem. C* **2008**, *112*, 11556–68.

102. Hiemstra, T.; Dewit, J. C. M.; Vanriemsdijk, W. H. *J. Colloid Interface Sci.* **1989**, *133*, 105–17.

103. Hiemstra, T.; Vanriemsdijk, W. H.; Bolt, G. H. *J. Colloid Interface Sci.* **1989**, *133*, 91–104.

104. Kreuer, K. D. *J. Membr. Sci.* **2001**, *185*, 29–39.

105. Wang, Z. B.; Tang, H. L.; Pan, M. *J. Membr. Sci.* **2011**, *369*, 250–57.

106. Pan, J. J.; Zhang, H. N.; Chen, W.; Pan, M. *Int. J. Hydrogen Energy* **2010**, *35*, 2796–801.

107. Damyanova, S.; Dimitrov, L.; Mariscal, R.; Fierro, J. L. G.; Petrov, L.; Sobrados, I. *Appl. Catal. A* **2003**, *256*, 183–97.

108. Lu, J. L.; Tang, H. L.; Lu, S. F.; Wu, H. W.; Jiang, S. P. *J. Mater. Chem.* **2011**, *21*, 6668–76.

109. Tang, H. L.; Pan, M.; Lu, S. F.; Lu, J. L.; Jiang, S. P. *Chem. Commun.* **2010**, *46*, 4351–53.

110. Tang, H. L.; Pan, M.; Jiang, S. P. *Dalton Trans.* **2011**, *40*, 5220–27.

111. Tang, H.; Pan, M.; Jiang, S. P. *Dalton Trans.* **2011**, *40*, 5220–27.

112. Han, W.; Kwan, S. M.; Yeung, K. L. *Top. Catal.* **2010**, *53*, 1394–400.

113. Smith, J. J.; Zharov, I. *Chem. Mater.* **2009**, *21*, 2013–19.

114. Yamada, M.; Honma, I. *J. Phys. Chem. B* **2006**, *110*, 20486–90.

115. Wei, M. L.; Li, H. H.; Wang, X. X.; Wang, J. H. *Struct. Chem.* **2012**, *23*, 129–36.

116. Cheng, C. C.; Yen, Y. C.; Ko, F. H.; Chu, C. W.; Fan, S. K.; Chang, F. C. *J. Mater. Chem.* **2012**, *22*, 731–34.

117. Wei, M. L.; Zhuang, P. F.; Wang, J. H.; Wang, X. X. *J. Mol. Struct.* **2011**, *995*, 51–57.

118. Wei, M. L.; Zhuang, P. F.; Miao, Q. X.; Wang, Y. J. *Solid State Chem.* **2011**, *184*, 1472–77.

119. He, R. H.; Li, Q. F.; Xiao, G.; Bjerrum, N. J. *J. Membr. Sci.* **2003**, *226*, 169–84.

120. Chen, L.; Hallinan, D. T.; Elabd, Y. A.; Hillmyer, M. A. *Macromolecules* **2009**, *42*, 6075–85.

121. Jin, Y. G.; Qiao, S. Z.; Xu, Z. P.; da Costa, J. C. D.; Lu, G. Q. *J. Phys. Chem. C* **2009**, *113*, 3157–63.

122. Oh, I.-H.; Kweon, J. J.; Oh, B. H.; Lee, C. E. *J. Korean Phys. Soc.* **2008**, *53*, 3497–99.

123. Haile, S. M.; Liu, H.; Secco, R. A. *Chem. Mater.* **2003**, *15*, 727–36.

124. Nogami, M.; Nagao, R.; Wong, C.; Kasuga, T.; Hayakawa, T. *J. Phys. Chem. B* **1999**, 9468–72.

125. Colomer, M. T. *J. Power Sources* **2011**, *196*, 8280–85.

126. Tong, X.; Zhu, W. M.; Wu, Q. Y.; Qian, X. Y.; Liu, Z.; Yan, W. F.; Gong, J. *J. Alloys Compd.* **2011**, *509*, 7768–72.

127. Zeng, J.; Jiang, S. P. *J. Phys. Chem. C* **2011**, *115*, 11854–63.

128. Honma, I.; Yamada, M. *Bull. Chem. Soc. Jpn.* **2007**, *80*, 2110–23.

129. Vuillaume, P. Y.; Mokrini, A.; Siu, A.; Theberge, K.; Robitaille, L. *Eur. Polym. J.* **2009**, *45*, 1641–51.

130. Yamada, M.; Honma, I. *J. Phys. Chem. B* **2004**, *108*, 5522–26.

131. Murata, T.; Maki, S.; Ohmoto, M.; Miyazaki, E.; Umemoto, Y.; Nakasaji, K.; Morita, Y. *CrystEngComm* **2011**, *13*, 6880–84.

132. Vilkman, M.; Lankinen, A.; Volk, N.; Kostamo, P.; Ikkala, O. *Polymer* **2010**, *51*, 4095–102.

Chapter 11

Electrocatalysis at Restructured Metal and Alloy Surfaces

Chun-Hua Cui and Shu-Hong Yu*

Division of Nanomaterials & Chemistry, Hefei National Laboratory for Physical Sciences at Microscale, Department of Chemistry, University of Science and Technology of China, Hefei 230026, P. R. China

*Fax: +86 551 3603040, E-mail: shyu@ustc.edu.cn

In this chapter, we review the studies of metal and alloy catalyst surfaces reconstructed in ultra-high vacuum (UHV) and gaseous conditions with respectively elevated temperatures and in electrochemical environments at room temperature and the electrochemical activities of these surface-restructured catalysts. We firstly summarize the geometric and compositional reconstructions in solid and solvent conditions, respectively, and then track their structural behaviors once these surface-restructured catalysts have been transferred into hostil electrochemical reactive conditions. The restructuring trajectories go along with the variational environmental impact factors that help to understand the catalytic selectivity and durability against the external environments (i.e., oxidative/reductive reaction gases, adsorbates with high adsorption energy, corrosively acidic electrolytes). Moreover, we discuss the studies of the surface reconstruction by *in situ* advanced photoelectron spectroscopies and scanning tunneling techniques and give the expectation on how to bridge this gap between solid and electrolyte conditions.

1. Introduction

Over last 20 years, a tremendous research and development effort for highly efficient and stable electrocatalysts used in polymer electrolyte membrane fuel

cells has been made to commercialize this environmentally clean and efficient energy supply technology (7). In particular, fundamental research on extended single crystal surfaces and nanostructured catalysts provides new understanding of their activity enhancement, selectivity and long-term stability in metal and alloy electrocatalysts (2, 3). For example, a concept of “Pt monolayer” was developed by Adzic and coworkers at Brookhaven National Laboratory (4). This kind of catalysts consist of a monolayer of Pt deposited on a Pt-free metal or alloy nanoparticles, which efficiently improve the Pt utilization holding the biggest advantage (5). Theoretically, all the Pt atoms are available for catalytic reactions owing to the complete exposure of Pt atoms on a nanoparticle’s surface. Stamenkovic and coworkers at Argonne National Laboratory developed a concept named “Pt-skin”, which driven a single Pt layer segregation from a homogenous alloy under ultrahigh vacuum (6). The clean single-crystal Pt₃Ni (111) surface with a thermodynamically stable Pt-skin “sandwich” structure results in distinctive electronic structure changes of the alloy surface and has demonstrated a 10-fold more active for the oxygen reduction reaction (ORR) than a corresponding Pt(111) surface and 90-fold more active than the current state-of-the-art Pt/C catalysts (2). Another catalyst concept by Strasser and coworkers at Technical University Berlin called “dealloyed core-shell” (7–9), which is accessible by a selective leaching of 3d transition metals such as Cu, Ni, and Co from the surfaces of alloy nanoparticles. The Pt shell thickness is sensitive to the electrochemical dealloying parameters and atomic fraction of surface non-noble metals (10). Dealloying on spherical Pt alloy nanoparticles make the formation of core-shell fine structures and porous nanostructures depend on the size of pristine particles (11–13). Interestingly, dealloying on shaped particles such as octahedral PtNi causes the formation of a more complex but basically octahedral structure (14). These three well-defined concepts provided a comprehensive and rational understanding of catalyst formation, electrocatalytic mechanism and potential practical applications in fuel cells.

It is well-known that a catalyst would not be consumed by the reaction itself during a catalytic reaction based on the definition of “catalyst”. However, in reactive and corrosive environments involving oxidizing/reducing reactive gases, acidic liquids and adsorbates, the surfaces of most materials restructure to adapt their geometrical and electronic structure to the environments and establish a new balance between them (15). Based on this phenomenon, it means that a catalytic reactivity of a catalyst should be investigated and specially considered both in the synthesis step and during the catalytic process. It implies that a catalyst even contains the same particle size, morphology and composition but it may present completely different catalytic reactivity if this catalyst is synthesized by different methods. Since in different synthesis environments, a surface microstructure difference and even a weak composition segregation will finally influence the catalytic reactivity and selectivity. That may be the key reasons why similar catalysts synthesized by different routes demonstrate different catalytic behaviors. On the other hand, a catalyst cannot hold the permanent catalytic activity under reaction environments owing to the surface restructuring induced by the changes of the adsorbates between reactants and products as well as the presence of some sorts of instantaneous intermediates. This associated environment changes

during the whole catalytic reaction and the catalyst changes with it all the time. Most of these changes on catalysts are irreversible. Therefore, the catalyst materials inevitably experience shape, microstructure and composition changes, that is, degradation. Furthermore, one of the unsolved problems in catalysis is to understand activation of a catalyst by restructuring (16).

To understand a catalyst with a “movement” or “thermodynamics” insight, we proposed a catalyst concept so-called “restructured surface/restructured catalyst” (17, 18). This catalyst concept could help one easily understand the catalytic activity, selectivity and stability by involving environmental factors (19). A certain catalyst can change the corresponding reactive environments and cause the changes of reactants and produced intermediates. In contrast, the changes of the external environments undoubtedly can make the catalyst change as well. Therefore, in electrochemical environments, electrocatalytic reactions take place at metal/solid-electrolyte interfaces, where the interfacial environments changes all the time owing to the potential-dependent adsorbates such as water, air and hydrated hydrogen and oxygenated species.

In this chapter, we provide a new concept so-called “restructured surface” on understanding the synthesis of metallic and alloyed catalysts in various conditions and implement this concept for a comprehensive coverage of recent advances in electrocatalytic reactivity and stability. Finally, we summarize the main conclusions and give an outlook of the role of restructured surface in understanding of a catalyst and an electrocatalytic reaction.

2. Construction of Restructured Surfaces in Various Environments

Noble metal catalysts are widely used in the fields of sensor, chemical production, energy conversion and storage. Design and synthesis of these metal and alloyed nanomaterials with well controlled shape, composition and size are very important in heterogeneous catalysis and low temperature fuel cell fields (20–22). In recent years, the synthesis of noble metal nanomaterials with complex structures and shapes through well-designed colloidal chemistry approach has achieved great progress (23). However, as we mentioned above, the as-prepared pristine nanomaterials have to adapt the new environments beyond synthesis conditions. For example, the active metal components of an alloy, such as Ni, Fe, and Co, will adsorb oxygen and water from air and segregate to the surface region even at room temperature (24). Thus, sometimes we have to treat as-synthesized nanomaterials in a specific environments to construct a special composition profile for a certain catalytic reaction (25). The metal and alloy surfaces in reaction conditions experience a lateral displacement called “geometric restructuring” and undergo a vertical displacement named “compositional restructuring”, respectively. In this part, we will summarize the shape and composition evolutions involving in solid state conditions and in electrochemical environments.

2.1. Restructuring in Solid State Conditions

The evolution of nanostructures on surfaces and the restructuring in surface chemistry, actually, are very wide and complex research field involving dynamical and experimental studies on crystalline surfaces, which have been reviewed and commented in the excellent reviews (26–28). In this section, we only summarize the evolution of nanostructures on the extended and nanoparticle surfaces including geometrical and compositional restructurings in ultrahigh vacuum and adsorption gases (H₂, Air/O₂, NO, CO, and N₂), respectively.

In general, the surface restructuring is to establish a new balance of surface energy. In many cases, the restructuring occurs spontaneously or as a result of adsorbate induced effects (29). For clean surface, since the surface atoms have fewer nearest neighbors than atoms in the bulk, the surface energy may be reduced for an arrangement which leads to closer packing in the top atomic layer. Meanwhile, a misfit between the surface and the bulk produced by restructuring increases the surface energy. Thus, the surface structure is determined by these effects (26, 30). On the other hand, in gaseous adsorption environments, the adsorbates on the catalyst surface broke the old energy balance and establish a new adsorption balance by adapting their surface atomic structure to the adsorbates.

On pure single component metal surface, geometric restricting plays a major role. The investigation of material surfaces under reactive conditions depends on the development of *in situ* characterization techniques including ambient pressure x-ray spectroscopies and high pressure high temperature scanning tunneling microscopes. Under oxidative environments, such as in the O₂, the oxygen atoms embed into the sublayers and increase the diffusivity of surface atoms. Understanding of the surface geometric restructuring under the influence of gaseous adsorbates plays a more key role in heterogeneous catalysis because catalytic reactions take place in the presence of reactant gases at pressures ranging from mTorr to atmospheres. Under gaseous conditions, the formation of dense layers of adsorbed molecules was determined by thermodynamics and kinetics (32). In 70 Torr O₂, for example, oxidation of single crystal Rh leads to a rearrangement of surface Rh atoms and forms an apparent rough surface microstructure. This process is irreversible (33).

In addition, Nolte et al reported that an oxygen-induced shape transformation of Rh nanoparticles on magnesium oxide (001) substrates is fully reversible when the surface oxide is removed by CO exposure (at 10⁻⁵ mbar) (Figure 1). A Wulff analysis of high-resolution *in situ* x-ray diffraction, combined with transmission electron microscopy, shows that this restructuring is driven by the formation of oxygen-rhodium-oxygen surface oxide at the rhodium facets, but the reversible shape transformation occurs after restoration of the surface environments (Figure 1). In addition, the dynamic reversible shape changes in response to changes in the gaseous environment were investigated in supported Cu nanocryst. The supports have a major influence on the changes of nanocrystals. For ZnO-supported Cu, the shape changes are caused both by adsorbate-induced changes in the surface energy and by changes in the interfacial energy in Figure 2. However, replacing ZnO with silica support, the support influence on the structure may be negligible. The detailed information for quite complex nanoparticle systems with different

surfaces and interfaces suggested that the structure sensitivity and dynamic morphology changes may be considered in realistic catalytic systems.

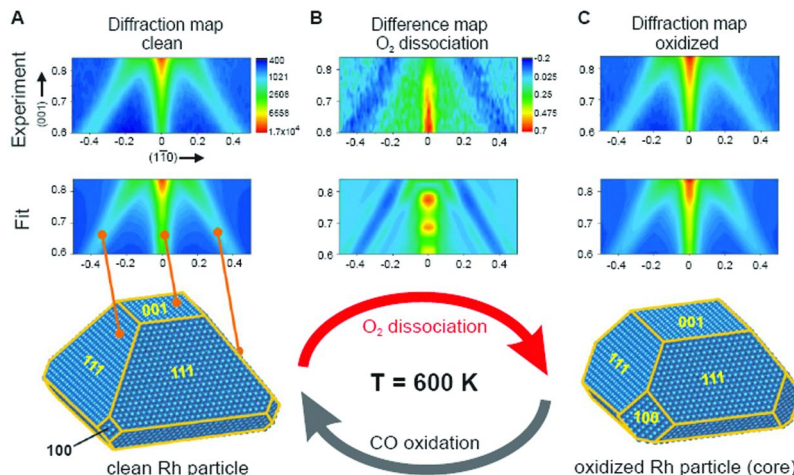


Figure 1. (A) (Top) (110) diffraction map of clean Rh particles at 600 K. (Middle) Fitted diffraction map corresponding to the average particle shape given below. (B) (Top) oxygen-induced change in the (110) plane. (Middle) Simulated signal change for particles with increased (100) side facet area. (C) (Top) Experimental (110) diffraction map at 600 K and 2×10^{-5} mbar O_2 pressure. (Middle) Fitted diffraction map for particles under oxygen exposure. (Bottom) Best-fit core particle shape after oxidation. Adapted with permission from reference (31). Copyright 2008 The American Association for the Advancement of Science.

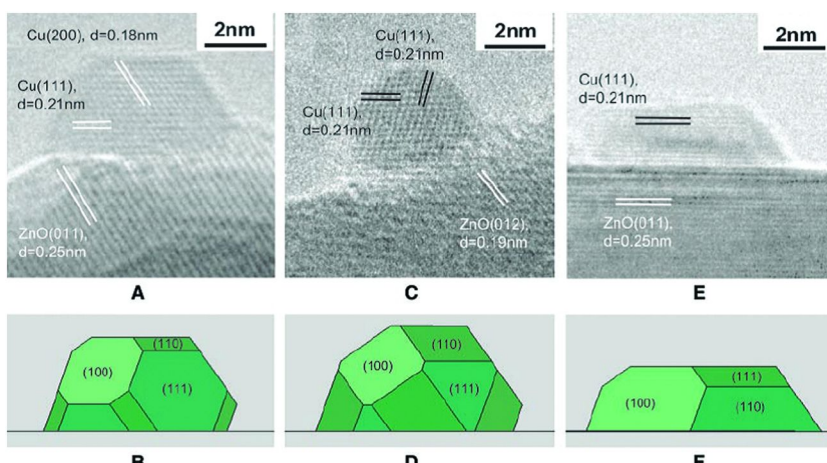


Figure 2. *In situ* TEM images (A, C, and E) of a Cu/ZnO catalyst in various gas environments together with the corresponding Wulff constructions of the Cu nanocrystals (B, D, and F). Adapted with permission from reference (34). Copyright 2002 The American Association for the Advancement of Science.

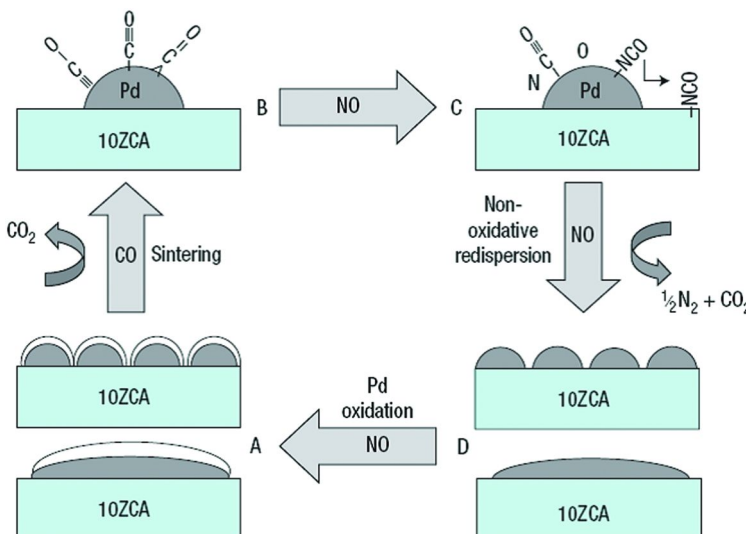


Figure 3. Schematic map of the fundamental steps underlying the reversible, non-oxidative, size and/or shape changes of Pd nanoparticles during CO/NO cycling. Points A–D mark the most salient positions within a CO/NO cycle. Adapted with permission from reference (35). Copyright 2007 Nature Publishing Group.

Supported nanoparticle catalysts based on precious metals, such as Pd, Ir and Pt hold a key to a range of catalytic applications including the reforming and hydrogenation reaction, low temperature fuel cell electrocatalysts, and water slitting (35). But the small size noble metal particles tend to coalesce or sinter into much larger aggregates under processing conditions. This process causes the deactivation of the catalysts owing to the reduction of surface area and active sites. In general, this process is an irreversible and exothermic reaction. Interestingly, Newton et al, by combining energy-dispersive extended X-ray absorption fine-structure spectroscopy with a vibrational spectroscopy (infrared) and mass spectrometry, at high time resolution, in a single *in situ* experiment, they found that very rapid, reversible sintering and novel, non-oxidative dispersion phenomena can be observed in supported 1 wt% Pd catalyst system during CO/NO cycling at 400 °C. At the start of feeding CO, the Pd exists as dispersed or quasi-two-dimensional particles with partially oxidized surfaces. But the surface oxygen can be rapidly removed by combining CO as CO₂ as shown in Figure 3. After the oxygen was completely removed from the Pd surface and Pd-support interface, atop and threefold adsorptions on metallic Pd can be observed. On switching to the NO feed, the adsorbed CO species on the Pd were removed and dispersion via particle splitting or flattening (initial stage; one cycle). The rapid and reversible dispersion of Pd nanoparticles is strongly enhanced when oxygen gas is introduced in the oxidizing step of the redox CO/(NO+O₂) cycle (36). At 400 °C, oxidation of the Pd nanoparticles is too slow to compete with this dispersion and only occurs after the Pd particles undergo significant size/morphological alteration. Alternatively, this process provides

more references in understanding the post-treatments of gaseous involved thermal annealing on supported metal catalysts.

Under reaction conditions, the restructuring of the surfaces of heterogeneous catalysts by adsorption molecules has been investigated visually by microscopy techniques in real space and time. After a long-term development, transmission electron microscopy (TEM) has taken a great step forward with the introduction of aberration-corrected electron optics, which allows the atomic-scale characterization of nanomaterials (37). Even though one of the challenges in TEM is still to visualize gas molecules interacting with supported nanoparticle catalysts at reaction conditions.

Very recently, Yoshida et al applied a newly developed aberration-corrected environment transmission electron microscopy to demonstrate restructuring of $\{100\}$ facets of a gold nanoparticle induced by the adsorption of the CO molecules during CO oxidation at room temperature. The CO molecules adsorbed on-top sites of gold atoms in the reconstructed surface in Figure 4. The ab initio calculations and image simulations confirm that this reconstructed structure is energetic favorability. As we know, a flat facet of a gold nanoparticle with high coordination number cannot adsorb CO molecules with a high coverage owing to the intrinsic weak interaction. Thus, CO molecules favor the low coordination sites such as steps, edges, kinks and corners. Interestingly, the present aberration-corrected environmental TEM revealed that the Au atoms on the topmost layer of the Au $\{100\}$ -hex reconstructed surface have unusual bonding configurations with the Au atoms on the second surface layer, which sustain the adsorption of CO molecules in high density (37).

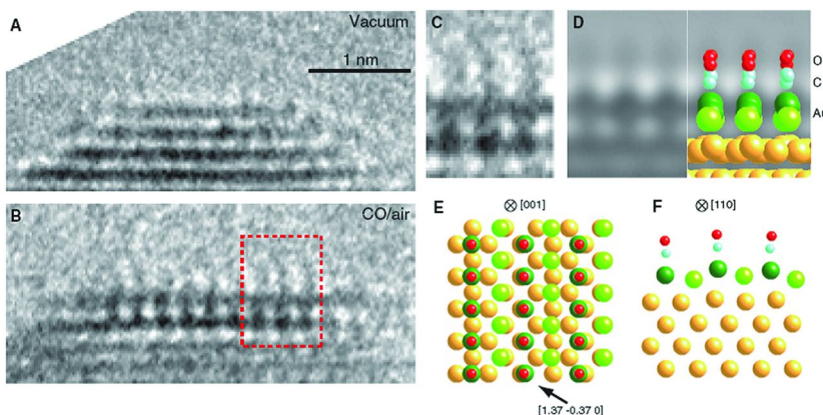


Figure 4. Adsorbed CO molecules on a Au $\{100\}$ -hex reconstructed surface under catalytic conditions. Aberration-corrected TEM images in (A) a vacuum and (B) a reaction environment. (C) The observed image in the rectangular region in (B) at higher magnification. (D) A simulated image based on an energetically favorable model. The model in (E) plan view along the $[001]$ direction of crystalline gold and (F) cross-sectional view along the $[110]$ direction of crystalline gold to show the undulating topmost Au layer. Adapted with permission from reference (38).

Copyright 2012 The American Association for the Advancement of Science.

The adsorption on Pt and Pd surface is much stronger relative to Au surface, especially on the low coordination sites. Tao et al reported a reversible restructuring on stepped Pt surfaces involving a large number of low-coordination sites (Figure 5) (39). Scanning tunneling microscopy and photoelectron spectroscopy studies revealed that the originally flat terraces of (557) and (332) oriented Pt crystals break up into nanometer-sized clusters when the CO surface coverage approaches 100%, and revert to the initial morphology after pumping out the CO gas under gaseous environments near ambient pressure at room temperature. In this case, the creation of increased concentrations of low-coordination Pt edge sites in the formed nanoclusters relieves the strong CO-CO repulsion via geometric restructuring. In addition, they reported the coadsorbate induced reconstruction of a stepped Pt(111) surface by sulfur and CO (40). During this process, the sulfur chemisorbs induced doubling of the terrace widths and step heights, the subsequent coadsorption of CO displaces the sulfur, compressing it to distance of root 3 times the Pt lattice spacing, as results of this, surface restructuring. These results suggested that this kind of large-scale surface restructurings on stepped Pt surface clarified the strong relationship between coverage of gaseous molecules and surface atomic structure under reaction conditions. Furthermore, we may reconsider the surface microstructure evolutions when catalytic reaction occurs on the high index planes, where the terrace may has already experienced surface restructuring relative to the pristine terrace.

For alloy or multicomponent materials under gaseous conditions involving NO, O₂, CO, and H₂, both the geometric and compositional restructurings occur, but sometimes compositional restructuring plays major role owing to the different adsorption energy on dissimilar metal atoms and thermodynamic equilibrium. For example in alternating H₂-O₂ atmosphere, the surface states of supported PtNi nanoparticles treated at alternating H₂ and O₂ atmosphere demonstrated a reversible structural change at the surface (41). The nanoparticles show Ni-O rich surface in oxidizing O₂ gases and Pt-rich surface in reducing H₂ gases. The dynamic behaviors can be attributed to two opposite gas-driven restructuring processes at bimetallic particle surfaces. The surface segregation of Pt at the bimetallic particles occurs in H₂ and encapsulation of the particles by NiO gets in O₂. Such emerging catalyst synthesis techniques can enable the large-scale preparation of highly active catalysts. As shown in Figure 6, three surface architectures were created at the PtNi catalysts including the Pt-skin or Pt-rich surface with subsurface Ni, the NiO-rich surface or Pt/NiO core/shell structure, and the Pt surface decorated with NiO or Ni patches (25). By changing the redox treatments at variable temperatures, it is very easy to establish the reversible switching among the three surfaces. The established treatment-structure-reactivity relationship for the PtNi bimetallic catalysts is very promising for a catalyst synthesis, such as for CO oxidation (42).

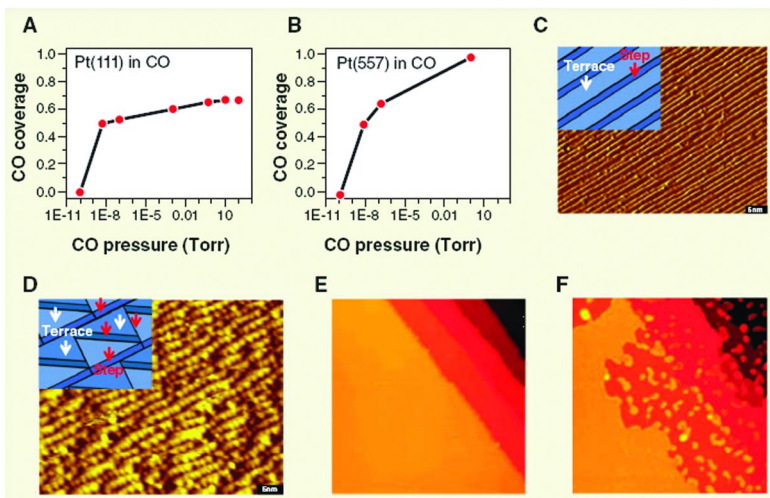


Figure 5. Represented coverage of CO on (A) Pt(111) and (B) Pt(557) in the presence of CO at various pressures, respectively. (C) STM image of Pt(557) with a homogeneous distribution of terraces in UHV; the inset shows the structural schematic. (D) STM image of the restructured surface consisting of triangular nanoclusters with a size of ~ 2 nm; the inset shows the structural schematic. (E and F) STM images (100 nm \times 100 nm) of the surface of a Au-Ni alloy catalyst in 10 torr of CO at 0 min and 75 min. Adapted with permission from reference (15).

Copyright 2011 The American Association for the Advancement of Science.

Tao et al. reported the structural and compositional evolutions of core/shell $\text{Rh}_{0.5}\text{Pd}_{0.5}$ and $\text{Pt}_{0.5}\text{Pd}_{0.5}$ nanoparticles during oxidizing, reducing, and catalytic reactions with alternating NO and $\text{NO} + \text{CO}$ (43). The atomic fraction of $\text{Rh}_{0.5}\text{Pd}_{0.5}$ in Figure 2B illustrates the changes in composition in the 0.7-nm shell measured by an X-ray energy of 645 eV. At 300 °C and in 100-mtorr NO, the Rh in the shell was oxidized. When 100-mtorr CO was feed to NO, CO_2 and N_2 was produced, then the total Rh atomic fraction in the shell decreased from 0.92 ± 0.03 to 0.46 ± 0.02 and that of Pd increased from 0.08 ± 0.03 to 0.54 ± 0.02 . These suggested the large-scale compositional restructuring from the shell to the core region other than in the surface several atomic layers. However, in the $\text{Pt}_{0.5}\text{Pd}_{0.5}$ nanoparticles, there is no obvious segregation under these conditions in Figure 6C. Moreover, the $\text{Pt}_{0.5}\text{Pd}_{0.5}$ nanoparticles even do not exhibit the strong segregation and reversibility characteristic relative to $\text{Rh}_{0.5}\text{Pd}_{0.5}$ nanoparticles because the Pt is not easier to be oxidized and pinned to the surface by formation of oxide.

Beyond nanoparticles materials, one can expect the systemic post material treatments on one-dimensional nanoarchitectures and extended single crystal surfaces. Yu and coworkers reported the gas involved thermal annealing on unique nanoparticle tubes (44–46). Thermal treatments on PtNi nanoparticle tubes in H₂/Ar gases cause the formation Pt-rich surface (18). However, for ternary PtPdCu materials, the thermal annealing in H₂/Ar makes the Pt and Pd segregate to the surface owing to adsorption-induced segregation of Pt and Pd in H₂ at 500 °C (47, 48).

Bandarenka et al. demonstrated a detailed construction of single-crystalline surface structures at different gaseous atmosphere in Figure 7. At the beginning 1 ML Cu atoms were electrodeposited on the Pt(111) surface to form a Cu overlayer. Then, this overlayer was thermal treated in Ar/H₂ at 400 °C for 2 min. The H₂-gas-adsorption causes the segregation of Pt to the surface via compositional restructuring (called near surface alloys, NSA). By switching Ar/CO gas, some Cu atoms migrate to the surface owing to the thermodynamical stability. This Cu/Pt NSA binds CO significantly more weakly than does Pt alone (49), and maybe there is a CO-CO repulsion on the terrace. Finally, the surface alloys, near surface alloys, and overlayers can be obtained by thermal treatments in atmosphere environments.

These adsorbate-induced resctriction strategies allow to build a catalyst with selectively controlled surface composition and structure for catalytic reaction. In addition, it helps for understanding of the real-time surface states in alloy catalysts.

2.2. Restructuring in Electrochemical Conditions

In electrolytes, surface reconstructions by a lowering of the surface energy are widely observed that is almost the same as those in solid state conditions. It contains reducing state at lower potential (< 0.4 V) and oxidizing state at higher potential (> 0.6 V) during potential cycling. Moreover, it involves gaseous adsorbates such as H₂, O₂, and CO, and ionic adsorbates such as halogen ions, SO₄²⁻, etc. In recent years, it has been demonstrated that in aqueous electrolytes by structure-sensitive techniques restructured surface of metal and alloy could be stable, which has allowed the determination of electrochemical properties of a restructured surface (51). However, since the established energy and charge balances of restructured surface in solid environments against the tough condition at a metal-electrolyte interface, a further surface restructuring in electrochemical conditions is too difficult to be avoided. At a specific potential in aqueous solution, the electrode surfaces receive different surface adsorbates. At lower and higher potentials, the water is split into hydrogen and oxygen which cause hydrogen and oxygen adsorptions, respectively. A reconstructed surface which is prepared by sputtering and annealing in ultrahigh vacuum conditions may be stable in the aqueous electrolyte and even survived potential cycling in the double layer charging region, but it may become unstable upon oxygen adsorption and CO adsorption. Herein, we summarize the key examples of potential-induced restructuring assisted by several adsorbates and investigate the stability of restructured surface.

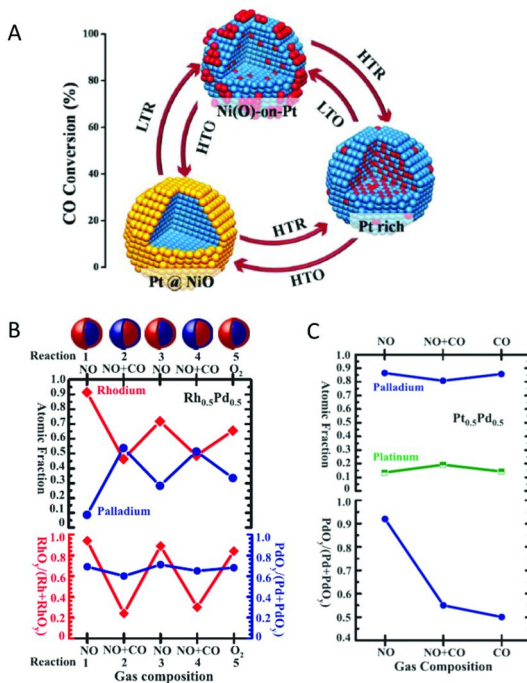


Figure 6. A, Reversible transformations between the Pt@NiO Core/Shell Structure, the Ni(O)-on-Pt Structure, and the Pt-rich Surface Structure during alternating reduction and oxidation (redox) treatments at variable temperatures.

LTO, low-temperature oxidation; HTO, high temperature oxidation; LTR, low-temperature reduction; HTR, high temperature reduction. Adapted with permission from reference (25) B, (Top) Evolution of Rh ($Rh^0 + Rh^{2+}$) and Pd ($Pd^0 + Pd^{2+}$) atomic fractions in the $Rh_{0.5}Pd_{0.5}$ NPs at 300°C under oxidizing conditions (100 mtorr NO or O_2) and catalytic conditions (100 mtorr NO and 100 mtorr CO) denoted in the x axis. (Bottom) Evolution of the fraction of the oxidized Rh (left y axis) and Pd atoms (right y axis). Schematic diagrams show the reversible segregation of Rh and Pd under alternating oxidizing and catalytic conditions. C, (Top) Evolution of the Pd and Pt atomic fractions in $Pt_{0.5}Pd_{0.5}$ NPs at 300°C under oxidizing (100 mtorr NO), catalytic (100 mtorr NO and 100 mtorr CO), and reducing (100 mtorr CO) conditions. The x axis represents the different gas environments. (Bottom) Evolution of the atomic fraction of the oxidized Pd atoms. Adapted with permission from reference (43). Copyright 2008 The American Association for the Advancement of Science.

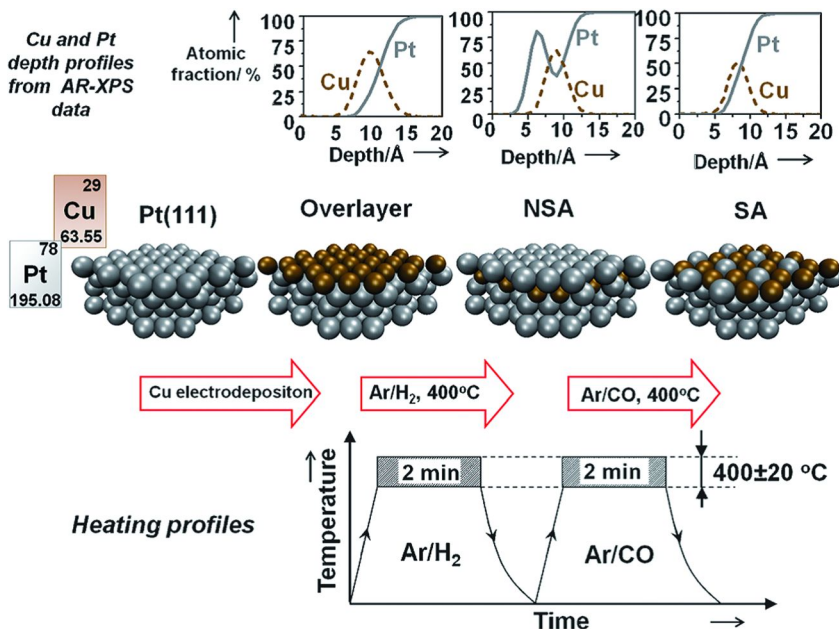


Figure 7. General scheme used to prepare Cu/Pt(111) overlayers, near surface alloys, and surface alloys. The corresponding depth profiles, obtained using AR-XPS, are shown at the top. Adapted with permission from reference (50).

Copyright 2012 John Wiley and Sons.

More than 30 years ago, surface electrochemists already started to investigate the surface faceting (geometric restructuring) of polycrystalline electrode surface by combining the scanning electron microscopy and voltammetry (52). By application of a repetitive scan at more than 10,000 V/s, the change of the surface structure observed is related to a specific hydrogen adatom voltammogram usually obtained for single crystal surfaces. Thus, the fast potential perturbations can induce structural changes in the surface and construct electrode surfaces with preferred orientations, or call surface faceting (53, 54).

For single-component metallic electrode, the most successful development of this electrochemical square-wave potential method should be the case on synthesis of tetrahedrahedral Pt nanocrystals (55). After the electrodeposition of Pt spherical particles, a square-wave potential treatment within the potential region between -0.2 to 1.2 V at 10 Hz in a solution of 0.1 M H₂SO₄ + 30 mM ascorbic acid for 10 to 60 min to transform the spherical particle into tetrahedrahedral Pt in Figure 8. The nature of the formation of tetrahedrahedral Pt may be considered as the adaption of the surface structure to the square-wave environment. At 1.2 V, Pt surface is oxidized and covered by oxygenated species originated from the dissociation of H₂O. On high coordination sites, such as Pt(111), the irreversible surface Pt-O displacement occurs and disorders the surface structure. However, for low coordination sites such as (730) terrace with coordination number of 6, the oxygen atoms preferentially adsorb at such stepped atoms without replacing them,

thus the ordered surface are preserved (55). By using the similar condition, the tetrahedrahedral Pd nanocrystals have been obtained (56). This potential-induced geometric restructuring strategy provides a realistic possibility for construction of nanocrystals with high index facets.

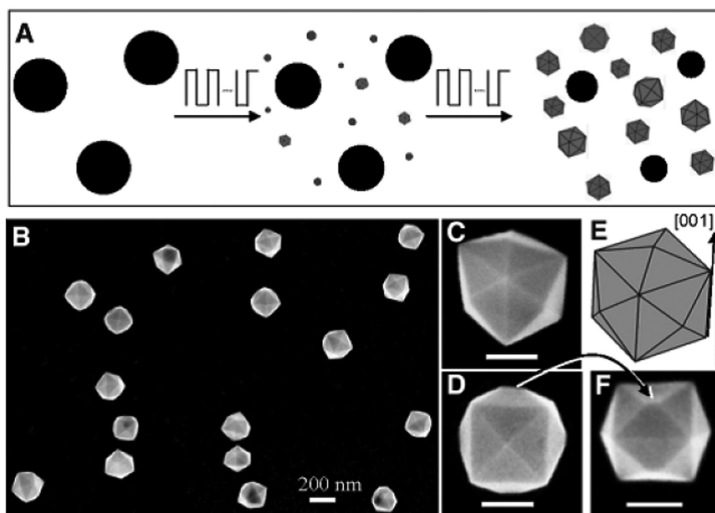


Figure 8. (A) Scheme of electrodeposition of tetrahedrahedral (THH) Pt nanocrystals from nanospheres. (B) SEM image of tetrahedrahedral (THH) Pt with growth time of 60 min. (C and D) SEM images of Pt THH viewed down along different orientations, showing the shape of the THH. (E) Geometrical model of an ideal THH. (F) SEM image of a THH Pt nanocrystal. Scale bars in (C), (D), and (F), 100 nm. Adapted with permission from reference (55). Copyright 2007 The American Association for the Advancement of Science.

The surface restructuring and surface ordering in electrochemical environments can be influenced by feeding gases and introducing ions. *In situ* surface X-ray scattering (SXS) in combination with cyclic voltammetry, Lucas et al. presented a potential-dependent surface reconstruction of Au(100) (57). The adsorption and ordering of Br anions on the Au(100) surface, and the adsorption and oxidation of CO on the Pt(111) in acidic electrolyte in the presence of anions represent a range of structural behaviors. In addition, Br anions can be used as “smoothing agent”. Low coordination sites, such as edges, kinks, and defects are very detrimental to oxygen reduction electrocatalysis, so the removal of these low coordination sites and removal of the roughness effect are challenging and attractive. Cai et al. reported an effective approach for smoothening of the particle surface by Br anions adsorption/desorption (Figure 9). This method synchronously increased the number of (111)-oriented facets during the potential cycling. This Br-induced geometric restructuring is more like adsorption ordering (Figure 9, bottom). After immersing the electrode in the Br containing solution, Br anions were immediately adsorbed on the low-coordination sites of the surface

owing to the stronger bond energy on these sites relative to the terrace sites. In the cathodic scan, the reductive desorption of the Br could trigger the low-coordinated Pd atoms and make them migration to the terrace sites to minimize the total surface free energy. In the following anodic scan, the low-coordinated Pd forms a Pd-Br pair in solution that is re-deposited onto the surface, accompanied by the oxidative adsorption of Br. Adsorbate-induced reconstruction during the potential cycling is a very attractive technique to modify the surface microstructure and even the morphology.

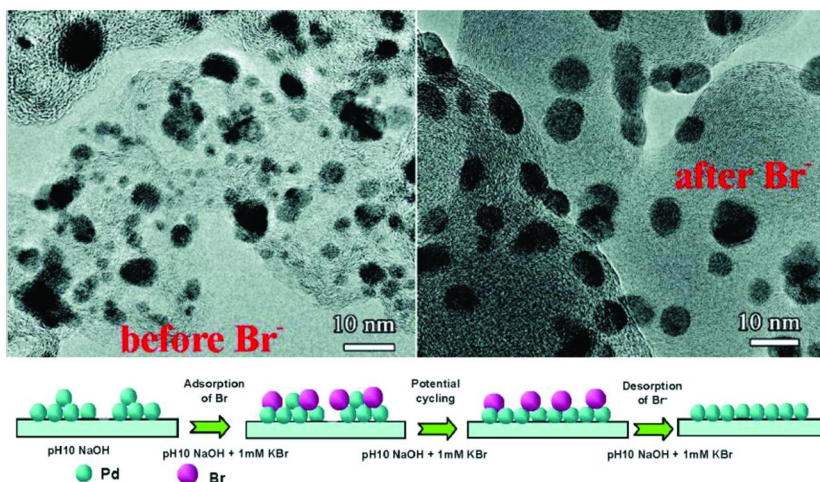


Figure 9. TEM images of Pd/C before (a) and after (b) Br treatment (top). Illustration of the removal of surface low-coordination sites via the oxidative adsorption and reductive desorption of a bromine layer (bottom). Adapted with permission from reference (58). Copyright 2011 American Chemical Society.

On the other hand, the adsorbate-induced reconstruction sometimes can increase the surface roughness and the surface active sites during potential cycling. Recently, Yu and coworkers reported a potential-induced reconstruction on Pt-rich surface of the PtCu nanoparticles assisted by the adsorption/desorption of oxygenated species in acid electrolyte (17). The driving force of this kind of morphology change may be from the release of surface compressed strain, which is caused by the differences of surface atomic arrangements or bond lengths in contrast to those in the core region (7). The intensity of surface strain correlates with the atomic fraction of Cu in the core region owing to the much shorter Cu-Cu and Cu-Pt bond lengths relative to Pt-Pt bond length in the surface. The high surface strain was released in electrochemical environments by oxygen-induce atom migration and O-Pt place exchange during the potential cycling. Under these conditions, the low-coordination Pt sites form on the surface and thus increase the surface area ten times than that before potential cycling (Figure 10). Of course, there are some Cu atoms have been leached out during the potential cycling because the Cu atoms in the core tend to migrate to the surface caused by the

adsorption of oxygenated species (17). A similar surface geometric restructuring was observed in PtNi bimetallic alloys (18), and ternary PtPdCu alloys (48). It must be noted that the geometric restructuring presented here should be directly related to the atoms migration. Atomic rearrangements during dealloying were predicted. The missing of the neighbor non-noble component metal atoms such as Cu, Ni, Co and Fe during leaching results in the formation of plenty of low-coordination and dangling atoms in the surface own high surface free energy (59). Thus, the rearrangements of Pt atoms in the surface spontaneously occur and further surface faceting may be caused by potential cycling.

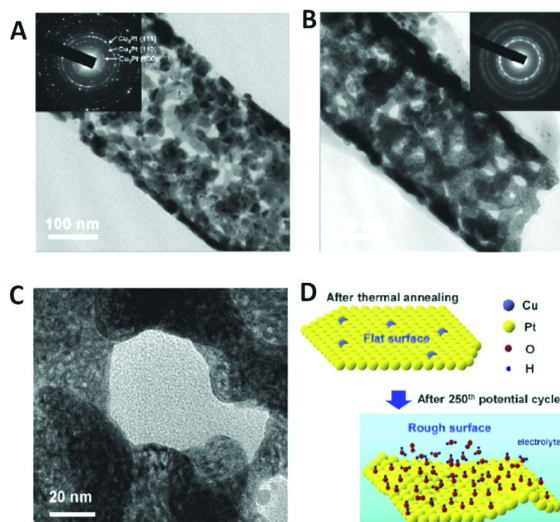


Figure 10. (A) TEM image of a part of a CuPt tube after annealing at 600 °C. (B) TEM image of a part of a CuPt restructured tube obtained after 250 cycles between 0.05 and 1.2 V vs RHE in Ar-saturated 0.1 M HClO_4 solutions. Insets show the ED patterns. (C) TEM image shows the highly rough surface. (D) Schematic of surface evolution after 250 cycles. Adapted with permission from reference (17). Copyright 2012 American Chemical Society.

In electrochemical environments, compositional segregation and restructuring play a key role in understanding the reactivity and stability of a catalyst, especially an alloyed catalyst. Potential voltammetry produces hydrogen adsorption at lower potential and oxygen adsorption at higher potential, respectively. Since the relatively weaker bond energy relative to oxygenated species, hydrogen adsorbate get insignificant effect on the morphology changes of the catalysts. However, oxygenated species has a much stronger adsorption on transition metals and even noble metals above 0.8 V versus reversible hydrogen electrode (RHE). Thus, in electrochemical conditions, oxygenated adsorbates could demonstrate a significant effect on the surface structure of catalysts.

Surface compositional restructuring of the non-noble component of a Pt bimetallic core–shell catalyst can occur under typical fuel cell cathode

application conditions or under reaction conditions at room temperature. In an alkaline electrolyte, electrochemical leaching may not occur, but the composition changes in the surface during potential cycling under the adsorption/desorption of oxygenated species above 0.7 V versus RHE (Figure 11A-C). In an acidic electrolyte, any non-noble alloying material at the surface would immediately dissolve into the electrolyte (60). Thus, such catalysts cannot escape degradation during operation in an acidic fuel cell. However, changing the reaction environment into CO saturated alkaline electrolyte, Pt segregates to the surface of the nanoparticles, and correspondingly displaces Co to the core because the adsorption enthalpy of CO on Pt is higher than on Co (61). In the whole process, the CO annealing would not change the particle size and cause the formation of well-defined core/shell Pt-Co/Pt structure. In a word, such adsorbate-induced compositional restructuring could be used to synthesize Pt-Co/Co_xO_y core/shell structure in an alkaline solution and prepare Pt-Co/Pt core/shell structure in CO saturated alkaline solution, respectively.

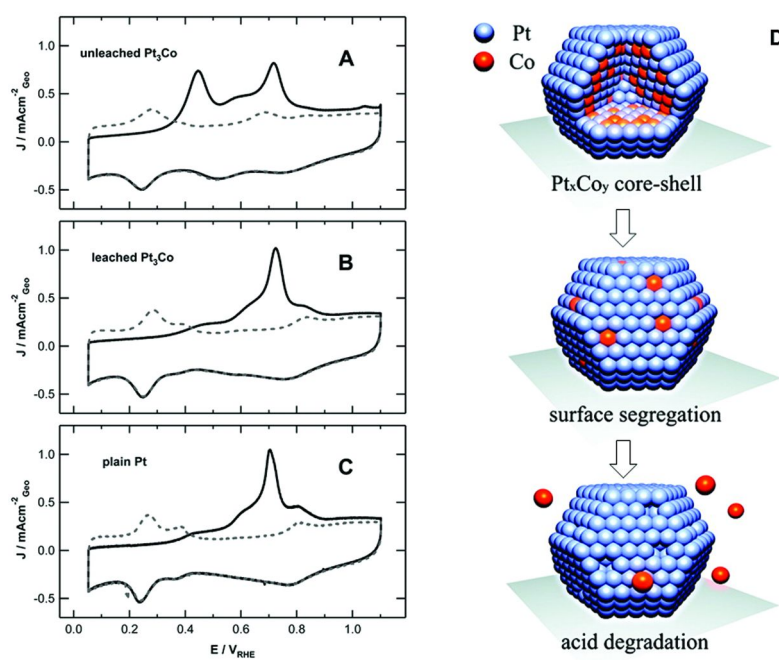


Figure 11. CVs in Ar-purged 0.1 M KOH electrolyte recorded at 50 mV s⁻¹ at room temperature (gray dashed curves) for (A) an unleashed Pt₃Co catalyst, (B) a leached Pt₃Co catalyst, and (C) a plain Pt catalyst for comparison. Black solid lines are CO-stripping curves for the same catalysts. (D) surface segregation in alkaline solution and followed degradation in acid electrolyte. Adapted with permission from reference (60). Copyright 2009 American Chemical Society.

In addition, adsorbate-induced compositional restructuring could redistribute the composition ratio in a mixed alloyed surface and cause surface atom ordering. For example, for the Pd-supported Pt-M mixed monolayers, where M = Ir, Ru, Re, or Os, with M adsorbing OH or O strongly, reflects the decreased OH coverage on Pt, caused by lateral repulsion between the OH adsorbed on Pt and the OH or O adsorbed on a neighboring surface metal atom, M (Figure 12 A). Thus, the role of the second metal is to lower the OH coverage on Pt. In addition, because of the lateral repulsion, the M redistribute orderly in the surface to minimize the surface energy (62). As we know, both Ir and Ru have a high coverage of OH at lower potentials relative to Pt. As shown in Figure 12 B, the kinetic current densities obtained from the Koutecky-Lev, which plots for oxygen reduction reaction (ORR) at 0.80 V for mixed Pt-Ir and Pt-Ru monolayers as a function of the M/Pt ratio. The repulsive interaction changed the atomic rearrangements on the surface and changed the binding energy of OH on Pt.

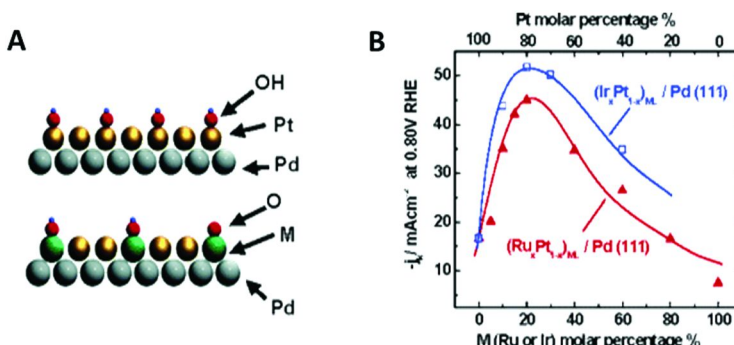


Figure 12. (A) Model for the decrease of the OH coverage on Pt, caused by a high OH or O coverage on a second metal M. (B) ORR activity of two mixed-metal monolayer electrocatalysts supported on Pd(111), expressed as the kinetic current density at 0.80 V as a function of the M/Pt ratio. Adapted with permission from reference (62). Copyright 2012 American Chemical Society.

Adsorbate-induced restructuring could further change the surface composition ratio (surface atomic redistribution). Recently, Yu and coworkers reported a surface atomic redistribution on Pt-Pd mixed alloy surface of PtPdCu materials (47). During potential cycling, non-noble metal Cu can be leached out from the surface in acidic electrolyte, and then the Pt-Pd mixed noble surface can be obtained. In this PtPdCu ternary system, the Cu did not show strong segregation from the core region, so plenty of Cu was confined in the core region. The Pd experienced segregation and leaching processes in the surface which continuously increased the atomic fraction of Pt. This is a very complex system. The further investigation will be carried out in the future.

Restructuring in electrochemical environments is still in its initial stage although D. M. Kolb already got very great progress in a few decades ago (51). The *in situ* investigations in solution condition is limited by the spectroscopy and scanning tunneling techniques. During that period, electrochemical scanning

tunneling technique has achieved significant development, but the revolution and stability of this technique still fall behind those techniques in UHV conditions. Thus, it is quite challenging to monitor the surface composition and morphology evolutions in solution compared to those in UHV or solid state conditions. As we discussed above, *ex situ* investigations on the surface from UHV or solid state conditions to solution environments have to consider the structural evolutions under different environments. However, the “restructured metal and alloy surfaces” will help us understand the structural and compositional differences in the surface between different conditions and thus understand the activation of catalysts by the restructurings.

3. Structural Behaviors of Restructured Surfaces in Electrocatalysis

The catalytic activity strongly correlates with the surface atomic arrangements and electronic structures. Surface atomic arrangements include surface atomic coordination number, atomic ensembles and atomic strain. Of course, electronic structure can be influenced by surface atomic arrangements and adsorbates as well as substrate supports. Unfortunately, surface atomic arrangements are not stable (63), such as (100) and (110) terraces which tend to restructure and form a quasihexagonal close-packed top layer. Low index (111) is relatively stable. In electrochemical hostile conditions, the high intensity adsorption of oxygenated species could change everything including the morphology, composition, and even particle size above 0.8 V versus RHE within typical fuel cell cathode application ranges. In this section, we briefly summary catalytic activation and deactivation by the restructurings, respectively, and provide alternative reference on understanding the activity and degradation in Electrocatalysis.

3.1. Activation by Restructuring

Fuel cells convert chemical energy directly into electrical energy with high efficiency and low emission of pollutants. However, optimal choice of fuels and the research and development of alternative catalytic materials in fuel cell stack for commercial applications still meet several important issues, such as cost and durability (64). The achievement of commercialization should go with the fundamental understanding of electrocatalysis and the development of materials science and surface science.

Investigations of electrocatalytic reactions on well-defined surfaces, especially on restructured surfaces, provide fundamental information on surface reactivity and guidelines for the understanding and design of practically catalytic materials (65). In my opinion, one of the most successfully restructured high active surfaces should be the “Pt-skin” (2, 6, 66), which was developed by Markovic and Stamenkovic in Argonne National Laboratory. In UHV conditions, the near-surface layer of single-crystalline Pt3Ni exhibits a highly compositional oscillation in the first third layers, which are Pt-rich, and in the second atomic layer, which is Ni-rich. It is called sandwich Pt-skin structure. By using *in situ*

surface X-ray diffraction, the atomic structure and stability of the Pt₃Ni(111) surface in the electrochemical environment have been determined (67). Surface segregation leads to a pure Pt(111) skin with enrichment of Ni in the second atomic layer (inset in Figure 13 A). This restructured structure modified the surface electronic structure (d band center position) (68) and altered the adsorption properties of the resulting Pt-alloys (Figure 13B and 13C) (69). The Pt-skin surface exhibits inward relaxation upon the adsorption of oxygenated species and this explains the surface stability compared to pure Pt(111). Using Monte Carlo calculations it is shown that nanoparticles with the same surface composition and stoichiometry are energetically stable (67). The ORR kinetic is accelerated on the segregated Pt(111)-skin relative to Pt(111), causing the positive shift of 100 mV in the half-wave potential in Figure 13D. In addition, Stamenkovic and coworkers extended this concept into mesostructured thin-film catalysts. The thin-film surface restructure to form high active Pt(111) skin structure under thermal treatments and this new kind of catalysts demonstrate 20-fold more active than the state-of-the-art Pt/C nanocatalyst (66).

On well-defined single-crystalline Pt(111) surface, Chorkendorff and coworkers demonstrated that the introduction of subsurface 3d transition metals can weaken the binding of a Pt surface to oxygenated species (50). By depositing different amount of Cu on the Pt(111) and a followed thermal annealing in a reductive atmosphere, the Cu atoms can be incorporated into the subsurface while retain its (111) orientation (50). After the surface compositional restructuring in a gaseous atmosphere, the electrode was then characterized in the same cell. Cyclic voltammetry in N₂ saturated solution was performed to detect the strength of the interaction of the Cu/Pt(111) near surface alloys with H and OH. The changes of the H and OH adsorption peaks inhibit that the presence of Cu in the subsurface destabilizes these adsorbates in Figure 14 A. *In situ* monitoring the binding energy change of an adsorbate OH on a single surface by incorporating continuously increased amount of Cu into the subsurface, only a slight weakening of the descriptor, ΔE_{OH} , by ~0.1 eV, relative to Pt(111), leads to optimal activity for the oxygen reduction reaction. This activity was achieved when about 0.5 ML Cu was deposited and incorporated into the subsurface in Figure 14B. The experimental descriptor for the activity of the surface is agreed with theoretical prediction that well demonstrated the Sabatier principle.

Beyond the investigations on well-defined single-crystalline, many excellent works have done on high surface area nanoparticle catalysts. As discussed above, on bulk Pt alloy surfaces, Pt can segregate in the topmost layer to form a “sandwich-segregated Pt-skin structure”. This structure is shown to weaken the metal-oxygen bond strength relative to pure Pt and increase the specific ORR area activity. However, for nanoscale catalysts, it quite difficult to directly synthesize this kind of sandwich skin structures, especially on specifically oriented surface such as (111) terrace. Yang and coworker used a two-step method to build sandwich skin structure on (100) by thermal annealing of acid-treated Pt-Co materials (71, 72). The enhanced ORR activity was attributed to compressive strains and ligand effects associated with the percolated and sandwich-segregation structures in the near-surfaces of nanoparticles. Wang et al used the similar acid-treatment/thermal annealing protocol to prepare multilayer

Pt-skin structure with a controlled Pt layer of 1 to 7 ML, and the 3 ML Pt-skin structure demonstrated exceptional specific ORR activity (73). These are typical cases that involve restructuring under solid conditions in a reductive atmosphere and characterize the electrocatalytic activity in electrolyte.

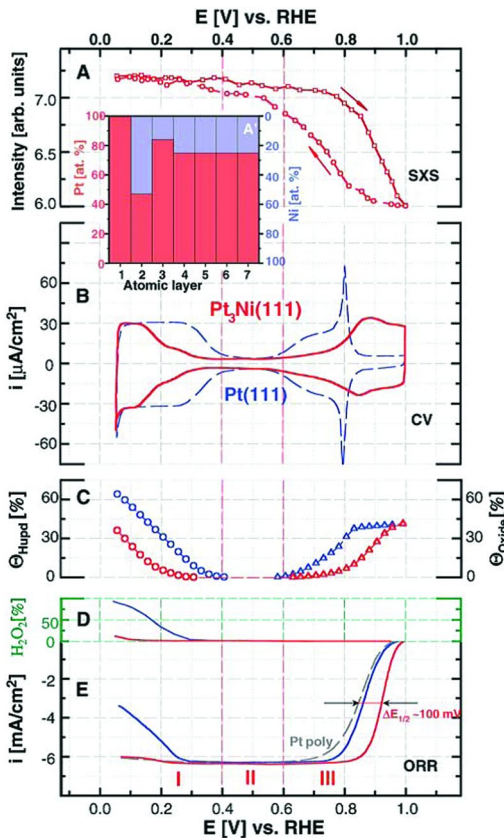


Figure 13. *In situ* characterization of the $\text{Pt}_3\text{Ni}(111)$ surface in 0.1 M HClO_4 at 333 K. (A) SXS data and (A') concentration profile revealed from SXS measurements. (B) Cyclic voltammetry (red curve) as compared to the voltammetry obtained from $\text{Pt}(111)$ surface (blue curve). (C) Surface coverage calculated from cyclic voltammograms of $\text{Pt}_3\text{Ni}(111)$ (red curve) and $\text{Pt}(111)$ (blue curve); (D) Green scale refers to hydrogen peroxide production in designated potential region and (E) ORR currents measured on $\text{Pt}_3\text{Ni}(111)$ (red curve), $\text{Pt}(111)$ (blue curve), and polycrystalline Pt (gray curve) surfaces. Adapted with permission from reference (2). Copyright 2007 The American Association for the Advancement of Science.

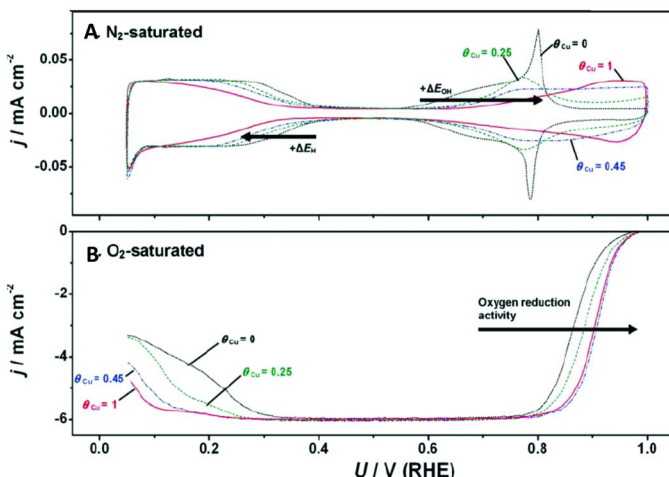


Figure 14. (A) in N_2 -saturated electrolyte; (B) LSV curves in O_2 -saturated electrolyte, 1600 rpm, 60 °C. θ_{Cu} denotes the amount of Cu initially deposited.

Adapted with permission from reference (70). Copyright 2011 American Chemical Society.

Recently, Yu and coworkers presented a highly active and stable CuPt catalyst which has been obtained by a compositional restructuring in a reductive atmosphere and a followed geometric restructuring in electrochemical conditions (17). The electrodeposited CuPt pristine materials firstly thermally treated in mixed H_2/Ar cause the formation of Pt-rich surface with high surface compressed strains. And then, the materials electrochemically treated in acid electrolyte to induce the release of surface strain and form a highly active and stable restructured surface.

As we know, electrochemical treatments (potential cycling) in a hostile acid solution leach out the non-noble components in the surfaces of alloys and make the formation of a core-shell structure (Figure 15 A) (74, 75). Based on the model by Strasser et al, more Cu present in the core, more strain in the core/shell interface (Figure 15 A and B). On the other hand, during the potential cycling, a mass of surface Cu leached out and dissolved into the solution and left vacancies, and then the surface Pt lost neighbor Cu atoms and became low-coordination Pt sites with a high surface free energy. Thus, surface restructuring occurred and Pt atoms migrated to fill in those vacancies, and finally dense Pt shell formed in Figure 15 C. Therefore, the strains on the topmost Pt shell depend on the shell thickness and surface roughness (76). These possible impact factors make the experimental descriptor cannot reach the optimal activity value predicted by DFT calculations in Figure 15D.

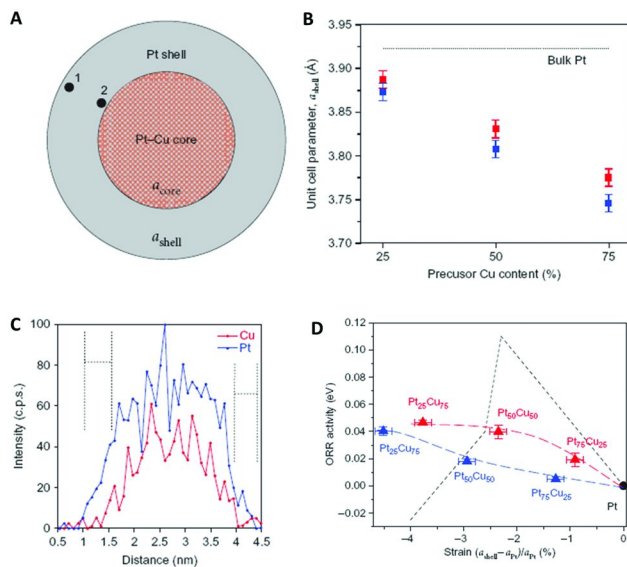


Figure 15. (A) Scheme of a simple two-phase structural model for the dealloyed state of a bimetallic particle. A real core–shell particle shows a gradient in lattice parameters, with strain in the surface layer (point 1) being less than in layers near the core (point 2). (B) Determination of a_{shell} for dealloyed Pt–Cu bimetallic particles, plotted as a function of the alloy precursor Cu atomic composition at precursor annealing temperatures of 950 °C (blue) and 800 °C (red). (C) HR-EDS line profile across an individual ~4 nm diameter dealloyed Pt–Cu alloy active-catalyst particle. The thickness of the Pt-enriched particle shell was ~0.6 nm. (D) Experimental and predicted relationships between electrocatalytic ORR activity and lattice strain. Adapted with permission from reference (7). Copyright 2010 Nature Publishing Group.

Potential cycling in electrochemical conditions causes surface atomic redistribution (48), which allows us to study a site-dependent electrochemical formic acid oxidation reaction on a mixed Pt/Pd alloy surface of ternary PtPdCu in an acidic electrolyte. The increased Pt/Pd atomic ratio in the topmost surface layer changes the formic acid oxidation mechanism owing to the adsorption differences for formic acid molecules in Figure 16A. For the formic acid oxidation, it is well known that the electro-oxidation of HCOOH to CO₂ proceeds through two parallel pathways: direct oxidation to CO₂ (pathway I) and oxidation to CO₂ (pathway II). In the direct oxidation (pathway I), the HCOOH molecules dehydrogenate to directly form CO₂ through one or more active intermediates. However, pathway II involves HCOOH dehydrogenation to form CO and subsequent electro-oxidation of the adsorbed CO to CO₂ at high potentials. For pathways I and II, the peak intensity appears at 0.35 and 0.9 V, respectively. As shown in Figure 16, the restructured mixed PtPd surfaces present both pathways only in one catalyst. In the case of the surface with low content Pt, the sites of a single Pt atom surrounded

by Pd atoms favor the direct oxidation of formic acid on these surfaces through the dehydrogenation of formic acid (pathway I). If more Pt atoms segregate to the topmost surface layer upon more potential cycles, the density of dimers and trimers of Pt atoms on the topmost surface is highly increased. The increase of the atomic fraction of Pt and density of sites of dimers and trimers on the surface will increase the adsorption of CO_{ad} on the surface, which favors pathway II and gives a high current density i_c .

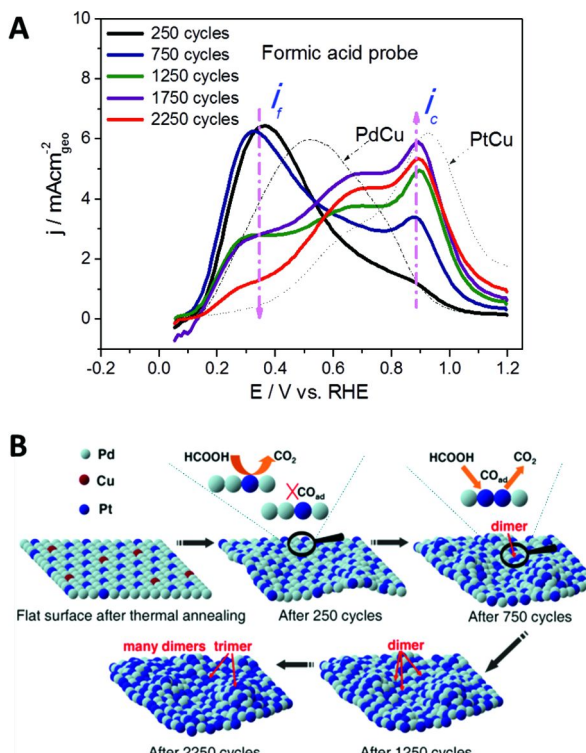


Figure 16. (A), CVs of the formic acid oxidation through the positive scan after a different number of potential cycles. i_f represents the peak current intensities of direct oxidation of HCOOH to CO_2 in pathway I and i_c denotes the peak current intensities of oxidation to CO_2 through the formation of an intermediate CO in pathway II. (B) Schematic illustration of the active site-dependent formic acid oxidation, the morphology restructuring and surface atomic redistribution of the surfaces after a different number of potential cycles. Adapted with permission from reference (47).

Although understanding activation of a catalyst by restructuring is still at its initial stage, it is still a very important reference for us to design the materials, track the change of surface and predict the activity in practical operation conditions.

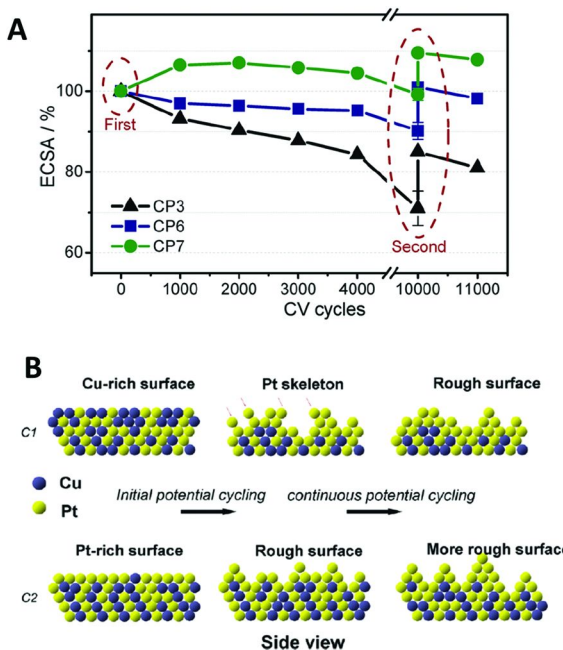


Figure 17. (A), Stability and restorability test. The loss percentage of ECSA was obtained after a specified accelerated stability test. The stability test was performed in an O_2 -saturated 0.1 M $HClO_4$ solution between 0.6 and 1.0 V (vs RHE). After 10k cycles of the stability test, the second 250 cycles were performed to measure the restorability. (B), Schematic of different surface morphology evolutions between C1 and C2 catalysts. Adapted with permission from reference (17). Copyright 2012 American Chemical Society.

3.2. Deactivation by Restructuring

In electrocatalysis, the loss of surface active sites, leaching of non-noble components in alloys and corrosive of carbon supports are the toughest issues that need to be addressed (77, 78). Stability of synthesized catalysts is one of the main requirements for commercializing fuel cell electrocatalysts for automotive applications (79).

Based on the reconstruction concept for catalysts, geometric restructuring including Ostwald-ripening, particle coalescence and loss of active facets should be the direct degradation for the loss of surface active sites (80). By using non-destructive transmission electron microscopy technique, Mayrhofer et al directly observed the morphology and size changes involving particle detachment and particle movement/agglomeration in electrochemical conditions (81). Recently, Yu et al reported a direct 3D visualization of nanoparticle trajectories before and after electrochemical treatments. The growth in the Pt shell thickness

and observation of coalescence decrease in the surface active sites and make the loss of the activity of Pt alloy nanocatalysts in fuel cell cathodes (82).

Restructured surfaces in electrochemical conditions could effectively prevent the loss of surface active sites by further restructuring. Yu and coworkers designed a CuPt bimetallic catalyst with a controlled Pt-rich shell. After electrochemical treatments on this catalyst between 0.06 and 1.2 V in acid solution, the surface active area increased 10 more times relative to the initial surface area before electrochemical treatment. This restructured surface held exceptionally structural stability, even after 10,000 cycles, the surface inhibited almost no loss of the ECSA value relative to the restructured surface in Figure 17 A. The reconstruction ability is related to the atomic fraction of Cu in the surface. As shown in Figure 17 B, for Cu-rich surface, the Cu leaching led to the roughness of the surface. The low-coordination Pt sites with high surface free energy would rearrange to decrease the surface area (loss of surface area). For Pt-rich surface, the flat Pt shell with high compressed strain would release the strain and roughen the surface, and thus increase the surface area. Therefore, both cases cause the surface restructuring by minimizing the surface free energy.

Furthermore, surface restructuring could help to understanding the stability of a ternary PtPdCu electrocatalyst. The PtPdCu catalyst demonstrated comparable catalytic activity for the ORR than that of the PtCu nanoparticle tubes after potential cycling but showed much higher catalytic stability (48). As shown in Figure 18A, the ECSAs of PtPdCu, PtCu and Pt/C catalysts decreased proportionally after stability tests, suggested the comparable loss of the active sites. The loss of ECSA for PtPdCu NNs was ~20 %, but the PtPdCu maintained ~90 % of the initial mass activity relative to PtCu and Pt/C in Figures 18B-18D. These results suggested that the increased intrinsic activity compensated the loss of the surface active sites. After stability test, the specific activity was even higher than that before stability test. Thus, the enhanced stability should be attributed to the improved activity per surface active site due to the surface-atomic redistribution-induced change of surface electronic structure (47).

4. Conclusions

We summarized the examples in this chapter in order to demonstrate the electrocatalytic reactions on restructured metal and alloy surfaces. We introduced the geometric and compositional restructurings in different gaseous atmospheres at the metal-gas interfaces and even in electrochemical conditions at the metal-electrolyte interfaces, respectively. We emphasized a strong relationship between structural behaviors of catalysts and the environments, and tried to understand the possible structural evolutions when transferring between solid condition and electrochemical environment. Our arguments reveal that the surface chemistry in electrocatalysis is still in its infancy, but we can incorporate this concept into research on understanding the activity and stability of a catalyst.

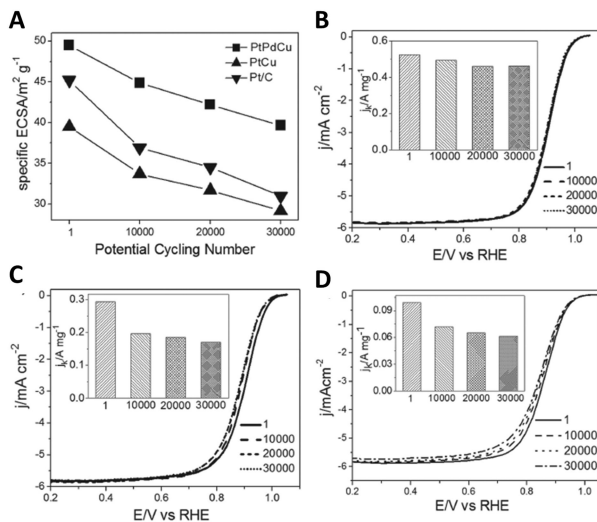


Figure 18. (A) Specific ECSA for PtPdCu nanoparticle tubes, PtCu nanoparticle tubes, and commercial Pt/C catalysts obtained prior to and following different potential cycles during durability testing. (B–D) ORR polarization curves for the PtPdCu nanoparticle tubes (B), PtCu nanoparticle tubes (C), and commercial Pt/C catalysts (D). The mass activity is shown as a function of durability cycling for the PtPdCu nanoparticle tubes, PtCu nanoparticle tubes, and commercial Pt/C catalysts at 0.9 V (versus RHE) in the insets to B, C, and D, respectively. Adapted with permission from reference (83). Copyright 2012 John Wiley and Sons.

In this field, electrochemists have benefitted from the corresponding surface science studies in ultrahigh vacuum and gaseous conditions by *in situ* techniques. In the future, more and more environmental TEM, STM, and spectroscopic analytic techniques have been introduced in an aqueous solution, thus electrochemists can *in situ* investigate the structural and compositional behaviors in electrochemical environments. Meanwhile, the *in situ* advanced spectroscopic analytic techniques can be used to detect the molecular adoptions of reactants, intermediates and products and the interactions with catalyst surfaces. Moreover, the investigations of practical metal-electrolyte interfaces by combining experimental tools and theoretical simulations could provide the basis for progress in electrocatalysis.

Acknowledgments

S. H. Yu acknowledges the funding support from the National Basic Research Program of China (Grant 2010CB934700), the National Natural Science Foundation of China (Grants 91022032, 912271932), the Chinese Academy of Sciences (Grant KJZD-EW-M01-1), the Principal Investigator Award by the National Synchrotron Radiation Laboratory at the University of Science and Technology of China.

References

1. Debe, M. K. *Nature* **2012**, *486*, 43–51.
2. Stamenkovic, V. R.; Fowler, B.; Mun, B. S.; Wang, G.; Ross, P. N.; Lucas, C. A.; Markovic, N. M. *Science* **2007**, *315*, 493–497.
3. Arico, A. S.; Bruce, P.; Scrosati, B.; Tarascon, J. M.; Van Schalkwijk, W. *Nat. Mater.* **2005**, *4*, 366–377.
4. Adzic, R. R.; Zhang, J.; Sasaki, K.; Vukmirovic, M. B.; Shao, M.; Wang, J. X.; Nilekar, A. U.; Mavrikakis, M.; Valerio, J. A.; Uribe, F. *Top. Catal.* **2007**, *46*, 249–262.
5. Zhang, J.; Vukmirovic, M. B.; Xu, Y.; Mavrikakis, M.; Adzic, R. R. *Angew. Chem. Int. Ed.* **2005**, *44*, 2132–2135.
6. Stamenkovic, V. R.; Mun, B. S.; Arenz, M.; Mayrhofer, K. J. J.; Lucas, C. A.; Wang, G.; Ross, P. N.; Markovic, N. M. *Nat. Mater.* **2007**, *6*, 241–247.
7. Strasser, P.; Koh, S.; Anniyev, T.; Greeley, J.; More, K.; Yu, C. F.; Liu, Z. C.; Kaya, S.; Nordlund, D.; Ogasawara, H.; Toney, M. F.; Nilsson, A. *Nat. Chem.* **2010**, *2*, 454–460.
8. Srivastava, R.; Mani, P.; Hahn, N.; Strasser, P. *Angew. Chem., Int. Ed.* **2007**, *46*, 8988–8991.
9. Koh, S.; Strasser, P. *J. Am. Chem. Soc.* **2007**, *129*, 12624–12625.
10. Strasser, P.; Koh, S.; Greeley, J. *Phys. Chem. Chem. Phys.* **2008**, *10*, 3670–3683.
11. Oezaslan, M.; Heggen, M.; Strasser, P. *J. Am. Chem. Soc.* **2012**, *134*, 514–524.
12. Heggen, M.; Oezaslan, M.; Houben, L.; Strasser, P. *J. Phys. Chem. C* **2012**, *116*, 19073–19083.
13. Gan, L.; Heggen, M.; Rudi, S.; Strasser, P. *Nano Lett.* **2012**, *12*, 5423–5430.
14. Cui, C.; Gan, L.; Li, H.-H.; Yu, S.-H.; Heggen, M.; Strasser, P. *Nano Lett.* **2012**, *12*, 5885–5889.
15. Tao, F.; Salmeron, M. *Science* **2011**, *331*, 171–174.
16. Tanaka, K. *Catal. Today* **2010**, *154*, 105–112.
17. Cui, C. H.; Li, H. H.; Liu, X. J.; Gao, M. R.; Yu, S. H. *ACS Catal.* **2012**, *2*, 916–924.
18. Cui, C. H.; Li, H. H.; Yu, S. H. *Chem. Sci.* **2011**, *2*, 1611–1614.
19. Abrasonis, G.; Wintz, S.; Liedke, M. O.; Aksoy Akgul, F.; Krause, M.; Kuepper, K.; Banerjee, D.; Liu, Z.; Gemming, S. *J. Phys. Chem. C* **2012**, *116*, 14401–14407.
20. Cabie, M.; Giorgio, S.; Henry, C. R.; Axet, M. R.; Philippot, K.; Chaudret, B. *J. Phys. Chem. C* **2010**, *114*, 2160–2163.
21. Xia, Y.; Xiong, Y. J.; Lim, B.; Skrabalak, S. E. *Angew. Chem., Int. Ed.* **2009**, *48*, 60–103.
22. Yu, S.-H.; Tao, F.; Liu, J. *ChemCatChem* **2012**, *4*, 1445–1447.
23. Gu, J.; Zhang, Y. W.; Tao, F. *Chem. Soc. Rev.* **2012**, *41*, 8050–8065.
24. Guo, X.; Fu, Q.; Ning, Y.; Wei, M.; Li, M.; Zhang, S.; Jiang, Z.; Bao, X. *J. Am. Chem. Soc.* **2012**, *134*, 12350–12353.
25. Mu, R.; Guo, X.; Fu, Q.; Bao, X. *J. Phys. Chem. C* **2011**, *115*, 20590–20595.
26. Somorjai, G. A.; Van Hove, M. A. *Prog. Surf. Sci.* **1989**, *30*, 201–231.

27. Somorjai, G. A. *Annu. Rev. Phys. Chem.* **1994**, *45*, 721–751.
28. Jeong, H.-C.; Williams, E. D. *Surf. Sci. Rep.* **1999**, *34*, 171–294.
29. Zhdanov, V. P.; Norton, P. R. *Langmuir* **1996**, *12*, 101–108.
30. Sandy, A. R.; Mochrie, S. G. J.; Zehner, D. M.; Grumbl, G.; Huang, K. G.; Gibbs, D. *Phys. Rev. Lett.* **1992**, *68*, 2192.
31. Nolte, P.; Stierle, A.; Jin-Phillipp, N. Y.; Kasper, N.; Schulli, T. U.; Dosch, H. *Science* **2008**, *321*, 1654–1658.
32. Tao, F.; Dag, S.; Wang, L. W.; Liu, Z.; Butcher, D. R.; Salmeron, M.; Somorjai, G. A. *Nano Lett.* **2009**, *9*, 2167–2171.
33. Logan, A. D.; Sharoudi, K.; Datye, A. K. *J. Phys. Chem.* **1991**, *95*, 5568–5574.
34. Hansen, P. L.; Wagner, J. B.; Helveg, S.; Rostrup-Nielsen, J. R.; Clausen, B. S.; Topsoe, H. *Science* **2002**, *295*, 2053–2055.
35. Newton, M. A.; Belver-Coldeira, C.; Martinez-Arias, A.; Fernandez-Garcia, M. *Nat. Mater.* **2007**, *6*, 528–532.
36. Newton, M. A.; Belver-Coldeira, C.; Martinez-Arias, A.; Fernandez-Garcia, M. *Angew. Chem., Int. Ed.* **2007**, *46*, 8629–8631.
37. Urban, K. W. *Science* **2008**, *321*, 506–510.
38. Yoshida, H.; Kuwauchi, Y.; Jinschek, J. R.; Sun, K. J.; Tanaka, S.; Kohyama, M.; Shimada, S.; Haruta, M.; Takeda, S. *Science* **2012**, *335*, 317–319.
39. Tao, F.; Dag, S.; Wang, L. W.; Liu, Z.; Butcher, D. R.; Bluhm, H.; Salmeron, M.; Somorjai, G. A. *Science* **2010**, *327*, 850–853.
40. Batteas, J. D.; Dunphy, J. C.; Somorjai, G. A.; Salmeron, M. *Phys. Rev. Lett.* **1996**, *77*, 534–537.
41. Mu, R. T.; Fu, Q.; Liu, H. Y.; Tan, D. L.; Zhai, R. S.; Bao, X. H. *Appl. Surf. Sci.* **2009**, *255*, 7296–7301.
42. Mu, R.; Fu, Q.; Xu, H.; Zhang, H.; Huang, Y.; Jiang, Z.; Zhang, S.; Tan, D.; Bao, X. *J. Am. Chem. Soc.* **2011**, *133*, 1978–1986.
43. Tao, F.; Grass, M. E.; Zhang, Y. W.; Butcher, D. R.; Renzas, J. R.; Liu, Z.; Chung, J. Y.; Mun, B. S.; Salmeron, M.; Somorjai, G. A. *Science* **2008**, *322*, 932–934.
44. Cui, C. H.; Li, H. H.; Yu, J. W.; Gao, M. R.; Yu, S. H. *Angew. Chem., Int. Ed.* **2010**, *49*, 9149–9152.
45. Cui, C. H.; Yu, J. W.; Li, H. H.; Gao, M. R.; Liang, H. W.; Yu, S. H. *ACS Nano* **2011**, *5*, 4211–4218.
46. Cui, C.-H.; Li, H.-H.; Yu, S.-H. *Chem. Commun.* **2010**, *46*, 940–942.
47. Cui, C.-H.; Li, H.-H.; Cong, H.-P.; Yu, S.-H.; Tao, F. *Chem. Commun.* **2012**, *48*, 12062–12064.
48. Cui, C.-H.; Liu, X.-J.; Li, H.-H.; Gao, M.-R.; Liang, H.-W.; Yao, H.-B.; Yu, S.-H. *ChemCatChem* **2012**, *4*, 1560–1563.
49. Knudsen, J.; Nilekar, A. U.; Vang, R. T.; Schnadt, J.; Kunkes, E. L.; Dumesic, J. A.; Mavrikakis, M.; Besenbacher, F. *J. Am. Chem. Soc.* **2007**, *129*, 6485–6490.
50. Bandarenka, A. S.; Varela, A. S.; Karamad, M.; Calle-Vallejo, F.; Bech, L.; Perez-Alonso, F. J.; Rossmeisl, J.; Stephens, I. E. L.; Chorkendorff, I. *Angew. Chem., Int. Ed.* **2012**, *51*, 11845–11848.

51. Kolb, D. M. *Prog. Surf. Sci.* **1996**, *51*, 109–173.
52. Cervino, R. M.; Arvia, A. J.; Vielstich, W. *Surf. Sci.* **1985**, *154*, 623–628.
53. Cerviño, R. M.; Triaca, W. E.; Arvia, A. J. *J. Electroanal. Chem. Interfacial Electrochem.* **1985**, *182*, 51–60.
54. Arvia, A. J.; Canullo, J. C.; Custodiano, E.; Perdriel, C. L.; Triaca, W. E. *Electrochim. Acta* **1986**, *31*, 1359–1368.
55. Tian, N.; Zhou, Z.-Y.; Sun, S.-G.; Ding, Y.; Wang, Z. L. *Science* **2007**, *316*, 732–735.
56. Tian, N.; Zhou, Z.-Y.; Yu, N.-F.; Wang, L.-Y.; Sun, S.-G. *J. Am. Chem. Soc.* **2010**, *132*, 7580–7581.
57. Lucas, C. A.; Thompson, P.; Cormack, M.; Brownrigg, A.; Fowler, B.; Strmenik, D.; Stamenkovic, V.; Greeley, J.; Menzel, A.; You, H.; Marković, N. M. *J. Am. Chem. Soc.* **2009**, *131*, 7654–7661.
58. Cai, Y.; Ma, C.; Zhu, Y.; Wang, J. X.; Adzic, R. R. *Langmuir* **2011**, *27*, 8540–8547.
59. Snyder, J.; McCue, I.; Livi, K.; Erlebacher, J. *J. Am. Chem. Soc.* **2012**, *134*, 8633–8645.
60. Mayrhofer, K. J. J.; Hartl, K.; Juhart, V.; Arenz, M. *J. Am. Chem. Soc.* **2009**, *131*, 16348–16349.
61. Mayrhofer, K. J. J.; Juhart, V.; Hartl, K.; Hanzlik, M.; Arenz, M. *Angew. Chem., Int. Ed.* **2009**, *48*, 3529–3531.
62. Zhang, J.; Vukmirovic, M. B.; Sasaki, K.; Nilekar, A. U.; Mavrikakis, M.; Adzic, R. R. *J. Am. Chem. Soc.* **2005**, *127*, 12480–12481.
63. Lucas, C. A.; Markovic, N. M.; Ross, P. N. *Phys. Rev. Lett.* **1996**, *77*, 4922–4925.
64. Steele, B. C. H.; Heinzel, A. *Nature* **2001**, *414*, 345–352.
65. Adzic, R. R.; Tripkovic, A. V.; Ogrady, W. E. *Nature* **1982**, *296*, 137–138.
66. van der Vliet, D. F.; Wang, C.; Tripkovic, D.; Strmcnik, D.; Zhang, X. F.; Debe, M. K.; Atanasoski, R. T.; Markovic, N. M.; Stamenkovic, V. R. *Nature Mater.* **2012**, *11*, 1051–1058.
67. Fowler, B.; Lucas, C. A.; Omer, A.; Wang, G.; Stamenkovic, V. R.; Markovic, N. M. *Electrochim. Acta* **2008**, *53*, 6076–6080.
68. Stamenkovic, V.; Mun, B. S.; Mayrhofer, K. J. J.; Ross, P. N.; Markovic, N. M.; Rossmeisl, J.; Greeley, J.; Norskov, J. K. *Angew. Chem., Int. Ed.* **2006**, *45*, 2897–2901.
69. van der Vliet, D. F.; Wang, C.; Li, D.; Paulikas, A. P.; Greeley, J.; Rankin, R. B.; Strmcnik, D.; Tripkovic, D.; Markovic, N. M.; Stamenkovic, V. R. *Angew. Chem., Int. Ed.* **2012**, *51*, 3139–3142.
70. Stephens, I. E. L.; Bondarenko, A. S.; Perez-Alonso, F. J.; Calle-Vallejo, F.; Bech, L.; Johansson, T. P.; Jepsen, A. K.; Frydendal, R.; Knudsen, B. P.; Rossmeisl, J.; Chorkendorff, I. *J. Am. Chem. Soc.* **2011**, *133*, 5485–5491.
71. Chen, S.; Ferreira, P. J.; Sheng, W.; Yabuuchi, N.; Allard, L. F.; Yang, S. H. *J. Am. Chem. Soc.* **2008**, *130*, 13818–13819.
72. Chen, S.; Sheng, W. C.; Yabuuchi, N.; Ferreira, P. J.; Allard, L. F.; Yang, S. H. *J. Phys. Chem. C* **2009**, *113*, 1109–1125.
73. Wang, C.; Chi, M.; Li, D.; Strmcnik, D.; van der Vliet, D.; Wang, G.; Komanicky, V.; Chang, K.-C.; Paulikas, A. P.; Tripkovic, D.; Pearson, J.;

More, K. L.; Markovic, N. M.; Stamenkovic, V. R. *J. Am. Chem. Soc.* **2011**, *133*, 14396–14403.

74. Strasser, P. *Rev. Chem. Eng.* **2009**, *25*, 255–295.

75. Oezaslan, M.; Strasser, P. *J. Power Sources* **2011**, *196*, 5240–5249.

76. Koh, S.; Yu, C.; Mani, P.; Srivastava, R.; Strasser, P. *J. Power Sources* **2007**, *172*, 50–56.

77. Rabis, A.; Rodriguez, P.; Schmidt, T. J. *ACS Catal.* **2012**, *2*, 864–890.

78. Hasche, F.; Oezaslan, M.; Strasser, P. *J. Electrochem. Soc.* **2012**, *159*, B25–B34.

79. Sasaki, K.; Naohara, H.; Choi, Y.; Cai, Y.; Chen, W.-F.; Liu, P.; Adzic, R. R. *Nat. Commun.* **2012**, *3*, 1–5.

80. Perez-Alonso, F. J.; Elkjaer, C. F.; Shim, S. S.; Abrams, B. L.; Stephens, I. E. L.; Chorkendorff, I. *J. Power Sources* **2011**, *196*, 6085–6091.

81. Mayrhofer, K. J. J.; Ashton, S. J.; Meier, J. C.; Wiberg, G. K. H.; Hanzlik, M.; Arenz, M. *J. Power Sources* **2008**, *185*, 734–739.

82. Yu, Y.; Xin, H. L.; Hovden, R.; Wang, D.; Rus, E. D.; Mundy, J. A.; Muller, D. A.; Abruna, H. D. *Nano Lett.* **2012**, *12*, 4417–4423.

83. Li, H.-H.; Cui, C.-H.; Zhao, S.; Yao, H.-B.; Gao, M.-R.; Fan, F.-J.; Yu, S.-H. *Adv. Energy Mater.* **2012**, *2*, 1182–1187.

Chapter 12

Butane Adsorption on Silica Supported MoO_x Clusters Nanofabricated by Electron Beam Lithography

J. Shan,¹ A. Chakradhar,¹ K. Anderson,¹ J. Schmidt,¹ S. Dhuey,² and U. Burghaus*,¹

¹Department of Chemistry and Biochemistry, North Dakota State University, Fargo, North Dakota 58108

²Nanofabrication Facility, Molecular Foundry, LBNL, Berkeley, California 94720

*E-mail: uwe.burghaus@ndsu.edu; Fax: 701.231.8831; URL: www.uweburghaus.us

Electron beam lithography was used to nanofabricate 77 nm Mo clusters supported on silica. Sample morphology and chemical composition were determined by scanning electron microscopy, Auger electron spectroscopy, and X-ray photoelectron spectroscopy. The chemical activity of metallic and oxidic Mo clusters towards butane adsorption was studied by thermal desorption spectroscopy and molecular beam scattering. Whereas butane adsorbs molecularly and non-dissociatively on the metallic clusters, the adsorption probabilities on MoO_x are below the detection limit of uptake experiments (< 0.05).

Introduction

Why Use Electron Beam Lithography in Surface Science and Catalysis?

Industrial catalysts for heterogeneously catalyzed gas-surface reactions typically consist of metallic, sulfidic, or oxidic clusters supported on a porous metal oxide or graphitic support (1). In order to mimic the structure of these systems in surface science, clusters supported on single crystal supports (2–4) and

thin films (5, 6) were studied at ultra-high vacuum (UHV) conditions. The clusters for these so-called model catalysts were mostly obtained by physical vapor deposition (PVD). Although a simple and inexpensive method, the drawback of PVD is an ill-determined morphology of the system. Consequently, a significant number of work hours were spent on just characterizing the growth of clusters on supports. Therefore, today more and more nanofabrication techniques are employed in catalysis and surface science. Among other fabrication techniques, a promising approach is utilizing electron beam lithography (EBL) to nanofabricate model catalysts with an *a priori* knowledge about the cluster morphology. EBL allows for engineering samples with predetermined cluster size, height, rim length, dispersion, and chemical composition (7, 8). In the simplest case, EBL is used to nanofabricate a regular pattern of clusters on a support. These model systems are named model-nano-array catalysts (MNAC) (9). We report here about an example of applying EBL to study model catalysts.

Why Study Molybdenum EBL Model Catalysts?

In prior studies we characterized Au, Cu, and Cu-oxide MNAC (10–17). In addition, one can find studies on Pt and Pd MNAC in the recent catalysis/surface science literature (see e.g. refs. (8, 18–23)). For this current project we looked at Mo MNAC. Mo single crystals have been studied extensively as a hydrodesulfurization (HDS) catalyst (24). Mo clusters and inorganic nanotubes were also recently considered as HDS catalysts (25–27). In regard of the topic of this meeting more interesting, however, is the observation that Mo clusters can decompose small organic molecules such as methanol (MeOH). Mo is very reactive, for example, decomposition of thiophene, CO, and CO₂ was reported (28, 29). A future proposal is using MeOH as an energy carrier to generate, for example, hydrogen for fuel cell vehicles using on-board catalysts and thereby circumventing the hydrogen gas storage problem. MeOH could be synthesized in the first place from hydrogen and CO₂. It has been envisioned to recycle CO₂ from air and to generate hydrogen by water splitting via sunlight, forming a sustainable cycle to fuel vehicles (30). Therefore, it is interesting to characterize the surface chemistry of small organic molecules interacting with Mo-based catalysts. However, rather than going through an additional loop (first synthesizing MeOH then decomposing it), at least in the foreseeable future, it would perhaps be more efficient to decompose methane (natural gas) directly to generate hydrogen. Therefore, in this study we characterized the adsorption of alkanes on Mo clusters utilizing nanotechnology to fabricate the samples.

Our motivation from an applied perspective was summarized in the preceding paragraph. Scientifically, it is interesting to compare the chemical activities of metallic and oxidic clusters. The properties of catalysts can be dramatically altered by surface oxidation (31–33). This gives one a means to tune the catalytic behavior of a given system or to prevent catalyst deactivation. To understand the underlying mechanism, molybdenum and molybdenum oxides have been extensively studied in recent years, as an important example (34–42).

Brief Literature Survey – Molybdenum

The decomposition of MeOH has been investigated on metallic and oxygen-modified Mo single crystals (43). Accordingly, methanol decomposes on clean Mo(100), and desorb without decomposition from oxygen-saturated Mo(100) (43, 44). The saturation coverage for MeOH on Mo(100) decreases with the extent of surface oxidation, similar to Mo(110) (see ref. (40)). These studies suggest that although Mo is quite reactive, complete oxidation makes the Mo surfaces inert.

Most early studies were conducted on various Mo single crystals. More recently, however, supported Mo and Mo oxides clusters were considered (45–47). Berkó, et. al, deposited Mo clusters on TiO₂(110) by PVD (46). The clusters were stable up to annealing temperatures of 900 K, and partial oxidation, probably by lattice oxygen, occurred at 900 - 1050 K. Mo clusters supported on SiO₂ via PVD, were oxidized by annealing at 600 K in 1x10⁻⁶ mbar molecular oxygen (48). In contrast, oxidizing Mo single crystals requires significantly harsher reaction conditions (40, 42). Therefore, one may speculate that real-world catalysts are strongly affected by oxidation, leading to catalyst deactivation. Thus, elucidating mechanistic details also has implications for applications.

Historically, Mo catalysts were used for HDS of coal (48, 49) and raw oil (24), while Mo oxides catalyze oxidations (50, 51).

Literature Survey – Alkanes

Bond activation of alkanes has been studied for decades as a model system, but with a historic focus on metal single crystal surfaces (see, e.g., refs. (52–59)). Only a few surface science projects about the adsorption of alkanes on non-metallic systems have been conducted. For MgO (60), ZnO (61), rutile TiO₂ (62, 63), silica (64, 65), and graphitic systems (66–68), only molecular adsorption is seen. Recently, for an alkaline earth metal oxide single crystal, CaO(100) (ref. (69)), bond activation of butane was evident. Later, bond cleavage on transition metal oxides, PdO thin films, was reported (70). At present, the only metal oxide single crystals/thin films studied in more detail with surface science techniques that promote alkane dissociation are Pd and Ca oxides. Palladium is quite rare and expensive and therefore not the best choice for a sustainable economy. Note that bond activation of alkanes was also present for anatase TiO₂ thin films (, probably the first system studied in this regard (63)), however, here the alkanes decompose entirely, which makes detailed characterization very cumbersome. In addition, the TiO₂ catalyst is poisoned in that process.

Silica is often used as a support for nanostructures, as also in our project, since it is cheap and quite inert. For example, CO basically does not adsorb on silica (11, 71). Physisorption of alkanes on silica, however, was seen before (64, 65). The earlier project was motivated by providing blind experiments for surface science studies on carbon nanotubes (CNTs); here CNTs are typically drop-and-dried on supports (at ambient pressure). Therefore, in the prior study, the silica samples were not UHV cleaned and probably covered with a carbon layer. Graphitic systems adsorb alkanes (67, 72).

In this report, the change in catalytic activity while oxidizing Mo clusters is characterized using an alkane (butane) as the probe molecule. The model catalyst was nanofabricated by electron beam lithography. As a main conclusion: metallic Mo clusters show some catalytic activity, whereas Mo oxides are completely inert towards alkane adsorption. Perhaps amazingly, even the metallic phase does not lead to bond activation in butane, although Mo decomposes a variety of other small organic molecules (43, 44, 73).

Experimental Setup

The measurements were conducted by a home-built, triply differentially pumped molecular beam scattering system (14). The supersonic molecular beam is attached to a scattering chamber, which houses two quadrupole mass spectrometers (QMS). One spectrometer is mounted perpendicular to the beam direction (for beam scattering measurements), and the other one is aligned with the direction of the beam (for time-of-flight (TOF) measurements). A double pass cylindrical mirror analyzer equipped with an electron gun is used for Auger electron spectroscopy (AES). In combination with an X-ray source, this analyzer is also utilized for X-ray photoelectron spectroscopy (XPS). In addition, a home-built metal evaporator, a commercial electron beam metal evaporator, a sputter gun, an atomic hydrogen source, and several leak valves are mounted on the scattering chamber.

In molecular beam and thermal desorption spectroscopy (TDS) experiments, n-butane was dosed with the beam on the sample, in order to suppress sample holder effects. The impact energy of n-butane was varied within $E_i = 0.1 - 1.2$ eV by using a pure beam or by seeding with Helium, combined with a variation of the nozzle temperature in the range of 300 - 750 K. The impact energies of n-butane were measured by TOF. The beam flux was determined to be $F = (2.0 \pm 0.1) \times 10^{13}$ butane molecules $\text{cm}^{-2} \text{ s}^{-1}$ for the pure butane beam. The initial adsorption probability, S_0 , of n-butane on Mo clusters was obtained by King and Wells type uptake experiments (74) directing the beam perpendicular to the surface plane. For a single measurement, the uncertainty in S_0 , as estimated from the signal-to-noise ratio, amounts to ± 0.05 .

The sample could be heated to 1000 K by electron bombardment and cooled down to 85 K by bubbling He gas through a liquid nitrogen containing dewar. The temperature was read by a K-type thermocouple. The reading of the thermocouple was calibrated in situ within ± 5 K by recording the condensation peaks of n-butane in TDS experiments. The heating rate amounted to 1.7 K/s. TDS data were collected with a shielded QMS. In TDS measurements, the distance from the sample to the shield amounts to only ~ 1 mm.

For AES, the electron energy amounts to 2 keV with a modulation voltage of 2 eV. For XPS, the Mg K α line (at 1253.6 eV) was used with pass energy of 50 eV of the electron analyzer. The XPS spectra were referenced with respect to the O 1s line at a binding energy of 532.9 eV (see ref. (75)). Uncertainties reported for AES intensities are based on the signal-to-noise ratio of the spectra.

Scanning electron microscopy (SEM) images of the samples were collected before the UHV experiments at Lawrence Berkeley National Laboratory with a Zeiss Ultra 60 equipped with a field emission gun. In addition, SEM imaging after the experiments was conducted at Brookhaven National Laboratory with a Hitachi S-4800 UHR.

Results and Discussion

Sample Morphology

The EBL sample was nanofabricated at Molecular Foundry (Lawrence Berkeley National Laboratory) (12). Mo clusters with a diameter of $d_s = (77 \pm 2)$ nm were arranged in a hexagonal pattern with a lattice constant of $a_s = 150$ nm, and a height of about 5 nm. A 5 mm by 5 mm area was covered with the Mo clusters on a 10 by 10 mm silica support. Although the Mo cluster size, shape, and height, as well as lattice constant were predetermined in the EBL fabrication, the sample was still inspected by scanning electron microscopy (SEM), see Fig. 1A.

The size distribution of the clusters is depicted in Fig. 1C as a bar diagram and was determined by using a commercial software tool (Pixcavator). The cluster size distribution is with $2/77 = 2.5\%$ narrow (, using the FWHM of the Gaussian fit shown in Fig. 1C as a solid line). The Mo coverage (total Mo area vs. support area) is calculated as 0.25 ML. (A monolayer, 1 ML, corresponds to a completely covered surface.) Fig. 1B depicts SEM images collected after the UHV experiments. Evidently the sample's morphology was conserved (cf., Fig. 1A and 1B). The cluster size distribution (shown in Fig. 1D) was also unaltered, i.e., significant sintering was absent. In order to better compare the cluster size distributions, Fig. 1C depicts the Gaussian fits together. A slight broadening of the distribution was evident for the used model catalyst. This may indicate the capture of small metal residuals from the lift-off process (or along the clusters rim) by the larger Mo clusters, cause by the sample annealing. Given the size of the clusters, a relaxation of grain boundaries appears unlikely.

Sample Cleaning – AES and XPS Characterization

Cleaning EBL samples without destroying the morphology or irreversibly changing the chemical composition is non-trivial (76, 77) and therefore described in more detail. Mo single crystals were usually cleaned by a thermal treatment at rather high temperature, e.g., annealing at ~ 1700 K under O_2 atmosphere followed by flashing to 2300 K was used (34–42). Unfortunately, this standard cleaning procedure is not applicable to EBL samples. Such a high temperature would likely result in cluster sintering, since the Tamman temperature of Mo may amount to only ~ 1450 K, assuming that it equals half of the bulk melting temperature. Note that, sintering of Mo clusters on TiO_2 and SiO_2 supports, respectively, has been observed experimentally already upon annealing at ~ 1050 K (refs. (46, 78)). Therefore, the Mo EBL sample studied here was initially cleaned by mild room temperature sputtering/annealing cycles (one minute each, sample current 2 μ A),

followed by annealing at 700 K in oxygen (1×10^{-8} mbar), and a flash to only 750 K.

During this cleaning procedure, the sample was inspected regularly by AES (Fig. 2A). The sputter cycles were continued up to a C/Mo AES peak ratio of 0.2. Thus, the C impurities did act as a buffer layer protecting the Mo clusters. A similar procedure was used before while cleaning thin film samples transferred through air (63). Afterwards, we switched from a “physical cleaning” to a “chemical treatment”: cycles of oxygen annealing at 700 K for 10 minutes were applied. Finally carbon containing impurities were below the detection limit of the AES system (Fig. 2B). Unfortunately, this procedure will also likely oxidize the Mo clusters (48). Again, the high-temperature (1050 K) (79) annealing used to reduce Mo single crystals does not work for EBL clusters. Therefore, as a final cleaning step, the EBL sample was annealed in a flux of atomic hydrogen ($p(H_2) = 1 \times 10^{-7}$ mbar, $T_s = 750$ K, for two hours). According to prior work in our group, this will successfully reduce the oxides (48, 80). Note that during the whole cleaning procedure, the Mo/Si AES intensity ratio remained constant and sample morphology was conserved (Fig. 1).

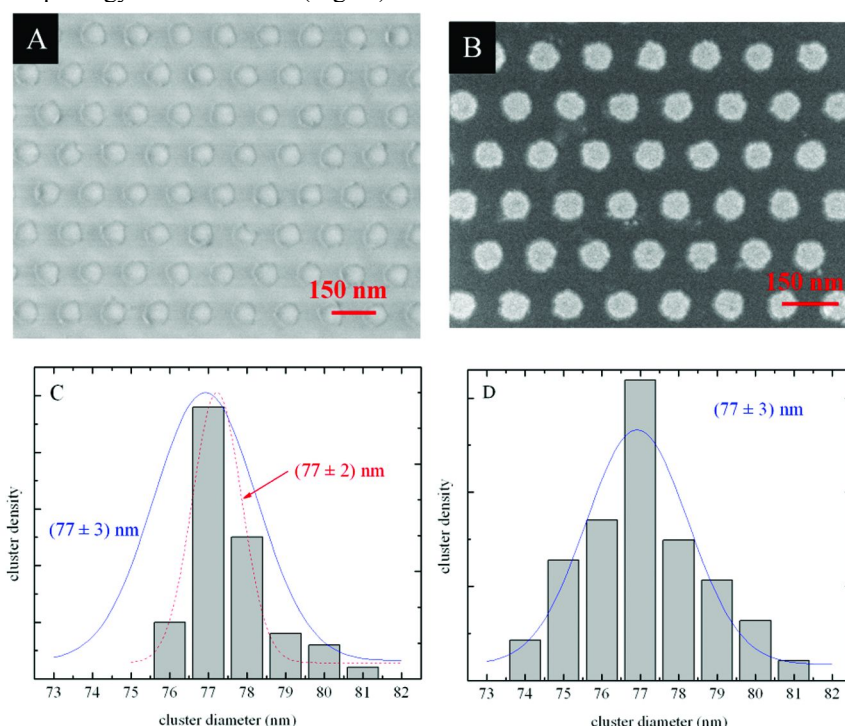


Figure 1. SEM images of the Mo EBL clusters supported on silica (A) before and (B) after the UHV experiments. The corresponding cluster size distributions are given in panel (C) and (D). Depicted is the cluster number (normalized with respect of the total cluster number) vs. the clusters' diameter. The lines are Gaussian fits of the cluster size distributions before (red dotted line) and after (blue solid line) the UHV experiments.

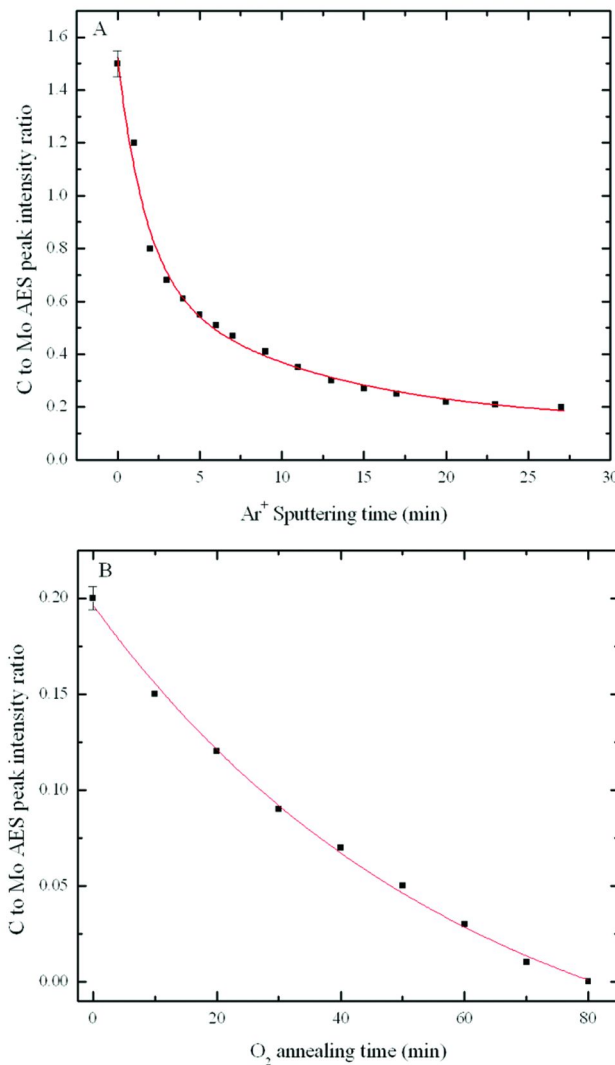


Figure 2. Cleaning procedure of the Mo EBL sample. (A) cleaning with Ar⁺ sputtering, (B) cleaning with O₂ annealing.

Fig. 3A depicts examples of AES survey scans of the as received and cleaned Mo EBL sample, respectively. Besides Si and O AES peaks from the support as well as Mo AES features (81), no other structures were evident for the cleaned sample. Similarly, a XPS survey scan of the cleaned Mo EBL sample is given in Fig. 3B. The spectra confirm that no carbon or other impurities are present on the cleaned surface. The XPS peak positions of Si, O, and Mo agree with reference data (75). The inset depicts the silica XPS 2p region. For fully oxidized silica only one peak is present, whereas partially reduced silica shows two peaks (75). Thus,

the cleaning procedure did not reduce the silica support (80, 82). This fact may be important, since silica is non-reactive, but silicon is highly reactive (64, 65).

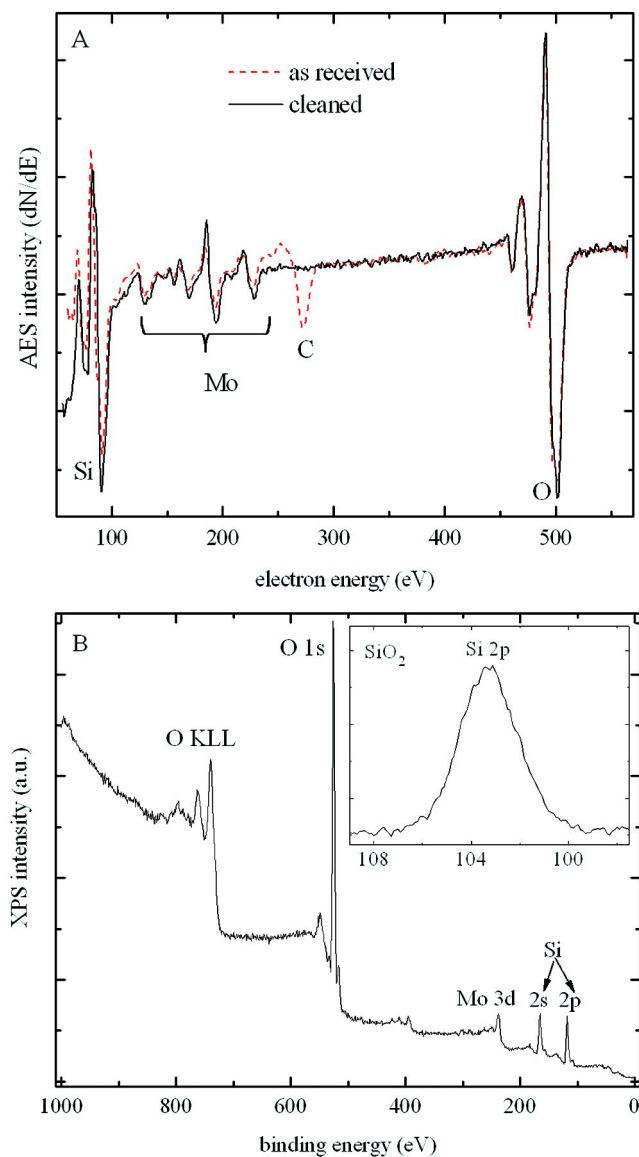


Figure 3. (A) AES spectra of the Mo EBL sample before cleaning (dashed line) and after cleaning (solid line). (B) XPS spectra of the Mo EBL sample after cleaning. The inset shows the XPS Si 2p region.

Both metallic and oxidic Mo clusters were considered in this study. Unfortunately, metallic and oxidic molybdenum have very similar XPS signatures (42, 83, 84). However, according to refs. (34, 40–42, 48, 79, 83) oxygen and hydrogen annealing, respectively, can be used to change the oxidation state of molybdenum. Therefore, Mo oxides were reduced in a flux of atomic hydrogen ($T_s = 750$ K, $t = 2$ h), while metallic clusters were oxidized by annealing in an oxygen ambient ($p = 1 \times 10^{-6}$ mbar, 750 K, 20 min).

Adsorption Dynamics - Typical Adsorption Transients

The adsorption dynamics of n-butane on the supported Mo clusters were characterized by molecular beam scattering. The solid lines in Fig. 4 show typical adsorption transient on Mo clusters, while the dashed lines depict results for oxidic clusters. Results of several experiments at identical measuring conditions are shown in order to illustrate the reproducibility of the measurements. Displayed is the exposure time (t), vs. the partial pressure of n-butane in the scattering chamber. At $t = 0$ s, a beam flag is opened and n-butane molecules start to strike the surface. If n-butane molecules do not adsorb on the surface, the transient resembles only a step function due to the increase in the equilibrium pressure. However, if the probe molecules adsorb, the alkane's partial pressure initially increases fast, but approaches the saturation level slowly hereafter. Once the surface is saturated, all butane molecules will be backscattered since thermal desorption and butane condensation can be neglected at the chosen adsorption temperature ($T_s = 115$ K). Saturation was reached for $t > 10$ s. The area above the transient and below the saturation level equals the number of adsorbed molecules. Therefore, it is evident from Fig. 4 that the alkane does not build up any significant concentration on the silica supported oxidic clusters, but does adsorb on supported metallic Mo clusters.

From the known geometrical size of the Mo clusters and the lattice constant of the array catalyst (see Fig. 1), the Mo coverage can be calculated as 0.25 ML. Since the surface density of a typical Mo surface amounts to 1.4×10^{15} atom cm^{-2} (ref. (85)), the atomic density of the Mo clusters supported on SiO_2 reads 3.5×10^{14} atom cm^{-2} . By integrating the transients shown in Fig. 4, we conclude that the total butane molecular density on the Mo clusters at saturation amounts to 1.0×10^{14} molecule cm^{-2} . In other words, at saturation coverage the ratio of butane molecules to Mo atoms is only about 0.3, i.e., approximately 3.5 Mo atom can accommodate one butane molecule. That result appears reasonable considering the size of n-butane (5.5 Å).

Furthermore, the adsorption probability, $S(t)$, of n-butane can be obtained from these adsorption transients (86). In Fig. 4, the curves are normalized such that $1 - S(t)$ vs. t is depicted. Thus, the adsorption probability can directly be read from these graphs. For example, the initial adsorption probability, S_0 , of pure n-butane can be determined at $t = 0$.

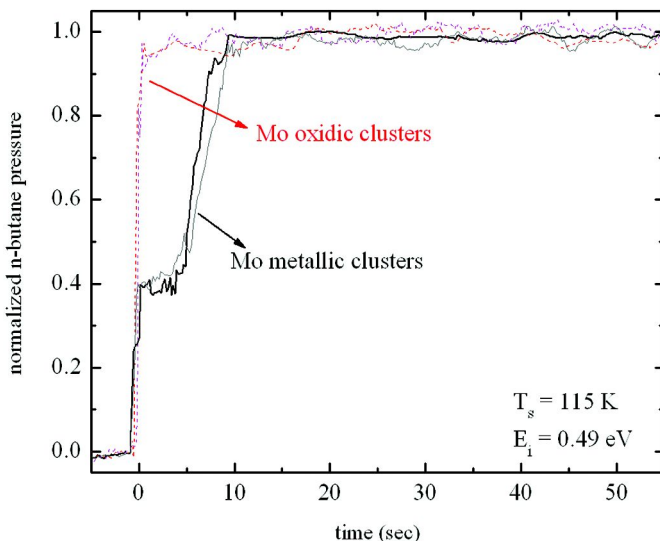


Figure 4. Typical adsorption transients of n-butane on metallic Mo clusters (solid lines), and on oxidic Mo clusters (dotted lines).

Energy Dependence of the Initial Adsorption Probability of n-Butane

In Fig. 5, S_0 on metallic Mo clusters is shown as a function of impact energy, E_i . The sample temperature was kept constant at 115 K. It is evident that S_0 decreases with increasing E_i . This trend reflects the decreasing efficiency of gas-to-surface energy transfer with increasing E_i . In simple terms, the larger E_i , the larger the speed of the molecules when impinging onto the surface and the smaller the interaction time with the surface. Therefore, the efficiency of the energy transfer processes of n-butane molecules decreases with E_i , hence S_0 decreases with E_i . This observation is consistent with non-activated and molecular adsorption of n-butane on metallic Mo clusters as is the absence of carbon after several adsorption/desorption cycles, evident from the AES/XPS experiments.

Kinetics of n-Butane on Mo Clusters

Fig. 6 summarizes butane TDS data on metallic Mo clusters (solid lines), as well as on oxidic Mo clusters (dashed line). Pure butane was dosed with the molecular beam system at $T_s = 90$ K. Therefore, the exposure, χ , is given as an exposure time in sec. We used exposures up to 30 sec for TDS. With the measured beam flux of $F = (2.0 \pm 0.1) \times 10^{13}$ butane molecules $\text{cm}^{-2} \text{ s}^{-1}$ that translates into a maximum exposure of ~ 1 Langmuir.

For the oxidized Mo clusters, no desorption of butane is seen. These data also suggest that the adsorption of n-butane from the silica support is below the detection level. This is consistent with the adsorption transient of butane on the oxidized sample (Fig. 4).

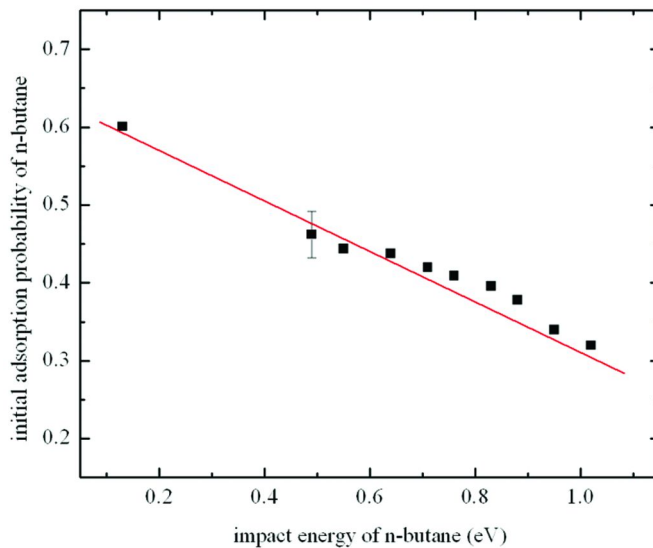


Figure 5. Initial adsorption probability of *n*-butane on metallic Mo clusters as a function of impact energy.

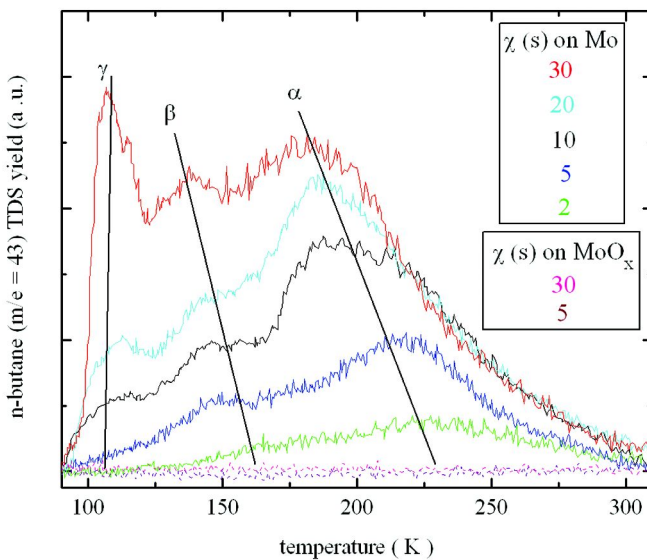


Figure 6. TDS of *n*-butane on metallic Mo clusters (solid lines), and on oxidic Mo clusters (dotted lines).

For metallic clusters, at the smallest exposure of $\chi = 2$ s, two TDS features are evident, one centered at 225 K (α peak), and the other centered at 160 K (β peak). With increasing χ , both features shift to lower temperatures. At the largest

exposure $\chi = 30$ s, the α peak shifts to 190 K while the β peak shift to 140 K. For $\chi = 10$ s, a new feature appears, first as a shoulder at 105 K. This shoulder develops into a distinct peak at $\chi = 30$ s. The low temperature onsets of the γ peaks line up, which is characteristic of condensed alkanes. Note also that, according to the beam scattering experiments (Fig. 4), the surface saturates for exposures of about 10 sec. Indeed, at about that exposure the γ peak develops in TDS.

The α and β peaks are related to the desorption of butane from the metallic Mo clusters; we assign these features to different types of adsorption sites. For example, the higher temperature structure is related to desorption from defect sites (such as the rim of the clusters), while the low temperature feature to pristine sites (terrace sites) (80, 87). The shift of α and β peak positions with butane exposure are likely due to repulsive lateral interactions among butane molecules. Due to the overlapping peaks, the magnitude of the peak shift is difficult to quantify. Repulsive interactions among alkanes have been seen before and were described by polarization effects induced by the support (88).

Fig. 7 shows multi-mass TDS data of n-butane on metallic Mo clusters (red bar), as well as the mass spectra of gaseous butane (gray bar), both detected with the same mass spectrometer. In the multi-mass TDS experiments, a constant exposure of $\chi = 5$ s was used. The peak intensities in the TDS spectra are normalized with respect to the intensity at $m/e = 43$ (where the strongest signal of n-butane is detected). Fig. 7 clearly shows that the mass scans for gaseous butane match those of the multi-mass TDS data. This indicates that only a molecular adsorption pathway is present. That conclusion is consistent with the absence of carbon in AES/XPS after TDS experiments, as well as the energy dependence of the initial adsorption probability.

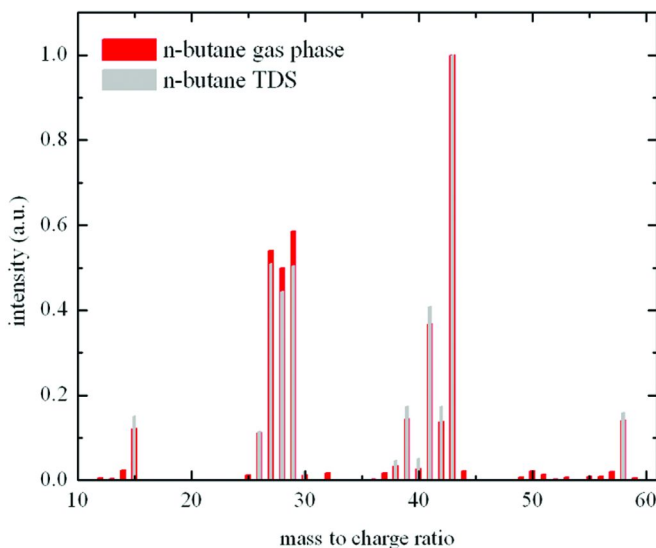


Figure 7. Multi-mass TDS of n-butane on metallic Mo clusters comparing with a mass scan of gaseous n-butane.

Conclusions

According to the molecular beam scattering data, n-butane adsorbs on silica supported Mo clusters with initial adsorption probabilities, S_0 , within the range of $S_0 = 0.60 - 0.32$, depending on impact energy, whereas on oxidic clusters S_0 was below the detection limit of $S_0 = 0.05$. Thus, the metallic clusters are reactive, but the oxidic clusters are not. Based on XPS and AES data, the adsorption is molecular, i.e., in both cases bond activation of the alkane was absent. TDS results consistently confirm adsorption on the silica supported Mo clusters. In contrast, even large exposures on the oxidic cluster sample did not allow for detecting n-butane desorption in TDS. Note that the silica support was UHV cleaned and the alkane was dosed onto the surface using a collimated molecular beam scattering system.

Similar results have been reported before: metallic Mo surfaces decompose efficiently methanol (34, 40) and thiophene (48), whereas oxidic Mo surfaces are rather inert. The crystal structure was invoked as a plausible explanation (89). For example, MoO_3 has an orthorhombic layered structure, consisting of MoO_6 octahedra, forming the basal plane of MoO_3 single crystals. That surface is oxygen terminated and therefore expected to be rather inert. The oxide formation would be one mechanism for catalyst deactivation. However, it perhaps remains surprising that even the metallic Mo clusters are catalytically not very active, since only molecular adsorption of the alkane was evident.

The advantage of using EBL samples for this project, in particular, is the *a priori* knowledge for samples' morphology. Thus, a time consuming morphology characterization is unnessesary. A detailed discussion of this approach in general can be found in ref. (9). In ref. (14, 15), the comparison of different cluster sizes, for example, allows to identify the clusters' rim as the active site of surface processes using simple kinetics techniques.

Acknowledgments

Discussions with Stephano Cabrini at Molecular Foundry are acknowledged and SEM images were collected by Ming Lu at Brookhaven national labs. Financial support was provided by a NSF-CAREER award (CHE-0743932).

References

1. Thomas, J. M.; Thomas, W. J. *Principles and Practice of Heterogeneous Catalysis*; VCH: 2005.
2. Choudhary, T. V.; Goodman, D. W. *Top. Catal.* **2002**, *21*, 25.
3. Goodman, D. W. *J. Chem. Phys.* **1996**, *100*, 13090.
4. Henry, C. R. *Surf. Sci. Rep.* **1998**, *31*, 235.
5. Freund, H. J. *Angew. Chem.* **1997**, *109*, 444.
6. Freund, H. J. *Surf. Sci.* **2007**, *601*, 1438–1442.
7. Avoyan, A.; Rupprechter, G.; Eppler, A. S.; Somorjai, G. A. *Top. Catal.* **2000**, *10*, 107–113.

8. Johanek, V.; Laurin, M.; Grant, A. W.; Kasemo, B.; Henry, C. R.; Libuda, J. *Science* **2004**, *304*, 1639.
9. Burghaus, U. In *Catalysis Series*; Spivey, J. J., Ed.; Royal Society of Chemistry: Cambridge, UK, in press.
10. Kadossov, E.; Justin, J.; Lu, M.; Rosenmann, D.; Ocola, L. E.; Cabrini, S.; Burghaus, U. *Chem. Phys. Lett.* **2009**, *483*, 250–253.
11. Kadossov, E.; Cabrini, S.; Burghaus, U. *J. Mol. Catal. A: Chem.* **2010**, *321*, 101–109.
12. Komarneni, M.; Shan, J.; Chakradhar, A.; Kadossov, E.; Cabrini, S.; Burghaus, U. *J. Phys. Chem. C* **2011**, *116*, 5792–5801.
13. Shan, J.; Komarneni, M.; Burghaus, U. *Chem. Phys. Lett.* **2011**, *517*, 59–61.
14. Chakradhar, A.; Shan, J.; Komarneni, M. R.; Lu, M.; Burghaus, U. *Chem. Phys. Lett.* **2012**, *544*, 70–72.
15. Shan, J.; Chakradhar, A.; Komarneni, M.; Burghaus, U. *J. Chem. Phys. C* **2012**, *116*, 18930–18936.
16. Kadossov, E.; Burghaus, U. *Catal. Lett.* **2010**, *134*, 228–232.
17. Shan, J.; Chakradhar, A.; Komarneni, M.; Kadossov, E.; Schmidt, J.; Burghaus, U.; Rosenmann, D.; Ocola, L. E.; Dhuey, S.; Cabrini, S. *Am. Chem. Soc., Div. Fuel Chem.* **2012**, in press.
18. Grunes, J.; Zhu, J.; Anderson, E. A.; Somorjai, G. A. *J. Phys. Chem. B* **2002**, *106*, 11463.
19. Grunes, J.; Zhu, J.; Yang, M.; Somorjai, G. A. *Catal. Lett.* **2003**, *4*, 157.
20. Jacobs, P. W.; Wind, S. J.; Ribeiro, F. H.; Somorjai, G. A. *Surf. Sci.* **1997**, *372*, L249.
21. Johanek, V.; Laurin, M.; Hoffmann, J.; Schauermann, S.; Grant, A. W.; Kasemo, B.; Libuda, J.; Freund, H. J. *Surf. Sci.* **2004**, *561*, L218–L224.
22. Laurin, M.; Johanek, V.; Grant, A. W.; Kasemo, B.; Libuda, J.; Freund, H. J. *J. Chem. Phys.* **2005**, *122*, 084713.
23. Laurin, M.; Johanek, V.; Grant, A. W.; Kasemo, B.; Libuda, J.; Freund, H. J. *J. Chem. Phys.* **2005**, *123*, 054701.
24. Topsoe, H.; Clausen, B. S.; Massoth, F. E. *J. Catal.* **1996**, *163*, 409.
25. Lauritzen, J. V.; Nyberg, M.; Vang, R. T.; Bollinger, M. V.; Clausen, B. S.; Topsoe, H.; Jacobsen, K. W.; Laegsgaard, E.; Norskov, J. K.; Besenbacher, F. *Nanotechnology* **2003**, *14*, 385–389.
26. Burghaus, U. Gas-carbon nanotubes interactions: a review of ultra-high vacuum surface science studies on CNTs. *Carbon nanotubes - Research Trends*; Nova Science: New York, 2009.
27. Burghaus, U.; Zak, A.; Rosentsveig, R. *Isr. J. Chem.* **2010**, *50*, 449–452.
28. Lopez-Carreno, L. D.; Heras, J. M.; Viscido, L. *Surf. Sci.* **1997**, *377*–379, 615.
29. Jaworowski, A. J.; Smedh, M.; Borg, M.; Sandell, A.; Beutler, A.; Sorensen, S. L.; Lundgren, E.; Andersen, J. N. *Surf. Sci.* **2001**, *492*, 185–194.
30. Olah, G. A.; Goeppert, A.; Prakash, G. K. S., 2003, *Beyond oil and gas: the methanol economy*, Wiley-VCH, 2003, ISBN 0-471-41782-3.
31. Evans, U. R. *The corrosion and oxidation of metals: scientific principles and practical applications*; St. Martin's Press: 1960.

32. Bond, G. C. *Heterogeneous catalysis: principles and applications*; Oxford University Press: 1974.
33. Kadosssov, E.; Goering, J.; Burghaus, U. *Surf. Sci.* **2008**, *602*, 811–818.
34. Miles, S. L.; Bernasek, S. L.; Gland, J. L. *J. Phys. Chem.* **1983**, *87* (9), 1626–1630.
35. Sierka, M.; Todorova, T. K.; Sauer, J.; Kaya, S.; Stacchiola, D.; Weissenrieder, J.; Shaikhutdinov, S.; Freund, H. J. *J. Chem. Phys.* **2007**, *126* (23), 234710.
36. Ko, E. I.; Madix, R. J. *Surf. Sci.* **1981**, *112* (3), 373–385.
37. Deiner, L. J.; Kang, D. H.; Friend, C. A. *J. Phys. Chem. B* **2005**, *109* (26), 12826–12831.
38. Deiner, L. J.; Kang, D. H.; Friend, C. M. *J. Phys. Chem. B* **2005**, *109* (16), 8085–8090.
39. Deiner, L. J.; Chan, A. S. Y.; Sheehy, M. A.; Friend, C. M. *Surf. Sci.* **2004**, *555* (1–3), L127–L132.
40. Street, S. C.; Liu, G.; Goodman, D. W. *Surf. Sci.* **1997**, *385* (2–3), L971–L977.
41. Sasaki, T.; Goto, Y.; Tero, R.; Fukui, K.; Iwasawa, Y. *Surf. Sci.* **2002**, *502*, 136–143.
42. Kaya, S.; Weissenrieder, J.; Stacchiola, D.; Todorova, T. K.; Sierka, M.; Sauer, J.; Shaikhutdinov, S.; Freund, H. J. *Surf. Sci.* **2008**, *602* (21), 3338–3342.
43. Miles, S. L.; Bernasek, S. L.; Gland, J. L. *J. Phys. Chem.* **1983**, *87*, 1626–30.
44. Ko, E. I.; Madix, R. J. *Surf. Sci.* **1981**, *109*, 221.
45. Chun, W. J.; Asakura, K.; Iwasawa, Y. *Chem. Phys. Lett.* **1998**, *288* (5–6), 868–872.
46. Berko, A.; Magony, A.; Szoko, J. *Langmuir* **2005**, *21* (10), 4562–4570.
47. Kitchin, J. R.; Barteau, M. A.; Chen, J. G. G. *Surf. Sci.* **2003**, *526* (3), 323–331.
48. Komarneni, M.; Kadosssov, E.; Justin, J.; Lu, M.; Burghaus, U. *Surf. Sci.* **2010**, *604* (13–14), 1221–1229.
49. Kibsgaard, J.; Lauritsen, J. V.; Laegsgaard, E.; Clausen, B. S.; Topsoe, H.; Besenbacher, F. *J. Am. Chem. Soc.* **2006**, *128* (42), 13950–13958.
50. Ozkan, U.; Schrader, G. L. *J. Catal.* **1985**, *95* (1), 120–136.
51. Tong, Y. D.; Lunsford, J. H. *J. Am. Chem. Soc.* **1991**, *113* (13), 4741–4746.
52. Mullins, C. B.; Weinberg, W. H. *Springer Series in Surface Science*; Springer GmbH: 1994; Vol. 34, Ch. 7.
53. Weinberg, W. H.; Sun, Y. K. *Science* **1991**, *253*, 542.
54. Weaver, J. F.; Carlsson, A. F.; Madix, R. J. *Surf. Sci. Rep.* **2003**, *50*, 107–199.
55. Zaera, F. *Catal. Today* **2003**, *81*, 149–157.
56. Juurlink, L. B. F.; Killelea, D. R.; Utz, A. L. *Prog. Surf. Sci.* **2009**, *84*, 69.
57. Wodtke, A. M.; Matsiev, D.; Auerbach, D. J. *Prog. Surf. Sci.* **2008**, *83*.
58. Ding, J.; Burghaus, U.; Weinberg, W. H. *Surf. Sci.* **2000**, *446*, 46.
59. Larsen, J. H.; Chorkendorff, I. *Surf. Sci. Rep.* **1999**, *35*, 163–222.
60. Tait, S. L.; Dohnalek, Z.; Campbell, C. T.; Kay, B. D. *J. Chem. Phys.* **2005**, *122*, 164708.
61. Wang, J.; Hokkanen, B.; Burghaus, U. *Surf. Sci.* **2005**, *577*, 158–166.

62. Hokkanen, B.; Funk, S.; Burghaus, U.; Ghicov, A.; Schmuki, P. *Surf. Sci.* **2007**, *601*, 4620–4628.
63. Goering, J.; Kadossov, E.; Burghaus, U.; Yu, Z. Q.; Thevuthasan, S.; Saraf, L. V. *Catal. Lett.* **2007**, *116*, 9.
64. Funk, S.; Nurkic, T.; Burghaus, U. *Appl. Surf. Sci.* **2007**, *253*, 4860–4865.
65. Funk, S.; Goering, J.; Burghaus, U. *Appl. Surf. Sci.* **2008**, *254*, 5271–5275.
66. Paserba, K. R.; Gellman, A. *J. Phys. Rev. Lett.* **2001**, *86*, 4338.
67. Kadossov, E.; Goering, J.; Burghaus, U. *Surf. Sci.* **2007**, *601*, 3421–3425.
68. Funk, S.; Hokkanen, B.; Nurkig, T.; Burghaus, U.; White, B.; O'Brien, S.; Turro, N. *J. Phys. Chem. C* **2007**, *111*, 8043–8049.
69. Chakradhar, A.; Liu, Y.; Schmidt, J.; Kadossov, E.; Burghaus, U. *Surf. Sci.* **2011**, *605*, 1534–1540.
70. Weaver, J. F.; Devarajan, S. P.; Hakanoglu, C. *J. Phys. Chem. C* **2009**, *113*, 9773–9782.
71. Gross, E.; Asscher, M.; Lundwall, M.; Goodman, D. W. *J. Phys. Chem. C* **2007**, *111*, 16197–16201.
72. Gellman, A. J.; Paserba, K. P. *J. Phys. Chem. B* **2002**, *106* (51), 13231.
73. Komarneni, M.; Kadossov, E.; Justin, J.; Ming, M.; Burghaus, U. *Surf. Sci.* **2010**, *604*, 1221–1229.
74. King, D. A.; Wells, M. G. *Surf. Sci.* **1972**, *29*, 454.
75. Moulder, J. F.; Stickle, W. F.; Sobol, P. E.; Bomben, K. D. *Handbook of x-ray photoelectron spectroscopy*; Perkin-Elmer-Corp: USA, 1980.
76. Ribeiro, F. H.; Somorjai, G. A. *Recl. Trav. Chim. Pays-Bas* **1994**, *113* (10), 419–422.
77. Wong, K.; Johansson, S.; Kasemo, B. *Faraday Discuss.* **1996**, *105*, 237–246.
78. Wang, F. P.; Cheng, L. S.; Wang, P. X.; Lu, K. Q. *Thin Solid Films* **2000**, *379* (1-2), 308–312.
79. Kim, B. S.; K., E. Y.; Jeon, H. S.; Lee, H. I.; Lee, J. C. *Mater. Trans.* **2008**, *49* (9), 2147–2152.
80. Komarneni, M.; Shan, J.; Chakradhar, A.; Kadossov, E.; Cabrini, S.; Burghaus, U. *J. Phys. Chem. C* **2012**, *116* (9), 5792–5801.
81. Hedberg, C. L. *Handbook of Auger Electron Spectroscopy*; Physical Electronics, Inc: USA, 1970.
82. Komarneni, M.; Shan, J.; Burghaus, U. *J. Phys. Chem. C* **2011**, *115* (33), 16590–16597.
83. Schroeder, T.; Zegenhagen, J.; Magg, N.; Immaraporn, B.; Freund, H. J. *Surf. Sci.* **2004**, *552* (1–3), 85–97.
84. Marin-Flores, O.; Scudiero, L.; Ha, S. *Surf. Sci.* **2009**, *603* (15), 2327–2332.
85. Zhang, X.; Linsebigler, A.; Heiz, U.; Yates, J. T. *J. Phys. Chem.* **1993**, *97*, 5074–5079.
86. King, D. A.; Wells, M. G. *Surf. Sci.* **1972**, *29* (2), 454.
87. Chakradhar, A.; S., J.; Komarneni, M.; Ming, L.; Burghaus, U. *Chem. Phys. Lett.* **2012**, in press.
88. Kadossov, E.; Burghaus, U. *Surf. Sci.* **2009**, *603*, 2494–2501.
89. Henrich, V. E.; Cox, P. A. *The Surface Science of Metal Oxides*; Cambridge University Press: New York, USA, 1994.

Subject Index

A

- Advanced lithium-ion batteries, 55
- AFM. *See* Atomic Force Microscope (AFM)
- Atomic force microscope (AFM), 26

B

- Band excitation (BE) method, 44
- Butane adsorption, silica supported MoO_x clusters
 - adsorption dynamics, typical adsorption transients, 303
 - brief literature survey
 - alkanes, 297
 - molybdenum, 297
 - conclusions, 307
 - experimental setup, 298
 - initial adsorption probability of n-butane, energy dependence, 304, 305*f*
 - kinetics of n-butane on Mo clusters, 304
 - metallic and oxidic Mo clusters
 - adsorption transients of n-butane, 304*f*
 - TDS of n-butane, 305*f*
- Mo EBL sample
 - AES and XPS spectra, 302*f*
 - before and after UHV experiments, 300*f*
 - cleaning procedure, 301*f*
 - multi-mass TDS of n-butane, 306*f*
 - sample cleaning, AES and XPS
 - characterization, 299
 - sample morphology, 299
 - study molybdenum EBL model catalysts, 296
 - surface science and catalysis, use of electron beam lithography, 295

C

- Carbon/metal oxide composite, 128
- CNT alignment in electrode, 130/*f*
- CNT/metal oxide composite flexible pseudo-supercapacitors, 129
- conductive wrapping method, 133
- graphene/CNT/MO composite flexible pseudo-capacitors, 134

- graphene/MO composite flexible pseudo-capacitors, 132
- MO nanowires, unique properties, 131
- RGO/MnO₂ hybrid papers, 132
- SWCNT/RuO₂ hybrid films, 131
- Contact-resonance AFM (CR-AFM), 46
- Co₃O₄/C composite nanofibers, 55
 - conclusion, 65
 - Coulombic efficiencies, 64*f*
 - cycling performance, 63*f*
 - discharge process, 61
 - electrochemical performance, 60
 - experimental, 56
 - fiber diameter distributions, 60*f*
 - galvanostatic charge-discharge curves, 62*f*
 - introduction, 56
 - morphology, 57
 - SEM images, 58*f*
 - TEM images, 59*f*
 - XRD pattern, 62*f*
- CR-AFM. *See* Contact-resonance AFM (CR-AFM)

D

- Density of states (DOS), 175
- DOS. *See* Density of states (DOS)

E

- Electrodeposited tin nanoarchitectures, 8
 - tin and tin oxides morphologies, 8
 - tin nanowires electrodeposition, different surfaces, 10*f*

F

- Flexible dye-sensitized solar cells (DSCs)
 - conclusion, 166
 - deposition techniques
 - dip coating, 151, 152*f*
 - doctor blading, 149
 - electrophoretic deposition (EPD), 150
 - Erichsen Coatmaster 509 MC-I, 151*f*
 - particle electrophoresis cell, 151*f*
 - screen printing, 152, 153*f*

spin-coating process, 149, 150/*f*
different dyes, chemical formula, 147/*s*
introduction, 144
mesoporous TiO_2 film, preparation, 146
nanoparticulate TiO_2 porous film,
 compression, 155/*f*
nanoporous semi-conducting films, 143
photoanodes, 146
photocurrent–voltage curve, 168/*f*
photoelectrode sintered at low
 temperature, 156/*t*
post treatment methods
 compression method, 154
 hydrothermal necking, 159
 hydrothermal treatment of films,
 experimental set-up, 159/*f*
 low temperature sintering, 153
 microwave irradiation process, 160
 spraying, 163
 UV light irradiation method, 161
 UV-assisted chemical vapor
 deposition method (CVD), 160
 UV-treatment route, 163/*f*
 vacuum cold spraying (VCS) system,
 164/*f*
PV cells, sweep curve, 147/*f*
schematic representation, 145/*f*
summary, 168
theory of photovoltaic device
 characterization, 147
 efficiency (η), 148
 fill factor (FF), 148
 maximum power (P_{max}), 148
 the open-circuit voltage (V_{oc}), 148
 short-circuit current (I_{sc}), 148
 TiO_2 photoelectrodes prepared
 compression method, 158/*t*
 UV light irradiation method, 162/*t*
 TiO_2 -coated ITO-PEN substrate, 167/*f*
 ZnO and SnO_2 photoanodes, low
 temperature preparation, 164
 ZnO photoelectrodes, 165/*t*
Flexible supercapacitors (SCs)
 all-solid-state SC, 104
 as-deposited SWCNT networks and thin
 film SC, 106/*f*
 assembling roll-designed SC, 108/*f*
 carbon materials-based flexible EDLCs,
 103
 carbon/polymer composite flexible
 pseudo-capacitors, 122
 CNT Bucky paper, 124
 CNT-conductive paper, 104
 CNT-graphene composites, 121
 CNTs/conductive polymer flexible
 pseudo-capacitors, 123
 conductive rGO films, 115
 constructing alternately multilayered
 GO/AuNP films, 119/*f*
 conventional SC, 102
 DNA-dispersed double-walled CNTs
 (DWCNTs), 104
 flexible pseudo-capacitors,
 graphene/CNTs/conductive polymer,
 128
 flexible pseudo-supercapacitors,
 graphene/conductive polymers, 126
 freestanding CNT/CL paper, 112/*f*
 graphene paper (GP)-based SCs, 120
 graphene-based flexible EDLCs, 111
 introduction, 101
 laser-scribed rGO SC, 115
 MWCNT films, 103
 PANI electrodeposition, 125/*f*
 perspectives, 134
 preparing ultrathin SWCNT films, 110/*f*
 rGO foams, 113, 114/*f*
 rGO/AuNP hybrid films, 118
 RGO/PANI hybrid film, 127
 single-walled CNT (SWCNT) film, 104
 in situ anodic electropolymerization, 127
 solvated graphene film, 117/*f*
 SWCNT films, 107
 applications, 108
 SWCNT/PANI hybrid films, 123
 variable sized graphene nanosheets, 116
Fuel cells, nanostructured proton exchange
 membranes
 acid-base composite proton conducting
 electrolyte materials, 256
 conductivity plots, 250/*f*
 diblock copolymers, 251
 high temperature inorganic proton
 conducting materials, 256/*t*
 hybrid nanocomposite PEMs via
 self-assembly, 252
 introduction, 244
 layer-by-layer (LbL) self-assembly, 244
 mesoporous Nafion membranes
 synthesized by self-assembly route,
 248
 methanol-crossover current of MEA,
 246/*f*
 modification of Nafion, LbL
 self-assembly technique, 245
 Nafion– SiO_2 nanoparticle, formation,
 253/*f*
 PEMs based on self-assembled block
 copolymers, 250
 samples with different structures and
 normalized proton conductivity, 252/*f*
 self-assembly, 243

small angle XRD pattern and N₂ adsorption/desorption isotherm, 255*f*
stability of single cells, 254*f*
stable polyelectrolyte membrane formation, 251
summary and outlook, 258
surface of Nafion membrane, self-assembly, 247*f*
surfactant-directed self-assembly process, 249*f*
UI-MDP composite materials, protonic conduction, 257*f*

L

LiCoPO₄ as high voltage cathode material, 67
bare or carbon coated LCP materials, lithium cell, 89*f*
carbon nanofibers/LCP composite, non aqueous sol-gel route, 81*f*
cell volume, 70*f*
chemical oxidation of LCP, 87
Co(II)-phosphate-H₂O system, solid state repartition and solubility diagram, 77*f*
conclusions, 95
effect of doping/substitution, 91
electrochemical lithium load curve, 86*f*
HF-scavenging SiO₂ separators, 94
hydro- and solvo-thermal LCP materials, SEM images, 82*f*
introduction, 68
isostructural LFP compound, 73
lattice constants, 71*t*
lattice constants and atomic positions, 89*t*
LCP carbon coated materials, lithium cell, 90*f*
LCP nanoparticle, CAM sol-gel route, 80*f*
LCP nanoparticle encapsulated into carbon hollow sphere, 79*f*
LCP particles coated in situ and one-step sol-gel synthesis, 85*f*
LCP sample, morphology, 79*f*
LDA+U approximation, 74*f*
LFP, LMP, LCP and LNP olivine compounds, properties, 69*t*
lithium cells, electrochemical activity of LCP, 86
metal doping, 92
parasitic processes, 93
physical properties, 70

PITT experiments, current measured, 88*f*
samples, low magnification SEM, 76*f*
spray pyrolysis LCP/carbon composite material, 83*f*

synthesis
carbon coating, 84
hydro- and solvo-thermal methods, 81
sol-gel method, 78
solid state method, 75
wet chemistry methods, 77

Lithium batteries, improved energy storage
anodized tin-based composites, 11
galvanostatic discharge/charge curves, 12*f*
¹¹⁹Sn Mössbauer spectra, 13*f*
tin-based electrodes, cycling study, 14*f*
composite materials, discharge/charge curves, 18*f*
conclusion, 17
electrodes “nano-structured”, 2
introduction, 1
low-cost carbon-tin heterostructures, 15
inexpensive carbonaceous products, use, 16
microwave plasma chemical vapor deposition (MPCVD), 16
scanning electron micrograph of Sn₈Co₄C₈₈, 17*f*
tin oxides, electrochemical behavior, 2
tin-based electrodes, 2
tin-polymer composites, 3
CoSn₂@PAN before and after annealing, 5*f*
polyacrylonitrile (PAN), 4
pyrolysis, 4

M

MEA. *See* Membrane-electrode-assembly (MEA)
Membrane-electrode-assembly (MEA), 244
Multi-walled carbon nanotubes (MWCNTs), 5
MWCNTs. *See* Multi-walled carbon nanotubes (MWCNTs)

P

PANI. *See* Polyaniline (PANI)
PEM. *See* Proton exchange membrane (PEM)

PET. *See* Polyethylene terephthalate (PET)
Polyaniline (PANI), 102
Polyethylene terephthalate (PET), 144
Proton exchange membrane (PEM), 244
 $\text{Pt}_{13}\text{H}_{24}$ cluster models
 anions *vs.* cations, 173
 catalytic properties
 H₂ desorption pathway, 181/*f*
 H₂ desorption rate, heat treatment
 temperature dependence, 180/*f*
 total energy, desorption rate and
 activation energy, 182/*f*
conclusion, 182
electronic properties, 175
 DOS, linear absorption spectra and
 radiative lifetime, 177/*f*
 linear absorption spectra and radiative
 lifetimes, 176
 partial charge density, 179/*f*
 spin-polarized DOS, 176
 spin-up and spin-down DOS, 178/*f*
introduction, 174
methodology, 174

R

Rechargeable Li-ion batteries, 23
AFM, EC-AFM and EFM techniques,
 morphological studies
 ex-situ AFM studies, 28
 in-situ electrochemical AFM
 (EC-AFM) studies, 30
 in-situ electrostatic force microscopy
 (EMF) studies, 33
all-solid-state thin film battery, in-situ
 EFM measurement, 35/*f*
charge and discharge processes, 25/*f*
composite graphite electrode surface, 32/*f*
conductive AFM (c-AFM) studies, 39
 c-AFM measurement and bias voltage
 dependent of tip current, 42/*f*
 Jahn-Teller phase transformation, 40
 summary, 40
 surface potential shift *vs* SPM scan
 number, 41/*f*
different SPM operation regimes, 27/*f*
in-situ characterization of Li-ion battery,
 EC-AFM set-up, 31/*f*
introduction, 24
ionic diffusion studies, Electrochemical
 Strain Microscopy (ESM) technique,
 42
 BE-ESM measurement, 45

displacement loop opening maps,
 evaluation, 46/*f*
ESM time spectroscopy, 45
LiMn₂O₄ thin film cathode, surface
 topography and current images, 43/*f*
 operation principle of ESM, 44/*f*
Kelvin Probe Force Microscopy (KPFM)
 studies, 37
 operation principle of KPFM, 38/*f*
Li-ion insertion/extraction cycles, 33
LiNi_{1/3}Co_{1/3}Mn_{1/3}O₂ thin film cathode
 surface morphology changes, 29/*f*
 surface roughness (RMS) changes, 30/*f*
SPM studies, future perspectives
 cathode materials, CR-AFM image,
 48/*f*
 CR-AFM technique, 47
 local mechanical property studies, 46
 study coupling effects, combining
 various SPM techniques, 48
studying techniques, 26
summary, 49
surface electrical properties, 37
surface topographic changes, 34
TiO₂ thin film anode, in-situ topography,
 amplitude and phase images, 36/*f*
Reduced graphene oxide (rGO), 111
Restructured metal and alloy surfaces,
 electrocatalysis
adsorption on Pt and Pd surface, 272
Au-hex reconstructed surface, adsorbed
 CO molecules, 271/*f*
bimetallic particle, dealloyed state, 286/*f*
concept of Pt monolayer, 265
conclusions, 289
CO/NO cycling, 270/*f*
Cu/Pt(111) overlayers, near surface
 alloys, and surface alloys, preparation,
 276/*f*
Cu/ZnO catalyst, in situ TEM images,
 269/*f*
diffraction map of clean Rh particles,
 269/*f*
formic acid oxidation, 287/*f*
geometric and compositional
 restructurings, 272
introduction, 265
LSV curves, N₂-saturated and
 O₂-saturated electrolytes, 285/*f*
OH coverage on Pt and ORR activity,
 281/*f*
part of CuPt tube after annealing, 279/*f*
Pd/C before and after Br treatment, TEM
 images, 278/*f*
Pt(111) and Pt(557), coverage of CO,
 273/*f*

restructured surfaces, construction, 267
restructuring in electrochemical conditions, 274
restructuring in solid state conditions, 268
reversible transformations, 275*f*
single-crystalline Pt(111) surface, 283
in situ characterization of Pt₃Ni(111) surface, 284*f*
specific ECSA, 290*f*
stability and restorability test, 288*f*
structural behaviors
activation by restructuring, 282
deactivation by restructuring, 288
tetrahedahedral (THH) Pt nanocrystals, electrodeposition, 277*f*
unleached and leached Pt₃Co catalysts, plain Pt catalyst and surface segregation, 280*f*
rGO. *See* Reduced graphene oxide (rGO)

S

Scanning probe microscopy (SPM), 25
Silver as possible dopant to anatase, 189
Silver doped TiO₂ anatase (100) surface, electronic properties, 187
all orbital energies, consistent shift, 209
conclusions, 208
density of states, 191
un-doped and silver doped anatase (100) surface, 196*f*
electron-hole relaxation rates, 198*t*
energy of orbitals, thermal fluctuations, 203*f*
excitations and relaxations
Ag doped model, 213*f*
un-doped model, 212*f*
geometry optimization, 191
introduction, 188
methods, 190
model creation and geometry optimization, 194
molecular dynamics, 201
molecular dynamics, fluctuations, and non-adiabatic couplings, 193
non-adiabatic relaxation dynamics, 203
silver doped model, 205*f*
un-doped model, 204*f*
optical absorption spectrum, 197
optical properties, 192
optimized geometry and schematic of relaxation, 190*f*
partial charge densities, 199, 200*f*, 202*f*

partial charge density, 192
electron states of un-doped model, 211*f*
holes of un-doped model, 210*f*
silver doped model, partial density of states, 199*f*
un-doped and silver doped anatase (100) surface, energies and properties, 195*t*
un-doped and silver doped model
hole cooling rate, 207*f*
holes and electron relaxation, 206
SPM. *See* Scanning probe microscopy (SPM)

T

TCO. *See* Transparent conducting oxide (TCO)
Tin-nanocarbon structures
hierarchical graphene-Sn@CNT composite, 7*f*
tin-carbon nanotubes, 5
tin-graphene, 6
Transparent conducting oxide (TCO), 144

W

Water splitting, hydrogen production, 219
CdS and titanate nanotubes, charge-separation, 224*f*
CdS modification, 233*t*, 237
CdS with different nanostructures, 222
cocatalysts, 228
function, 229*f*
future application, 237
hybridization of CdS with inorganic or organic matrix materials, 225
hybridization of CdS with other materials, 222
hybridization of CdS with other semiconductor, 224
hybridization of CdS with sulfides, 223
introduction, 220
organic matrix, charge separation and transfer, 227*f*
other factors, 232
sacrificial reagents
photocatalytic reactions, basic principle, 230*f*
S²⁻/SO₃²⁻, 231
sample CdS and CdS-GR, 227*f*
semiconductor-based photocatalytic water splitting, 221*f*

summary and prospects, 232

synthesis of heteromatrices, 226